Proceedings of NEWRAD 2011

Edited by

Seongchong Park, KRISS

and

Erkki Ikonen, MIKES

FOREWORD

These Proceedings contain the extended abstracts of the NEWRAD 2011 Conference, on Maui, Hawaii, 18-23 September 2011. The oral and poster presentations are listed in the conference program at http://newrad2011.org/program.php

In addition, the NEWRAD Scientific Committee has invited the authors of the following extended abstracts to submit a related paper to the NEWRAD special issue of Metrologia:

EAO_OR_003, jonathan.gero@ssec.wisc.edu
EAO_OR_005, khlevnoy-m4@vniiofi.ru
EAO_OR_018, samantha.lavender@argans.co.uk
EAO_OR_024, dennis.helder@sdstate.edu
SSR_OR_007, Greg.Kopp@LASP.Colorado.edu
SSR_OR_009, andre.fehlmann@pmodwrc.ch
SBR_OR_002, yqdeng@nim.ac.cn
SBR_OR_007, saulius.nevas@ptb.de
SBR_OR_013, saulius.nevas@ptb.de
SBR_OR_016, petri.karha@aalto.fi
SBR_PO_018, khlevnoy-m4@vniiofi.ru
OPM_OR_011, a.koo@irl.cri.nz
OPM_OR_017, christopher.chunnilall@npl.co.uk
OPM_PO_019, fengguojin@nim.ac.cn
OPM_OR_021, heather.patrick@nist.gov
OPM_OR_027, hanssen@nist.gov
DBR_OR_001, lehman@boulder.nist.gov
DBR_OR_009, e.theo@npl.co.uk
DBR_OR_021, julian.groebner@pmodwrc.ch
DBR_OR_031, george.eppeldauer@nist.gov
DBR_OR_038, terubumi.saito@tohtech.ac.jp
DBR_OR_039, yuqin.zong@nist.gov
DBR_PO_044, jag@justervesenet.no
DBR_OR_045, tuomas.poikonen@aalto.fi
OT_OR_004, alexander.gottwald@ptb.de
OT_OR_008, marco.lopez@ptb.de
SFR_OR_002, ingmar.mueller@ptb.de
SFR_OR_005, silke.peters@ptb.de

The above corresponding authors have made a strong personal commitment that they will submit the related article to Metrologia before 18 September 2011.

The extended abstracts of these proceedings are organized in numerical order under the following categories:

INV – Invited talks

Part A
EAO – Earth observation
SSR – Solar/stellar radiometry
SBR – Source-based radiometry
OPM – Optical properties of materials/components

Part B
DBR – Detector-based radiometry
OT – Other topic
SFR – Single/few-photon radiometry

Erkki Ikonen and Seongchong Park

INVITED TALKS

PART-A

PART-B

Calibration Accuracy for Cimate-Quality Data Sets from Space Observations.

K. Thome[1], M. Mlynczak[2], B. Wielicki[2], D. Young[2]

[1]*NASA Goddard Space Flight Center, Greenbelt, MD*
[2]*NASA Langley Research Center*

Highly accurate, space-based measurements of parameters relevant for decadal change observations are vital for understanding the accuracy of climate change projections. This work summarizes new methods used to determine the observing system requirements including the use of infrared and reflected solar spectra as fingerprints of climate change. The studies lead toward a set of requirements for space-based observations SI-traceable uncertainty of temperature of 0.07 K (*k = 2*), and of reflectance of 0.3% (*k = 2*). Instrument approaches and calibration methods to meet the above accuracies are presented.

The 2007 Earth Science Decadal Survey concluded that the single most critical issue for current climate change observations was their lack of accuracy and low confidence in observing the small climate change signals over decade time scales. Studies done related to the Climate Absolute Radiance And Refractivity Observatory (CLARREO) mission, one of the Tier 1 missions recommended by the 2007 Earth Science Decadal Survey, show that such observations are feasible.

The current work summarizes the methods used to determine the observing system requirements needed to meet the Decadal Survey in terms of the accuracy of decadal change versus a perfect observing system limited only by natural variability. One approach described is climate model OSSEs (Observing System Simulation Experiments) that predict a sensor's utility in testing climate models and understanding climate forcings, response, and feedbacks to anthropogenic change.

The OSSE studies and theoretically-based statistical studies of climate systems lead to a requirement for climate-quality observations that have SI-traceable uncertainty <0.07 K (95% confidence or *k=2* for metrology) for the infrared spectra, and <0.3% (*k=2*) for reflected solar spectra. Defining a set of mission requirements in terms of accuracy of the entire observation system for decadal change trends permits a trade space in mission design between calibration, spectral fingerprint, orbit sampling, and instrument noise. These requirements would allow a space-based sensor to achieve decadal change accuracy within 20% of a perfect observing system, and time to detect trends within 15% of a perfect observing system.

Instrument approaches to meet the above accuracies require factors of 3 to 10 improvement in benchmark accuracy over current observations. This work describes a dual-instrument concept that is capable of achieving the stringent accuracy requirements. Long-wave measurements of the earth's emitted radiation would be provided by a nadir viewing infrared interferometer covering the spectral region of 200 to 2000 cm^{-1}, with 0.5 cm^{-1} unapodized spectral resolution with a 25-km spatial resolution. The second instrument would retrieve at-sensor reflectance over the spectral range from 320 to 2300 nm with 500-m GIFOV and a 100-km swath width

The infrared instrument would be designed to record an entire double-sided interferogram from an Earth view in a period of 8 seconds. This is followed by views of internal calibration targets and deep space. The process is repeated every 30 seconds, resulting in the recording of an Earth spectrum approximately every 200 km in the along track direction.

The systematic error on each measured Earth spectrum will be 0.1 Kelvin in brightness temperature (k = 3). Measurement precision of a single spectrum will typically be less than 2 Kelvin. The accuracy of the long-term means (zonal to global; annual to decadal) will be realized through averaging of spectra over these domains. The effect of averaging is to reduce the random component of the measurement error (i.e., the precision) to insignificance, thus leaving the systematic uncertainty as the only uncertainty in the long-term average spectrum.

The proposed instrument design relies on calibration of the infrared spectra that is traceable directly to the Kelvin through an on-orbit blackbody used in its calibration. The blackbody

temperature would be continually referenced to the International Temperature Scale (ITS) through small amounts of pure materials (water, gallium, mercury) whose melt points are known and specified on the ITS. These materials are encapsulated throughout the blackbody and routinely cycled in temperature through their melt points. This approach allows the traditional thermistors in the blackbody to be continuously calibrated and provides the fundamental tie to the SI through the unit of the Kelvin.

The measurement precision for the reflected solar instruments is presently calculated to be about 30 (signal-to noise ratio). As with the infrared measurements, averaging of the reflected solar spectra over large time and space scales will be used to drive down the random noise on the measurement, yielding a time and space averaged spectrum whose accuracy is determined by the systematic error of the measurements.

The calibration approach to achieve the ambitious 0.3% absolute calibration uncertainty is predicated on a reliance on heritage hardware, reduction of sensor complexity, and adherence to detector-based calibration standards. The proposed design is a typical Offner spectrometer with two separate focal planes each with its own entrance aperture and grating covering spectral ranges of 320-640, 600-2300 nm. Such a design would limit stray light effects. Reflectance is obtained from the ratio of measurements of radiance while viewing the earth's surface to measurements of irradiance while viewing the sun. Key components in the error budget are geometry differences between the solar and earth views, knowledge of attenuator behavior when viewing the sun, and sensor behavior such as detector linearity and noise behavior. Methods for demonstrating this error budget are also presented.

The approach described here would provide the accurate measurements of infrared emission spectra and reflected spectra of solar radiation. All measurements are fundamentally traceable to international measurement standards and fundamental or derived SI units. These data would provide a benchmark that could be used to assess both the natural variability and climate change of the Earth and its atmosphere.

NIST Efforts for Calibrations in Earth Observation Programs

B. C. Johnson
National Institute of Standards and Technology, Gaithersburg, MD, USA
Corresponding e-mail address: cjohnson@nist.gov

We describe the overall philosophy of the NIST program that supports the radiometric calibration and characterization of remote-sensing studies of the Earth, provide a historical perspective highlighting major accomplishments, and indicate future directions.

INTRODUCTION

National standards laboratories such as NIST are responsible for realizing and maintaining fundamental radiometric scales and developing the means to disseminate them to the user community by use of calibrated artifacts [1]. Artifacts such as FEL-type lamp standards of spectral irradiance, diffuse reflectance standards, lamp-illuminated integrating spheres, detectors, apertures, and contact thermometers are utilized at the user facility in various schemes to establish the traceability of values for the reflected-solar and emitted thermal spectral regions of the Earth's surfaces and atmosphere generated or measured by various sources and radiometers, including space-borne sensors.

A significant aspect of establishing traceability is in the uncertainty estimation for the resultant values. It is often difficult to assess the veracity of these values. For remote sensing programs with the objective to detect subtle changes in the Earth's physical properties over decadal time scales, the uncertainty requirements are stringent and the effort to validate the results is therefore critical [2]. One part of the solution, advocated by NIST and the international metrology community, is to perform intercomparison activities. In the early 1990s NIST, with NASA support, began to execute spectral radiometric comparisons. This required the development of field-deployable transfer radiometers (XRs) and integrating sphere sources (ISSs).

It was found that complete characterization of the XRs or ISSs represents the majority of the effort to understand these artifacts and estimate uncertainties; absolute calibration is the assignment of an overall scale factor to the full measurement equation that describes all possible influencing parameters. Also, along the way, novel ideas and advances have been realized, and NIST efforts have expanded to include participation in programs beyond the scope of what was imagined at the beginning. In this talk, we give examples of the accomplishments in these areas.

INTERCOMPARISONS

Table 1 lists some of the intercomparison activities related to Earth Observation that have involved NIST and US and international partners. In the late 1980s, a portable irradiance bench equipped with calibrated D_2 and FEL lamp standards of spectral irradiance was circulated multiple times in order to assess the scales assigned to flight sensors in the SOLSPEC, SSBUV, SOLSTICE, and SUSIM programs. In the 1990s NIST supported the downwelling surface UV spectral irradiance network by piloting field intercomparisons, developing *in situ* methods to characterize and calibrate the participants' radiometers, and uniformly analyze the results. Also in the 1990s, a strong partnership with NASA's EOS and ocean color (SeaWiFS) programs led to portable Vis/NIR filter radiometers, spectroradiometers, and vacuum-compatible TIR radiometers. On the source side, portable spectral radiance standards (an ISS and a water-bath blackbody) as well as sources specifically designed to be stability monitors for field radiometers were developed and transferred to the user community.

Table 1. Partial listing of key intercomparisons; type is S for source, R for radiometer, O for other.

Designation(type)	Program(s)
D_2/FEL bench(S)	UV exoatmospheric solar spectral irradiance
UV Network(S,R)	Surface solar irradiance, stratospheric ozone
Vis/NIR/SWIR/TIR (R,S)	Space and ground-based sensors (EOS Program, SeaWIFS, MOBY, etc.)
BRDF(O)	Reflectance of flight diffusers
Aperture Area(O)	Total solar irradiance

Bi-directional reflectance impacts the realization of spectral radiance from irradiance standards, both for laboratory and flight systems. The value of the defining aperture area affects the derived value of

Total Solar Irradiance (TSI) as measured from space. With support of the EOS Program, we investigated these scales: for BRDF samples prepared by NIST were circulated; for aperture area NIST measured selected apertures from TSI programs.

Lessons learned from these activities are the usual ones, and serve to reinforce the notion that radiometry is susceptible to many types of systematic effects, many of which seemed difficult to anticipate but obvious after the fact, e.g, "black" that is not black enough; unidentified scattered radiation; stability of standards; wavelength error, geometric error, incomplete or incorrect characterization (e.g. polarization).

FACILITIES

Several facilities at NIST have been influenced by the requirement to support remote sensing programs; an overview is given in Table 2.

Table 2. Partial listing of NIST facilities related to Earth Observation implemented in the last 20 years.

Designation(type)	Objective
SIRCUS(S)	Radiance or irradiance responsivity
STARR(O)	Bi-directional and directional-hemispherical reflectance
Aperture Area(O)	Optical-based dimensional metrology
FASCAL II(R)	Spectral Irradiance Scales
RSL(S,R)	Validating, characterizing, developing NIST artifacts; hosting intercomparisons
HIP(S)	Development of digitally-controlled, hyperspectral image projectors
Theoretical	Diffraction, Stray Light Correction Algorithm(s), Monte-Carlo modeling

To fulfill the requirement to determine the responsivity of the transfer radiometers, the SIRCUS facility was developed [3]. It provides system level, full entrance pupil, tunable-monochromatic calibration of radiometers. The STARR facility was expanded to include BRDF capability over the entire reflected solar spectral region, motivated by MODIS and related space sensor requirements. To enhance performance, the Aperture Area Facility was reconfigured (hardware and software). FEL-type lamps are now calibrated in a new facility, FASCAL II, using a detector based scale that substantially reduced the uncertainties in the UV and SWIR. The Remote Sensing Laboratory (RSL) is used for study of the NIST artifacts and for hosting intercomparisons. Sources based on digitally controlled spectral filtering and spatial control of broadband light sources to create custom scenes [4] are developed in the Hyperspectral Image Projector (HIP) laboratory. Finally, in order to fully correct radiometric measurements for systematic effects, modelling is often necessary. NIST has developed theory and algorithms to correct for diffraction from optical apertures, spectral and spatial stray light in spectrographs, performance of ISS collectors or blackbody cavities, and scattering of particles on surfaces. In some of these examples, the software has been made for distribution to the community.

CONCLUDING REMARKS

As the program has matured, NIST involvement has grown from review of cal/val plans and execution of intercomparisons to involvement at a more fundamental level. Examples include participation in sensor design and characterization, transfer of the techniques to related fields such as stellar radiometer and medical imaging, and efforts to determine the spectral radiance of the moon, for use as an on-orbit standard. The objective continues to be to reduce our uncertainties in order to meet program requirements, and to design artifacts that are least sensitive to systematic effects.

REFERENCES

1. B. C. Johnson *et al.*, Metrology for remote sensing radiometry, in *Post-Launch Calibration of Satellite Sensors*, edited by S. A. Morain & A. M. Budge, 7-16, A. A. Balkema, New York, 2004.
2. J. J. Butler *et al.*, The calibration and characterization of Earth remote sensing and environmental monitoring instruments, in Optical Radiometry, edited by A. C. Parr, R. U. Datla, & J. L. Gardner, 453-534, Elsevier Academic Press, New York, 2005.
3. S.W. Brown, *et al*. Facility for Spectral Irradiance and Radiance responsivity Calibrations using Uniform Sources (SIRCUS), *Appl. Optics*, **45**, 8218-8237, 2006.
4. J. P. Rice, *et al*. Hyperspectral image projectors for radiometric applications, *Metrologia*, **43**, S61-S65, 2006.

Future Long-term Measurements of Solar Spectral Irradiance by the TSIS Spectral Irradiance Monitor: Improvements in Measurement Accuracy and Stability

Erik Richard[1], Dave Harber[1], Joel Rutkowski[1], Kasandra O'Malia[1], Matthew Triplett[1], Ginger Drake[1], Jerald Harder[1], Peter Pilewskie[1], Steven Brown[2], Allan Smith[2], and Keith Lykke[2]

[1]*Laboratory for Atmospheric and Space Physics (LASP),*
University of Colorado, Boulder, Colorado 80303 USA
[2] *Optical Technology Division, National Institute of Standards and Technology (NIST)*
Gaithersburg, Maryland 20899 USA
Corresponding e-mail address: Erik.Richard@LASP.colorado.edu

The TSIS Spectral Irradiance Monitor (SIM) is the next-generation space-borne spectrometer that is designed to measure twice daily the solar spectral irradiance (SSI) between 200 and 2400 nm and meet the requirements for the long-term SSI data record. Significant design improvements have been implemented over that of the first-generation (SORCE) SIM. Key performance advances include improved radiometric detector design, reduced uncertainties in long-term stability, and significant improvement in pre-launch calibration of absolute accuracy.

INTRODUCTION

In order to advance understanding of how natural and anthropogenic processes affect climate it is important to maintain accurate, long-term records of climate forcing. In particular, the continuation of solar spectral irradiance (SSI) measurements is needed to characterize poorly understood wavelength-dependent climate processes. For example, the strong reliance on radiative transfer modeling for interpretation and quantification of the deposition of solar radiation in the atmosphere makes it imperative that the spectral distribution of radiant energy entering the atmosphere be known to a high degree of absolute accuracy[1]. Major measurement challenges in quantifying the influence of SSI variability on climate are achieving sufficient radiometric absolute accuracy and maintaining the long-term relative accuracy of the data record.

The Total and Spectral Solar Irradiance Sensor (TSIS) is a dual-instrument package that will acquire solar irradiance in the present decade. The TSIS instruments include a Total Irradiance Monitor (TIM) and a Spectral Irradiance Monitor (SIM) that will continue the simultaneous measurements of total solar irradiance (TSI) and SSI, which began with the NASA SOlar Radiation and Climate Experiment (SORCE), launched in 2003. NASA and NOAA have recently established the Joint Polar Satellite System (JPSS), which will provide stewardship for TSIS.

The TSIS SIM, which derives heritage from SORCE SIM, is a solar spectral radiometer that monitors the SSI across a continuous wavelength region spanning the ultraviolet, visible and near infrared (200 nm – 2400 nm, encompassing 96% of the TSI) [2]. The instrument incorporates a single Féry prism for refractive spectral dispersion and focusing onto a focal plane with an absolute bolometric detector and various photodiode detectors.

The SORCE SIM has now monitored SSI over a wide range in solar activity to unfold wavelength-dependent variability [3]. Moreover, the measurements have revealed areas for instrument design and calibration improvements to better quantify long-term SSI variability. The TSIS SIM development specifically includes improvements in the pre-launch *SI*-traceable calibration, the measurement precision, and the long-term relative stability needed to meet the requirements for establishing a climate record of SSI into the future.

SSI MEASUREMENT REQUIREMENTS

The measurement requirements for SSI are derived from an analysis of the solar spectral variability expected over a solar cycle. The requirement is that SIM have measurement stability no worse than 100 ppm/year in the visible/near infrared and 500 ppm/year in the ultraviolet. These measurement requirements flow-down directly into the instrument design requirements. Specifically for the TSIS SIM, these include implementing refractive dispersion (via single optical element), extremely precise wavelength control, accurate radiometric detectors, and robust, long-term optical degradation correction methods.

Table 1 lists the high level measurement requirements for the SSI record to address current needs for improved understanding of the climate system response to solar-cycle spectral variability.

Table 2. TSIS SSI Level-1 requirements.

Specification	Requirement

Irradiance Range	10^{-4} – 10^{1} $Wm^{-2}nm^{-1}$
Spectral Range	200 – 2400 nm
Measurement Accuracy	0.25%
Measurement Precision	0.01%
Long-term Stability	$\lambda \leq 400$ nm: 0.05%/yr $\lambda > 400$ nm: 0.01%/yr
Spectral Resolution	$\lambda < 280$ nm: 2 nm 280 nm-400 nm: 5 nm $\lambda > 400$ nm: 45 nm
Reporting Frequency	2 spectra/day

PRE-LAUNCH CHARACTERIZATION AND CALIBRATION

The full characterization and calibration for TSIS SIM follows a measurement equation approach at the unit-level for full validation of the end-to-end performance at the instrument-level. Following this approach, we characterize the SIM instrument as an "absolute" sensor tied to a Cryogenic Radiometer traceable to the NIST Primary Optical Watt Radiometer (POWR), the primary US standard for radiant power measurements.

The measured solar spectral irradiance is derived from the fundamental measurement equation (1) in units of $Wm^{-2}nm^{-1}$:

$$E(\lambda_s) = \frac{P_{ESR}(\lambda_s)}{A_{slit}\int \alpha_\lambda T_\lambda \Phi_\lambda S(\lambda,\lambda_s) d\lambda} \qquad (1)$$

Each term in (1) represents a directly measureable unit- or instrument-level quantity. The primary radiant power detector is an ambient temperature, electrical substitution, null-balance radiometer (ESR). The standard Watt is derived from ultra-stable voltage and resistance references. The POWR calibrated ESR provides absolute power measurements covering four orders of magnitude in solar spectral power in the 200-2400 nm range, $P_{ESR}(\lambda_s)$. The integral in (1) accounts for the wavelength-dependent contributions to the radiometric response and includes the absorptance efficiency of the ESR, α_λ, the full prism transmission, T_λ, the entrance slit diffraction loss, Φ_λ, and the spectral instrument profile, $S(\lambda,\lambda_s)$.

To quantify the absolute accuracy over the full spectral range, we have developed a comprehensive calibration program utilizing the NIST *Spectral Irradiance and Radiance Responsivity Calibrations using Uniform Sources* (SIRCUS) facility [4]. The complete SIRCUS system provides continuously tuneable laser light sources from the ultraviolet to the near infrared that are matched in radiant power to the solar spectrum. Based on the standard uncertainties (u_i) determined for the individual quantities in (1) we achieve a combined standard uncertainty (u_c) of 0.25%

ON-ORBIT CALIBRATION MAINTAINACE

The pre-launch absolute spectral power calibration is transferred to orbit and maintained through the ESR. The dominant uncertainty in the long-term stability of the measurements is the exposure-dependent optical transmission loss of the prism as a function of wavelength. The TSIS SIM design incorporates three independent channels that are duty cycled in solar exposure to allow for spectral cross calibration of the primary (highest exposure) channel to maintain a relative stability of 100 ppm/year.

CONCLUSION

The TSIS SIM is the next generation space-borne SSI monitor that will fly as part of the joint agency (NASA/NOAA) JPSS program scheduled for launch by 2014. The instrument has been designed and calibrated to achieve unprecedented levels of measurement accuracy and on-orbit stability required to meet the needs of establishing a complete solar spectral irradiance climate data record.

REFERENCES

1. P. Pilewskie, G. Rottman and E. Richard, An overview of the deposition of solar radiation in the lower atmosphere: connections to the SORCE mission and climate change, Sol. Phys., 230, 55-69, 2005.
2. J. W. Harder J., *et al.,* The Spectral Irradiance Monitor: Scientific Requirements, Instrument Design, and Operation Modes, Solar Phys., **230**, 141-167, 2005.
3. J. W. Harder, *et al.* , Trends in solar spectral irradiance variability in the visible and infrared, Geophys. Res. Lett., 36, L07801, 2009.
4. S. W. Brown, G. P. Eppeldauer, and K. R. Lyyke, Facility for spectral irradiance and radiance responsivity calibrations using uniform sources, Applied Optics, 45, 8218-8237, 2006.

A new cryogenic absolute radiometer for total solar irradiance

Wolfgang Finsterle[1], Rainer Winkler[2], André Fehlmann[1], Peter Blattner[3], Nigel Fox[2] ,and Werner Schmutz[1]

[1]PMOD/WRC, Davos Dorf, Switzerland, [2]NPL, Teddington, UK, [3]METAS, Wabern, Switzerland

Corresponding e-mail address: wolfgang@pmodwrc.ch

We will report on the first solar irradiance measurements with the Cryogenic Solar Absolute Radiometer (CSAR). The CSAR is intended to replace the World Standard Group of Pyrheliometers (WSG) in its role as a primary reference for ground-based total solar irradiance. The first-light measurements yield encouraging results.

INTRODUCTION

Since 1978 a group of ambient-temperature absolute radiometers has been serving as the primary reference for ground-based total solar irradiance measurements [1]. This group is termed the World Standard Group (WSG). At any given time the mean irradiance measured by the WSG is referred to as the World Radiometric Reference (WRR). In order to provide a stable WRR the WSG is required to consist of at least four absolute radiometers of different design [2]. It currently consists of six radiometers.

Most of the WSG radiometers are more than 30 years old and will need to be replaced within the next decade. To this effect and to benefit from the technological progress which was made since the 1970's PMOD/WRC together with NPL and METAS have developed and built the Cryogenic Solar Absolute Radiometer CSAR [3]. While the WRR is a conventional standard, the CSAR measurements are fully traceable to SI primary standards for optical power and length (via aperture area). The major challenges with the implementation of cryogenic technology in solar radiometry were the relatively high power level of ~20 mW, the determination of the broad-band transmittance of the entrance window, and optical effects such as stray light and diffraction induced by the illuminated apertures. To account for the variable attenuation effect due to the changing spectrum of the incoming radiation a Monitor for Integrated Transmittance (MITRA) was developed and built [4].

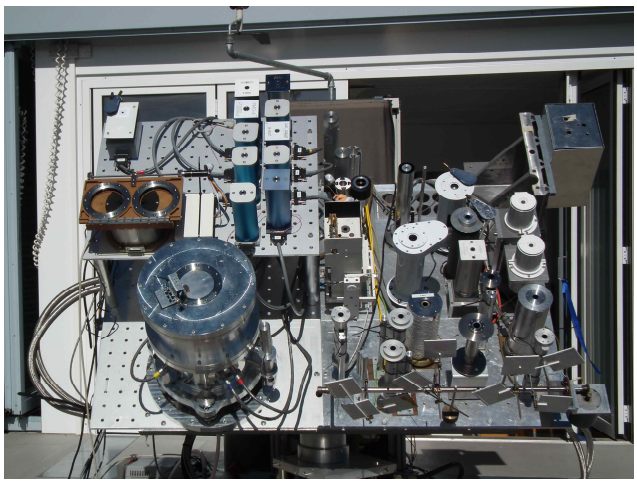

Figure 1. The CSAR on the solar tracking platform at PMOD/WRC (lower left). The right-hand side of the platform is mainly occupied by the WSG instruments. The MITRA is mounted to the left above the CSAR.

FIRST-LIGHT MEASUREMENTS

The CSAR was commissioned for participation in the 11th International Pyrheliometer Comparison (IPC-XI) which took place in September/October 2010. Figure 1 shows the CSAR on the solar tracking platform at PMOD/WRC together with the WSG and other radiometers. During the IPC-XI the CSAR suffered from high noise levels. The noise source was identified in the sensing wires which acted as thermal bridges causing temperature fluctuations of the cryogenic reference block (~20 K). Subsequently the cavity was re-wired and the thermal noise was

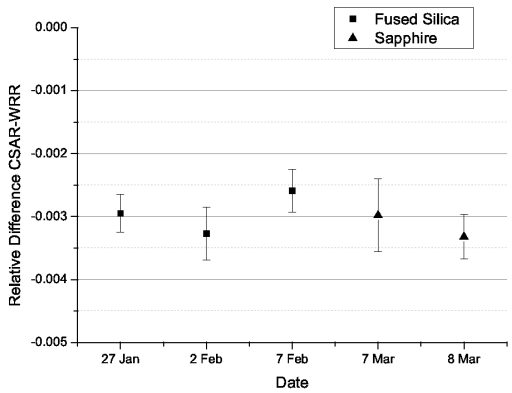

Figure 2. During the comparison in early 2011 the CSAR measured consistently *lower* solar irradiance than the WSG. Here daily averages are shown because the MITRA was not yet ready to compensate diurnal trends in the integrated transmittance of the entrance windows (fused silica or sapphire).

eliminated. Optical power calibrations against the NPL cryogenic radiometer confirmed conformance of the CSAR power measurements with SI units. A second set of CSAR-to-WRR comparison measurements took place in early 2011. The CSAR measured consistently lower than the WRR by ~0.3% (see Figure 2). This difference is similar to the difference observed by different space radiometers.

DISCUSSION AND OUTLOOK

The CSAR was designed and built to replace the decades-old conventional standard for solar irradiance, the WRR, with state-of-the-art technology. The CSAR measurements are fully traceable to SI primary standards through optical power calibration against the NPL primary standard and aperture area calibrations. The CSAR will also be able to participate in BIPM key comparisons with other cryogenic radiometers. Thorough and long-term testing will be required to establish the new standard. The most obvious issues are still the determination and monitoring of the integrated transmittance of the entrance window to the vacuum chamber. Other aspects include stray light characterization and validation of the diffraction correction, which is based on theoretical calculations. Therefore and for various administrative reasons we do not expect to replace of the WRR by the CSAR before 2015 at the earliest.

The relevance of the observed ~0.3% scale difference between the CSAR and the WRR is not yet fully understood. Nevertheless, the difference is remarkably similar to what solar radiometers measure in space depending on which calibration they use (WRR or SI). Because currently only one space radiometer (PREMOS on PICARD) is strictly traceable to SI a definite decision on whether the discrepancy between the WRR and SI is larger than the expected ±0.14% [5] is still premature.

REFERENCES

1. C. Fröhlich, World Radiometric Reference, in CIMO-VII Final Report, WMO-No. 490, 1978
2. Guide to Meteorological Instruments an Methods of Observations, WMO-No. 8, Seventh edition 2008
3. R. Winkler et al., Design Features and Test of the Cryogenic Solar Absolute Radiometer, NEWRAD 2011
4. Fehlmann et al., Monitor to measure the Integrated Transmittance (MITRA) of Windows, NEWRAD 2011
5. Finsterle et al., Third comparison of the World Radiometric Reference and the SI radiometric scale, Metrologia, Vol. 45, Issue 4, 377-381, 2008

Integrating Sphere Photometers Designed for Solid State Lighting Measurement

Seongchong Park, Dong-Hoon Lee, Seung-Nam Park

Korea Research Institute of Standards and Science (KRISS), Daejeon, Rep. Korea
Corresponding e-mail address:spark@kriss.re.kr

We present designs of two new integrating sphere photometers. The first one with a special auxiliary lamp can measure total luminous flux of large-area surface-emitting light sources without self-screening error. The second one is featured by multiple detection ports, which can measure total luminous flux of directive lamps without spatial mismatch error. The validity of the new designs is tested by numerical simulation. We expect that combination of two designs will improve the accuracy and practicability of integrating sphere photometers especially for solid-state lighting products.

MOTIVATION

Accurate measurement of total luminous flux (TLF) becomes more important as more LED-based solid state lighting (SSL) products appear in the market. In particular, TLF is the key measurement quantity to specify the energy efficiency of the SSL products. The optical properties of SSL products, however, are completely different from the "classical" sources such as incandescence lamps, which make the accurate measurement more challenging.

Conventionally, integrating sphere (IS) photometers have been widely used to measure TLF of light sources due to its speedy and simple procedure. For new types of SSL products, however, IS photometers are often regarded as not accurate and even not applicable. For example, large-area surface-emitting light sources could not be measured using an IS photometer because the source itself acts as a highly absorptive baffle to change the flux distribution in the IS. The flux loss by the absorptive screening cannot be corrected with a conventional IS configuration.

In addition, highly directive SSL lamps such as MR- or PAR-type lamps are also difficult to measure with a conventional IS photometer because of a significant spatial mismatch between the SSL lamps and a point-like reference source.

In this talk, we present two new IS photometers, which are designed to overcome the limitations to SSL application [1, 2]. The target SSL products are large-area surface-emitting sources and directive SSL lamps with a narrow angular emission. The validity of the designs is tested by numerical simulation based on the geometrical radiative transfer equation for the realistic dimensions as described in Ref. [3].

DESIGN FOR LARGE-AREA SOURCES

The first design enables us to apply an IS photometer to measure TLF of large-area surface-emitting light sources. Figure 1 shows the schematic diagram of the proposed design.

The major problem of using an IS photometer for a large-area source is the change of the sphere response due to self-screening by the test source itself. We calculated that, for a conventional IS photometer, this self-screening effect can be as large as 50 % for a 1 m-diameter light source inside an 2 m-diameter IS. Our solution is to specialize the auxiliary lamp that is usually used for self-absorption correction. We modify the spatial emission characteristics of the auxiliary lamp and adjust its location so that its illuminating area matches to that of the test source. For a surface-emitting test source, illumination will cover only a half sphere of the IS inner wall. In this case, the conventional correction procedure of self-absorption mismatch between the test and the reference lamps can compensate also the self-screening effect simultaneously.

To demonstrate the feasibility of our design, we calculated the residual error of TLF measurement for different size of a test source and different spatial

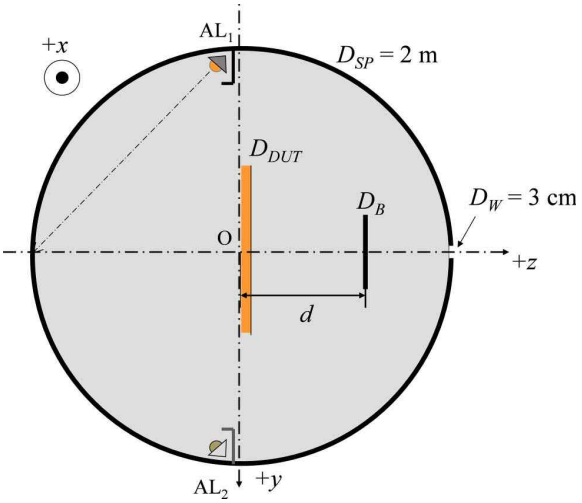

Figure 2. Schematic diagram of the IS photometer design with the specialized auxiliary lamp to measure large-area surface-emitting light sources.

distribution of an auxiliary lamp, and also for different design parameters indicated in Fig. 1. As a result, for a Lambert-like test source with a diameter up to 1 m, the measurement error of the IS photometer with a diameter of 2 m is reduced to be less than 2 % after the self-screening correction by using the specialized auxiliary lamp with a cosine-like angular distribution.

The conclusion of this part is that the proposed design and method provides a simple but accurate correction of the self-screening effect. This will extend the application field of an IS photometer to large-area surface-emitting sources. The method requires only a minor modification of the auxiliary lamp and thus can be generally adopted to the conventional design of the IS photometer without limiting its performance.

DESIGN WITH UNIFORM SPATIAL RESPONSE

The second design we propose is an IS photometer with uniform spatial response, which practically eliminates the spatial mismatch error even for highly directive lamps. Figure 2 shows the schematic diagram of the proposed design.

As the angular distribution of test lamps becomes narrower, the error due to spatial mismatch between the test lamp and the reference lamp that is commonly a point-like incandescent lamp. In principle, such a spatial mismatch error can be corrected by calculating spatial correction factor (SCF) from the spatial response distribution function (SRDF) of the IS photometer and the angular distribution of the test source illumination. However, the procedure to determine SCF requires a lot of time and effort. It is simply not practical to perform the spatial mismatch correction for every single lamp.

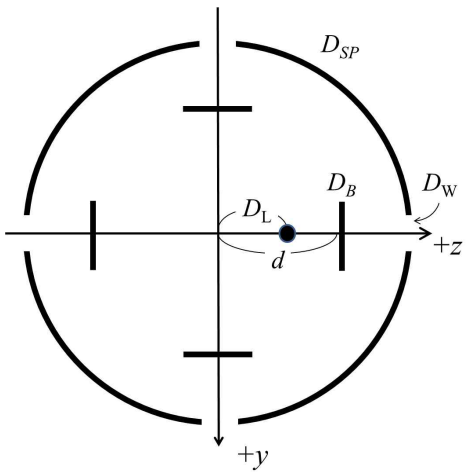

Figure 2. Schematic diagram of the IS photometer design with six detection ports to produce a uniform spatial response.

This problem can be solved if the spatial response of the IS photometer is as uniform as possible, i.e. the SRDF is a close to a constant with respect to the whole 4π-solid angle. The main idea is to realize a superposition of six identical one-port spheres by using six identical detection ports placed as uniformly as possible on the sphere surface, e.g., at the poles of the +z, -z, +x, -x, +y, and -y axes. Based on numerical simulation, we confirmed that the resultant SRDF is almost independent on the direction inside the IS.

In detail, we calculated SCF for a conventional one-port IS photometer and for the six-port IS photometer for various test lamps with an angular distribution from $\cos^1\theta$ (120º FWHM) to $\cos^{60}\theta$ (17º FWHM). For the conventional IS photometer, the deviation of SCF from unity varies more than ±5 % as the emission orientation changes. In contrast, the deviation of SCF from unity was within ±0.3 % for the six-port IS photometer. We also tested the sensitivity of the performance on the design parameters such as wall reflectivity, baffle reflectivity, and baffle size.

In this part, we confirmed the feasibility and the expected performance of the new six-port design of IS photometer. The spatial mismatch error and its sophisticated correction procedure, which were critical obstacles to the practical application of an IS photometer for SSL products, are expected not to be necessary in the new design, without a significant loss of accuracy.

Finally, we note that the two designs presented here can also be combined to realize a practical IS photometer useful for various types of SSL products. In KRISS, we are currently preparing an experimental realization and validation of the new design IS photometers.

REFERENCES

1. S. Park, S.-N. Park, and D.-H. Lee, “Correction of self-screening effect in integrating sphere-based measurement of total luminous flux of large-area surface-emitting light sources,” Appl. Opt. **49**, 3831-3840 (2010).
2. S. Park, D.-H. Lee, and S.-N. Park, “Six-port integrating sphere photometer with uniform spatial response,” Appl. Opt. **50**, 2220-2227 (2011).
3. Y. Ohno, “Integrating sphere simulation: application to total flux scale realization,” Appl. Opt. **33**, 2637–2647 (1994).

Tuneable Lasers at PTB for Photometry and Radiometry

Armin Sperling

Physikalisch-Technische Bundesanstalt (PTB), 381116 Braunschweig, Germany
Corresponding e-mail address: armin.sperling@ptb.de

The spectral characterisation of detectors is mostly done with lamp and monochromator-based facilities such as the spectrally tuneable "light" sources. The measurement uncertainty of this approach is mainly determined by the limited optical power and wavelength offsets of the spectrally filtered lamp radiation [1]. Due to the rapid progress in laser technology, such setups can nowadays be replaced by tuneable laser facilities. The advantages of tuneable laser radiation are much higher output power levels combined with simultaneously narrow bandwidth. Both are essential for the measurement of steep spectral response functions with the lowest uncertainties. This paper gives an overview on the current status of the laser-based characterisation of detectors, cameras and spectroradiometers, as well as on the first results of exclusively detector-based calibrations of light sources, carried out at PTB.

CALIBRATION SETUPS

SI-traceable measurements of spectral detector responsivity or optical radiation quantities are of the highest interest in many applications in photometry and radiometry. At PTB, narrow-band wavelength-tuneable continuous-wave (cw) laser systems started to be used for absolute radiometry over limited spectral ranges more than twenty years ago. The TULIP setup (Tuneable Lasers in Photometry) now covers the broad spectral range from about 360 nm to 1000 nm [2] and has been upgraded with a tuneable quasi-cw femtosecond laser system covering the entire spectral range between 230 nm and 2500 nm. This is sufficient to calibrate most radiometric detectors. The total spectral range of the different setups is given in Figure 1 [3].

Different light path geometries to achieve uniform tuneable radiation can be selected within the TULIP setup. Depending on the spectral range and the design and measurement geometry of the DUT, a Ba_2SO_4 painted integrating sphere or a holographic diffuser combined with a microlens array can be used as light output ports. A tapered multimode fibre (TMF) or a liquid lightguide support the proper incoupling of the different laser beams along with the uniformity in the measurement plane and foster the necessary beam conditioning techniques to avoid speckle effects. A sketch of this setup showing the different light path geometries is given in Figure 2.

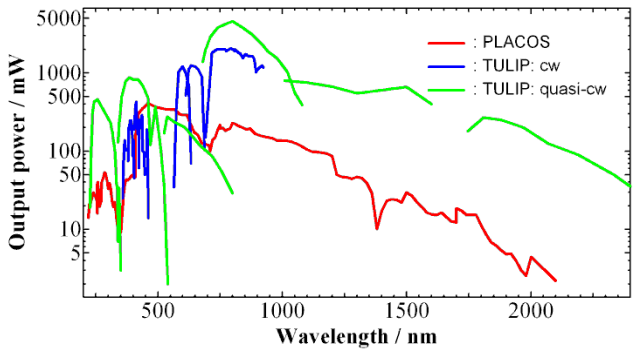

Figure 1. Spectral range of the tuneable laser facilities used for the calibration of detectors, spectroradiometers and sources at PTB

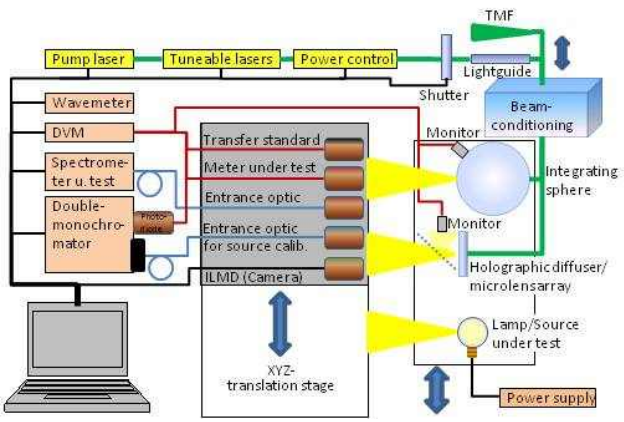

Figure 2. Sketch of the TULIP setup with its various beam geometries depending on the measurement task and the spectral range used

The well-known side effects of coherent laser radiation - emergence of interference - are corrected by a numerical analysis of the measured data based on Discrete Fourier Transform (DFT) analysis and digital filtering techniques (see Figure 3).

However, not only single detectors but also imaging luminance and radiance measurement devices, i.e. camera systems, have been spectrally characterised with respect to their linearity, uniformity and spectral responsivity at the laser-based setup TULIP.

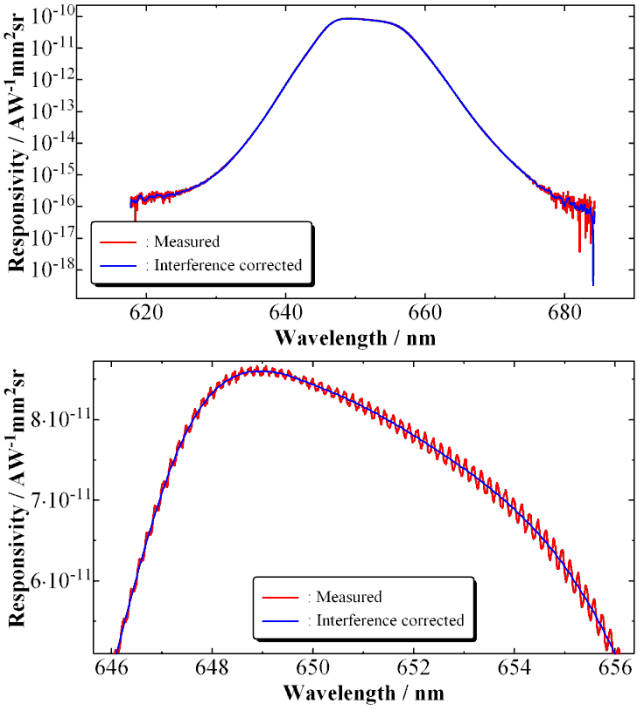

Figure 3. Responsivity of a broadband detector before (red) and after the process of digital filtering (blue) to remove the periodic contributions of the interference fringes. The diagram below shows the magnified central part of the responsivity curve

CHARACTERISATION OF SPECTRORADIOMETERS

In addition to TULIP, a second laser facility, PLACOS (Pulsed Laser for Advanced Characterisation of Spectroradiometers), is employed. It provides low repetition nanosecond pulses for the spectral characterisation of array spectroradiometers. With the PLACOS setup, the so-called line spread function of CCD array spectroradiometers can be measured for any wavelength within the spectral range from 220 nm to 2200 nm. Based on such measurements (see Figure 4), a correction matrix can be determined that allows us to correct not only the stray light but also the bandpass effects of such devices.

CALIBRATION OF LIGHT SOURCES

Finally, the first investigations to use the tuneable laser setup TULIP for the calibration of broadband sources directly against trap detectors have been successfully realised [4]. The aim of this work is to avoid the necessary calibration of filtered radiometers, which are needed to determine the exact temperature of a black body radiator within the classical calibration chain for radiometric sources. Although the measurements were only carried out within part of the spectral range of the cw-TULIP setup, the results are very promising. Lower uncertainties compared to black-body-based calibrations are expected, especially in the UV spectral range.

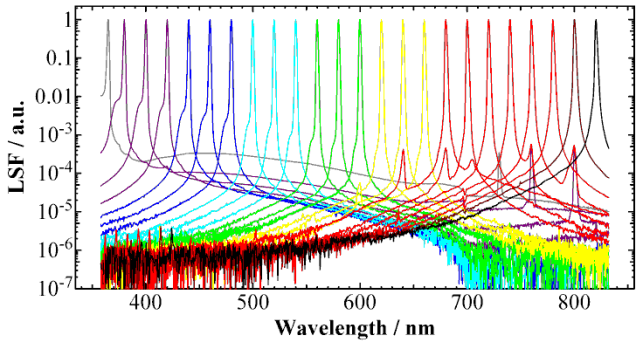

Figure 4. Typical series of line spread functions of an array spectroradiometer used to correct for stray-light effects and bandpass distortion

REFERENCES

1. S. Winter, A. Sperling, “Uncertainty Analysis of a Photometer Calibration at the DSR Setup of the PTB”, in Proc. 2nd Expert Symposium on Measurement Uncertainty (Braunschweig 2006), pp. 139-142, CIE x029:2006, ISBN 3-9810021-4-8.
2. A. Sperling, O. Larionov, U. Grusemann, S. Winter, “Stray-light correction of array spectrometers using tuneable pulsed and cw lasers,” in Proceedings of the 9th international conference on new developments and applications in optical radiometry (NEWRAD), p. 93, Davos, 2005, ISBN-10 3-033-00570-5.
3. S. Nevas, M. Lindemann, A. Sperling, A. Teuber and R. Maass, “Colorimetry of LEDs with Array Spectroradiometers”, MAPAN - Journal of Metrology Society of India, Vol. 24, No. 3, 2009; pp 153-162.
4. A. E. Abd El Mageed, S. Winter, S. Nevas, P. Sperfeld, S. Kück, A. Sperling; ”Detector based traceability chain for spectral irradiance using tunable lasers, independent from blackbody radiators”; BulLight 2010, XIV National Conference with International Participation, Varna, 10-12 June 2010, http://bullight2010.cie-bg.org/EN/Proceedings-BulLight.pdf, p. III3 – III7.

Predictable Quantum Efficient Detector (PQED)

Farshid Manoocheri[1]
on behalf of the PQED consortium
Meelis Sildoja[1], Mikko Merimaa[1], Erkki Ikonen[1], Ingmar Müller[2], Lutz Werner[2], Jarle Gran[3], Stian Hoem[3], Toomas Kübarsepp[4], Geiland Porrovecchio[5], Marek Smîd[5], Giorgio Brida[6] and Maria Luisa Rastello[6]
[1]Aalto University and Centre for Metrology and Accreditation (MIKES), Espoo, Finland, [2]Physikalisch-Technische Bundesanstalt (PTB), Berlin, Germany, [3]Justervesenet, Kjeller, Norway, [4]AS METROSERT, Tartu, Estonia, [5]Cesky metrologický institut, Brno, Czech Republic, [6]Istituto Nazionale di Ricerca Metrologica, Torino, Italy
Corresponding e-mail address: farshid.manoocheri@aalto.fi

The internal quantum efficiency of silicon photodiodes can be made very close to unity [1-3]. This has raised interest to use induced-junction photodiodes [4] as absolute radiometric detector standards with measurement uncertainty in the parts-per-million (ppm) range [5,6]. The design and construction of a Predictable Quantum Efficient Detector (PQED) is aimed to test how small internal quantum deficiency (IQD) of such a device can be obtained [7-10]. Our preliminary experimental results are very encouraging and support the expectation that the PQED can provide a new underpinning scale for optical power measurements with 1 ppm uncertainty.*

INTRODUCTION

The close to ideal quantum detector performance of the PQED is based on dedicated photodiodes made of low-doping *p*-type silicon and a trap detector structure where the reflectance losses are controlled down to ppm level. The dedicated photodiodes can have large area and IQD well below 1 ppm, which are essential features for the PQED. High relative uncertainty in the calculation of the IQD can be tolerated in the total uncertainty budget, if the absolute value of the IQD is sufficiently low.

PHOTODIODES & DETECTOR STRUCTURE

The photodiodes for the PQED were produced by the Technical Research Center of Finland (VTT). Figure 1 shows the schematic cross section of the manufactured photodiodes on a 525 µm thick wafer. The impurity density of the *p*-type substrate is about $2 \cdot 10^{12}$ cm^{-3}. The active area of the photodiodes is 11 x 22 mm^2 and the thickness of the oxide layer between 100 and 300 nm for different diodes [7]. Test measurements of spatial uniformity and nonlinearity of single photodiodes have given promising results [8].

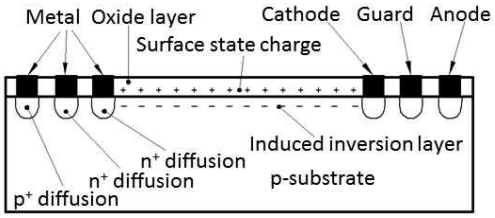

Figure 1. Cross section of the induced junction photodiode (not to scale).

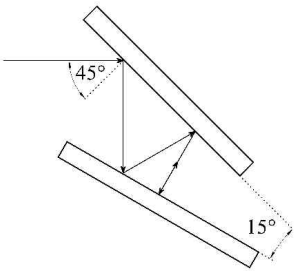

Figure 2. Schematic structure of the PQED consisting of two photodiodes and having 7 reflections altogether. The oxide thickness of the upper (lower) diode is 300 nm (220 nm).

As shown in Fig. 2, the PQED consists of two photodiodes aligned in such a way that 7 specular reflections take place before light leaves the detector [6,7]. The remaining reflectance of 30 to 50 ppm can be used for diagnostics and alignment purposes. For operation between 77 K and 300 K, the two-photodiode detector is mounted into liquid nitrogen cryostat equipped with a Brewster window for high transmission of *p* polarized light.

OPERATION PRINCIPLE

In the produced photodiodes, the oxide layer surface charge of $6.2 \cdot 10^{11}$ *e*/cm^2 induces the *np* junction of the diode with a depletion layer width of about 30 µm [9]. As shown in Fig. 3, the electric field is still large in the depletion layer and thus any generated charge carriers are efficiently collected within this region. Figure 3 also shows the distribution of charge carriers generated by absorbed light at 476 nm and 760 nm wavelengths. For the former wavelength, photons are almost fully absorbed within the depletion region at

both 77 K and 300 K, whereas a fraction of the 760 nm radiation penetrates beyond the depletion region.

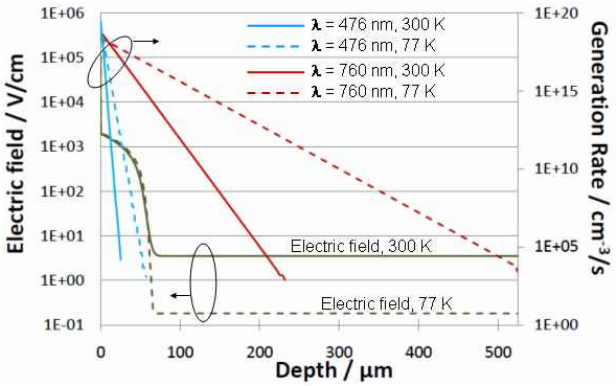

Figure 3. Generation rate of charge carriers at two different wavelengths (λ) and temperatures as a function of depth into the PQED photodiode and compared with the induced electric field. The doping concentration is $2.3 \cdot 10^{12}$ cm^{-3} and bias voltage 5 V.

Losses of charge carriers are caused by recombination at impurity atoms and crystal defects. The advantage of low temperature operation is the improved mobility of charge carriers, which reduces the recombination losses especially if all the photons are absorbed within the depletion layer: One-dimensional PC1D software predicts that the IQD is below 0.03 ppm at 77 K within the spectral range 400-600 nm [10], where the $1/e$ absorption length is smaller than 4 µm [11]. Beyond the depletion layer, the charge carriers are not driven by electric field, but move slower by diffusion. Nevertheless, a large fraction of the charge carriers can still contribute to the measured photocurrent, although the recombination probability is increased as compared to that within the depletion layer.

The uncertainty components of the predicted spectral responsivity of the PQED include losses of charge carriers, reflection/absorption losses of photons, and measurements of photocurrent and wavelength. When the three latter contributions are controlled within 1 ppm uncertainty, the PC1D simulation results suggest that the spectral responsivity can be calculated with similarly low uncertainty [10].

PRELIMINARY TEST RESULTS

Test measurements of the PQED responsivity were carried out against cryogenic radiometers at CMI (λ=476 nm) and PTB (λ=760 nm). Data at 476 nm are in agreement with the notion that the charge carriers are efficiently collected within the depletion region (see Table I). As estimated from Fig. 3 and Ref. [11] for 760 nm, about 0.5% (15%) of the photons are absorbed beyond the depletion layer at 300 K (77 K) and 5 V bias voltage. At 20 V bias, the depletion layer width is doubled and the losses reduced by a factor of four as compared with the values with 5 V bias (Table I). The results at 760 nm thus indicate that only something like one hundredth of charge carriers generated beyond the depletion layer are lost. These are impressively low losses and verify the presence of low density of recombination centers due to impurities and crystal defects. The preliminary results provide evidence for less than ppm level losses of the PQED, when the photons are almost fully absorbed within the depletion layer (i.e. λ = 400 to 600 nm).

Table I. Preliminary internal quantum deficiency (IQD) results of the PQED. The standard uncertainty is given in parentheses.

λ (nm)	Temperature (K)	Bias (V)	IQD (ppm)
476	300	5	20(100)
476	77	5	20(100)
760	300	5	130(30)
760	77	5	600(30)
760	77	20	160(30)

*The research leading to these results has received funding from the European Community's Seventh Framework Programme, ERA-NET Plus, under Grant Agreement No. 217257.

REFERENCES

1. J. Geist, E. Liang and A. R. Schaefer, Complete collection of minority carriers from the inversion layer in induced junction diodes, J. Appl. Phys. **52**, 4879-4881, 1981.
2. E. F. Zalewski and C. R. Duda, Silicon photodiode device with 100% external quantum efficiency, Applied Optics **22**, 2867-2873, 1983.
3. N. P. Fox, Trap detectors and their properties, Metrologia **28**, 197-202, 1991.
4. T. E. Hansen, Silicon UV-Photodiodes using natural inversion layers, Phys. Scripta **18**, 471-475, 1978.
5. J. Geist, G. Brida and M. L. Rastello, Prospects for improving the accuracy of silicon photodiode self-calibration with custom cryogenic photodiodes, Metrologia **40**, 132-135, 2003.
6. M. Sildoja, F. Manoocheri and E. Ikonen, Reflectance calculations for a predictable quantum efficient detector, Metrologia **46**, S151-S154, 2009.
7. M. Sildoja et al, PQED I: Photodiodes and design, these proceedings DBR_OR_047.
8. I. Mueller et al, PQED II: Characterization results, these proceedings DBR_OR_029.

9. S. Hoem et al, Physics of self-induced photodiodes, these proceedings DBR_PO_042.
10. J. Gran et al, Simulations of PQED with PC1D, these proceedings DBR_PO_044.
11. http://www.ioffe.ru/SVA/NSM/Semicond/Si/optic.html

Single-photon sources with near unity efficiency

Stephan Götzinger[1], Kwang-Geol Lee[1], Xuewen Chen[1], Hadi Eghlidi[1], Alois Renn[1], Vahid Sandoghdar[2]
[1]*Laboratory of Physical Chemistry, ETH Zürich, CH-8093 Zürich, Switzerland*
[2]*Max Planck Institute for the Science of Light, D-91058 Erlangen, Germany*
Corresponding e-mail address: Stephan.Goetzinger@phys.chem.ethz.ch

We report on a single-photon source based on an oriented single organic molecule with record photon count rates exceeding 48 MHz. By designing a dielectric antenna around the molecule, we succeed to collect 96% of the photons emitted into a 120° cone. New theoretical calculations show that it is possible to modify the current scheme and reach collection efficiencies beyond 99% for emitters with arbitrarily oriented dipole moments. Furthermore, we provide antenna parameters to realize ultra-bright single-photon sources in high-index materials such as semiconductor quantum dots and color centers in diamond. Because the extraction efficiency is insensitive to design parameters, we can predict the photon emission rate. Such antenna based single-photon sources hold great promise as new primary intensity standards in the pW range.

INTRODUCTION

During the last decade single-photon sources haven been extensively studied for their potential as building blocks in emerging quantum technologies – so far mostly for quantum information processing but also for metrology applications [1, 2, 3]. When a single emitter is excited in a pulsed fashion, one and only one photon is emitted per excitation pulse. If one could collect every photon emitted by the single-photon emitter, one would have a fully noise-free light source with an intensity given by the repetition rate of the excitation. The realization of such a new primary intensity standard has been previously prevented by the difficulty to attain a bright source. Furthermore, precise determination of the source efficiency has been a challenge since the total collection efficiency is usually extremely sensitive to the exact collection angle of the collection optics, the refractive index in the vicinity of the emitter, and its dipole orientation.

EXPERIMENTAL

We fabricated a device consisting of oriented, photostable terrylene molecules [4], embedded in two dielectric layers of PVA (see Fig. 1). A high-index substrate made of sapphire completes the structure, which acts as a dielectric antenna. Theoretical calculations show that an emitter with a dipole moment perpendicular to the substrate emits 96.1% of the photons in a 120° cone towards the immersion objective. The remaining 3.9% are emitted into the other half-space above the antenna. Because the full collection angle of our objective is larger than the emission cone, we collect all of the photons emitted into the half-space on the objective side. By considering the losses in all optical components and the quantum efficiency of the CCD detector, we can achieve a total detection efficiency of 52% and photon detection rates of 48.1 MHz [5]. This information together with the photon emission probability, obtained from photon correlation measurements, allows us to assess the number of collected photons. At high excitation powers, strong anti-bunching is still observable. The extraordinary count rates allowed us to perform photon correlation measurements in less than one second.

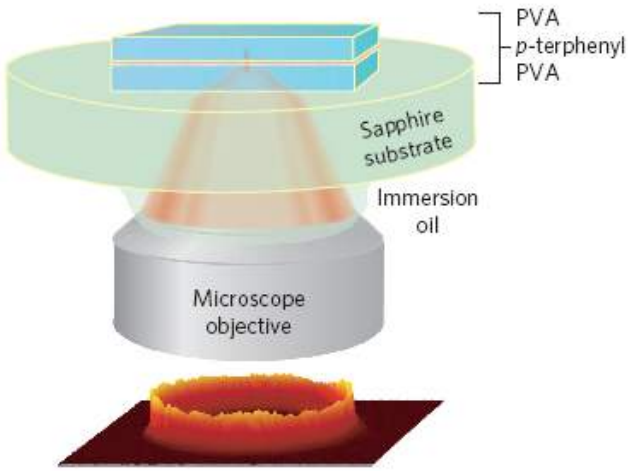

Figure 1. Schematics of the photon collection strategy.

EXTENTION OF THE PHOTON COLLECTION CONCEPT TO OTHER EMITTERS

The normal orientation of the molecules is an integral part of our antenna design. Unfortunately this condition cannot be met by every solid state emitter. To remedy this shortcoming, we added another low index spacer layer and a metallic mirror on top of our first antenna design. Calculations show that it is now possible to collect 99% of the fluorescence independently of the emitter orientation [6]. By

employing high-refractive index solid immersion lenses and a careful tailoring of the antenna structure, we show that the methodology is also applicable to emitters embedded into high index materials such as InAs quantum dots or NV centers in diamond.

CONCLUSIONS

We have introduced a robust metallo-dieletric planar antenna with 99% efficiency for collecting photons emitted by randomly oriented emitters. Some of the outstanding features of our antenna design are that its operation is broadband, it does not require sophisticated lateral nanofabrication, and it is compatible with essentially all materials. In particular, extension of this concept to single emitters at cryogenic conditions will allow one to realize ultra-bright sources of narrow-band single photons [7,8]. In summary, the photon collection strategy we are presenting does not only yield record photon count rates, but it is also extremely versatile and promises the realization of predictable bright single-photon sources for metrology applications.

REFERENCES

1. Lounis, B. & Orrit, M. Single-photon sources. *Rep Prog Phys* **68**, 1129-1179 (2005).
2. Scheel, S. Single-photon sources-an introduction. *Journal of Modern Optics* **56**, 141-160 (2009).
3. Polyakov, S. V. & Migdall, A. L. Quantum radiometry. *Journal of Modern Optics* **56**, 1045-1052 (2009).
4. Pfab, R. J. *et al.* Aligned terrylene molecules in a spin-coated ultrathin crystalline film of p-terphenyl. *Chem Phys Lett* **387**, 490-495 (2004).
5. K. G. Lee *et al.,* A planar dielectric antenna for directional single-photon emission and near-unity collection efficiency, *Nature Photonics* **5**, 166-169 (2011).
6. X. W. Chen, S. Götzinger, V. Sandoghdar, 99% efficiency in collecting photons from a single emitter, submitted (2011).
7. R. Lettow *et al,*. Realization of two Fourier-limited solid-state single-photon sources, *Optics Express* **15**, 15842-15847 (2007).
8. R. Lettow *et al.*, Quantum interference of tunably indistinguishable photons from remote organic molecules, *Physical Review Letters* **104**, 123605 (2010).

Novel photon detector utilizing superconducting optical detection technology and its application to a few-photon radiometry

D. Fukuda[1], G. Fujii[1,2], A. Yoshizawa[1], T. Numata[1], K. Amemiya[1], S. Inoue[2], and H. Tsuchida[1]

[1]*National Institute of Advanced Industrial Science and Technology, Tsukuba, Japan*
[2]*Institute of Quantum Science, Nihon University, Tokyo, Japan*
Corresponding e-mail address: d. fukuda@aist.go.jp

We have been developing a high detection efficiency photon number resolving detector with a superconducting transition edge sensor. The detector consists of a titanium-based superconductive film with the superconducting transition temperature from 0.3 K to 0.4 K. By using dielectric multi-layered structure to enhance photon absorption, we have achieved the system detection efficiency of 98 % and 84 % with optimized devices at wavelengths of 850 nm and 1550 nm, respectively. An intrinsic dark count in TES devices is negligible, while several hundreds of dark counts were observed due to black body radiation for devices optimized at 1550 nm. We also applied this device to characterize a non classical light source, which is base on polarization entangled photons. High fidelity of >98 % was obtained by quantum tomography, that shows these devices would be powerful tools to exactly evaluate the non-classical optical sources in a few-photon radiometry.

INTRODUCTION

A generation and evaluation of quantum states with a non-classical light source are very important issues in a few-photon metrology. Especially in terms of the evaluation, it is difficult to precisely characterise the photon number distributions of non-classical optical sources because of limited detection efficiency (DE) of conventionally used photon detectors. This is more serious with increasing the number of photons because the detection probability of the *n*–th photon state is proportional to DE of the *n*–th power. A superconducting transition edge sensor (TES) is one solution to resolve this problem. The TES detector is a kind of calorimeters, thus the temperature change resulted from photon absorption is measured as the resistance change in its superconducting-to-normal phase transition. The output signal of the TES is proportional to the incident photon energy so that the spectral information to the single photon or the number of photons in incident optical pulses can be obtained. Besides, optical absorption enhancement can be possible with an optical resonant structure, which leads to high detection efficiency. The high DE photon number resolving detector (PNRD) allows us to characterise photon number distribution of non-classical sources with low uncertainty. The high DE photon detectors will also open new applications such as a generation of non-Gaussian states for optical quantum computing[1], or quantum optimal receiver with bit-error rate lower than shot-noise limit[2,3].
For these purposes, we are now trying to develop TES photon detectors with high DE, fast response, and low dark noise. In this presentation, we will show the current status of our developed TES photon detectors. Moreover, we will show results of quantum tomography to characterize a polarization-entangled photon source by applying the TES technology.

HIGH DE PHOTON NUMBER RESOLVING DETECTORS

In NMIJ/AIST, titanium (Ti) single-layers or titanium-gold (Ti/Au) proximity bi-layers are used as the TES superconducting films. The typical transition temperature of these films is controllable from 0.3 K to 0.4 K. This relatively higher temperature enables the fast response time less than 1 μs. The superconducting films are photon absorbing layer

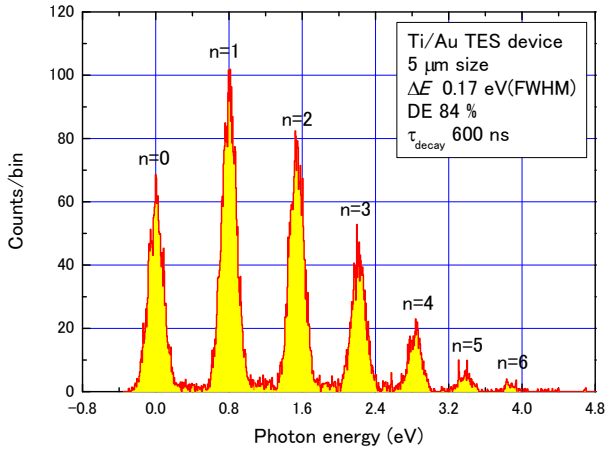

Figure 3. A distribution of observed signal pulses for a laser pulses at 1.5 μm wavelength.

embedded in the optical resonant cavity to enhance the DE, which is composed of dielectric multi-layered films[4]. The optical cavity is designed and optimized at the wavelengths of the interest used in the laser source. The figure 1 is the pulse height distribution for the coherent light pulses with the incident mean photon number μ=0.5/pulse at a laser repetition frequency 50 kHz. The energy resolution for the single photon state (n=1) is 0.18 eV, and makes it possible to clearly resolve the photon number. In order to determine the system detection efficiency η, we have used a comparison method[4] of detection probabilities $P_{\mathrm{TES}}(n|\mu)$ with the Poisson distribution $P_{\mathrm{Poisson}}(n|\mu)=(\eta\mu)^n\exp(-\eta\mu)/n!$. Figure 2 is an example of the DE determination for the TES optimized at the 850 nm wavelength. From the least χ^2 fitting, we obtain η=98.42 %±0.10 %. The dark count of the TES is typically hundreds of counts because of the black body radiation through fibres at the room temperature, which is much smaller than that of conventional photon detectors.

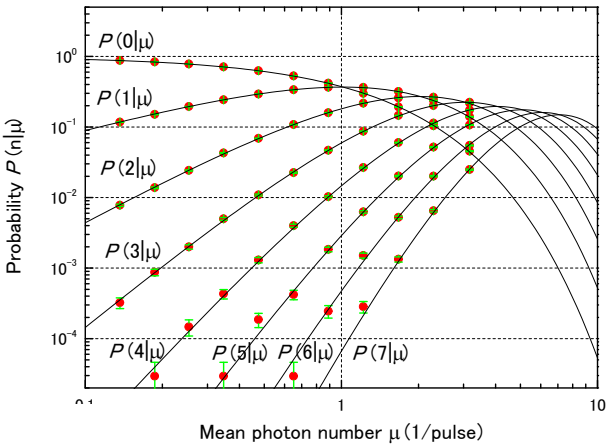

Figure 2. A DE determination result for a TES detector. The circles are measured values of $P(n|\mu)$. The solid lines are the Poisson distribution with η =0.9842.

EVALUATION OF POLARIZATION ENTALGLED PHTON PAIRS

Correlated or entangled photon pairs, generated by parametric down conversion, are very important light sources for detection efficiency calibration or quantum information. The measurement techniques of the fidelity and the purity of these light sources are indispensable to develop the high performance light sources. In these measurements, a large number of coincident counts and less accidental coincidence count are preferable to avoid the degradation of the fidelity. The TES photon detectors, due to its high DE and low dark counts, are very suitable for this measurement. Here we have applied the TES

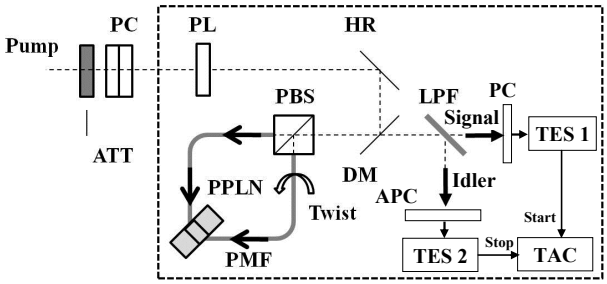

Figure 3. An experimental setup for a polarization entangle photon source and TES devices(Att: attenuator, PL: Polarizer, HR: high reflection mirror, DM: dichroic mirror, PBS: polarization beam splitter, PMF: polarization maintaining fiber, LPF: long wavelength pass filter, TAC: time to amplitude converter). Pump rejection filters and an optical delay are not shown.

detectors to evaluate a polarization entanglement at 1550 nm telecom band. Our entangle source consists of a CW-pumped periodically poled lithium niobate (PPLN) waveguide in a polarization-diversity loop[5], as shown in Figure 3. Both signal and idler photons were measured by two sets of TES detectors via an automatic polarization controller (APC) and a phase controller (PC). By changing the polarization states of photon pairs, we measured coincident counts from TES signals. A coincident time window was set to 150 ns, nonetheless the time jitter of each TES detector was ~20 ns. From these results, we obtain a density matrix reconstructed by quantum-state tomography. A high fidelity of 98.5 % was obtained without subtracting accidental coincident counts, which shows our TES is very effective to evaluate an intrinsic nature of the light sources.

ACKNOWLEDGEMENTS

A part of this work was conducted at the AIST Nano-Processing Facility, and supported by the program “Strategic Information and Communications R&D Promotion Programme (SCOPE)” of the Ministry of Internal Affairs and Communications (MIC).

REFERENCES

1. N. Namekata et al., Non-Gaussian operation based on photon subtraction using a photon-number-resolving detector at a telecommunications wavelengths, Nature Photonics 4, 655-660, 2010.
2. K. Tsujino et al, Sub-shot-noise-limit discrimination of on-off keyed coherent signals via a quantum receiver with a superconducting transition edge sensor, Opt. Express, 18, 8107-8114, 2010.

3. K. Tsujino et al, Quantum receiver beyond the standard quantum limit of coherent optical communication, accepted to Phys. Rev. Lett.
4. D. Fukuda et al, Titanium-based transition-edge photon number resolving detector with 98 % detection efficiency with index-matched small-gap fiber coupling, Opt. Express, 19, 870-875, 2011.

Bridging the Gap: Radiometry from Watts to Single-Photons

A. Migdall[1], B. Calkins[2], C. Cromer[2], M. Dowell[2], J. Fan[1], T. Gerrits[2], J. Lehman[2], A. Lita[2], D. Livigni[2], R. P. Mirin[2], S. W. Nam[2], S. V. Polyakov[1], M. Stevens[2], N. Tomlin[2] , and I. Vayshenker[2]

[1] *Joint Quantum Institute and National Institute of Standards and Technology, 100 Bureau Dr, Gaithersburg, MD 20899*
[2] *National Institute of Standards and Technology, 325 Broadway, Boulder, CO 80305*

Making optical power and energy measurements have always been challenging, as seen by the best uncertainties achieved in radiometry relative to the uncertainties achieved in most other areas of metrology. See this, for example, on a fundamental level in the uncertainty of the radiometrically relevant Stefan-Boltzmann constant which is already one of the least certain constants[1] and radiometric measurements cannot compete even with that already relatively poor uncertainty[2]. On a more utilitarian level we see this issue in radiometric detector scale uncertainties[3]. There are many challenges that limit this uncertainty, and the current interest in single-photon devices is only increasing the challenge, with the dynamic range of interest now covering at least 20 orders of magnitude. This large range, and in particular the interest in measurements at the lowest levels, has spurred discussions as to whether the advances in single-photon tools can be fruitfully applied as a new approach to radiometry with improved uncertainty[4]. While no one knows specifically how this might be achieved, one reason for the interest and hope in this area is that if existing radiometric measurements can somehow be transformed into a problem where uncertainties depend on the counting of a large number of highly certain events, instead of on issues such as losses or inefficiencies of a substitution-based or equivalence-based detector devices or similar inefficiencies and design limitations of conventional sources.

While we are long way from realizing the dream of this transformation, there are a number of efforts toward this goal. These efforts include the demonstrated metrology uses, where photon pair sources are used to create what is effectively a single-photon gun for the radiometric application of detector efficiency metrology[5, 6], and that same pair production process becomes a tool for source radiance metrology[7]. Other efforts underway are focused on stretching existing technology beyond the ranges where they traditionally operate. One example is the extension of cryo-based radiometers from the milliwatt range down to a range where power levels begin to be compatible with photon-counting detectors. An example of an extension in the other direction, i.e. from low levels up to high levels, is where photon-counting detectors are pushed to operate beyond the range where photon counting is possible, that is these detectors are made to operate in analog mode when they exceed the maximum rates they can handle in photon-counting mode. There are similar such efforts to extend the range of single-photon sources from the typical maximum rate limits of $\approx 10^6$ photon/s upward to create "countable photon super sources" that can operate as standards for conventional radiometry applications.

We review these efforts and discuss issues and prospects related to the overall goals of these efforts.

REFERENCES

[1] P. J. Mohr, B. N. Taylor, and D. B. Newell, "CODATA recommended values of the fundamental physical constants: 2006," Rev. Mod. Phys **80**, 633-730(2008) .

[2] B Fellmuth, Ch Gaiser and J Fischer, "Determination of the Boltzmann constant—status and prospects," Meas. Sci. Technol. **17** R145–R159(2006).

[3] H. W. Yoon, C. E. Gibson, and P. Y. Barnes, "A Realization of the National Institute of Standards and Technology detector-based spectral irradiance scale," Applied Optics **41**, 5879(2002).

[4]http://www.quantumcandela.org/

[5] G Brida, S Castelletto, I P Degiovanni, C Novero and M L Rastello, "Quantum efficiency and dead time of single-photon counting photodiodes: a comparison between two measurement techniques," Metrologia **37** 625 (2000).

[6] S.V. Polyakov and A.L. Migdall, "High accuracy verification of a correlated photon-based method for determining photon-counting detection efficiency," Opt. Express **15**, 1390-1407 (2007).

[7] A. Migdall, E. Dauler, A. Muller, and A. Sergienko, "Tests of an Omnipresent Standard for Absolute Spectral Radiance Measurements," Analytica Chimica Acta **380**, 311-316 (1999).

New measurements of the intensity and geometrical structure of the upwelling and downwelling underwater light fields (radiance distributions)

David Antoine[1], Edouard Leymarie[1], André Morel[1], Amel Houyou[1,2], Stéphane Victori[2], Didier Crozel[2], and Bertrand Fougnie[3]

[1]*Laboratoire d'Océanographie de Villefranche (CNRS-LOV), Villefranche sur mer, France,* [2]*CIMEL Electronique, Paris, France,* [3] *Centre National d'Etudes Spatiales (CNES), Toulouse, France*

Corresponding e-mail address: antoine@obs-vlfr.fr

New measurements of the intensity and geometrical structure of the upwelling and downwelling underwater light fields (radiance distributions) are presented. They are obtained from new miniaturized underwater radiance cameras. The instruments are succinctly presented along with sample data. Better knowing the radiance distribution is fundamental for interpretation of ocean color remote sensing observations. Potential for renewing the way we measure ocean optical properties is also explored. Extension of the methods and instrument capabilities to atmospheric optics is also discussed.

INTRODUCTION

A paradox in marine optics is that we ignore the geometrical structure of the underwater light field when we measure and interpret underwater optical properties whereas it has a strong impact on these properties. By "geometrical structure" one means the spatial distribution of the fundamental radiometric quantities: radiance, L. Its distribution over an hemisphere is noted L(Ξ) (subscript "u" and "d" for the upwelling and downwelling hemispheres). Optical properties are of tremendous importance for many domains of oceanography and marine operations, e.g., heating rate of the upper ocean, bio-geochemistry and carbon cycle, water transparency, coastal zones monitoring, assimilation into global coupled physical-biological models, underwater imaging. Improving their quality and consistency is therefore an important goal. L(Ξ) is anisotropic, including the image of the sun and much dimmer radiances from the deep. The distribution of radiances emerging from the ocean, and possibly remotely-sensed from satellites, depends on L(Ξ) and is accordingly also anisotropic (an effect to be removed before proper interpretation of satellite signals).

Measuring L(Ξ) has been for long an elusive task because of technological limitations, whereas an accurate knowledge of its changes with depth would actually allow all optical properties to be derived consistently [1]. $L(\Xi_u)$ is partially known in open ocean waters [2, 3, 4] and totally undocumented in coastal turbid waters. Pushing back this frontier is important for the fundamental knowledge of how light interacts with matter in the ocean. It also has multiple implications and applications for better field measurements of optical properties, better interpretation and use of these properties as they are remotely sensed from satellites (the so-called "ocean color" remote sensing observations, with major challenges for their current interpretation in coastal areas and from the geostationary orbit), and underwater imaging. Accurate and simultaneous measurements of L(Ξ) over 4π steradians are now possible thanks to miniaturized radiance cameras we have recently developed.

THE INSTRUMENTS

Two prototypes were designed to meet specific requirements, i.e., miniaturization (to minimize self-shading when measuring the upwelling radiances $L(\Xi_u)$), multi-spectral capability, high dynamic range and no blooming in order to measure low radiances from the deep as well as high radiances from the direct sun, high SNR.

Figure 1. Overall external view of the miniaturized multi-spectral "CE-600" underwater fish-eye radiance camera (joint development by LOV and CIMEL Electronique).

The system built from these requirements is shown on Fig. 1. The 200-m rated container hosts a patented specifically-designed telecentric optics

collecting radiances from all directions of one hemisphere (actually over 184°, allowing $L(\Xi_u)$ and $L(\Xi_d)$, to be linked up to form $L(\Xi)$), a filter wheel with 6 positions (from 406 to 628 nm), a CMOS array detector (selected for absence of blooming), and a fiber-optic transmission to the command and data acquisition PC on board the ship. Auxiliary sensors provide internal temperature (monitoring of dark currents) and humidity (leaks detection), tilt (quality control), compass (orientation w.r.t the sun), and pressure (depth).The cameras can be deployed either floating at the surface to collect $L(\Xi_u)$ (when the aim is to determine the distribution above the surface for remote sensing purposes) or head to tail on a profiling system, allowing simultaneous measurements of $L(\Xi_u)$ and $L(\Xi_d)$ at depths down to 200m.

SAMPLE RESULTS

The capabilities of the CE-600 cameras are illustrated on Fig. 2. The colored polar plots show $L(\Xi_d)$ measured at different depths and under different sky conditions, and the curves are data extracted from $L(\Xi_d)$ (see figure legend).

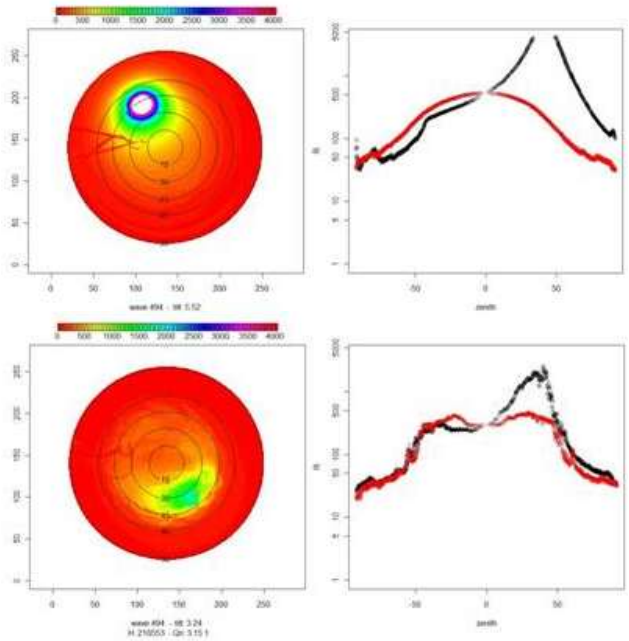

Figure 2. $L(\Xi_d)$ for a clear sky and near the 1% light level (top panels) and overcast conditions near the surface (bottom panels). Black and red curves are the principal and perpendicular planes extracted from the full distributions.

These plots show the image of the sun and the dimmer radiances from slant directions, for instance. By making several images with different integration times, it is possible to get measurements of the very high radiances close to the sun direction and much lower radiances from other directions. The CMOS sensitivity and noise levels are adapted for this purpose. Comparison of $L(\Xi_u)$ with the only other similar available instruments is shown on Fig. 3.

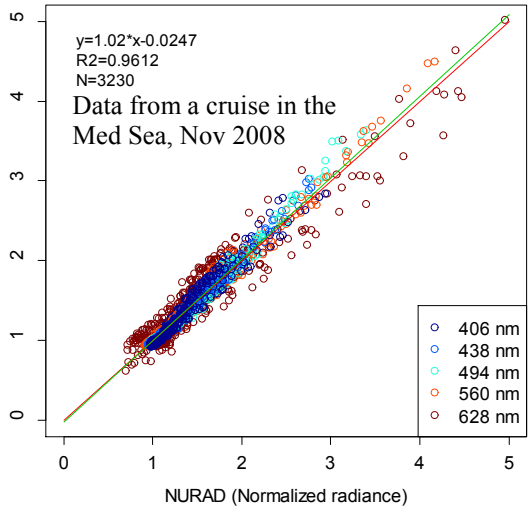

Figure 3. Comparison of radiances normalized to nadir for all directions of the upward hemisphere, between our camera (vertical axis) and the "NURADS" [5].

PERSPECTIVES

Data exploitation is ongoing. Two of our goals are directly related to a better interpretation of satellite ocean color observations: (1) to complete data bases of $L(\Xi_u)$ in very clear as well as eutrophic Case 1 waters, (2) document $L(\Xi_u)$ in turbid coastal Case 2 waters (no data exist for the moment). Other objectives are more fundamental: develop numerical inversion procedures using both $L(\Xi_u)$ and $L(\Xi_d)$ measured at several depths to determine all optical properties, and extend the methods and instrument capabilities to atmospheric optics.

REFERENCES

1. Zaneveld, R.J.V., An asymptotic closure theory for irradiance in the sea and its inversion to obtain the inherent optical properties, Limnology and Oceanography, 19, 1442-1452, 1989.
2. Voss, K., A. Morel, and D. Antoine, Detailed validation of the bidirectional effect in various Case 1 waters for application to Ocean Color imagery, Biogeosciences, 4, 781-789, 2007.
3. Voss, K. and A. Morel, Bidirectional reflectance function for oceanic waters with varying chlorophyll concentration Measurements versus predictions, Limnology and Oceanography, 50, 698-705, 2005.
4. Morel, A., and B. Gentili, Diffuse reflectance of oceanic waters. 2. Bidirectional aspects, Applied Optics, 32, 6864-6872, 1993.
5. Voss, K., and A. L. Chapin, Upwelling radiance distribution camera system, NURADS, Optics Express 13, 4250-4262, 2005.

On-orbit Absolute Blackbody Emissivity Determination Using the Heated Halo Method

Jonathan Gero, Joe Taylor, Fred Best, Henry Revercomb, Robert Knuteson, David Tobin

Space Science and Engineering Center, University of Wisconsin—Madison, Madison, WI, USA
Corresponding e-mail address: jonathan.gero@ssec.wisc.edu

Reliable calibration of high-accuracy spaceborne infrared spectrometers requires knowledge of both blackbody temperature and emissivity on-orbit, as well as their uncertainties. The Heated Halo is a broadband thermal source that provides a robust and compact method to measure emissivity. Measurements of spectral emissivity are demonstrated with this apparatus in the laboratory with an uncertainty of 4×10^{-4} (k=3) for a 0.999 emissivity blackbody.

INTRODUCTION

Measurements of spectral infrared radiance from space are an effective benchmark of global climate change and provide powerful constraints on climate models, if they are made with demonstrable on-orbit accuracy. Recent studies [1] call for measurements of thermal infrared radiance with combined uncertainties better than 0.1 K (k=3) in radiance temperature for the detection of spectral climate signatures. Furthermore, instrument uncertainty must be demonstrated on-orbit, to confirm that the uncertainty budgets obtained during pre-launch calibration remain tenable [2]. This level of uncertainty has not yet been accomplished by space-based high-resolution infrared sounders.

Spaceborne measurements of infrared radiance can be most accurately calibrated with blackbodies. The spectral radiance $B_{\tilde{\nu}}(T)$ emitted by a blackbody cavity of uniform temperature T with an infinitesimal aperture is described by the Planck function

$$B_{\tilde{\nu}}(T) = 2hc^2\tilde{\nu}^3 / \exp(hc\tilde{\nu}/k_B T) - 1 \quad (1)$$

where $\tilde{\nu}$ is the spectral index in cm^{-1}. The spectral radiance $I_{\tilde{\nu}}$ emitted by a cavity with a finite aperture with Lambertian reflectance is

$$I_{\tilde{\nu}} = \varepsilon_{\tilde{\nu}} B_{\tilde{\nu}}(T) + (1-\varepsilon_{\tilde{\nu}}) I_{\tilde{\nu},bg} \quad (2)$$

where $\varepsilon_{\tilde{\nu}}$ is the cavity emissivity, and $I_{\tilde{\nu},bg}$ is the radiation from the background environment. The dominant source of uncertainty in a well designed blackbody arises from the measurement of the cavity temperature and the effect of the nonunity emissivity of a practical blackbody with a macroscopic aperture. In this paper we address the on-orbit monitoring of blackbody cavity emissivity using the Heated Halo.

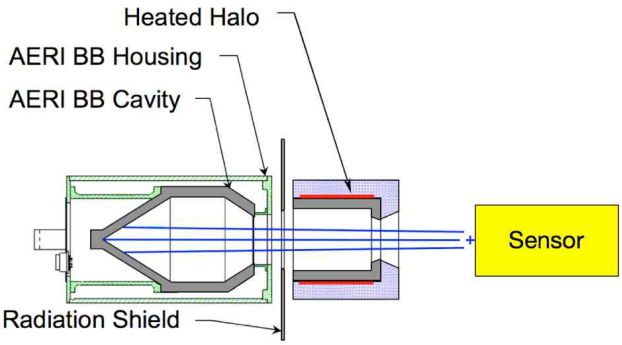

Figure 4. Schematic cross-sectional representation of the first generation Heated Halo. A radiation shield reduces radiative heating of the blackbody by the Heated Halo.

APPARATUS

The Heated Halo is a broadband thermal radiation source designed to fill a large fraction of the solid angle of a given blackbody's field of view, while being physically outside of the field of view of the detector observing the blackbody. The Heated Halo used in this experiment is a hollow aluminum cylinder, painted black and heated with Kapton thermofoil heaters to 95°C (Fig. 1).

We measure the emissivity of the Atmospheric Emitted Radiance Interferometer (AERI) blackbody [3] for this experiment. The blackbody employs a light-trapping cavity geometry, is painted with diffuse Aeroglaze Z306, and its temperature is measured by embedded thermistors to within a combined uncertainty of 0.05 K (k=3). The blackbody is operated at ambient room temperature (about 23°C).

Two different spectrometer systems are used to observe the AERI blackbody: (1) the Scanning High-resolution Interferometer Sounder (S-HIS), a Fourier transform spectrometer (FTS) designed for autonomous operation on board research aircraft, covering the 580-2800 cm^{-1} spectral range using an InSb and two HgCdTe detectors [4]; and (2) the Absolute Radiance Interferometer (ARI), a laboratory-based FTS covering the 200-1700 cm^{-1} spectral range using a pyroelectric detector [5].

METHODOLOGY

When the Heated Halo is placed in the optical chain between the spectrometer and the blackbody, the background radiance in Eq. 2 becomes,

$$I_{\varrho,\mathrm{bg}} = FB_{\varrho}(T_{\mathrm{ha}}) + (1-F)B_{\varrho}(T_{\mathrm{rm}}^{\mathrm{eff}}) \quad (3)$$

where F is the geometrical view factor characterizing the fraction of the blackbody solid angle viewing the Heated Halo, T_{ha} is the Heated Halo temperature, and $T_{\mathrm{rm}}^{\mathrm{eff}}$ is the effective temperature of the background environment. Eq. 2 can be rewritten as

$$\varepsilon_{\varrho} = (I_{\varrho} - I_{\varrho,\mathrm{bg}})/(B(T) - I_{\varrho,\mathrm{bg}}) \quad (4)$$

where $I_{\varrho,\mathrm{bg}}$ is given by Eq. 3. All of the terms on the right hand side of Eq. 4 can be measured or modelled accurately, thus the spectral emissivity for a given blackbody can be evaluated.

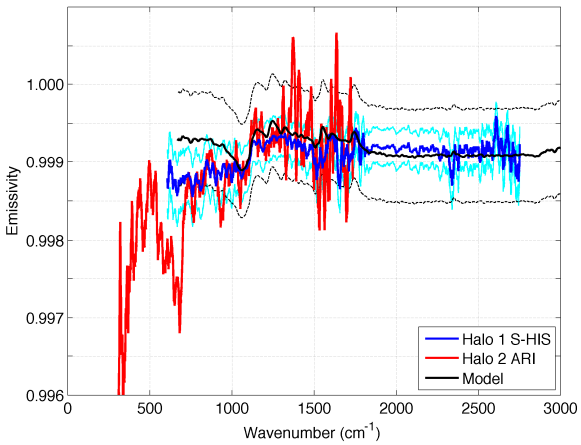

Figure 2. Comparison between two versions of Heated Halo measurements, S-HIS (blue) and ARI (red), as well as the modelled emissivity of the AERI blackbody. The dashed curves represent the systematic (type B) uncertainty (k=3) for the S-HIS and the model result.

RESULTS AND DISCUSSION

The emissivity spectrum of the AERI blackbody, measured by both the S-HIS and the ARI using the Heated Halo method, is shown in Fig. 2, compared to a model result from a Monte Carlo simulation [6]. The overall shape of the observed emissivity curve, notably the step in emissivity around 1200 cm^{-1}, is consistent with the properties of the Aero glaze Z306 paint [7]. Some of the high frequency oscillations in the measurements can be attributed to detector noise (type A uncertainty), as well as spectral lines of carbon dioxide (near 667 cm^{-1}) not fully eliminated by the purge employed in the experiment. The lower measured values in emissivity between 600-1000 cm^{-1}, compared to the model result, indicate an error in the model parameterization due to extrapolation.

The six main sources of systematic measurement uncertainty (type B: stray radiation, view factor, calibration accuracy, Heated Halo temperature, effective room temperature, blackbody temperature) are calculated by applying variational analysis to Eq. 4. The overall root-sum-of-squares (RSS) uncertainty is less than 4×10^{-4} (k=3) between 500-2800 cm^{-1}, and has a maximum value of 1.2×10^{-3} (k=3) at 200 cm^{-1}.

CONCLUSIONS

Using the S-HIS and ARI spectrometers, the spectral emissivity of the AERI blackbody was measured in the 200-2800 cm^{-1} spectral range with the Heated Halo method. The measurements are in agreement with each other, as well as with a Monte Carlo model, within their uncertainties. Furthermore they are in agreement with several other measurements of the AERI blackbody emissivity using physically independent methods in experiments performed by NIST. The low level of systematic (type B) experimental uncertainty across most of the infrared spectrum (4×10^{-4}, k=3) is encouraging that the Heated Halo can be deployed on space-based instruments to monitor calibration blackbody emissivity, on-orbit, throughout the lifetime of satellite missions.

REFERENCES

1. National Research Council, Earth Science and Applications from Space: National Imperatives for the Next Decade and Beyond, National Academies Press, Washington D. C., 2007.
2. J. A. Dykema and J. G. Anderson, A methodology for obtaining on-orbit SI-traceable spectral radiance measurements in the thermal infrared, Metrologia, 43, 287–293, 2006.
3. R. O. Knuteson and Coauthors, Atmospheric Emitted Radiance Interferometer. Part I: Instrument Design, J. Atmos. Oceanic Technol., 21, 1763–1776, 2004.
4. H. E. Revercomb and Coauthors, Highly accurate FTIR observations from the scanning HIS aircraft instrument, in Proc. SPIE 5655, 41–53, 2005.
5. J. K. Taylor and Coauthors, The University of Wisconsin Space Science and Engineering Center Absolute Radiance Interferometer (ARI), in Proc. SPIE 7857, 78570K, 2010.
6. F. A. Best and Coauthors, Determination of the Atmospheric Emitted Radiance Interferometer (AERI) blackbody emissivity and radiance using multiple techniques, in Proc. Characterization and Radiometric Calibration for Remote Sensing, Logan, UT, 2009.
7. M. J. Persky, Review of black surfaces for space-borne infrared systems, Rev. Sci. Instrum., 70, 2193–2217, 1999.

Current activity of Russia in measurement assurance of Earth optical observation

V.I. Sapritsky[1], V.N. Krutikov[2], V.S. Ivanov[1], A.S. Panfilov[1], M.A. Pavlovich[1], A.A. Burdakin[1], V.V. Rakov[1], S.P. Morozova[1], B.E. Lisyansky[1], B.B. Khlevnoy[1], V.R. Gavrilov[1], S.A. Ogarev[1], A.V. Pusanov[1], M.L. Samoylov[1], M.V. Solodilov[1]

[1]*All-Russian Research Institute for Optical and Physical Measurements (VNIIOFI), Moscow, Russia*
[2]*Federal Agency on Technical Regulating and Metrology, Moscow, Russia*
Corresponding e-mail addresses: VSapritsky@gmail.com, khlevnoy-m4r@vniiofi.ru

The current results obtained at VNIIOFI within Global Earth Observation System of Systems project are presented. The newly created standard radiometric facility for precise calibration of instruments for Earth observation and the project on precise monitoring of in-flight stability of the instruments are described, and activity on documentation harmonization in this field is discussed.

INTRODUCTION

In 2006 a "10-year implementation plan" to establish a Global Earth Observation System of Systems (GEOSS) was launched [1]. The key objective of GEOSS is synergistic usage of data delivered by various Earth observation systems belonging to the countries – members of the Group on Earth Observations (GEO). To accomplish this vision it is obligatory to meet requirements on the data consistency. At NEWRAD2005 VNIIOFI proposed an approach to metrological assurance of optical measurements within GEOSS [2] and a framework for activities in this field.

Here we present current results obtained at VNIIOFI in this activities and discuss the further plans, namely:

- description of the newly created traceable to SI standard radiometric facility for precise calibration of instruments for the Earth observations,
- project on precise monitoring of stability of instruments in-flight performance,
- VNIIOFI activity for implementation of the document «Quality Assurance Framework for Earth Observation» [3] developed within GEOSS community.

STANDARD RADIOMETRIC FACILITY FOR EARTH OBSERVATION INSRUMENTS

The standard radiometric facility was developed at VNIIOFI for ground high accuracy calibration of the Earth observation instruments with apertures up to 500 mm. The facility consists of two parts. The first one is for spectral range from 300 nm to 3000 nm. It includes two large-area sources: integrating sphere source (IS) with measured spectral radiance and monochromatic source (MS). The MS is for measurements of relative spectral responsivity of the instruments, and the IS is for determining absolute responsivity. The second part is based on a large-area low temperature blackbody (LABB) and intended for spectral range from 3 μm to 25 μm.

The diameter of the IS is 2 m. It has an aperture with diameter of 600 mm. The IS is equipped with a set of 24 tungsten halogen lamps of 150W each located inside the sphere along the aperture perimeter. The IS realizes 24 levels of spectral radiance in the range $(6\cdot10^4 \div 8\cdot10^8)$ $W\cdot m^{-3}\cdot sr^{-1}$. Radiance homogeneity of the IS at 650 nm is within about 2% over the aperture area, whereas the central-point radiance differs from the weighted average radiance by about 0.2%.

Calibration of IS is carried out by comparison with a high temperature blackbody (HTTB), which temperature varies from 1800K to 3300K. The HTTB temperature is determined through the use of filter radiometers (FR) calibrated in terms of spectral irradiance responsivity against a trap detector directly linked to a cryogenic radiometer. The spectral radiance scale realization accuracy for the range $(2\cdot10^6 \div 8\cdot10^8)$ $W\cdot m^{-3}\cdot sr^{-1}$ is presented in Table 1.

Table 3. Relative standard uncertainties u_c (k=1) of the spectral radiance scale of IS and the relative distribution of spectral radiant power of MS.

λ, μm	0.3	0.6	0.9	1.0	1.5	2.5
u_c(IS),%	1.5	0.5	0.5	0.6	1.0	1.5
u_c(MS),%	1.71	0.33	0.39	0.76	1.76	1.76

The basic components of the MS are a tungsten lamp, focusing optics, a double diffraction monochromator and a mirror collimator with

diameter of 600 mm. For the MS calibration a set of standard detectors is used. The MS realizes the relative distribution of spectral radiant power in the range from 0.001 to 1.0 with uncertainties presented in Table 1.

The LABB with radiating-area diameter of 500 mm and working temperature range from 213K to 453K realizes the spectral radiance scale in the wavelength range from 3.0 μm to 25.0 μm. The LABB is intended for use in a cryogenic vacuum chamber. The LABB the spectral radiance scale is realized by means of comparison with a gallium fixed-point blackbody in the range $(7.8 \cdot 10^{1} \div 7.3 \cdot 10^{7})$ $W \cdot m^{-3} \cdot sr^{-1}$. The uncertainty of the LABB is presented in Table 2.

Table 2. Relative standard uncertainty u_c (k=1) of the spectral radiance scale at the LTBB temperature of 300K.

λ, μm	3.0	6.0	8.0	10.0	12.0	14.0
u_c, %	0.85	0.33	0.24	0.20	0.17	0.15

LABB's radiance homogeneity measured by a detector with a band from 2 μm to 5 μm is within 1.5% at the temperature level of 300K.

The method of "linear quadrature rule" [4] was applied to evaluate the uncertainties of the Earth observation instruments calibration against the standard radiometric facility.

To maintain the uniformity of measurements in the framework GEOSS it's expedient to carry out intercomparisons of national facilities for the Earth observation instruments calibration. Thus, the facility described above will be compared with the similar facilities of other countries.

CURRENT ACTIVITIES

In order to get reliable satellite data both pre-flight calibration and in-flight precise monitoring characteristics of the instruments are essential. It was suggested [2] that within the thermal IR spectral range this task can be solved through the development and the use of space-born reference radiation sources that incorporate the phase transition phenomenon of substances occurring in the relatively low-temperature range. Since then the most prospective substances have been selected on the basis of analysis of relevant data and preliminary ground experiments. Promising results have been obtained for the phase transition phenomenon studies for Ga and the eutectic alloys Ga-In, Ga-Sn, and Ga-Zn in cells with a mass of working substances ~ 100 g. Thus, repeatability values (1σ) of these melting fixed points in a small cell were found to be ≤ 3 mK [5]. The results obtained have made it possible to begin development of the space experiment to investigate the phase transition phenomenon of the above mentioned substances under zero-gravity conditions. By now research facilities required for this purpose has been developed. Meanwhile elaboration of basic design of the super-stable onboard standard IR radiation source incorporating the phase transition phenomenon is in progress. Space experiment with the low-temperature fixed-point blackbody prototype is scheduled. Keeping stability at the level of the order of 10 mK will meet the most stringent requirements of the global climate change monitoring.

In 2006-2008 the international document "Quality Assurance Framework for Earth Observation" (QA4EO) had been developed by the Committee on Earth Observation Satellites' Working Group on Calibration and Validation (WGCV), in partnership with the Institute of Electrical and Electronics Engineers (IEEE). This document contains basic principles of establishing uniformity of measurements in the field of Earth Observation. Since implementation of the QA4EO at the level of national agencies is highly desirable, VNIIOFI originated arrangements to its implementation in Russia by means of developing national normative document harmonized with the QA4EO.

REFERENCES

1. Global Earth Observation System of Systems GEOSS. 10-Year Implementation Plan. GEO 1000. 2005.
2. V.N. Krutikov, V.I. Sapritsky et al., The Global Earth Observation System of Systems (GEOSS) and Metrological Support for Measuring Radiometric Properties of Objects of Observations, Metrologia, 43, 94-97, 2006.
3. http://qa4eo.org/.
4. M.G. Cox, The area under a curve specified by measured values, Metrologia, 44, 365-378, 2007.
5. A. Burdakin, B. Khlevnoy et al., Melting points of gallium and of binary eutectics with gallium realized in small cells, Metrologia, 45, 75-82, 2008.

Travelling SIRCUS calibration of NPP VIIRS

Steven W. Brown[1], Keith R. Lykke[1], Robert A. Barnes[2] and Thomas Schwarting[3], Bruce Guenther[4], Frank DeLuccia[5], Christopher Moeller[6]

[1]National Institute of Standards and Technology, Gaithersburg, MD USA, [2]Science Applications International Corporation, Beltsville MD USA, [3]SigmaSpace Corporation, Lanham, MD USA [4]National Oceanic and Atmospheric Administration, Seabrook, MD USA, [5]Aerospace Corporation, El Segundo, CA USA, [6]University of Wisconsin Madison, WI USA

Corresponding e-mail address: swbrown@nist.gov

Results of recent system-level radiometric tests on the National Polar-orbiting Operational Environmental Satellite System (NPOESS) Preparatory Project (NPP) Visible Infrared Imaging Radiometer Suite (VIIRS) using the NIST Travelling Spectral Irradiance and Radiance responsivity Using uniform Sources (SIRCUS) system are presented. End-to-end absolute spectral radiance responsivity (through the Earth viewport) and absolute irradiance response (through the solar port) measurements were performed. This presentation focuses on the results of the absolute spectral radiance responsivity testing.

INTRODUCTION

Radiometric sensors involved in satellite observations of the Earth in the reflected solar region typically have relatively large entrance apertures to meet mission signal-to-noise requirements. Historically, spectral measurements of sensor band relative spectral responsivities (RSRs) have been done using lamp-monochromator systems. These sources do not have the flux for full-aperture integrating sphere illumination of the sensor. A combination of piece-parts measurements along with broad-band lamp-illuminated integrating spheres are used to provide a calibration of the sensor. The SIRCUS laser systems, with radiant flux levels 3 orders of magnitude or more greater than lamp-monochromator systems, provide the possibility of full aperture integrating sphere-based absolute spectral responsivity measurements of satellite sensor bands.

To evaluate the potential of the new calibration approach for satellite sensors, the NPP Project management group at NASA's Goddard Space Flight Center (GSFC) and the Integrated Program Office (IPO) at the National Oceanic and Atmospheric Administration (NOAA) funded a special test of NPP VIIRS using a portable version of SIRCUS at Ball Aerospace and Technologies Corporation (BATC) in early 2010. This test was performed immediately after the integration of the completed flight instrument onto the spacecraft platform.

The VIIRS sensor was at room temperature; as a consequence, testing was limited to the spectral range from 380 nm to 980 nm. The principal objective of the testing was to demonstrate the capability of Travelling SIRCUS determine the Absolute Spectral Responsivity (ASR) of the VIIRS visible/near infrared bands with an in-band response target uncertainty of 1 % and an out-of-band noise floor less than 10^{-4}. An additional goal of the testing was to provide a data set that could be used to corroborate the previous piece-parts determination of band RSR's.

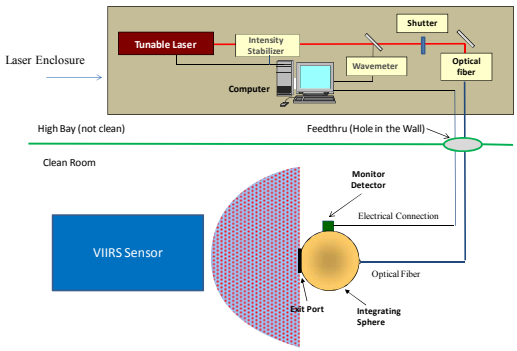

Fig. 1. Schematic diagram of the Traveling SIRCUS setup at BATC.

SETUP

VIIRS is a 22-band sensor with 9 spectral bands in the visible and near infrared. Seven bands have spectral widths less than 40 nm. Labelled M1 through M7 in order of increasing band center wavelengths, their band centers range from 410 nm to 860 nm, approximately,.

A schematic diagram of the Traveling SIRCUS setup at BATC is shown in Fig. 1. The output from a tunable laser system is intensity stabilized and coupled into an optical fiber. The optical fiber runs from the laser enclosure through a small hole in the

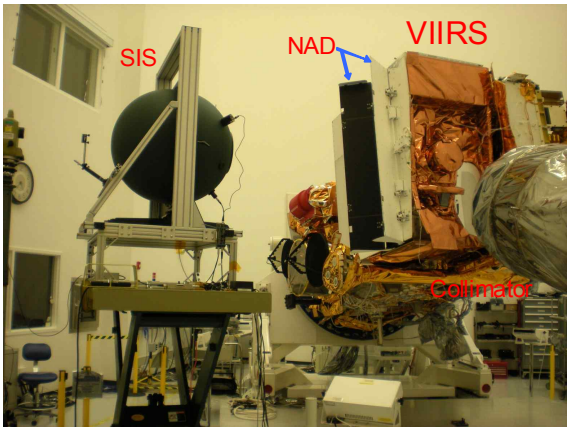

Fig. 2 VIIRS looking at the Integrating Sphere through the Nadir aperture doors (NAD).

BATC clean room wall into a 76.2 cm diameter spherical integrating sphere (SpIS) equipped with a 25.4 cm diameter exit aperture. Two monitor photodiodes mounted on the sphere wall are calibrated for sphere radiance pre- and post-VIIRS testing. Figure 2 shows the SpIS in front of the VIIRS nadir (Earth-viewing) port. During testing, the laser is sequentially tuned through a series of wavelengths while the monitor photodiode signal and the VIIRS signal are recorded.

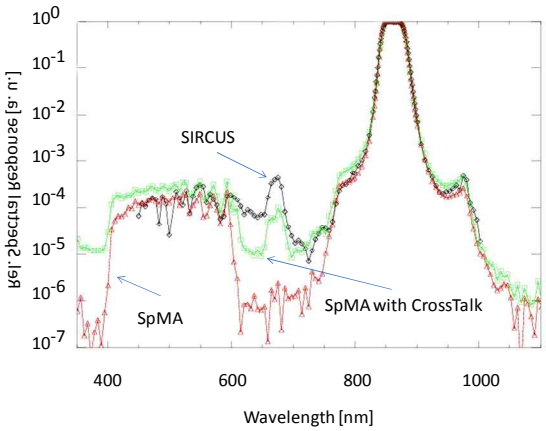

Fig. 3. RSR comparison between the SpMA results and the SIRCUS results.

RESULTS

There are a total of 16 sensors for each band at the focal plane. Fig. 3 compares band-normalized results from Travelling SIRCUS with the previous lamp monochromator-based results (labelled SpMA in the figure) for VIIRS Band 7, detector 8. The data show good agreement between the two approaches down to the 10^{-4} level. Fig. 4 shows detector-to-detector differences in the centroid wavelength of band M7. SpMA again refers to the lamp monochromator-based results. Differences in the centroid wavelength on the order of 1 nm were observed for this Band.

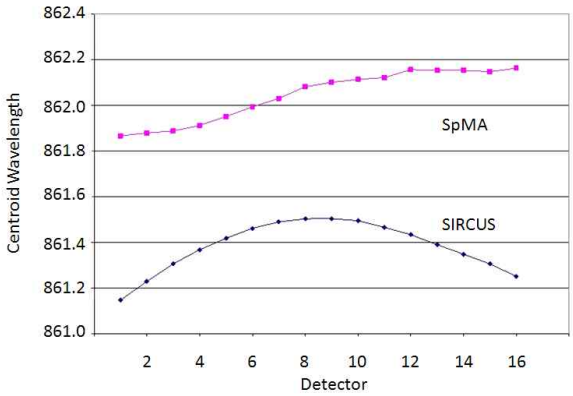

Fig. 4. Comparison of VIIRS band M7 detector-to-detector centroid wavelengths between SpMa and SIRCUS.

CONCLUSIONS

The SIRCUS full aperture measurements of VIIRS ASR provided a great deal of useful information about the sensor performance. The SIRCUS measurements validated the lamp monochromator-based piece-parts RSR. The measurements also alleviated concerns about optical cross-talk due to scattering from the individual channel bandpass filters.

SIRCUS measurements provided the ASR for each band, enabling verification of the VIIRS on-board solar diffuser calibration system.

Finally, while versions of the Travelling SIRCUS have been used at a number of sites for instrument characterization and calibration, this was the first deployment of Travelling SIRCUS to characterize and calibrate an Earth-observing satellite sensor. Consequently, there were a number of lessons learned about the usefulness of the Traveling SIRCUS system for system-level characterization of large aperture systems. These lessons come into play if laser-based systems are used in the future to calibrate Earth-observing sensors.

ACKNOWLEDGEMENTS

The authors wish to thank Robert Lambeck, QSS Group; Craig Kent, Stellar Solutions; Chungsan Lin, Space Dynamics Laboratory; and Thomas Gonzales and the staff at the Ball Aerospace and Technology Corporation, Boulder CO.

The University of Wisconsin Space Science and Engineering Center Absolute Radiance Interferometer (ARI)

Joe K. Taylor[1,3], Henry E. Revercomb[1], Henry Buijs[2], Frederic J Grandmont[2], P. Jonathan Gero[1], Fred A. Best[1], David C. Tobin[1], Robert O. Knuteson[1], Daniel D. LaPorte[1], Richard Cline[1], Mark Schwarz[1], Jeff Wong[1]

[1]*Space Science and Engineering Center, University of Wisconsin-Madison, Madison, USA*
[2]*ABB-Bomem Inc., Quebec, Canada*
[3]*Université Laval, Québec, Canada*
Corresponding e-mail address: joe.taylor@ssec.wisc.edu

A summary of the development of the Absolute Radiance Interferometer (ARI) at the University of Wisconsin Space Science and Engineering Center (UW-SSEC) is presented. This effort is funded under the NASA Instrument Incubator Program (IIP).

INTRODUCTION

CLARREO [1] will measure spectrally resolved radiance from the earth and atmospheric bending of GPS signals related to atmospheric structure (refractivity) as benchmark measurements of long-term climate change trends.

To reduce the time to unequivocally resolve climate trends, IR radiance spectra and GPS refractivity were selected as quantities with high information content that can be measured with high calibration accuracy referenced to international standards provided on orbit (SI-traceable measurements). For the infrared radiance spectra, a brightness temperature accuracy of 0.1 K, k = 3, confirmed on orbit is practical.

The challenge in the IR FTS sensor development for CLARREO is to achieve ultra-high accuracy with a design that can be flight qualified, has long design life, and is reasonably small and affordable. In this area, our approach is to make use of components with strong spaceflight heritage (direct analogs with high TRL) combined into a functional package for detailed performance testing.

THE UW-SSEC ARI

The objective of this effort is to develop and demonstrate the technologies needed to measure IR spectrally resolved radiances with ultra high accuracy for the CLARREO climate benchmark. The effort combines the development of fundamentally new devices including (1) an On-orbit Absolute Radiance Standard (OARS), high emissivity blackbody source that uses multiple miniature phase-change cells to provide a revolutionary on-orbit standard with absolute temperature accuracy proven over a wide range of temperatures; (2) On-orbit Cavity Emissivity Modules (OCEMs), providing a source (quantum cascade laser, QCL, or "Heated Halo") to measure any change in the cavity emissivity of the OARS and calibration reference sources; and (3) an On-orbit Spectral Response Module (OSRM), a source for spectral response measurements using a nearly monochromatic QCL source configured to uniformly fill the sensor field-of-view. The OARS, OCEMs, and OSRM form the On-orbit Test and Validation (OTV) system that is key for maintaining IR measurement traceability to absolute standards on-orbit. These new technologies are combined with the advancement of Dual Absolute Radiance Interferometers (DARI), one of which is the UW-SSEC ARI, providing spectral coverage from 3.3 to 50μm that can be inter-compared to dissect any unexpected systematic errors in overlapping spectral regions.

On-orbit, the UW-ARI would be radiometrically calibrated using views of a dedicated blackbody reference and space. For laboratory testing during the IIP development, the space reference will be replaced by a second dedicated blackbody reference. The FTS will also be designed to minimize potential biases related to non-linear response and polarization effects, allowing the 0.1 K, k = 3 measurement accuracy requirement to be met. On-orbit tests to demonstrate that linearity and polarization characteristics do not change are also planned.

A Gold 45º scene mirror is used to select viewing targets. The target options are the nadir earth view defined to be 0º, standard calibration views of the onboard calibration source at 90º and space at 180º, the OARS at -90º, a second space view for polarization characterization at -135º, and finally the OSRM for ILS monitoring at 135º. The normal

operational concept is very simple. To collect the primary climate record, sequential views of the earth are separated by several samples of the calibration blackbody and the primary space view. Much less frequently, views of the OARS are collected over the full range of earth scene brightness temperatures. The other scenes that are also viewed infrequently include (1) the secondary space view, (2) the OARS with emissivity monitoring sources of the OCEM turned on, and (3) the OSRM.

The calibration advantages of high spectral resolution [2] are very important to achieving CLARREO goals. The spectral resolution for CLARREO (0.5 cm^{-1} unapodized) has been chosen for the information content it provides on the vertical structure of the atmosphere, for the lineshape and position determination, and for this calibration advantage. A very stable metrology laser will be used to make the interferometer spectral calibration highly stable, but the absolute spectral calibration will be derived from atmospheric spectra themselves as has been demonstrated with AIRS [3], S-HIS [4], NAST-I, and IASI. The fundamental physics that determines line positions will not be altered by climate change, and line positions are known with very high accuracy. We have demonstrated the capability to calibrate from the atmosphere with an accuracy exceeding 1 ppm.

The UW-SSEC ARI is comprised of

- Fore and aft optics designed specifically for high radiometric accuracy
- A cube corner, rocking arm interferometer with a diode laser-based metrology system
- A Cooled semi-conductor detector and dewar assembly
- A DTGS pyrolectric detector assembly
- A small mechanical cooler for the semi-conductor detector / dewar subassembly

Each are chosen for their strong spaceflight heritage such that detailed performance testing can be conducted on a system with a clear path to space [5]. For compatibility with an IIP budgets, the electronics are not flight designs.

Testing of the first breadboard will be completed in April 2011. The sensor prototype testing will be conducted April – July 2011. Key test results along with calibration budgets and expected performance will be presented.

SUMMARY

An excellent, low cost, climate benchmark mission has been defined, and the proposed IR measurement requirements are supported by excellent technical readiness. The UW-SSEC ARI and On-orbit Test and Validation (OT/V) module will allow us to demonstrate the technology necessary to measure IR spectrally resolved radiances (3.3 – 50 μm) with ultra high accuracy (< 0.1 K, k = 3 brightness temperature at scene temperature) for the CLARREO benchmark climate mission. The UW-SSEC ARI subsystems have been selected and developed to provide a system with a clear path to space.

REFERENCES

1. National Research Council (NRC), [Earth Science and Applications from Space: National Imperatives for the Next Decade and Beyond], The National Academies Press, Washington, D.C., 64 (2007).
2. Goody, R. and R. Haskins, “1998: Calibration of Radiances from Space”, J. Climate 11, 754-758 (1998).
3. Strow L. L., S. E. Hannon, S. De-Souza Machado, H. E. Motteler, D. C. Tobin (2006), “Validation of the Atmospheric Infrared Sounder radiative transfer algorithm”, J. Geophys. Res. **111**, D09S06, (2006).
4. Tobin, D. C., H. E. Revercomb, R. O. Knuteson, "On-orbit Spectral Calibration of the Geosynchronous Imaging Fourier Transform Spectrometer (GIFTS)", 2003 CALCON Technical Conference, Characterization and Radiometric Calibration for Remote Sensing, Space Dynamics Laboratory / Utah State University, Logan, Utah, 15-18 September, (2003).
5. Taylor, J.K., H.E. Revercomb, P.J. Gero, F.A. Best, D.C. Tobin, R.O. Knuteson, D.D. LaPorte, R. Cline, M. Schwarz, J. Wong, “The University of Wisconsin Space Science and Engineering Center Absolute Radiance Interferometer (ARI)”, Proc. SPIE 7857, 78570K (2010); doi:10.1117/12.869581

Primary Realization of Both Spectral Radiance and Reflectance in the Mid- and Far-Infrared for Climate Change Science Support

Sergey Mekhontsev[1], Leonard Hanssen[1], Steven Lorentz[2], and Joseph Rice[1]
[1]National Institute of Standards and Technology, Gaithersburg MD, USA, [2]L-1 Standards and Technology Inc., New Windsor MD, USA

Corresponding e-mail address: snm@nist.gov

Long term absolute measurements of the Earth spectral radiance in the infrared are essential for climate change modelling and prediction. Proposed climate science missions, such as CLARREO, along with weather sounders, require rigorous pre-flight radiometric calibration, as well as validation of techniques for maintaining traceability to fundamental units in space. This paper provides an update on recent progress in the area of thermal emission metrology standards at NIST, and discusses the techniques and instrumentation under development, which may help to achieve "climate benchmark" data quality for future space missions, as well as support other applications.

BACKGROUND

Understanding of the driving forces of climate change and the role of anthropogenic factors can be enhanced by long -term absolute measurements of the Earth spectral radiance [1, 2]. Measurement requirements include spectral coverage from 3 μm up to 50 μm with radiance uncertainty at the level corresponding to 0.1 K (k=2) expressed in radiance temperature over the duration of the mission. Achieving proven accuracy and traceability of spaceborne measurements requires development of fundamental and reproducible physical standards, which can be used for pre-flight radiometric calibration, as well as validation of techniques for maintaining the traceability in space [3,4].

PROJECT OBJECTIVES

NIST's Fourier Transform Infrared Spectrophotometry (FTIS) and Advanced Infrared Radiometry and Imaging (AIRI) facilities, among other functions, are providing primary national level support for measurements of absolute spectral emissivity and spectral radiance of materials [5] and blackbody sources [6] at near-ambient temperatures and ambient environment. At the same time capabilities of these facilities are limited in temperature and spectral range due to the fact that measurements are performed at the normal laboratory environment.

A new project, aimed at the construction of the Controlled Background Spectroradiometry and Spectrophotometry System (CBS3), will add capability to calibrate targets and blackbodies in the spectral range of 1 μm to 100 μm and over the temperature range of 190 K to 520 K under strictly controlled background conditions and in vacuum or high purity gas (Fig.1).

It is anticipated that upon completion of the project, the facility will support measurements of IR reflectance and emittance of materials, reflectance of

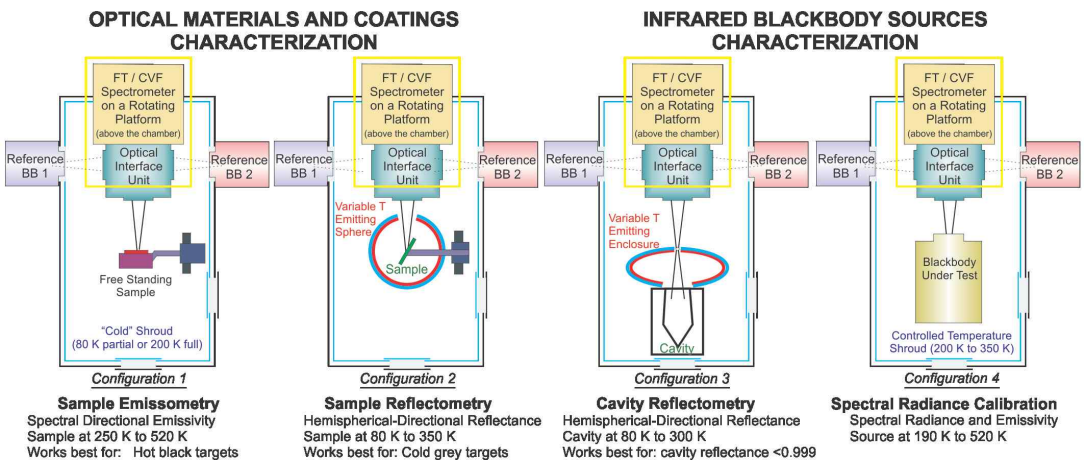

Figure 5. Main configurations of the CBS3 Facility (shown on a simplified top view)

cavities, and spectral radiance of thermal radiation sources. Another function will be support of the NIST Thermal Infrared Transfer Radiometer [7].

RADIANCE SCALE REALIZATION

Capitalizing on already proven approaches and techniques, the spectral radiance realization will be based on complementary sets of fixed point and variable temperature primary blackbodies (Fig. 2).

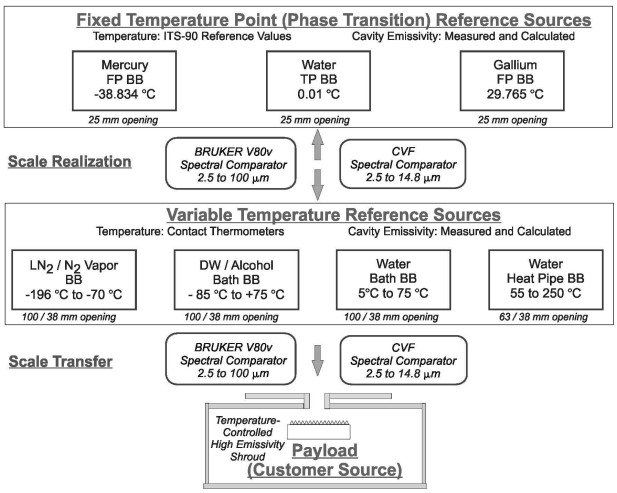

Figure 2. Radiance scale realization

To measure emissivity of primary blackbody cavities in the thermal and far IR, a recently developed experimental laser reflectometer [8] will be used, with addition of far IR lasers and potentially utilizing a synchrotron radiation source.

REFLECTANCE SCALE REALIZATION

A radiometric technique, involving placement of the sample in a high emittance enclosure at a well known temperature [5], will be realized at our facility to derive a directional-hemispherical reflectance scale.

This approach has a number of unique advantages, which are especially useful for characterizing targets at sub-ambient temperatures, as well as for dealing with such difficult issues as port loss component and variable incidence angle reflectometry. This paper will include discussion of several varieties of this method implementation, including Gier-Dunkle and two-temperature techniques [5].

A practically important case of measuring the directional-hemispherical reflectance of blackbody cavities will also be addressed using a variable background technique (Configuration #3 in Fig. 1).

A direct realization of angle-dependent spectral directional emittance is also feasible (Configuration #1 in Fig. 1), although extreme precautions are necessary to avoid contamination of the chamber.

CONCLUSIONS

An approach to the primary realization of spectral radiance, emittance and reflectance, using a suite of primary blackbody sources, a background controlled vacuum chamber, and a spectral comparator, are described. The new CBS3 facility, based on fundamental and reproducible physical standards, will substantially expand the spectral and temperature coverage of existing NIST capabilities,. To our knowledge, the selected approach will enable us to achieve the uncertainty levels necessary for supporting climate missions. At the same time, additional analysis, modelling and prototyping are necessary to produce more reliable uncertainty estimates.

REFERENCES

1. J. G. Anderson, J. A. Dykema, R. M. Goody, H. Hu and D. B. Kirk-Davidoff, Absolute, spectrally-resolved, thermal radiance: a benchmark for climate monitoring from space, J. Quant. Spectrosc. & Rad. Transf., 85, 367–383, 2004.
2. Earth science and applications from space: national imperatives for the next decade and beyond, The National Academies Press, 456 pp., 2007.
3. J. A. Dykema and J. G. Anderson, Infrared Standards in Space, Proc. SPIE 6678, 66781B1-66781B10, 2007.
4. P. J. Gero, J. A. Dykema, J. G. Anderson, and S. S. Leroy, On-Orbit Characterization of Blackbody Emissivity and Spectrometer Instrument Line-Shape Using Quantum Cascade Laser Based Reflectometry, Proc. SPIE 7081, 7081Q1-7081Q11, 2008.
5. L. M. Hanssen, S. N. Mekhontsev., and S. G. Kaplan, NIST Program For The Infrared Emittance Characterization Of Materials, in Proc. of the 29th Intern. Thermal Conductivity Conf. and the 17th Intern. Thermal Expansion Symp., 2008, pp. 523-534
6. S. N. Mekhontsev, V. B. Khromchenko, and L. M. Hanssen, NIST Radiance Temperature and Infrared Spectral Radiance Scales at Near-ambient Temperatures, Int. J. Thermophys. 29, 1026–1040, 2008.
7. J. P. Rice and B. C. Johnson, The NIST EOS Thermal-Infrared Transfer Radiometer, Metrologia 35, 5052509, 1998.
8. L. M. Hanssen, S. N. Mekhontsev, J. Zeng, and A.V. Prokhorov. Evaluation of Blackbody Cavity Emissivity in the Infrared Using Total Integrated Scatter Measurements, Int. J. Thermophys. 29, 352-369, 2008.

Blackbody and Radiometer Cavity Reflectometry for Satellite Instrumentation

Leonard Hanssen,[1] Jinan Zeng,[2] Jeff Morrill, [3] Steven Lorentz,[4] and Harri Latvakoski[2]

[1]*National Institute of Standards and Technology (NIST), Gaithersburg, MD, USA*
[2]*Space Dynamics Laboratory (SDL), Logan UT, USA*
[3]*Naval Research Laboratory (NRL), Gaithersburg, MD, USA*
[4]*L-1 Standards and Technology (L-1), New Windsor, MD, USA*
Corresponding e-mail address: hanssen@nist.gov

We report the results of reflectance measurements of two very different cavities, both designed for space-operated instrumentation. One is an 8 mm diameter aperture radiometer cavity in the Active Cavity Radiometer Irradiance Monitor (ACRIM) instrument for monitoring solar irradiance levels above Earth's atmosphere and the second is a 100 mm x 125 mm rectangular aperture blackbody cavity (the Internal Calibration Target (ICT)) used for calibration of the Cross track Infrared Sounder's (CrIS) in the Joint Polar Satellite System (JPSS). The measurements were made using the NIST Complete Hemispherical Infrared Laser-based Reflectometer (CHILR) instrument and at L-1. The reflectance measurements are used to validate previously estimated performance parameters of the radiometer cavity absorptance and the blackbody cavity emittance.

INTRODUCTION

High accuracy on-board blackbodies are being designed and built to meet the increasing accuracy needs of Earth observing instrumentation. Such blackbodies are typically designed to accommodate the space, weight and power limitations on board a satellite, while still based on cavities designed for high emissivity. Similarly, radiometers based on cavity designs with nearly ideal unity absorption are used for high accuracy solar irradiance measurements. The cavity emissivity or absorptance is generally determined in the design phase from theoretical and ray tracing simulation modelling, using available reflectance and/or emittance data for the cavity coating.

Verification of the calculated or modelled emissivity/absorptance is often a challenge, but important to establishing confidence is the instrument's performance and uncertainty budget. There are several possible means to verify cavity blackbody and radiometer performance. In this paper we employ the CHILR facility at NIST for infrared measurements as well as a setup for visible measurements at L-1. CHILR uses multiple lasers and a gold coated integrating sphere to accurately measure the reflectance of a cavity at several laser wavelengths across the spectrum of interest.

CAVITY DESCRIPTIONS

The Internal Calibration Target blackbody cavity, shown in Figure 1, is formed by flat sections arranged in a trap design. [1] The surfaces are coated with a specular black paint. The entire viewed region of the blackbody is a flat surface tilted at a 45° angle, so that external light is reflected down to a second flat surface, where the light will be retro-reflected, resulting in 3 reflections before exiting the cavity. The entrance aperture has a rectangular shape of approximately 10 cm x 12.5 cm.

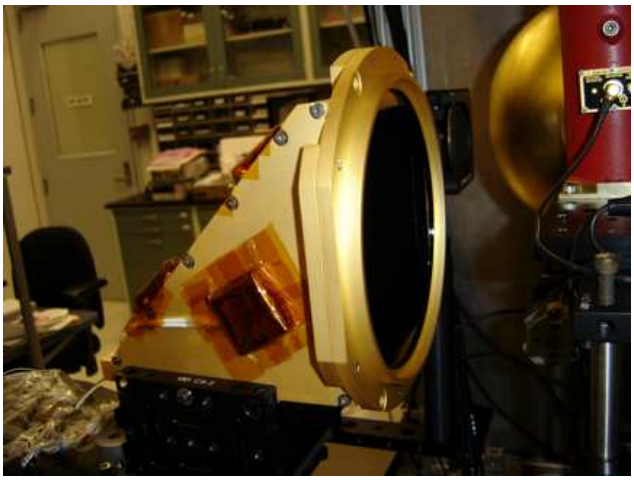

Figure 6. Photo of Internal Calibration Target cavity, side view.

The Active Cavity Radiometer Irradiance Monitor cavity, shown in the right side of Figure 2, has a simple cone shape with a small flared region near its front aperture. [2] The surface is also coated with a specular black paint. The front aperture of the cavity is 13 mm in diameter. However, a smaller

8 mm dia. aperture, shown in the left side of Figure 2, is used to define the irradiated area of the ACRIM radiometer.

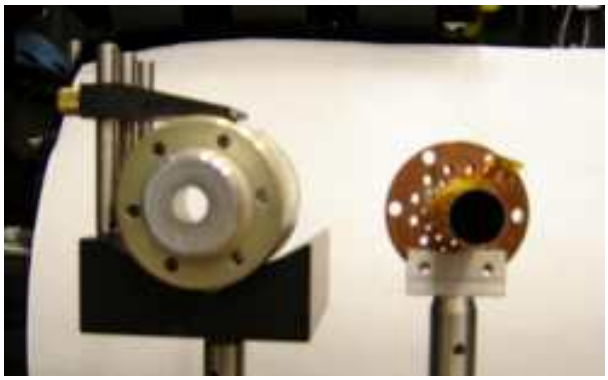

Figure 7. Photo of Active Cavity Radiometer Irradiance Monitor cavity (on right) and aperture assembly (on left).

REFLECTANCE MEASUREMENTS

The CHILR and L-1 systems are used to perform reflectance measurements on the cavities. The general setup involves sending a small diameter laser beam, through a small diameter entrance port of an integrating sphere, where the beam transverses the sphere and enters the cavity mounted onto the reflectance sample port of the sphere. [3] The reflected laser light that leaves the cavity then enters the sphere, where it is distributed over its surface by diffuse reflection, which is sampled by a detector placed at a detector port on the sphere. The signal is compared to that of a second measurement, where the cavity is replaced with a previously calibrated black reflectance standard. A third "empty port" measurement is often required in order to measure and subtract the extraneous signal component due to light scattered by the sphere entrance port and light in the wings of the beam, which reflects directly off the sphere wall or front of the cavity aperture and other exposed structure. The small laser beam size (1 mm to 2mm dia.) enables spatial "mapping" of the cavity reflectance over its full aperture. Integration over the resulting reflectance map is used to obtain effective emissivity values as a function of viewed area.

Each cavity presents a challenge to the measurement systems. In the case of the ICT cavity, its sizable aperture is larger than the CHILR sphere sample port. This means that the sphere cannot capture all of the reflected light from the cavity, requiring an analysis of the reflectance behaviour of the coating and cavity geometry. Corrections are performed to account for the size differences. In addition, the specular interior surfaces' reflectance are polarization sensitive so that separate measurements need to be made with vertically and horizontally polarized incident light, and averaged after corrections are applied. An example map result is shown in Figure 3.

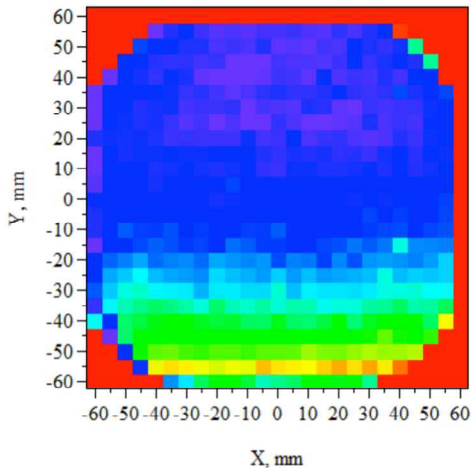

Figure 8. Uncorrected reflectance map of ICT cavity at 10.6 μm, with values ranging from approx. 0.0003 (top) to 0.0008 (bottom) (inverted from photo in Fig. 2).

The ACRIM cavity, in contrast, has a very small opening, especially when assembled with its dedicated aperture. In this case it is difficult to achieve accurate reflectance data near the edge of the aperture due to the high signal levels from the wings of the input beam reflecting off the front of the aperture. This problem was overcome by performing measurements of both the isolated cavity and the assembled cavity – aperture unit.

Effective emissivity and absorptance results on the cavities will be presented at various laser wavelengths across the infrared (ICT and ACRIM) and visible (ACRIM) regions.

REFERENCES

1. R. J. Glumb and D. C. Jordan, "Enhancements to the crosstrack infrated sounder (CrIS) for improved radiometric accuracy," Proc. SPIE. **4131**, 323 – 333 (2000).
2. R. C. Wilson, "Active cavity radiometer type V," Appl. Opt. **19**, 3256 – 3257 (1980).
3. L. M. Hanssen, A. V. Prokhorov, J. Zeng, S. N. Mekhontsev "Evaluation of Blackbody Cavity Emissivity in the Infrared Using Total Integrated Scatter Measurements," Int. J. Thermophys. **29**, 352-369 (2008).

Vicarious calibration of OCM-2 sensor using KAVARATTI Cal/Val site

A.K.Shukla, K.N.Babu, Ajai

Space Applications Centre(ISRO), Ahmedabad-380 015,INDIA.
Email address : akshukla@sac.isro.gov.in

INTRODUCTION

Calibration and Validation is an important aspect in remote sensing to ensure the quality of data received from spaceborne sensors. India's second mission of ocean color observations is realized by launching Oceansat-II satellite on 24th September, 2009. This mission consists of two payloads namely, Ocean Color Monitor OCM-2 primarily for the estimation of chlorophyll-a in the ocean and a pencil beam scatterometer for sea surface wind measurements. Prior to launch of Oceansat-II, a reference site was established successfully off Kavaratti island in Lakshadweep with automated data collection platforms. The data collected over this site has been used to carry out OCM-2 in-orbit vicarious calibration as against its measured radiance at the Top-of-the-atmosphere.

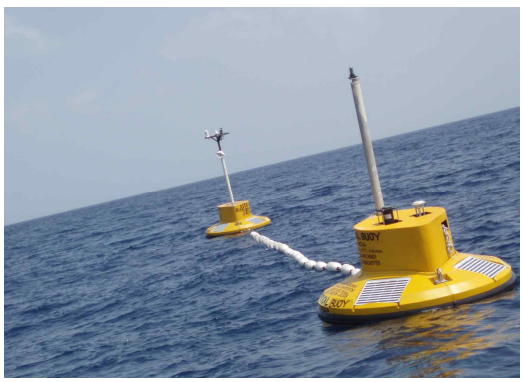

Figure-1 : OPTICAL and MET Buoys

OCM-2 SENSOR

OCM-2 is a 8-band multi-spectral camera operating in the visible & near infrared spectral range with spatial resolution of 360m covering a swath width of 1420km. Each lens assembly contains a CCD of 6000 pixels in the focal plane and the spectral band pass filter in front of the CCD. Out of 6000 pixels, 3730 pixels in the center are used to cover the image field. To avoid sun glint due to specular reflection from the ocean surface, there is provision to tilt the OCM-2 by ±20^{o} in along track direction.

CAL-VAL SITE & IN-SITU DATA

Figure 1 shows a pair of buoys developed and deployed in the open ocean for optical, meteorological, and biological parameter measurements. These two buoys are separated by a distance of 30 meters. The data collection systems are unmanned and fully automated and INSAT-3C satellite transmission technology has been adopted for data transmission & reception. The optical in-situ observations in-air and in-water at three discrete depths over the site are collected synchronously at hourly interval for a duration of 30 seconds. These radiance measurements are used to derive water leaving radiance, *Lw*, remote sensing reflectance, *Rrs*, diffuse attenuation coefficient, *Kd*, etc. The hyperspectral radiometers provide 1nm hyperspectral data from 350-850nm and thus matches the spectral response of each of the eight OCM-2 bands. The *Lw* processing procedure adhere to the ocean optics protocols (Mueller et al, 2003). Three hourly meteorological observations are recorded continuously on the site. The fully automated CIMEL robotic sun-photometer on the CAL-VAL Island laboratory is shown in **Figure 2**. The data from this system is also transmitted via INSAT-3C. Aerosol optical depth is computed from direct-sun observations. The measured sun irradiance and sky radiance values are inverted to derive the aerosol radiative characteristics e.g. single scattering albedo, aerosol phase function, etc. over the site, which in-turn, are used to compute the atmospheric path radiance at the given time over the site.

Figure 2: Sun photometer on the Island

METHODOLOGY & RESULT

Kavaratti site data has been used to compare in-situ derived TOA radiance with OCM-2 measured TOA radiance using forward RT modeling approach. Kavaratti The site measured parameters (from the Optical buoy, Met-buoy and sun photometer) are used in this model for TOA radiance computation. *Lw* is taken from Optical buoy observations. The atmospheric pressure, air temperature, water temperature, and wind speed are taken from the Met-buoy observations. The single scattering albedo, ω, aerosol optical thickness is obtained from the sun photometric observation. The sun and sensor geometry over Kavaratti site is taken from OCM-2 level L1B product. Following Franz et al, 2007, the exclusion criteria applied to the data as the baseline for this study include : chlorophyll-*a* concentration less than 0.25 mg/m^3, AOD (870) less than or equal to 0.21, solar zenith angle less than 70^o, sensor zenith angle less than 56^o. The data which are having band 8 (865nm) radiance greater than 1 μW/cm^2/sr/nm are excluded. Data are also excluded which are contaminated by stray light, and sun glint. We also excluded extreme variation between pixels in the defined box (coefficient of variance greater than 0.1). Here, OCM-2 TOA radiance is the filtered mean value from 5x5 pixels window centered on the geo-location of optical buoy and is taken for the analysis.

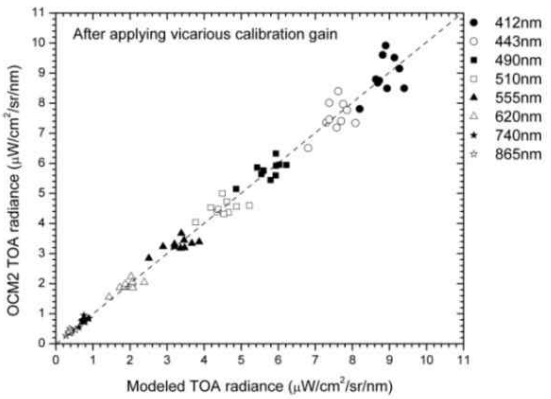

Figure-3 : Matchup of TOA radiances

Figure-3 shows the matchup between in-situ derived TOA and OCM-2 TOA radiance after applying derived vicarious gain. The derived vicarious gain coefficients for all eight spectral bands of OCM-2 using Kavaratti CAL/VAL site are given in Table-1. These gains are applied to generate OCM-2 chlorophyll products operationally.

Table-1: Vicarious gain coefficient

Band	**1**	**2**	**3**	**4**
Gain	1.035	1.003	0.954	1.019
Band	**5**	**6**	**7**	**8**
Gain	1.035	1.104	1.049	0.914

REFERENCES

Franz, B. A., et.al. Sensor independent approach to the vicarious calibration of satellite ocean color radiometry, Appl. Opt. 46, 5068 – 5082. 2007.

Muller, J. L., et.al. Ocean optics protocols for satellite ocean color sensor validation, Revision 4: Introduction, background and conventions. NASA Tech. Memo. 2003-211621, NASA, GSFC, Greenbelt, MD.

Radiometric Characterization of a Hyperspectral Image Projector

J. P. Rice, S.E. Maxwell, H.W. Yoon, and S.W. Brown

NIST Optical Technology Division, Gaithersburg, MD, USA

Corresponding e-mail address: joe.rice@nist.gov

We describe characterization results for the prototype Hyperspectral Image Projector (HIP). This is a novel light source that produces high-resolution programmable spectra and projects them into dynamic two-dimensional images. It has applications in imaging spectrometer radiometric calibration and performance validation, medical imaging, and photovoltaic device characterization. The prototype HIP has a spectral range from 450 nm to 2500 nm, spectral resolution of 2 nm, spatial resolution of 1024 × 768 pixels (XGA), and spectral radiance exceeding that of solar-illuminated top-of-atmosphere (TOA) Lambertian Earth scenes. We present measurements of the HIP output spectral radiance, spectral resolution, spatial uniformity, and temporal stability.

INTRODUCTION

Realistic scenes are spatially and spectrally complex. However, radiometric sources such as lamp-illuminated integrating spheres traditionally used for calibration of sensors such as multispectral imagers and imaging spectrometers are typically spatially uniform and spectrally Planckian. The HIP can be used as a scene projector that overcomes this limitation by enabling the projection of spatially and spectrally complex scenes into such sensors in controlled, laboratory conditions, for radiometric calibration and performance validation [1-4]. Other potential applications of the HIP include use as a digital tissue phantom for performance validation of medical imagers [5], an absolute detector-based source [6], structured microscope illumination, and as a solar simulator for testing photovoltaic devices.

NIST originally demonstrated the concept of the scene projector application of the HIP using simple lamp-based breadboard systems [1-4]. For the past several years NIST has led the development of a high-performance prototype HIP based upon a supercontinuum source. This paper will first provide a short description of this prototype HIP. Then it will describe the measured performance of the HIP in the spectral, spatial, radiometric, and temporal domains. Finally, a few examples of matching the HIP output spectrum to that of realistic scenes will be presented.

HIP DESIGN

Light from a supercontinuum source is fiber-coupled to a collimator, then sent to a spectral engine, where it is split between a visible-near-infrared (VNIR) spectrograph operating from 450 nm to 1100 nm and a short-wavelength infrared (SWIR) spectrograph operating from 1000 nm to 2500 nm. Each spectrograph uses prisms to disperse the spectrum across a digital micromirror device (DMD) having a spatial resolution of 1024×768. The reflected light from the on-state pixels of both the VNIR and SWIR DMDs is re-combined and sent to a spatial engine, either directly or through a liquid light guide (LLG). Light from the LLG can be also used directly or with an integrating sphere, without the spatial engine.

Within the spectral engine, wavelength is mapped to the columns of the VNIR and SWIR DMDs, and the relative intensity at any wavelength is determined by the number of DMD mirrors that are on in a given column. Thus, the output spectral radiance can be programmed to match realistic spectra by simply writing images to the VNIR and SWIR DMDs. The frequency of the display of these binary images can also be varied from DC to 11 kHz.

The spatial engine includes a homogenizer and an optical system that provides uniform illumination of the light onto another DMD, which is in turn at the focus of an output collimator. A sensor under test is focussed at infinity with its optical axis co-aligned with the HIP output collimator, thereby focussing the HIP spatial engine DMD image onto the sensor focal plane array.

When the spectral engine is coupled to the spatial engine to make the full HIP, the spectrally-programmed light globally illuminates the 1024×768 pixels of the spatial engine DMD. Grey scale at this DMD enables realistic 2-dimensional images to be displayed, as in conventional projectors. The difference here is that the time-integrated spectra projected from each spatial engine DMD pixel can be individually controlled, using a compressive projection algorithm described previously, enabling projection of realistic spatial/spectral image cubes into sensors under test [3,4].

CHARACTERIZATION RESULTS

The spectrum that results from turning on a single DMD column of mirrors in the VNIR spectral engine, with all other DMD mirrors off, is shown in Fig. 1. These data were measured with a single-grating-based spectrograph having spectral resolution of 0.24 nm. Similar results were obtained for single-column spectra throughout the VNIR spectral range, always indicating a full-width-half-maximum (FWHM) of less than 2 nm, in accord with ray trace predictions of spectral resolution. Away from this line, the spectral response falls to a value below 10^{-3}.

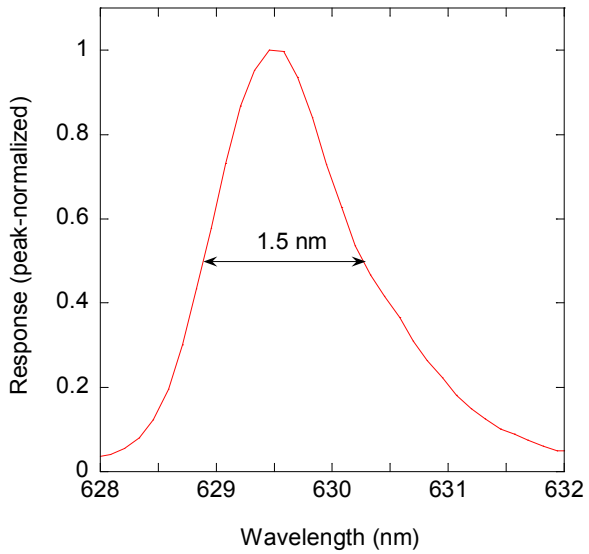

Figure 4. Example of a measured single-column spectrum.

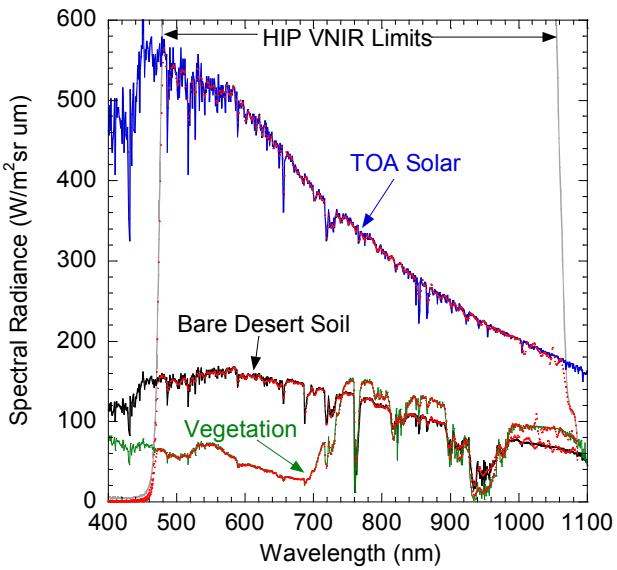

Figure 2. Examples of the HIP VNIR output spectral radiance (red) matched to realistic spectral radiance spectra (TOA Solar:blue; Soil:black; Vegetation:green).

The HIP output can match Earth-reflected solar spectral radiance and even direct solar spectral irradiance. Example spectra for spectrally and radiometrically matching the HIP VNIR output radiance (over its 10.5 mm x 14 mm image area at f/3) to realistic radiance spectra are shown in Fig. 2. Example spectra for spectrally and radiometrically matching the irradiance of the HIP VNIR spectral engine (at its 8 mm diameter, f/1 LLG output) to standard solar irradiance spectra are shown in Fig. 3. In this figures, the overlaid spectra (red) are the HIP output spectra, each matched to its respective desired spectrum, as measured by a calibrated spectroradiometer having 4 nm resolution.

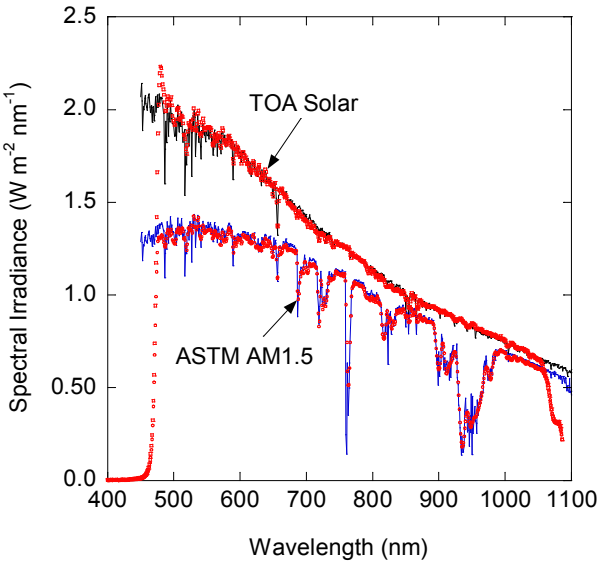

Figure 3. Examples of the HIP VNIR spectral engine spectral irradiance (red) matched to standard solar irradiance spectra (TOA:black; ASTM Atmospheric Mass (AM) 1.5:blue).

REFERENCES

1. J. P. Rice, S. W. Brown, B. C. Johnson, and J. E. Neira, "Hyperspectral image projectors for radiometric applications," *Metrologia* **43**, S61-S65 (2006).
2. J. P. Rice, S.W. Brown, J.E. Neira, and R.R. Bousquet, "A hyperspectral image projector for hyperspectral imagers," *Proc. SPIE* **6565**, 65650C (2007).
3. J. P. Rice and D. W. Allen, "Hyperspectral image compressive projection algorithm," *Proc. SPIE* **7334**, 733414 (2009).
4. D. W. Allen, J. P. Rice, and J. A. Goodman, "Hyperspectral projection of a coral reef scene using the NIST hyperspectral image projector," *Proc SPIE* **7334**, 733415 (2009).
5. S. W. Brown, J. P. Rice, D. W. Allen, K. Zuzak, E. Livingston, and M. Litorja, "Dynamically programmable digital tissue phantoms," *Proc. SPIE* **6870**, 687003 (2008).
6. S. W. Brown, R. D. Saunders, Z. Li, A. Fein, and R. A. Barnes, "An absolute detector-based spectral radiance source," *Proc. SPIE* **7807**, 78070A-1 (2010).

Characterization of the Airborne Compact Atmospheric Mapper during the Global Hawk Pacific Campaign

Matthew Kowalewski[1,2], Scott Janz[2], Xiong Liu[3]

[1]*University of Maryland Baltimore County, Catonsville, MD USA,* [2]*NASA Goddard Space Flight Center, Greenbelt, MD, USA,* [3]*Harvard Smithsonian Center for Astrophysics, Cambridge, MA, USA*

Corresponding e-mail address: matthew.g.kowalewski@nasa.gov

Abstract The Airborne Compact Atmospheric Mapper (ACAM) is a hyper-spectral aircraft instrument capable of performing ultraviolet (UV), visible and near infra-red (VIS/NIR) air quality measurements. These measurements can be used to optimize satellite instrument spatial, temporal, and spectral requirements for such products as: ozone (O_3), nitrogen dioxide (NO_2), aerosols, and ocean color. We present the characterization techniques, results, and uncertainties for ACAM performance as tested for the Global Hawk Pacific (GloPac) campaign. Our evaluation indicates that the primary instrument parameters affecting performance are a 8% wavelength dependent radiometric change in the ultraviolet over the course of the mission, out of band scattered light performance on the order of 0.1%, and non-linearity of 4% corrected to an uncertainty of 0.5% [k=2].

INSTRUMENT DESCRIPTION

ACAM is a small, self contained imaging and hyper-spectral instrument package that requires minimal operator interaction [1]. The instrument contains a nadir viewing high-definition visible imager and two, fiber-fed commercial, crossed Czerny-Turner mini-spectrometers for UV and VIS/NIR measurements. A galvanometer mounted scan mirror illuminates the spectrometer fiber input in order to provide nadir viewing cross-track scanning capabilities. Table 1 summarizes the capabilities of the instrument.

Table 5. ACAM Capabilities Summary

Size	22”x10”x16”
Weight	60lbs
Nadir IFOV	4^o
Nadir FOV	40^o ($+15^o$ to -25^o)
Zenith FOV	24^o
Spectral Range	304 – 520nm (UV) 465 – 900nm (VIS)
Spectral Resolution	0.8nm (UV) 1.6nm (VIS)

The primary science goals of ACAM are to provide cloud and surface information for AURA satellite instruments and associated airborne instrument packages; make remote sensing observations of tropospheric pollutants; provide derived products at high spatial and temporal resolution for use in the formulation of Geostationary Coastal And Pollution Event (GeoCAPE) science and instrument design requirements.

CHARACTERIZATION RESULTS

In order to take advantage of ACAM’s spectral resolution, range and sampling size the trace gas science products are derived using methods outlined in Lui [2] (O_3) and Platt [3] (NO_2, CHCO). These retrieval methods rely on the normalization of the nadir viewing radiances with those measured from the zenith or other reference locations along the flight track.

Aerosols and ocean color products (such as colored dissolved organic material, CDOM) are derived using the directly observed radiances. For these products, errors in the absolute and wavelength dependent radiometric calibration propagate directly into the retrievals.

Radiometric calibration of ACAM was performed prior to, and after the GloPac campaign using a 20” diameter, polytetrafluoroethylene (PTFE) integrating sphere. The PTFE sphere is internally illuminated via four, 150W quartz tungsten halogen (QTH) bulbs; serially powered by a single power supply and current monitored by an external calibrated shunt and meter. A 6” diameter PTFE integrating sphere, ACAM Calibration Source (ACS) was used in the lab and in the field in order to track radiometric changes during the campaign. The ACS is illuminated via a single 150W QTH lamp whose power supply is monitored by an external calibrated shunt and meter.

Figure 1 shows the relative sensitivity change of the instrument’s nadir viewing direction with different colors representing different field calibration dates.

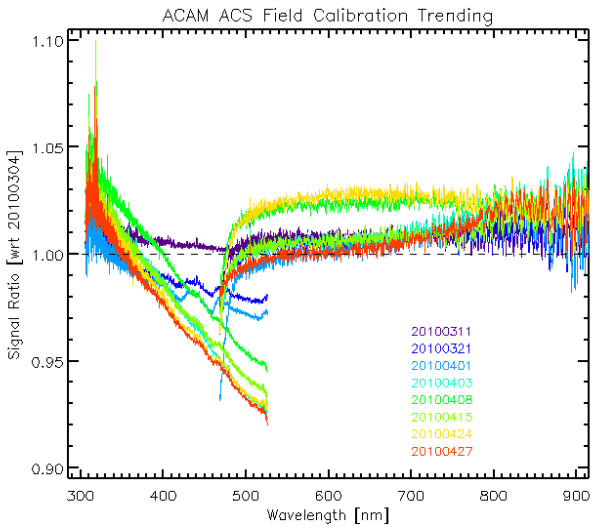

Figure 1. Nadir viewing sensitivity change as a function of wavelength relative to pre-mission lab calibration. Different colors represent different field calibration dates.

Noise in the lower UV wavelengths is due to the relatively low output of the ACS in that region and the enhanced noise in the upper near infrared wavelengths is caused by minor differences in etaloning of the VIS/NIR spectrometer caused by small test to test temperature differences in the back-thinned CCD.

Laboratory calibration transfers of the ACS made before and after the missions have shown the source to be stable to within 1% [k=2] for all wavelengths. Repeat measurements made without breaking instrument setup have shown that an additional 2% [k=2] field set up and repeatability uncertainty contributes to the source's trending accuracy. Therefore, the UV calibration trend dependencies shown in Figure 1 are mostly due to real instrument changes and demonstrate the need for radiometric field calibrations.

Wavelength calibration was performed prior to the campaign using spectral line sources and monitored during each flight using multiple solar Fraunhofer lines observed in the data. Analysis has shown that the wavelength temperature sensitivity of the spectrometers is primarily dependent on the difference between the top and bottom housing temperatures to the order of -0.07nm/ ^{o}C.

Spectrometer scattered light performance was measured using two methods; discrete laser line sources used to build a correction matrix [4] and long pass filters to confirm correction matrix performance. Figure 3 shows example slit functions as measured by two helium cadmium (HeCd) lasers for the UV spectrograph. The functions are located in the spectral regions where O_3 and NO_2 are derived. Nearly four orders of magnitude scattered light rejection exists approximately 20nm away from the peak. Other optical artefacts on the order of 10^{-3} can be seen due to multiple reflections within the system.

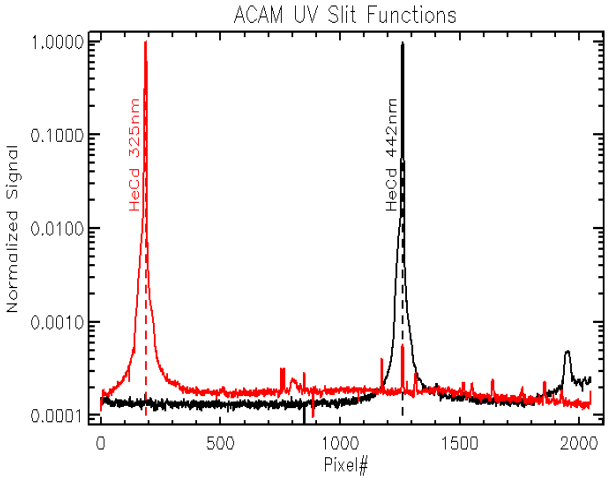

Figure 3. ACAM UV spectrometer slit functions for 325nm and 442nm. Secondary features can be seen due to multiple reflections within the system.

CONCLUSIONS

The ACAM instrument experienced an 8% wavelength dependent change over the course of the GloPac campaign. Spectrometer scattered light performance on the order 10^{-4} has been measured and is in the expected range for this type of miniature spectrometer. In-flight wavelength stability has been observed to be better than 1 Angstrom/^{o}C.

Through the use of a field calibration source, it has been possible to track the radiometric calibration trends with approximately 3% accuracy. The wavelength dependent nature of this change is not typical for UV instrumentation however, it does tend to stabilize slowly over the course of the mission.

REFERENCES

1. M. Kowalewski, S. Janz, Remote Sensing Capabilities of the Airborne Compact Atmospheric Mapper, in Proc. SPIE Int. Soc. Eng, edited by J. Butler, X. Xiong, X. Gu, 74520Q, SPIE, Bellingham, 2009.
2. X. Lui, *et al*., Mapping tropospheric ozone profiles from an airborne UV/Visible spectrometer, Appl. Opt., 44, 3312-3319, 2005.
3. U. Platt, Differential Optical Absorption Spectroscopy, in Air Monitoring by Spectroscopic Techniques, edited by M. Sigirst, 37-84, John Wiley and Sons, New York, 1994.
4. Y. Zong, *et* al, Simple spectral stray light correction method for array spectroradiometers, Appl. Opt., 45, 1111-1119, 2006.

Applying Uncertainties to Ocean Colour Data.

LAVENDER Samantha[1], BARKER Kathryn [1], FANTON D'ANDON Odile Hembise[2], KAY Susan[3], BOURG Ludovic[2], KENT Chris [1], EMSLEY Stephen[1], MCCULLOCH Mike[1], GORYL Philippe[4] and Sentinel-3 L2 Products and Algorithm Team.

[1]ARGANS Limited, Plymouth, Devon, UK
[2]ACRI-ST, Sophia Antipolis, France
[3]University of Exeter, Exeter, UK
[4]European Space Agency, Frascati, Italy

SLavender@argans.co.uk, KBarker@argans.co.uk, CKent@argans.co.uk, SEmsley@argans.co.uk and MMcCulloch@argans.co.uk
oha@acri-st.fr and lb@acri-st.fr
sk284@exeter.ac.uk
Philippe.Goryl@esa.int

Uncertainty analysis is essential for the quality control and validation of satellite data. The results from two linked studies are presented: an investigation into the dependence of Envisat's Medium Resolution Imaging Spectrometer (MERIS) variability on sub-pixel size; determining uncertainties for ocean colour products as part of the Sentinel-3 Level 2 Optical Prototype Processor development.

Quantification of errors in MERIS data at the sub-pixel scale is especially emphasised in optically complex waters. The results of an initial study aimed at quantifying, using ratios of sub-pixel areas to megapixel areas of a number of randomly selected MERIS scenes, and empirically defining the relationship at the MERIS visible bands are presented.

The Sentinel-3 satellite, scheduled to launch in 2013/14, is the third in a series of five space missions within the European GMES programme. The mission aims to produce consistent long-term datasets with both an improved accuracy and reliability; this abstract concentrates on the Ocean Land Colour Instrument (OLCI) that is the MERIS follow-on. The requirement of the Quality Assurance framework for Earth Observation (QA4EO) applies to all products so a method to determine uncertainties must be investigated and applied. Research has focused on several techniques including error sensitivity analysis / propagation where Gaussian noise is added to the input parameters of an equation / processing step that is being evaluated. OLCI simulations will be presented.

Together these two studies look at different aspects of uncertainty with both being important for the subsequent transfer of uncertainties to models that import satellite data.

Calibration and Characterization Advances Applied to the NPP Sensor Suite for Optical Radiation Measuring Devices in Space

B. Guenther[1], Frank DeLuccia[2], James McCarthy[3], Gail Bingham[4], and Scott Janz[5]

[1]National Oceanic and Atmospheric Administration, Seabrook, MD USA, [2]Aerospace Corporation, El Segundo, CA USA, [3]Northrop Grumman Aerospace Systems, Redondo Beach, CA USA, [4]Space Dynamics Laboratory, Utah State University, Logan, UT USA, [5]NASA's Goddard Space Flight Center, Greenbelt, MD USA.

Corresponding e-mail address: bruce.guenther@noaa.gov

The NPP Observatory is scheduled to launch in 2011. This Observatory will be the first flight of a new Observatory class with multiple new, large sensors to launch since the launch of the Earth Observatory System Aura mission that launched in 2002. NPP offers 4 new instruments plus the re-flight of an EOS-heritage CERES mission. The objective of this presentation is to provide a description of the new contributions made to space-based observations by the NPP mission.

INTRODUCTION

The NPOESS Preparatory Project (NPP) spacecraft is fully occupied with science sensors and has completed the Observatory thermal vacuum testing and is ready for launch in the near future. Table 1 identifies the sensors and the recent legacy instruments from which these sensor requirements are derived.

The National Polar-orbiting Operational Environmental Satellite System (NPOESS) was initiated in 1994, and the NPP mission was designated to be the pre-cursor mission for NPOESS was authorized in 2004.

The NPP sensors were built under contract to either in NPOESS Integrated Office (CrIS, OMPS and VIIRS), the NASA-Goddard Space Flight Center (ATMS) and the NASA-Langley Research Center (CERES). The ATMS sensor is a microwave sensor has a measurement capability that covers spectral ranges not normally covered within the meeting structure of the New Developments and Advances in Optical Radiometry conference series. The CERES unit on NPP is the designated FM-5 and is built and tested consistent with the designs and approaches used for the EOS satellite series.

CRIS

CrIS is an infrared Michelson interferometer that has a full sampling range of the interferometer of 0.8 cm. It has 3 bands (LWIR of 650 to 1100 cm^{-1}, MWIR 1210 to 1760 cm^{-1} and SWIR for 2150 to 2550 cm^{-1}) and 9 fields of view on each band. The two point calibration is accomplished with in Internal Calibration Target and cold space and both sources are sampled every 9 s. The primary ground calibration is performed with an External Calibration Target (ECT) and the flight calibration blackbody is the Internal Calibration Target (ICT). The CrIS is large aperture sensor and that leads to special problems for high accuracy blackbody calibrations. The ICT has a 5" aperture. One response to the problems related to a large aperture source involves a separate calibration of the accuracy and the emissivity of the ECT.

There is a critical need to measure performance for the high-accuracy blackbodies. These measurements in turn give greater insight into performance and characterization of the flight sensor. Measurements greatly enhance models to give a complete picture of how the system performs. These measurements reduce the uncertainty of the system and give better science results. The NPOESS (now JPSS) program has worked closely with NIST to do two tests of blackbodies related to the CrIS sensor. The first was to make reflectance measurements of the ECT. The second was to perform characterization measurements of the ICT to better develop the on-board re-calibration capability.

The absolute reflectance and radiance of the ECT was measured using NIST's TXR transfer radiometer. The TXR is NISTs working transfer radiometer and holds the NIST calibration working standard. The ECT test includes multiple viewing angles of the ECT to derive angular components of the reflectance.

The CHILR (Complete Hemispherical Infrared Laser-based Reflectometer) was used to measure blackbody

emissivity for the ICT. Measurements were made to characterize blackbody emissivity at multiple incidence angles of the input laser, multiple rotation angles of the blackbody cavity, and multiple laser wavelengths; resulting in a more complete understanding of the overall blackbody performance. We have worked with NIST to develop some of the testing procedures that are being used to better understand the spectral emissivity of the CrIS ICT.

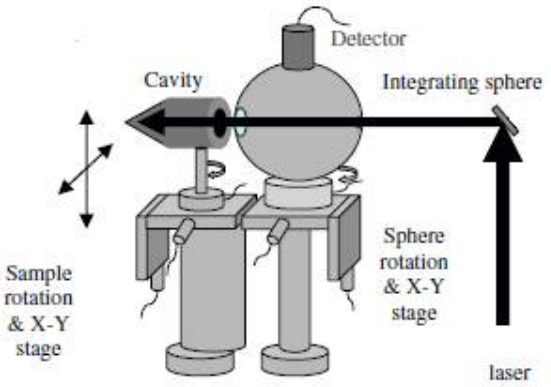

Figure 1. CHILR (Complete Hemispherical Infrared Laser-based Reflectometer) is a NIST apparatus to measure blackbody emissivity.

OMPS

The Ozone Mapping and Profiler Suite performs the nadir mapping measurements with a CCD array, where spectral sampling and along-track spatial resolution are mapped onto the two dimensional CCD array. Goniometric mapping of diffuser response will be provided.

VIIRS

The contributions for VIIRS calibration are made in the reflected solar bands (RSB) covering the spectral range of 0.4 to 2.5 µm. Four major additions have been made to the testing of the VIIRS-MODIS class of sensors. The main test and test result reported here is improved polarization sensitivity testing.

The third test of note is the development and application of a test for residual polarization sensitivity in the VisNIR from 0.4 to 0.9 µm. The polarization testing will be covered in this presentation.

There are a total of 16 sensors for each band at the focal plane on VIIRS in the moderate resolution bands on the VisNIR focal plane. The spacing of the bands on the focal plane is much tighter for VIIRS than was the case for MODIS, and the integrated filter assembly has a demonstrated filter spray function that leads to appreciable spectral cross-talk in these bands. We found non-uniform polarization sensitivity across the detectors in the bands, and then that non-uniformity was eliminated when we placed a block filter into the setup to reduce sensitivity to filter scatter (which is known to change with state of polarization of incident signal)

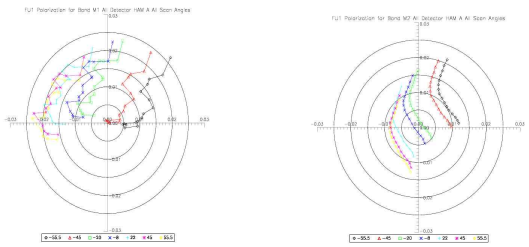

Figure 2. VIIRS polarization sensitivity for band M2 (0.443 µm) A-side of Half Angle Mirror without and with long wavelength blocking filterr.

The figure is a polar plot and represents the results of a fourier filtering of the measured data. The degree of linear polarization is represented by the distance from the center of the graph, and phase is represented by the orientation around the polar plot from the vertical in the curve.

CONCLUSIONS

The testing of the NPP sensors has created several important advances in radiometric testing of space-borne devices. This presentation will bring all those advances together in a single place for the community to exploit in future opportunities. Brief references are provided for the advances that continue in the development stage and more extensive discussions are contained here and other materials at this Conference for the testing that is sufficiently mature to be used directly by other investigations.

Vicarious Calibration of the IKONOS Earth Observing Sensor Using The Specular Array Radiometric Calibration (SPARC) Method

Stephen Schiller, John Silny
Raytheon Space and Airborne Systems
El Segundo, CA
&
Martin Taylor
GeoEye Inc.
Thornton, Co

Physics-based exploitation of image data from electro-optical remote sensing systems requires knowledge of the accuracy, stability and repeatability of the sensor's radiometric response. Vicarious calibration methods, using ground based targets, provides a powerful approach to obtaining this knowledge by evaluating performance under true post launch operational conditions for both the sensor and target of interest.

The standard reflectance-based vicarious calibration method has proven to be effective at delivering accurate at-sensor radiance knowledge. However, in general, the method explicitly relies on using large natural uniform surfaces (i.e. desert playa) and extensive surface and atmospheric ground truth collected coincident with the sensor acquisition.

For high spatial resolution airborne and orbiting sensors, bright sub-pixel intensity sources (watts/str) become a useful alternative. Radiometric performance characterization is achieved by providing a known at-sensor irradiance spectrum from a small target. Such calibration references can be created using specular reflectors producing point sources with a controlled upwelling intensity traceable directly to the solar spectral constant.

A new vicarious method by which to perform in-flight spatial and radiometric calibration of satellite and airborne earth observing radiometers will be described in this presentation with application to GeoEye's IKONOS sensor. The Specular Array Radiometric Calibration (SPARC) method uses spherical convex mirrors to create a collection of ground-based "solar stars" with well defined radiometric properties directly traceable to the exo-atmospheric solar spectral constant.

The specular reflectors are deployed as two separate target groups. The first is an array of single mirrors, each with different pixel phasing, used to oversample the sensor's point spread function (PSF). The second is a set of panels consisting of multiple mirrors designed to stimulate detector response of the sensor under test with known at-sensor radiance. The combination provides a spatial characterization that supports radiometric analysis of small targets. The capability achieves improved accuracy, repeatability and traceability compared to other in-flight vicarious techniques because of reduced uncertainties in target reflectance, atmospheric effects, and temporal variability. The only ground truth needed, for the prediction of at-sensor radiance is the measurement of atmospheric transmittance with a sun photometer. Validation of the technique is presented based on multiple collects by IKONOS of SPARC targets over a five month period in 2009. The analysis includes a direct comparison of gain coefficients for the multispectral bands derived by other investigations utilizing reflectance-based vicarious calibration methods.

Recent Surface Reflectance Measurement Campaigns With Emphasis on Best Practices, SI Traceability and Uncertainty Estimation.

Dennis Helder[1], Kurt Thome[2], Dave Aaron[1], Larry Leigh[1], Jeff Czapla-Meyers[3], Nathan Leisso[3]

[1]*South Dakota State University, Brookings, SD*
[2]*NASA Goddard Space Flight Center, Greenbelt, MD*
[3]*University of Arizona, Tucson, AZ*

A significant problem facing the satellite calibration community is the knowledge of the uncertainties associated with fundamental measurements, such as surface reflectance, used to derive calibration estimates. This paper reports on a recent field campaign that incorporated an experimental design to isolate estimate common uncertainties within and across calibration groups and do so in an efficient, cost effective manner using simple spectrally flat targets in a round robin exercise.

In the past year two field campaigns have been conducted with a primary goal of developing best practices for surface reflectance measurement as applied to calibration of remote sensing satellite VNIR and SWIR systems. In addition, these campaigns have emphasized traceability of measurements to national laboratories, such as NIST and NPL, as well as the estimation of measurement uncertainties. The first campaign was conducted in Turkey in August 2010 with ten international teams participating. During this campaign measurements of instrument calibrations were conducted in the laboratory, as well as in the field. In addition, surface reflectance measurements were made by all teams over a 10 day time period at the CEOS Landnet site known as Tuz Golu which is operated and maintained by Tubitak Uzay, the Turkish space agency. Tuz Golu is a large lake in central Turkey that partially dries out in the summer months of July and August. The dry lake bed is composed primarily of salt crystals and forms a very bright target in the VNIR that is highly suitable for satellite calibration. Results from this campaign are being documented at the time of this writing and will be available for discussion at the time of the NEWRAD 2011 meeting.

Based on the Tuz Golu field campaign experience, a subgroup of participants developed a field campaign on a smaller scale designed to take the lessons learned from Tuz Golu and apply them in an efficient manner to achieve the same set of goals. In this campaign, teams from NASA Goddard Space Flight Center, South Dakota State University and the University of Arizona were hosted on the University of Arizona campus to conduct both laboratory calibration and field campaigns. Combined, these three teams have over 40 man-years of experience in satellite radiometric calibration which was applied to optimize calibration accuracy, minimize uncertainties, as well as minimize cost of obtaining surface reflectance measurements.

Figure 1. Calibration targets (tarps), instruments (ASDs and Labsphere panels), and participants.

Similar to the Tuz Golu campaign, the Tucson campaign began with laboratory calibration of instruments from each team which included spectroradiometers from Analytical Spectral Devices (ASDs) and Labsphere calibration panels. All laboratory calibration was conducted with NIST primary standards. Data from these calibrations is being analyzed at the time of this writing with results will prsented at the the NEXRAD conference indicating the differences between instruments and their uncertainties.

Following laboratory calibration, multiple targets were deployed on the University of Arizona campus mall as shown in Figure 1. Primary targets consisted of three Tracor tarps with reflectances of

2%, 8%, and 48%. In addition, concrete and grass targets were also utilized to represent common targets of opportunity that are often used in satellite calibration field campaigns. The spectral signatures of these targets are shown in Figure 2. The figure clearly illustrates the flat spectral response that is possible with the Tracor tarps. Use of this type of target can minimize errors due to spectral signature and allow better separation of error sources in data analysis. Data were collected from these targets on two consecutive dates with multiple collects at the same sun angles.

The experimental design of the Tucson field campaign allowed collection of test data with varying reflectance, sun angle, calibration panels, ASDs, and differing fields of view. As a result, these data will be analyzed to isolate the effects of each of these variables to estimate their uncertainties. Initial analysis is focused on internal consistencies from each group. For example, each group will analyze their data sets with all of the other variables fixed. Multiple data sets collected from each target provide estimates of surface reflectance and uncertainties at each wavelength. These analyses will provide information on consistency of measurement due to instrumentation and operators with minimal influence on targets and sun angle. Following this analysis, intergroup comparisons of surface reflectance will be conducted. Data will be analyzed at two different sun angles, as well as at multiple tarp reflectances. These comparisons will illustrate the ability of differing groups to reproduce the same measurements, and is a fundamental concern for consistent calibration of satellite imagers.

The results of these analyses will be presented with emphasis on overall uncertainties, including both Type A and Type B. Comparisons of these results to those from Tuz Golu will also be presented, particularly with respect to data produced by the SDSU group who participated in both campaigns. The ability for multiple groups to produce consistent measurements will be emphasized as a fundamental limitation on overall precision and accuracy possible from ground-based vicarious calibration methods.

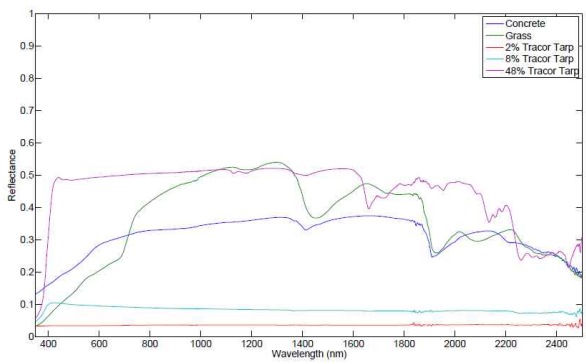

Figure 2. Spectral signature of targets. Note exceptional flat response of Tracor tarps past 1600 nm.

Calibration of the relative spectral radiance responsivity of EO instruments using grating monochromators: Problems and solutions

E. Theocharous[1] and M. Caldwell[2]

[1]*National Physical Laboratory, Hampton Road, Teddington, TW11 0LW, UK*
[2]*STFC Rutherford Appleton Lab Space Dept., DIDCOT, OX11 OQX, UK*
Corresponding e-mail address: e.theo@npl.co.uk

We discuss how grating monochromators can be used for the relative spectral radiance responsivity calibration of Earth Observation instruments, and in particular the three Broad Band Radiometers (BBR)s due to fly on the EarthCARE space mission. While grating monochromators offer very high wavelength tunability (300 nm to 24 μm), their output must also be able to overfill the spatial and angular Field of View (FoV) of the test instruments. We discuss how the selection of the appropriate optics can fulfil these conditions and describe the feasibility tests which have already been completed at NPL on the calibration of the BBRs. The use of a grating monochromator as a wavelength selector for this type of calibration introduces additional, less obvious, problems which must also be overcome. This presentation will discuss these issues and identify methods of overcoming them.

INTRODUCTION

The majority of Earth observation (EO) instruments are being used to measure the Earth's radiance. The calibration of the relative spectral radiance responsivity of these instruments requires a monochromatic source which can be tuned over the wavelength range of interest. The source size must also be large enough to overfill the instrument FoV both spatially and angularly. Although laser illuminated integrating sphere sources are available, they have very limited wavelength coverage due to the narrow tuning range of available lasers. Furthermore, the large loss introduced by integrating spheres means that these sources struggle to achieve the spectral radiance levels required for the calibration of some EO instruments, particularly those which observe the total radiance from the surface of the Earth or the top of the clouds.

Although grating monochromators are widely used in spectral radiant power responsivity calibrations [1], and less frequently in spectral irradiance responsivity calibrations, their application in the calibration of radiance instruments has been hindered by the limited area over which they emit quasi-monochromatic radiation (limited by the area of the monochromator exit slit), and by the limited angular extent of the emission (limited by the f/number of the monochromator).

NPL was asked to calibrate the relative spectral radiance responsivity of the three BBRs [2] due to fly on the EarthCARE mission [3] in 2013. Each BBR consists of a linear array (3 mm by 0.1 mm) of 30 pixels, each 100 μm by 100 μm in area and arranged in a vertical configuration, and a telescope of 67 mm focal length. Each BBR has a 30 mm by 30 mm aperture located in front of the telescope.

For the calibration of the BBRs, the entrance aperture of the telescope can be overfilled by the output of the monochromator, using the appropriate optic, e.g. an Off Axis Parabolic (OAP) mirror. However, overfilling the entrance aperture of the telescope is only one requirement. Overfilling the instrument FOV for all the pixels of the detector array presents a harder task.

The choice of the focal length of the collimating mirror is critical. Choosing a collimating mirror with a short focal length (e.g. 150 mm focal length) results in a longer length of the array (i.e. a larger number of pixels) being illuminated for a particular length of the monochromator exit slit. It also results in higher radiant powers reaching each pixel, something which is highly desirable in the calibration of BBR-type instruments. However, the use of a short focal length mirror results in difficulties in overfilling the aperture and FoV of the instrument under test. Conversely, choosing a collimating mirror with a long focal length results in fewer array pixels being illuminated and lower radiant powers reaching the illuminated pixels. However, the use of a long focal length collimating mirror (e.g. 600 mm focal length) increases the number of pixels which can have their FoV fully illuminated. The selection of a 300 mm focal length OAP mirror to collimate the output of the monochromator was a compromise. This mirror

allows the 30 mm by 30 mm aperture of the BBR instruments to be overfilled by the collimated beam. The use of the same collimator also means that the illuminating beam will overfill the FoV of 20 pixels of the detector array[1] without under-filling the 30 mm by 30 mm telescope aperture. The illumination of at least 20 pixels on the BBR array would require the exit slit of the monochromator to be at least 10 mm in length, something that is easily achievable. This, in turn, implies that two calibration runs will be sufficient to cover all 30 pixels of the array. Using a 1.6 mm wide monochromator exit slit means that a 360 μm wide area will be illuminated in the plane of the array. This is more than sufficient to overfill the width of the array (100 μm wide) as well as the horizontal FoV of the pixels.

Figure 1 shows the layout of the arrangement used in a feasibility study to calibrate the relative spectral radiance responsivity of the BBRs. Radiation emerging from the exit slit of the monochromator is collimated using a 300 mm focal length OAP mirror, M1. The collimated beam is steered using a plane mirror, M2, and directed into the vacuum chamber containing the BBR under test using a second plane mirror, M3. A second OAP mirror, M4, which is mounted on a PC-driven linear translation stage, is periodically inserted into the beam so it focuses the collimating beam onto the active area of the reference detector. This means that the standard software used by NPL for spectral radiant power responsivity calibrations [1] can be used for the calibration of the BBRs.

The vacuum chamber uses a CaF_2 window to cover the 300 nm to 8 μm wavelength range, while a KRS-5 window is used to cover the 8 μm to 40 μm wavelength range. A 17.4 Hz modulation frequency is used for all BBR calibrations to simulate the chopping frequency of the BBR chopper [2].

The NPL infrared spectral responsivity measurement facility [4] will be used to cover the 1.3 μm to 24 μm wavelength range, while the NPL UV/Vis/NIR spectral responsivity measurement facility will be used to cover the 300 nm to 1.6 μm wavelength range. Spot measurements using band-pass filters will extend the wavelength range of calibration to 40 μm.

[1] The distance between the 300 mm focal length collimator and the aperture of the BBR is approximately 1 m.

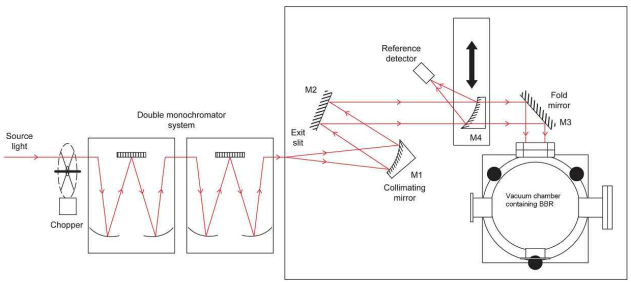

Figure 1: Layout of the arrangement used to calibrate the relative spectral radiance responsivity of the BBRs.

When a grating monochromator is used as a wavelength selector for this type of calibration, it introduces additional serious calibration problems which must also be overcome. These include variations in the transmission of the monochromators due to changes in the effective aperture of the diffraction gratings due to rotation, spectral variations across the width of the monochromator exit slit and variations in the spectral irradiance along the length of the monochromator exit slit. This presentation will discuss these issues and describe methods which can overcome them.

In conclusion, grating monochromators can be used to calibrate the relative spectral radiance response of instruments. They offer wide wavelength tunability, although care is needed to ensure that their output overfills the spatial and angular FoV of the test instruments. A number of other calibration problems must also be overcome.

REFERENCES

1. E. Theocharous, The establishment of the NPL infrared relative spectral response scale using cavity pyroelectric detectors, Metrologia, 43, S115-S119, 2006.
2. K. Wallace, N. Wright, K. Ward and M. Caldwell, The BroadBand Radiometer on the EarthCARE Spacecraft, Proc. SPIE, 7453, Infrared Spaceborne Remote Sensing and Instrumentation XVII, 2009.
3. R. Gelsthorpe, A. Heliere, A. Lefebvre, J. Lrmanczyk, E. Mateu and K. Wallace, EarthCARE and its payload, Proc SPIE, 7152, Remote Sensing of the Atmosphere and Clouds II, 715207-1, 2008.
4. E. Theocharous, F. J. J. Clarke, L. J. Rogers, N. P. Fox, Latest measurement techniques at NPL for the characterization of infrared detectors and materials, Proc. SPIE, 5209, 228-239, 2003.

The calibration of earth observe image using BRDF model

Liu Zilong[1,2],Lian Yusheng[2], Wang yu1, Liao Ningfang[1]

[1]*National Institute of Metrology, Beijing 100013, China*
[2]*Beijing Institute of Technology, Beijing 100081,China*
Corresponding e-mail address: liuzl@nim.ac.cn

A new BRDF model of earth objects is established for the calibration of earth observe image by the national metrology equipment. This model colligate the solar radiance、the atmosphere status、the object type and the space camera parameter, etc. The output data of this model is the enter radiance data for the space camera. The earth observe image can be appeared more "true" through this calibration. A kind of ground glass for architecture is measured and the correspond remote sensing image is simulated. After calibrated, the chromatism of this image is improved by 2 and the luminance contrast of that is improved by 3.

Keyword: BRDF earth observe image calibration chromatism

INTRODUCTION

The objects of earth observe receive different radiance and emit different wavelength light at the same time. BRDF (Bidirectional Reflectance Distribution Function) combine these incident light、reflect light and scatter light in one variable and it is the best variable to describe the space radiance performance of objects. The complex BRDF model for earth observe objects is based on the BRDF fundament equation, colligate the solar radiance、the atmosphere status、the object type and the space camera parameter, etc. In this model, the solar radiance and it's change through atmosphere are considered in the incident variable of BRDF, and the proximity effect of atmosphere and the parameter of space camera are considered for the reflect variable of BRDF, for example, the BRDF performance of aerosol.[1] Then the BRDF value of some typical objects are measured and calibrated. The absolute BRDF value are achieved and simulated using the complex BRDF model. Thus the earth observe image which is calibrated is achieved. The whole procedure is shown in figure 1.

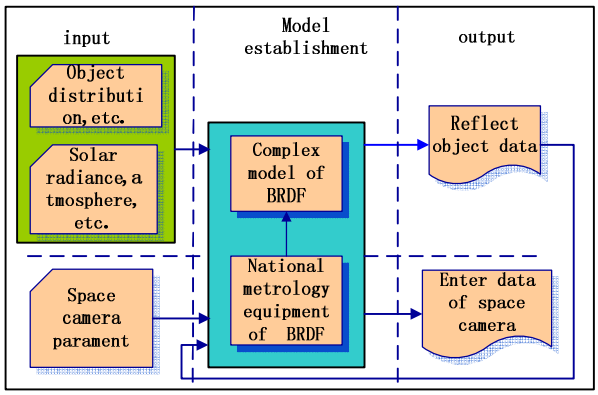

Figure 9. The establish procedure of the complex BRDF model for earth observe

THE ESTABLISHMENT OF THE COMPLEX BRDF MODEL

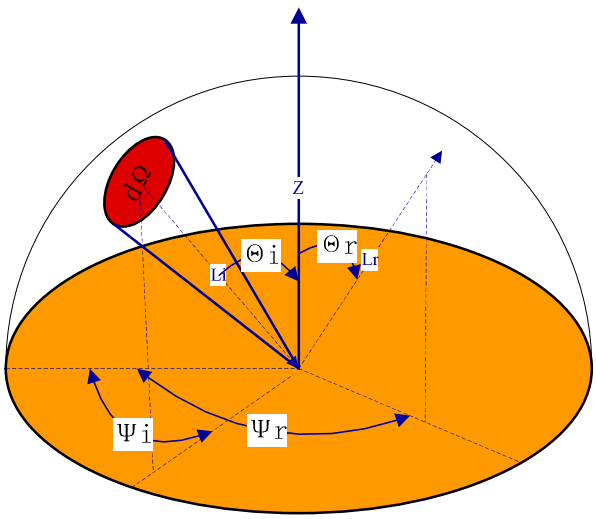

Figure 2 The schematic of BRDF

1) The basement equation of the complex BRDF model is established by the definition of BRDF as shown in Eq.1 which defined as the ration of the reflect radiance and the incident irradiance on the appearance of the objects.[2] The Eq.1 is true in the controllable incident solid angle $d\Omega_i$, which is shown in figure 2.

$$f_r(\theta_i,\varphi_i,\theta_r,\varphi_r)=\frac{dL_r(\theta_i,\varphi_i,\theta_r,\varphi_r)}{dE_i(\theta_i,\varphi_i)}=\frac{L_r(\theta_r,\varphi_r)}{E_i(\theta_i,\varphi_i)} \quad (1)$$

2) The calibration equation of this BRDF model is est ablished by using the national metrology equipment. A operator K_f which named BRDF absolute calibr ation operator is defined based on Eq1 as shown belo

w.[3]

$$K_f = \frac{1}{L_r(0,0,180,0)\Omega_r}$$

K_f is achieved by measuring the incident radiance at the vertical angle and the corresponding solid angle. Then the BRDF absolute calibration model can be represented as shown in Eq2.

$$f(\theta_i,\varphi_i,\theta_r,\varphi_r) = K_f \frac{L_r(\theta_i,\varphi_i,\theta_r,\varphi_r)}{\cos\theta_i} \qquad (2)$$

3) The incident solar radiance is changed when it pass the atmosphere. So the incident radiance of the earth objects includes the direct solar light and the scatter solar light. All these lights can be reflect by the earth objects.[4] The direct solar light can be calculated according to the distance between the earth and the sun - r and the solar constant- $E_0(\lambda)$ as shown in Eq3.

$$E_r(\lambda) = (r/r_0)^2 E_0(\lambda) \qquad (3)$$

This solar light irradiate at zenith angle σ_s, the transmit ratio of the atmosphere is $\tau_i(\lambda)$,then the solar radiance which reach at the earth object- $E_s(\lambda)$ can be represented as shown in Eq4.

$$E_s(\lambda) = E_r(\lambda)\tau_i(\lambda)\cos\sigma_s \qquad (4)$$

The scatter solar light may be scatted and reflected by the atmosphere many times. These scatter solar lights considered only once because other lights are little and the influence is also limited. Then the scatter incident radiance $E_d(\lambda)$ is represented as shown in Eq5.

$$E_d(\lambda) = \int_{\varphi=0}^{2\pi}\int_{\delta=0}^{\pi/2} L_d(\delta,\varphi,\lambda)\cos\sigma\sin\delta d\sigma d\varphi \qquad (5)$$

$L_d(\delta,\varphi,\lambda)$ represent the radiance on the earth object from the scatter solar light.

Thus the BRDF absolute model through reflection by the earth object is established as shown in Eq6.

$$L_r(\theta_i,\varphi_i,\theta_r,\varphi_r,\lambda) = [E_s(\theta_i,\varphi_i,\lambda) + E_d(\lambda)]f(\theta_i,\varphi_i,\theta_r,\varphi_r,\lambda) \qquad (6)$$

4) The absorption of the atmospheric molecules and aerosol will influent the radiance procedure for the existing of atmosphere and aerosol. [5] So the proximity effect of the atmosphere should be considered. All these influence can be integrated as one weight function which as shown in Eq7 for earth object unit (x,y).

$$F(x,y,\lambda) = \int_0^H \frac{\beta(\lambda)\rho(\theta)\cos\theta\tau_i(x,y,z,\lambda)\tau_r(z,\lambda)}{4\pi(x^2+y^2+z^2)\tau(\lambda)}dz \qquad (7)$$

$\beta(\theta)$ represent the sum of the scatter coefficients of the atmospheric molecules and the aerosol. $\rho(\theta)$ represent scatter phase function.

$F(x,y,\lambda) = \frac{1}{dxdy}$ when $x = y = 0$.

Thus the BRDF absolute model including the proximity effect can be represented as shown in Eq8.

$$L(\lambda) = [E_s(\lambda) + E_d(\lambda)]\tau_r(\lambda)\iint f(x,y,\lambda)F(x,y,\lambda)dxdy \qquad (8)$$

Eq8 is the final model of the complex BRDF model for earth observe.

MEASUREMENT AND SIMULATION BY CALIBRATION

The BRDF of a kind of ground glass for architecture is measured using the national metrology equipment. θ_i represent incident zenith angle, φ_i represent azimuth angle, θ_r represent reflect zenith angle, φ_r represent reflect azimuth angle. Some typical measurement angles are selected as φ_i =0°, φ_r =180°, θ_i is changed between 20°and 85°, θ_r is changed between 85°and - 85°. The results of the absolute BRDF measurement are shown in Fig3(wavelength=512nm).

Furthermore, the BRDF in different reflect azimuth angles φ_r are measured when φ_i =0°and φ_i =60°, φ_r =60°and φ_i =85°, φ_r =85°. The results of these absolute BRDF measurement are shown in Fig4 (wavelength=512 nm).

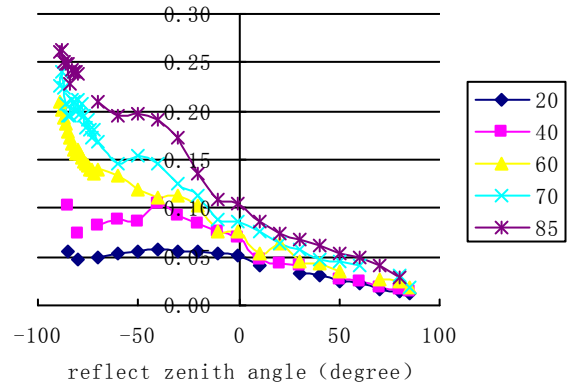

Figure 3 The absolute BRDF curve 1 of a kind of ground glass for architecture

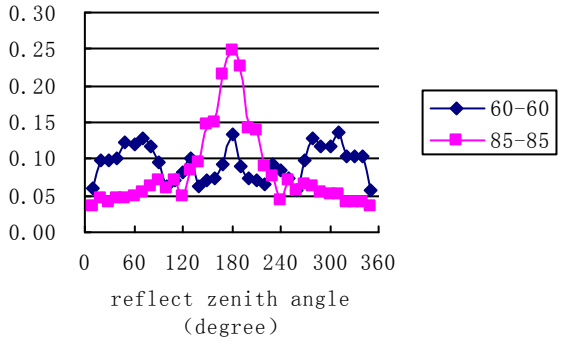

Figure 4 The absolute BRDF curve 2 of a kind of ground glass for architecture

The performance of this ground glass for architecture when zenith angle and azimuth angle change separately is achieved through these two kind of measurements. All these data are the input of the simulate procedure and the simulated image with calibration is achieved. Fig5 show the image of the ground glass architecture before calibration and the same image which is calibrated by the BRDF absolute model and corresponding measurement data. The maximum chromatism $\Delta E^* ab$ and luminance contrast ΔL^* in every image are given below.

$\Delta E^* ab = 8, \quad \Delta L^* = 10$

the image before calibration

$\Delta E^* ab = 10, \quad \Delta L^* = 13$

the image after calibration

Figure 5 The image of the ground glass architecture before calibration (up) and the same image which is calibrated(down)

CONCLUSION

The chromatism of this image is improved by 2 and the luminance contrast of that is improved by 3 from the calibration result of the ground glass architecture, Furthermore, this complex BRDF model can be used in the establishment and correct of remote sensing data, and the simulation of space camera.[6][7] Next work should be concerned on the different correct requirement of BRDF model for different earth observe objects in order to achieve more “true” earth observe image.

REFERENCES

1. H.Echtler, K.Segl, C.Dickerhof.Isograde Mapping and Mineral Identification on the Island of Naxos, Greece, Using DAIS 7915 Hyperspectral Data. SPIE Remote Sensing for Environmental Monitoring, GIS Applications,and Geology II,Agia Pelagia, Greece, 2003
2. ASTM Standard E-1392, “Standard practice for angle resolved optical scatter measurements on specular or diffuse surface.”
3. Xu tianzhou, [applied function analysis], the press of Science, China,(2002)
4. L.Li,H.Fukushima,et al. Optimization of Cox and Munk Sun-Glint Model Using ADEOS/II GLI Data and SeaWinds Data. SPIE, 2007
5. Brner A,Wiest L,Reulke R,et al.SENSOR: a Tool for the Simulation of Hyperspectral Remote Sensing Systems. ISPRS Journal of Photogrammetry and Remote Sensing, 2001
6. J.P.Kerekes,J.E.Baum. Full-Spectrum spectral Imaging System Analytical Model. IEEE Transactions on Geoscience and Remote Sensing, 2005
7. R.L.Sundberg, R.Kennett, J.Gruninger, et al. Extraction of Spatial and Spectral Scene Statistics for Hyperspectral Scene Simulation. IEEE International Geoscience and Remote Sensing Symposium, Anchorage, USA, 2004

On-Orbit Absolute Radiance Standard for Future IR Remote Sensing Instruments

Fred A. Best[1], Douglas P. Adler[1], Claire Pettersen[1], Henry E. Revercomb[1], P. Jonathan Gero[1], Joseph K. Taylor[1], Robert O. Knuteson[1], and John H. Perepezko[2]

[1]*University of Wisconsin, Space Science and Engineering Center, Madison, WI, USA,*
[2]*University of Wisconsin, Materials Science and Engineering, Madison, WI, USA,*
Corresponding e-mail address: fred.best@ssec.wisc.edu

Space borne IR remote sensing instruments in the future will require higher accuracies than now available, and the ability to perform absolute on-orbit calibrations traceable to SI standards. An On-Orbit Absolute Radiance Standard (OARS) is being developed to provide these on-orbit calibrations. The OARS uses a high emissivity (>0.999) blackbody cavity with imbedded thermistor temperature sensors that can be periodically calibrated using the transient melt signatures from three different reference materials also imbedded in the cavity. Emissivity measurements of the blackbody can be made periodically by measuring the reflection of a carefully baffled heated cylinder placed in front of the cavity.

INTRODUCTION

Future NASA infrared remote sensing missions, including the climate benchmark CLARREO mission will require better absolute measurement accuracy than now available, and will most certainly rely on the emerging capability to fly SI traceable standards that provide irrefutable absolute measurement accuracy [1]. As an example, instrumentation designed to measure spectrally resolved infrared radiances with an absolute brightness temperature error of better than 0.1 K will require high-emissivity (>0.999) calibration blackbodies with emissivity uncertainty of better than 0.06% (k=3), and absolute temperature uncertainties of 0.045K (k=3). Key elements of an On-Orbit Absolute Radiance Standard (OARS) meeting these stringent requirements have been demonstrated in the laboratory at the University of Wisconsin and are undergoing further refinement under the NASA Instrument Incubator Program (IIP). This work will culminate with an integrated subsystem that can provide on-orbit end-to-end radiometric accuracy validation for infrared remote sensing instruments.

APPROACH

Figure 1 illustrates the key features of the OARS in a section view. The blackbody design is based on the on-board calibration system developed for the NASA Geosynchronous Imaging Fourier Transform Spectrometer [2]. A temperature controlled light-trapping blackbody cavity contains thermistor temperature sensors and miniature phase change cells that provide on-orbit temperature calibration [3]. Three or more phase change cells with different reference materials can be used, thus providing multiple calibration temperatures. The heatable conical frustum (heated halo) out in front of the cavity provides the broadband source for periodic measurement of emissivity [4]. These measurements are made by the spectroradiometer that normally views the cavity for calibration verification, but in this case it is measuring the reflected signal of the heated halo. With the knowledge of the heated halo and effective background temperatures, and the solid angle view factor of the cavity view to the halo, the cavity emissivity can be calculated. Laboratory measurements of an OARS type blackbody, with a spectral emissivity greater than 0.999, have been made with uncertainties less than 0.0004 (k=3).

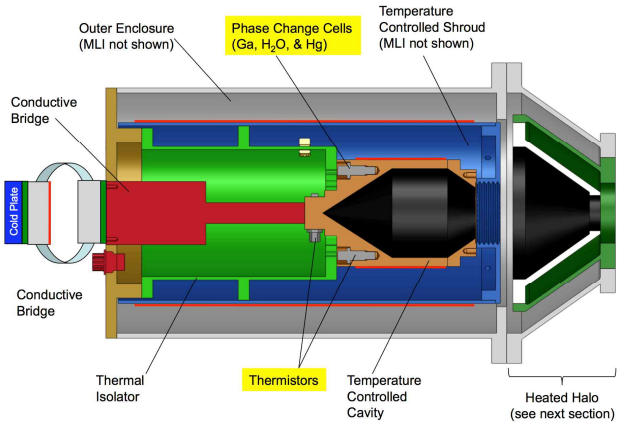

Figure 10. The key features of the OARS.

A temperature calibration point is obtained by measuring the transient cavity temperature response to a small increase in power. The sequence

of events during a typical melt of gallium is illustrated in Figure 3. After initial stabilization in the constant temperature mode, a constant power is used to transition through the melt plateau, where the phase change signature is observed. Other melt materials have been demonstrated, including H_2O, Hg, and a Ga-Sn eutectic. Using this technique, the thermistors imbedded in the cavity can be calibrated to uncertainties of better than 5 mK (k=3). With the inclusion of all other error sources, this leads to a total uncertainty of the OARS blackbody T_{eff} of 45 mK (k=3).

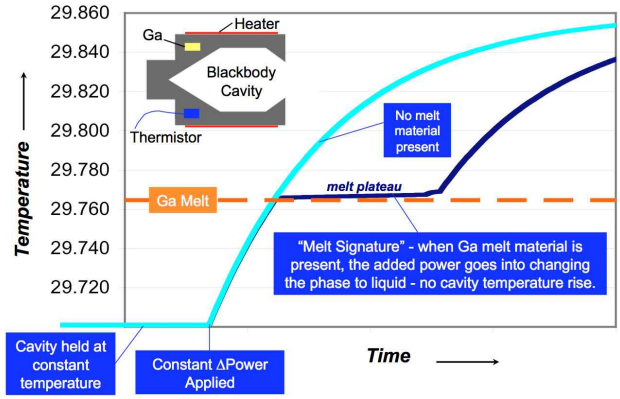

Figure 11. Key elements of a transient melt signature, in this case for Gallium. The melt plateau is approximately 4,000 seconds in duration.

The radiance from the OARS can be expressed as

$$I(\upsilon) = \varepsilon(\upsilon)B(\upsilon, T_{eff}) + (1-\varepsilon(\upsilon))B(\upsilon, T_{bg}) \qquad (1)$$

where $\varepsilon(\upsilon)$ is the cavity spectral emissivity, $B(\upsilon, T_{eff})$ is the Planck radiance at the effective cavity temperature T_{eff}, and $B(\upsilon, T_{bg})$ represents the plank radiance from the background at T_{bg}. The effective temperature is determined by a weighting of the different thermistors imbedded at key locations within the cavity. The weighting has been determined from analysis that uses a Monte-Carlo ray trace model of the cavity with a temperature distribution calculated from a thermal model.

CONCLUSIONS

Key aspects of an on-orbit absolute radiance standard, capable of periodic self-calibration traceable to SI standards, have been demonstrated in the laboratory, to accuracies required for future IR remote sensing instruments. Temperature calibration is conducted using melt signatures of miniature phase change cells. Emissivity of the blackbody is measured by the spectroradiometer that views the reflected signal from a heated halo that is located in front of the cavity.

REFERENCES

1. National Research Council, Earth Science and Applications from Space: National Imperatives for the Next Decade and Beyond, National Academies Press, Washington D. C., (2007)
2. Best, F. A., Revercomb, H. E., Tobin, D. C., et al.; Performance verification of the Geosynchronous Imaging Fourier Transform Spectrometer (GIFTS) on-board blackbody calibration system. Proceedings of SPIE Vol. 6405, 64050I (2006).
3. Gero, P. J., Taylor, J. K., Best, F. A., et al.; On-orbit absolute blackbody emissivity determination using the heated halo method. Proceedings of SPIE Vol. 7857, 78570L (2010).
4. Best, F. A., Adler, D. P., Pettersen, C., et al.; On-orbit absolute temperature calibration using multiple phase change materials: overview of recent technology advancements. Proceedings of SPIE Vol. 7857, 78570J (2010).

Satellite Observational Strategies for Climate Monitoring and Trend Detection

Benjamin K. Johnson[1] and Daniel B. Kirk-Davidoff[1]

[1]*Department of Atmospheric and Oceanic Science*
University of Maryland, College Park USA
Corresponding e-mail address: bjohnson@atmos.umd.edu

Precise in-orbit measurement of Earth's outgoing radiation is a critical goal for climate diagnosis and climate forecast validation. We determine the appropriate satellite design and orbit trajectory (instrument aperture, sampling frequency, cross track sampling strategy, orbit inclination and ground track repeat pattern) to minimize observational sampling error by orbiting virtual satellites above two proxy radiance datasets: a 4-8km resolution, geographically limited dataset from GOES East and the CERES SSF1 1° global assimilated dataset. We conclude that precessing orbits decrease sampling errors compared to sun-synchronous orbits; cross-track sampling decreases error and a specific combination of inclination and altitude decreases error by randomizing the ground track repeat cycle.

INTRODUCTION

Sampling bias, how the statistics of a sample of a time series differ from the entire time series since satellites are only able to take limited measurements from low-earth orbit, must be considered in the error budget when designing climate-monitoring satellites.

In this study we fly virtual satellites over proxy datasets to determine the effect of satellite design, orbital trajectory, sampling pattern and configuration within a constellation of satellites have on sampling bias and examine how sampling error correlates with natural variability to see if sampling errors can be predicted from what data collected in orbit.

An instrument with such long-term accuracy is needed for both testing climate models [2][3][5], and detecting decadal trends for the purpose of climate monitoring [1][6].

The minimum length of a time series with stable error characteristics necessary to detect a linear climate trend with certain confidence assuming that variability unrelated to the trend can be decomposed into orthogonal components of natural variability and measurement error depends on the ratio of measurement error to natural variability [7]:

$$\sigma_{meas} \propto \sigma_{\mathrm{var}} (t^3 - 1)^{1/2} \quad (1)$$

where σ_{meas} is the measurement error, σ_{var} is the natural variability and t is the time to trend detection. To limit this time to ten percent more than the time to zero measurement error detection, $\sigma_{meas} < 0.57\,\sigma_{\mathrm{var}}$.

This requirement relaxes the constraints on measurement error in regions with high natural variability (i.e. heavily clouded regions) but strengthens the constraints on measurement error in other regions (i.e. global means in optically thick regions of the IR spectrum).

METHODS

We fly a virtual satellite (or constellation of virtual satellites) over proxy radiance two datasets, one from GOES East and the other CERES SSF1, taking the radiances as the truth and measuring the sampling error of each observation strategy. This setup improves upon the approach of previous studies [4][8][9] by incorporating two higher resolution complimentary datasets, using new methodology to predict errors from what is observable in orbit and to determine the impact of satellite design choices on measurement error.

Sampling errors are calculated by orbiting 72 virtual satellites with identical altitudes and inclinations initialized 5° longitudinally apart at the equator. The expected error for one satellite is calculated as the standard deviation of the measured means for a given region and time period calculated by each orbiter. For a constellation of two satellites, we used the standard deviation of means for 36 pairs of satellites; for a constellation of 3 satellites, we used the standard deviation of means for 24 trios of satellites. In each case, the measured radiances were then converted to brightness temperature using the Planck Function.

To compare the datasets, we divide the CERES dataset into larger grid squares (typically, 5°x5°, 10°x10°, 15°x15° or 20°x20° squares) and examine the effect of taking statistics over larger areas.

To avoid aliasing the diurnal signal into climate trends, it is important to have a satellite make equal number of observations in the ascending and

descending nodes of an orbit [6]. We select four orbital inclinations that avoid this by causing the satellite to precess an integral number of times per year: 98° sun-synchronous, 90° polar, 82° one-time precessing, 74° two-time precessing.

To predict errors on orbit, we derive a formula that accounts for both seasonal and aperiodic variability:

$$e = \frac{\sigma}{\left(n \frac{(1-\rho_1)(1+\rho_2)}{(1+\rho_1)(1-\rho_2)} \right)^{1/2}} \qquad (2)$$

where e is the grid point error, σ is the standard deviation of observations in the grid point, n is the number of observations in each grid point ρ_1 is the average lag-one temporal autocorrelation along the scan track for each overpass of the grid square and ρ_2 is the lag-one autocorrelation of the time series of grid square averages for each overpass. The first fraction of n adjusts for the independence of the data while the second adjusts σ for the lack of randomness of seasonally varying radiances.

RESULTS

We make specific recommendations regarding the design and observational strategy for any Earth-Observing mission where it is desirable to minimize sampling error ab initio. One discovery is the altitude of the orbit must be closely controlled for a given orbit to ensure the ground-track repeat pattern is minimized (Figure 1).

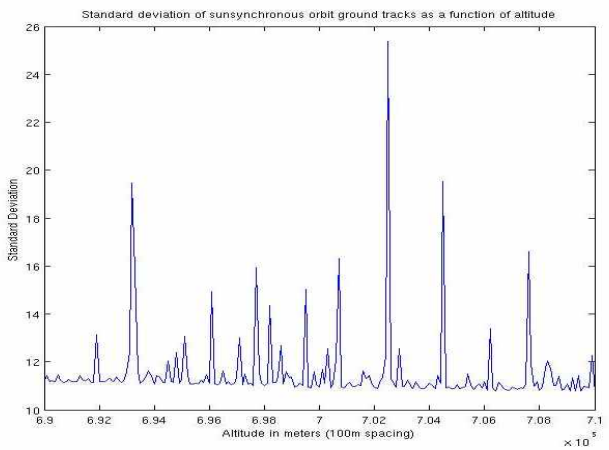

Figure 12. Standard deviation of number of observations over 15°x15° squares as a function of altitude.

Further recommendations are as follows:

- Cross-track sampling decreases sampling error as long as the off-nadir view is wide enough to sample areas of the surface typically beyond the decorrelation length scale (about 300km).
- Aperture size does not significantly affect error.
- Polar orbits give the least amount of sampling error with the greatest spatial coverage.
- Once-precessing orbits give a comparable amount of sampling error and provide for the highest number of simultaneous nadir overpasses of satellites in sun-synchronous orbit.
- Sun-synchronous orbits in singles and pairs give the largest sampling errors.
- Paired satellites with different inclinations have about 10% larger errors than paired satellites with like inclinations.
- Sampling error dependence on grid size scales roughly as the inverse of the area.

REFERENCES

1. Anderson, J. G., J. A. Dykema, R. M. Goody, H. Hu, and D. B. Kirk-Davidoff, 2004: Absolute, spectrally-resolved, thermal radiance: a benchmark for climate monitoring from space. Journal of Quantitative Spectroscopy & Radiative Transfer, 85, 367-383.
2. Goody, R., J. Anderson, and G. North, 1998: Testing climate models: An approach. Bulletin of the American Meteorological Society, 79, 2541-2549.
3. Haskins, R. D., R. M. Goody, and L. Chen, 1997: A statistical method for testing a general circulation model with spectrally resolved satellite data. Journal of Geophysical Research-Atmospheres, 102, 16563-16581.
4. Kirk-Davidoff, D. B., R. M. Goody, and J. G. Anderson, 2005: Analysis of sampling errors for climate monitoring satellites. Journal of Climate, 18, 810-822.
5. Leroy, S., J. Anderson, J. Dykema, and R. Goody, 2008a: Testing climate models using thermal infrared spectra. Journal of Climate, 21, 1863-1875.
6. Leroy, S. S., 2001: The effects of orbital precession on remote climate monitoring. Journal of Climate, 14, 4330-4337.
7. Leroy, S. S., J. G. Anderson, and G. Ohring, 2008b: Climate signal detection times and constraints on climate benchmark accuracy requirements. Journal of Climate, 21, 841-846.
8. Lin, X., L. D. Fowler, and D. A. Randall, 2002: Flying the TRMM Satellite in a general circulation model. Journal of Geophysical Research-Atmospheres, 107, 17.
9. Pirscher, B., U. Foelsche, B. C. Lackner, and G. Kirchengast, 2007: Local time influence in single-satellite radio occultation climatologies from Sun-synchronous and non-Sun-synchronous satellites. Journal of Geophysical Research-Atmospheres, 112, 13.

Infrared Laser-based Reflectance Measurements for Blackbody Cavity Emissivity Determination

John Dykema[1], Mark Witinski[1], and James Anderson[1]

[1]*School of Engineering and Applied Sciences,*
Harvard University, Cambridge, MA, USA
Corresponding e-mail address: dykema@huarp.harvard.edu

Reflectance measurements of near ambient blackbodies illuminated by monochromatic infrared lasers are presented. Meausrements are made with different illumination geometries and with different laser sources. These measurements are compared with theoretical results from optical modeling software. By making measurements of multiple blackbody sources sharing the same geometry but utilizing different paints, the optical modeling results are empirically validated. An analysis of the geometrical factors together with laser characteristics and blackbody properties supports the design of deployable blackbody testing sub-systems appropriate to meeting the needs of Earth science applications.

INTRODUCTION

Spectral measurements of thermal infrared emission play a key role in contemporary Earth science. More demanding calibration requirements for these measurements have created the need for technological solutions to the demonstration of measurement performance during the course of measurement campaigns, whether conducted from space or from other remote environments. Since the calibration of these systems relies on the use of thermal infrared blackbodies, the optical and thermodynamic properties of the blackbodies must be known in the environment and at the time measurements are acquired.

The need for this knowledge has motivated the development of compact, deployable techniques for measuring blackbody cavity emissivity. In this study, we examine the possibility of deriving blackbody cavity emissivity information from reflectance measurements obtained by illuminating the blackbody under test with monochromatic infrared laser radiation.

TECHNICAL APPROACH

Developments in semiconductor technology have led to the rapid progress in mid-infrared devices that make it possible to use a compact, non-cryogenic, single mode laser to both illuminate the blackbody for emissivity testing and to investigate the optical performance of the interferometer system. Of particular interest is the Quantum Cascade Laser (QCL). QCLs are capable of reaching high powers (>100 mW) at moderate temperatures (accessible from thermoelectric coolers) with narrow linewidths (<1 cm^{-1}). These characteristics are ideal not only for implementing on-orbit analogs of laser-based optical materials measurements performed by institutions such as NIST, but also for creating uniform, monochromatic sources for optical system testing [1]. The recognition of the suitability of the QCL for these purposes motivated a proof-of-concept study to integrate a QCL into a blackbody-calibrated interferometer system to investigate different options for laser coupling and optical measurement. It was found that a 40 mW QCL emitting at 8 μm enabled a measurement of the reflectivity of a blackbody cavity with emissivity of 0.9996 with an uncertainty of 10% [2], equivalent to 9 mK compared to the CLARREO requirement of 100 mK (3-σ).

A detailed analysis of the relationship between blackbody hemispheric-normal emissivity (relevant for CLARREO calibration) and directional-normal reflectivity (as measured by QCL) is presented here. The design of an accurate, reliable emissivity measurement subsystem requires detailed information about the optical properties of cavities and their interactions with optical radiation. Materials characterization and numerical modeling must be incorporated to successfully predict the optical properties of absorbing cavities in the mid-infrared. Materials characterization is provided by witness samples of various geometries of blackbody cavity surface treatments to allow direct measurement of relevant optical properties. These properties are used to define realistic diffuse and specular reflection in numerical modeling software capable of representing

blackbodies geometry and the details of the QCL-based reflectometer experiment with high fidelity. This analysis supports refinement of the CLARREO infrared sensor design and avenues for further development of QCL devices.

SUMMARY

Multiple blackbodies with the same cavity geometry but different surface paints were fabricated and measured, including Aeroglaze Z306 and Alion MH2200. Reflectance measurements utilized both QCL sources and monochromatic radiation at 10.6 μm from a CO_2 gas laser. The combination of these different experimental conditions provides a basis for evaluation of the fidelity of the optical modelling software used to relate reflectance to cavity emissivity. These results lead to recommendations for implementing this calibration blackbody testing technique for practical measurement systems.

REFERENCES

1. M. Chamberland, F. Williams, P. Tremblay, V. Farley, R. Desbiens, L. Belhumeur, and J. Lawrence, " The Instrument Lineshape, an imperative parameter for the absolute spectral calibration of an FTS.," in Fourier Transform Spectroscopy, A. Sawchuk, ed., Vol. 84 of OSA Trends in Optics and Photonics (Optical Society of America, 2003), paper FWC1.
2. Gero, P. Jonathan, John A. Dykema, James G. Anderson, 2009: A Quantum Cascade Laser–Based Reflectometer for On-Orbit Blackbody Cavity Monitoring. J. Atmos. Oceanic Technol., 26, 1596–1604.

A Differential Spectral Responsivity Measuring System for Solar Cell Calibration

Gan Xu and Xuebo Huang

National Metrology Centre, Agency of Science, Technology and Education, Singapore
Corresponding e-mail address: xu_gan@nmc.a-star.edu.sg

A differential spectral responsivity measuring system has been developed for primary calibration of reference solar cells of sizes up to 156 mm x 156 mm under IEC standard testing conditions. The system can also be used to measure the temperature coefficient, spatial uniformity of the solar cell under test. This paper presents the system design, method validation and preliminary results of calibration.

MEASUREMENT PRINCIPLE

Solar cell calibration under standard testing conditions (STC) can be carried out either outdoor under natural sunlight conditions or indoor under an artificial solar simulator. While the latter is able to provide full I-V characteristics of a solar cell, it is not considered a primary calibration as its accuracy relies on the reference solar cell used to set the standard irradiance conditions including correction for spectral mismatch between the AM1.5 reference solar spectrum and that of the solar simulator. On the other hand, determination of the short-circuit current by measurements of differential spectral responsivity (DSR) of the solar cell at different bias conditions is widely recognised as the most accurate method of calibration especially for solar cells with poor linearity. The best reported uncertainty using such method is ~ 0.25% [1].

For a non-linear solar cell, its DSR under bias irradiance E_b is given by the slope of its short-circuit current (SCC, I_{sc}) curve:

$$\tilde{s}(E_b) = \left.\frac{\Delta I_{sc}(E_b)}{\Delta E_b}\right|_{E_b} \qquad (1)$$

while DSR as function of SCC of the solar cell under test in accordance with AM1.5 spectrum is given by

$$\tilde{s}_{AM1.5}(I_{sc}(E_b)) = \frac{\int_0^\infty \tilde{s}(\lambda, I_{sc}(E_b)) E_{\lambda,EM1.5}(\lambda) d\lambda}{\int_0^\infty E_{\lambda,EM1.5}(\lambda) d\lambda} \qquad (2)$$

If DSRs at sufficient bias levels are measured, the SCC under STC can be decided by finding the upper limit of the following equation

$$1{,}000 W/m^2 = E_{STC} = \int_0^{I_{STC}} \frac{dI_{sc}}{\tilde{s}_{AM1.5}(I_{sc})} \qquad (3)$$

where E_{STC} is the irradiance under STC.

SYSTEM DESIGN AND FEATURES

In order to fully calibrate and characterise solar cells with the highest accuracy, we have designed and constructed a DSR calibration system based on the same principle originated from PTB [2] with some special built-in features.

A quasi-monochromatic probe beam used in the test is produced by a light source (1600W Xe discharge or 1000W halogen lamp) through a double-grating monochromator. The insertion of a specially designed micro-lens array in the collimating optics ensures good spatial uniformity of the probe beam on the sample stage. As the distance of the sample stage increases from the probe beam optics, the slightly diverging beam can give uniformity better than 0.5% and 1.5% over an area of 50 mm x 50 mm and 160 mm x 160 mm respectively. This enables accurate measurement on solar cells of sizes up to 156 mm x 156 mm. A sample stage capable of holding a large solar cell (156 mm x 156 mm), two WPVS reference cells (20 mm x 20 mm) and two reference photodiodes (Si- and InGaAs) is mounted on an automated X-Y-Z stage. The temperature of the sample stage is normally set at 25°C controlled by a closed loop temperature control chillier. The temperature of the solar cells can also be individually controlled by a temperature controller from 20°C to 60°C for temperature coefficient measurement.

An array of 24 50W halogen lamps is used to provide the required bias irradiance on the test solar cell for DSR measurement with the level of bias to be adjustable by changing the combinations of the lamps

light up and the distance between bias light with the sample stage.

To correct for variation of probe beam power, two monitor photodiodes (Si- and InGaAs) are inserted in the optical path of the probe beam.

In the detection system, a current transformer and standard phase-sensitive AC technique is used to separate the weak probe beam (modulated ac signal) from the strong bias background irradiance (DC signal). When the reference photodiode is aligned with the probe beam, both ac signals from reference and monitoring photodiodes are simultaneously recorded during each wavelength scan at every wavelength and their ratio is used as reference. When the probe beam is aligned to the test solar cell, both ac signals from the solar cell and monitoring photodiode is also simultaneously recorded and their ratios calculated. If no bias is applied, the spectral responsivity of the solar cell can be calculated from the calibration data of the reference photodiode multiplied by the ratio of the two recorded ratios. With a bias applied, the DSR is measured instead and the SCC from the test solar cell is directly obtained by a DC source meter when the probe beam is blocked. Any errors caused by the fluctuation of the probe beam power during the two scans are corrected by this procedure.

The system can be used to perform the following functions: calibration of spectral responsivity (w/o bias) or DSR at bias levels of 0.1 to 1.2 STC irradiances of single solar cells of sizes up to 156 mm x 156 mm at temperatures from 20°C to 60°C. The wavelength range is currently from 280 nm to 1200 nm, sufficient for silicon based PV cells and can be easily extended to 1600 nm without changing any major parts. In addition, the system is also programmed to measure the spatial uniformity of the bias beam and probe beam (at selected wavelengths). It can also be used to measure the spatial uniformity as well as temperature coefficient of the spectral responsivity of the cell.

Details of the system design, construction, method validation and experimental results will be presented.

REFERENCES

1. S Winter, T Wittchen and J Metzdorf, Primary Reference Cell Calibration at the PTB based on Improved DSR Facility, 16th European Photovoltaic Solar Energy Conference, Glasgow, 2000
2. J Metzdorf, Calibration of Solar Cells – the differential spectral responsivity method, Applied Physics, 26, 1701-1708, 1987

Traceable calibration of a very low photon flux source for the NIRSpec Instrument of the James Webb Space Telescope

R. D. Taubert[1], C. Monte[1], C. Baltruschat[1], J. Hollandt[1],
D. Kochems[2], C. Küchel[2], and M. te Plate[3]

[1]*Physikalisch-Technische Bundesanstalt (PTB), Berlin, Germany,*
[2]*EADS Astrium GmbH, Munich, Germany,*
[3]*European Space Agency (ESA), Noordwijk, The Netherlands*
Corresponding e-mail address: dieter.taubert@ptb.de

The Radiometrically Calibrated Spectral Source (RCSS) is a source with very low photon flux for the calibration of the Near Infrared Spectrograph (NIRSpec) of the James Webb Space Telescope (JWST). It was calibrated in the wavelength range from 0.7 µm to 1.55 µm at the Spectral Radiance Comparator Facility (SRCF) of the PTB under space similar conditions, in vacuum and at temperatures below 90 K. Calibration results are presented for different RCSS configurations, covering photon flux ranges from $2.4 \cdot 10^7$ µm^{-1}·s^{-1} down to $1.2 \cdot 10^5$ µm^{-1}·s^{-1} and relative standard uncertainties, depending on wavelength and photon flux, as low as 5 % (k=2).

INTRODUCTION

In 2014, succeeding the Hubble Space Telescope and the Spitzer Space Telescope, the James Webb Space Telescope (JWST) [1] will be launched as one of the major future space observation platforms. Part of the JWST scientific instrumentation is the Near InfraRed multiobject dispersive Spectrograph (NIRSpec) covering the wavelength range from 0.7 µm to 5 µm.

To fulfil the stringent traceability requirements, NIRSpec undergoes a pre-flight calibration against the Radiometrically Calibrated Spectral Source (RCSS) at the Optical Ground Support Equipment (OGSE) facility [2]. The RCSS, a combination of integrating spheres and small apertures, has a pinhole output port of 10 µm diameter acting as a point-like radiation source [3]. The RCSS design was optimized to operate in vacuum at cryogenic temperatures and to emit the very low photon flux required for the NIRSpec calibration, ranging from 10^5 to 10^7 photons µm^{-1}·s^{-1}[4].

For the absolute radiometric calibration of the RCSS in the wavelength range from 0.7 µm to 1.55 µm, the PTB has significantly improved the detector instrumentation of the Spectral Radiance Comparator Facility (SRCF) [5] and has developed new schemes for the calibration of very low photon flux sources traceable to blackbody radiation.

CALIBRATION SETUP

The spectral photon flux of the RCSS was calibrated at the SRCF of the PTB by direct comparison with a calibrated cavity radiator operated in the temperature range from 250 °C to 650 °C, whose radiance

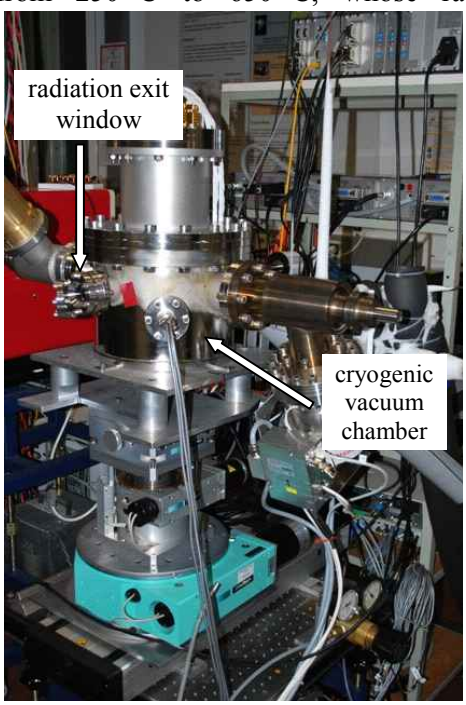

Figure 13. The Radiometrically Calibrated Spectral Source in its cryogenic vacuum chamber for the absolute measurement of its spectral photon flux with the Spectral Radiance Comparator Facility

temperature is traceable to the International Temperature Scale of 1990 (ITS-90).

For calibration, the RCSS was clean-room assembled by EADS Astrium in a PTB-built dedicated cryogenic vacuum chamber, its optical radiation being measured through a wedged CaF_2 window with calibrated transmittance. To assure the accurate and reproducible alignment of the 10 µm diameter source pinhole, the RCSS/vacuum chamber assembly was mounted on a kinematic stage allowing

two rotational and two translation degrees of freedom with the pivot point set in the centre of the RCSS pinhole (Figure 1). During the calibration, the RCSS was kept at a temperature below 90 K via a controlled liquid nitrogen flow.

RESULTS

The results of the spectral photon flux calibration of the RCSS are presented in Figure 2. The calibration was performed for five of the eight internal RCSS so-called "Lamp-in-Light-Sources" (LiLS), each LiLS consisting of two separately controllable lamps as radiation sources for redundancy, selected to match with respect to their electrical characteristics.

The RCSS, to be applied as a transfer standard radiation source for the calibration of NIRSpec, was calibrated at this setup using a dedicated calibration scheme for five different photon flux configurations under space similar conditions in the wavelength range from 0.7 µm to 1.55 µm.

The calibration results obtained for the different RCSS photon flux configurations range from $2.4 \cdot 10^7$ $\mu m^{-1} \cdot s^{-1}$ at 1.55 µm down to $1.2 \cdot 10^5$ $\mu m^{-1} \cdot s^{-1}$ at 0.7 µm, which is more than eight orders of magnitude lower than a typical spectral radiance standard, a tungsten strip lamp operated at a radiance temperature of 2300 K. Relative uncertainties as low as 5 % (k=2 at λ=0.7 µm) were achieved.

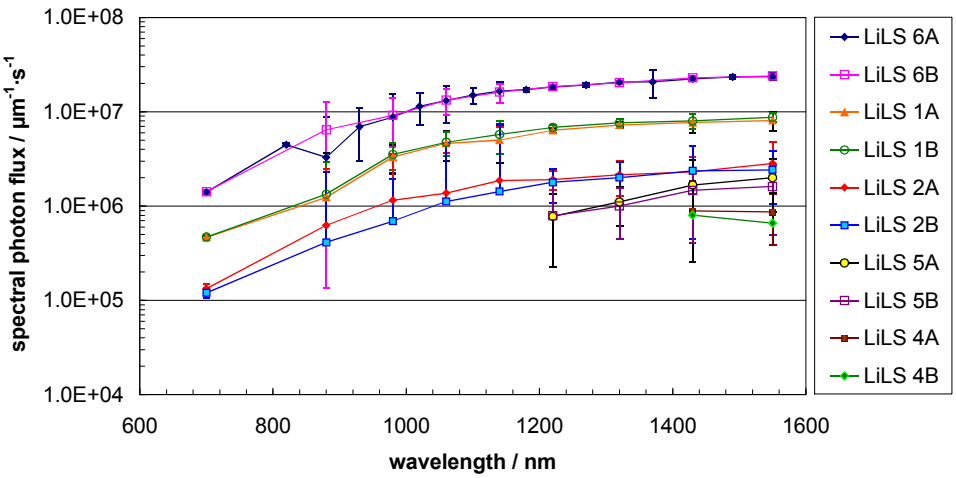

Figure 2. Spectral photon flux of the RCSS for different LiLS configurations. The uncertainty bars denote the expanded standard uncertainty (k=2).

For identification the LiLS are marked as "1", "2", "4", "5" and "6" whereas the individual lamps within the LiLS are labelled as "A" respective "B". All LiLS were operated at a lamp current of 17 mA, excepting LiLS "4" and "5" which were operated at a lamp current of 10 mA.

The total uncertainty shown in Fig. 2 was calculated including the uncertainty contributions from noise, the SRCF solid angle measurement, the monochromator wavelength, the monochromator entrance aperture area measurement, the cryogenic chamber window transmittance measurement and the spectral radiance of the cavity radiator.

CONCLUSIONS

For the traceable calibration of the NIRSpec instrument on the JWST, the PTB has developed on the basis of the existing SRCF a new experimental setup with an improved detector instrumentation and a gated photon counting technique for the absolute calibration of ultra-low photon flux radiation sources.

REFERENCES

1. J. P. Gardner et al., The James Webb Space Telescope, Space Science Reviews, 123, 485-606, 2006
2. G. Bagnasco et al, The on-ground calibration of the Near Infrared Spectrograph (NIRSpec) instrument onboard the James Webb Space Telescope (JWST), in Proceedings SPIE, 7010, 2008
3. R. D. Taubert, C. Monte, C. Baltruschat, A. Schirmacher, B. Gutschwager, J. Hartmann, J. Hollandt, D. Kochems, C. Küchel, M. te Plate, The spectral photon flux of the radiometric calibration spectral source fort he NIRSpec instrument of the James Webb Space Telescope, Metrologia, 46, S207-S212, 2009
4. R. D. Taubert, C. Monte, C. Baltruschat, B. Gutschwager, J. Hartmann, J. Hollandt, D. Kochems, C. Küchel, M. te Plate, Radiometric calibration of the NIRSpec instrument on the James Webb Space Telescope in the wavelength range from 0.7 µm to 5.0 µm, in Proceedings OPTO 2009 & IRS² 2009, ed. AMA Service GmbH, Wunstorf/Germany, ISBN 978-3-9810993
5. R. Friedrich, J. Fischer, New spectral radiance scale from 220 nm to 2500 nm, Metrologia, 37, 539-542, 2000

Spatial Uniformity Measurements of Photo-Voltaic Cells Using Digital Micro-mirror Device

Seung Kwan Kim[1], Jae-Keun Yoo[2], Seung-Nam Park[1,2]

[1]*Division of Physical Metrology, Korea Research Institute of Standards and Science, Daejeon, Republic of Korea*
[2]*Department of Measurement Science, University of Science and Technology, Daejeon, Republic of Korea*

Corresponding e-mail address: sk@kriss.re.kr

We proposed and implemented a measurement method to inspect spatial uniformity of conversion efficiency of photo-voltaic cells using a digital micro-mirror device. Irradiance over 1.5 m × 0.8 m area on the cell plane was equalized within ±2.6 % through gray scale of the device. We demonstrated that a commercial photo-voltaic cell would exhibit conversion efficiency difference of more than 10 %.

INTRODUCTION

Spatial uniformity of conversion efficiency (CE) of a photo-voltaic (PV) cell is an important measurement quantity to improve its product quality and thus extend the life time. Bad spatial uniformity is normally resulted from local defects, cracks, bad interconnection, etc., which degrades CE and make the local points of PV cell overloaded to decrease the life time. Visual inspection, photo-luminescence, or electro-luminescence can be used to detect such fault locations but all these methods are not directly related to CE [1-3].

We have sought a direct method to enable fast measurement of CE distribution without bulky mechanical movement. One potential method that we have focused is to use digital micro-mirror device (DMD) that is widely used for projection display. DMD is capable of producing patterns with arbitrary shapes and changing the patterns easily and quickly as time. With the appropriate projection lens, the pattern image can be formed on to the large area plane, which is ideal for testing large area PV cells or modules.

In this paper, we describe our development of CE distribution measurement setup for PV cells using a beam projector utilizing DMD.

MEASUREMENT SETUP

We designed the measurement setup that can cover the rectangular image area of 1.5 m and 0.8 m on the test table in x and y direction, respectively, on which the light from the projector irradiated from the height of about 1 m as shown in Figure 1. The beam projector had the resolution of 1024×768 (XGA), ANSI lumen of 3000, and contrast ratio of more than 2000 in specification. The projector was fixed to a stage attached to the ceiling of a mechanical frame covered with black fabric for dark room environment.

In order to measure the irradiance distribution of the white image from the projector, we installed 20 identical silicon photodiodes (PD) on a straight bar in y direction to form a PD array that could translate along x direction on the test table. The spacing between the neighbouring PDs was 4.0 cm. The photo-current of each PD was sequentially selected by a 1×20 electronic switch and measured with an ampere meter. An additional photodiode was installed near the edge of the image and its photo-current was used to compensate the drift of the light during the measurement. Once the irradiance distribution measurement was completed, the PD array was set aside to the edge of the table.

When a PV cell or module was placed on the test table with the same surface height of the PD array and irradiated by the image pattern of the projector, its short circuit (SC) current was measured with a source-meter while the image pattern was being scanned.

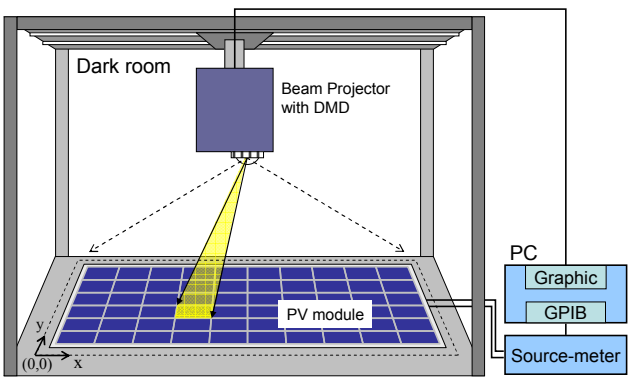

Figure 1. Measurement setup for conversion efficiency distribution of photo-voltaic module.

IRRADIANCE UNIFORMITY

Irradiating the test table with full white image, we measured the photo-current distribution at 300 points covering the entire area with 0.1 m spacing in x direction by translation and 0.04 m in y direction by photodiode array with switch. As a result, the photo-current was maximum near x=0.7 m, y=0.4 m and it decreased as the position became away from it, and the maximum was twice as much as the minimum. Therefore, we needed to make this mountain like irradiance distribution flat and we proposed to use gray level adjustment at each pixel of DMD.

In order to implement it, we first measured the photo-current change as a function of 8 bit gray level (0 – 255) at several sampled pixels and obtained a polynomial fitting function to calculate the gray level required to give a certain photo-current. For unmeasured pixel points, we assigned values by 2D spline interpolation using the 300 data points. Then, we applied the appropriate gray level to each pixel so that it could produce the same minimum photo-current. As a result, we could obtain the flat irradiance distribution with the maximum deviation of ±2.6 % when we re-measured the photo-current distribution as shown in Figure 2.

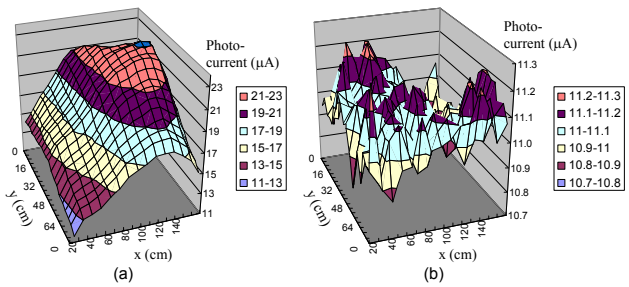

Figure 2. Irradiance distribution of full white image of the beam projector (a) before and (b) after gray scale adjustment.

EFFICIENCY UNIFORMITY

The PV cell that we measured its conversion efficiency uniformity was a square shaped poly-crystalline silicon cell with a dimension of 15 cm in both x and y. The SC current of the cell was 5.6 mA when the white image with the same size as the cell irradiated on the cell. Then we applied a small white image with black background on the cell and mapped the SC current distribution while scanning the small white image over the entire cell surface. The measured SC current was subtracted by the SC current measured when the image was all black (superscript K) as shown in equation (1) because the black image with all 0 gray levels also produced small background current.

$$I_{sc}(x,\mathrm{y}) = I_{sc}^{\mathrm{W}}(x,\mathrm{y}) - I_{sc}^{\mathrm{K}} \qquad (1)$$

Four CE distribution maps with white image area of 10×10, 7×7, 5×5, and 2×2 pixels, where 1 pixel size corresponded to about 1.5 mm, showed good reproducibility and we could see more detailed feature as the pixel size became smaller (better resolution). Figure 3 shows the CE distribution map of the cell when it was scanned by 2×2 pixel image where the two thick black vertical lines corresponded to the shaded area by the electric bus lines attached to the cell. Even the single PV cell exhibited conversion efficiency difference of more than 10 % for different position as shown in Figure 3.

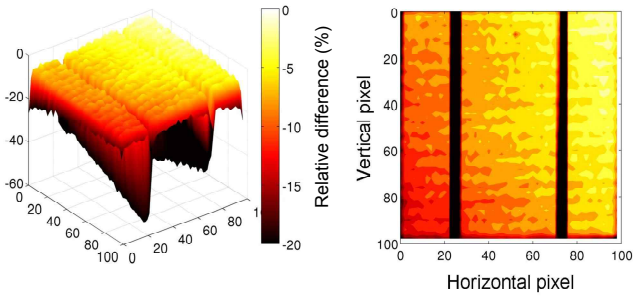

Figure 3. Conversion efficiency distribution of a PV cell scanned by 2x2 pixel image.

CONCLUSION

We successfully demonstrated our implementation of measuring conversion efficiency distribution using a beam projector with DMD.

The key advantage of this method is that we can easily and quickly provide any kind of irradiance pattern over wide area and obtain conversion efficiency distribution of PV cell or module without mechanical movement.

REFERENCES

1. A.R. Gxasheka, E.E. van Dyk, E.L. Meyer, Evaluation of performance parameters of PV modules deployed outdoors, Renewable Energy, 30, 611-620, 2005.
2. Otwin Breitenstein, Jan Bauer, Thorsten Trupke, Robert A. Bardos, On The Detection of Shunts in Silicon Solar Cells by Photo- and Electroluminescence Imaging, Progress in Photovoltaics: Research and Applications, 16, 325-330, 2008.
3. Takashi Fuyuki, Athapol Kitiyanan, Photographic diagnosis of crystalline silicon solar cells utilizing electroluminescence, Applied Physics A, 96, 189-196, 2009.

Design Features and Test of the Cryogenic Solar Absolute Radiometer

Rainer Winkler[1], André Fehlmann[2], Nigel Fox[1], Eric Usadi[1], Wolfgang Finsterle[2], Peter Blattner[3], Werner Schmutz[2]

[1]*National Physical Laboratory, Teddington, United Kingdom*
[2]*Physikalisch-Meteorologisches Observatorium Davos / World Radiation Center, Davos, Switzerland*
[3]*Federal Office of Metrology, Bern, Switzerland*
Corresponding e-mail address: rainer.winkler@npl.co.uk

The World Standard Group (WSG) is the current representation of the World Radiometric Reference (WRR). Since the individual instruments of the WSG are already over 30 years old, it is necessary to take steps towards a future replacement [1] and in so doing seek to improve the rigour of SI traceability. Extending the range of application of cryogenic radiometry to enable direct measurements of solar radiation is the obvious solution. This paper provides an overview of the design and performance of the "Cryogenic Solar Absolute Radiometer (CSAR)" – the first to achieve this goal.

INTRODUCTION

The Cryogenic Solar Absolute Radiometer was primarily developed to serve as a potential replacement for the World Standard Group. The aim was to fully exploit the advantages of cryogenic radiometry in order to significantly reduce the systematic uncertainties – with a target overall uncertainty of <0.03% (k=1) and also to establish robust traceability to SI units.

While this terrestrial application was the primary design focus, CSAR was also developed with space flight in mind – to not only make extra-terrestrial Total Solar Irradiance (TSI) measurements but also to serve as an engineering model for the primary standard on the proposed TRUTHS mission [2]. The uncertainty goal for TSI is ~0.01% (k=1).

The following sections outline the principle design features.

HIGHLY ABSORBING CAVITY

One of the main advantages of operation at cryogenic temperatures is the significant reduction in heat capacity of typical cavity materials, when compared to room temperature. This allows the use of a larger cavity, which enables a much higher absorptivity, while maintaining a small time constant. In the case of CSAR, the cavity has an absorbance of 0.99998 (theoretical and confirmed by measurement). The reflectivity is therefore approximately a factor of ten smaller than the current state-of-the-art ambient temperature radiometers.

But despite of the high absorptivity and consequential size, the detector cavity has a response time of <10 seconds, which is comparable to current room-temperature radiometers.

EQUIVALENCE OF OPTICAL AND ELECTRICAL HEATING

The measurement principle of CSAR is electrical substitution radiometry – like in all other current TSI instrument designs. However, the non-equivalence of optical and electrical heating can be reduced to negligible levels if operating at low temperature.

A surrounding cold-shield which is maintained at a similar temperature to the gold-coated cavity prevents any significant radiative heat transfer between the detector cavity and its immediate environment. In addition, the operation in vacuum implies that there is no significant heat exchange by convection or conduction through air.

Another important source of non-equivalence in ambient-temperature radiometers are the current-carrying heater wires. In cryogenic radiometers, this effect can be completely avoided through the use of super-conducting leads. Although the detector temperature of CSAR is slightly too high to allow the use of conventional superconductors (for reasons given below), Ø50 µm steel-sheathed MgB_2 [3] were used to exclude this effect.

ARRANGEMENT OF APERTURES

A precision aperture is needed to define the irradiated detector area to enable a measure of irradiance. An additional field-of-view-limiting aperture is required to reduce the influence of indirect sky-irradiation. In conventional TSI-radiometers, the smaller (precision) aperture is placed directly in front of the cavity, which allows for a smaller cavity design than if the

view-limiting aperture was placed in front of the cavity. However, a major drawback of such a conventional design is that it admits a lot of excess solar radiation into the radiometer, which then needs to be absorbed by a light trap.

Since operation at cryogenic temperature relaxes the constraints regarding the cavity size, the optically superior configuration was chosen, i.e. the field-of-view limiting aperture directly in front of the cavity and the precision aperture closer to the Sun.

The chosen aperture configuration is similar to that used for the Total Irradiance Monitor, TIM [4]; however, in contrast to TIM, CSAR was specifically built for ground use – the optical geometry has therefore been made to comply to the rules set out in the CIMO guide [5] as much as possible. This ensures that CSAR does not measure significantly different amounts of circumsolar radiation than the existing radiometers.

The precision aperture is diamond-turned from aluminium and has an edge thickness of slightly less than 20 μm. The front face of the precision aperture is shaped in such a way that inter-reflections between the aperture and the window cannot make their way into the detector cavity.

WINDOW TRANSMISSION

In order to create a vacuum, but also allow the solar radiation to reach the detector at the same time, a highly transmitting window is used. Two different window materials (fused silica and sapphire) were used to confirm the robustness of the correction for the window transmission. In addition, theoretical values were compared with experimental results and they have been found to agree very well. Great care has been taken to evaluate the effect of the window and to minimise the uncertainty arising from its use. More detail will be given in another contribution to this NEWRAD conference [6].

PROTOTYPE FOR SPACE

The requirements needed for a space instrument have been taken into account in the design phase. The main restrictions regarding the use of CSAR in space are related to the available cooling power and the mechanical resistance to launch vibrations.

The radiometer was designed to cope with the limited cooling power available from a mechanical space cooler, but to have Eigenfrequencies of sub-components higher than 120Hz.

While the mechanical cooler used for ground operation provides enough cooling power to operate the detector cavities at 4K, the actual operating temperature was set at 20K – in order to demonstrate CSAR's performance under the more restricted conditions of space use.

COMPARISONS AGAINST EXISTING STANDARDS

Comparisons have been made against the SI quantity of radiant power and also against the WSG. The results are still subject to analysis at the time of writing this extended abstract, however, first results will be available at NEWRAD 2011.

CONCLUSIONS

This paper discusses the design of CSAR and presents first test results. The CSAR based on this design will be able to significantly reduce the uncertainty in TSI measurements, both on the ground and in space, and should lead to the eventual replacement of the WSG.

REFERENCES

1. W. Finsterle et al., Cryogenic absolute radiometer for total solar irradiance, NEWRAD 2011.
2. N. Fox et al., Traceable Radiometry Underpinning Terrestrial- and Helio-Studies (TRUTHS), Advances in Space Research, **32**(11): 2253-2261, 2003.
3. S.I. Schlachter, W. Goldacker, et al., Properties of MgB2 superconductors with regard to space applications, Cryogenics, **46**(2-3): 201-207.
4. G. Kopp and G. Lawrence, The Total Irradiance Monitor (TIM): Instrument design, Solar Physics, **230**(1-2): 91-109, 2005.
5. WMO, WMO Guide to Meteorological Instruments and Methods of Observation (CIMO guide WMO-8), 2008
6. A. Fehlmann et al., Monitor to measure the Integrated Transmittance (MITRA) of Windows, NEWRAD 2011.

ACKNOWLEDGEMENTS

We would like to acknowledge the contribution of Sonja Schlachter from the Karlsruhe Institute of Technology, who provided the MgB_2-wires. We also gratefully acknowledge substantial financial funding by the UK Department for Business, Innovation and Skills and the Swiss National Science Foundation.

Total Solar Irradiance Data Record Accuracy and Consistency Improvements

Greg Kopp[1], André Fehlmann[2], Wolfgang Finsterle[2], David Harber[1], and Karl Heuerman[1]

[1]*Laboratory for Atmospheric and Space Physics, Univ. of Colorado, Boulder, CO, USA*

[2] *Physikalisch-Meteorologisches Observatorium Davos / World Radiation Center, Davos, Switzerland*

Greg.Kopp@LASP.Colorado.edu

Continuity of the 33-year long total solar irradiance record has allowed corrections for offsets due to calibration differences between instruments, providing a quality solar data record for Earth climate studies. Recent laboratory tests have 1) improved measurement absolute accuracy to mitigate against potential future data gaps, 2) helped explain the causes of the instrument offsets, and 3) improved consistency between the international references upon which various instrument calibrations are based.

INTRODUCTION

Total solar irradiance (TSI) is a measure of the spectrally- and spatially-integrated radiant energy from the Sun, which is the dominant energy source driving the Earth's climate system. The 32-year spaceborne TSI record is used in climate studies for attributing the portion of global and regional climate effects due to solar variability over modern and – via proxies – historical times [1,2].

Such studies utilize composite records that are based on the spaceborne TSI instrument measurements shown in Figure 1. The offsets between these measurements, which are as large as 0.35% for current instruments, are due to calibration differences, which, along with differing instrumental drifts, must be corrected to create a composite TSI record needed for climate studies.

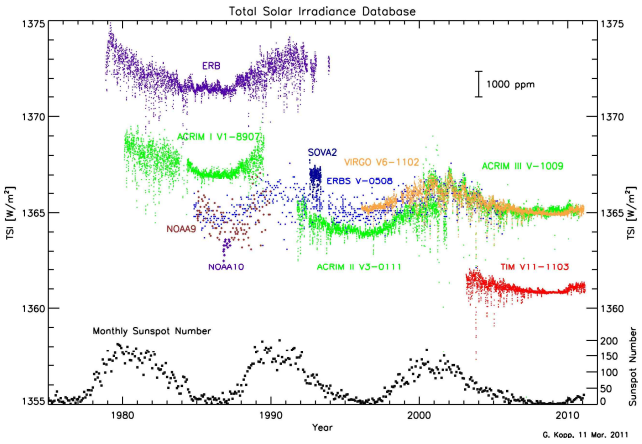

Figure 14. The 32-year TSI record is the result of several instruments. Measurement overlap helps correct for the majority of the differences between instruments.

Because of the offsets between instruments, measurement continuity has been imperative and has led to requirements for improvements in absolute accuracy as well as a desired understanding of the causes of the offsets [3,4]. Recent tests with ground-based versions of the flight TSI instruments at the new TSI Radiometer Facility (TRF) [5] have provided an improved understanding of the causes of these instrument offsets and suggest higher than stated uncertainties associated with current flight measurements. Internal instrument scatter appears to be the cause of erroneously high reported TSI values, favoring a TSI value of 1360.8±0.5 W m^{-2} as best representative of solar minimum [6].

TRF CALIBRATION FACILITY VALIDATES MEASUREMENT ACCURACY

None of the spaceflight instruments in Figure 1 has been calibrated as an end-to-end system for irradiance as no facility capable of providing the needed accuracies existed prior to launch. The new TRF provides such capability, being the world's only facility to validate TSI instruments for irradiance directly against a NIST-calibrated cryogenic radiometer at full solar power levels while operating under vacuum. Additionally, incident beam control with the TRF allows diagnostics to determine the causes of instrument differences.

Newer spaceflight instruments, particularly the PICARD/PREMOS instrument launched in 2010 and the follow-on instrument (which was unfortunately lost in the Glory launch failure) to the Total Irradiance Monitor (TIM) currently flying on NASA's SORCE mission, benefitted from these reference calibrations. Ref. [6] reports the Glory/TIM flight instrument reads lower than the SI-traceable TRF irradiance reference scale by an average of 0.012±0.020%, while the SORCE/TIM ground unit is lower by 0.037±0.032%, consistent with the instrument's stated accuracy. The PREMOS has now transferred this reference SI-traceable calibration to space. Baselined to the reference TRF, the flight PREMOS instrument could help link the existing on-orbit instruments with future TSI

instruments compared on the TRF, helping mitigate against potential future – and still undesirable – measurement gaps.

SCATTER IS CAUSE OF INSTRUMENT DIFFERENCES

Diagnostics during TRF tests have helped understand the causes and magnitudes of the on-orbit differences. Instruments tested to date include a ground-based SORCE/TIM, a PMO6 radiometer representative of the SoHO/VIRGO, a ground representative of the ACRIMSat/ACRIM-3, and the flight plus a ground-based PICARD/PREMOS.

A fundamental optical design difference between the TIM and all other radiometers is the layout of the precision aperture that defines the sunlight collected by the instrument. The TIM locates this small aperture at the front of the instrument, allowing only the light intended for measurement into the instrument. All other radiometers have a larger entrance aperture at the front and this small precision aperture inside, close to the radiometer cavity itself. This layout allows two to three times the light intended for measurement into the instrument interior, where it can scatter into the radiometer cavity and cause erroneously high signals.

By expanding the uniform entrance TRF light beam from underfilling to overfilling an instrument's precision and larger entrance apertures, an instrument interior is progressively illuminated and scatter sources are diagnosed. The PREMOS flight instrument shows scatter effects of 0.04% while a ground-based version has higher measured scatter at 0.10%. The VIRGO ground unit shows measured scatter of 0.15% while the ACRIM-3 has scatter contributions as large as 0.73%. The magnitudes of these scatter effects are comparable to the measured instrument offsets in Figure 1, and likely explain the majority of the on-orbit differences between TSI instruments; although applying these monochromatic lab scatter measurements to flight instruments that have been on orbit for several years requires adding large additional uncertainties to the corrections.

LINKING INTERNATIONAL REFERENCES

Via comparisons at NPL, the NIST-calibrated TRF, and the World Radiation Reference (WRR), the PREMOS instrument has linked the national labs at NPL with those at NIST, showing agreement in optical power measurement of 999989±0.000297 (k=1) [7]. Similar comparisons indicate the WRR reads slightly higher than SI in optical power by 1.001785±0.001064 (k=1) and higher yet in irradiance (1.003249±0.001112), likely due to internal scatter in the WRR instruments.

Similarly, SORCE/TIM participation in the 2010 International Pyrheliometer Comparison XI linked the TIM to the WRR, albeit with higher uncertainties due to the air-to-vacuum corrections needed for these ambient temperature comparisons. That comparison showed offsetting effects of the WRR measuring higher than the TIM in irradiance due to internal scatter while the TIM measured higher signals due to large atmospheric scatter during the campaign combined with the TIM's larger field of view.

SUMMARY

Recent ground tests with the TSI Radiometer Facility indicate the cause of the offsets between TSI instruments is internal instrument scatter, which causes erroneously high readings in non-TIM optical layout instruments. This facility helps validate instrument accuracy, making the existing TSI climate data record more robust against a potential data gap. The NPL and NIST radiometric references are in good agreement for measuring optical power, while the WRR reads slightly higher in both optical power and irradiance, based on comparisons with the TIM and PREMOS radiometers.

REFERENCES

1. Lean, J. and Rind, D., "How natural and anthropogenic influences alter global and regional surface temperatures: 1889 to 2006," *GRL*, **35**, L18701, 2008.
2. Gray, L.J., *et al.*, "Solar Influences on Climate," *Reviews of Geophysics*, **48**, RG4001, 2010.
3. Ohring, G., *et al.*, "Achieving Satellite Instrument Calibration for Climate Change," *EOS*, **88**, No. 11, 2007.
4. Butler, J.J., *et al.*, "Sources of differences in on-orbital total solar irradiance measurements and description of a proposed laboratory intercomparison," *J. of Res. of the NIST*, July 1, 2008.
5. Kopp, G., *et al.*, "The TSI Radiometer Facility - Absolute Calibrations for Total Solar Irradiance Instruments", *SPIE Proc*. **6677-09**, 26-28 Aug. 2007.
6. Kopp, G. and Lean, J.L., "A New, Lower Value of Total Solar Irradiance: Evidence and Climate Significance," *GRL*, **38**, L01706, 2011.
7. Fehlmann, A., *et al.*, "Fourth World Radiometric Reference to SI Radiometric Scale Comparison and Implications to On-Orbit Measurements of the Total Solar Irradiance," NEWRAD, Sept. 2011.

Absolute flux calibration of standard stars

John T. Woodward[1], Claire E. Cramer[1], Ping-Shine Shaw[1], Keith R. Lykke[1], Peter C. Zimmer[2], John T. McGraw[2], Peter Doherty[3], Christopher W. Stubbs[3,4], Emilio Falco[4]

[1]National Institute of Standards and Technology, Gaithersburg, USA, [2]University of New Mexico, Albuquerque, NM, USA, [3]Harvard University, Cambridge, MA, USA, [4]Harvard-Smithsonian Center for Astrophysics, Cambridge, MA, USA
Corresponding e-mail address: john.woodward@nist.gov

We have undertaken a campaign to calibrate the top-of-the-atmosphere absolute spectral flux for a catalogue of standard stars using a terrestrial telescope. Our approach involves calibrating a telescope-spectrometer system by imaging a terrestrial, spectrally calibrated source, then measuring the spectral flux from the target star. These measurements must be corrected for the atmospheric attenuation of the light along the respective paths. We will describe our overall approach to this challenging calibration problem and present preliminary results for the telescope-spectrograph calibration and measurement of the horizontal atmospheric transmission.

INTRODUCTION

Absolute stellar spectroradiometry is based on measurements in the 1970s of α Lyr (Vega) calibrated against a terrestrial blackbody source.[1] More recent observations have indicated that Vega may not be a suitable star for a radiometric standard. It is believed to be a pole-on, rapidly rotating star and contains a debris disk, both of which greatly complicate the modelling required to extend the calibration beyond the measured wavelengths.[2;3]

In the intervening decades, there have been significant advances in both radiometry and in measuring and modelling the effect of the atmosphere on light during its path to the telescope. A well calibrated (<1% uncertainty) catalogue of standard stars would have benefits for fundamental astronomy research, as well as potential applications in other scientific and commercial fields. We have previously reported the development of the Telescope Calibration Facility (TCF) at NIST for the calibration and testing of instrumentation for a field campaign.[4]

EXPERIMENTAL APPROACH

Our fundamental experimental approach to stellar radiometric calibration adheres closely to the 1970s measurements and is being performed at the same location, the F. L. Whipple Observatory at Mt. Hopkins, AZ. A calibrated light source is placed on the summit of Mt. Hopkins and observed with a telescope located on the Mt. Hopkins Ridge. The telescope then observes the target stars for calibration. Measurements of the atmospheric transmission along the light path from the summit to the telescope (horizontal transmission) and the telescope to the star (vertical transmission) are then used to correct the calibration for the atmospheric transmission.

The telescope we are using is the 60 inch Tillinghast telescope at the Mt. Hopkins ridge with the FAST spectrometer. This telescope can point at the Mt Hopkins summit, allowing observation of the calibration source during each night's observations.

The source on the summit consists of an integrating sphere illuminated either by a small lamp or by a spectrally tunable light source. A spectrometer with an irradiance head calibrated to NIST standards is used to calibrate the output of the source before and after it is observed by the telescope. The stability of the source is measured by a spectrometer fiber-coupled to the sphere.

Figure 1. Prototype of the calibration source mounted on a rail and tripod on Mt. Hopkins summit. The black box on right contains a 2 inch integrating sphere, shutter, and light source. The blue cube at left is the irradiance calibration head. A removable LED for initial alignment with the telescope is in between. The spectrometer and electronics are inside the window at right.

To correct for the horizontal atmospheric transmission we directly measure the radiance from a large integrating sphere located near the telescope at the ridge. A small telescope with a spectrometer measures the radiance a few meters from the sphere at the ridge and then is moved to the summit to repeat the measurement while the large telescope is observing the calibration source. The ratio of the radiance measurement from the summit to the one at the ridge yields the atmospheric transmission which is used to correct the calibration of the large telescope.

The calibration source and the horizontal transmission measurement are under going final testing in the laboratory and will be deployed at Mt. Hopkins in the spring of 2011. Preliminary results from this deployment will be presented.

The correction for the vertical atmospheric transmission will be done with a combination of LIDAR measurements and atmospheric modelling. A portable system based on the University of New Mexico's Atmospheric LIDAR for Extinction (ALE)[5] is under development and scheduled to be deployed at Mt. Hopkins later this year.

CONCLUSIONS

We have undertaken a campaign to create a catalogue of standard stars with absolute, top-of-the-atmosphere, spectral flux measured to <1% uncertainty. A calibration source and methods for measuring the atmospheric transmission have been developed and tested in the laboratory and will be deployed to Mt. Hopkins this year.

REFERENCES

[1] D. S. Hayes, D. W. Latham, and S. H. Hayes, "Measurements of the monochromatic flux from Vega in the near-infrared," *Astrophysical Journal*, vol. 197, pp. 587-592, 1975.

[2] D. M. Peterson, "Vega is a rapidly rotating star," *Nature*, vol. 440, pp. 896-899, 2006.

[3] C. Mégessier, "Accuracy of the astrophysical absolute flux calibrations: visible and near-infrared," *Astronomy and Astrophysics*, vol. 296, pp. 771-778, 1995.

[4] A. W. Smith, J. T. Woodward, C. A. Jenkins, S. W. Brown, and K. R. Lykke, "Absolute flux calibration of stars: calibration of the reference telescope," *Metrologia*, vol. 46, no. 4, p. S219-S223, 2009.

[5] P. C. Zimmer, J. T. Mcgraw, M. R. Ackermann, D. C. Hines, A. B. Hull, L. Rossmann, D. C. Zirzow, S. W. Brown, C. E. Cramer, G. T. Fraser, K. R. Lykke, A. W. Smith, C. W. Stubbs, and J. T. Woodward, "Space-based photometric precision from ground-based telescopes", *SPIE Proceedings*, vol. 7735, 2010.

Fourth World Radiometric Reference to SI radiometric scale comparison and implications to on-orbit measurements of the total solar irradiance

André Fehlmann[1], Greg Kopp[3], Werner Schmutz[1], Rainer Winkler[2], Wolfgang Finsterle[1], Nigel Fox[2]

[1]*Physikalisch-Meteorologisches Observatorium Davos / World Radiation Center, Davos, Switzerland*
[2]*National Physical Laboratory, Teddington, United Kingdom*
[3]*Laboratory for Atmospheric and Space Physics, Boulder, CO, United States of America*
Corresponding e-mail address: andre.fehlmann@pmodwrc.ch

Unlike the three previous World Radiometric Reference (WRR)-to-SI comparisons [1,2,3], we performed the fourth comparison in vacuum and thus avoid the air-to-vacuum corrections, which are generally the largest sources of uncertainty in such comparisons. Additionally, the Total solar irradiance Radiometer Facility (TRF) [4] allows, for the first time, an SI-traceable irradiance comparison to the WRR. We find that the WRR measures 0.17 % higher than SI in optical power and 0.32 % higher when measuring irradiances.

INTRODUCTION

Spaceborne total solar irradiance (TSI) instruments have shown poorly-understood offsets since the beginning of these measurements in 1978. Although all TSI instrument teams claim to have either fully characterized or calibrated their radiometers, there is a difference in measured TSI between the Total Irradiance Monitor (TIM), launched in 2003, and the previously existing space experiments, with the newer TIM measuring lower by 0.33 %. A workshop [5] dedicated to find the possible reasons for these differences identified stray light as a possible cause, noting that the older radiometers could potentially be susceptible to scattered light because their large entrance view-limiting apertures allow much more sunlight than is intended for measurement into the instrument interior, where, if not completely blocked, it can scatter through the smaller precision aperture and into the radiometer cavity itself, causing an erroneously high signal. The TIM has an inverted aperture geometry with a small precision entrance aperture, and thus averts this stray light problem, as explained in [6].

METHODS

Two PMO6-type absolute radiometers were selected for flight on the French PICARD spacecraft with intended improved SI-traceability in their calibrations, enabled via three comparisons to national standards:
1) Radiant power calibrations against the SI radiometric scale were performed at NPL [7]. These were purely optical power calibrations with an entering laser beam under-filling all radiometer apertures, as in the three previous WRR-to-SI comparisons. Placing the PREMOS radiometers in a vacuum chamber for the new results reported here avoids the air-to-vacuum corrections, which are generally the largest sources of uncertainty in such comparisons.
2) Calibrations of two PREMOS radiometers at the Laboratory for Atmospheric and Space Physics's TSI Radiometer Facility (TRF) allowed the first comparisons of flight radiometers in irradiance mode against a cryogenic radiometer that is traceable to the NIST radiant power scale. By varying the diameter of the uniform incident beam generated by the TRF, the PREMOS apertures were successively over-filled to determine the stray light originating from back reflections off the precision aperture and internal instrument scatter effects.
3) Comparisons of the PREMOS radiometers to the WRR in Davos were performed, allowing the PREMOS radiometers to become transfer instruments to compare the three different radiometric scales.

RESULTS

The optical power scales from NPL and NIST were linked via the TRF measurements of the PREMOS radiometers and found to be in very good agreement, having a ratio of 0.999989 ± 0.000297 (k=1). The

corresponding WRR-to-SI optical power ratio is 1.001785 ± 0.001064 (k=1) (Fig. 1), where the uncertainty is dominated by the uncertainties in the WRR calibration and its air-to-vacuum correction.
Irradiance mode comparisons, where all PREMOS apertures are over-filled by the TRF's uniform incident beam, raised the PREMOS signals by 0.14%. We conclude that this is due to stray light in the instrument.
Using the TRF irradiance calibration to compare the WRR and the SI scales gives a WRR-to-SI ratio of 1.003249 ± 0.001112 (k=1) (Fig. 1), where the uncertainty is again dominated by the uncertainties in the WRR calibration and the its air-to-vacuum correction.
Using the WRR calibrations, the PREMOS TSI measurements agree with those of VIRGO, which is not surprising as VIRGO also uses a WRR calibration. The ratio of these two radiometer measurements is 1.000064. However, utilizing the TRF irradiance calibrations, which include corrections for PREMOS's stray light, the PREMOS measurements agree with the TIM TSI values, giving a ratio of 0.999882 with PREMOS measuring slightly less than the TIM.

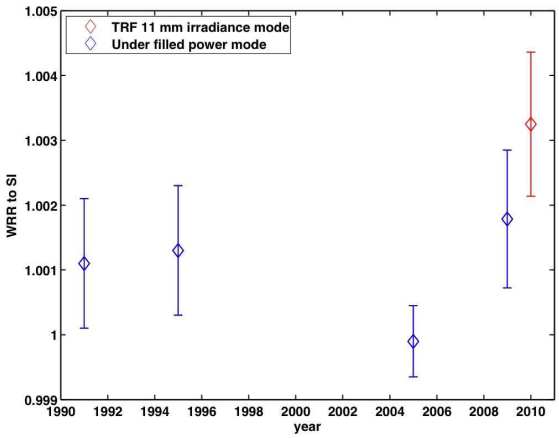

Figure 15. Results from the four WRR-to-SI radiometric scale comparisons. In blue are the results from optical power comparisons, showing the WRR measures 0.18% higher than the SI scale, and in red is the result from the irradiance comparison, which is 0.14 % higher still due to contributions from stray light in the WRR.

CONCLUSIONS

The TRF allowed us for the first time to determine the stray light measured by a PMO6-type radiometer when measuring irradiances. This value has been underestimated in the past, and explains half of the observed difference between the TIM and VIRGO in on-orbit TSI measurements. The other half is explained by the WRR-to-SI difference observed in optical power comparisons.
Thus we explain the on-orbit difference between the VIRGO and the TIM TSI values by the utilization of two different scales and it will be interesting to see what other TSI teams (DIARAD, ACRIM) find when they perform similar calibration experiments.

REFERENCES

1. J. Romero et al., First comparison of the solar and an SI radiometric scale, Metrologia, 28, 125-128, 1991.
2. J. Romero et al., Improved comparison of the World Radiometric Reference and the SI radiometric scale, Metrologia, 32, 523-524, 1995.
3. W. Finsterele et al., Third comparison of the World Radiometric Reference and the SI radiometric scale, Metrologia, 45, 377-381, 2008.
4. G. Kopp et al., Earth Observing Systems XII, Vol. 6677, 667709, 2007.
5. J. J. Butler et al., Sources of Differences in On-Orbit Total Solar Irradiance Measurements, Journal of Research, 4, 187-203, 2008
6. Kopp, G. and Lean, J.L., A New, Lower Value of Total Solar Irradiance: Evidence and Climate Significance, Geophys. Res. Letters Frontier article, 38, L01706, doi:10.1029/2010GL045777, 2011.
7. W. Schmutz et al., The PREMOS/PICARD instrument calibration, Metrologia, 46, 202-206, 2009.

Calibration of photovoltaic reference cells traceable to spectral irradiance standards of KRISS and its comparisons with PTB

Seung-Nam Park[1], Dong-Hoon Lee[1], Seongchong Park[1], Jae Keun Yoo[1], Seung-Kwan Kim[1], Dong-Joo Shin[1], Stefan Winter[2]

[1]*Korea Research Institute of Standards and Science (KRISS), Daejeon, Korea*
[2]*Physikalisch-Technische Bundesanstalt (PTB), Braunschweig, Germany*
Corresponding e-mail address: snpark@kriss.re.kr

We have calibrated photovoltaic reference cells (PVRCs) under a solar simulator in terms of its shot-circuit currents (I_{sc}) at the standard test condition (STC) traceable to the spectral irradiance standard of KRISS. The calibration uncertainty is evaluated to be 2.0 % (k = 2). The calibration is compared with that of PTB, which gives an agreement within 0.3%.

INTORDUCTION

Recently renewable energy industries in Korea requires primary calibration capability of PVRCs as PV industries is increasing production of silicon-based solar cell and intensifying development of the next generation solar cells.

Calibrations of PVRCs are to obtain I_{sc} at STC defined by

$$I_{sc}^{STC} = I_{sc}^{Meas} \cdot \frac{\int \Phi_s(\lambda) \cdot S(\lambda) d\lambda}{\int \Phi_m(\lambda) \cdot S(\lambda) d\lambda} \quad , \qquad (1)$$

where I_{sc}^{Meas} is short-circuit current of the PVRC under a certain irradiance of which absolute spectral irradiance is described by $\Phi_m(\lambda)$, $S(\lambda)$ the spectral responsivity of the PVRC, and $\Phi_s(\lambda)$ is the spectral irradiance of the standard AM 1.5 [1].

TRACEABILITY

Spectral irradiance of FEL lamps are realized by comparing them with a high-temperature blackbody using a spectroradiometer from 0.25 μm to 2.5 μm. The spectral irradiance of the blackbody is obtained by Planck's radiation law where the blackbody temperature is determined by a radiation thermometer. The spectral irradiance scale was verified by a bilateral comparison with VNIIOFI [2].

The spectral responsivity is measured against a Si and InGaAs photodiodes. The photodiodes are calibrated traceable to the KRISS cryogenic radiometer via Si trap detectors and a thermal detector.

CALIBRATION FACILITY

The PVRC comparator mainly consists of a solar simulator, a translator and instruments as shown in Figure 1. The solar simulator (Oriel 92251) has a 150 W Xenon lamp filtered an AM1.5 correction filter and a working area of 2.5 cm x 2.5 cm. A high-power LED is attached on the solar simulator to check linearity of PVRC near 1 kW/m^2 based on two-beam addition. The translator can install two PVRCs on two cold-plates whose temperatures are separately controlled by thermistors, temperature controllers and TECs. Positioning the PVRCs is controlled by the 2-axis translator. The temperatures of the PVRCs are monitored by reading the PRT sensors in them. The I_{sc} and I-V curve of two PVRCs are separately measured by a source-meter (Keithley 2400) through the front and rear terminals, respectively.

When we measure the spectral irradiance of the solar simulator, one of cold-plates is replaced with an integrating sphere collector of spectro-radiometers. CAS-140CT-154 (Instrument Systems GmbH) is used to cover the range from 0.25 μm to 0.9 μm and SP-320-R5 (Instrument Systems GmbH) to cover the range until 1.6 μm.

Beside the comparator, KRISS is running a differential spectral responsivity comparator which measures spectral responsivity of the PVRCs at 1 kW/m^2 [3].

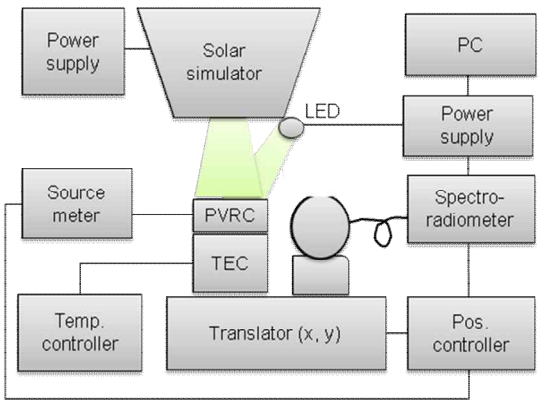

Figure 16. Schematics of RPVC comparator.

CHARACTERIZATION OF FACILITY

The spatial uniformity of irradiance on an area range of 2.4 cm × 2.4 cm over the reference plane was measured by a PVRC masked by an aperture with 3 mm in diameter. The irradiance difference between on the integrating sphere aperture (1.6 cm in diameter) of the spectroradiometer and on the active area (2 cm × 2 cm) of a PVRC under calibration was calculated to correct the irradiance on the PVRC. The reflection difference between from the integrating sphere aperture and from the PVRC was also measured to correct its effects on the irradiance measurements.

The temporal irradiance stability of the solar simulator was measured by a PVRC for 30 min after its initial stabilization, which enables us to estimate the relevant uncertainty. The I_{sc}-temperature coefficient of a PVRC was measured by comparison of two PVRCs. During the comparison, one of the cells maintained 25 ℃ while the other cell changed from 30 ℃ to 20 ℃. The temperature coefficient is 0.072 %/K. In general, PVRCs must be linear until more than 1 kW/m^2, which is confirmed by adding irradiance from the auxiliary LED lamp to that of the solar simulator.

This calibration facility may also be used as a secondary reference cell calibrator. To avoid any systematic effect on positioning two cells, the comparison is repeated after exchanging the cell positions on the hotplates. Final I_{sc} ratio of two cells is obtained by taking a geometric mean of the two comparison configurations. A product of three I_{sc} ratios of two combinations of 3 PVRCs yields unit within 0.1 %, which can be considered as the comparison uncertainty.

UNCERTAINTIES

The uncertainty of PVRC calibrations originates from the solar simulator PVRC under calibration as shown in Eq. (1) and Table 1. Measurements of spectral irradiance of the solar simulator and spectral responsivity of PVRC independently contribute to the uncertainty of the ratio of the integrations in Eq. (1).

The uncertainty contribution of spectral irradiance measurements consists of the spectral irradiance standard lamp (0.6 %), distance setting on the reference measurement (0.3 %), linearity (0.5 %), spectral stray light (0.2 %), reproducibility (0.2 %), wavelength accuracy (0.2 %) , etc., which totally amounts to 0.9 %.

The contribution of the spectral responsivity is derived by assuming the worst case of its measurements. The contributions from spatial uniformity and temporal stability of the solar simulator occur during comparison of the spectro-radiometer and the PVRC. The contribution from the spatial uniformity is obtained from the spatial uniformity test by assuming spatial mismatch of 1 mm between the integrating sphere collector and the active area of the PVRC.

The contribution from the cell temperature is reduced from the temperature range of PRT during comparison. Exposure of PVRC to the solar simulator causes temperature deviation of ± 0.5 ℃ from 25 ℃. The PVRCs are turned out to be linear near 1 kW/m^2 by adding irradiance of the auxiliary LED lamp. The contribution in the linearity measurements is included in the uncertainty.

Table 6. Calibration uncertainty of PVRCs at STC.

Origin	Contribution	Std. uncertainty
Solar simulator	measurement	0.9 %
	spatial uniformity	0.2 %
	temporal stability	0.1 %
PVRC	spectral responsivity	0.3 %
	temperature	0.04 %
	linearity	0.1 %
	current measurement	0.02 %
Combined std. uncertainty (k=1)		0.98 %

COMPARISON WITH THE PTB PV SCALE

Two PVRCs were hand-carried to PTB to compare them with the PTB scale. The comparisons of I_{sc} showed agreements within 0.3 % for both cells. The drift of the artefacts was checked after retuning back to KRISS, which was insignificant within 0.1 %.

REFERENCES

1. Metzdorf J., Winter S., Wittchen T., Radiometry in photovoltaics: calibration of reference solar cells and evaluation of reference values, Metrologia, 37(5), 573-578, 2000.
2. Shin D-J., Park C-W., Kolesnikova S.S., Khlevnoy B.B., Final report on bilateral comparison APMP.PR-K1.a.1-2008 between KRISS (Korea) and VNIIOFI (Russia): Spectral irradiance from 250 nm to 2500 nm, Metrologia, 47, Tech. Suppl., 02005, 2010.
3. Zaid G., Park S-N., Park S., Lee, D-H., Differential spectral responsivity measurement of photovoltaic detectors with a light-emitting-diode based integrating sphere source, Appl. Opt. 49(35), 6772-6783, 2010.

Modernized Absolute Radiometer for Solar Irradiance Measurement

S. P. Morozova, M. N. Pavlovich, A. A. Stacharny, B. E. Lisyansky, V. I. Sapritsky

All-Russian Research Institute for Optical and Physical Measurement (VNIIOFI), Moscow, RUSSIA

Corresponding e-mail address: morozova-m4@vniiofi.ru

The absolute radiometer MAR-1 with electrical substitution designed for use in solar irradiance measurements at the All-Russian Research Institute for Optical and Physical Measurement (VNIIOFI) was modified. The principle of operation of the radiometer is described. The composition of the radiometer and its software is described. The results of international comparisons of the radiometer MAR-1 with World Radiometric Reference (WRR), which were carried out at the World Radiation Center in Davos are given.

INTRODUCTION

Appearance of two modified radiometers MAR-1 installed on the Sun tracker STR 22 is shown in Fig. 1.

Figure 17. Appearance of two modified radiometers MAR-1 installed on the Sun tracker STR 22.

Primary standards for realization of the units of irradiance are established with the use of absolute radiometers with electrical substitution.

The modernized absolute radiometer MAR-1 with electrical substitution consists of a radiation receiver and automatic temperature stabilization and data processing systems, based on the notebook and also Sun tracking system.

The absolute radiometer measures irradiance by comparing optical power with electrical power dissipated in a substitution winding. Irradiance value in the Absolute Radiometer MAR-1 is computed as difference between electrical power values during reference and observation phases taking into account the area of the precision aperture and an overall correction factor which includes the cavity absorption coefficient [1.2]. The receiving unit of the radiometer is installed on the Sun Tracker STR 22 (EKO Instruments Co., Ltd, Japan). The Sun Tracker STR 22 is exceedingly accurate at Sun tracking and can calculate the solar position in everywhere throughout the world. The Sun Tracker has double arms and it is possible to mount two receiving units. The software of the absolute radiometer is written in LABVIEW 8.

The software provides completely an automatic operating mode of radiometer with changing of the reference and observation phases of work with representation of the current information and results of its processing. The software allows to record on a computer screen a current and voltage on the substitution winding during the observation and reference phases for all the measurement cycles. The precision and accuracy of the reproduction of the irradiance unit have been confirmed during the international comparisons with World Radiometric Reference (WRR), which were carried out at the World Radiation Center in Davos in 1995, 2000, 2005 and 2010 (IPC-VIII, IPC-IX, IPC-X, IPCX1).

The results of these comparisons have shown, that during 10 years a divergence of the results of the absolute radiometer MAR-1 and World Standard Group (WSG) does not exceed 0.14 %.

REFERENCES

1. V. I. Sapritsky, M. N. Pavlovich, Metrologia, 26, 81-86 (1989).
2. S. P. Morozova, V. I. Sapritsky and M. N. Pavlovich, Metrologia, 28, 117-120 (1991).

Monitor to measure the Integrated Transmittance (MITRA) of Windows

André Fehlmann[1], Wolfgang Finsterle[1], Werner Schmutz[1], Rainer Winkler[2], Nigel Fox[2], Peter Blattner[3]

[1]*Physikalisch-Meteorologisches Observatorium Davos / World Radiation Center, Davos, Switzerland*
[2]*National Physical Laboratory, Teddington, United Kingdom*
[3]*Federal Office of Metrology, Bern, Switzerland*
Corresponding e-mail address: andre.fehlmann@pmodwrc.ch

This work forms part of the Cryogenic Solar Absolute Radiometer (CSAR) project [1] - also presented at this conference by [2] - seeking to bring the advantages of cryogenic radiometry to ground based total solar irradiance measurements. One of the most critical issues that we must address to achieve this is how to precisely measure the transmittance of the entrance window to the vacuum chamber. We have built a Monitor to measure the Solar spectrally weighted, Integrated Transmittance (MITRA) of windows and will present the first measurement results acquired in front of the sun.

INTRODUCTION

We have built a cryogenic solar absolute radiometer (CSAR) for ground based measurements of Total Solar Irradiance (TSI). The advantages of CSAR stem from its operational temperature, which in turn enforces operation under vacuum and consequently the need for a window. In this context it is essential to be able to precisely determine the transmittance of the entrance window to the vacuum chamber over the full spectral range of interest. In contrast to cryogenic radiometers currently operated as primary standards for spectral responsivity in national metrology institutes where the interest is largely in monochromatic transmittance values over a relatively narrow spectral range, we have to deal with the transmission of the entire solar spectrum. We decided to use fused quartz (Suprasil) and alternatively sapphire windows on the cryogenic radiometer. Although these materials cut-off some of the solar radiation, their mechanical stability and resistance to atmospheric moisture made them the best choice. Theoretical calculations (Fig. 1) show that the integrated transmittance through a suprasil window will change by up to 0.15 % during a day depending on the air mass along the line of sight. We also expect seasonal variations of the same order which we want to track with MITRA.

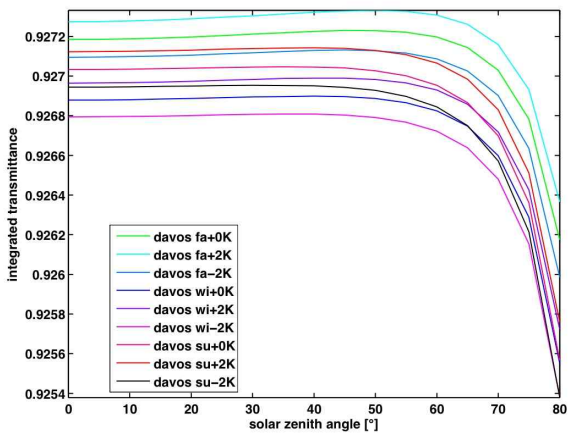

Figure 18: Calculated integrated transmittance through a suprasil window for different seasons and atmospheric temperature profiles. Depending on the solar elevation, the integrated transmittance varies by up to 0.15 %.

DESCRIPTION OF MITRA

The MITRA design is based on the principle of a dual-cavity monitor radiometer working at ambient temperature (Fig. 2). One of the monitor cavities views TSI through an identical window to that used on CSAR. Thus the monitor can determine the attenuation caused by the window relative to the unobstructed monitor cavity. Because the monitor radiometer will perform relative rather than absolute measurements the normal drawbacks of ambient temperature radiometry are largely irrelevant. All multiplicative correction factors, such as reflectivity of the cavities or area of the precision aperture, will cancel out in these relative measurements. Moreover, the monitor radiometer will be operated in "passive mode" i.e. not using electrical substitution. Hence the corrections for non-equivalence, lead heating, and the control loop electronics (CUI) also vanish. With all these sources of uncertainty eliminated we expect to measure the integrated (solar/atmosphere weighted) transmittance of the entrance window to better than one part in 10^4.

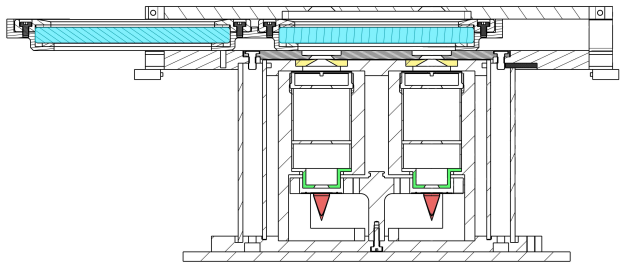

Figure 19: Darwing of MITRA with the two cavities in red. The precision respectively view limiting apertures in yellow and green. MITRA has two window inserts (blue) which allow different operation modes.

CHARACTERISATION OF MITRA

From experience with PMO6-type radiometers which make use of two cavities we know that a difference in the thermal relaxation time constant between the two cavities introduces a spurious signal. Thus we developed new silver cavities which are ultrasonically welded to an aluminium thermal resistor. This highly reproducible technique yields cavity pairs which have almost the same thermal relaxation time constant allowing it to be "fine-tuned" much more easily.

The temperature rise of a MITRA cavity is proportional to the absorbed solar irradiance. We determine this temperature rise by measuring the resistance of the thermometer on the cavity and on the heat sink. When we assume a linear response of the thermometer resistance with temperature then the solar irradiance generates a signal that is proportional to

$$\frac{R^{cavity}\ T}{R_0^{cavity}\ T_0} - \frac{R^{heatsink}\ T}{R_0^{heatsink}\ T_0}$$

Since the temperature rise of a cavity is approximately 1 degree Celsius, the measured signals will be small. Thus, the calculated ratio of the two cavities is sensitive to disturbances of the measured resistances. We first performed thermal stability tests of the cavity ratio by measuring the dark signals with closed shutters. Since we are interested in the variations that we have to expect when the cavities are illuminated, we introduced a virtual temperature rise of 1 degree in the cavity by adding 0.38 Ohm to the cavity resistance. Then we determine the cavity ratio during a night where the ambient temperature changed by more than 12 degrees Celsius. Since both cavities are mounted on the same heat sink, we expect that a change of the ambient temperature should have no effect on the cavity ratio. And indeed, our measurements show that the mean cavity ratio is 1.000005 (Fig. 3). Hence, we have designed a monitor that is not sensitive to ambient temperature changes. The standard deviation of 220 ppm of the measurements represents the intrinsic thermal fluctuations in the thermometers which seems to be the natural limit of the current system. However, increasing the sampling rate and applying the appropriate fitting should allow us reduce the uncertainty in the integrated transmittance measurements.

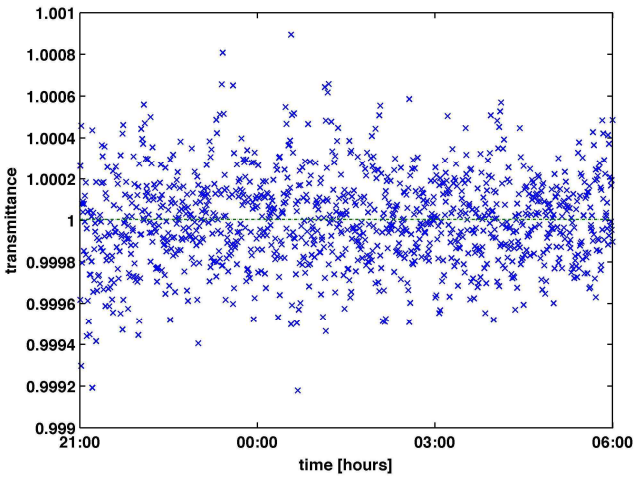

Figure 20: The stability test of the MITRA cavity ratio reveals that the entire system is not sensitive to ambient temperature changes of 12 degrees Celsius during the night.

CONCLUSION AND OUTLOOK

We have shown that the MITRA cavity ratio is not influenced by the ambient temperature. Integrated transmittance measurements in front of the sun with the CSAR entrance windows are still ongoing and we will be ready to present the first results at NEWRAD 2011.

REFERENCES

1. J.E. Martin, N.P. Fox, P.J. Key, Cryogenic Solar Absolute Radiometer (CSAR), Metrologia, 30, 305, 1993.
2. W. Finsterle, Cryogenic absolute radiometer for total solar irradiance, NEWRAD 2011 invited talk.
3. R. Winkler et al, Design Features and Test of the Cryogenic Solar Absolute Radiometer, NEWRAD 2011 abstract.

Aerosols and cloud effects on solar spectral irradiance

Uwe Feister[1] and Steffen Franke[2]

[1]*German Meteorological Service, Meteorological Observatory Lindenberg – Richard-Aßman-Observatory, Lindenberg, Germany*,

[2]*Leibniz Institute for Plasma-Science and Technology, Greifswald, Germany*
Corresponding e-mail address: uwe.feister@dwd.de

Spectroradiometric measurements of solar irradiance at the Earth's surface from the UV to the NIR have been performed to study wavelength dependent actions of radiation. Instrument calibration and stability are important prerequisites. Atmospheric extinction of solar spectral irradiance by air molecules, aerosols and clouds affects the relation between different actions. In this study, the relationship between melatonin suppression and photopic vision (illuminance) in dependence of atmospheric conditions will be discussed.

INSTRUMENTATION AND CALIBRATION

A CCD spectroradiometer Avantes Avaspec-2048 USB2 with 1.5 nm step width was applied for the measurements. The instrument is equipped with an optics head consisting of a Teflon diffuser (2π), which is heated to 25 °C. It is connected via an 8 m fiber optics bundle to the entrance aperture of the spectroradiometer. The integral cosine error is less than 2.5%. Calibration of the whole system is based on an FEL 1000 W quartz halogen lamp OSRAM Sylvania SL206, which was calibrated by the Physikalisch-Technische Bundesanstalt (PTB). The diffuser has been installed on the rooftop platform having free horizon at Lindenberg (52.2086° N, 14.1213° E, 127 m asl), while the spectro-radiometer itself has been placed in a thermostatted box at 22 ± 0.5 °C in the floor below the platform, after its temperature dependence had been checked in the Lindenberg climate chamber. Monthly calibration checks of the Avantes instrument, which were performed by a portable lamp source KS-041 of 200 W based on a design by PTB [1], showed deviations within ±5%. The KS041 lamp source had been also absolutely calibrated by an Optronics spectro-radiometer OL750 based on the FEL 1000 W SL206. Its absolute calibration allows us roof-top instrument re-calibrations without having to transport the instrument back to the laboratory.

Spectra of solar spectral irradiance from 300 to 922 nm have been acquired from August 2010 onwards. Groups of 10 spectra typically at exposure times of 20 ms to 200 ms have been averaged at time steps of 1 minute to resolve fast irradiance changes due to moving clouds.

SOLAR SPECTRAL IRRADIANCE

Solar spectral irradiance was compared for the region 300 – 450 nm with spectra operationally measured by fast scanning UV spectroradiometers of the type SPECTRO 320 D, which are double monochromators. The comparisons showed that the Avantes CCD instrument is capable of providing spectral irradiance with small uncertainties for wavelengths of >350 nm, whereas with shorter wavelengths higher uncertainties become evident that need to be analyzed. Fig. 1 illustrates solar spectral irradiance at distances of 30 minutes in the morning of August 21, 2010 between 5 and 11 UTC. The thin Cirrus clouds did not significantly alter the irradiance compared to clear sky. Spectral irradiance increases with decreasing solar zenith angle (SZA). The ratios between spectra at 11 UTC (SZA=40^0) and 5 UTC (SZA=81.5^0) plotted in the upper panel of Fig. 1 show a decrease with increasing wavelengths, i.e. a stronger increase of irradiance at shorter wavelengths than at longer wavelengths ('blue-shift'). While the Fraunhofer absorption lines, that arise from the sun's photosphere and that are mainly a phenomenon in the UV and short-wavelengths visible region, are not evident in the *ratios* of spectral irradiance, the absorption features of atmospheric gases (CO_2, O_2, H_2O) appear as maxima (peaks) due to the smaller band-absorption with shorter radiation path-lengths at small SZA.

In this study, we focus on the relationship between melatonin suppression (MEL) [2] and photopic vision [3], or illuminance (ILL) if converted to photometric units. Melatonin suppression is important for the sleep-awake cycle and is considered to be effective in

treating seasonal affective disorders (SAD) or seasonal depression.

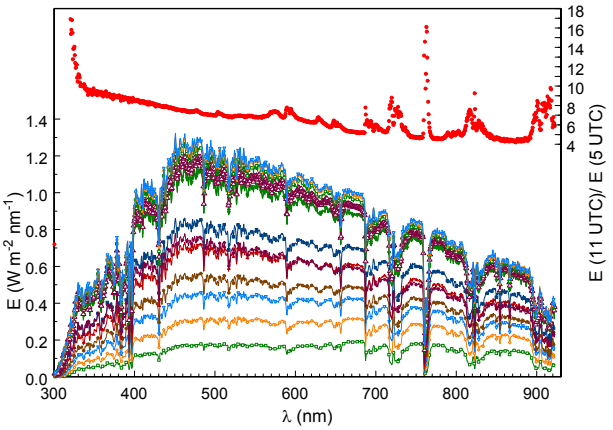

Fig. 1 Solar spectral irradiance as a function of wavelength at Lindenberg on August 21, 2010 at 30 minutes distance between 5 and 11 UTC (lower curves with left-hand ordinate), and ratios between spectral irradiance at 11 UTC and 5 UTC (upper panel and right-hand ordinate scale)

The action spectrum of MEL extends from about 365 nm to 625 nm, and it reaches its peak in the blue at about 470 nm. Illuminance extends from about 370 nm to 810 nm, and it reaches its peak in the green region around 560 nm.

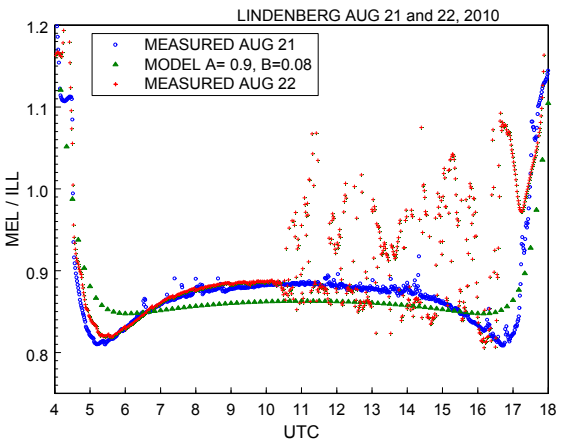

Fig. 2 Ratios between melatonin suppression (MEL) and photopic vision (ILL) both in radiometric units on August 21 and 22, 2010 from spectroradiometric measurements and model calculations

As is shown in the left-hand panel of Fig. 2, a typical diurnal variation of the ratios MEL/ILL reaches a broad maximum around local noon time. Minimum values are reached at SZA of about 75° in the early morning and late afternoon. The ratios increase again with further increasing SZA due to the dominating portion of diffuse radiation scattered from angles close to the zenith at very large path lengths of direct irradiance.

The measurements have been compared with model calculations for clear sky using a radiative transfer model [4]. The results of the model calculation for clear sky with an Angstrom coefficient of α=0.9 and a turbidity parameter of β=0.08 derived from aerosol optical depth measurements at the site provide a diurnal variation of the ratios MEL/ILL quite similar to the measurements, though with somewhat smaller diurnal amplitude.

In the morning hours of the following day August 22, 2010 only Cirrus clouds occurred as well. Beginning around 11 UTC low-level Cumulus and mid-level Altocumulus clouds of 5 to 7 Okta appeared. Due to increased scattering of shortwave radiation by cloud particles and increased absorption due to cloud water at longer visible and NIR wavelengths, the ratios MEL/ILL significantly increased in the afternoon hours of August 22. The few lower ratios compared to modelled clear sky on August 22 are assumed to be caused by anisotropy of clear-sky radiance and the cloud distribution that modifies this anisotropy. We note that the optical characteristics of atmospheric aerosols affect the ratios MEL/ILL [5].

Further objectives of this study will be to characterize and test the instrument for its suitability for solar radiation measurements and to provide a data base to derive dependencies of spectral irradiance on atmospheric conditions.

REFERENCES

1. Metzdorf, J., K. D. Stock, P. Sperfeld, A. Sperling, S. Winter, T. Wittchen, Aspects of quality assurance in monitoring solar UV irradiance, *Metrologia* 40, 66 – 69, 2003.
2. Thapan, K, J. Arendt, D.J. Skene, An action spectrum for melatonin suppression: evidence for a novel non-rod, non-cone photoreceptor system in humans. *J. Physiol.* 535 (1), 261 – 267, 2001.
3. CIE Publication 086-1990 CIE 1988 2 Degree Spectral Luminous Efficiency Function for Photopic Vision 1988.
4. Mayer, B. A. Kylling , Technical Note The LibRadtran software package for radiative transfer calculations – description and examples of use. *Atmos. Chem. and Phys. Disc*. 5, 1855 – 1877, 2005.
5. Feister U., G. Laschewski, and R.-D. Grewe, UV index forecasts and measurements of health-effective radiation. *J. Photochem. Photobiol. B*, 102, 55 – 68, 2011.

Development of a 365 nm LED Source as a UV Transfer Standard

Shen Zhu,

US Army Primary Standard Laboratory, Redstone Arsenal, Alabama

Yuqin Zong,

National Institute of Standards and Technology, Gaithersburg, Maryland

Currently high pressure mercury lamps are used as 365 nm ultraviolet (UV) sources in the US military laboratories for material characterizations and sample inspections. The mercury lamps are susceptible to electric shock (due to high voltage operation) and mercury contamination. These bulky, hazardous mercury lamps require long stabilization time and have poor repeatability and reproducibility. Thus, a detector-based device must be used as the UV transfer standard. Due to unwanted additional spectral lines (other than the 365 nm line), a 365 nm narrow-band filter must be added in the detector-based transfer standard, which introduces additional errors from the filter transmittance and inter-reflection between the filter and the detector unless they are calibrated as a single device.

Solid-state high-power UV light-emitting diodes (LEDs) have been developed in recent years which may be used in many applications where mercury lamps are used traditionally. We have developed a compact 365 nm UV LED transfer standard source. The prototype LED source is temperature-controlled which is stabilized within one minute and has one-week stability of less than 0.1 %. The prototype UV LED source were characterized for relative spectral power distribution, spatial uniformity of LED beam, irradiance level, and stability. Details will be presented and discussed.

Automatic and Accurate Characterization of Femtosecond Optical Pulses

Yuqiang Deng[1], Qing Sun[1], Shiying Cao[2], Jing Yu[1] Ching-yue Wang[3] and Zhigang Zhang[4]

[1]*Division of Metrology in Optics and Laser, National Institute of Metrology, Beijing 100013, P. R. China*
[2] *Division of Electricity Quantum Metrology, National Institute of Metrology, Beijing 100013, P. R. China*
[3]*School of Precision Instrument and Optoelectronics Engineering, Tianjin University, Tianjin 300072, P. R. China*
[4]*School of Electronics Engineering and Computer Science, Beijing University, Beijing 100871, P. R. China*
Corresponding e-mail address: yqdeng@nim.ac.cn

We introduce a technique for measurement of femtosecond optical pulses automatically and accurately. With this technique, electric field, phase, waveform, as well as duration of femtosecond optical pulses are precisely characterized. The simulated autocorrelation traces from measured pulses electric field agrees excellently with the measured ones; and the pulse reconstruction procedure needs no manual operation.

INTRODUCTION

A femtosecond optical pulse has extreme short duration period, extreme broad spectral bandwidth, and extreme peak power; it therefore plays a key role in a variety of applications, such as ultrafast pumping and detection, time-resolved spectroscopy, ultra-fine microfabrication, and nonlinear optics. Femtosecond optical pulses have brought revolutions in recent time and frequency metrology [1], terahertz metrology [2], and ultrafast electric pulse metrology [3]. Accurate measurement and characterization of femtosecond optical pulse have become anticipated in various applications.

We introduce a technique for measurement femtosecond optical pulse accurately and automatically in this paper. With this technique, electric field and waveform of femtosecond optical pulses are precisely characterized.

EXPERIMENTAL DEMOSTRATION

Spectral phase interferometry for direct electric-field reconstruction (SPIDER) [4] is a technique for measurement spectral phase of femtosecond optical pulse. Pulses waveform is constructed combined with spectrum based on Fourier transform. In the traditional phase retrieval procedure, phase is extracted from the filtered alternating current component of Fourier transform. The filter is manual selection and adjustment, and different widths or shapes of filter windows produced different phases.

We introduce wavelet transform [5] for spectral phase retrieval of femtosecond optical pulses. The phase is directly extracted from the ridge of wavelet transform. There are no filter in this procedure, and uncertainty form filter width or/and shape is therefore avoided.

We have home made a spectral phase interferometer based on SPIDER technique. The spectral interferogram is produced from a 100 μm thick BBO crystal with type II phase match, as is shown in Fig. 1.

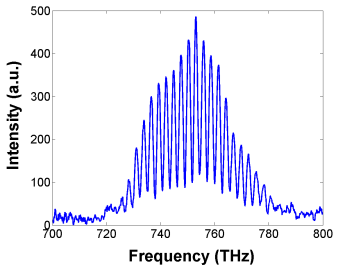

Figure 1. Measured spectral interferogram.

Wavelet transform was applied on the measured spectral interferogram, and the time and frequency distributions are exhibited on a two-dimensional plane. The intensity map and phase map are shown in Fig. 2(a) and 2(b), respectively.

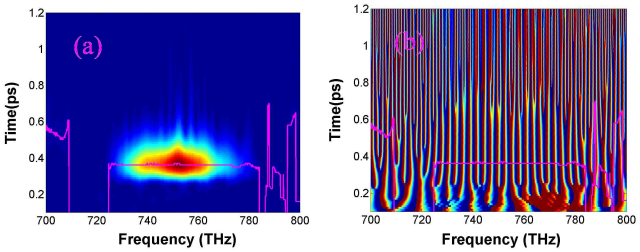

Figure 2. Wavelet-transform of spectral interferogram. (a) Intensity topography, (b) phase topography. The ridge of wavelet transform is indicated with pink colour line.

The phase of spectral interferogram can be directly extracted from the ridge of wavelet transform. The ridge was superposed on Fig. 2 with pink lines.

With the extracted interferometry phase, we can retrieve the spectral phase (Fig. 3). Figure 3 also shows the measured spectrum of the femtosecond optical pulse. The electric field (Fig. 4(a)) and

waveform (Fig. 4(b)) of the femtosecond optical pulse is reconstructed from the spectrum and spectral phase with Fourier transform technique. Figure 4(b) shows the pulse width (FWHM) is 18.2 fs.

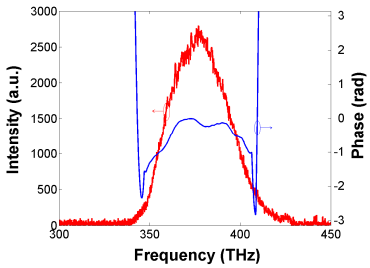

Figure 3. Measured spectrum and retrieved spectral phase.

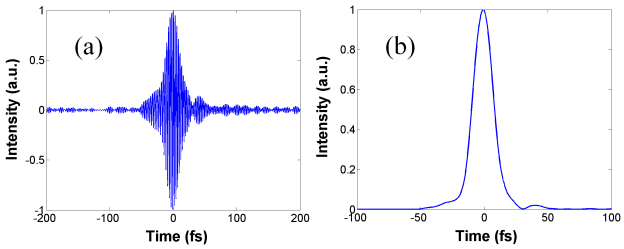

Figure 4. Reconstructed electric field and waveform. (a) Electric field, (b) waveform.

RESULTS ANALYSIS

From the reconstructed electric field in Fig. 4(a), we simulate the autocorrelation traces of the pulses. The simulated interferometric autocorrelation and intensity autocorrelation are shown in Fig. 5(a) and 5(b), respectively. The intensity autocorrelation in Fig. 5(b) shows the width of autocorrelation (FWHM) is 26.6 fs. We can obtain that the ratio of autocorrelation width to the pulse width is 1.462.

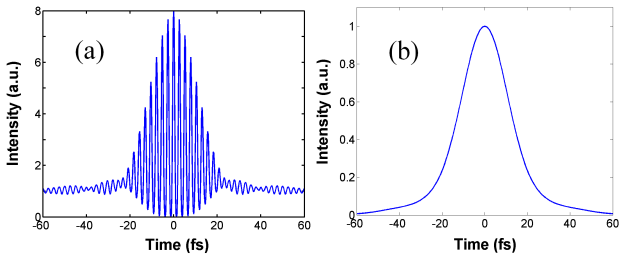

Figure 5. Simulated autocorrelation traces with reconstructed pulse electric field. (a) Interferomatric autocorrelation, (b) intensity autocorrelation.

We have also home made an autocorrelator for autocorrelation measurement [6] of the femtosecond optical pulses. The measured interferometric autocorrelation and intensity autocorrelation are shown in Fig. 6(a) and 6(b), respectively.

Figure 6 shows there are an excellent agreement in comparison with the simulated autocorrelation in Fig. 5. This proves the accuracy of the measurement results. The repetitious measurements with different interferometry delay or from type I phase match of BBO crystal are in good agreement. The deviation is within ± 1 fs.

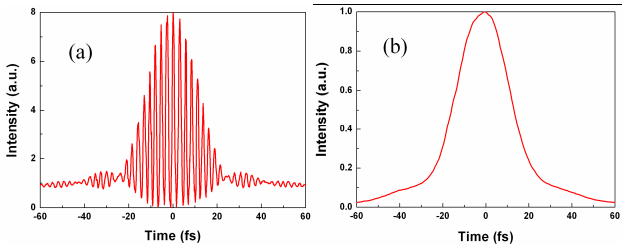

Figure 6. Measured autocorrelation traces. (a) Interferomatric autocorrelation, (b) intensity autocorrelation.

CONCLUSIONS

We have introduced a technique for spectral phase retrieval of femtosecond optical pulses. This technique needs no filter; therefore, automatic phase retrieval and pulse reconstruction is realized because of no manual operation of selection and adjustment filter. The simulated autocorrelation traces agree excellently with measured ones. This technique is useful in accurate characterization of ultrashort optical pulses, precise measurement of pulse peak power, and determination of instantaneous electric field intensity of the pulse. With this technique, the ratio of autocorrelation width to pulse width can be identified, which is helpful in improving the precision of pulses width measurement with autocorrelation technique.

REFERENCES

1. J. L. Hall and J. Ye, "A new era of frequency standards and optical frequency measurement," Optics & Photonics News 12, 44-50, 2001.
2. T. Yasui, S. Yokoyama, H. Inaba, K. Minoshima, T. Nagatsuma, and Tsutomu Araki, "Terahertz frequency metrology based on frequency comb," IEEE J. Sel. Top. Quant. 17, 191-201, 2011.
3. D. F. Williams, P. D. Hale, T. S. Clement, and J. M. Morgan, "Calibrated 200-GHz waveform measurement," IEEE T. Microw. Theory. 53, 1384-1389, 2005.
4. C. Iaconis and I. A. Walmsley, "Self-referencing spectral interferometry for measuring ultrashort optical pulses", IEEE J. Quantum Electron. 35, 501-509, 1999.
5. Y. Deng, Z. Wu, L. Chai, C. Wang, K. Yamane, R. Morita, M. Yamashita, and Z. Zhang, "Wavelet-transform analysis of spectral shearing interferometry for phase reconstruction of femtosecond optical pulses," Opt. Express 13, 2120-2126, 2005.
6. J-C. M.Diels, J. J. Fontaine, I. C. McMichael, and F. Simoni, "Control and measurement of ultrashort pulse shapes (in amplitude and phase) with femtosecond accuracy," Appl. Opt. 24, 1270-1282, 1985.

Simultaneous Correction of Bandpass and Stray Light Effects in Array Spectroradiometer Data

Saulius Nevas, Gerd Wübbeler, Armin Sperling, Annette Teuber and Clemens Elster
Physikalisch-Technische Bundesanstalt (PTB), Braunschweig and Berlin, Germany,

Corresponding e-mail address: saulius.nevas@ptb.de

A method for a simultaneous correction of bandpass and stray light effects in array spectroradiometer data is presented. The method is based on the inversion of the instrument matrix of a device determined with the help of tuneable lasers. By applying an established regularization technique, a straightforward deconvolution of the measurement results is possible. Application examples on the basis of LED measurement data are provided.

INTRODUCTION

Both radiometry and modern photometry rely heavily on spectroradiometric measurements, e.g. for the purpose of the photometric and colorimetric characterization of new types of light sources for SSL lighting applications, the spectral power distribution of UV radiators for the determination of the spectral mismatch corrections of UV meters or the spectral assessment of solar simulators for PV testing equipment, to mention a few. The spectroradiometric applications increasingly employ compact, fast, cost-efficient and easy-to-handle CCD array spectroradiometers. The devices, however, are far from being perfect in terms of their spectral transfer (response) functions, i.e. they typically have a finite bandpass and also a non-zero response in the out-of-band range. Hence, both the bandpass and the stray light corrections often need to be applied to the measurement data. A complete spectral correction with respect to the bandpass and stray light properties of a spectroradiometer is commonly known as a spectral deconvolution. Unfortunately, the deconvolution of measured spectra faces the well-known problems related to the stability of the solutions. Therefore, existing correction techniques typically divide the problem into two parts and deal separately with either the bandpass [1-4] or the stray light correction [5-6]. In this paper, we present a matrix inversion-based method that makes possible a simultaneous correction of both the bandpass and the stray light effects in array spectroradiometer data.

SPECTRAL DECONVOLUTION OF ARRAY SPECTRORADIOMETER DATA

A starting point for enabling spectral deconvolution is the determination of the instrument functions (relative response of the spectroradiometer to a monochromatic excitation) within the spectral range of the device. This task is nowadays considerably simplified due to the increasing commercialization and affordability of wavelength-tuneable solid-state lasers. At PTB, a setup based on a cost-efficient slow repetition-rate laser system is used for that purpose [7]. For a CCD array spectroradiometer, the instrument functions can be expressed as a square matrix. Hence, the measured spectrum X is described in terms of matrix multiplication

$$X = AY, \tag{1}$$

where A denotes the instrument matrix and Y the vector of the true spectrum. Thus, a correction for the instrument function may be achieved by the inversion of (1). However, for array spectroradiometers, the instrument matrix A is typically ill-conditioned. Therefore, the direct solution of (1) by the matrix inversion yields results which are unstable with respect to small perturbations of the measured spectrum as well as perturbations of the estimated instrument matrix. In order to achieve a stable solution of (1), regularization techniques can be applied. We propose applying the Tikhonov regularization [8] for the solution of (1) by minimizing

$$\left\|AY - X\right\|^2 + \left\|\Gamma Y\right\|^2, \tag{2}$$

where $\|\ \|$ is the Euclidian norm and Γ denotes a suitably chosen regularization matrix. Here $\Gamma = \alpha I$ is used, where I is the identity matrix. The regularization parameter α is usually chosen as a trade off between a small residual norm ($\|AY - X\|$) resulting from a small value of α and a small norm of the solution Y, which is achieved for large α. This approach is also followed when applying the L-curve criterion for selecting an α [8]. For the

Tikhonov regularization, the approximate solution of (1) is given by

$$Y_\alpha = (A^T A + \alpha^2 I)^{-1} A^T X . \qquad (3)$$

That is, the matrix $(A^T A + \alpha^2 I)^{-1} A^T$ can be used as a spectral correction matrix.

Note that the matrix-based stray light correction method by Zong *et al*. [6], where the bandpass region surrounding the main diagonal of the instrument matrix is manipulated, also results in a regularization of the instrument matrix. However, there the bandpass region of the instrument function is mainly discarded and, hence, bandpass effects are not corrected. In contrast, when applying the Tikhonov regularization (3), the full instrument matrix is taken into account. Therefore, the proposed method simultaneously corrects for stray light as well as bandpass effects induced by the instrument function.

APPLICATION EXAMPLE

The matrix inversion-based method for the simultaneous bandpass and stray light corrections was tested on several CCD array spectroradiometers. The instrument matrices A of the devices were determined using the **P**ulsed **L**aser **S**etup for **A**dvanced **C**haracterisation **o**f **S**pectroradiometers (PLACOS) at PTB [7]. Fig. 1 demonstrates the effectiveness of the spectral corrections applied to the spectral power distribution of a deep blue and blue LEDs measured by an array spectroradiometer with a nominal bandwidth of 1.7 nm. For comparison purposes, results of only stray light corrections using the method of [6] as well as the measurement data by a double-monochromator spectroradiometer with a 1.0 nm bandwidth are also shown.

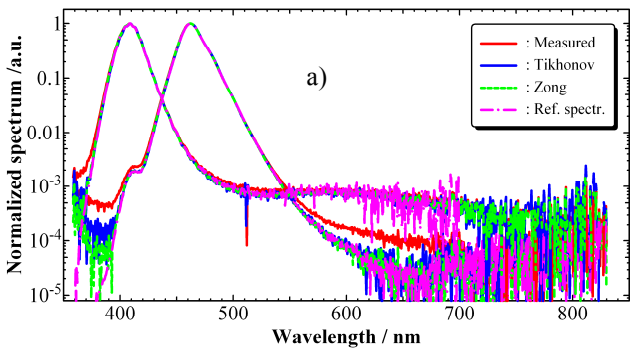

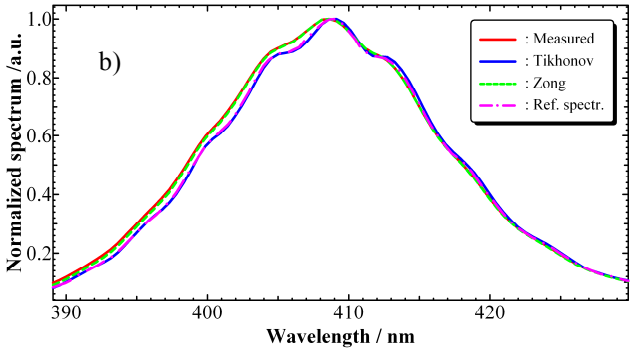

Figure 1. Spectral power distribution of blue LEDs: a) measurement result by a CCD array spectroradiometer with a 1.7 nm bandwidth, result of the spectral deconvolution by means of Tikhonov regularization, result of the stray light correction by the method of Zong *et al*. and measurement result by a double-monochromator spectroradiometer (Ref. spectr.) with a 1.0 nm bandwidth; b) close up on the bandwidth region of the deep blue LED.

REFERENCES

1. E. I. Stearns, R. E. Stearns, An example of a method for correcting radiance data for bandpass error, Color Res. Appl., 13, 257-259, 1988.
2. E. R. Woolliams, M. G. Cox., P. M. Harris, H. M. Pegrum, Correcting for bandwidth effects in monochromator measurements, in Proceedings of NEWRAD 2005: 9th International Conference on New Developments and Applications in Optical Radiometry, Davos, 2005.
3. Y. Ohno, A flexible bandpass correction method for spectrometers, in Proc. AIC'05, Granada, 2005.
4. J. L. Gardner, Bandwidth correction for LED chromaticity, Color Res. Appl., 31, 374-380, 2006.
5. S. W. Brown, B. C. Johnson, M. E. Feinholz, M. A. Yarbrough, S. J. Flora, K. R. Lykke, D. K. Clark, Stray light correction algorithm for spectrographs, Metrologia, 40, S81-83, 2003.
6. Y. Zong, S. W. Brown, B. C. Johnson, K. R. Lykke, Y. Ohno, Simple spectral stray light correction method for array spectroradiometers, Appl. Opt., 45, 1111-1119, 2006.
7. S. Nevas, M. Lindemann, A. Sperling, A. Teuber, R. Maass, Colorimetry of LEDs with array spectroradiometers, MAPAN - Journal of Metrology Society of India, 24, 153-162, 2009.
8. H. W. Engl., M. Hanke, A. Neubauer, Regularization of Inverse Problems, Kluwer, Dordrecht, 1996.

In Situ Measurements of OLED Lifetime

Thorsten Gerloff, Armin Sperling, Detlef Lindner, Maic Meyer, Stefan Pendsa[1]

[1]*Physikalisch-Technische Bundesanstalt, Braunschweig, Germany*

Corresponding e-mail address: Thorsten.Gerloff@PTB.de

OLEDs are flat light sources with an extended emitting area and OLEDs are already commercially available. Key parameters for quality are high luminous efficacy and a long lifetime in terms of luminance decay as well as colour stability. However, up to now no standardised measurement procedures have been established.

In this article we describe in situ measurements of OLED lifetimes which have recently started at PTB. The results will be used to derive proposals for standardisation.

INTRODUCTION

A long lifetime of Organic Light Emitting Diodes (OLEDs) is one important key parameter for this technology to become sufficiently reliable as a mass product for lighting applications.

Although degradation effects of OLEDs under operation have been intensively investigated for (small area) OLEDs, a fundamental understanding of the mechanisms is still lacking. [1]

A statistical analysis of lifetime measurements under standard conditions as well as accelerated ageing conditions (higher current and / or higher temperature) is necessary to develop a mathematical model that allows calculating a mean OLED lifetime based on accelerated lifetime tests.

Within the OLED100.eu project [2] a lifetime measurement setup for large area OLEDs with some unique features was established at PTB.

MEASURING METHODS

The basis for our investigations is a 17 m long segment of the photometer bench system at PTB to measure different optical and electrical properties of 60 OLEDs.

30 OLEDs are mounted on the wall with a horizontal light output direction and an additional 30 OLEDs are mounted below the ceiling facing downwards.

All OLEDs are operated under constant current conditions. Due to the different OLED types provided by the OLED100.eu consortium, we have to use more than 30 power supplies to operate each OLED with its appropriate current.

The OLEDs are mounted on specific holders with separate contacts for current supply and voltage measurement (4-pole technique). We use a digital voltmeter (DVM) with a 60 channel multiplexer to measure each OLED voltage separately.

In addition, these OLED holders are mounted, thermally isolated, on the wall and ceiling, respectively. Therefore, the thermal equilibrium condition of the OLED is mainly affected by the ambient temperature only.

A motor-driven bench carriage, equipped with several photometers, a spectroradiometer, and an imaging luminance measuring device (ILMD) are used for the optical measurements.

Figure 21. PTB bench carriage with several optical and electrical measurement devices and a large area OLED mounted on a turning device.

The bench carriage is computer controlled and comes with an absolute position encoding system. The optical measurement devices are mounted on a rotating table in a light tight cabinet (as seen in figure 1). The option to move and rotate the detectors freely along the 17 m long bench (parallel to the row of mounted OLEDs) enables us to measure not only under a perpendicular viewing angle but also under any viewing angle up to approximately 45°.

Furthermore, we have installed a front surface mirror beside the bench carriage to determine the photometric and radiometric properties of the

OLEDs mounted below the ceiling. A computer simulation of the setup is shown in figure 2. The distance between the optical detectors and the front surface of the OLED is approximately 1.65 m.

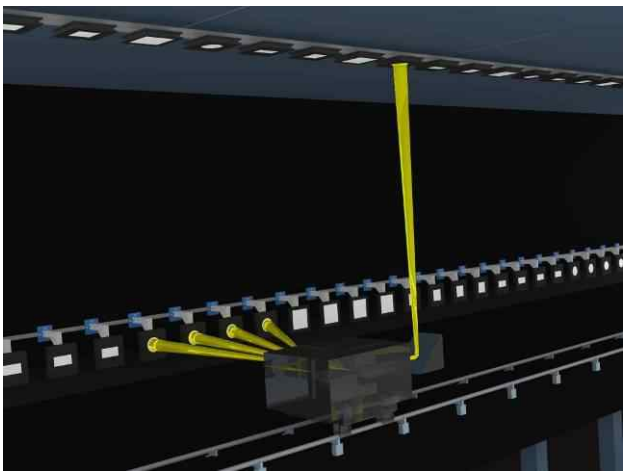

Figure 22. Computer simulation of PTB's OLED lifetime measurement setup. The cabinet on the bench carriage is shown in the front. The yellow cones illustrate the field of view for different viewing angles. A front surface mirror beside the bench carriage reflects the emitted light of the OLEDs from the ceiling to the various detectors inside the cabinet.

The measurements are fully automated. This includes the movement of the bench carriage, changing detectors, the settings of photocurrent amplifiers as well as the data acquisition by DVMs, the ILMD, the spectroradiometer, the temperatures of the devices and environmental quantities.

Figure 23. Row of real objects investigated with the lifetime measurement setup.

One characteristic of the presented measurement setup is the possibility of in situ measurements.

Furthermore, we are able to identify changes in the spatial distribution of luminous intensity and chromaticity coordinates.

SUMMARY

The presented measurement setup at PTB is able to measure the following in situ:

- Luminous intensity*
- Average luminance*
- Chromaticity coordinates*
- Spectral measurements*
- Luminance distribution (ILMD)
- Chromaticity distribution (ILMD)
- OLED current
- OLED voltage
- OLED temperature (on the reverse)
- Ambient temperature

*for different viewing angles (approximately 0-45°)

Figure 24. PTB's OLED lifetime measurement setup with several OLED types mounted on wall and ceiling.

OUTLOOK

We will present the results of our lifetime measurements at the conference. This includes the analysis of the ageing behaviour as well as a first interpretation of the parameters which have to be taken into account for the evaluation of the OLED lifetime.

ACKNOWLEDGMENT

The work leading to these results has received funding from the European Community's Seventh Framework Programme under grant agreement n° FP7-224122 (OLED100.eu)

REFERENCES

1. Appl. Phys. Lett. **87**, 213502 (2005)
2. http://oled100.eu/homepage.asp

OLED Transfer Standards

Thorsten Gerloff, Armin Sperling, Maic Meyer, Mario Taddeo[1]

[1]*Physikalisch-Technische Bundesanstalt, Braunschweig, Germany*
Corresponding e-mail address: Thorsten.Gerloff@PTB.de

Light sources of different technologies vary in their photometric properties. For the calibration or adjustment of measurement equipment it is always desirable to use transfer standards having similar properties compared to the light sources under test.
The best match is achieved when a transfer standard relies on the same technology as the light sources under evaluation.
Thus, PTB analysed OLED device parameters to develop a transfer standard using commercially available OLEDs [1].
This is, to our knowledge, the first and only existing OLED transfer standard.
The characterisation of this standard in terms of reproducibility and geometrical alignment is described in this article.

TRACEABILITY

To ensure the continuity of a production process, in most cases it is sufficient to carry out relative measurements of optical quantities and device parameters, i.e. to refer to measurement results based on a defined production test method. However, to compare measurement results of different manufacturers and vendors or measurement laboratories, absolute measurements are required.

For safeguarding the reliability of the properties of an Organic Light Emitting Diode (OLED), it is therefore necessary to indicate measurement results with respect to internationally recognised units together with their associated measurement uncertainty. The link-up of all measurement steps within the measurement chain is called "traceability". Traceable measurement results are normally related to a reference standard through a documented unbroken chain of calibrations with validated measurement procedures.

PHOTOMETRIC STANDARDS

For luminous quantities, it is convenient to use special light sources as transfer standards. During their operation under defined conditions, they produce a stable amount of light for the quantity they should transfer which is stated in a certificate. Such standard light sources are necessary for substitution procedures to deliver the required traceable measurement at the lowest effort with regard to the measuring technique.

Frequently, incandescent lamps are used as transfer standards. If small measurement uncertainties are to be achieved by means of substitution procedures, it is important that all properties of the transfer standard and of the measurement objects match to a large extent.

For sources with spectral distributions different from Planckian radiators, the NMIs can also provide other light sources such as LEDs as transfer standards, mostly for a selection of colours and for different - most similar - colour temperatures.

OLED TRANSFER STANDARD

To develop a transfer standard, it is essential to account for all possible operational and ambient influences on the device. The optical properties of OLEDs are strongly influenced by the ambient temperature. Additionally, the warm-up time behaviour of OLEDs reaching thermal equilibrium makes it necessary to develop a special OLED transfer standard design with active temperature stabilisation.

Figure 25. Temperature stabilised OLED transfer standard and power source.

The presented OLED transfer standard was developed as a mobile stand-alone solution for easy

operation. The complete system is shown in figure 1 and consists of a commercially available OLED in a special housing and a software controlled power source.

All relevant electrical data of the OLED are monitored during operation and saved onto a USB flash drive and can be used for software-assisted data analysis.

REPRODUCIBILITY

The reproducibility of the total luminous flux Φ_{OLED} was measured in an integrating sphere as shown in figure 2.

Figure 26. OLED transfer standard mounted in a temperature stabilised 2.5 m diameter integrating sphere.

The OLED standard was operated for 10 minutes with a permanent active control of the current and voltage and afterwards turned off for 5 minutes. This procedure was repeated 70 times and the response of the sphere photometer in dependence on the cycle number is shown in figure 3. The subsequent figure shows the response for 1 cycle and indicates that thermal stabilisation is reached after approximately 5 minutes.

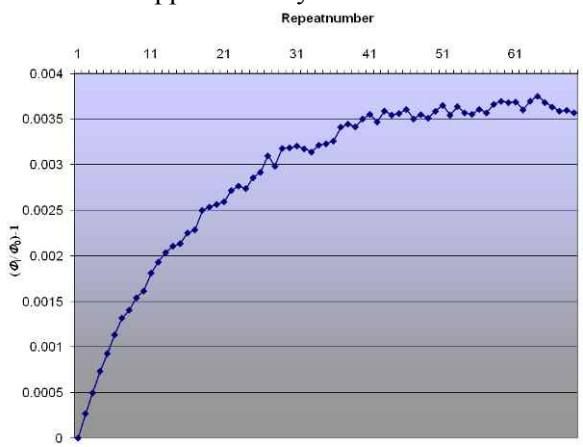

Figure 27. Relative changes of the total luminous flux Φ_1 of the OLED compared to the initial value Φ_0.

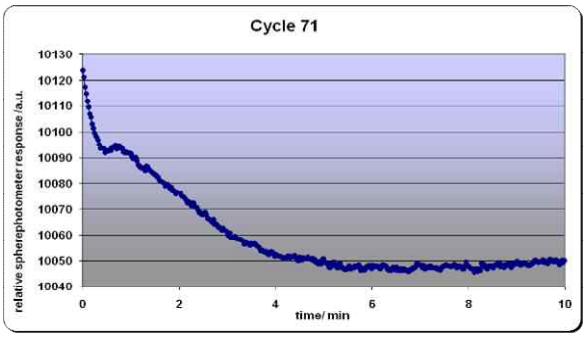

Figure 28. Typical warm-up behaviour of the temperature-regulated OLED. After about 5 minutes the total luminous flux of the OLED has stabilised.

GEOMETRICAL ALIGNMENT

The luminance distribution of a large area OLED without temperature stabilisation is significantly influenced by its geometrical alignment. In dependence of the OLED-stack and -design we measured local luminance changes up to 15% for different alignments caused by warm air moving along the light output area by thermal convection due to the heat of the OLED. [2]

The changes of the luminance caused by thermal convection of the same OLED with and without thermal management are shown in figure 5.

The presented OLED transfer standard with thermal management is hardly affected by its geometrical alignment.

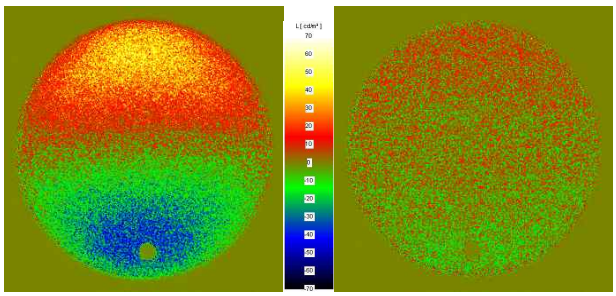

Figure 29. The images show luminance changes for different geometrical alignments. An OLED in a housing without thermal management is shown in the left image and the same OLED with thermal management in the right image. The mean luminance is about 1000 cd/m².

ACKNOWLEDGMENT

The work leading to these results has received funding from the European Community's Seventh Framework Programme under grant agreement n° FP7-224122 (OLED100.eu)

REFERENCES

1. http://www.osram.com/osram_com/LED/OLED_Lighting/ORBEOS_Products/index.html
2. CIE Tutorial and Expert Symposium for Photometry and Radiometry. Bern, Switzerland (2010).

Stability of Array Spectroradiometers and their Suitability for Absolute Calibrations

Saulius Nevas, Annette Teuber, Armin Sperling, and Matthias Lindemann
Physikalisch-Technische Bundesanstalt (PTB), Braunschweig and Berlin, Germany,

Corresponding e-mail address: saulius.nevas@ptb.de

An investigation on the short- and long-term stability of various low-end and high-end array spectroradiometers is presented. The influence of ambient conditions, such as temperature and the relative humidity of air, on relevant instrumental characteristics and their temporal stability was evaluated. Potentially weak points of array spectroradiometer construction with respect to their suitability for absolute calibrations are discussed.

INTRODUCTION

Compact array spectroradiometers are increasingly replacing conventional scanning spectroradiometer systems for spectroradiometric measurements in the health and cosmetics sectors, solar irradiance monitoring, various industrial applications, the photometry and the colorimetry of modern light sources, etc. The calibration of such devices with respect to their spectral irradiance responsivity should typically be accomplished directly before/after the measurements at a user site by means of a portable source-based transfer standard with traceability to the national standard of spectral irradiance. Sometimes, respective quality assurance systems require the calibration of the array spectroradiometers to be carried out at an accredited calibration laboratory. However, such a calibration scheme is only possible if the spectroradiometer is suitable for the calibration, i.e. the transfer of the spectral irradiance unit from one source to another is feasible. For this purpose, the calibration factor determined under the given measurement conditions should be maintained in the array spectroradiometer. In this paper, we examine properties of array spectroradiometers that are critical with respect to their absolute calibration capability. Relevant characteristics of a number of low-end as well as high-end devices have been monitored over a time frame of up to five years.

CALIBRATION CAPABILITY OF ARRAY SPECTRORADIOMETERS

The requirements for array spectroradiometers used for absolute calibrations are as follows. The instruments should have entrance optics appropriate for the measurement geometry. They must be stable and reproducible throughout time periods between consecutive recalibrations and should be insensitive with respect to ambient conditions. They should have a linear(-ised) response with respect to the measured quantity, have adequate stray light properties, bandpass, etc.

In addition to an appropriate diffuser head, entrance optics of array spectroradiometers typically include a piece of optical fibre. This is potentially a weak point of the spectroradiometer that is susceptible to mechanical and thermal influences. For compact devices, a multimode fibre with an SMA-type connector is often used. Therefore, the reproducibility of the spectroradiometer properties is generally poor (see Fig. 1). This is related not only to the mechanical tolerances of the connector type, but also to the numerical aperture of the fibre and the quality of the diffuser. Thus, either a choice of a fibre-optic adapter with lower tolerances, such as the FC type, or an inseparable connection between the entrance optics and the array spectroradiometer are recommended.

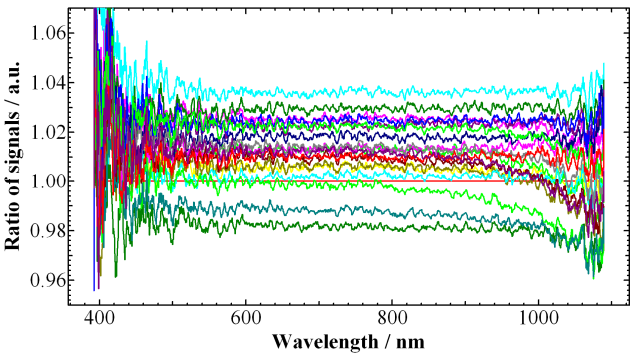

Figure 1. Reproducibility of the fibre-based entrance optics of an array spectroradiometer due to the usage of SMA-type connectors. The ratios of signals to the first measurement of a stable quartz-tungsten-halogen lamp are shown. The connector was removed from the spectroradiometer adapter and refitted again before every consecutive measurement.

Since the temporal stability of spectroradiometers is typically poor, portable calibration sources are normally used for the calibration of the instruments in close proximity to measurements applications. Whether the relevant properties of an array spectroradiometer remain stable, depends on many details of the opto-mechanical design as well as on properties of the optical components used. Depending on their individual construction, array spectroradiometers could be sensitive to extreme ambient conditions, such as high air humidity. This might also have an adverse effect on the stability of both the wavelength calibration (see Fig. 2) and the spectral response.

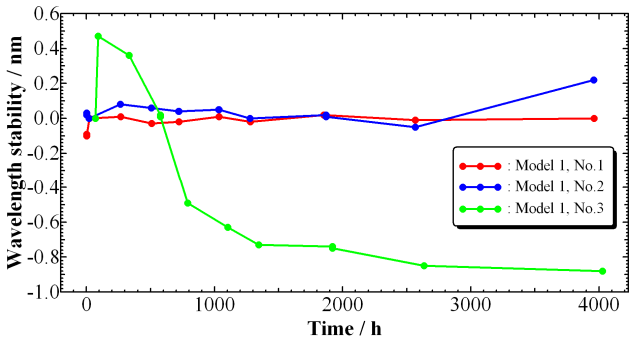

Figure 2. Wavelength scale stability of three low-end array spectroradiometers at a nominal wavelength of 450 nm. During the first 60 h, between the first and the second data points, spectroradiometer No. 3 was kept in a climate chamber under the relative air humidity of > 95 %. The other spectroradiometers were kept under normal ambient conditions.

Without an active temperature stabilisation, which is typical for low-end instruments, the temperature dependence of the spectral responsivity of the CCD detector has a significant effect on the spectroradiometer signals (see Fig. 3). For some spectroradiometers, we have also observed additional temperature effects, e.g. a wavelength-independent shift of spectroradiometer signals as a function of temperature. The stability of the wavelength scale calibration with respect to ambient temperature can also be completely different depending on the construction of a specific instrument (see Fig. 4).

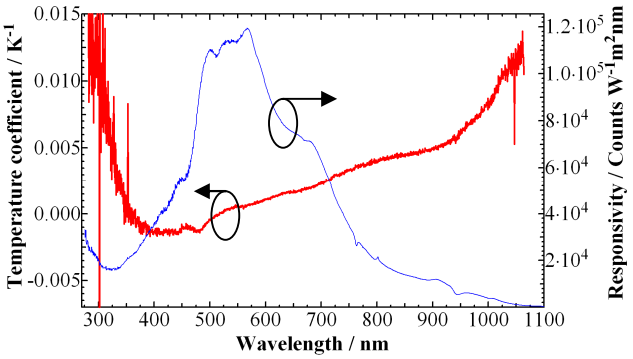

Figure 3. Temperature coefficient for spectral responsivity of a CCD array spectroradiometer (left axis, red curve) and spectral irradiance responsivity of the instrument (right axis, blue curve).

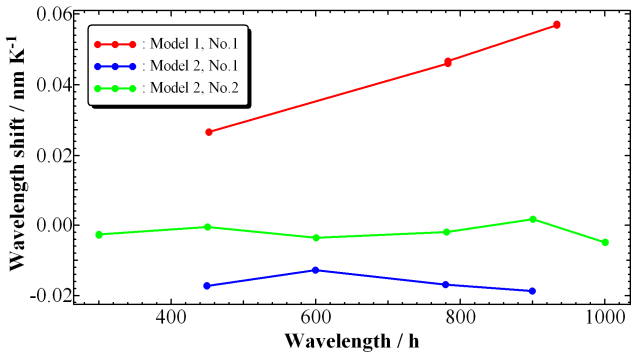

Figure 4. Effect of ambient temperature on wavelength scale calibration of different array spectroradiometers.

CCD detectors are often assumed to be linear with respect to the measured radiometric quantity. Thus, linearity corrections implemented in array spectroradiometers are typically meant to account only for the linearity of the signal processing electronics. Results for the radiometric linearity measurements of different array spectroradiometers will be presented in the conference contributions.

SUMMARY

Comprehensive characterisations of various low-end as well as high-end array spectroradiometers have been carried out. Relevant instrumental parameters of the devices have been monitored over a time frame of several years to determine their stability and suitability for the assignment of an absolute calibration factor for given measurement conditions. Significant differences among array spectroradiometers of different manufacturers were observed.

Uniform broad-band UV irradiance measurements of 365 nm LED sources

George P. Eppeldauer

National Institute of Standards and Technology
Gaithersburg, Maryland, USA
Corresponding e-mail address: george.eppeldauer@nist.gov

Broad-band UV measurements are analyzed when UV-A irradiance meters measure optical radiation from 365-nm UV sources. The CIE standardized rectangular-shape UV-A function cannot be easily realized. The spectral mismatch of the realized functions to the standard function is large. The spectral power distribution of the 365-nm excitation source is not standardized. Accordingly, the readings, made with different types of UV meters, even if they measure the same UV source, can be very different. Commercially available UV detectors and UV meters were measured for spectral responsivity. The spectral product of the source-distribution and the meter's spectral-responsivity were calculated to estimate broad-band signal measurement errors. Standardization of both the UV source-distribution and the meter spectral-responsivity is recommended here to perform uniform broad-band measurements with low uncertainty. It is shown what spectral responsivity function(s) are needed for new and existing UV irradiance meters to perform low-uncertainty broad-band 365-nm measurements.

INTRODUCTION

UV irradiance meters measure optical radiation from broad-band UV sources that peak at 365 nm for performing non-destructive testing of metal parts. Commercially available UV-A irradiance meters read different irradiance values when they measure the same 365-nm source. The differences in the readings can increase to higher than 20 % when different UV radiometer models are involved in the irradiance measurements [1]. The reason of the large measurement errors is lack of a proper standard spectral responsivity function for the UV meters. The CIE standardized UV-A function has a square-shape between 320 nm and 400 nm. Since filter combinations are to be used to realize this square-shape band-pass function, the spectral mismatch errors are large. A reasonable calibration (correction) factor for broad-band UV measurements cannot be assigned based on the CIE UV-A standard responsivity function. Also, the spectral power distribution of the excitation 365-nm sources has not been standardized which is a must if the realized spectral responsivity function of the UV meter is different from the standard function. The wavelength range of the presently used CIE standard function is too broad for the required tests where 365-nm excitation sources are used. At present, the 365-nm Hg line is utilized for non-destructive material tests. LED sources should be used in future tests instead of filtered mercury lamps. The goal is to develop UV sources and meters (and to find suitable commercial UV meters) that can satisfy the measurement requirements described as a definition in this paper.

UV METERS

Several commercial UV irradiance meters have been measured for spectral irradiance responsivity. Figure 1 shows how different the peak-normalized spectral responsivities are. Both the peak responses and the spectral bandwidths (wavelength coverage) are different. The graph also shows the spectral distribution of the filtered Hg-source. The errors obtained with these different meters compared to the measurement of the UDT 268 UVA meter when they

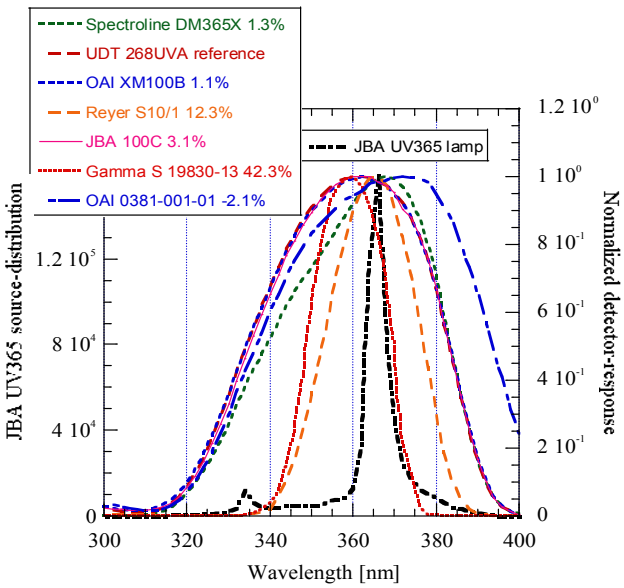

Figure 1. Normalized response of UV meters and the distribution of the filtered 365-nm Hg-source.

all measured the same 365-nm source in the figure, are shown in the legend of the graph. The UDT268 UVA meter was arbitrarily selected here as a reference meter to compare the measurement results obtained with the different UV meters. Some of the shown measurement uniformity-errors are small but

others (where the shapes of the spectral responsivity functions were not adequate) increased to 42.3 %.

SPECTRAL MODELLING

A spectral responsivity function that can be easily realized and used as a standard function has been designed using three filters (UG11 and BG39 both 1 mm thick and WG345 of 2 mm thick) and a UV-damage resistant silicon photodiode (UVG100). The modelled and normalized function is shown in Fig. 2 together with the spectral distribution of a UV projector and the normalized spectral response of a commercial UV meter. This commercial meter (UDT268 UVA) was used as a reference meter in Fig.1 to compare the readings of the different meters.

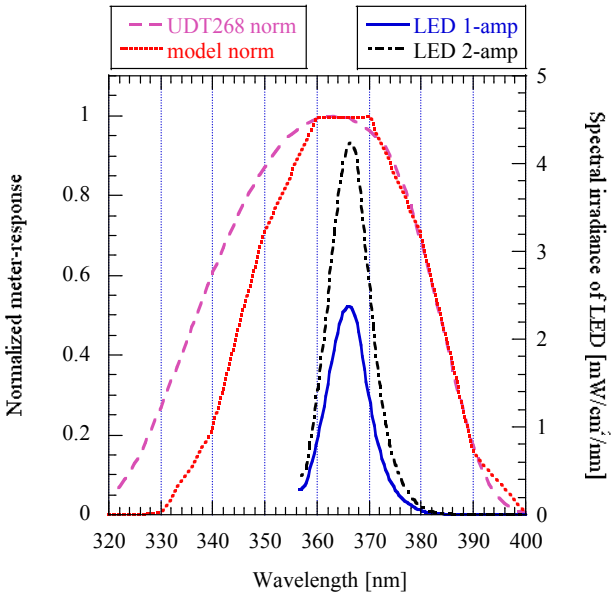

Figure 2. Comparison of the modelled 365-nm response to a commercial meter. The distribution of the LED projector is shown at 1 A and 2A currents.

The first step in the modelling and in the following standardization is to establish the spectral band-limits and peak tolerances for the 365-nm LEDs. The suggestion is to use LEDs with 365 nm +/- 5 nm peaks and a maximum spectrum-half-width (FWHM) of less than 15 nm to keep the spectral mismatch errors and the uncertainties of the spectral products (signals) at a reasonably low level even if different meters and/or sources are used.

LED SOURCES

Figure 3 shows the design of a high-power LED source that can produce a uniform irradiance, larger than 1 mW/cm^2 within a diameter of 7.5 cm at a distance of 40 cm from the source.

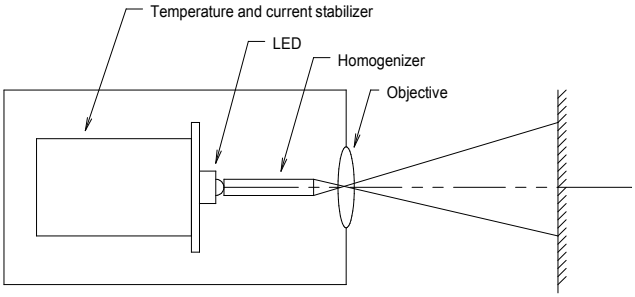

Figure 4. UV-LED irradiance source.

DEFINITION

First, satisfy the requirements for source-distribution: Use LEDs with 365 nm +/- 5 nm peaks and a maximum spectrum-half-width (FWHM) of less than 15 nm. In the next step, match the spectral response of the UV meters to the 365-nm source-distribution-function such that the spectral product of the source-distribution and the meter-responsivity will produce an error which is less than the required measurement-uncertainty when different UV meters (types) and/or different 365-nm sources are used. The standardization of the broad-band UV measurements makes sense only if more than one UV meter and/or more than one 365-nm sources are used.

ACKNOWLEDGEMENTS

The author thanks T. C. Larason for supplying the spectral responsivity data and J. D. Schanda for the design of the UV-LED source.

DISCLAIMER

Certain commercial equipment, instruments, or materials are identified in this paper to foster understanding. Such identification does not imply recommendation or endorsement by the NIST, nor does imply that the equipment are necessarily the best available for the purpose.

REFERENCES

1. T. C. Larason and C. L. Cromer, Sources of error in UV radiation measurements, J. Res.NIST, Vol. 106, No. 4, p. 649-656, 2001.

Tungsten Filament Lamps as Absolute Radiometric Reference Sources

Petri Kärhä[1,2], Maija Ojanen[3], Saulius Nevas[4], and Erkki Ikonen[1,2]

[1]Aalto University, Espoo, Finland, [2]Centre for Metrology and Accreditation (MIKES), Espoo, Finland, [3]presently with LNE, Paris, France; from June 2011 with MIKES[2], [4]Physikalisch-Technische Bundesanstalt, Braunschweig, Germany
Corresponding e-mail address: petri.karha@aalto.fi

We have developed a physical model for the spectral behaviour of the radiation of tungsten filament lamps. The model is based on Planck's radiation law, published values for the emissivity of tungsten, measurement geometry, and measured values for a residual correction function. The model can interpolate and extrapolate spectral irradiances of 1-kW FEL and DXW type lamps, with additional uncertainties better than 1 % within the wavelength range 340 – 850 nm. The model makes it possible to estimate spectra of incandescent lamps with uncertainties of the order of 2.5 % based on illuminance and colour temperature, or even illuminance and resistance measurements only.

LAMP MODEL

The spectral irradiance of an incandescent tungsten halogen lamp can be expressed as a function of lamp temperature T and wavelength λ as

$$E(\lambda,T) = B(T)\varepsilon_W(\lambda,T)\varepsilon_\Delta(\lambda)\frac{2hc^2}{\lambda^5\left[\exp\left(\frac{hc}{\lambda kT}\right)-1\right]}, \quad (1)$$

where, $\varepsilon_W(\lambda,T)$ is the emissivity of tungsten [1,2], $\varepsilon_\Delta(\lambda)$ is the residual correction factor for the emissivity of the lamp, h is the Planck's constant, c is the speed of light in vacuum, and k is the Boltzmann constant. [3] The geometry of the lamp and the receiving detector is accounted for by $B(T)$, which is practically constant. The filament size is slightly affected by thermal expansion. Thus we express the $B(T)$ as

$$\underline{B}(T) = B_0[1 + b(T)], \text{ where} \quad (2)$$

$$B(T) = 0.000016\ \mathrm{K}^{-1}\ (T - T_0), \quad (3)$$

and $T_0 = 2770$ K.

The biggest difference between the spectra of an incandescent lamp and a black body radiator is the emissivity of the tungsten filament. Tungsten is a grey body with emissivity close to 0.42 and spectral dependence of the order of 5 % in the spectral region studied. Accounting for the emissivity of tungsten does not fully explain the spectral behaviour of lamps. In addition, one needs to account for the bulb transmittance, absorption of the filling gas, and impurities, material variation, and structure of the filament. Some of these effects can be studied with further measurements, such as determination of the transmittance difference in lamp-on and lamp-off states using a wavelength tuneable laser.

We measured the net effect of the unknown factors of the lamp, and derived the residual correction factor presented in Fig. 1. The measurement was made by changing the current of an FEL lamp, thus altering its temperature, and finding a common solution for $\varepsilon_\Delta(\lambda)$ that models all measured spectra.

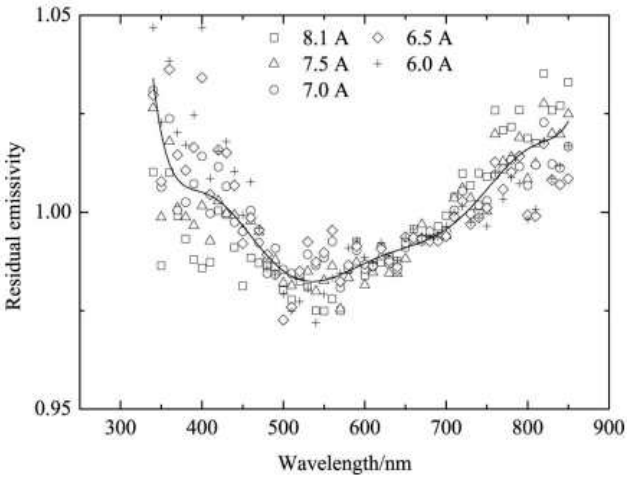

Figure 30. Residual correction factor for emissivity of tungsten lamps, after taking into account Planck's law, emissivity of tungsten, and the measurement geometry. [3] Symbols denote correction values obtained for different lamp currents and temperatures. Solid line is an 8th degree polynomial fitted to the average of the results.

The final model presented has two free parameters only – temperature T and the geometrical factor B_0. It can thus interpolate and extrapolate measured irradiances based on two measurements only. In practice, three measurements give more reliability.

TEST MEASUREMENTS

The model was tested on a group of four FEL and four DXW type lamps that have been calibrated at the Aalto University School of Electrical Engineering

(former Helsinki University of Technology). Irradiances at three wavelengths, 380, 570, and 800 nm, were selected and interpolated / extrapolated with the model. The maximum deviation between the interpolated values between 340 and 850 nm wavelengths was 0.8 %, and the standard deviations were of the order of 0.4 %.

Figure 2 presents results of a similar intercomparison for lamps that were calibrated by NPL as part of the international key comparison CCPR-K1.a. [4] The spectral irradiance values at wavelengths of 380, 555, and 800 nm were selected, and other values were interpolated with the model. The agreement of the modelled values was within ±1 %, and the standard deviation was 0.3 %.

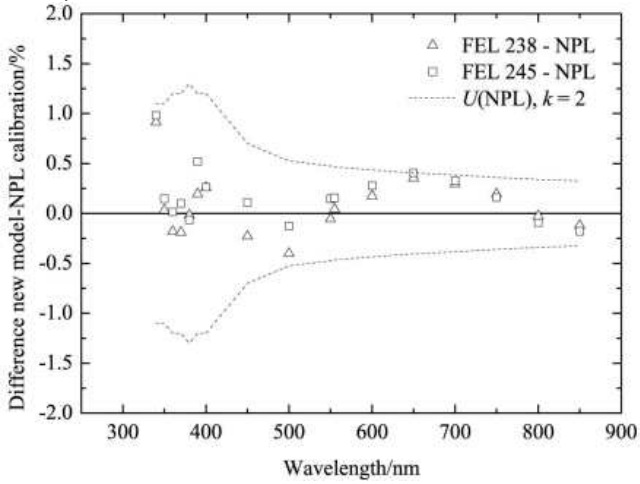

Figure 31. Deviation between the modelled irradiances and irradiances measured by NPL for two FEL lamps (symbols). Thin lines denote the uncertainties of the NPL measurements. [3]

PRACTICAL APPLICATIONS

The model developed has two free parameters only. Thus, two measurements giving information about the lamp spectrum should be adequate to fix the model. We studied possibilities of deriving spectral irradiances of lamps with moderate accuracies using data ordinarily available or easily obtainable for lamps. These techniques can not supersede high-accuracy calibrations in national standards laboratories, but may give end users valuable information on their lamps. The scenarios tested included extrapolations using:

1. two spectral irradiance values,
2. illuminance and colour temperature, and
3. illuminance and electrical measurements.

It would be relatively cost effective to build two filter radiometers using apertures, photodiodes and interference filters. To study the feasibility of such an approach, we selected randomly two spectral irradiance values at the wavelengths of 366, 380, 440, 570, 700, and 800 nm, modelled the spectral irradiances, and compared the rest of the values. The standard deviations of the differences were 0.50 %, 0.14 %, and 0.26 % in the UV, visible and NIR wavelength regions, respectively.

For photometric standard lamps, users typically have calibrated values for illuminance and colour temperature. We therefore calculated these for our lamps, and fitted the spectral irradiance model so that it replicates the same values. Sensitivity analysis was carried out studying how large uncertainties are introduced when colour temperature and illuminance have expanded uncertainties of 20 K and 2 %. It turned out that with these values, the resulting expanded uncertainty in the spectral irradiance values is within 2.6 %.

We finally tested, whether electrical measurements can be used to derive information on the lamp spectrum. We measured the resistance of the cold filament of the lamp. During the lamp operation, we calculated the temperature-dependent resistance of the filament from the lamp current and voltage. The resistivity and the mechanical dimensions of the filament vary with temperature. According to our measurements, a reasonable estimate for the filament temperature T can be obtained from the hot resistance $R(T)$ and the room temperature resistance $R(295\ \mathrm{K})$ as

$$T = R(T) / [0.0062\ \mathrm{K}^{-1} R(295\ \mathrm{K})] + 319\ \mathrm{K}. \quad (4)$$

By combining the temperature obtained from resistances with an illuminance measurement, we can obtain a spectral irradiance scale with an uncertainty of the order of 3 %.

REFERENCES

1. J.C. de Vos, A new determination of the emissivity of tungsten ribbon, Physica 20, 690–714, 1954.
2. R. M. Pon and J. P. Hessler, Spectral emissivity of tungsten: analytic expressions for the 340 nm to 2:6 μm spectral region, Appl. Opt. 23, 975–976, 1984.
3. M. Ojanen, P. Kärhä, and E. Ikonen, Spectral irradiance model for tungsten halogen lamps in 340–850 nm wavelength range, Appl. Opt. 49, 880–886, 2010.
4. E.R. Woolliams, N.P. Fox, M.G. Cox, P.M. Harris, and N.J. Harrison, Final report on CCPR-K1.a: Spectral irradiance from 250 nm to 2500 nm, Metrologia 43, (Tech. Suppl.) 02003, 2006.

TiC-C Fixed Point Measurement Using a Linear Pyrometer and a Filter Radiometer

A.D.W. Todd and D.J. Woods

Institute for National Measurement Standards, National Research Council of Canada,

Ottawa, Ontario Canada

Corresponding e-mail address: andrew.todd@nrc-cnrc.gc.ca

At the Institute for National Measurement Standards of the National Research Council Canada, two TiC-C fixed points are currently available: one large (~8 mm dia.) and one smaller (~4 mm dia.) aperture fixed point. The melting plateaus of the large-aperture (LA) fixed point were measured using a filter radiometer and a linear pyrometer (LP3) and the small-aperture fixed point was measured using the LP3. The melting plateaus of the two cells were compared.

INTRODUCTION

The melting point of the TiC-C eutectic is near 3033 K, which makes it of interest as both a temperature and radiance standard. A number of studies of the TiC-C fixed point have been reported [1-5].

Here, one large-aperture and one small-aperture fixed point were measured and compared. The large-aperture fixed point was measured with an absolutely-calibrated filter radiometer (FR1) and a linear pyrometer (LP3) and the small-aperture cell was measured with the LP3 only.

PROCEDURES AND RESULTS

The filter radiometer used in this work was constructed using coloured glass filters designed to achieve a peak wavelength near 650 nm and a bandwidth of approximately 100 nm (FR1). Details of the filter radiometer can be found in Ref. 6. The calibration of FR1 is traceable to NRC's cryogenic radiometer. The details of this calibration can be found in Ref. 7.

To facilitate the measurement of the LA fixed point with FR1, a precision aperture (2.896 mm in dia. with an uncertainty of 0.006 mm (k = 1)) installed in a water-cooled copper housing was placed in front of the high temperature blackbody (HTBB) opening. A gauge bar of length 913.063 mm was used to align the HTBB aperture to the aperture integrated into FR1 and to set the distance between the two apertures. A flow of 19.5 ºC water was maintained through the HTBB aperture housing. The temperature of the FR was maintained at 30.0 °C using the integrated thermo-electric coolers.

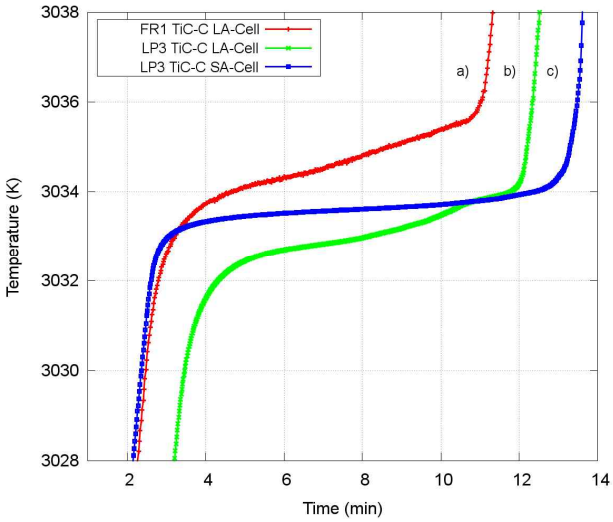

Figure 1: Melting plateaus measured using the filter radiometer with the large-aperture fixed point (red), and using the LP3 with the large-aperture (green) and small-aperture (blue) fixed points.

The HTBB (BB3500M, see Ref. 8) was brought close to the desired operating temperature by ramping up the HTBB current at a rate of 7 A/min so that a temperature of 20 K below the fixed-point transition temperature was realized. Melting was achieved by raising the furnace operating current by nominally 40 A from the lower set point to achieve a furnace temperature close to 20 K above the fixed point transition temperature.

Figure 1 shows melting plateaus measured using the FR1 (a) and LP3 (b) for the large-aperture fixed point and using the LP3 for the small-aperture fixed point (c). The two plateaus corresponding to the LP3 and FR1 measurements of the large-aperture fixed point were taken on the same day. One melt and freeze were measured using FR1. Then, the blackbody aperture was removed, and the LP3 moved into place and one melt and freeze were measured. The LP3 was focused in such a way that the area

from which light was collected inside the fixed-point cavity was comparable to that defined by the FR apertures. For measurements made using the LP3 with the small-aperture fixed point, the LP3 was focused just inside the fixed-point aperture.

CONCLUSIONS AND FUTURE WORK

The melting plateaus of a TiC-C fixed point with an 8 mm diameter aperture have been measured with both a filter radiometer and an LP3. These measurements have been compared to melting plateau measurements of a TiC-C fixed point with a 4 mm diameter aperture that have been made with only the LP3. The melting temperatures determined by the LP3 and the FR agree within their uncertainties. The values for the measured melting temperatures (inflection points) and the associated uncertainties are given in Table 1. The dominant contribution to the uncertainty of the LP3 measurements comes from the transfer calibration from the FR1.

Table 1: Temperatures that were determined for the two TiC-C fixed points with the LP3 and FR1.

	Temperature (K)	Uncertainty (k = 1) (K)
LA cell, LP3	3033.646	0.95
LA cell, FR1	3034.359	0.60
SA cell, LP3	3033.672	0.95

Further work on these fixed points will include reducing the uncertainty of the thermodynamic LP3 calibration at this temperature, a better quantification of uncertainties due to the geometrical aspects of the FR measurement of the fixed point, and further steps to ensure the equivalence of the FR and LP3 measurements to each other. It is also suspected that the location of the large aperture fixed point within the furnace could be optimized to achieve melting plateaus with less slope. The work presented here is preliminary and it is expected that a considerable amount of new work will be completed in the coming months.

REFERENCES

1. J. Hartmann, K. Anhalt, P. Sperfeld, J. Hollandt, M. Sakharov, B. Khlevnoy, Yu. Pikalev, S. Ogarev, and V. Sapritsky, Thermodynamic temperature measurements of the melting curves of Re-C, TiC-C and Zr-C-C eutectic irradiance fixed-point cells, Proceedings of the 9th Symposium on Temperature and Thermal Measurements in Industry and Science, Dubrovnik-Cavtat, Croatia, June 22-25, 189-194, 2004.
2. B.B. Khlevnoy, V.I. Sapritsky, S.A. Ogarev, M.K. Sakharov, M.L. Samoylov, Yu.A. Pikalev, Development of fixed points above 2700 K based on M-C and MC-C eutectics at VNIIOFI for radiation thermometry and radiometry, Proceedings of the 9th Symposium on Temperature and Thermal Measurements in Industry and Science, Dubrovnik-Cavtat, Croatia, June 22-25, 203-208, 2004.
3. M.K. Sakharov, B.B. Khlevnoy, V.I. Sapritsky, M.L. Samoylov and S.A. Ogarev, Development and investigation of high-temperature fixed point based on TiC-C eutectic, Proceedings of the 9th Symposium on Temperature and Thermal Measurements in Industry and Science, Dubrovnik-Cavtat, Croatia, June 22-25, 319-324, 2004.
4. N. Sasajima, M. Sakharov, B. Khlevnoy, Y. Yamada, M. Samoylov, S. Ogarev, P. Bloembergen and v. Sapritsky, A comparison of Re-C and TiC-C eutectic fixed-point cells among VNIIOFI, NMIJ and BIPM, Proceedings of the 9th Symposium on Temperature and Thermal Measurements in Industry and Science, Dubrovnik-Cavtat, Croatia, June 22-25, 1107-1114, 2004.
5. N. Sasajima and Y. Yamada, Investigation of TiC-C eutectic and WC-C peritectic high-temperature fixed points, Int. J. Thermophys., 29, 944-957, 2008.
6. L.P. Boivin, C. Bamber, A.A. Gaertner, R.K. Gerson, D.J. Woods and E.R. Woolliams, Wideband filter radiometers for blackbody temperature measurements, J. Modern Optics, 57:17, 1648-1660, 2010.
7. L.P. Boivin and K. Gibb, Monochromator-based cryogenic radiometry at the NRC, Metrologia, 32, 565-570, 1995/96.
8. S.A. Ogarev, B.B. Khlevnoy, M.L. Samoylov, V.I. Shapoval, V.I. Sapritsky and M.K. Sakharov, New high-temperature pyrolytic graphite blackbody sources for precision measurements in radiation thermometry, in Proceedings of the 9th Symposium on Temperature and Thermal Measurements in Industry and Science, Dubrovnik-Cavtat, Croatia, June 22-25, 2004.

Low, Middle and High Temperature Blackbodies developed at VNIIOFI for Various Applications

S.A. Ogarev, S.P. Morozova, B.B. Khlevnoy, M.L. Samoylov, B.E. Lisyansky, A.V. Pusanov, N.A. Parfentyev and V.I. Sapritsky

All-Russian Institute for Optical and Physical Measurements (VNIIOFI), Moscow, Russia,

Corresponding e-mail address: ogarev-m4@vniiofi.ru

The paper is concerned with cavity-type blackbodies developed at VNIIOFI within the last years for wide temperatures range from -173 °C to 3200 °C and various applications such as vacuum- and middle-background calibration facility, spectral irradiance and other radiometric applications. The principles of operation, design, controlling software and investigation results of the blackbodies are described.

LOW AND MIDDLE TEMPERATURE BLACKBODIES

Two blackbodies (BBs), VTBB and BB100K1 models, were developed at VNIIOFI for the Middle Background Calibration Facility of KRISS [3]. VTBB was designed to serve as highly stable reference source with 30-mm aperture diameter in the temperature range from -60 °C to 90 °C under medium-vacuum conditions ($1 \cdot 10^{-4}$ mbar). The BB100K1 blackbody featuring 100-mm aperture, demonstrated stable operation as inside vacuum chamber in the temperature range from -60 °C to 90 °C, so as in dry-air or inert gas environment in the temperature range from -40 °C to 90 °C, with the usage of an extra hood with an aperture. Effective emissivity of these BB's radiating cavities, covered with Aeroglaze Z306 black paint, was estimated as 0.9997 for VTBB and 0.997 for BB100K1using a Monte-Carlo simulation software. The cavities temperature of both BBs were stabilized at the level of ±0.01°C by means of HUBER UNISTAT 705 thermostat. Temperature gradient along the VTBB cavity under vacuum conditions does not exceed ±40 mK at the temperature range from -60 °C to 90 °C. Temperature gradient across BB100K1 cavity bottom does not exceed ±50 mK under dry-air environment in the temperature range from –40 °C to 90 °C.

Two blackbodies, the Vacuum Low-Temperature BB (VLTBB) and the Vacuum Middle-Temperature BB (VMTBB), were developed for vacuum reduced background calibration facility of PTB.

The VLTBB was constructed as a highly stable reference radiation source for the temperature range from -173 °C to 177 °C under medium-vacuum conditions (10^{-3} Pa) and a medium-background environment (liquid-nitrogen-cooled cryo-shroud) [1]. The VLTBB represents a deep radiation cavity with cooled 20-mm aperture. The VLTBB cylindrical cavity (Ø40 mm × 250.6 mm length) with cone-shaped bottom is made of oxygen-free copper. Inner walls of the cavity are covered by a black Aeroglaze Z306 paint. The temperature control of the three-zonal VLTBB is provided with the help of rough and precision controllers. The rough stabilization is performed both by cooling with liquid nitrogen and heating by electrical heaters. The precision system provides a stability and gradient of temperature along the cavity within the limits of 20 mK in the whole operating temperature range. Effective emissivity of the VLTBB at 150 K in the spectral range from 10 μm to 25 μm is 0.9996.

The VMTBB has a temperature range from 150 °C to 430 °C and output diameter of 20 mm [2]. Operating conditions of the VMTBB are the same as for the VLTBB. The VMTBB cavity design is almost the same as that of the VLTBB, but with dimensions of (Ø26 mm × 240 mm length). As a result of investigations at PTB a special procedure of coating the surface of the cavity by paint with high emissivity has been developed. The cavity surface is coated by chemical nickel plating prior to covering it by high-emissivity paint. The VMTBB effective emissivity is 0.9994. To achieve best temperature uniformity along the cavity a 3-module design is used based on two precision PID controllers. The temperature of the cavity is measured by precision PRTs. The investigation of the VMTBB carried out at PTB, demonstrated radiating temperature stability of ± 20 mK and uniformity of ± 100 mK in the whole temperature range.

HIGH TEMPERATURE BLACKBODIES

The high temperature blackbodies (HTBB) of BB3200/3500 series are well known due to their ultra high working temperature, high emissivity and stability, and are used spectral radiometric measurements [6].

Three HTBB for 800 °C to 3400 °C temperature range with a wide variety of cavity sizes (from 15 mm to 59 mm inner diameter) are developed and investigated recently. Cylindrical cavities of these HTBBs were made of graphite, pyrolytic graphite (PG) or their combination. PG differs by significantly lower sublimation rate, which makes it a more preferable material for temperatures above 2500 °C.

The BB3500MP has the largest PG cavity with inner diameter of 59 mm. It can be used both for spectral irradiance and high-temperature fixed-point application, especially for heating large-size cells. In addition to the previous investigation of BB3500MP [5], the paper presents the results of its temperature uniformity investigation carried out using a W-Re thermocouple at temperatures of about 2170 °C, 2360 °C and 2550 °C. For example, at the level of 2556 °C the temperature varied along the 200 mm zone from the cavity bottom within 100 °C.

The BB-PyroG is the smallest blackbody featuring a cavity made from PG rings, with two modifications: BB-PyroG/2500 and BB-PyroG/3000. These BB sources feature a cavity with 15 to 25 mm inner diameter, with 10-mm opening, and low-consuming power supply. With maximal working temperature of 3200 °C, this "budget" BB is intended for both SR and SI measurements. The paper presents the results of BB-PyroG investigation. BB-PyroG emissivity was estimated as 0.9996±0.0003 in the spectral range 300 nm to 2000 nm.

The graphite BB2000/40 blackbody was developed for calibration of radiation. Operating within the temperature range from 800 °C to 2000 °C, it features large cavity opening of 40 mm. The BB2000/40 is built using the BB3500YY furnace [4] housing as a basis, but it has a normal graphite tube radiator instead of a heater consisting of PG rings. The radiator consists of a few tube pieces with an outer diameter of 55 mm that are separated from each other by the cavity bottom and the graphite baffles in the rear part, the latter reducing radiation heat losses. At both ends the radiator is supported by PG rings, which serve as additional heaters and improve the temperature uniformity. The emissivity of the BB2000/40 cavity was estimated as 0.995 ± 0.003 in the spectral range from 350 nm to 2000 nm. The uniformity along the cavity axis, accounting for 10 °C, was measured using a B-type thermocouple at 1500 °C. The BB2000/40 is equipped with the same type of a power supply unit as the BB3500YY furnaces, and, if necessary, can be easily modified by replacing the graphite radiator with a set of PG rings to be able to reach temperatures as high as 3200 °C.

Another BB series is modification of the BB3500M/BB3500MP blackbodies with the usage of combined graphite-pyrographite radiator designed to become more widely available for potential users.

The safety and reliability of the latest versions of BB3500M series BB is improved with the new elbow design of their water-cooled copper-made flanges.

All the mentioned new HTBB are equipped with an optical feedback temperature control system mounted on the rear flange of BB. Based on a lens, optical fiber and filtered Si photodiode assembled with an amplifier in the same case, the system allows BB stabilizing within 0.1 °C. This rear-view feedback allows the whole BB aperture to be used for measurements.

REFERENCES

1. S.P. Morozova et al., Vacuum Variable Temperature Blackbody VLTBB100, International Journal of Thermophysics, 29, 341-351, 2008.
2. S.P. Morozova et al., Vacuum Variable Medium Temperature Blackbody (VMTBB), International Journal of Thermophysics, 31, 1809-1820, 2010.
3. S. Ogarev et al., Low temperature blackbodies for temperature range from -60°C up to 90°C, in Proc. of TEMPMEKO & ISHM 2010, Portorož, Slovenia. Book of Abstracts, Vol.A, 135, 2010.
4. B. Khlevnoy et al., Investigation of Furnace Uniformity and its Effect on High-Temperature Fixed-Point Performance, International Journal of Thermophysics 29, N.1, 271-284, 2008.
5. P. Sperfeld et al., Perfomance limitations of carbon-cavity blackbodies due to absorption bands at the highest temperatures, Metrologia, 46,170-S173, 2009.
6. J. Hartmann et al., Blackbody and Other Calibration Sources, Chapter 6, 241-295, in RADIOMETRIC TEMPERATURE MEASUREMENTS, I. Fundamentals. Experimental Methods in the Physical Sciences, Volume 42, edited by Z.M.Zhang, B.K.Tsai, G.Machin, Academic Press is an imprint of Elsevier, USA, 2010, p.368.

Facility for the calibration of radiation sources in the UV and VUV at the Metrology Light Source

Reiner Thornagel, Rolf Fliegauf, Roman Klein, Wolfgang Paustian, Mathias Richter and Gerhard Ulm

Physikalisch-Technische Bundesanstalt (PTB), Berlin, Germany

Corresponding e-mail address: roman.klein@ptb.de

The Physikalisch-Technische Bundesanstalt, the German national metrology institute, performs the calibration of radiation sources traceable to an electron storage ring as a calculable primary source standard in the UV and VUV spectral range for more than 25 years. A facility for the calibration of radiation sources covering the UV and VUV spectral range from 7 nm to 400 nm using the Metrology Light Source as a primary radiation source standard is now under construction and will be fully operational at the end of 2011.

INTRODUCTION

The Physikalisch-Technische Bundesanstalt (PTB) performs synchrotron radiation-based radiometry for more than 25 years [1]. Based on the calculation of the spectral radiant intensity of synchrotron radiation (SR) according to the Schwinger theory [2], electron storage rings can be operated as primary source standards and thus serve as the reference standard for source – based radiometry. The SR spectrum covers a wide spectral range from the IR up to the X-ray region and thus allows the extension of the spectral region as compared to that covered by blackbody radiators, which are routinely used for conventional source-based radiometry from the IR to the UV region. The radiation of the SR primary source standard is used to calibrate energy-dispersive detectors or wavelength-dispersive spectrometers or, by means of a suitable transfer device, to calibrate other radiation sources traceable to the primary source standard. These calibration schemes have been employed by PTB, routinely for the calibration of deuterium lamps or hollow cathode sources as transfer standards [3].

Outstanding examples have been, e.g., the calibration of transfer sources, which then have been used for the calibration of the CDS (*Coronal Diagnostics Spectrograph*) [4] and SUMER (*Solar Ultraviolet Measurements of Emitted Radiation*) [5] telescopes on board of the SOHO (*SOlar and Heliospheric Observatory)* satellite.

FACILITY AND CALIBRATION SCHEME

The Metrology Light Source (MLS), the dedicated electron storage ring of PTB, is operated as a primary source standard from the IR to the VUV spectral region [6]. The MLS is equipped with all the instrumentation for the determination of the parameters needed for the calculation of the SR spectral intensity. The MLS can be operated in a highly flexible mode, i.e. the electron beam current can be changed over more than 11 decades [7]. The spectral intensity of the SR is directly proportional to the electron beam current, thus by adjustment of it, the spectral intensity can be adjusted to be similar to that of a source to be calibrated. Moreover, the spectral shape of the SR spectrum can be changed by variation of the electron energy.

The direct, undispersed radiation of a MLS bending magnet is used at an already operational so-called white-light beamline [8] for the calibration of energy-dispersive detectors or wavelength-dispersive or selective [9] spectrometers. At this beamline a suitable transfer device will be implemented for the calibration of radiation sources. The transfer device consists of a mirror-monochromator-detector system that can be moved to either be illuminated by the calculable radiation of the MLS or by the source to be calibrated. By this, the source to be calibrated can be directly compared to the primary source standard

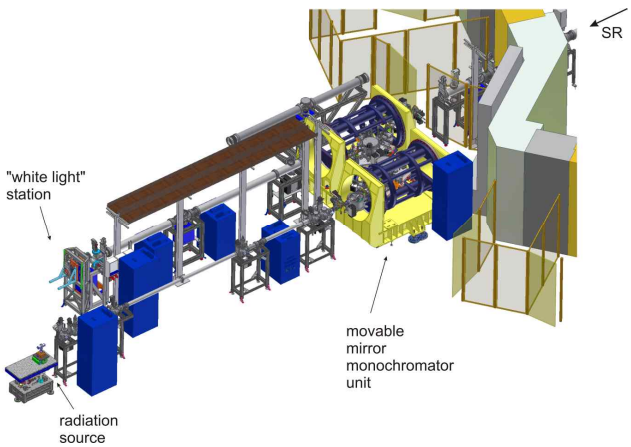

Figure 32. Overview of the source calibration facility.

within the spectral range covered by the monochromator (see illustration in Figure 1).

MONOCHROMATOR STATION

The spectral range of the monochromator will cover the UV and VUV region from 7 nm to 400 nm and thus considerably expand the spectral region at shorter wavelengths as compared to a similar station [10] operated at the BESSY II electron storage ring in the spectral range from 40 nm to 400 nm. The monochromator station consists of a focusing elliptical mirror and a dedicated grating monochromator with a normal incidence (NI) and a grazing incidence (GI) configuration for the respective wavelength region. Table 1 lists the available gratings in the NI and the GI branch. The gratings are mounted on a revolver and can be exchanged under vacuum.

The entire mirror - monochromator ensemble can be rotated around the axis of the incoming SR beam to account for the high degree of polarization of the SR. Moreover, the monochromator can be flooded with gas in the region between the entrance and the exit slits, thus acting as a gas filter for the reduction of higher order effects in the mid VUV spectral range. The illustration in Figure 2 shows the main components of the set-up. The whole set-up can be moved by means of air cushions to be either directed to the primary source standard or the source under test (see Figure 1).

The radiation sources can be characterized either in terms of spectral intensity or spectral radiance. For the latter, precision apertures can be placed into the image plane behind the focusing mirror at the entrance of the monochromator. These circular entrance apertures of different size, ranging from 60 µm to 1 mm in diameter, are arranged on a sheet and are made of gold plated copper, which has been galvanically molded from a micro-mechanically fabricated PMMA master [11]. They show exceptionally well-formed shapes and edges as can be seen from the electron microscope photography in Figure 3.

The facility will be fully operational at the end of 2011 and will enable PTB to perform the calibration of radiation sources at VUV wavelengths as short as 7 nm. The first task performed at the facility after its validation will be the characterization of a novel gas-jet source in the accessible spectral range.

Table 1. Wavelength range covered by the available gratings.

Branch	Grating / lines mm^{-1}	Wavelength range / nm
NI	900	160 to 400
NI	1800	80 to 200
NI	3600	40 to 100
GI	600	20 to 50
GI	1200	10 to 25
GI	2400	7 to 13

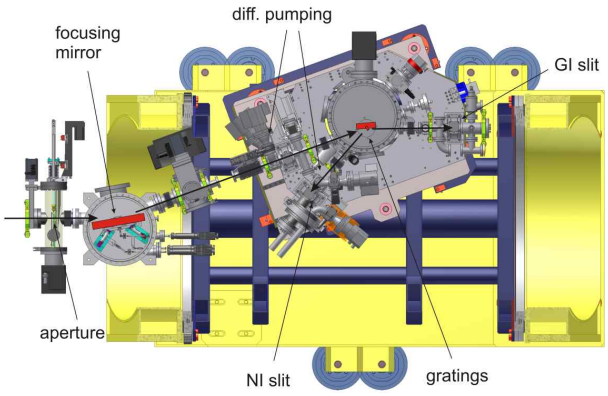

Figure 2. Monochromator station.

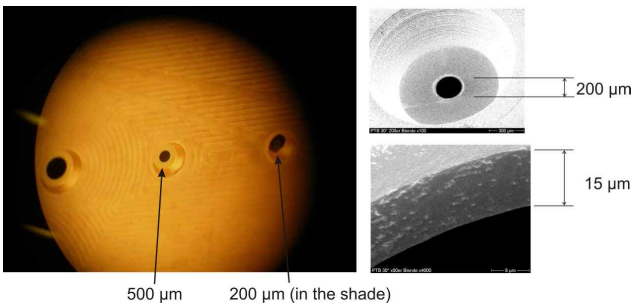

Figure 3. Photograph of the pinhole aperture sheet.

REFERENCES

1. B. Beckhoff et al., Phys. Status Solidi B 246, 1415, 2009.
2. J. Schwinger, Phys. Rev. 75, 1912, 1949.
3. M. Richter et al., Metrologia 40, S107, 2003.
4. J. Hollandt, M. Huber, and M. Kühne, Metrologia 30, 381, 1993.
5. K. Wilhelm et al., Appl. Opt. 36, 6416, 1997.
6. R. Klein et al., Phys. Rev. ST – Accel. Beams 11, 110701, 2008.
7. R. Klein, R. Thornagel, and G. Ulm, Metrologia 47, R33, 2010.
8. R. Klein et al., Metrologia 46, S266, 2009.
9. R. Klein et al., Metrologia 46, 359, 2009.
10. M. Richter et al., Nucl. Instr. and Meth. A 467-468, 605, 2001.
11. Fabricated by M. Schmidt, Mikro- und Feingeräte, Technical University, Berlin, Germany.

The Research of Numerical Analysis Methods For Interpolating Spectral Irradiance of Standard Lamps

Bo Huang, Caihong Dai, Jialin Yu, Zhifeng Wu, Huiquan Ouyang

National Institute of Metrology , Beijing, China

huangbo@nim.ac.cn; daicaihong@nim.ac.cn; wuzf@nim.ac.cn; oyhq@nim.ac.cn

Some numerical analysis methods are introduced to interpolate the spectral irradiance of standard lamp in needed area, including how to build a mathematical model, calculating the parameters and analyzing the errors. A new three segment fitting function of spectral irradiance of standard lamp and an optimizing method for non-linear parameter are put forward. Compare relative errors of different interpolating methods and curve fitting methods by a new successive error analysis method. The relative deviation of the new curve fitting function is 0.27% between 250nm and 2500nm which is acceptable comparing to the uncertainty of national primary standard of spectral irradiance lamp.

INTRODUCTION

The spectral irradiance of standard lamp is metrological maintain which is used to preserve and transfer the quantity of spectral irradiance. Its spectral range is from 250nm to 2500nm which covering ultraviolet, visible light and near-infrared. In order to obtain accuracy quantities from spectral irradiance of standard lamps, the sampling time should be limited that not over than 30 minutes in each region or the sensitivity of the system will drift. Considering of NIM's primary standard system we use the sampling intervals as follow 10nm at ultraviolet region, 50nm at visible light region and 100nm at near-infrared region, then use the interpolating or fitting functions to interpolate standard lamps' irradiances to users' wavelengths.

PROCEDURE

The spectral irradiance of standard lamp departs from the ideal Planckian distribution, and is generally approximated by multiplying the Planck function as follows:

$$L(\lambda,T)=\frac{c_1}{\pi\cdot\lambda^5}\cdot\frac{1}{\exp(\frac{c_2}{\lambda\cdot T})-1} \tag{1}$$

Traditional fitting function:

$$\begin{cases}\lambda<450nm, f(\lambda)=\dfrac{e^{c(1)+c(2)/\lambda}}{\lambda^5}\cdot e^{c(3)\lambda-c(4)\left|\frac{\lambda-\lambda_0}{500}\right|c(5)}\\ \lambda\geq 450nm, f(\lambda)=\dfrac{e^{c(1)+c(2)/\lambda}}{\lambda^5}\cdot e^{c(3)\lambda+c(6)\left|\frac{\lambda-\lambda_0}{500}\right|c(7)}\end{cases} \tag{2}$$

Where λ is the wavelength, and c(i) is fitting parameter, and the $\exp(a+\frac{b}{\lambda})\cdot\frac{1}{\lambda^5}$ is an approximation to a Plank function which as a constant factor. The rest is correction factor that is needed to account for differences between the spectral irradiance of standard lamps and the high black-body irradiance. So the correction factor reflects different spectral properties of different spectral irradiance of standard lamps.

The function that be fitted to the spectral irradiance of standard lamps of NIM:

$$\begin{cases}\lambda<300nm, f(\lambda)=\dfrac{e^{c(1)+c(2)/\lambda}}{\lambda^5}\cdot(e^{d(1)\cdot\lambda}-d(2)\cdot\left|\lambda-300\right|^{d(3)})\\ 300nm\leq\lambda<450nm, f(\lambda)=\dfrac{e^{c(1)+c(2)/\lambda}}{\lambda^5}\cdot e^{d(1)\cdot\lambda-d(4)\cdot(|\lambda-450|+|\lambda-300|)d(5)}\\ \lambda\geq 450nm, f(\lambda)=\dfrac{e^{c(1)+c(2)/\lambda}}{\lambda^5}\cdot e^{d(1)\cdot\lambda+d(6)\cdot|\lambda-450|c(7)}\end{cases} \tag{3}$$

We minimize the relative deviation between the measured values and the calculated values by the least-squares method in each spectral region:

$$E'_{\Delta}=\sum_{k=1}^{N}[\frac{f(x_k)-y_k}{y_k}]^2=\min \tag{4}$$

Suppose:

$$\Delta=\begin{vmatrix}\sum_{k=1}^{N}\frac{f_1(x_k)\cdot f_1(x_k)}{y_k^2},\sum_{k=1}^{N}\frac{f_1(x_k)\cdot f_2(x_k)}{y_k^2},\sum_{k=1}^{N}\frac{f_1(x_k)\cdot f_3(x_k)}{y_k^2},\cdots\cdots\\ \sum_{k=1}^{N}\frac{f_2(x_k)\cdot f_1(x_k)}{y_k^2},\sum_{k=1}^{N}\frac{f_2(x_k)\cdot f_2(x_k)}{y_k^2},\sum_{k=1}^{N}\frac{f_2(x_k)\cdot f_3(x_k)}{y_k^2},\cdots\cdots\\ \sum_{k=1}^{N}\frac{f_3(x_k)\cdot f_1(x_k)}{y_k^2},\sum_{k=1}^{N}\frac{f_3(x_k)\cdot f_2(x_k)}{y_k^2},\sum_{k=1}^{N}\frac{f_3(x_k)\cdot f_3(x_k)}{y_k^2},\cdots\cdots\\ \vdots\end{vmatrix} \tag{5}$$

$f_1(x_k)=1$, $f_2(x_k)=x_k$, $f_3(x_k)=x_k^2$, $f_4(x_k)=x_k^3$, $f_5(x_k)=x_k^4$, $f_6(x_k)=x_k^5$.

We get the parameters as follow:

$$
\begin{cases}
c(1) = \dfrac{1}{\Delta} \cdot \begin{vmatrix} \sum_{k=1}^{N} \frac{f_1(x_k)}{y_k}, \sum_{k=1}^{N} \frac{f_1(x_k)\cdot f_2(x_k)}{y_k^2}, \sum_{k=1}^{N} \frac{f_1(x_k)\cdot f_3(x_k)}{y_k^2}, \cdots\cdots \\ \sum_{k=1}^{N} \frac{f_2(x_k)}{y_k}, \sum_{k=1}^{N} \frac{f_2(x_k)\cdot f_2(x_k)}{y_k^2}, \sum_{k=1}^{N} \frac{f_2(x_k)\cdot f_3(x_k)}{y_k^2}, \cdots\cdots \\ \sum_{k=1}^{N} \frac{f_3(x_k)}{y_k}, \sum_{k=1}^{N} \frac{f_3(x_k)\cdot f_2(x_k)}{y_k^2}, \sum_{k=1}^{N} \frac{f_3(x_k)\cdot f_3(x_k)}{y_k^2}, \cdots\cdots \\ \vdots \end{vmatrix} \\
c(2) = \dfrac{1}{\Delta} \cdot \begin{vmatrix} \sum_{k=1}^{N} \frac{f_1(x_k)\cdot f_1(x_k)}{y_k^2}, \sum_{k=1}^{N} \frac{f_1(x_k)}{y_k}, \sum_{k=1}^{N} \frac{f_1(x_k)\cdot f_3(x_k)}{y_k^2}, \cdots\cdots \\ \sum_{k=1}^{N} \frac{f_2(x_k)\cdot f_1(x_k)}{y_k^2}, \sum_{k=1}^{N} \frac{f_2(x_k)}{y_k}, \sum_{k=1}^{N} \frac{f_2(x_k)\cdot f_3(x_k)}{y_k^2}, \cdots\cdots \\ \sum_{k=1}^{N} \frac{f_3(x_k)\cdot f_1(x_k)}{y_k^2}, \sum_{k=1}^{N} \frac{f_3(x_k)}{y_k}, \sum_{k=1}^{N} \frac{f_3(x_k)\cdot f_3(x_k)}{y_k^2}, \cdots\cdots \\ \vdots \end{vmatrix} \\
c(3) = \dfrac{1}{\Delta} \cdot \begin{vmatrix} \sum_{k=1}^{N} \frac{f_1(x_k)\cdot f_1(x_k)}{y_k^2}, \sum_{k=1}^{N} \frac{f_1(x_k)\cdot f_2(x_k)}{y_k^2}, \sum_{k=1}^{N} \frac{f_1(x_k)}{y_k}, \cdots\cdots \\ \sum_{k=1}^{N} \frac{f_2(x_k)\cdot f_1(x_k)}{y_k^2}, \sum_{k=1}^{N} \frac{f_2(x_k)\cdot f_2(x_k)}{y_k^2}, \sum_{k=1}^{N} \frac{f_2(x_k)}{y_k}, \cdots\cdots \\ \sum_{k=1}^{N} \frac{f_3(x_k)\cdot f_1(x_k)}{y_k^2}, \sum_{k=1}^{N} \frac{f_3(x_k)\cdot f_2(x_k)}{y_k^2}, \sum_{k=1}^{N} \frac{f_3(x_k)}{y_k}, \cdots\cdots \\ \vdots \end{vmatrix} \\
c(4) = \cdots\cdots \\
c(5) = \cdots\cdots \\
c(6) = \cdots\cdots
\end{cases}
\tag{6}
$$

The following Figure reflects the results of three methods which are spline interpolation, traditional fitting function and fitting function for standard lamps of NIM.

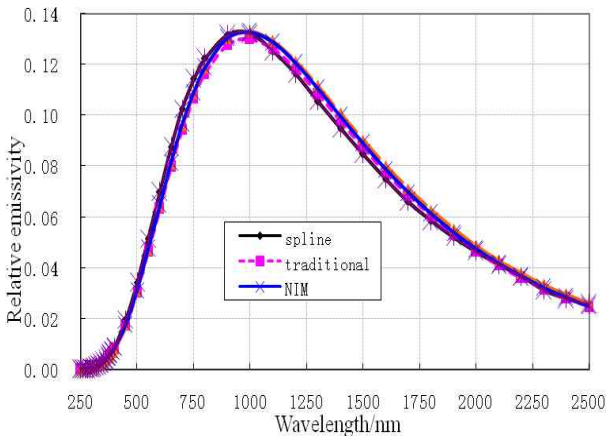

Figure 33. Interpolating the spectral irradiance of standard lamps by three methods.

We calculate three methods' relative deviation that compare with measured values as follow:

Table 7. The relative deviation of three methods between 250nm and 2500nm

function	relative deviation
Spline	0.56%
Traditional	0.44%
NIM	0.27%

The relative deviation distribution of three methods are shown below:

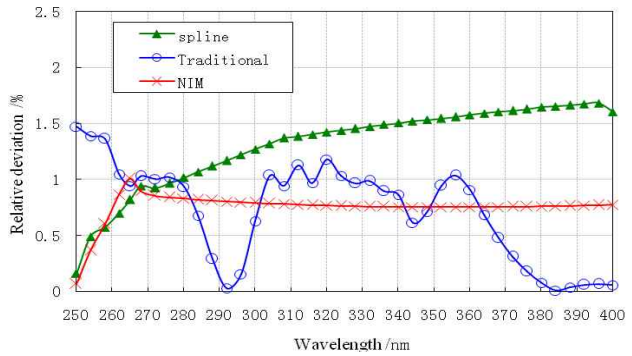

Figure 2. The relative deviation distribution of three methods between 250nm and 400nm

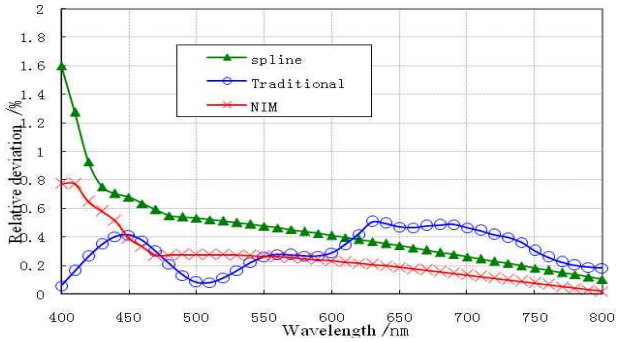

Figure 3. The relative deviation distribution of three methods between 400nm and 800nm

CONCLUSION

This part introduces a new three segment fitting function of spectral irradiance of standard lamp of NIM, and put forward an optimizing method for non-linear parameter. The relative deviation of the new curve fitting function is 0.27% between 250nm and 2500nm which is more suitable and acceptable comparing to the uncertainty of national primary standard of spectral irradiance lamp. It can reduce relative deviation remarkably.

REFERENCES

1. L. K. Huang, R. P. Cebula and E. Hilsenrath., New procedure for interpolating NIST FEL lamp irradiances, Metrologia, 35,381~386(1998).
2. G. Andor, Approximation function of spectral irradiance of standard lamps, Metrologia. 35, 427-429(1998).
3. Bevington P.R.,[Data Reduction and Error Analysis for the Physical Sciences], McGraw-Hill, New York, 96-164(1969).
4. John H.Mathews, Kurtis D.Fink, Numerical methods using MATLAB (Fourth Edition), Publishing House of Electronics Industry, Beijing, 5, 195-246(2005).

Performance Calibration of Solar Simulators According to IEC 60904-9

Haifeng Meng[1], Limin Xiong[1], Hao Sun[1], Yingwei He[1], Dingpu Liu[1], Wei Wang[2], and Tian Qin[2]

[1]*National Institute of Metrology, Beijing, P. R. China,* [2]*Institute of Metrology, Yangzhou, P. R. China*
Corresponding e-mail address: menghf@nim.ac.cn

Solar simulators are widely used for indoor I-V measurement as well as irradiance exposure tests of terrestrial photovoltaic (PV) modules. In the case of PV performance measurements, the influence of solar simulator's spectral mismatch and uniformity/temporal stability of irradiance can never be ignored. Herein, a practicable procedure calibrating solar simulator's performance according to IEC 60904-9 is demonstrated, then defines classifications of solar simulators, including spectral mismatch compared with AM1.5G spectrum, non-uniformity and temporal instability of irradiance. This procedure is applicable to various kinds of solar simulators. Furthermore, it's portable so that satisfy the requirements of in-situ serve for the solar simulator users.

INTRODUCTION

With the rapid development of photovoltaic industry, solar simulator, as an optimal substitute of natural solar irradiance, plays an increasingly great role in the performance measurements of PV modules, I-V characteristics, typically [1]. According to the I-V characteristic result, important parameters of PV modules, such as short-circuit current (Isc), open-circuit voltage (Voc), maximum power (Pmax), conversion efficiency (η), fill factor (FF) and so on, can be obtained. These parameters can reflect the performance of solar cells and modules, and provide significant reference for the producing techniques. Moreover, the price of PV product in trade is determined on the basis of Pmax, to avoid conflicts during trade, it's extremely important to guarantee the accuracy of the parameters. Therefore, solar simulator which used to obtain these parameters should be calibrated according to a criterion. The two leading standards organizations, ASTM International and International Electrotechnical Commission (IEC) have recognized that three most critical parameters related to the optical output should be standardized.

According to IEC 60904-9, it provided us a standard to define classifications of solar simulators: class A, B and C based on criteria of spectral distribution match, irradiance non-uniformity on the test plane and temporal instability [2]. This standard endowed us the required methodologies for determining the rating achieved by a solar simulator in each of the categories, but concrete method to calibrate solar simulators according to this standard is rarely reported.

In this article, we describe a practical and universal procedure for the performance calibration of solar simulators with items including spectral mismatch compared with AM1.5G spectrum, non-uniformity and instability of irradiance, resulting in a solar simulator classification.

CALIBRATION PROCEDURE

Among the three parameters of solar simulator's performance calibration, the spectral mismatch was traditionally the hardest to address. Spectral mismatch can demonstrate the extent of simulation between a solar simulator and an AM1.5G solar spectrum [3]. Considering precise simulation of an AM1.5G spectrum using artificial light could be very difficult, three classifications for the spectral accuracy of solar simulators were set up in international standards. For a class A designation, the irradiance fraction must be within ±25% of AM1.5G for each wavelength interval; class B, it must be within ±40%; and class C, within -60% to +100% [2]. Here, we employed a calibrated optical fibre spectrometer with good performance to measure the spectrum of solar simulator; it was traceable to standard light source so that proved reliable results. Below is a typical class A spectrum curves (Figure 1), and its corresponding data of irradiance fractions (Table 1).

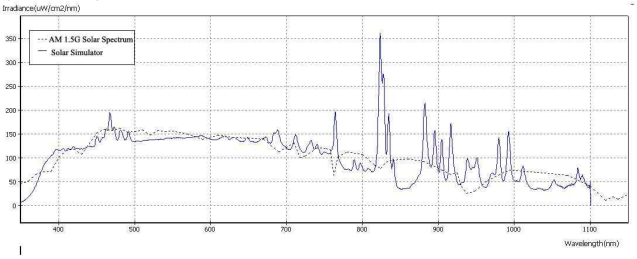

Figure 1 Comparison of a typical solar simulator's spectrum and AM1.5G solar spectrum.

Table 8. Percentage of total irradiance for AM1.5G solar spectrum and a typical solar simulator.

Wavelength range (nm)	Percentage of total irradiance (AM1.5G)	Percentage of total irradiance (simulator)	Spectral match
400-500	18.4%	18.0%	0.98
500-600	19.9%	18.7%	0.94
600-700	18.4%	18.6%	1.01
700-800	14.9%	14.7%	0.99
800-900	12.5%	13.5%	1.08
900-1100	15.9%	16.4%	1.03

To identify the irradiance non-uniformity on the test plane and temporal instability, we integrated a system composed of Si solar cell, IV convertor, and data acquisition card, as its equipment scheme shown in Figure 2. It technically used an IV convertor to convert the Isc signal of the Si solar cell (here as a uniformity detector) to voltage signal, which collected by the data acquisition, and finally display the irradiance of solar simulators.

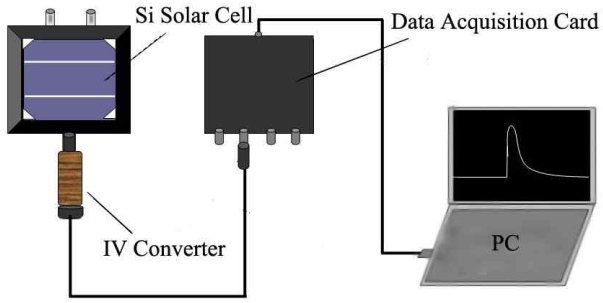

Figure 2 Equipment schemes of the irradiance non-uniformity and temporal stability measurements.

An example of the non-uniformity measurement was described. After divide the designated test area (1.4m*1.1m) to 64 equally sized blocks, we detected the voltage signal of each test block, data shown in Figure 3. Then, according to the definition of non-uniformity of irradiance in IEC 60904-9, we get a corresponding equation, that is Non-uniformity (%) = (Max Isc×R–Min Isc×R)/(Max Isc×R+Min Isc×R) ×100%, R stands for the resistance of the IV convertor, Isc×R equals the detected voltage. In Figure 3, Max Isc×R = 126.8 mV, Min Isc×R = 122.2 mV, its non-uniformity (%) of irradiance can be calculated to be 1.8%, small than 2%, so it should be classified as class A [2]. If the value is in the range of 2% and 5%, it should be class B; while between 5% and 10%, it is class C.

	1	2	3	4	5	6	7	8
A	122.7	122.6	122.2	122.3	123.1	122.8	123.2	124.4
B	123.7	123.3	123.2	123.5	123.8	123.8	124.3	125.0
C	122.6	122.4	122.5	123.1	123.5	124.0	124.3	124.7
D	124.5	124.8	125.2	126.1	126.8	126.7	126.5	126.5
E	124.7	125.0	125.3	126.2	126.6	126.1	125.7	125.8
F	123.0	123.4	123.3	124.0	124.1	123.8	123.4	123.9
G	124.7	125.0	124.4	124.8	124.7	124.8	125.1	125.1
H	124.1	123.7	123.2	123.8	122.6	122.0	123.2	123.1

Figure 3 Data acquired in irradiance non-uniformity measurement (Unit: mV).

Temporal instability is traditionally divided into short term instability (STI) and long term instability (LTI). If the solar simulator can simultaneously measure and store values of irradiance, current and voltage, the temporal instability is class A for STI. We detect the LTI by detecting a fixed block with the same equipment as the non-uniformity measurement. Similar to the calculation of non-uniformity (%), long term instability (%) = (Max Isc×R–Min Isc×R)/(Max Isc×R+Min Isc×R), and then determine its classification according to IEC 60904-9.

Repeated calibrating issues testified that this procedure for measuring all these three parameters is effective for various kinds of solar simulators.

CONCLUSIONS

A whole concrete procedure of solar simulators' performance calibration has been developed in this work. Three important parameters of solar simulators were taken into concern according to IEC 60904-9. This procedure provided a reasonable procedure to accomplish the classification of solar simulators; it is applicable to various kinds of solar simulators, as well as convenient for in-situ calibration.

REFERENCES

1. H. B. Serreze, R. G. Little, Large-area solar simulator: critical tools for module manufacturing, Technical Papers in PV Modules, Edition 1-Photovoltaics International, 2008.
2. IEC 60904-9, 2nd edition, 2007.
3. A. M. Andreas, D.R. Myers, Pulse analysis spectroradiometer system for measuring the spectral distribution of flash solar simulators, SPIE Opitics and Photonics Conference: Optical Modeling and Measurements for Solar Energy Systems II, San Diego, California, 2008.

Characterization and Traceability of Broadband UV Radiometers

Dai Caihong, Huang Bo, Yu Jialin, Wu Zhifeng, Ouyang Huiquan

National Institute of Metrology , Beijing, China

daicaihong@nim.ac.cn; huangbo@nim.ac.cn; yujialin@nim.ac.cn; wuzf@nim.ac.cn; oyhq@nim.ac.cn

Five kinds of traceability methods of UVA radiometers are described and analyzed. Spectral mismatch and correction method for different UV sources, long wavelength range response error and directional response error are investigated and evaluated for commercial UV radiometers. Multi-spectral UV irradiance for different types of UV sources and radiometric measurement for weathering tests standard apparatus were set up at NIM.

INTRODUCTION

Broadband UV radiometers are widely used for measuring UV irradiance or radiant exposure in various areas of health, industry, and science, such as in weather aging of materials, semiconductor lithography, non-destructive testing, UV curing, catalytic process, environmental monitoring, atmospheric research, water purification, medical diagnostics and therapy, space-based astrophysical observations and other applications. The accuracy of measurement is influenced by many factors such as the characteristics of the radiometer, operating conditions, environmental conditions and the UV sources to be measured. Due to the lack of spectral resolving power, significant measurement errors may occur if the radiometer has poor quality. Five kinds of traceability methods and experiments of UVA radiometers are compared and analyzed in this paper. Spectral mismatch and correction method for different UV sources, long wavelength range response error and directional response error of commercial UV radiometers were investigated and evaluated.

TRACEABILITY METHODS COMPARISON FOR UVA RADIOMETERS

Five kinds of traceability methods of UVA radiometers are discussed and analyzed (Table 1), including absolute spectral irradiance method based on standard lamps, absolute spectral power responsivity of detectors, absolute thermoelectric radiometer method, electrically calibrated pyroelectric radiometer method and method of comparing with the standard radiometer. On the basis of the above theories and methods, the uncertainty of broadband ultraviolet irradiance under the defined conditions was cut down to 2.0%(k=1) from 10%(k=1) at NIM.

Table 1. Five kinds of traceability methods comparison of UVA radiometers

Traceability methods	UVA irradiance responsivity R_{UVA} /(A·cm^2/W	Uncertainty / %	Relative deviation compared to method 1 /%
Method 1	0.00560	2.0	0.00
Method 2	0.00561	3.9	0.18
Method 3	0.00574	5.5	2.50
Method 4	0.00543	6.8	-3.04
Method 5	0.00583	10.0	4.11

SPECTRAL MISMATCH AND CORRECTION METHOD

When the measuring sources and calibrated sources have different spectral distributions, large errors result from calibrating UV radiometers with one kind of UV sources. Because the spectral responsivity of the UV radiometers are not ideal which are well-defined as "1" within its specific spectral region and "0" outside of this region, the out-band signal will effect the measuring result.

A special experiment was designed to compare the test signal of two UVA radiometers which are calibrated by high-voltage mercury lamp, and measuring under different type of UV sources. Results are listed in Table 2 and 3.

Table 2. Measuring errors when the spectral of test and calibrated sources mismatched for UVA-1 radiometer.

Source Type	Standard value /μW/cm^2	Test value /μW/cm^2	Relative deviation /%
H-Mercury	192.69	195.00	1.20
CHG-200	553.53	383.00	30.81
Xenon	34.62	16.00	53.78
Tungsten Halogen	67.20	33.00	50.89

Table 3. Measuring errors when the spectral of test and calibrated sources mismatched for UVA-2 radiometer.

Source Type	Standard value /μW/cm^2	Test value /μW/cm^2	Relative deviation /%
H-Mercury	192.69	196.50	1.98

CHG-200	553.53	458.04	17.25
Xenon	34.62	19.98	42.29
Tungsten Halogen	67.20	45.86	31.76

The measurement results are various by using different UVA radiometer, and different relative deviations will occur when a UVA radiometer was calibrated by one source and measured other different type source.

Define the spectral mismatch correction factor and spectral matching characteristic factor as follow:

$$F[E_t(\lambda),E_c(\lambda)]=\frac{R_c}{R_t}=\frac{\int_0^\infty E_c(\lambda)\cdot S_{rel}(\lambda)\cdot d\lambda}{\int_0^\infty E_c(\lambda)\cdot S_{act,rel}(\lambda)\cdot d\lambda}\cdot\frac{\int_0^\infty E_t(\lambda)\cdot S_{act,rel}(\lambda)\cdot d\lambda}{\int_0^\infty E_t(\lambda)\cdot S_{rel}(\lambda)\cdot d\lambda} \quad (1)$$

By using the spectral mismatch correction factor, the measurement result can be corrected as,

$$Y = Y_t \cdot F[E_t(\lambda),E_c(\lambda)] \quad (2)$$

The corrected results of UVA-1 radiometer are listed in Table 4.

Table 4. The corrected results of UVA-1 radiometer

Test source	Standard value /μW/cm^2	Test value /μW/cm^2	Relative deviate of tested value /μW/cm^2	Relative deviate of corrected value /%
H-Mercury	192.69	195.00	1.20	/
CHG-200	553.53	383.00	30.81	1.06
Xenon	34.62	16.00	53.78	1.10
Tungsten Halogen	67.20	33.00	50.89	1.29

DIRECTIONAL RESPONSE

The directional response function is determined by the shape and the optical properties of the acceptance area as well as the geometric and optical construction of the radiometer head. 20 kinds of commercial UV radiometers were measured by cosine response measurement system developed by NIM. The results are listed in figure 1 and figure 2.

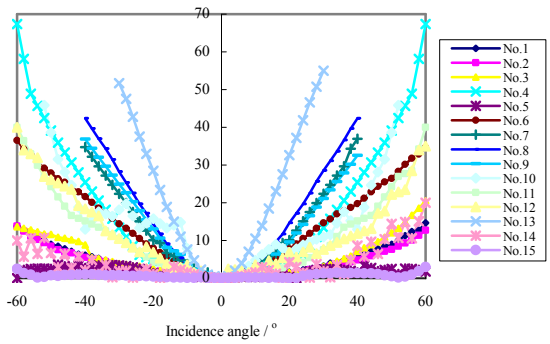

Figure 1. Directional response of UVA radiometers.

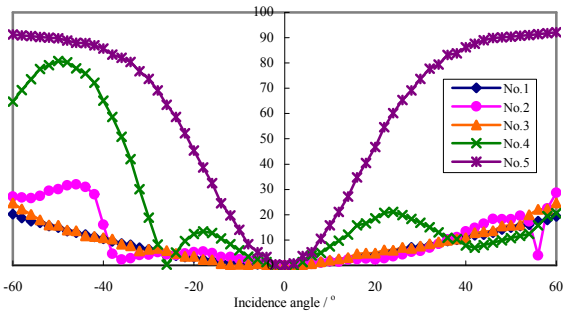

Figure 2. Directional response of UVC radiometers.

LONG WAVELENGTH RANGE RESPONSE

The long wavelength range response of a radiometer head is according to Eq.(3),

$$u = \left|\frac{Y_s}{Y} - u_0\right| \quad (3)$$

Where u_0 is according to Eq.(4),

$$u_0 = \frac{\int_0^\infty S_{\lambda,S}\cdot\tau(\lambda)\cdot s_{act,rel}(\lambda)\cdot d\lambda}{\int_0^\infty S_{\lambda,S}\cdot s_{act,rel}(\lambda)\cdot d\lambda} \quad (4)$$

Long wavelength range response results of 28 kinds of commercial UV radiometers are listed in Figure 3.

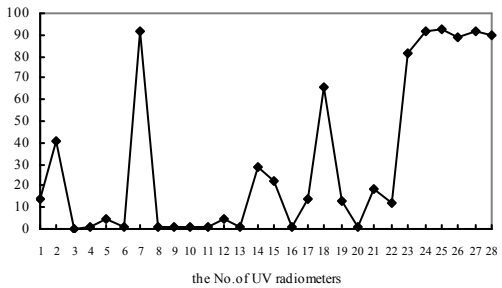

Figure 3. Long wavelength range response results of radiometers.

REFERENCES

1. G. Xu and X. Huang, Calibration of broadband UV radiometers-methodology and uncertainty evaluation[J], *Metrologia*, 2003, 40: S21~S24.
2. G. Xu and X. Huang, Characterization and calibration of broadband ultraviolet radiometers[J], *Metrologia*, 2000, 37: 235~242.
3. Thomas C. Larason, Christopher L. Cromer, Sources of error in UV radiation measurements[J], *J. Res. Natl. Inst. Stand. Technol.*, 2001, 106: 649~656.
4. Gan Xu, Xuebo Huang and Yuanjie Liu, APMP.PR-S1 comparison of irradiance responsivity of UVA detectors[J], *Metrologia*, 2007, 44, Tech. Suppl., 02001.

Study on Standard White Field of Liquid Crystal Display and Threshold Viewing Angle

Wende Liu[1], Chi Chen[1], Yingying Xu[1], Qiming Fan[1], Jing Zhang[1]

[1] *National Institute of Metrology , Beijing, China*

Corresponding e-mail address: chenchi@nim.ac.cn

The standard white-field instrument, which is traceable to to the national spectral radiometric, photometric and colorimetric primary standards, was built for applications in characterizing photometric and colorimetric parameters of displays. The instrument was characterized and its spectral, stability and photometric-colorimetric parameters were presented. Using the instrument to study the viewing-angle of the main-stream liquid crystal displays, the influence of the usually ignored varied area of the light-emitting surface during the measuring procedure was considered. The results indicate a difference of more than 8% for the absolute-luminance-based viewing-angle threshold method, which should be considered and avoided in the measurement.

INTRODUCTION

Recent years have witnessed rapid progress in color television/displays. During the process of manufacturing, different colorimeters need to be used for the adjustment and verification of their color. For the unification of the testing results by these devices, calibration by using standard white field is necessary. Formerly the CRT white field was used for calibrating colorimeters, which, however, is no longer suitable for present mainstream color televisions and displays. Therefore, it is necessary to develop a new standard white field of display to enable precise measurement or calibration.

Furthermore, we used the instrument to study the threshold of viewing angle for different displays. TCO'06 standard[1] set strict rules for various specifications of the flat panel display, without clear notes on threshold viewing angle. But TCO'06 gives detailed description on how the variation of the luminance, chromaticity and their homogeneity with the viewing angle should reach certain requirements. This can be used for reference when measuring viewing angle performance. On the other hand, the Video Electronics Standards Association (VESA) has issued the Flat Panel Display Measurements Standard (FPDM version 2) early in 2001[2], which is still an important specification in use by the industry. In FPDM, several threshold viewing angle definitions are suggested, based on luminance, threshold color difference and gray scale inversion. The empirical formula for the threshold viewing-angle based on subjective vision proposed in literature[3] is also discussed with the above objective quantities in the present work.

Not only the changes of the luminance, contrast ratio, color difference versus the viewing angle are presented here, the correction of the viewing-angle measurement is discussed by considering the changed area of the tested region on the display during the rotation of the display panel.

INSTRUMENT, METHOD OF MEASUREMENT AND RESULTS

For increasing requirements of measuring photometric and colorimetric values of the color TV/displays, the tristimulus colorimeter is usually used devices. However, the mismatch of the spectral responsivity and the color matching function is unavoidable. And the error becomes even worse when the spectral power distribution of the displays differs largely with standard light source. Standard light source A was usually employed for the calibration. The solution for calibrating displays is to use the standard white field produced by display having a similar spectral distribution to the display under test to calibrate the measuring devices. Some authors[4] use the standard light source A to calibrate the spectral radiometer, which is then used as standard detector. The detailed steps include the following calibration period: firstly using the uncalibrated measuring device to set the display to its white field status, secondly using the calibrated spectral radiometer to measure this white field and then set to the target white field. Repeat of this period is considered to make the display gradually approaching the standard value. The display is used as a reference light source and cannot be uses as a stand-alone standard light source. Moreover, the error can not be conveniently evaluated during the repeated calibration process.

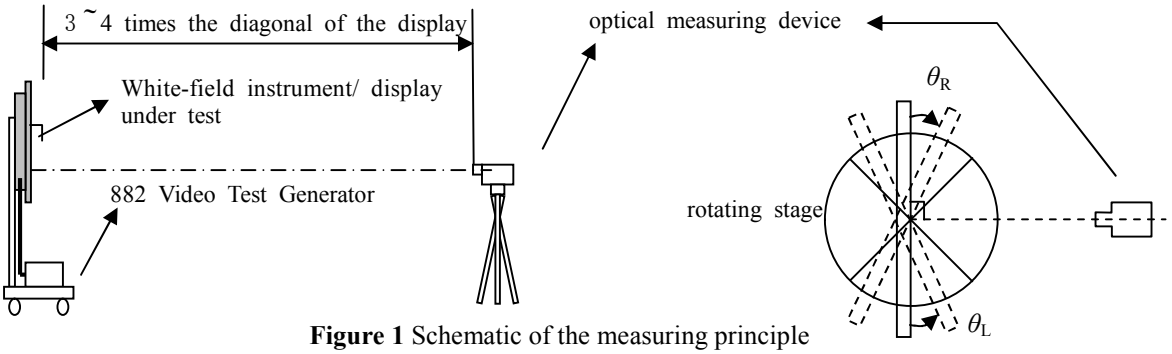

Figure 1 Schematic of the measuring principle

We established the standard LCD white field instrument, employing the primary standard maintained by Chinese National Institute of Metrology. The principle of measurement is shown in Fig. 1. Figure 2 shows the idea that we used to correct the results of the threshold of the viewing angles. As the display rotates, the area of the region under test also changes. For the left case in Fig. 2, the pixels outside the tested region is covered by black paper so that the effective area in the field of view becomes smaller. On the other hand, without coverage, the number of effective pixels in the field of view increases, which should be corrected in a more precise consideration. Figure 3 gives the spectral responsivity curve of the monochromatic field output from the established LCD standard white field instrument with CCFL (cold cathode florescent lamp) as its backlight. Meanwhile, we investigate the temporal variation of the luminance, chromaticity coordinates of each monochromatic field, as shown in Fig. 4 The correction made for the luminance test and viewing angle test based on IQ factor are shown in Figs. 5 and 6, respectively.

REFERENCES

1. TCO'06 Media Display, version 1.2, The Swedish Confederation of Professional Employees, 2006.
2. Flat Panel Display Measurements Standard (FPDM) version 2.0, VESA Display Metrology Committee, 2001.
3. Teunissen K, Qin S, Heynderickx I, A perceptually based metric to characterize the viewing-angle range of matrix displays, J. Soc. Info. Display, 16, 27-36, 2008.
4. Yao Jun, Study on the Way of Quickly Setting up the Standard White Field of TV. Chinese Journal of Scientific Instrument, 23, 79-81, 2002. (in Chinese with an English abstract)

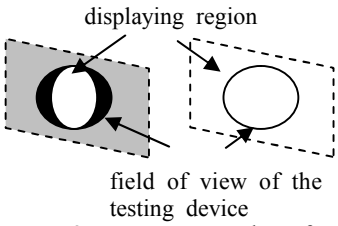

Figure 2 Two approaches for measuring display

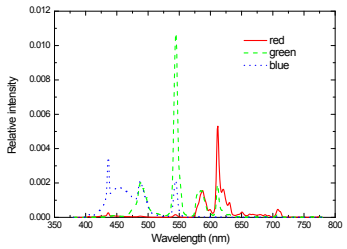

Figure 3 Spectral responsivity of red, green and blue monochromatic field

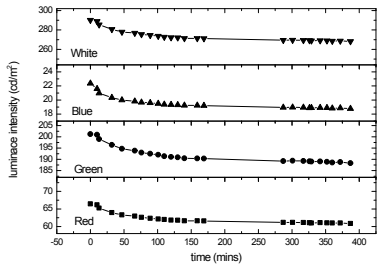

Figure 4 Time dependence of white field and red, green, blue monochromatic field

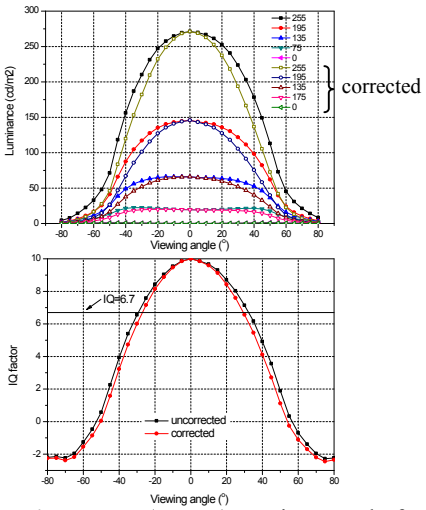

Figure 5 (Upper)Luminance before and after the correction (for LCD2). (Lower) Image quality factor before and after the correction (for LCD1)

Characterization of LED light sources in power and wavelength

Anne Andersson[1], Stefan Källberg[1], Sylvain Dubé[2], and Håkan Skoogh[1]

[1]*SP Swedish Technical Research Institute, Borås, Sweden* [2]*Heliospectra AB, Borås, Sweden*

Corresponding e-mail address: anne.andersson@sp.se

This paper reports on characterization of LED light sources and LED luminaires in power and wavelength in sphere sizes 50 cm and 300 cm in diameter.[1]

LED reference sources[2] and LED greenhouse luminaries are measured. The large sphere system is tested with a LED luminaire for each wavelength individually and compared with all wavelengths "on".

THE FIRST SECTION

Traditionall light sources to be used in the greenhouse industry are characterized photometrically. Plants are rather considered as photon counters and make use of radiation in the range of wavelengths from UVB up to Far Red. Green is however greatly reflected by green leaves. One can note that HPS (High Pressure Sodium) lamps are very energy inefficient for plants due to high reflectivity of leaves in green and yellow wavebands. They also lack blue wavebands which are important for optimal photosynthesis. Hence, to optimize a greenhouse light source[3] one needs to know the power at each wavelength also outside the photometric V(λ)-function. In diagram 1 below the spectra for a LED (HS-LED) and one HPS luminaire are compared.

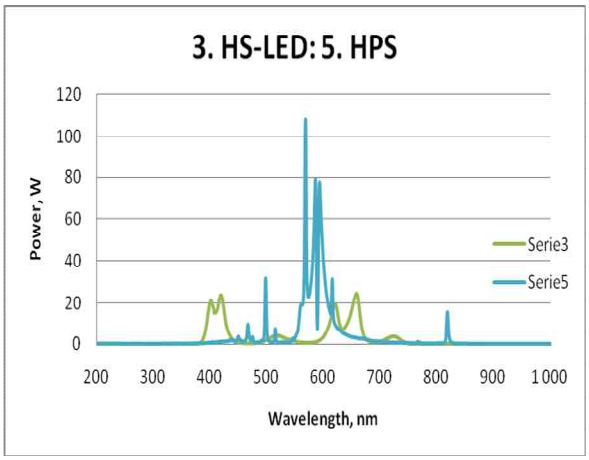

Figure 1: spectra for a LED greenhouse luminare and one HPS luminare.

Several traceable steps were used to calibrate a large, 300 cm diameter sphere, for measurements of total power and spectral properties of large luminaires. Spectral Responsivity of the 300 cm sphere set-up can be studied in Fig 2.

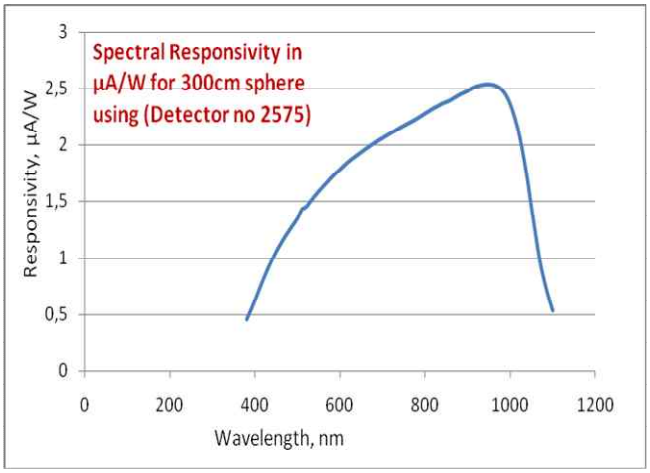

Figure 2: spectral responsivity of 300cm sphere set-up

In the first step a 50 cm sphere set-up was calibrated using Argon laser light at 514.5 nm.

Secondly, a multi-chip green LED source was calibrated using the 50 cm sphere to be used as a reference LED source. This reference LED source was a high intensity single wavelength, cooled LED array, composed of 25 LEDs mounted in a square 7X7 mm^2(Enfis, UNO Tile array, 515nm). The total power of the LED array and the peak wavelength, as functions of the driving current, were evaluated.

Total power of the reference LED array was also measured using an Ophir radiometer with a thermal detector, calibrated with a measurement uncertainty of 2 % in power. A small discrepancy (< 3 % less for the "Ophir method") between the two methods was found, and is attributed LED side- stray- light effects. In an integrating sphere all light will go into the sphere, which is difficult to get in the thermal radiometer measurement set-up.

The calibrated reference LED array was used as reference LED light source in the 300 cm sphere. The reference LED conditions were: stabilized drive current of 2.0 A, peak wavelength 515.0 nm and 3,26 W giving a reference detector value of 1.425 µA/W in the 300 cm diameter sphere. The 300 cm sphere was equipped with an auxiliary lamp.

Compensation factors were estimated for each luminaire before power measurement. Compensation factors, ranging from 1.01 to 1.07, were used to compensate for self-absorption of the luminaires.
The same Si- detector was used in the 50 cm and 300 cm spheres.
The center wavelength for the measured light sources was calculated and used to evaluate the responsivity at that wavelength to obtain the total power output from the sources.

Table 9. Uncertainty calculation for LED luminaire power calibration..

Uncertainty estimation LED power calibration	factor incl
Measurement	0,010
Detector current	0,001
Detector calibration	0,012
Calibration of sphere at 515 nm	0,021
Responsivity at centre wavelenth	0,021
Centre wavelength of source	0,007
Helplamp compensation	0,007
k=1	0,035
k=2	0,070

RESULTS

One standard HPS greenhouse luminaire and a prototype greenhouse LED luminaire were characterized in power and measured spectroradiometrically in the 300 cm sphere. The HS LED luminaire total power output, (see table) was determined two ways.

Table 2. Power and Wavelength characterization of two Greenhouse Luminaires

	uA	**nm**	**uA/W**		**W**
HPS	176	589	1,75	1,07	108,1
LED	38,8	554	1,60	1,02	24,7
nm					
735	6,47	727	2,42	1,02	2,73
660	18,25	660	1,96	1,02	9,50
620	7,62	622	1,86	1,02	4,19
530	1,98	519	1,50	1,02	1,35
420	2,51	420	0,82	1,02	3,11
400	2,08	402	0,63	1,02	3,35
sum	38,91				24,2

First, by summing outputs of single channels LED lights by driving each wavelength LED group separately and, secondly by having all LED groups turned ON at one time. A lower value (approximately 2 %) was obtained when adding optical power levels of individual wavelength groups, compared with lighting all groups simultaneously (at full LED electrical power). The total detector current added up to same values but the optical output power did not. The full reason for that has not been analyzed. The spectral responsivity of the sphere system must be judged as not fully linear over the total range, but still is within the stated measurement uncertainty.

FUTURE WORK

Suggestion for future work will be to further look into and improve methods for characterizing light sources by radiometry rather than photometry. [4].

REFERENCES

1. Commission Internationale de l' clairage: Measurement of LEDs, CIE 127
2. IESNA standards on LED and SSL: LM-79 and LM-80.
3. Pinho, P., Nyrhilä, R., Särkkä, L., Tahvonen, R., Tetri, E., Halonen, L., Evaluation of Lettuce Growth under Multi-spectral-component Supplemental Solid State Lighting in Greenhouse Environment. International Review of Electrical Engineering (I.R.E.E.), 2007, vol. 2(6), pp. 854-860.
4. JONES, C. F. and OHNO, Y., Colorimetric Accuracies and Concerns in Spectroradiometry of LEDs, Proc., CIE Symposium '99, Budapest, 173-177 (1999).

Reflectance Study of Blackbody Fixed-Point Crucible Graphite at Elevated Temperatures

Leonard Hanssen,[1] Sergey Mekhontsev,[1] Vladimir Khromchenko,[2] Boris Wilthan,[2] Jinan Zeng,[2] Heather Patrick,[1] and Thom Germer[1]

[1]*National Institute of Standards and Technology (NIST), Gaithersburg, MD, USA*
[2]*Space Dynamics Laboratory (SDL), Logan UT, USA*
Corresponding e-mail address: hanssen@nist.gov

We report on a study of the emittance properties of graphite at 405 nm and 658 nm at ambient and elevated temperatures. This study is part of an effort to accurately determine the emissivity of high temperature fixed point cavities, which are being evaluated for inclusion as high temperature reference points in a new practical temperature scale. This effort is being conducted in coordination with the Consultative Committee for Thermometry (CCT) Working Group 5 on Radiation Thermometry of the International Committee of Weights and Measures (CIPM).

INTRODUCTION

The WG5 of the CCT is pursuing an investigation of high temperature fixed point blackbody (HTFP) sources containing the eutectics Co-C, Pt-C and Re-C, with eutectic temperatures of 1597 K, 2011 K, and 2747K, respectively, for their suitability to serve as reference points for dissemination of T (and T90) within the context of the "Mise en pratique of the definition of the Kelvin" (MeP-K) at high temperature. A critical component of the overall investigation is an accurate determination of the cavity effective emissivity. The primary available approach to obtaining the cavity emissivity is through modelling that employs measured optical properties of the cavity wall material – graphite.

In this paper we present an overview of our plan for determination of the HTFP emissivities, along with a description and results of the study of graphite emittance and reflectance over a range of temperatures from ambient to 2700 K.

CAVITY EMISSIVTY APPROACH

The overall program for evaluation of HTFP cavities, is summarized in seven steps below. It involves diverse measurements on representative graphite samples and calculations of the cavity emissivity dependencies. All measurements are performed at 405 nm and 658 nm using laser sources to obtain cavity emissivity values at wavelengths comparable to those used by existing and anticipated pyrometers employed for high temperature radiometric temperature measurements. The steps are:

1) Hemispherical spectral reflectance of graphite samples under neutral gas purge at temperatures above ambient (up to a maximum of about 1200 K), to obtain the near-normal directional emittance.

2) Complete room temperature bi-directional reflectance distribution function (BRDF) of the graphite samples at 405 nm and 650 nm. A second paper at this conference describes this step and results in detail.[1] These measurements can be validated with hemispherical reflectance at the same wavelengths obtained in step 1. At the same time, the BRDF results can validate the restricted BRDF measurement set in step 3.

3) Temperature dependent BRDF of the graphite samples at a few fixed geometries up to 2750 K. Assuming that the relative BRDF angular distribution does not change with temperature, these measurements will allow scaling the reflectance (from step 1), and hence the near-normal emittance.

4) Angle-dependent relative spectral radiance at 405 nm and 650 nm under vacuum at temperatures up to 2750 K in the same setup as step 3 to obtain the angle dependent emittance.

5) Furnace-temperature profiles of the radiation-shield structure in front of the cavity are measured at the eutectic temperatures of the eutectics in study. These results are found in Reference 2.

6) Calculations of the temperature distributions within the cavity and along its outer environment, using a software package utilizing finite volume analysis, with input from step 5. These results are found in References 2 and 3.

7) Monte Carlo ray trace modeling of the effective spectral cavity emissivity with input of the results of all steps 1 to 6, including the high-temperature angle dependent graphite emissivity and BRDF as well as

the cavity temperature non-uniformities. Preliminary results using nominal values for graphite emittance at room temperature were recently reported in Reference 4.

We will report on the progress of the final elements of the study, including DHR and BRDF measurements at elevated temperatures (steps 1, 3 and 4), as well as updated modelling results, using the recent ambient temperature graphite BRDF results.[1]

REFERENCES

1. H. J. Patrick, L. M. Hanssen, J. Zeng and T. A. Germer, "BRDF Measurements of Graphite Cavity Material used in High-Temperature Fixed Point Blackbodies for Temperature Scale Dissemination: a multi-angle study at 405 nm and 658 nm," *NEWRAD 2011 Abstract Book*, 2011.
2. P. Bloembergen, B. B. Khlevnoy, P. J. Largo, Y.Yamada, "Spectral and total effective emissivity of a high-temperature fixed-point radiator considered in relation to the temperature drop across its back wall", Int. J. Thermophys **29**, 370-385 (2008).
3. P. Castro, P. Bloembergen, Y.Yamada, M.A. Villamanan, G. Machin, "On the uncertainty in the Temperature Drop across the Backwall of High-Temperature Fixed Points", Acta Metrologica Sinica **29**, 253 – 260 (2008).
4. P. Bloembergen, L. M. Hanssen, S. N. Mekhontsev, P. Castro, and Y. Yamada, "Spectral and total effective emissivity of a high-temperature fixed-point radiator considered in relation to the temperature drop across its back wall", submitted to Int. J. Thermophys (2011).

Development and Investigation of WC-C Fixed Point Cells

B. B. Khlevnoy and I. A. Grigoryeva

All-Russian Research Institute for Optical and Physical Measurements (VNIIOFI), Moscow, Russia
Corresponding e-mail address: khlevnoy-m4@vniiofi.ru

Two WC-C fixed-point cells were built using materials of 5N purity and two different methods of filling, and then investigated. The cells showed the similar melting plateau shapes with melting range of 100 mK. The repeatability of melting temperatures was estimated as 24 mK. The melting temperature of WC-C was measured by comparing with Cu fixed point and was found to be 3020.8 K with uncertainty 1.1 K (*k*=2).

INTRODUCTION

Recently suggested a new high temperature fixed point based on the WC-C peritectic [1] is especially attractive for people involved in radiometry. Its melting temperature (about 3022 K) is close to the colour temperature of tungsten halogen lamps, usually used for spectral irradiance measurements.

However, up to now only one laboratory [1, 2] has published the results of investigation of the WC-C fixed point. To make certain of its high reproducibility comparisons of cells built in different laboratories have to be carried out.

VNIIOFI has built cells out of 5N tungsten powder using two different methods of cell filling. The cells showed almost identical melting plateaus with the melting range of about 100 mK and repeatability of 20 mK. The paper will present the experience in developing the WC-C cells, the results of the cells investigation and ehe WC-C melting temperature measured by means of comparison with the Cu fixed point.

FABRICATION OF THE CELLS

Cell crucibles were manufactured from graphite and had an outer diameter of 24 mm and a length of 49 mm. The crucible contains a blackbody radiating cavity with a diameter of 5 mm, a depth of 35 mm and an opening of 3 mm. Thickness of the cavity wall was 1.5 mm. The inner volume of the cell between the cavity and outer walls are filled with a WC-C ingot. The cells had a hybrid structure, i.e. in between the outer walls and the ingot there was an insulator combined from a graphite sleeve and a C/C sheet, the latter was between the sleeve and outer walls. Fig. 1 shows a cross-section of the cell. The graphite used for the crucibles was the Ringsdorff R4550 type with nominal purity of 99,998 %. The crucibles were purified chemically after machining and finally baked together with the C/C sheet at temperature of 3000 °C for 30 minutes in an argon atmosphere.

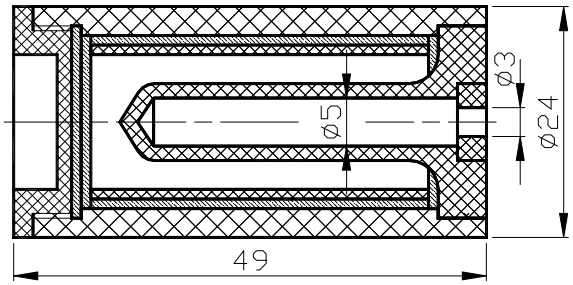

Figure 1. Cross-section of WC-C cells

The materials used for smelting WC-C were: tungsten powder with nominal purity of 99.999% (supplier: Alfa Aesar, lot: B15Q07) and graphite powder with nominal purity of 99.9999% (supplier: Carbotec, lot: OC4-8-4).

Two cells were filled using different procedures. The cell WC-C4 was filled by pouring a mixture of tungsten and graphite powders (mass portion of graphite was 6.0 %) directly into the crucible. Then the crucible was heated up in vertical furnace in an argon atmosphere to melt the mixture, then filled and melted again five steps more until the crucible was full. The mass of the WC-C4 ingot was 43,0 g.

The cell WC-C5 was filled using the new “drop method” of filling. The powders were mixed in the reduced proportions: 5.0 % of graphite powder. In this method the mixture is not introduced into the crucible directly, but into an additional container located just above the crucible. The WC-C pritectic forms and melts inside the container and the already molten alloy drops through a small hole in the container bottom and fills the crucible. We believe that the new method enables to get more homogeneous ingot and avoid contamination during filling. The mass of the WC-C5 cell ingot was 58.8 g. Difference in masses of WC-C4 and WC-C5 denotes the better filling of the latter one.

INVESTIGATION OF THE CELLS

The cells were heated in a high-temperature furnace of the BB3500MP type with a pyrolytic-graphite cavity with inner diameter of 59 mm. The furnace temperature was controlled by means of an optical feedback system. Melting and freezing plateaux were realized by applying to the furnace a certain temperature step ΔT with a heating/cooling rate of 15 K/min. For most cases ΔT equalled +15 K for melts and -30 K for freezes as compared to the melting temperature. The temperature of the cells was measured using an imaging radiation thermometer of the TSP-2 type with central wavelength of 650 nm and a bandpass of 20 nm.

Fig. 2 shows melting plateaux measured for both cells. The WC-C5 cell demonstrated a slightly higher (by about 45 mK) temperature and longer plateauex: 7 min in comparison with 5 min for the WC-C4 cell. The difference in durations could be explained by the lower mass of the latter. Except the duration, both cells had similar shape of plateaux with melting rage of about 100 mK.

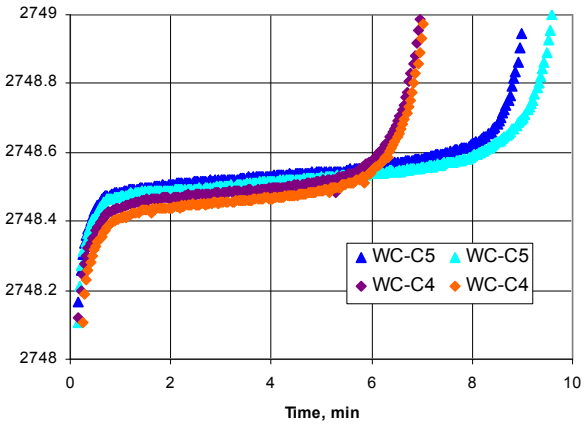

Figure 2. Melting plateaux of WC-C cells

The repeatability of the WC-C5 cell was investigated during four days measurements as estimated as 24 mK. The WC-C4 had the similar repeatability (22 mK), which, however, was calculated for measurements done during one day.

The investigation showed that the distinguishing feature of the WC-C cells are deep supercool. Although supercool happen sometimes with other metal-carbon fixed points as well, for the WC-C it could be a real problem. Fig.3 demonstrates a typical measurement records showing that all four realized melts were followed by deep supercools, and one of them lasted for 40 minutes. Moreover, one day we were able to measure only three melts during five and half working hours because of three deep supercools lasted for 40 minutes, 1 hour and even 2 hours respectively. The paper will discuss possible ways to avoid this problem.

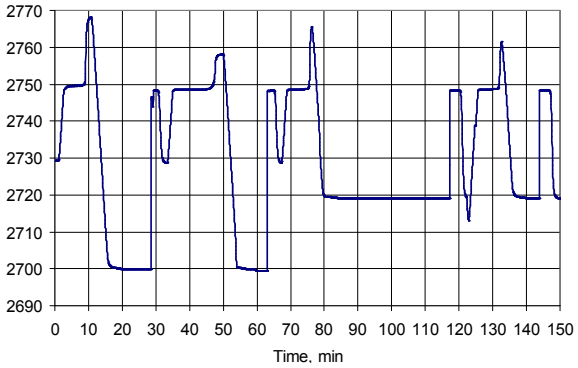

Figure 3. WC-C curves with deep supercools

MELTING TEMPERATURE MEASUREMENT

The WC-C melting temperature was measured by means of comparison with a Cu fixed-point blackbody using a radiation thermometer with known relative spectral responsivity.

The Cu point cell used was made using 5N purity copper. The geometry of the Cu cell and WC-C cell was almost the same including sizes of the radiating cavities, therefore there was no need to apply a correction for emissivities. The Cu blackbody and WC-C furnace stood next to each other with the same distance between the cells and the thermometer. Both cells were measured during the same day, and alignment and focusing of the thermometer were not changed when it moved from cell to cell. Thus, the corrections for thermometer drift and refocusing were not needed.

The WC-C melting temperature measured was 3020.8 K with uncertainty of 1.1 K (k=2). The main uncertainty components were associated with spectral responsivity, realisation of Cu point and size-pf-source effect of the thermometer.

REFERENCES

1.Y. Yamada, Y. Wang, N. Sasajima, Metal carbide-carbon peritectic systems as high-temperature fixed points in thermometry, Metrologia 43, L23,2006.

2. N. Sasajima and Y. Yamada, Investigation of TiC–C Eutectic and WC–C Peritectic High-Temperature Fixed Points, Int J Thermophys, 29, 944–957, 2008

Measurement of divergence for large beam diameter lasers

Ian C.M. Littler

National Measurement Institute, Sydney, Australia
Corresponding e-mail address: ian.littler@measurement.gov.au

Determining the divergence of long range targeting lasers is complicated by the size of the beam and the low beam divergence encountered. We describe a method which provides fast and accurate measurement of large laser beam diameters to yield the beam divergence. Pixel level resolution and accuracy is achieved.

INTRODUCTION

The measurement of the divergence of targeting lasers requires the measurement of relatively large beams, i.e. 10 mm to 100 mm in diameter over a displacement covering some 60 metres from the laser. These beam diameters are too large for most commercially available beam profilers. In addition, either the profiler or laser must be placed on a moveable trolley, raising issues of supplying remote power to either of the systems.

In order to measure such beam diameters, several approaches have been used, each with its advantages and disadvantages [1]. We required a method which would be sufficiently accurate and transportable but also fast whilst satisfying the requirements of a quality management system and providing operator safety.

The scanning of a pinhole or slit across the beam provides accurate measurement, but the measurement is not instantaneous therefore taking quite some time to complete. If the laser is placed on the trolley power must be supplied, laser safety is degraded and subtle beam angle changes as the trolley is relocated lead to misalignment at the scanning system. Mounting the scanning system on the trolley presents issues of power supply and data connectivity.

Since the beams are too large for directly shining onto a CCD array, an imaging system is required. There are two approaches; reflection or transmission, both of which require scattering from a diffuser. In the transmission system, the camera is mounted directly behind a translucent scattering surface. The issue here is finding a suitably thin and translucent scattering material which can also dissipate heat in the case of high power lasers.

We have chosen to operate in a reflective mode since uniform scattering surfaces can be made with little depth penetration and good heat conduction.

While perhaps not as accurate as scanning systems, with care such systems can provide sufficient accuracy with careful attention to the following issues.

1) Skew and perspective correction
2) Lens distortion
3) Speckle

METHODOLOGY

The camera, screen and laser are arranged in the geometry depicted in Fig. 1. The scattering surface is a steel sheet over-coated with an ultra-flat paint.

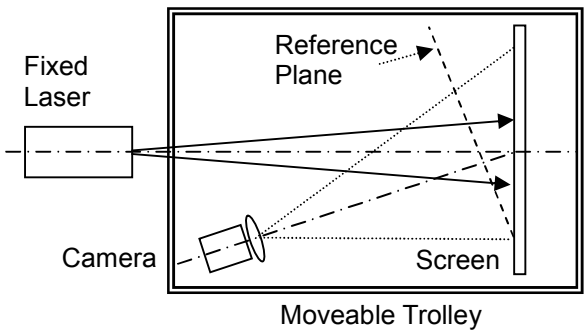

Figure 34. Schematic of the experimental set-up

Since the camera views the screen at an angle, the image on the screen is compressed or skewed in the horizontal direction. Also since points on the far edge of the screen are further away from the camera than the near edge, that part of the image appears smaller due to perspective. Therefore, geometric corrections are required.

Skew can be corrected relatively easily by scaling the pixels in the horizontal by the secant of the angle of the camera axis to the screen normal.

To correct perspective, a reference plane is chosen onto which the image is to be normalised. The plane chosen is perpendicular to the camera axis intersecting the nearest side of the screen in the field of view as in Fig. 1. Then the distances to planes intersecting the screen and parallel to the reference plane are computed, and these used to calculate the magnification factor required by which to expand the pixels intersecting each plane.

The image field is calibrated using a fiducial to scale pixel number into position and to test the efficacy of the transformation.

Other distortions, such as barrelling, occur only at the corners of the field. It is not necessary to correct for these, since they are well beyond the beam limits.

Speckle occurs when spatially coherent light reflected from an irregular surface interferes at the image plane. The spatial frequency cut-off of the speckle depends on the aperture size. Therefore, it is important to regulate the light reaching the image plane by using appropriate filters and exposure time rather than reducing the lens iris diameter.

RESULTS

The efficacy of the skew and perspective correction can be seen in Fig. 2. Here, the deviation from true field for the horizontal axis, as measured with a fiducial, is shown for the uncorrected field (dashed) and the corrected field (solid). The noise observed in the measurement is due to the discrete nature of the pixels.

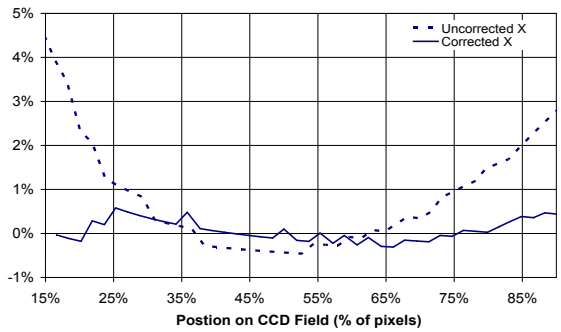

Figure 2. Comparison: corrected vs. uncorrected field

For validation, a series of uniformly backlit apertures of known diameter were imaged, corrected and measured using an algorithm to determine the diameter of the smallest circle containing 63% of the power. The results are compared with the calculated values from the known aperture diameters in Table 1.

Table 10. Measured diameters of known apertures

Diameter Calculated 63% (mm)	Diameter Measured 63% (mm)	Error (mm)	Error (pixels)
23.84	24.12	0.14	2.1
15.92	16.14	0.11	0.9
11.98	12.14	0.08	0.6
5.60	5.62	0.01	0.2

Thus pixel level resolution and accuracy is achieved for measurement of the diameter of these known disks. Scatter from the aperture edge may cause the slight over estimate.

To perform a measurement, the radius containing 63% of the power is plotted as a function of displacement from the laser. Typically, the far-field divergence is reached after 15 m. The points more distant than this point are used to compute the steady state divergence angle from the slope by a linear least squares fit to the data. The divergence angle is defined as

$$\theta = 2 \cdot \arctan(slope), \qquad (1)$$

where the slope is the change in radius with displacement. The standard uncertainty in the slope is computed using standard statistical techniques and gives a measure of the scatter of the shot-to-shot variation in the laser divergence. Typical uncertainties (95% confidence interval) are ± 5% (for divergences of hundreds of μrad) with the coverage factor k = 2.4.

However, beyond the accuracy and efficacy of the technique, the data can be recorded rapidly for end-to-end processing within one computer program.

CONCLUSION

A method for measuring the divergence angle for large diameter beams has been presented. It yields pixel level resolution and sufficient angular accuracy for measurement of low divergent laser beams. Most importantly, the method is time-effective.

REFERENCES

1. R. M. Herman, John Pardo, and T. A. Wiggins, Diffraction and focusing of Gaussian beams, Appl. Opt. 24, 1346-1354, 1985.

LED-based tunable monochromatic uniform source for calibration of imaging sensors and cameras

Khaled Mahmoud Abd-Elfattah[1,3], Seongchong Park[2], Seung-Nam Park[1,2], and Dong-Hoon Lee[1,2]

[1]*Science of Measurement, University of Science and Technology (UST), Daejeon, Rep. Korea*
[2]*Division of Physical Metrology, Korea Research Institute of Standards and Science (KRISS), Daejeon, Rep. Korea*
[3]*National Institute of Standards (NIS), Geza, Egypt*
Corresponding e-mail address: dh.lee@kriss.re.kr

We are developing a tunable uniform source consisting of changeable LEDs, single-grating monochromator, and an integrating sphere. The target application is the spectral responsivity calibration of imaging sensors and cameras. Irradiance level between 1 nW/cm^2 and 100 nW/cm^2 at a bandwidth of < 5 nm (FWHM) is achieved in a wavelength range from 380 nm to 950 nm at a distance of 1 cm from the output port of the integrating sphere. A compact and cost-effective setup with high spectral purity, high temporal stability, and easy modulation possibility can be counted as the important advantages.

MOTIVATION

To calibrate two-dimensional imaging sensors and imaging systems such as cameras, one needs a uniform source with calibrated irradiance or radiance [1]. The spectral responsivity measurement of imaging sensors and cameras, in particular, requires a monochromatic uniform source tunable in a wide wavelength range.

A combination of an incandescent lamp and a monochromator as a tunable spectral filter is the conventional choice for realizing a tunable monochromatic uniform source. Low spectral purity due to out-of-band stray of the monochromator and low spectral radiance level are the general shortcomings of such sources. A more sophisticated uniform source based on tunable lasers is also demonstrated [2], but this usually requires a large and expensive facility to cover the whole visible spectral range.

Light-emitting diodes (LEDs) are now available at different wavelengths covering a wide wavelength range. Advantages such as high efficiency, high spectral power, high stability, and excellent modulation characteristics by using LEDs for a tunable quasi-monochromatic source are demonstrated [3]. However, the relatively large spectral bandwidth ranging from 20 nm to 50 nm limits its applicability.

In this work, we propose to develop a LED-based tunable uniform source with a spectral bandwidth smaller than 5 nm in the spectral range from 380 nm to 950 nm, which is of importance for Si-based imaging sensors. To overcome the large spectral bandwidth of LEDs, we used a compact single-grating monochromator as a tunable spectral filter between LEDs and an integrating sphere. The experimental setup and the preliminary results of its characterization are described in this paper.

EXPERIMENTAL SETUP AND RESUTS

Figure 1 schematically shows the experimental setup of the LED-based tunable monochromatic uniform

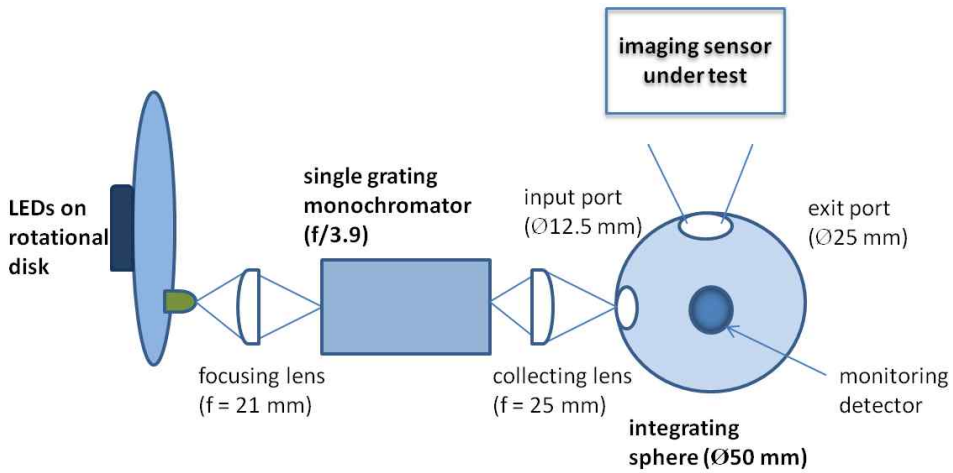

Figure 35. Schematic setup of the LED-based tunable monochromator uniform source.

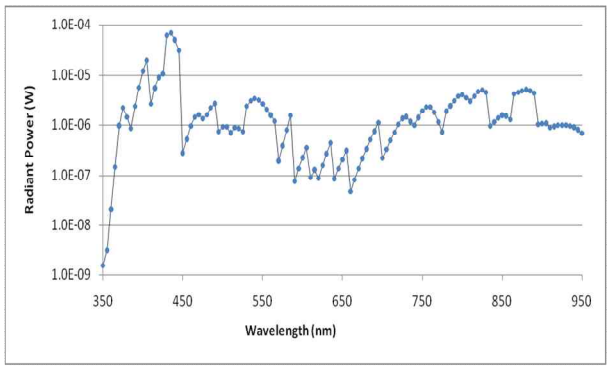

Figure 36. Radiant power output from the monochromator as a function of set wavelength (log-scale). The dots indicate the measurement values at a wavelength interval of 5 nm. The connecting line is only for better visibility.

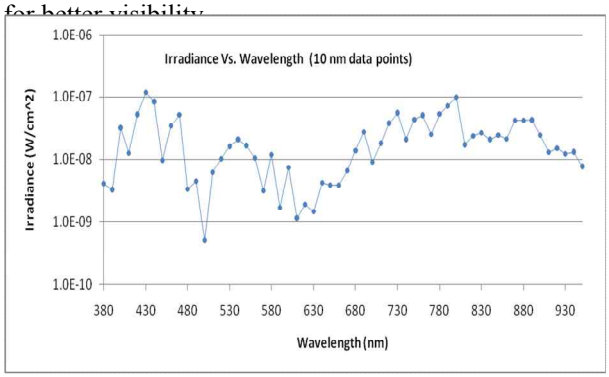

Figure 38. Irradiance output from the integrating sphere as a function of wavelength (log scale), measured at a distance of 1 cm from the output port by using a spectroradiometer. The dots indicate the measurement values at a wavelength interval of 10 nm. The connecting line is only for better visibility.

source. It consists of LEDs mounted on a rotational disk, a single-grating monochromator (CM110, Spectral Products, f = 110 mm, slit width 0.6 mm), and a PTFE coated integrating sphere with an inner diameter of 50 mm. We used 23 LEDs of different wavelengths to cover the wavelength range from 350 nm to 950 nm. The emitted radiation of one selected LED is coupled into the monochromator with a focusing lens. A computer controls the LED driving circuit, rotational disk position, and the set wavelength of the monochromator so that the selection of a LED is correlated with the set wavelength of the monochromator to provide the maximum available radiant power at the set wavelength.

Figure 2 shows the radiant output power measured at the output slit of the monochromator. In a wavelength range from 380 nm to 950 nm, radiant power of more than 100 nW is available at a wavelength interval of 5 nm without interruption. By using spectral discharge lamps, the wavelength scale

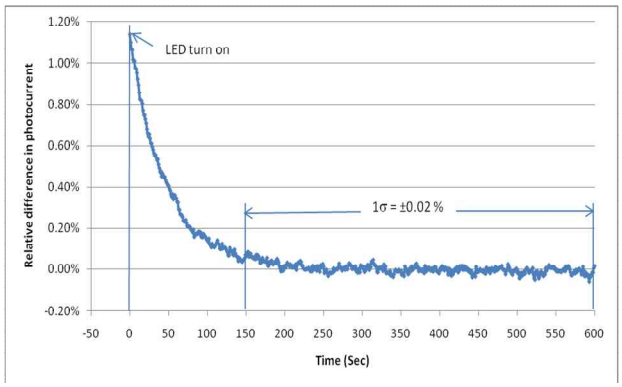

Figure 37. Temporal characteristics of the LED-based monochromatic source measured at 550 nm with an integration time of 10 ms and a sampling interval of 1 s.

is calibrated within ±0.2 nm, and the spectral bandwidth at each wavelength is measured to be less than 5 nm (FWHM) in the whole wavelength range shown in Fig. 2.

The monochromatic radiation from the monochromator is coupled into the integrating sphere to make a uniform spatial distribution. In order to improve the spatial uniformity, no baffle is used inside the sphere. Figure 3 shows the irradiance output measured at a distance of 1 cm from the output port of the integrating sphere. A CCD-based spectroradiometer (Instrument System, CAS 140) is used to measure the spectral irradiance and calculate the irradiance at each set wavelength. Irradiance level between 1 nW/cm^2 and 100 nW/cm^2 is available, which correspond to a radiance level of 0.52 nW/ cm^{2}sr and 52 nW/ cm^{2}sr, respectively.

Figure 4 shows the temporal stability of the source measured at 550 nm by using a photodiode with a sampling rate of 1 Hz. After turning on the LED, there exists a slow drift due to temperature change at the LED junction. After the initial drift is stabilized, we measured the stability of better than ±0.02 % as a relative standard deviation interval (1σ) for a time duration of 7.5 minutes, which indicates an excellent long-term stability of LEDs operated by a constant current.

REFERENCES

1. Alejandro Ferrero *et al.*, Low-uncertainty absolute radiometric calibration of a CCD, Metrologia, 43, S17-S21, 2006.
2. S. W. Brown, G. P. Eppeldauer, K. R. Lykke, Facility for spectral irradiance and radiance responsivity calibrations using uniform sources, Appl. Opt., 45, 8218–8237 2006.
3. Ghufron Zaid *et al.*, Differential spectral responsivity measurement of photovoltaic detectors with a light-emitting-diodebased integrating sphere source, Appl. Opt., 49, 6772-6783, 2010.

Interpolation functions for spectral irradiance standards

V. B. Khromchenko[1], C. E. Gibson[2], H. W. Yoon[2]

[1]*Space Dynamics Laboratory, North Logan, UT, USA,* [2] *NIST, Gaithersburg, MD, USA*

Corresponding e-mail address: vladimir.khromchenko@nist.gov

The different methods for the interpolation of FEL spectral irradiance standards are compared, both with each other and against spectral measurements using a tungsten strip lamp and a blackbody. The advantages and the disadvantages of the different interpolation methods are discussed. These comparisons are performed in a spectral region from 250 nm to 2400 nm. We find that to obtain the interpolations with the lowest uncertainties, spectral irradiances determined using one of the polynomial fitting method and the least-square fitting method should be compared.

INTRODUCTION

NIST calibrates FEL lamps as sources of spectral irradiance from 250 nm to 2400 nm at 35 selected wavelengths. However, spectral irradiances are often needed at different wavelengths than those issued with the calibrations. The interpolated spectral irradiances are used to calibrate irradiance responsivities of spectrographs used for remote sensing, photometry and photovoltaics among other uses. In the past, the optimum interpolation approach for spectral irradiance standards has been extensively discussed [1].

Until now, these comparisons have only utilized modelling of NIST-calibrated spectral irradiances without other validating measurements, and thus, it was difficult to determine which interpolation scheme was optimal [2]. Here we compare the cubic-spline, the Lagrange and the 4th order polynomial-modified Planck function (NIST) interpolation schemes [3]. We further compare the interpolated values with those obtained using a calibrated tungsten-strip lamp and a blackbody with a known temperature and emissivity to provide a physical check of the interpolated values.

EXPERIMENTAL SETUP

The FEL lamp was placed at 50 cm away from a Spectralon* panel, and the spectral irradiances of the FEL lamp is determined using spectral radiance,

$$L = \frac{E(50\,\mathrm{cm})}{\pi} \cdot \rho(45/0, \lambda) \quad (1)$$

where E is the spectral irradiances of the lamp and ρ is the bidirectional reflectance factor. The 45°/0° bidirectional reflectance factors were measured in the NIST STARR facility. The measurements were performed using a custom modified Cary 14 prism-grating monochromator with Si and extended InGaAs detectors. The spectral radiances from the FEL lamp were compared with the Planckian radiances from a variable-temperature cavity blackbody with a > 0.99 emissivity and a known temperature. The spectral radiances were also compares with a NIST-calibrated tungsten-strip lamp whose spectral radiances were also interpolated.

INTERPOLATION METHODS

The spectral irradiances are interpolated using a cubic-spline with the condition that the slope is continuous, with a Lagrange interpolation which is restricted to 4 consecutive datapoint, and lastly, using the interpolation function used at NIST which is a 4th order polynomial-modified Wien approximation,

$$E_\lambda = \left(A_0 + .. + A_4 \cdot \lambda^4\right) / \lambda^5 \cdot \exp\left(A_5 + \frac{c_2}{\lambda T}\right) \quad (2)$$

where λ is the wavelength, T is the fitted temperature, c_2 is the second radiation constant, and A_0 to A_5 are fitted parameters.

COMPARISON OF INTERPOLATIONS

A purely mathematical-based fitting such as the cubic spline or the Lagrange interpolation forces the interpolation function to exactly match the value at the datapoint. Although these polynomial interpolations can be easily implemented, such fittings cannot provide additional information on the uncertainties of the original datapoints or the quality of the fit.

In Fig. 1, the residuals of the fits using Eq. 2 with spectral irradiances published in the NIST Special Publication (SP250-20) are shown. The

large deviations in the fit are due to the erroneous value at 555 nm in the publication. When the value is adjusted to be in closer agreement with the other fitted values using Eq. 2, the residuals are smaller overall. Such analysis would not be possible with either the cubic spline or the Lagrange interpolations.

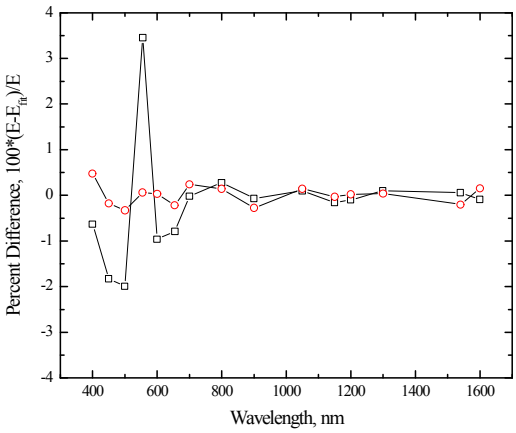

Figure 39. Comparison of the residuals of the fit using Eq. 2 with and without the erroneous value at 555 nm. The erroneous value results in wide deviations of the residuals.

VALIDATION OF INTERPOLATIONS

The interpolated spectral irradiances can only be validated by a separately calibrated source which should preferably exhibit a spectrally smooth continuum. For these studies, in the visible wavelength a calibrated tungsten-ribbon filament lamp was used, and in the near infrared spectral region a variable-temperature blackbody was used as continuous spectral sources.

Fig. 2 shows the plots of the discrete spectral irradiances of the FEL with the interpolated values and those determined using the blackbody in the spectral region between 800 nm to 2400 nm. The FEL spectral irradiances are found to be spectrally smooth with deviations of < 1 % from those spectral irradiances determined from the blackbody. Although the envelope of the FEL lamp is constructed from quartz, there is no evidence of any OH absorption features near 2200 nm.

The only substantial deviations are seen at the atmospheric absorption features since the monochromator used for these measurements was not purged for these measurements.

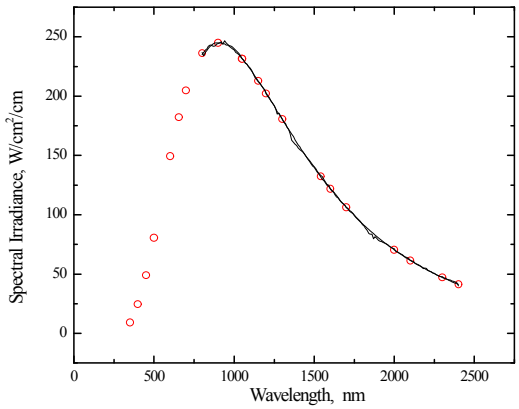

Figure 2. Comparison of the interpolated spectral irradiances with those determined using the spectral radiances from the blackbody.

The interpolations in the ultraviolet to the near-infrared are compared to a separately calibrated tungsten-strip lamp whose spectral radiances are also interpolated to 1 nm.

*Certain commercial equipment, instruments, or materials are identified in this paper to foster understanding. Such identification does not imply recommendation or endorsement by the National Institute of Standards and Technology, nor does it imply that the material or equipment are necessarily the best available for the purpose.

REFERENCES

1. L.K. Huang, R. P. Cebulla and E. Hilsenrath, New Procedure for interpolating NIST FEL lamp irradiances, Metrologia 35, 381-386 (1998).
2. J. Gardner, Uncertainty Propagation for NIST Visible Spectral Standards, J. Res. Natl. Inst. Stand. Technol. 109, 305-318 (2004).
3. NBS Special Publication 250-20 Spectral Irradiance Calibrations

Infrared hemispherical reflectance of carbon nanotube mats and arrays in the 5 μm to 50 μm wavelength region

C. J. Chunnilall[1], J. H. Lehman[2] and E. Theocharous[1]

[1]*National Physical Laboratory, Teddington, TW11 0LW, UK*
[2]*National Institute of Standards and Technology, Boulder, Colorado 80305, USA*
Corresponding e-mail address: lehman@boulder.nist.gov

We present the absolute infrared (5 μm to 50 μm) reflectance of films produced from commercially available carbon nanotubes. Data were obtained using the upgraded NPL directional-hemispherical reflectance measurement facility. A brief description of this facility is presented, along with the results of the measurement of the test samples. One group of samples consisted of mats of carbon nanotubes with potassium silicate binder sprayed on copper or silicon substrates. Another group consisted of vertically aligned carbon nanotubes grown on silicon. The emphasis of our study is the evaluation of materials suitable for radiometric applications such as thermal detectors, baffles and broadband absorbers in the infrared.

INTRODUCTION

Carbon nanotube coatings have been reported in the literature as having very low reflectance throughout the optical and infrared spectrum. For applications that require high absorptance such as coatings for thermal detectors, light baffles and optical instruments, carbon nanotubes are an attractive technology. Carbon nanotubes are produced in very large quantities for industrial use in products such as plastics and paints and are no longer a laboratory curiosity. Therefore, we have undertaken the investigation of the optical properties of carbon nanotubes that are commercially produced and readily available.

DIRECTIONAL-HEMISPHERICAL MEASUREMENTS

The infrared directional-hemispherical reflectance facility at NPL was used to quantify the directional-hemispherical reflectance of the samples [1]. The facility is based on the absolute directional-hemispherical reflectance measurement facility developed by F. J. J. Clarke [2], but includes significant improvements, the most important being the use of an FT spectrometer instead of a grating spectrometer to generate spectrally resolved data. Other improvements include the adoption of improved alignment procedures using visible radiation, the use of aspheric reflective optics to minimize aberrations, better definition of the dark measurement, and minimizing the effects generated due to heating of the test samples by the illuminating radiation. The new facility is able to cover the 2.5 μm to 50 μm wavelength region, and uses all-reflective imaging and beam steering optics. The only non-reflective optics are the FT spectrometer beamsplitter and the windows which seal the hygroscopic deuterated l-ananine triglycine sulfate (DLATGS) pyroelectric detectors. For the present work, witness samples having an area of 25 mm x 25 mm or larger were evaluated.

RANDOM MATS OF TUBES

Two types of mats were prepared. One was based on multiwall carbon nanotubes (MWCNTs) and the other on MWCNTs surrounded by a shell of boron-doped silicon carbon nitride (BSiCN). The MWCNTs were produced commercially by Nanocyl† and are described by the manufacturer as being greater than 96 % carbon nanotube content and approximately 10 nm in diameter. In addition, this material is sold as being COOH functionalized to facilitate dispersion and mixing. The BSiCN surrounding the MWCNTs is a polymer derived ceramic similar to that described elsewhere.[3] In both instances, the mats were sprayed from solution containing 100 mg of nanotube-based material, 20 ml distilled water, 0.5 mg dodecylbenzensulfonic acid (DBS) and 0.5 ml potassium silicate solution. The distilled water, MWNCTs (or BiSiCN/MWCNTs), and DBS were sonicated with a horn sonicator for 10 minutes. The potassium silicate was then added and the complete solution was stirred for one minute.

The solution was applied by means of an airbrush with nitrogen gas propellant with a pressure of 124 kPa. The solution was sprayed on to copper or silicon (Si) substrates maintained at a temperature of 95 °C. Approximately 20 mL of solution were

†Trade names are identified only for reference purposes and does not represent or imply an endorsement by the authors.

sprayed on to the coupon, with some over-spray landing off the coupon. The coated coupon was further baked at 100 °C for 1 hour in order to drive off any remaining water and fully cure the silicate. We measured the thickness of the coating by mechanical means and find that it is approximately 20 µm. This should be considered an estimate, however, and we state this measurement without an uncertainty value.

ARRAY OF 150 µm LONG TUBES

A vertically aligned MWCNT forest was grown by FirstNano†, a division of CVD Equipment Corporation, using a water-assisted chemical vapor deposition (CVD). To facilitate CNT growth, a 20 nm aluminum buffer layer and 2 nm iron catalyst were deposited on top of a Si substrate. Thereafter, a 2.5 minute growth at 750 °C with 100 standard cubic centimetres per minute (sccm) ethylene, 195 sccm hydrogen, 1.1 standard litres per minute (slpm) argon, and 40 sccm argon were passed through a water bubbler at room temperature and injected into the reactor. This process resulted in a uniform MWCNT forest aligned perpendicular to the substrate and approximately 150 µm in height.

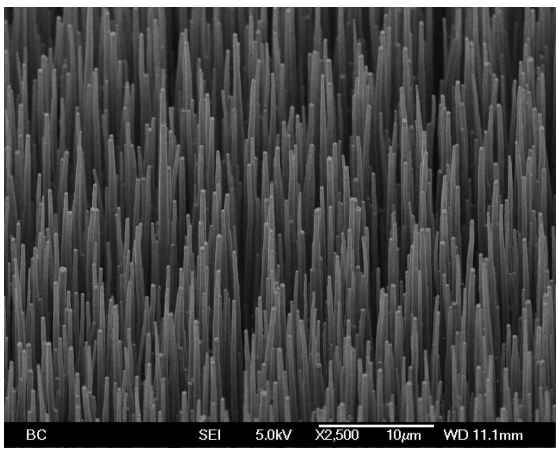

Figure 1. Scanning electron micrograph of 40 µm long vertically aligned nanotubes.

ARRAY OF 40 µm LONG TUBES

Vertically aligned MWCNTs, 40 µm long were grown by Nanolab† on Si substrates by plasma enhanced chemical vapor deposition (PECVD). The substrate was coated with a metal catalyst layer consisting of 300 nm thick chromium (purity 99.99%) and then 10~50 nm thick nickel (purity 99.99%). PECVD process is accomplished by introduction of ammonia gas at 4 kPa and heating a tungsten filament. Thereafter, acetylene gas is incorporated while powering the plasma source at 0.47 A. The carbon nanotube length, diameter and site density are verified by means of scanning electron microscopy.

RESULTS AND DISCUSSION

Fig. 2 shows the hemispherical reflectance of four of the test samples in the 5 µm to 50 µm wavelength range, measured at 15°C. The vertically aligned VA40 and VA150 samples maintain their low reflectance properties throughout this range, whereas the reflectance of the sprayed MWCNTs (nCylSi in Fig. 2) and BSiCN/MWCNT (BSiCN in Fig. 2) test samples is higher than that of the vertically aligned test samples and increases monotonically with wavelength. The peak observed in the nCylSi sample near 10 µm is not due to nanotubes nor COOH functionalization, but due to silicate [4].

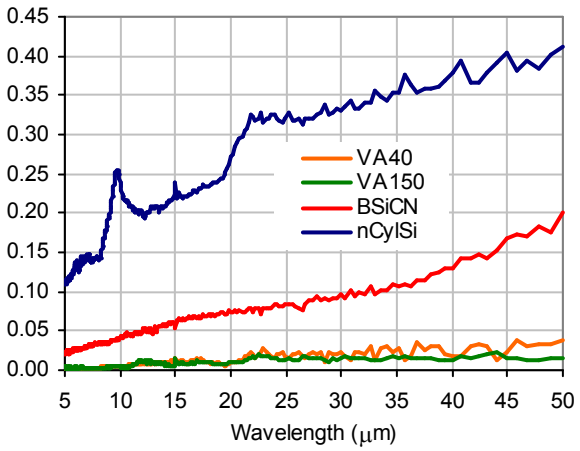

Figure 2: Hemispherical reflectance of MWCNT samples in the 5 µm to 50 µm wavelength range.

REFERENCES

1. C. J. Chunnilall & E. Theocharous, Infrared hemispherical reflectance measurements in the 2.5 µm to 50 µm wavelength range using an FT spectrometer, NEWRAD2011 abstracts.
2. F. J. J. Clarke, C. J. Chunnilall, L. J. Rogers, Recent progress at NPL in the development of mid-infrared spectrometric measurements, Proc. SPIE, 5192, 111-122, 2003.
3. J. H. Lehman, K. E. Hurst, G. Singh, E. Mansfield, J. D. Perkins, C. L. Cromer, Core–shell composite of SiCN and multiwalled carbon nanotubes from toluene dispersion, J. Mater. Sci 45, 4251–4254, 2010.
4. J. Osswald, K. Fehr, FTIR spectroscopic study on liquid silica solutions and nanoscale particle size determination, Journal of Materials Science, 41, 1335-9, 2006.

†Trade names are identified only for reference purposes and does not represent or imply an endorsement by the authors.

Color Measurement of Flexible Surface Sources and Flexible Objects

C.C. Hsiao and H.L.Yu

Center for Measurement Standards, ITRI, Hsinchu, Taiwan, R.O.C.
Corresponding e-mail address: cchsiao@itri.org.tw

Flexible displays are highly attractive for next generation electronic products. Colorfulness is one of the most important parameters to evaluate display quality. Unlike the luminance measurement of flexible products which strongly depends on the measurement conditions, color measurement results depend more on the characteristics of the material itself. This paper presents the variation of color when bending the display.

INTRODUCTION

The development trend for high-tech products is toward the capability of flexibility, since flexibility means not only thin and light, but, most importantly, break-resistant. In particular, flexible displays are highly attractive, including both the active display which has its own backlight and passive displays commonly used for electrical paper (e-paper) which need environmental lighting. As the market expects that flexible displays will become ubiquitous, it is time to start the research of measurement to support the manufactures' needs in the near future.

This paper focuses on the color measurement of curved surface sources and curved surface objects since curved is the basic shape for flexible displays. Unlike the luminance measurement of curved surface sources [1] which depends on the curvature of the surface, the viewing angle of the meter, the distance between the source and the meter, the measured position of the surface source, and how alike the source is to a Lambertian surface, the color measurement results for curved display are more dependent on the characteristics of the material itself such as the variation of stresses caused by bending the surface.

MEASUREMENT SETUP

Figure 1 shows the schematic diagram of the setup for scanning the color distributions of the curved surface source on the X-Y and ω-Y coordinates by moving the spectroradiometer with an XYZ stage and rotating the test sample with the rotating stage. The meaning of X-Y distribution is as though an observer passes through the curved surface source and watches it along the horizontal direction. The ω-Y distribution is analogous to an observer watching the source from different direction along the curve. The test sample in Figure 1 is designed by MCL/ITRI, and made with LED side lighting with a flexible light guide plate. The sample is a Lambertian-like surface with distribution index of approximately 3.5. For a Lambertian surface the index is equal to 1 [2].

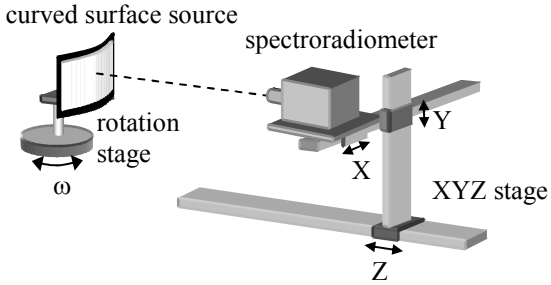

Figure 1. The setup of color measurement for flexible surface source.

Figure 2 is the d/0 geometry color measurement setup for flexible surface object. The test sample is cholesterin liquid crystal e-paper supplied by DTC/ITRI. The colors of the e-paper are light blue, blue, pink, and red. Since the sample port of the integrating sphere in Figure 2 can not be completely covered by the curved sample, to reduce the color measurement error due to light leakage from the sample port, a mat white paper with known color and with the same curvature as the sample is used as the white standard. Here it is assumed that the white paper remains the same color no matter whether its shape is plane or curved.

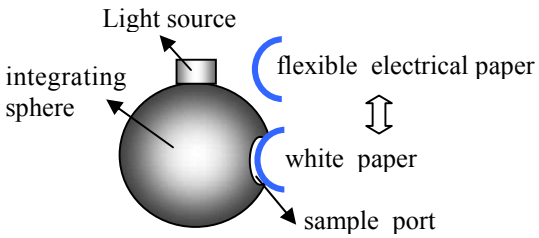

Figure 2. The setup of color measurement for flexible electrical paper.

EXPERIMENTAL RESULTS

Figure 3(a) and 3(b) are the color distributions of the curved surface source on the X-Y and ω-Y coordinates, respectively. From Figure 3, the color

distributions on the X-Y and ω-Y coordinates are quite similar. This means that, unlike the luminance measurement, the color measurement of a Lambertian-like curved surface source is less dependent on the measurement method.

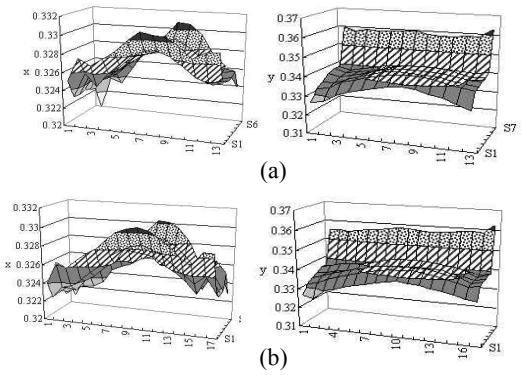

Figure 3. (a) The distribution of the chromaticity coordinate (x, y) of the curved surface source on the X-Y plane. (b) The (x, y) distribution of the curved surface source on the ω-Y plane.

Table 1 and Figure 4 show the $L^*a^*b^*$ color difference ΔE of the cholesterin liquid crystal e-paper at the central position and at the position near the edge for various curvature R. The reference color for ΔE calculation is set as the color when the e-paper is flat.

Table 11. Color difference of e-paper for different curvature and location.

Color	Location (C: center, E: edge)	ΔE (Color difference)			
		R 17 cm	R 9 cm	R 6 cm	R 5 cm
Light blue	C	1.3	3.2	8.2	9.0
	E	1.6	3.7	9.8	10.3
Pink	C	1.4	3.3	9.7	9.9
	E	1.7	3.6	10.3	12.2
Blue	C	1.1	2.5	6.8	6.8
	E	1.4	2.8	7.0	7.4
Red	C	1.1	2.6	7.3	8.3
	E	1.2	2.3	8.6	10.5

The results show that no matter whether the color of the e-paper is light blue, blue, pink, or red, the smaller the R is, the larger the ΔE is obtained. This is because the stress of the e-paper increases as the curvature of the e-paper gets smaller. The stress disturbs the position of the cholesterin liquid crystal inside the e-paper and thus causes color variation. Higher stress induces more significant color variation, therefore ΔE is larger for smaller R. Except that, at the edge of the e-paper, ΔE is higher than that at the central position since the edge sustains the highest force when the e-paper is curved.

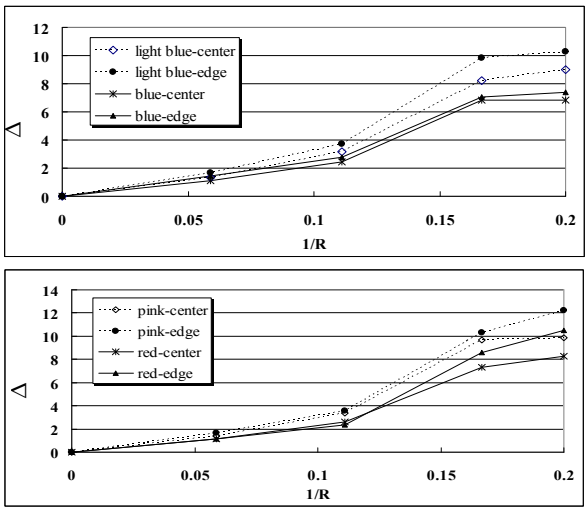

Figure 4. The $L^*a^*b^*$ color difference of the e-paper for various curvature R. The reference color is set to be the color when the e-paper is flat.

CONCLUSIONS

For a Lambertian-like curved surface source, the color distributions on the X-Y and ω-Y coordinates are similar. This means the results of color measurement for this type of surface source are less dependent on the measurement method. Theoretically, the result will become more and more reliant on the measurement method as the source gets more and more unlike a Lambertian surface. An experiment will be performed to verify this viewpoint in a future work.

Considering the color measurement for the flexible e-paper, a mat white paper with the same curvature as the test e-paper is employed as the white standard. The color difference between the flat e-paper and curved e-paper increases as the curvature decreases, except that the color difference is larger at the position near the edge of the e-paper than at the central position. The color difference is induced by the force when bending the e-paper.

As the color may change during rolling the e-paper, a standard of color measurement for flexible surface object is necessary in the future to help the manufacturers utilize the appropriate metrology.

REFERENCES

1. H.-L. Yu and Z.-Y. Chung, Luminance Measurement of Curved Surface Sources, 2011.
2. I. Moreno, M. Avendano-Alejo, R.I. Tzonchev, Designing light-emitting diode arrays for uniform near-field irradiance, Appl.Opt., 45, 2265-2272, 2006.

STARR II: Progress towards a new NIST facility for UV-SWIR gonioreflectance calibrations

Heather J. Patrick[1], Clarence J. Zarobila[1,2], and Thomas A. Germer[1]

[1]*National Institute of Standards and Technology, Gaithersburg, MD 20899 USA,* [2]*Jung Research and Development Corp., Washington, DC 20009 USA*

Corresponding e-mail address: heather.patrick@nist.gov

We report on the status of STARR II, a planned facility for angle-resolved BRDF measurements with out-of-plane capability and spectral coverage from the UV-SWIR. A tunable supercontinuum-based light source with output from 500 nm to 2500 nm will be demonstrated, and prototype beam delivery optics presented. The gonioreflectometer design and the impact of the supercontinuum source on gonioreflectance measurement capabilities will be discussed.

INTRODUCTION

The Optical Technology Division of NIST provides reference measurements of specular and diffuse reflectance of materials, including wavelength- and angle-resolved bidirectional reflectance distribution function (BRDF) measurements of diffuse scatterers that provide traceability for diffuser plaques used as onboard calibration standards in remote sensing. We are currently expanding these measurement capabilities to include increased spectral coverage into the short-wave infrared (SWIR) spectral region, out-of-plane measurement capability to replicate customer measurement geometries over a wide range of polar and azimuthal incident and scatter angles, and improved accuracy and speed of measurement. The STARR II project is being constructed to meet these needs and to eventually replace the current facility, STARR (the spectral, tri-function automated reference reflectometer).[1,2]

SYSTEM LAYOUT

Figure 1 shows the proposed system layout, including the goniometer, which is modeled on the NIST Goniometric Optical Scatter Instrument (GOSI)[3] and will allow angle-resovled BRDF measurements over nearly a full hemisphere, and the tunable supercontinuum (SC) fiber laser-based light source that we plan to use from 500 nm to 2500 nm.[4] A separate source (not shown) will be used for UV illumination down to 250 nm. The light source provides a circular illumination area of about 1 cm diameter (in the prototype) on the sample when illuminating at normal incidence. The receiver is designed both to view the full illuminated area on the sample, and to capture the full incident beam for input power measurements, so that scattered power can be directly compared to the incident power without use of a reference sample.

SUPERCONTINUUM SOURCE

Obtaining sufficient power for BRDF measurements from a tunable source can be problematic, especially in the short-wave infrared (SWIR) where detectors tend to have higher noise-equivalent power and smaller active areas than VIS-NIR detectors.[5] SC sources are attractive for their broad band, laser-like directional output but until recently did not extend to

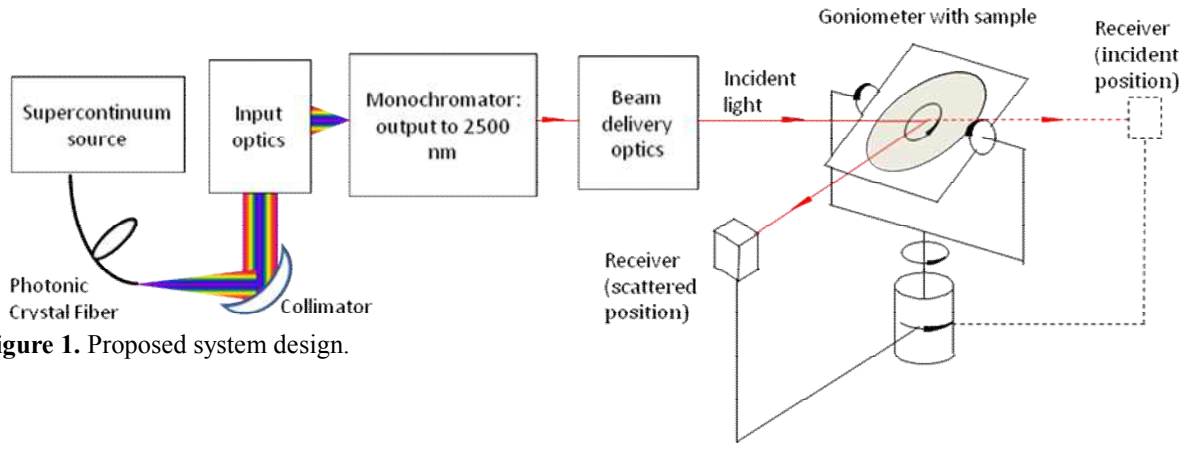

Figure 1. Proposed system design.

2500 nm. Additionally, the stock optics provided on SC sources are not optimized for use beyond 1000 nm.[4] Recently, however, we have obtained a 6 W SWIR-enhanced SC source with output to 2500 nm and bare fiber termination. Using a reflective collimator (see Fig. 1) we are able to obtain a collimated, near-Gaussian mode beam from 450 nm to 2500 nm. Figure 2 shows the spectral density of the source's fiber output, measured by inputting the light to an integrating sphere and measuring with a spectroradiometer as described in Ref. [4]. Typical power densities are in the 2-3 mW/nm range, with 0.26 mW/nm at 2500 nm. We estimate the uncertainty (1-σ) in the accuracy of the spectral density to be ± 15%.

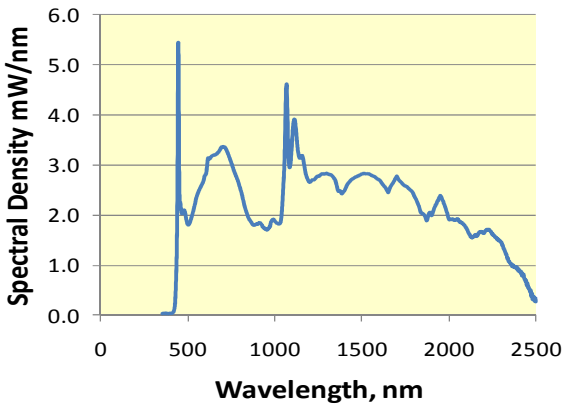

Figure 2. Spectral density from fiber output of SWIR-enhanced supercontinuum source.

WAVELENGTH SELECTION AND BEAM DELIVERY

We use a Newport 257 monochromator with 4-grating turret to filter the SC source to a tunable, quasi-monochromatic output. Because the SC source output is laser-like, light can be very efficiently coupled into the monochromator. However, care must be taken that the input optics control the divergence into the monochromator such that the monochromator optics are not overfilled.[4]

An example layout for coupling the SC source into the monochromator and delivering the beam to the sample plane is shown in Fig. 3. The input optics can be translated to optimize the input divergence, and the output wavelengths selected by the grating flood an aperture and are then projected to the sample using an off-axis parabola (OAP). Initial measurements indicate it should be possible to deliver incident powers in the 100's of μW, with a 10-15 nm bandwidth, over the SC source's spectral range. For comparison, the existing STARR uses a 100 W Quartz-Tungsten Halogen (QTH) lamp focused into a monochromator. At 1000 nm, the output power from the monochromator is about 1 μW in a 14 nm bandwidth,[6] and at 2500 nm, has been estimated at < 200 nW.

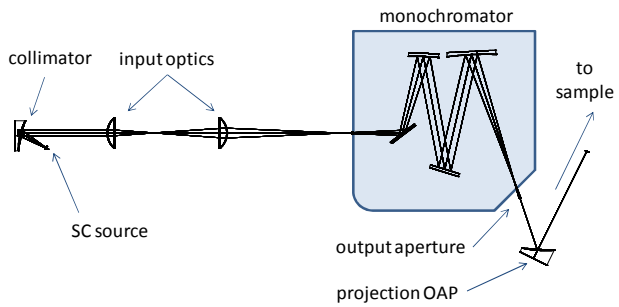

Figure 3. Layout of monochromator for wavelength selection, and beam delivery optics to sample.

SUMMARY

In this presentation, we give a detailed update on STARR II, with particular emphasis on demonstration of a supercontinuum-based light source tunable from 500 nm to 2500 nm, the prototype projection system to illuminate the sample, and the impact of the supercontinuum source on our measurement capabilities. In addition, we will discuss options for expanded coverage in the UV down to 250 nm and considerations for receiver design. Angle-resolved hemispherical BRDF measurement capability using the current, laser-based Goniometric Optical Scatter Instrument (GOSI) will be shown, and we plan to demonstrate measurements on GOSI using the supercontinuum-based source in the near future.

REFERENCES

1. http://www.nist.gov/pml/div685/grp06/starr2.cfm
2. http://www.nist.gov/pml/div685/grp03/spectrophotometry_starr.cfm
3. T.A. Germer and C.C. Asmail, Goniometric optical scatter instrument for out-of-plane ellipsometry measurements, Rev. Sci. Instr., 70, 3688-3695, 1999.
4. H.J. Patrick and C.J. Zarobila, Supercontinuum fiber laser source for reflectance calibrations in remote sensing, in Proc. SPIE 7807, 78070B, SPIE, Bellingham, WA, 2010.
5. H.W. Yoon, M.C. Dopkiss and G.P. Eppeldauer,Performance comparisons of InGaAs, extended InGaAs, and short-wave HgCdTe detectors between 1 μm and 2.5 μm, in Proc. SPIE 6297 629703, SPIE, Bellingham, WA, 2006.
6. H.W. Yoon, D.W. Allen, G.P. Eppeldauer and B.K. Tsai, The extension of the NIST BRDF scale from 1100 nm to 2500 nm, in Proc. SPIE 7452, 745204, SPIE, Bellingham, WA, 2009.

Characterization of new optical diffusers used in high irradiance UV radiometers

Bettina Barton[1], Peter Sperfeld[1], Stefan Nowy[1], Andreas Höpe[1], Sven Teichert[1], Gabriel Hopfenmüller[2], Michael Baer[3] and Thomas Kreuzberger[3]

[1]*Physikalisch-Technische Bundesanstalt (PTB), Braunschweig, Germany,*
[2]*sglux SolGel Technologies GmbH, Berlin, Germany,* [3]*SGIL Silicaglas Ilmenau GmbH, Langewiesen, Germany*
Corresponding e-mail address: bettina.barton@ptb.de

Diffusers are essential components of UV radiometers used, for example, as transfer standards. Diffusers improve the insensitivity to differing radiation situations. In combination with a beam limiting aperture, a diffuser defines the irradiated area. A detailed study of the transmittance of UV diffusers is shown.

INTRODUCTION

A suitable diffuser should meet the following requirements:
The transmittance should be spectrally flat. It should not change the spectral sensitivity of the UV radiometer in general. The transmittance should be temporally stable independent of surrounding conditions and it should not degrade through a high radiation load. The diffusers should be homogenous, i.e. the transmittance should be more or less constant over the entire surface. Finally, the influence of the angle of incident radiation should be cosine. Various test measurements were made to verify these requirements. Furthermore, combinations of several different diffusers were investigated in order to see whether the total transmittance of a diffuser package could be calculated from the transmittance of the single diffusers. Diffusers with a diameter of 25 mm and various thicknesses were examined.

STUDY OF HOMOGENEITY

Each diffuser was irradiated by a high UV irradiance level. A silicon photodiode (Hamamatsu S1227, ∅ = 3 mm) scanned the distribution of the transmitted light right behind the diffuser.
It was shown that the transmission of silica glass diffusers investigated is quite homogenous over the central spot of its area and decreases gradually to its edges. This was expected for this volume type diffuser.

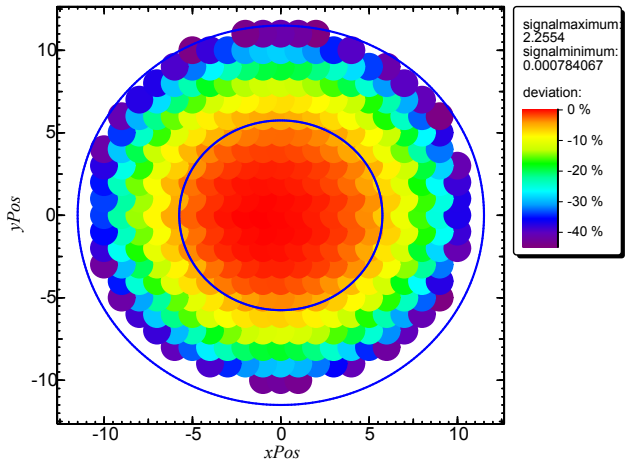

Figure 1: Homogeneity of the relative transmission measured at a distance of 3 mm behind the diffuser

STUDY OF TRANSMISSION

The direct spectral transmission of the investigated diffusers was determined with a Cary 5000 spectrophotometer (Varian) within the wavelength range from 230 nm to 800 nm. Since a diffuser scatters the incident radiation very strongly, the measurement results represent only relative values.

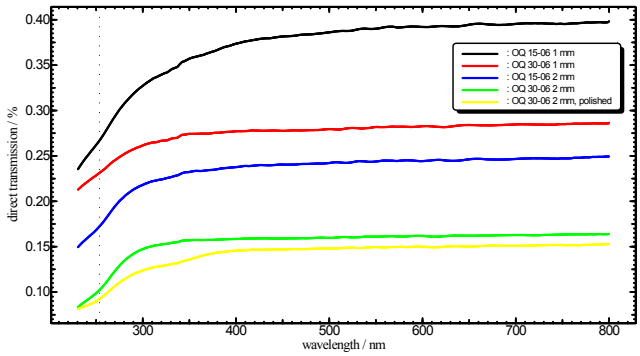

Figure 2: Direct transmission of different diffusers

Figure 2 shows the detected direct transmission of diffusers with different opacities and thicknesses. Obviously, the transmission in the visible spectral range is spectrally independent in contrast to the UV range where it strongly decreases. In the visible range all curves have the same characteristics. However, in

the UV range the decrease of the transmission depends on the thickness and the opacity of the diffusers. This characteristic has to be taken into account for the determination of the spectral responsivity of UV sensors.

COMBINATION OF SEVERAL DIFFUSERS

The relative transmission of two single diffusers is compared to the transmission of the combined diffusers.

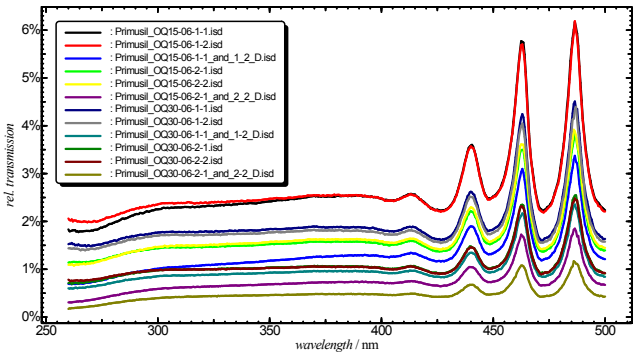

Figure 3: Relative transmission of two single diffusers in comparison with the combination of both

The combination of two silica glass diffusers has the same spectral behaviour regarding the relative transmission as the single diffusers. Because of reflections at the multiple surfaces the relative transmission of the combined diffusers is smaller than that one of the singles.

STUDY OF UV RESISTANCE

Different diffusers were irradiated in the radiation field of a 2 kW medium pressure Hg lamp at a 20 cm distance to the source. Their transmittance was measured before, as well as directly after a 14-hour irradiation, after a three-day rest interval and after a following 15-hour irradiation. All diffusers showed a degradation of transmission in the spectral range below 450 nm. The strongest degradation was observed for the polished diffuser Primusil OQ 30/6 with a thickness of 2 mm. At 254 nm the transmission increases by an amount of about 4 %. Other diffusers showed uneven characteristics. In general, after the first irradiation, no considerable change of transmission was detected.

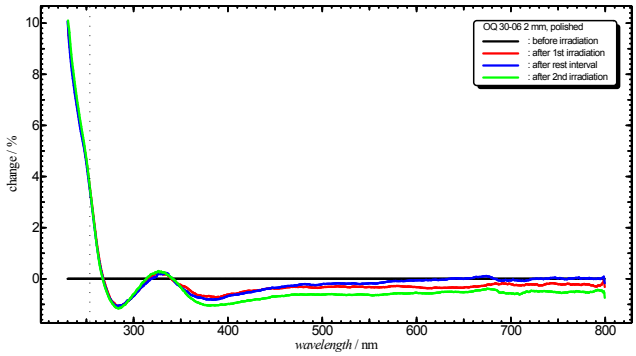

Figure 4: Change of a polished Primusil OQ 30/6 2 mm diffuser after UV irradiation

REFERENCES

1. Technische Regel Arbeitsblatt W 294-3 June 2006, UV-Geräte zur Desinfektion in der Wasserversorgung; Teil 3: Messfenster und Sensoren zur radiometrischen Überwachung von UV-Desinfektionsgeräten; Anforderungen, Prüfung und Kalibrierung
2. D. R. Gibbs, F. J. Duncan, R. P. Lambe and T. M. Goodman, Ageing of materials under intense ultraviolet radiation, Metrologia, 32, 601-607, 1995
3. S. Nevas, P. Sperfeld, C. Reichold, A. Heinrich, B. Seiferling, K. Haberstroh, and R. Gruler, New transfer standards for high UV-irradiances – investigation of Xe-Hg lamps, NEWRAD 2008

Temporal and temperature dependence of transmittance standards

Annette Koo[1] and John Hamlin[1]

[1]*Measurement Standards Laboratory, Lower Hutt, New Zealand*
Corresponding e-mail address: a.koo@irl.cri.nz

The temperature and temporal dependences of the transmittance of transmittance standards have been characterised. Both effects are shown to contribute significantly to the uncertainty associated with standards of this type. Relative data showing the changes in transmittance with time and temperature are reported.

INTRODUCTION

In preparation for the comparison of spectral regular transmittance (CCPR-K6.2010), sets of filters were manufactured at MSL with nominal transmittances of 90% (BK7), 50% (NG11), 10% (NG5), 1% (NG4) and 0.1% (NG3) [1].

To determine the stability of the filters, four sets were chosen and monitored for several months. Strong temperature and temporal dependences were observed in the glasses. Measurements were made on the MSL Reference Spectrophotometer [2]. The source is a 17 mm diameter, collimated, monochromatic and 1 nm bandwidth beam.

RESULTS

The transmittance of the filters was shown to be independent of the effects of rotation, translation by 2 mm, tilt of the filter with respect to the beam of up to 1° and polarization of the beam.

Initial measurements were carried out on the W set of filters at each of the wavelengths required for the comparison (380 nm, 400 nm, 500 nm, 600 nm, 700 nm, 800 nm, 900 nm and 1000 nm). Strong temperature dependence in the transmittance values obtained for several of the filters was noted and so several measurements over the range 20 °C to 23 °C were carried out. Repeating the measurement a few weeks later also showed that there were significant shifts in the transmittance with time. To confirm the results, similar tests were carried out on three additional sets, designated as X, Y and Z. The same temperature dependences and drift characteristics were found in the filters of these sets. In particular it was found that the BK7 had no temperature or time dependence while the remaining filters had significant temperature dependence. The temperature coefficients are shown in figure 1.

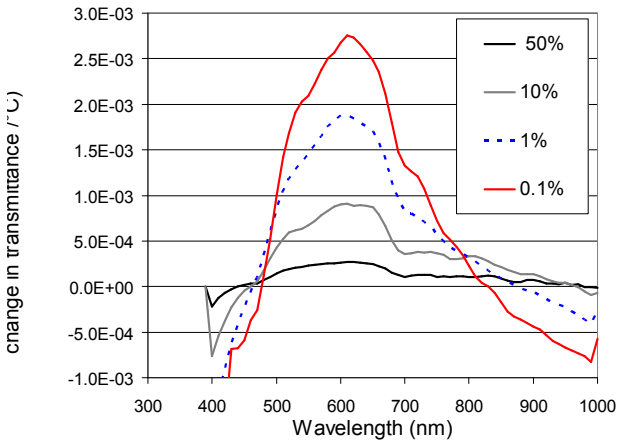

Figure 40. Change in transmittance of NG filters with temperature.

The temperature coefficients reported here are consistent with a previous study of NG4 over the visible range [3] and NG9 at 1064 nm [4]. In the latter study the temperature coefficient was shown to correlate with thickness of the filter, showing that the effect was not a surface effect but rather a bulk effect. Supporting this conclusion is the fact that the temperature coefficients in figure 1 grow stronger as the optical density of the glass increases; i.e. as the density of absorbing centres in the bulk of the glass increases. In many cases, the temperature coefficient is large enough that, given the temperature uncertainty in a typical laboratory (0.5 °C), the influence of temperature may become the dominant component of an uncertainty budget.

The absorbing centres in Schott NG glasses are reported to be Fe^{3+} in the blue region of the spectrum, Co^{2+} dominating the green-red region and Fe^{3+} ions absorbing in the near infrared [5, 6, 7]. It is generally understood that absorption bands shift to longer wavelengths with temperature [8]. The simple transformation, red-shifting absorption bands with temperature, is not sufficient to explain the temperature coefficients we have observed. It is likely that some other temperature induced changes

in the environment of the colouring ions are occurring. Some possibilities include shifting of the redox equilibrium between Fe^{2+} and Fe^{3+}, the movement of ions from tetrahedral to octahedral environments or vice versa, increasing polarizability of the ions as thermal expansion occurs, and decrease of the ligand field strength as thermal expansion occurs.

Similar processes occurring irreversibly over time, or surface modification due to oxidation or adsorption of water and organic matter may be responsible for the temporal changes that have been observed in filter transmittance. The relative change in transmittance over a 4-month period is shown for the coloured glasses in figure 2.

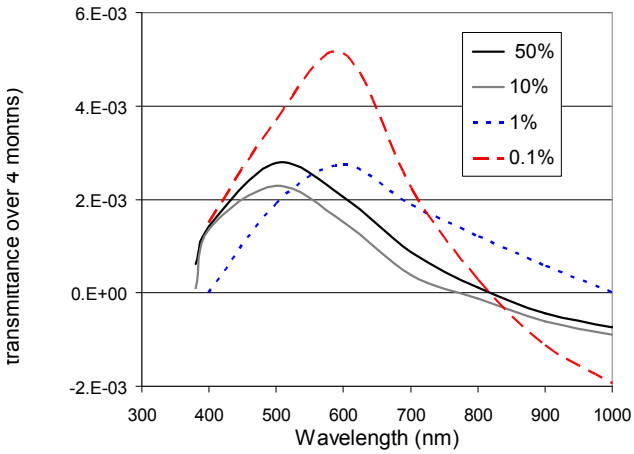

Figure 2. Change in transmittance of NG filters with time.

Previous studies have been made of the stability of NG glasses. NG5 glass has been shown to exhibit a relative change in transmittance of ~2e-4 over a 35 year period across the visible range of the spectrum [9]. The relative change between repeat measurements made by NIST during intercomparisons of regular transmittance, usually with several months elapsed between measurements, contributed a significant fraction of the overall uncertainty [10,11] associated with the comparisons and are of the same order as those in figure 2.

Similarly, the previous CCPR-K6 comparison encountered strong drift in the transmittance values of the artefacts as measured by the pilot laboratory before and after other participants' measurements [12]. The large changes observed in the BK7 filters (~ 2e-4) cannot be explained by the results obtained here. The four NG filters follow the same wavelength trend, having positive drift with time at wavelengths below 700 nm and generally negative drift with time at longer wavelengths. The spread of changes is broad in the filters used in the previous comparison, and in some cases may be accounted for by either the types of drift we observe with time here, or simply temperature variations (within the range of 22.5 ± 0.6 C reported) between the two measurements made.

CONCLUSION

The neutral density glasses used as transmittance standards exhibit temperature and temporal instability. Understanding and control of both effects is necessary in order to attain the levels of uncertainty often associated with values assigned to transmittance standards. Investigations into the origins of instability are being carried out.

REFERENCES

1. CCPR-K6.2010 *Key Comparison Technical Protocol*, available at http://kcdb.bipm.org/appendixB/AppBResults/CCPR -K6.2010/CCPR-K6.2010_Technical_Protocol_Dec-10.pdf
2. A Koo and J Hamlin *Maintenance and development of the MSL reference spectrophotometer* IRL Report 2469, 2010
3. Z M Zhang T R Gentile A L Migdall and R U Datla Transmittance measurements for filters of optical density between one and ten *Appl. Opt.* B 8889-95, 1997
4. R Mavrodineau and J R Baldwin Glass filters as a standard reference material for spectrophotometry *NBS Special Publication 260-51* (Washington: US Government Publishing Office), 1975
5. U Kolberg Coloured Glasses *The properties of optical glass* ed H Bach and N Neuroth (Heidelberg: Springer-Verlag), 1995
6. T Bates Ligand field theory and absorption spectra of transition–metal ions in glasses *Modern aspects of the vitreous state vol 2* ed J D MacKenzie (London: Butterworths), 1960
7. C R Bamford *Colour generation and control in glass (Glass science and technology 2)* (Amsterdam: Elsevier), 1977
8. W A Weyl and E C Marboe The constitution of glasses, a dynamic interpretation vol II, part 2 (New York: Interscience), 1967
9. J Bastie and B Mercier Stability of coloured glass filters over a period of about 35 years *Proc of the CIE Meeting Venezia* 203, 1987
10. K L Eckerle E Sutter G H C Freeman G Andor and L Fillinger International intercomparison of regular transmittance scales *Metrologia* **27** 33-38, 1990
11. K L Eckerle J Bastie J Zwinkels V Sapritsky and A Ulyanov Comparison of regular transmittance scales of four national standardizing laboratories *Col. Res. Appl.* **18** 35-40, 1993
12. G Obein and J Bastie *Report on the CCPR Key Comparison K6* (Paris: BIPM), 2008

Infrared hemispherical reflectance measurements in the 2.5 μm to 50 μm wavelength region using an FT spectrometer

C. J. Chunnilall and E. Theocharous

National Physical Laboratory, Teddington, TW11 0LW, UK

Corresponding e-mail address: christopher.chunnilall@npl.co.uk

The NPL hemispherical-directional reflectance facility has recently been upgraded, the most significant change being the replacement of the grating spectrophotometer with a Fourier transform spectrometer. Other improvements include better alignment (using visible radiation), the use of an intermediate field stop, minimisation of the effects of heating of the test sample, and correcting for instrumental and relay optics drift by using a blackbody. Measurements obtained with the new facility are presented and discussed.

The NPL spectral absolute hemispherical-directional mid-infrared (MIR) reflectance measurement facility is comprised of the absolute hemispherical reflectometer (AHR), relay optics, and a Fourier transform spectrometer (FTS). The AHR is based on a specially modified electroplated copper hemisphere mirror which collects the output of a cylindrical Oppermann source and illuminates the test sample with a uniform hemisphere of -radiation, and is a development of the earlier relative hemispherical reflectometer which derived its traceability from measurements of a reference mirror and a near-Lambertian scatterer. The hemispherical mirror has one small aperture which is only slightly larger than the cross section of the beam passing through it. By rotating and sliding the hemisphere to reproducible positions, the hemispherical mirror radiance and reflected sample radiance can be measured. The radiance directly from the source is also measured with and without the sample present to take into account inter-reflections between the source and the test sample [1].

Until recently, the output of the hemisphere was spectrally analysed using a Perkin-Elmer 580B IR grating spectrophotometer which used four different gratings to cover the wavelength range from 2.5 μm to 56 μm (4000 cm^{-1} to 180 cm^{-1}). The output of the modified hemisphere is now spectrally analysed using a Bruker Equinox 55 FTS, which has a much better signal-to-noise performance than the grating spectrometer. KBr (2.5 μm - 22 μm) and multilayer Mylar (16 μm – 50 μm) beamsplitters enable the wavelength range from 2.5 μm to 50 μm (4000 cm^{-1} to 200 cm^{-1}) to be covered. A gold-black-coated deuterated L-alanine triglycine sulphate (DLATGS) pyroelectric detector with a KBr window is used with the KBr bemsplitter, and a similar detector, but with a polythene window, is used with the Mylar beamplitter.

Figure 1 shows the layout of the upgraded facility. Radiation leaving the hemisphere is collimated using an Off Axis Parabolic (OAP) mirror. A second OAP mirror re-images the collimated beam on a 1.8 mm diameter pinhole which is in good thermal contact with a metal block to increase its heat capacity. Radiation passing though the pinhole enters the FTS where it is analysed. The intermediate aperture between the two OAP mirrors ensures that the collected radiation is not vignetted by the aperture on the reflecting hemisphere.

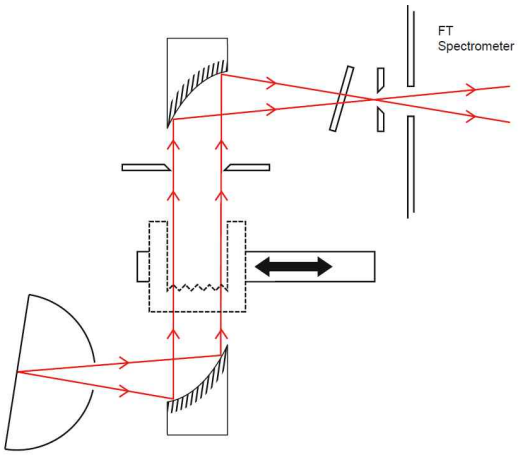

Figure 1. Layout of the FT spectrometer-based IR hemispherical-directional reflectance facility.

The standard alignment of the spectrometer aligns a beam from an internal source through the interferometer optics, brings it to a focus in the internal sample compartment, and then refocuses it onto the detector(s). Once this has been carried out, visible radiation is used to illuminate an aperture placed at the focus in the sample compartment,

which then forms a focus at the emission port of the spectrometer (a mirror is used to switch from the internal source to the emission port, and a 'dummy' quartz beamsplitter is used which will transmit visible radiation). The visible radiation is then used to align the relay optics and the AHR (in all of its required orientations). The source is removed from the sample compartment, the 'dummy' beamsplitter is replaced by the appropriate beamsplitter, and the AHR and its relay optics are properly aligned.

One potentially serious disadvantage of using the unfiltered output of the Oppermann source to illuminate the test sample is the very high irradiance which reaches the sample. This is a particular problem in absorptive samples because the temperature of the sample can be raised and the contribution due the thermal radiation emitted by the sample itself can become a significant problem for wavelengths longer than 20 μm. Although the test samples are mounted on a copper block whose temperature is controlled by flowing water, the thermal conductance of the sample substrate will be critical. Copper substrates are preferred, whenever possible, for measuring the reflectance of absorptive coatings such as black paints. The effect of the thermal emission of the test sample was studied by making measurements with the Oppermann source at different temperatures. For black samples, the reflectance exhibits a small decrease for long wavelengths as the source temperature is decreased and asymptotically reaches a minimum level which is taken as the reflectance value without any contributions from thermal emission from the sample. This requires the source to operate at relatively low temperatures, necessitating long measurement times for wavelengths longer than 10 μm. In this time the response of the interferometer and relay optics may drift. In order to correct for this, a blackbody, shown in dotted lines in Figure 1, is mounted on a PC-driven linear translation stage which allows it to be sequentially inserted and viewed by the spectrometer. The blackbody is kept at a temperature stable to within ±0.05 ^{o}C using flowing water.

A second issue is the treatment of the 'dark', or 'source off' measurements. There are spectral components in the interference functions for the measurements which are in anti-phase to those arising from light from the AHR entering the FTS through the emission port, and which are due to thermal radiation from the FTS detector and sample compartments passing through the interferometer and being reflected back onto the detector. Therefore all subtraction of 'dark' or 'source off' measurements, as well as any corrections for drift, must be carried out in the interferogram (time) domain, before Fourier transformation into the frequency (wavelength) domain.

The investigation of these effects was carried out using various samples, as well as very low reflectance carbon nanotube samples provided by NIST, Boulder. Figure 2 gives an example of measurements carried out with the new facility. The material, Nextel black, is an example of a low reflectance material, and was measured at 15 ^{o}C.

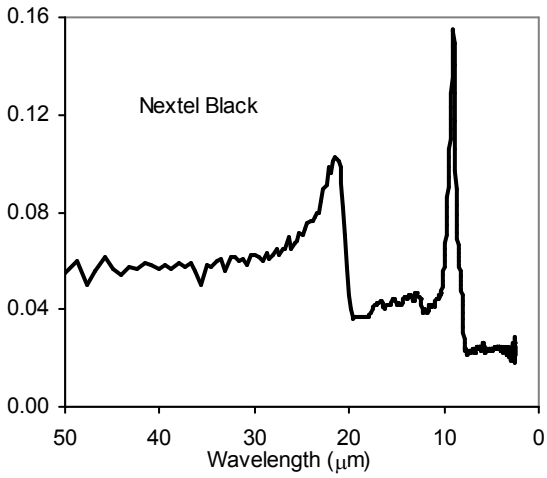

Figure 2. Reflectance of Nextel black sample measured at 15 ^{o}C.

The new facility has also been used to measure carbon nanotube samples to evaluate their suitability for use such as thermal detectors, baffles and broadband absorbers in the infrared [2]. A full description of the facility and measurement process will be presented, together with measurements of low and high reflectance samples and an evaluation of their associated uncertainties.

REFERENCES

1. F. J. J. Clarke, C. J. Chunnilall, L. J. Rogers, Recent progress at NPL in the development of mid-infrared spectrometric measurements, Proc. SPIE, 5192, 111-122, 2003.
2. C J Chunnilall, J H Lehman, E Theocharous, Infrared hemispherical reflectance of carbon nanotube mats and arrays in the 5 μm to 50 μm wavelength region, NEWRAD 2011 Abstracts.

BRDF measurements of graphite used in high-temperature fixed point blackbody radiators: a multi-angle study at 405 nm and 658 nm

Heather J. Patrick, Leonard Hanssen, Jinan Zeng and Thomas A. Germer

National Institute of Standards and Technology, Gaithersburg, MD 20899 USA
Corresponding e-mail address: heather.patrick@nist.gov

We have measured angle- and polarization-resolved, hemispherical bidirectional reflectance distribution function (BRDF) for four types of graphite samples illuminated at angles of incidence varying from normal incidence to 70°. Measurements were made at room temperature using 405 nm and 658 nm laser sources. All of the samples exhibited non-isotropic scattering, including enhanced forward scatter at high incident angles. The directional-hemispherical reflectance (DHR) obtained from integrating the BRDF ranged from 0.08 to 0.1, depending upon sample and incident angle. The impact of these measurements on emissivity models for graphite blackbody radiators and radiance temperature scale dissemination will be discussed.

INTRODUCTION

The eutectic alloys Co-C, Pt-C and Re-C are being considered as reference points for the dissemination of temperature at 1597 K, 2011 K, and 2747 K, respectively.[1] A critical issue in their use is the knowledge of the emissivity of the graphite blackbody radiator cavities used in the measurement. (See Fig. 1). Modeling of the emissivity requires characterization of the reflectance of the cavity, ideally as a function of incident angle, scattering angle, polarization, wavelength and temperature, which is described by BRDF of the graphite walls. The cavity reflectance is then input to Monte Carlo-based ray tracing models to obtain the effective emissivity. In current models, the BRDF of the graphite is approximated either as Lambertian, or as a generalized specular plus diffuse (GSD) function.[2]

In this work, we utilized two laser sources at 405 nm and 658 nm, to measure full angle-and polarization-resolved, hemispherical BRDF for graphite samples illuminated at angles of incidence varying from normal incidence to 70°. The wavelengths were chosen for their proximity to two common operating wavelengths for filter radiometers used in radiation thermometry, 400 nm and 650 nm. The measurements were performed at ambient temperature using the NIST Goniometric Optical Scatter Instrument (GOSI).[3] The measurements show that the graphite used is not well-described by either the Lambertian or GSD models. Non-isotropic scattering, including enhanced forward scatter at high incident angles, was seen for all of the samples. The results of this study will be used to guide further emissivity model development, and where possible, as inputs to current emissivity models to better estimate cavity contributions to the uncertainty in radiation thermometry.

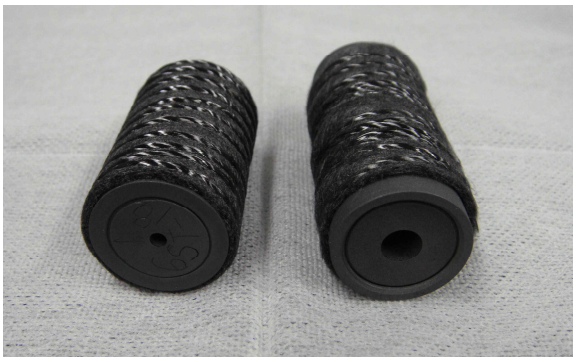

Figure 1: Blackbody cavities, with two aperture sizes and protective sleeves. Photo courtesy Y. Yamada.

MEASUREMENTS

Four graphite samples, taken from material used in the construction of high temperature fixed point blackbody cavities, were used in this study. The samples are shown in Fig. 2. Samples appeared diffuse, with little evidence of specular reflection but with some non-uniformity, such as scratches and tooling marks, on the surface.

Figure 2: Graphite samples. Ruler is in inches.

BRDF measurements were made using GOSI. This instrument uses near-collimated laser light to illuminate a sample at a selectable angle of incidence

(θ_i). A multi-axis goniometer holds the sample, and, along with a rotating detector arm, allows the scattered light to be measured at any polar and azimuthal scattering direction (θ_s and ϕ_s) in the hemisphere above the sample. Laser sources at 405 nm and 658 nm wavelengths were used to illuminate a few millimeter spot on the sample. The incident laser polarization was linear. At each θ_i, two angle-resolved hemispherical data sets were taken, one for s-polarization (polarization perpendicular to the plane of incidence) and the other for p-polarization (polarization in the plane of incidence). To obtain the BRDF that would be measured for unpolarized light, the s- and p-polarization values at each θ_s and ϕ_s point were averaged.

RESULTS

Figure 3 shows the unpolarized hemispherical BRDF for one of the samples, measured at θ_i = -60° using the 405 nm laser. The data were measured at points spaced by 0.1 on an *x,y* grid, where

$$x = \sin\theta_s \cos\phi_s \quad (1)$$

$$y = \sin\theta_s \sin\phi_s \quad (2)$$

In the figure, the line along y = 0 is the in-plane direction, with the position x,y = -0.86,0 corresponding to retro-reflection, and x,y = +0.86,0 corresponding to specular reflection. Regular spacing of the data in *x,y* coordinates is used to simplify integration of BRDF to the DHR, ρ. Since ρ is given by[4]

$$\rho = \iint \mathrm{BRDF} \cos\theta_s \sin\theta_s \, d\theta_s d\phi_s \quad (3)$$

it can be shown that by substituting variables to *x,y* then ρ is the average BRDF over the *x,y* grid, multiplied by π. For the data shown in Fig. 3, ρ = 0.089. Uncertainties in ρ and in the BRDF data will be discussed in the presentation.

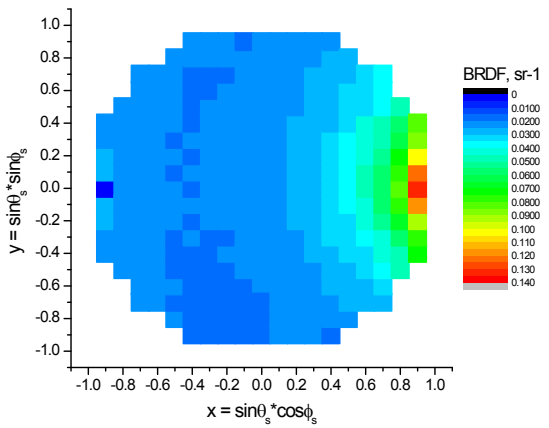

Figure 3. BRDF as a function of scattering direction, unpolarized 405 nm light, θ_i= -60°.

DISCUSSION

In typical emissivity models, the BRDF of the graphite is approximated either as Lambertian, or as a GSD model. In one study, the different models lead to very different behavior of the effective emissivity when a known temperature non-uniformity was input along the cavity length.[5] Fig. 3 suggests that the graphite is not well-described by either the Lambertian or GSD models. For Lambertian scattering, the BRDF would be isotropic over the scattering hemisphere. Instead, the BRDF shown in Fig. 3 increases in the forward-scattering direction. The increase is not part of a specular peak, but rather a general enhancement of the forward scattering, and was seen, to varying degrees, in all the samples at high incident angles. In the presentation, we will discuss full results, including the comparison of BRDF and DHR at 405 nm vs. 658 nm, polarization and incident direction dependence, and variation of BRDF and DHR between samples and at different positions on a given sample due to surface non-uniformities. We also hope to compare the DHR measurements integrated from Eq. 3 to DHR obtained by other techniques. While the effect of temperature on the BRDF has not been considered here, we plan to conduct BRDF and/or DHR measurements at elevated temperature in future studies. The results of the current work will help to guide further development of emissivity models to correctly account for more complicated BRDF distributions. The impact of these measurements on emissivity models and radiance temperature will be discussed.

REFERENCES

1. http://www.bipm.org/wg/CCT/CCT-WG5/Allowed/Miscellaneous/CCT-WG5-docs-01.pdf
2. A.V. Prokhorov and L.M. Hanssen, Effective emissivity of a cylindrical cavity with an inclined bottom: I. Isothermal cavity, Metrologia, 41, 421-431, 2004.
3. http://www.nist.gov/pml/div685/grp06/scattering_bidirectional.cfm
4. ASTM E2387-05, Standard Practice for Goniometric Optical Scatter Measurements, ASTM International, West Conshohocken, PA, 2005.
5. A.V. Prokhorov and L.M. Hanssen, Effective emissivity of a cylindrical cavity with an inclined bottom: II. Non-isothermal cavity, Metrologia, 47, 33-46, 2010.

Measurement Setups and Methods for UV Action Spectra of Materials

Petri Kärhä[1,2], Anu Heikkilä[3], and Merja Kaunismaa[4]

[1]Aalto University School of Electrical Engineering, Espoo, Finland, [2]Centre for Metrology and Accreditation (MIKES), Espoo, Finland, [3]Finnish Meteorological Institute, Helsinki, Finland, [4]Elastopoli Ltd., Sastamala, Finland
Corresponding e-mail address: petri.karha@aalto.fi

Two spectrographs have been developed for measuring UV action spectra of materials. The setups include 1-kW Xe lamps and concave holographic gratings for spectral separation of light. In one setup, the temperature of the sample can be heated up to 75 °C. Various polymer, plastic, and paper samples have been aged and analysed in the wavelength region 250 – 450 nm. Samples have been measured e.g. for colour and hardness. In order to accurately reveal the action spectrum from the measurement results, varying irradiance levels at different wavelengths and spectral convolutions need to be accounted for.

SPECTROGRAPHS

Ultraviolet (UV) radiation damages materials in many ways. Common ageing methods include yellowing, hardening, and cracking of the material surface. Materials to be used outside are regularly tested for UV duration. The methods used include placing samples under the Sun. The exposure may be accelerated by concentrating the radiation with solar trackers and mirrors. Materials can also be aged with artificial UV sources such as Hg or Xe lamps.

Interpreting the ageing results is complicated. The solar spectrum in the testing site and in the location where the materials are to be used may vary. In addition to the obvious difference in the solar intensity, the spectral shape of the radiation varies in different parts of the Earth. When ageing with artificial sources, the comparison is even more complicated. For example, the spectrum of a Hg lamp is far from the solar spectrum. Predicting the life time expected at a certain location requires knowledge of the spectra involved in ageing and use, and the action spectrum of the material, i.e., knowledge on how different wavelengths damage the material.

We have built two setups for measuring the action spectra of materials. The optical layout of the first prototype is presented in Fig. 1. The design has been described in details in [1]. The design is essentially based on [2] but the device has been reduced in size so that it fits on an ordinary table of 75 × 150 cm^2 in area.

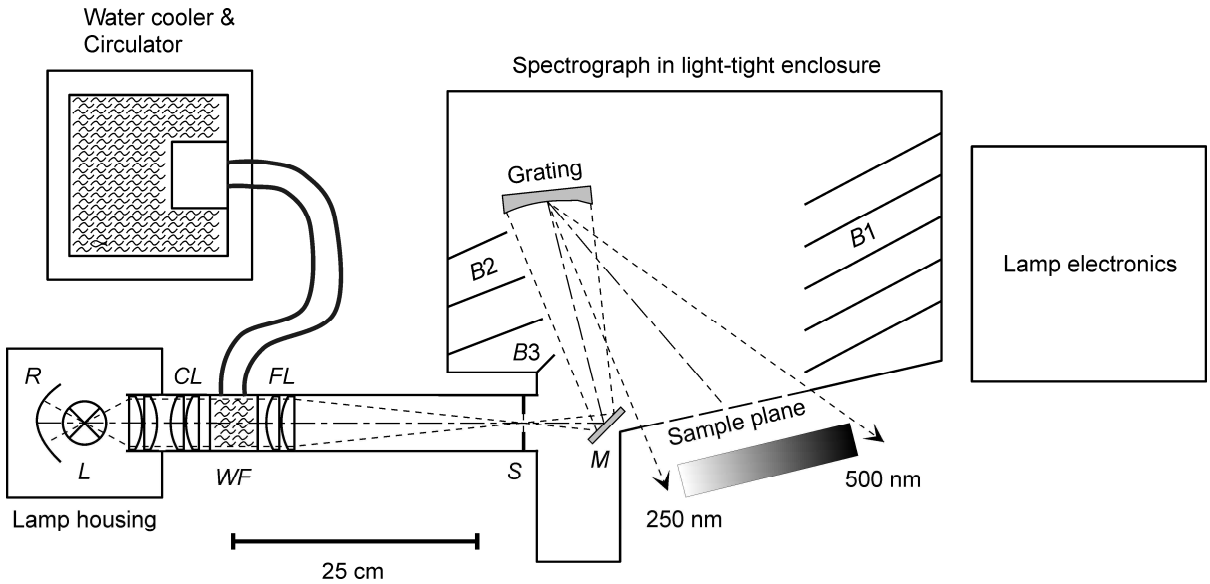

Figure 41. Spectrograph for ageing samples with spectrally resolved UV radiation. Hard sample plates with minimum size of 2 × 21 cm^2 are attached to the sample plane opening in the enclosure. [1]

The essential parts of the spectrograph are a 1-kW Xe lamp (*L*) imaged with lenses (*CL*, *FL*) to a concave holographic grating. Radiation in the sample plane contains wavelengths within 250 – 500 nm. The slit (*S*) width is adjustable from 1 to 6 mm, which varies the bandwidth within 6 – 9 nm. In the

improved prototype, the wavelength range has been limited to 280 – 420 nm, because the extended regions have no relevance. Most materials age slowly with radiation above 420 nm, and the intensity of the radiation at wavelengths below 280 nm is very low in the solar UV. In the improved prototype, the sample can be heated to accelerate the ageing.

TEST MEASUREMENTS

Various materials have been aged with the spectrographs including paper, stretched and unstretched rubber, polymers, and painted surfaces.

The samples were mainly measured for surface colour (*Yxy*), hardness, and FTIR depending on the damage type expected. Also video images, 3D microscope images, and X-ray diffraction spectra were tested to quantify cracking of the surfaces.

Figure 2 shows an example of the samples tested – two plates of fibre reinforced polymers that have been aged in the spectrograph for approximately 300 h. The damage caused by the radiation can be seen as yellowing of the samples in the wavelength region 250 – 350 nm.

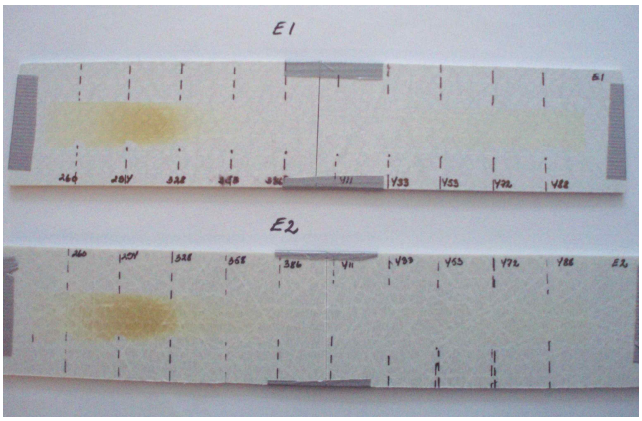

Figure 42. Two fibre reinforced polymer samples aged in the spectrograph.

The samples in Fig. 2 were measured for surface colour on 10 locations marked with stripes. Each location corresponds to a certain wavelength. The wavelengths have been calibrated with a spectroradiometer. The brightness values (*Y*) measured are presented in Fig. 3.

The samples were also measured for hardness, but this did not change notably. Obviously the damage in this case takes place on the surface only. FTIR measurements were analysed for ester groups and carboxyl groups in the wave number region 1500 – 1800 cm^{-1}. Ageing of the polymers could also be seen in these measurements.

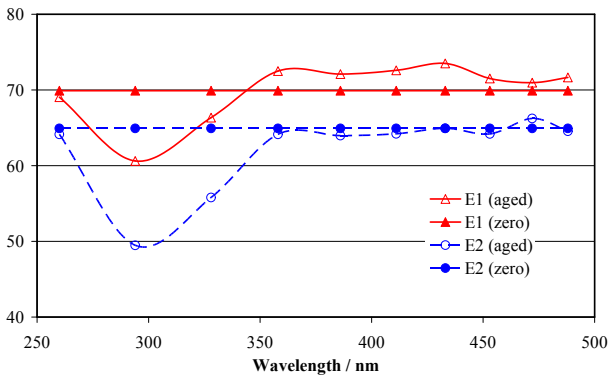

Figure 43. Measured surface brightness (*Y*) for the polymer samples of Fig. 2. Closed symbols indicate measurements of unaged control samples. Results with open symbols are for aged materials.

DERIVING ACTION SPECTRA

Work is underway to derive methodology to convert results such as those in Fig. 3 to action spectra.

In typical action spectra, such as the well known erythema action spectrum, certain wavelength region is assigned to have a value of 1. In our example this would quite naturally be the wavelength with maximum change at around 300 nm. At wavelengths above 370 nm, there is practically no change, so these could be assigned the value 0.

However, if accurate action spectra are needed, one needs to consider various corrections. The intensity in the output is not constant as a function of wavelength, but resembles that of a Xe lamp. The different exposure doses need to be taken into account, e.g., by producing a set of samples with varying exposure times. The yellowing may not be linear either. Finally, one also needs to take into account various convolutions. The bandwidth of the spectrograph is typically ~7 nm. The colour meter used to measure brightness values has an aperture diameter of 10 mm. Results could be improved by taking a spectrally dense set of measurements and deconvoluting them for the slit scattering function of the spectrograph, and the spatial responsivities of the measurement instruments.

REFERENCES

1. P. Kärhä, A. Heikkilä, K. Ruokolainen, and M. Kaunismaa, A novel facility for ageing materials with narrow-band ultraviolet radiation exposure, Rev. Sci. Instrum., 82, 023107, 2011.
2. M. Watanabe, M. Furuya, Y. Miyoshi, Y. Inoue, I. Iwahashi, and K. Matsumoto, Design and performance of the okazaki large spectrograph for photobiological research, Photochem. Photobiol., 36, 491 – 498, 1982.

Optical properties of Al_2O_3 and $Al_2O_3/BaSO_4$ reflecting diffusers processed with plasma powder spraying

Hiroshi Shitomi[1], Shinobu Ito[2], Motohiro Yamada[3] and Masahiro Fukumoto[3]

[1] *National Metrology Institute of Japan (NMIJ), AIST, Tsukuba, JAPAN,* [2] *OPTCOM Co., Ltd., Iwata, JAPAN*
[3] *Department of Mechanical Engineering, Toyohashi University of Technology, Toyohashi, JAPAN*
Corresponding e-mail address: h-shitomi@aist.go.jp

As a new approach to prepare rigid reflecting diffusers used for reflectance standards, reflection targets and integrating spheres mainly in industries, plasma powder spraying technique was introduced. The optical properties of reflecting diffusers based on Al_2O_3 and its compounds with $BaSO_4$ processed with plasma powder spraying are described together with some noticeable results about the way to improve their optical properties.

INTRODUCTION

Reflecting diffusers are one of the key elements in the field of photometry, radiometry and colorimetry. They are widely used in various types of instruments as optical components such as reflectance standards for calibration, reflection target and integrating spheres to make the optical radiation spatially uniform. Many kinds of reflecting diffusers, most of which are made of white reference materials, are commercially available and their reflection properties have been investigated in detail [1].

$BaSO_4$ is the most commonly used reflecting diffusers that shows high reflectance over the wide wavelength range from UV to near-IR and has a lot of excellent properties [1]. General ways in the use of $BaSO_4$ as the reflecting diffuser are pressing powder and/or spraying the powder with a binder such as PVA (Polyvinyl alcohol) aqueous solution, which inherently has the fragile surface. Such fragility often causes serious problems for many industrial applications such as product inspections and field measurements that are accompanied by vibration, impact, mechanical contact, harsh environmental condition etc.

Plasma powder spraying [2] is one of the common industrial thermal spraying processes for coating on materials such as metals and ceramics. Most plasma powder spraying processes don't intend to fabricate the diffusing surface, but recently we found that mechanically hard and spatially uniform reflecting diffusers with the thickness of sub-millimeters can be fabricated for Al_2O_3 under the condition that the particle size of powder is highly controlled. This paper describes the basic optical properties of Al_2O_3 reflecting diffuers processed with plasma powder spraying technique together with the effectiveness of the improvement in the reflection properties by containing $BaSO_4$ powder in the process. It also discusses the possibility to improve the reflection properties in the visibel and near-UV region by introdicing a new technique, suspension thermal spraying, to realize minuter surface.

EXPERIMENTAL SETUP

The general plasma spray apparatus comprises a water-cooled copper anode and tungsten cathode as shown in Fig.1. Plasma gas such as argon and hydrogen is used with powdered material to be deposited on the substrate. The powdered material is injected into electrically generated plasma flame, in which it is heated and melted, and accelerated with high velocity. Then it impacts on the substrate, rapidly cooled and is deposited over the substrate to form the coating.

In this study, reflecting diffusers were prepared on 50 mm squared aluminum substrates with the thickness of 3 mm. The approximate thickness of the samples onto the substrates was from 0.20 mm to 0.40 mm depending on the sprayed condition. For the samples based on the plasma powder spraying, pure Al_2O_3 powder, two types of $Al_2O_3/BaSO_4$ compounds with different mixture ratio (3:1 and 7:1) were prepared. The purity of the Al_2O_3 powder used in this study is more than 99.8 %.

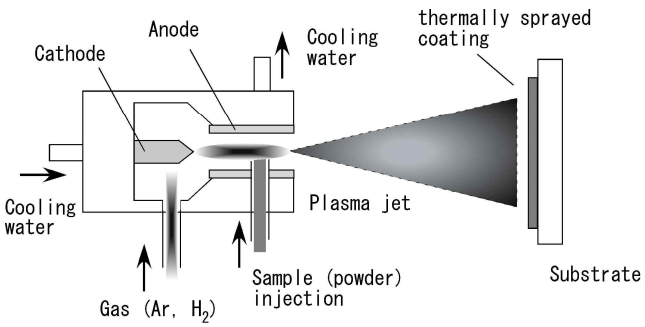

Figure 1. Schematic diagram of the plasma powder spraying process

Optical properties of the prepared reflecting diffusers were evaluated based on the spectral diffuse reflectance. It was measured with a calibrated commercial spectrophotometer (Perkin-Elmer Inc., Lambda 900) attached with a 150 mm integrating sphere. The measured wavelength range is from 300 nm to 900 nm with 5 nm intervals and the measurement geometry is $8°/d_i$.

RESULTS AND DISCUSSION

All the reflecting diffusers prepared by the plasma powder spraying have Vickers hardness of 400 HV to 500 HV, which indicates the surface has high robustness strong enough to stand intense vibration and metal scratch with a metal spatula.

Fig.2 shows the spectral diffuse reflectance of Al_2O_3, $Al_2O_3/BaSO_4$ (3:1) and $Al_2O_3/BaSO_4$ (7:1) reflecting diffusers processed with plasma powder spraying. Comparison between the samples with the thickness of 0.20 mm and that of 0.40 mm in Fig.2 reveals clear thickness dependence, which implies the existence of significant amount of transmitted radiation. Theoretically plasma powder spraying can produce a coating with the thickness more than a few millimeters, which will improve the reflection properties of the samples.

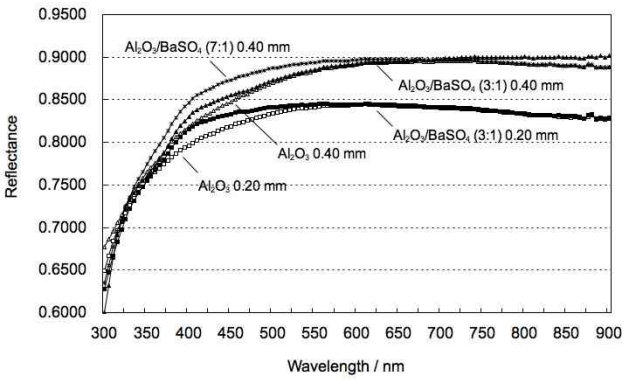

Figure 2. Spectral diffuse reflectance of Al_2O_3 and $Al_2O_3/BaSO_4$ reflecting diffusers processed with plasma

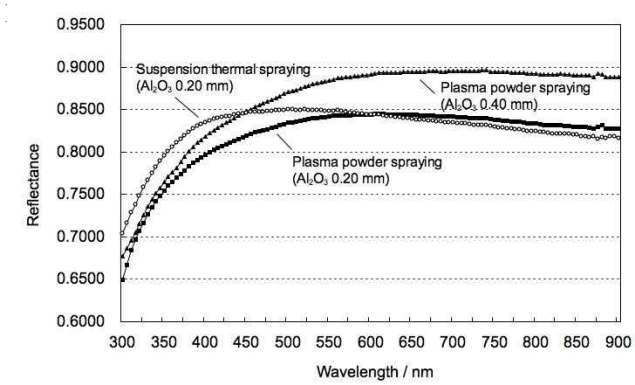

Figure 3. Spectral diffuse reflectance of Al_2O_3 reflecting diffusers based on the plasma powder spraying and that based on the suspension thermal spraying.

Al_2O_3 samples show spectrally neutral reflection properties at the wavelength range from 500 nm to 900 nm whereas relatively large drop in reflectance is observed at the shorter wavelength range. The comparison among three samples made of different mixture ratio shown in Fig.2 reveals that the reflection drop is improved by containing the $BaSO_4$ into the Al_2O_3 in the plasma power spraying process at the wavelength range from 380 nm to 500 nm. The more the sample contains $BaSO_4$, the higher the reflectance of the sample in that region becomes.

Another approach examined in this study is suspension thermal spraying technique, which is relatively new process developed to fabricate nano-structured coatings. It utilizes powdered materials with aqueous or alcoholic suspensions for injection into the plasma flame [3]. Fig.3 shows the spectral diffuse reflectance of an Al_2O_3 reflecting diffuser based on the suspension thermal spraying, which indicates the noticeable improvement in reflection properties especially in the near-UV region.

CONCLUSION

The reflecting diffusers processed with the plasma powder spraying have high mechanical strength and relatively good spectral properties in the visible region. Containing $BaSO_4$ in the process resulted in the improvement of the reflection properties in the shorter wavelength part of the visible region. Preliminary investigation on the reflecting diffusers based on the suspension thermal spraying indicates high possibility to improve the reflection properties especially in the near-UV region. In conclusion, both spraying processes are promising to manufacture the reflecting diffusers that have high robustness and good reflection properties sufficient for industrial applications that integrating spheres currently in use don't necessarily meet the requirements.

REFERENCES

1. A. W. Springsteen, Standards for the measurement of diffuse reflectance - an overview of available materials and measurement laboratories, Analy. Chim. Acta. 380, 379-390, 1999.
2. L. Pawlowski, The Science and Engineering of Thermal Spray Coatings, Wiley, New York, 1995.
3. F.-L. Toma, L.-M. Berger, T. Naumann, S. Langner: Microstructures of nanostructured ceramic coatings obtained by suspension thermal spraying, Surface and Coatings Technology, 202, 4343-4348, 2008.

Characterizing Silicon Photodiodes using Spectroscopic Ellipsometry for High Accuracy Radiometry

Ping-Shine Shaw, Lee J. Richter, Steven W. Brown,, and Keith R. Lykke
National Institute of Standards and Technology

Gaithersburg, MD 20899, USA
Corresponding e-mail address:shaw@nist.gov

In high-accuracy radiometry, the silicon photodiode is the foundation for radiation detection throughout the near infrared to ultraviolet. The response of a silicon photodiode is determined by two factors; the internal quantum efficiency and reflection loss due to the optical structure of the photodiode. The latter not only affects the responsivity but also the wavelength-dependent uniformity of the photodiode. Here, we show how a fast and easy to use ellipsometer can accurately determine the optical structure of a photodiode throughout its active detection area. Such diagnostic information allows one to predict the response and spatial uniformity throughout the wavelength range. We discuss the technique and compare the prediction based on ellipsometry with monochromatic light measurements from ultraviolet to near infrared.

INTRODUCTION

In the pursuit of ever higher light-detection accuracy, the performance of silicon photodiodes becomes ever more important. With the maturity of silicon processing, silicon photodiodes have become more reliable and their performance can be predicted by characterizing fundamental properties. For example, the internal quantum efficiency of silicon photodiodes has been modelled and shows good agreement with measurements. [1,2] The consistency of the internal quantum efficiency allowed the development of high-accuracy trap detectors by minimizing reflection losses.

For a more general use, a single silicon photodiode for light detection is preferred and commonly used. In this case, the reflection loss becomes a major factor in the response of a photodiode. Moreover, the wavelength-dependent reflection loss varies from one position to another over the active area and contributes to the measurement uncertainty. Characterizing such effects is tedious using monochromatic light, requiring spatial scans at various wavelengths.

We describe a technique of characterizing silicon photodiodes using mapping ellipsometry. Ellipsometric measurements provide a high-precision silicon dioxide film thickness map of the photodiode from which reflectance at any wavelength can be predicted. Other effects, such as contamination, can also be determined. Using a commercial ellipsometer, measurement across the whole photodiode surface is fast and easy to setup.

ELLIPSOMETRY FOR SILICON PHOTODIODE CHARACTERIZATION

Typical silicon photodiodes have a simple structure of a thin silicon dioxide film on a silicon substrate. With a spectroscopic ellipsometer, which measures the complex ratio of the amplitude reflectance for TE and TM polarizations over a wide wavelength range, one can accurately determine the thickness of the oxide film. Figure 1 shows the result of mapping a 1 x 1 cm^2 silicon photodiode. The precision in thickness across the measurement area is better than 0.01 nm with only 1 second data acquisition time per point. By using Fresnel formulae, the map of Fig. 1 can be translated into the reflectivity at any position on the photodiode at any wavelength. We will compare such prediction with

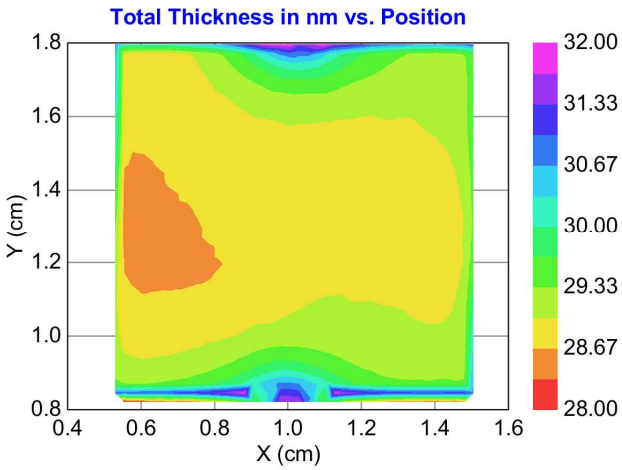

Figure 44. Silicon dioxide film thickness map of a silicon photodiode measured by an ellipsometer.

single wavelength uniformity measurements throughout the near infrared to ultraviolet range using NIST's facilities of the Synchrotron Ultraviolet Radiation Facility III (SURF III) and also the Spectral Irradiance and Radiance Responsivity Calibrations using Uniform Sources (SIRCUS). A variety of silicon photodiodes with different nominal oxide thicknesses will be measured and discussed.

REFERENCES

1. T.R. Gentile, S.W. Brown, K.R. Lykke, P.S. Shaw, and J.T. Woodward, "Internal quantum efficiency modelling of silicon photodiodes", Appl. Opt. 49, 1859-1864 (2010).
2. T.R. Gentile, J.M. Houston, and C.L. Cramer, "Realization of a scale of absolute spectral response using the National Institute of Standards and Technology high-accuracy cryogenic radiometer" Appl. Opt. 35,4392-4402 (1996).

NIST – PTB Joint Study of Far Infrared Selected Black Coatings

Leonard Hanssen,[1] Boris Wilthan,[1] Sergey Mekhontsev,[1] Christian Monte,[2] and Jörg Hollandt[2]

[1]*National Institute of Standards and Technology (NIST), Gaithersburg, MD, USA,*
[2]*Physikalisch-Technische Bundesanstalt (PTB), Berlin, Germany*
Corresponding e-mail address: hanssen@nist.gov

NIST and PTB are pursuing an investigation of selected black coatings for multiple applications including reflectance and emittance standards, cavity coatings for blackbody sources and radiometers, and coatings for baffles and temperature controlled shrouds in background controlled chambers. The investigation consists of spectral reflectance and emittance measurements, at temperatures from near ambient to several hundred degrees Celsius, over the mid and far infrared range of 2 µm to 50 µm. Implementation of these coatings and accurate knowledge of their optical properties should ultimately benefit calibration support of a number of remote sensing satellite programs.

INTRODUCTION

The spectral emittance of available blackbody coatings plays a critical role in the design and performance of blackbodies. In particular, the high accuracy goals of spectroradiometric systems such as the planned infrared spectral radiance instrument of the Climate Absolute Radiance and Refractivity Observatory (CLARREO) mission requires detailed knowledge of the infrared optical properties of such coatings. There exists a large body of infrared data on many blackbody coatings in the infrared, especially in the 2 µm to 14 µm spectral region. However, available data at longer wavelengths, such as 50 µm as planned for CLARREO measurements, is much more sparse. In addition, as time proceeds, some widely used coatings may be discontinued, as for example Aeroglaze Z-302, requiring substitute coatings, which in turn will require careful characterization and study prior to being useful for blackbody sources.

The Optical Technology Division of NIST is in the process of upgrading its spectrophotometric and spectroradiometric capabilities to support both materials studies and radiance source and detector characterization and calibration for programs such as CLARREO. The improved facilities will require black coatings for blackbody sources, as well as for baffling and cold shrouds over the complete spectral range (2 µm to 50 µm).

To meet the requirements described above, an extensive effort extended over time and multiple laboratories will be necessary. The study reported here consists of both reflectance and emittance characterization of candidate blackbody coating materials. Measurements have been performed at both NIST and the PTB. The compilation of results includes overlap of spectral ranges, different instrumentation and measurement methods. Comparison of results provides confirmation and validation of the cited uncertainties.

MEASUREMENT METHODS

Both PTB and NIST operate systems based on the comparison of spectral radiance for determination of the emittance of materials and coatings. Schematics of the systems are shown in Figures 1 and 2. Both systems employ reference blackbody sources and Fourier transform spectrometers. The PTB system shown in Figure 1 is geared for larger samples (up to 90 mm diameter) and temperatures in the near ambient range of 80 °C to 500 °C.[1,2] The NIST system is designed to cover a broader temperature range of 150 °C to 900 °C, with a restriction of sample size of 25 mm for temperatures below 500 °C, and 19 mm diameter for higher temperatures.[3,4]

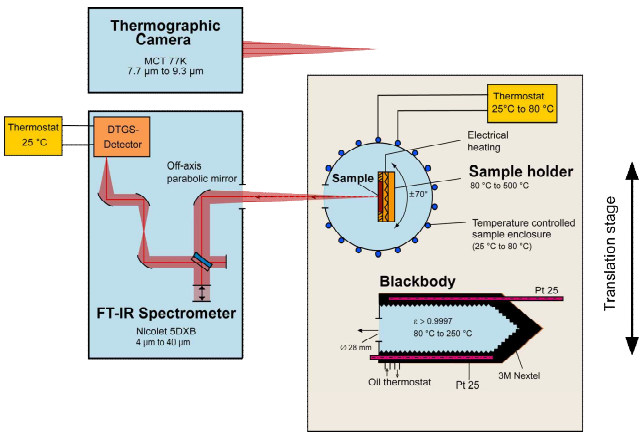

Figure 45. Diagram of the PTB Facility for infrared spectral emittance.

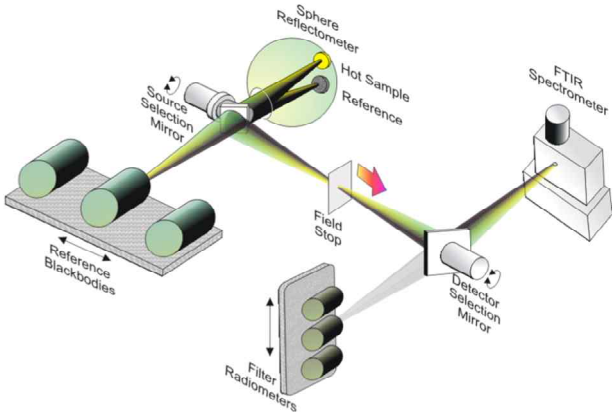

Figure 46. Diagram of the NIST Facility for infrared spectral emittance.

An integrating sphere based directional hemispherical reflectance (DHR) measurement system is used at NIST to measure the DHR of materials and coatings from 23 °C to 200 °C.[5,6]

MEASUREMENT RESULTS

All three systems described here have been used to examine several candidate black paint coatings. One of the coatings examined is a high temperature diffuse black paint with low reflectance from 8 µm to 40 µm: Rolls Royce HE23. Figure 3 shows a

Figure 47. Comparison of PTB and NIST measurements of Rolls Royce HE23 paint samples at

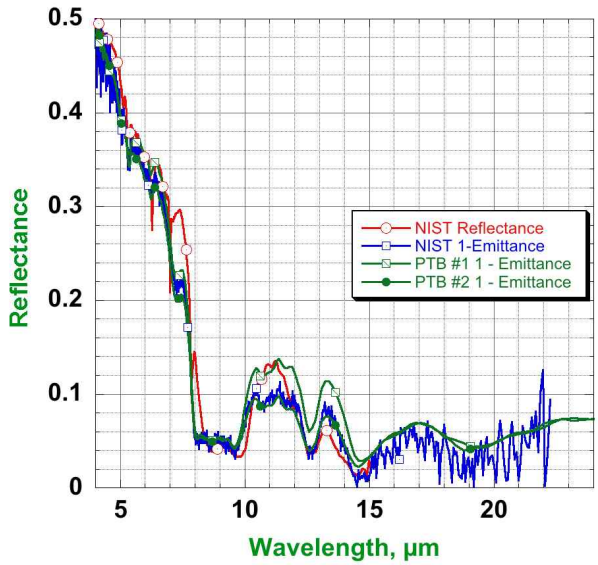

200 °C.

comparison of its reflectance spectra using the three systems. Due to the difference in sample size requirements, PTB and NIST measured different samples, which were simultaneously coated and baked under identical conditions. Nevertheless some sample-to-sample variation can be observed. Figure 3 shows spectra obtained from emittance measurements at PTB on 2 samples, as well as spectra obtained from NIST's reflectance and emittance measurement systems.

Complete results on HE23 and additional black paints including both specular and diffuse types, will be presented.

FUTURE DEVELOPMENT

Both PTB [7] and NIST are in the process of establishing additional emittance and reflectance measurement capabilities employing vacuum and controlled / cooled background to enable characterization at lower temperatures for wavelengths up to 100 µm.

REFERENCES

1. C. Monte and J. Hollandt, "The measurement of directional spectral emissivity in the temperature range from 80 ºC to 500 ºC at the Physikalisch-Technische Bundesanstalt," High Temp. High Press. **39** , 151-164 (2010).
2. C. Monte and J. Hollandt, "The determination of the uncertainties of spectral emissivity measurements in air at the PTB," Metrologia **47**, S172-S181 (2010).
3. L. M. Hanssen, S. N. Mekhontsev, and V. B. Khromchenko, "Infrared spectral emissivity characterization facility at NIST," Proc. SPIE **5405**, 1-12 (2004).
4. C. P. Cagran, L. M. Hanssen, Mart Noorma, Alex V. Gura, and S. N. Mekhontsev, "Temperature-Resolved Infrared Spectral Emissivity of SiC and Pt–10Rh for Temperatures up to 900◦C," Int. J. Thermophys. **28**, 581-597 (2007).
5. L. M. Hanssen and S. G. Kaplan, "Infrared diffuse reflectance instrumentation and standards at NIST," Analytica Chimica Acta **380**, 289-302 (1998).
6. L.M. Hanssen, "Integrating-sphere system and method for absolute measurement of transmittance, reflectance, and absorptance of specular samples," Applied Optics **40** (19), 3196-3204 (2001).
7. C. Monte, B. Gutschwager, S. P. Morozova, and J. Hollandt, "Radiation Thermometry and Emissivity Measurements Under Vacuum at the PTB." Int. J. Thermophys. **30**, 203-219 (2009).

Refractive index of silicon with various doping levels at high temperatures

Maksim Shpak[1], Lauri Sainiemi[1], Petri Kärhä[1], Martti Heinonen[2], Sami Franssila[1], Erkki Ikonen[1,2]

[1]*Aalto University, Espoo, Finland,* [2]*Centre for Metrology and Accreditation, Espoo, Finland*

Corresponding e-mail address: maksim.shpak@aalto.fi

We present the first measurement results of complex refractive index of doped silicon at temperatures between 800 ºC and 1200 ºC in the wavelength range of 500 – 2200 nm. The silicon samples under study have conductivities of about 0.01 Ω·cm, 1 Ω·cm and 3000 Ω·cm. Our measurement method is based on heating a multi-layer sample in a furnace to a known temperature and measuring the spectrum radiated by the sample. The refractive index is then determined from the interference patterns caused by the layered structure of the sample.

INTRODUCTION

Accurate temperature measurement is critical for the control of thermally dependent processes, such as RTP (rapid thermal processing). In semiconductor processes radiation thermometry is an attractive method, providing a contaminant-free temperature monitoring. Such method requires knowledge of the emissivity of the object.

Radiative properties, including the emissivity, can be determined from the temperature, refractive index, direction and surface roughness of an object, and are affected by presence of thin-film coatings. For optically smooth surfaces emissivity can be theoretically predicted based on thicknesses and optical constants of the materials. Uncertainty in the emissivity of silicon and related materials is the limiting factor in such measurements, due to its dependence on temperature and impurity concentration.

Silicon is a widely studied material, and fundamental physical mechanisms governing its optical behavior have been well established. Although a number of model expressions for optical constants of silicon exist [1–3], there are large gaps in wavelength ranges, temperatures and doping concentrations covered, and extrapolations to higher temperatures and doping concentrations show large differences [4].

For the extinction coefficient of silicon in particular, there are no earlier experimental studies covering temperatures above 800 ºC and different doping concentrations, which is the focus of this work. This study is the application of the method presented in Ref. 5, covering a wide range of temperatures and doping concentrations of silicon.

MATERIALS AND METHODS

The samples under study are three SOI (silicon on insulator) wafers with different resistivities of the device layers. The thicknesses of the wafers are between 500 µm and 660 µm and those of the buried oxide layer between 1 µm and 2 µm. The thickness of the device layer is 2 µm in all samples. Main characteristics of the device layers of the samples are presented in Table 1.

Table 12. Properties of studied silicon samples

Sample	1	2	3
Resistivity (Ω·cm)	3000–5000	1–10	< 0.01
Doping density (cm^{-3})	$8.6 \cdot 10^{11}$ – $1.4 \cdot 10^{12}$	$4.4 \cdot 10^{14}$ – $4.8 \cdot 10^{15}$	$> 8 \cdot 10^{18}$
Dopant type	N / Phosph.	N / Phosph.	P / Boron
Lattice orientation	1-1-1	1-1-0	1-0-0

For measurements, the samples are placed vertically in the horizontal tube furnace (Carbolite STF), with both ends of the tube open. The temperature of the sample is monitored from the sample holder with a thermocouple. Spectral radiance of the sample is then measured at various temperatures with focusing optics of a spectroradiometer. We avoid the glow of the working tube and the sample holder to affect the measurement by ensuring that the sample stays vertical and has low diffuse reflectance component (measured separately at the room temperature).

The radiance spectrum of the multi-layer sample has interference patterns (figure 1), which

are modeled using thin-film techniques based on the Fresnel equations. The modeled radiance is fitted to the measurement results by adjusting the real and the imaginary parts of the refractive index of the device layer spectrally. Accurate knowledge of thicknesses of the layers is needed to calculate the refractive index. The thicknesses are obtained from reflectance measurements of the sample at the room temperature before and after the heat cycle.

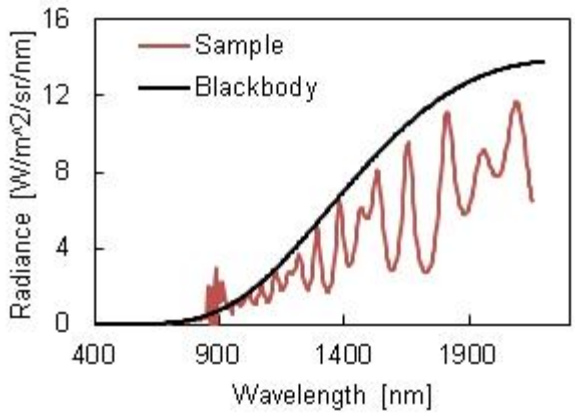

Figure 1. Radiance spectrum of a sample compared to that of a blackbody at 1000 ºC temperature. The radiance data consists of two superimposed interference patterns due to the multi-layer structure of the sample.

At the higher temperatures thermal oxidation of the device layer introduces a silicon dioxide layer on top of the sample, which has to be accounted for in the model. The thickness of the oxide layer, as well as the decreasing thickness of the device layer, is a function of time.

RESULTS AND DISCUSSION

Results obtained for the temperature dependence of the extinction coefficient k of sample 3 are presented in figure 2. The dashed portions of the curves at the two lowest temperatures are interpolations, and represent the likely upper limits of k in those regions. The increasing trend of k with temperature is evident from the data, which is attributed to increasing absorption by thermally generated carriers at high temperatures.

Also plotted on figure 2 are data from Timans [2] at 800 ºC, extrapolated to shorter wavelengths by Lee et al. [4]. These data are in general agreement with our measured k at 800 ºC in the wavelength range 800–1200 nm. The comparison data is, however, for lightly doped silicon, whereas sample 3 is heavily doped.

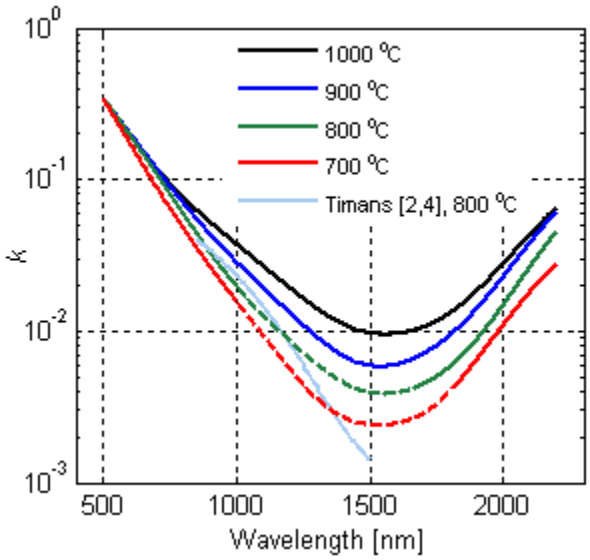

Figure 2. Extinction coefficient of sample 3 at 4 different temperatures.

The results to be presented at NEWRAD 2011 cover temperatures from 700 ºC to 1200 ºC for all three samples, as well as comparisons with existing models.

REFERENCES

1. T. Satō, Spectral emissivity of silicon, Jpn. J. Appl. Phys. 6, 339–347, 1967.
2. P. J. Timans, Emissivity of silicon at elevated temperatures, J. Appl. Phys. 74, 6353–6364, 1993.
3. G. E. Jellison, Jr., F. A. Modine, Optical functions of silicon at elevated temperatures, J. Appl. Phys. 76, 3758–3761, 1994.
4. B. J. Lee, Z. M. Zhang, E. A. Early, D. P. DeWitt, B. K. Tsai, Modeling radiative properties of silicon with coatings and comparison with reflectance measurements, J. Thermophys. Heat Transf. 19, 558–565, 2005.
5. M. Shpak, P. Kärhä, M. Ojanen, E. Ikonen, M. Heinonen, Optical temperature measurement method for glowing microcomponents, Int J Thermophys. 31, 1762–1770, 2010.

A Method for Inspecting the Full-field Residual Stress with Large Area on a Flexible Indium Tin Oxide Film

Yen-Liang Chen*, Bor-Jiunn Wen, Shau-Wei Hsu, and Kuei-Neng Wu

Center for Measurement Standards / Industrial Technology Research Institute (ITRI)
Hsinchu, Taiwan
**Corresponding e-mail address: yenz@itri.org.tw*

The full-field phase retardation of a flexible indium tin oxide film related to its residual stress is measured under unbending/bending with large area. A narrow-band linear polarized panel light passes through a liquid crystal cell, the tested sample and an analyzer, full-field interference signal are taken by a camera. The driving voltage of the crystal cell is adjusted for the four-step phase shifting method. After the 2-D phase unwrapping calculation, the full-field phase retardation can be obtained. Its validity is demonstrated.

INTRODUCTION

The indium tin oxide (ITO) film is widely used as the electrode for flat panel display devices, solar cells and organic light emitting diodes (OLED) [1]. Due to the temperature variation during the coating or laser patterning processes [2], the residual stress exists in part areas and affects the quality and lifetime of the ITO film. The previous article described that the material phase retardation is related to its stress or optical activity [3]. To know the uniformity of the birefringence material, some methods were proposed to measure their full-field phase retardation [4-5]. However they use a laser and an electro-optic modulator to be a modulated light source which is not easy to be expanded to a large area. An alternative method for measuring the full-field phase retardation with large area is proposed in this paper. A cold cathode fluorescent lamp (CCFL) panel light passes through an optical filter, a polarizer, a twisted nematic (TN) liquid crystal cell, the tested ITO film, and an analyzer. Full-field interference signals are taken by a CCD camera. The driving voltage of the TN cell is adjusted for alternating different interference phases. Based on the four-step phase shifting method [6], the full-field phase retardation can be obtained. An ITO film is tested under unbending/bending with measurement area around 230 mm × 110 mm to show the validity of this method.

PRINCIPLE

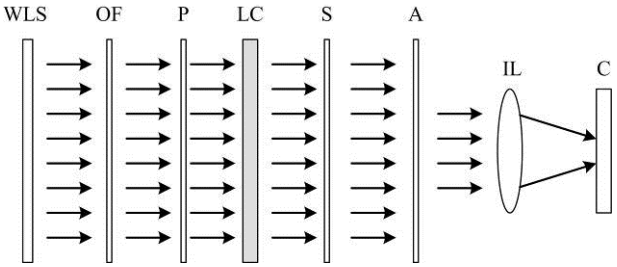

Figure 48. Schematic diagram for the full-field common-path interferometer: WLS, CCFL white light siurce; OF, optical filter; P, polarizer; LC, liquid crystal cell; S, sample; A, analyzer; IL, imaging lens; C, camera.

The schematic diagram of this method is shown in Fig. 1. A white CCFL panel light (WLS) passes through an optical filter (OF) with 620 nm central wavelength and a polarizer (P) to become a narrow-band linear polarized light at 45° with respect to the x axis. Next, the light passes through a liquid crystal cell (LC), a tested sample (S), an analyzer (A) with the transmission axis at 45°, and an imaging lens (IL), and finally enters a camera (C). The light amplitude E can be derived and written as

$$E = A \cdot S \cdot LC \cdot P(45°) = \frac{1}{\sqrt{2}} \begin{bmatrix} \cos[(\phi + \delta)/2] \\ \cos[(\phi + \delta)/2] \end{bmatrix}, \quad (1)$$

where δ is the difference of the phase retardation caused by the LC and $\phi(x,y)$ is the phase retardation distribution of S. The associated intensity can be expressed as

$$I(x,y) = I_0[1 + \cos(\phi(x,y)) + \delta]. \quad (2)$$

According to four-step phase shifting algorithm [6], δ = 0°, 60°, 120°, 180° are alternated by different

driving voltage of LC. The associated intensities are I_1, I_2, I_3 and I_4. Therefore we have

$$\phi(x,y) = \tan^{-1}\frac{5(I_1 - I_2 - I_3 + I_4)}{\sqrt{3}(2I_1 + I_2 - I_3 - 2I_4)} \quad (3)$$

In addition, the 2-D phase unwrapping technique [7] is applied to solve the phase ambiguity, and the full-field phase retardation distribution $\phi(x,y)$ is obtained.

EXPERIMENTS AND RESULTS

To demonstrate the validity of this method, we tested an ITO film coated on PET layer (CPFilms/ OC 100). The film was originally a plane plate which was set under unbending. A 230 mm × 110 mm area was measured as shown in Fig. 2. After the first experiment, the sample was bent and kept with a bending machine (ITRI-CMS/FCIS/08) under 25° bending angle. The associated measurement results were shown in Fig. 3. After the phase calculations by Eq. (3) and the 2-D phase unwrapping processing [7], the results of above two experiments were shown in Fig. 4(a) and 4(b), respectively.

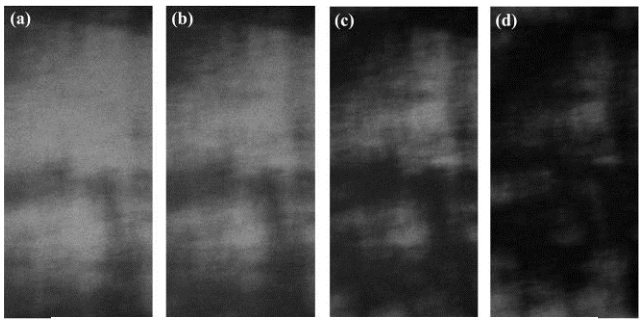

Figure 2. Interferometric images of the unbent sample with four-step phase shifting method where δ = (a) 0°, (b) 60°, (c) 120°, and (d) 180°.

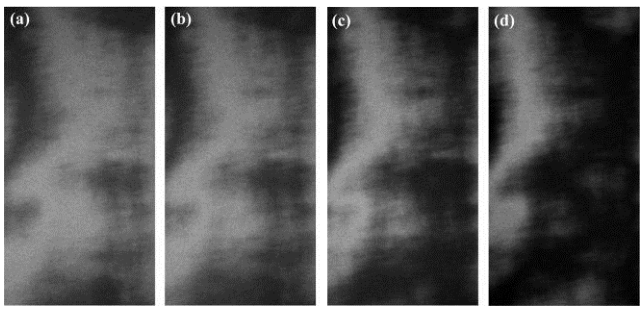

Figure 3. Interferometric images of the bent sample with four-step phase shifting method where δ = (a) 0°, (b) 60°, (c) 120°, and (d) 180°.

In Fig. 4, the mean values of the measured area can be calculated and they are 1.224 rad and 5.630 rad, respectively. Their associated standard deviations can also be derived and they are 0.712 rad and 1.455 rad. Because the bending test can make the effect of the residual stress to be more obvious [8-9], it also can be seen by comparing Fig. 4(a) and 4(b) in the circular region. The deviation between maximum and minimum of the circle region in Fig. 4(a) is at least double than it in Fig. 4(b). The validity of this method is demonstrated.

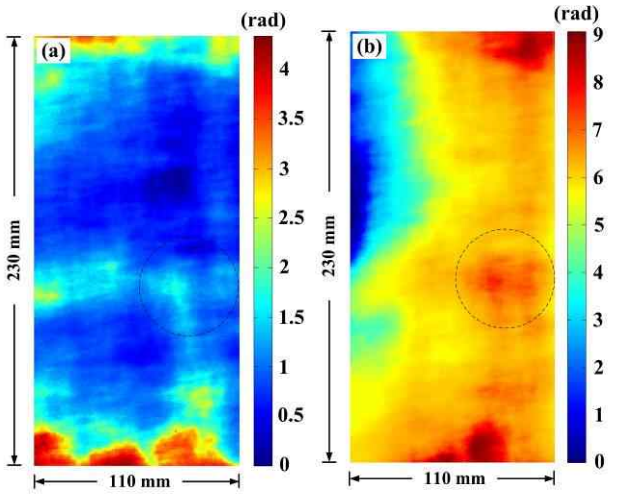

Figure 4. Measurement results of the full-field phase retardation. (a) sample is unbent; (b) sample is bent.

REFERENCES

1. C. Sujatha, G.M. Rao, and S. Uthanna, Characteristics of indium tin oxide films deposited by bias magnetron sputtering, Mater. Sci. Eng., B94, 106-110, 2002.
2. H.Y. Tsai, H. Yangm, C.T. Pan, and M.C. Chou, Laser patterning indium tin oxide (ITO) coated on PET substrate, Proc. SPIE, 4230, 156-163, 2000.
3. E. Hecht, Optics, 4th edition, Addison Wesley, 2001.
4. Y.L. Lo, H.W. Chih, C.Y. Yeh, and T.C. Yu, Full-field heterodyne polariscope with an image signal processing method for principal axis and phase retardation measurements, Appl. Opt., 45, 8006-8012, 2006.
5. Y.L. Chen and D.C. Su, Full-field measurement of the phase retardation for birefringent elements by using common path heterodyne interferometry, Opt. Las. Eng., 47, 484-487, 2009.
6. R.S. Sirohi, Optical methods of measurement, 2nd edition, CRC Press, 2009.
7. J. A. Quiroga and E. Bernabeu, Phase-unwrapping algorithm for noisy phase-map processing, Appl. Opt. 33, 6725-6731, 1994.
8. S. Grego, J. Lewis, E. Vick, D. Temple, Development and evaluation of bend-testing techniques for flexible-display applications, J. Soc. Inf. Display, 13, 575-581, 2005.
9. B.J. Wen, T.S. Liu, C.H. Chen, H.Y. Ko, Z.Y. Chung, and S.C. Liao, P-72: optical- characteristic measurement of flexible display for reliability test, In: SID Symp. Dig. Tech. Papers, 40, 1378-1381, 2009.

Analysis and reduction of fluorescence on PTFE-coated integrating spheres

S. Pape, P. Sperfeld, B. Barton, K. Stock

Physikalisch-Technische-Bundesanstalt, Braunschweig, Germany
Corresponding e-mail address: sven.pape@ptb.de

The transmission of PTFE-coated integrating spheres can be heavily corrupted by fluorescence effects. This effect was proofed using a 30 watt deuterium lamp with and without an edge filter applied. The fluorescence effects were eliminated by specific heating and irradiation treatments.

ANALYSIS OF FLUORESCENCE

The Physikalisch-Technische Bundesanstalt (PTB) uses two different measurement set-ups to calibrate deuterium lamps and quartz halogen lamps. The facilities differ especially in the entrance spheres: one spectrometer uses a BaSO4-coated sphere and the other one a PTFE-coated sphere.

A comparison of the spectral irradiance of deuterium lamps and quartz halogen lamps using both measurement set-ups shows considerably different results, especially in the wavelength range from 270 nm to 365 nm. A measurement with a 30 W deuterium lamp with and without an edge filter applied confirmed the assumption of the adulterant influence of fluorescence.

Lamp radiation in the wavelength range below 280 nm is disabled by using an edge filter. Thereby, the fluorescence is eliminated. The fluorescence disappears due to the fact that the fluorescence is excited solely outside the filter bandpass.

The fluorescence beyond the filter edge at 280 nm could be estimated on the basis of the ratio of the actually measured radiation and the expected calculated radiation (see curve a in Fig. 1). The spectral transmittance of the applied edge filter is well known.

REDUCTION OF FLUORESCENCE BY UV IRRADIATION

The fluorescence could be minimized or rather eliminated by the following procedure: heating the integrating spheres in light vacuum [1] and then exposing them to UV radiation of high irradiance (more than 500 mW/cm^2) [2]. Finally, there was almost no fluorescence anymore (see curve b in Fig. 2).

Fig. 1.: Fluorescent PTFE integrating sphere under UV radiation

RE-INCREASE OF FLUORESCENCE

Unfortunately, this state was not stable in the long run. The fluorescence increased again up to approximately 15% over a period of 6 to 7 months within the spectral range of 270 nm to 400 nm (see curve c in Fig. 2).

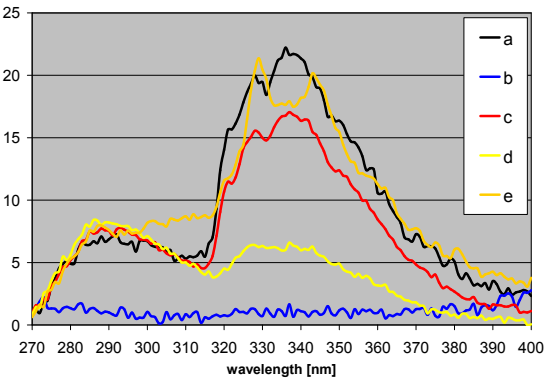

Fig. 2: Reduction and re-increase of the fluorescence (curves: a = untreated sphere, b = directly after UV treatment, c = 27 weeks after UV reatment, d = directly after ozone treatment, e = 16 weeks after ozone treatment)

PARTIAL REDUCTION AND RE-INCREASE AFTER OZONE TREATMENT

Following the experiments described above, the integrating spheres were treated by means of another method: ozone of more than 10 ppm under low-pressure atmosphere was applied (see curve d in Fig. 2). Also here the fluorescence was reduced; however, this effect was limited to wavelengths of more than

320 nm, only. Similar to the UV treatment experiment this state was not stable in the long run (see curve e in Fig. 2).

REFERENCES

1. Ping-Shine Shaw, Zhiang Li, Uwe Arp, and Keith R. Lykke, "*Ultraviolet characterization of integrating spheres*", APPLIED OPTICS, Vol. 46, No. 22, 1 August 2007
2. Saulius Nevas, Peter Sperfeld, Sven Teichert, and Andreas Höpe, "*Extraordinary Changes in PTFE-Based Integrating-Sphere Properties under High Levels of UV-Irradiation*", Proceedings of NEWRAD 2008: 10th International Conference on New Developments and Applications in Optical Radiometry", (Daejeon 2008), pp. 333-334

Measurement of the spatial distribution of the absolute transmittance of optical components at NPL

E. Theocharous

National Physical Laboratory, Teddington, TW11 0LW, UK
Corresponding e-mail address: e.theo@npl.co.uk

The result of a measurement of absolute transmittance corresponds to the average transmittance of the test sample over the area illuminated by the probe beam. This is usually sufficient when the test sample has spatially uniform transmittance. However, we have found that a number of optical components, such as non-linear crystals, bandpass filters and anti-reflection (AR) coated optical windows, exhibit large spatial variations in transmittance and therefore cannot be adequately quantified by a single, average, transmittance value. NPL has developed a facility which measures the spatially resolved absolute transmittance of optical components as large as 50 mm by 50 mm with a spatial resolution down to 8 μm. Measurements can be performed anywhere in the 300 nm to 20 μm wavelength range. This contribution will describe the facility and will provide examples of its use.

The NPL spatial uniformity of absolute transmittance measurement facility is based on the NPL spatial uniformity of response measurement facility [1] but with major modifications to the "detector chamber". Figure 1 shows the layout of the "detector chamber" of the new facility. Two optically polished Off-Axis Parabolic (OAP) mirrors are used to form a real image of the pinhole through which monochromatic radiation enters into the chamber. The real image is formed in the plane of the component under test. Radiation passing through the test sample is imaged onto the active area of the test detector. A pellicle beam splitter located immediately before the test piece (see Figure 1) diverts a fraction of the radiant power onto another detector, which provides a reference measurement which is used to eliminate the effects of any drifts in the radiation illuminating the test piece. The diameter of the spot illuminating the test piece is equal to the diameter of the pinhole and can be selected to vary from 8 μm to 3 mm. The wavelength is selected using bandpass filters placed immediately before the pinhole [1]. The test piece is placed on two computer-controlled linear translation stages which provide movement in the horizontal and vertical directions. This allows the probe spot to (sequentially) illuminate an area of the test piece up to 50 mm by 50 mm. Optical encoders ensure that the positioning accuracy of the spot on the sample is ± 2 μm in both the horizontal and vertical directions.

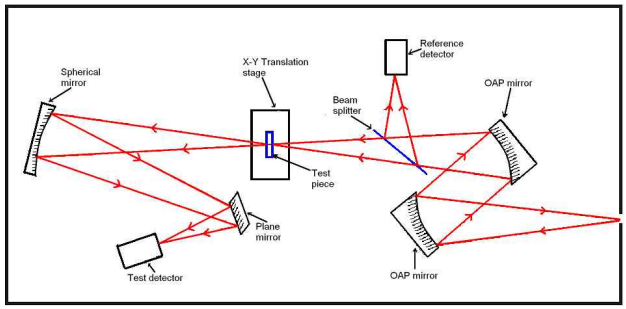

Figure 1: Layout of part of the facility for measuring the spatial distribution of the absolute transmittance of optical components.

The new facility has been used to measure the spatial distribution of transmittance of optical windows (CaF_2, ZnSe, KRS-5, fused silica and sapphire), bandpass filters, and anti-reflection (A/R) coated non-linear crystals. Examples of these measurements are summarised below.

An A/R-coated beta-barium borate (BBO) crystal is used to measure the detection efficiency of a photon counting device using correlated photons. When in use, a 2 mm diameter area of the crystal is illuminated by a laser. The absolute transmittance of this crystal is required to calculate the losses suffered by the signal photons from the point of down-conversion until they exit the crystal. The BBO crystal was mounted on a dedicated mount which allowed angular alignment of the crystal about two orthogonal axes passing through the centre of the crystal. Measurements could therefore be performed at any angle of incidence. The measurement wavelength was selected using bandpass filters (FWHM bandwidth of 10 nm). Measurements were carried out at 400 nm, 500 nm, 633 nm and 700 nm, with the axis of the incident beam normal to the BBO crystal surfaces, as well as at angles of incidence of 6° and 15°. The quasi-monochromatic radiation was focused to a 0.4 mm diameter spot in the plane of the BBO crystal. The

beam was focused on the crystal within an f/6.2 cone. Measurements were extended beyond the edge of the BBO crystal so each horizontal scan included at least 10 measurements for which the BBO crystal did not interrupt the beam. These latter measurements correspond to the radiant power incident on the crystal and were used to calculate the absolute transmittance of the BBO crystal during each horizontal scan.

Figure 2 shows the transmittance of the BBO crystal measured at 633 nm, at 6° angle of incidence, with 0.1 mm step. The uniform band on the right of the Figure indicates the radiant power (or 100% transmittance) measurements, taken when the crystal was not intersecting the beam. Figure 3 shows the transmittance of the BBO crystal measured at 500 nm, at normal angle of incidence, with 0.1 mm step. The absolute transmittance of the crystal at 500 nm is much lower than at 633 nm due to the 700 nm A/R coatings deposited on the crystal surfaces. However, the fine structure is reproduced in both figures.

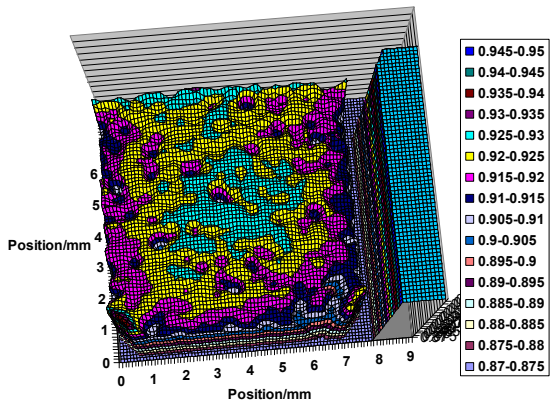

Figure 2: The transmittance of the BBO crystal measured at 633 nm, at 6° angle of incidence. The uniform band on the RHS indicates the radiant power measurements, taken when the crystal was not intersecting the beam.

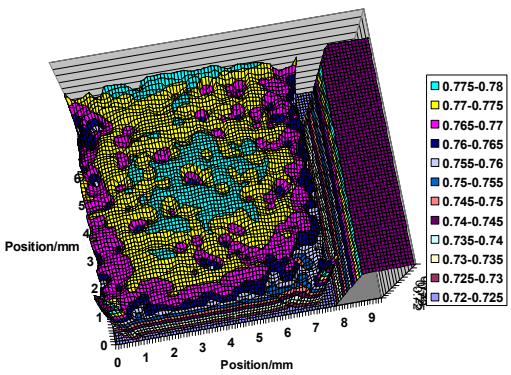

Figure 3. The transmittance of the BBO crystal measured at 500 nm, at 0° angle of incidence.

Figure 4 shows the spatial uniformity of transmittance of an 800 nm bandpass filter measured with a 0.6 mm diameter spot, at normal incidence. Periodic variations in transmittance of up to 2% are evident. Figure 5 shows the corresponding plot for a 720 nm bandpass filter which exhibits 10% variations in its transmittance.

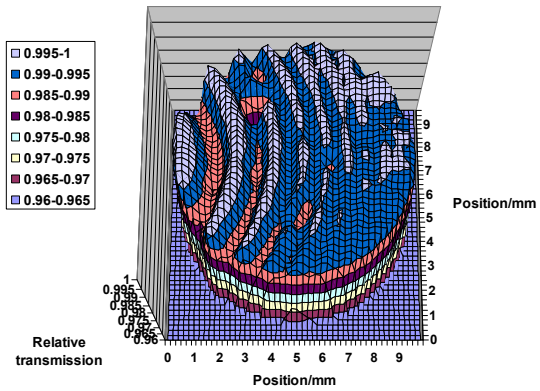

Figure 4: Transmittance of an 800 nm bandpass filter measured with a 0.6 mm diameter spot, at normal incidence.

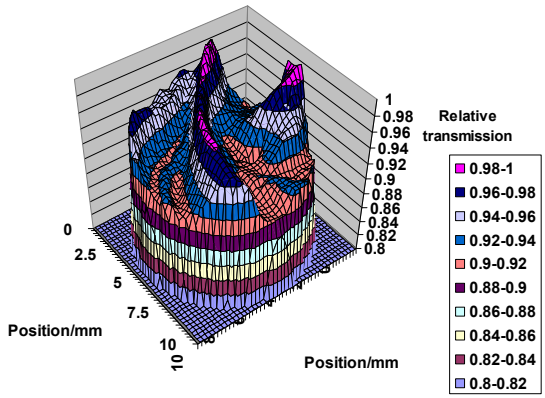

Figure 5: Transmittance of a 720 nm bandpass filter illuminated at normal incidence with a 0.4 mm diameter spot.

SUMMARY

The spatial uniformity of transmittance of most optical components evaluated was shown to exhibit fine structure which may introduce significant uncertainties in high accuracy radiometric measurements. NPL can routinely measure the spatial uniformity of transmittance of optical components in order to identify and select the component with the most uniform transmittance.

REFERENCES

1. E. Theocharous et al., Latest techniques at NPL for the characterisation of infrared detectors and materials, Proc. SPIE, 5209, 228-239, 2003.

Nonlinear Alignment Effect in Molecules Induced by Femtosecond Laser

Nan Xu, Jian Li, Jianwei Li and Zhixin Zhang

Division of Metrology in Optics and Laser
National Institute of Metrology
Beijing, China
e-mail: xunan@nim.ac.cn

A technique was present to nonintrusively measure the field-free alignment of molecules caused by femtosecond laser pulse. Based on the nonlinear Kerr effect, molecular alignment measurement can be employed for the study of interaction between laser and materials.

INTRODUCTION

When molecules are irradiated by strong laser field with intensity below the ionization threshold of molecules, the interaction between molecules and the laser electric field tends to align the molecules with the most polarizable axis along the laser polarization vector [1]. If the laser pulse duration is less than the molecular rotational period, the laser-molecule interaction gives the molecules a rapid "kick" to make the molecular axis toward the laser field vector. After extinction of the laser, the transient alignment can periodically revive as long as the coherence of the rotational wave packet is preserved, which called field-free alignment [2].

One-dimensional field-free alignment of molecules has been successfully dealt with by rotational wave packet theory, in which a rotational wave packet with an aligned many *J* hybrid is formed when molecules are irradiated by a strong laser pulse [3-5]. Following the short pulse, the molecules will evolve subject to the field-free Hamiltonian and move through a moment of collective alignment. Then they continue to rotate and the wave packet will dephase. But through a full rotational period, they will move through the collective alignment moment again. The degree of alignment of a rotational wave packet is given by the average of $\langle\cos^2\theta\rangle$, where θ is the angle between the molecular axis and the polarization vector of the laser field. $\langle\cos^2\theta\rangle = 1/3$ represents an isotropic angular distribution evenly distributed across all θ. If $\langle\cos^2\theta\rangle > 1/3$, the molecule is predominantly aligned along the laser polarization. If $\langle\cos^2\theta\rangle < 1/3$ the probability distribution for the molecular axis is concentrated around a plane orthogonal to the laser polarization. All the directions in this plane have the same probability and labeled as antialignment.

Due to the lower molecular density, field-free alignment of gas sample is more obvious than liquid and solid, which could be used in rapid detection of gas molecules. Results about field-free alignment of gas molecules (N_2, O_2, CO and N_2O) are present as follows at room temperature under the same laser properties.

The experimental results also demonstrated that gas mixture of N_2 and O_2 present a mixed alignment structure in which N_2 and O_2 present their own alignment structure. This result shows a feasibility of rapid detection of gas molecules.

EXPERIMENTAL SETUP

The laser pulse of 110fs was split into two parts to provide a strong energy pump beam and a weak energy probe beam both linearly polarized at 45° with respect to each other. The relative separated times between the two pulses is precisely adjusted using an optical translational stage controlled by a stepping motor. Both the pump beam and the probe beam are focused with a 30cm focal length lens into a 20cm long gas cell at a small angle. The gas cell was filled with different gases at room temperature under one atmosphere pressure at room temperature. After the cell, the depolarization of the probe, which represents the alignment degree, is analyzed with a polarizer set at 90° with respect to its initial polarization detection. The alignment signals and the reference laser signals were detected by two homotypical photoelectric cells and transformed into a computer via a four-channel A/D converter for analysis.

RESULTS AND DISCUSSION

Figure 1 shows the alignment signal for diatomic molecules (a) N_2, (b) O_2, and (c) CO irradiated by 800nm, 110fs at an intensity of 6×10^{13} W/cm^2. The classical rotational period T_r of molecules is determined by the equation $T_r = 1/2\ B_0 c$ where B_0 is rotational constant in the ground vibronic state and *c*

is the speed of the light. For N_2, O_2 and CO, B_0 is 2.010, 1.4456, 1.9772 cm^{-1}, respectively[13]. The corresponding rotational period T_r is therefore 8.3 ps for N_2, 11.6 ps for O_2 and 8.5 ps for CO. It is clearly noted from figure 1 that the alignment signal fully revives every molecular rotational period. However, there are also moments of strong alignment that occur at smaller intervals. The difference at quarter full revival for N_2, O_2 and CO can be well explained by the different nuclear spin weights of the even and odd J states in the initial distribution. At 1/4, 3/4, 5/4, … full revivals, the odd wave packet has maxima (minima) whereas the even wave packet has minima (maxima). For homonuclear diatomic molecules, the nuclear spin statistics controls the relative weights between even and odd J states. In the case of N_2, the relative weights of the even and odd J are 2:1. As a result, the temporary localization of the even wave packet at T_r /4 is only partially cancelled by its odd counterpart. Thus, some net N_2 alignment and antialignment is observed near t = n T_r /4, where n is an odd number. In the case of O_2, only odd J states are populated. Since only a single localized wave packet exists, strong net alignment and antialignment is observed near the time of a quarter revivals. For heteronuclear diatomic molecule CO, the even and odd J states are equally populated, the opposite localizations would cancel and therefore no net alignment would be observed at the time of the quarter revival.

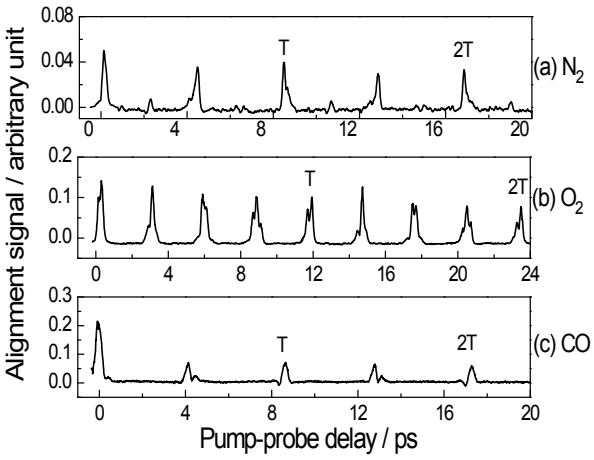

Figure 1. Alignment signal for (a) N2, (b) O2, and (c) CO

Figure 2 shows the alignment signal for (a) N_2, (b) O_2, and (c) air at room temperature under one atmosphere pressure. As we know, air mainly contains N_2 and O_2. It is clearly seen that alignment structure of gas sample can be derived from alignment signal of pure N_2 and O_2. It is possible that one can identify the component from gas mixture rapidly if the alignment structure of pure component is obtained. Precision of this alignment detection method just depends on the value of polarization anisotropy for different molecules.

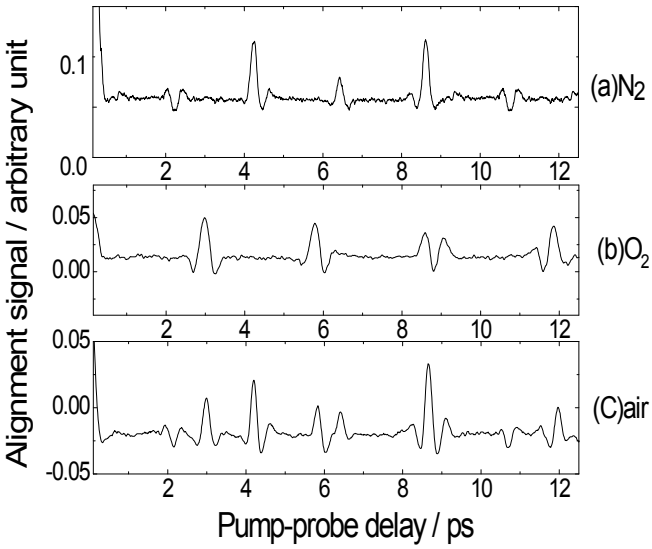

Figure 2. Alignment signal for (a) N2, (b) O2, and (c) air.

CONCLUSION

In summary, we have realized field-free alignment of N_2, O_2, CO and N_2O at room temperature using strong femtosecond laser pulses. Different gas samples present different alignment structure. We also demonstrated that N_2 and O_2 component can be identified by measuring alignment structure of an air sample. This result will promote the applications of femtosecond laser in air components analysis and other fields.

REFERENCES

1. Friedrich, B. and D.R. Herschbach, Polarization of Molecules Induced by Intense Nonresonant Laser Fields, J. Phys. Chem., 99, p. 15686,1995.
2. H. Stapelfeldt, T. Seideman, Controlling the rotation of asymmetric top molecules by the combination of a long and a short laser pulse, Rev. Mod. Phys., 75, 543, 2003.
3. T. Seideman, Revival structure of aligned rotational wave packets, Phys. Rev. Lett. 83, 4971, 1999.
4. F. Rosca-Pruna, M. J.J. Vrakking, Experimental Observation of Revival Structures in Picosecond Laser-Induced Alignment of I2, Phys. Rev. Lett., 87, 153902, 2001.
5. E. Hamilton, T. Seideman, T. Ejdrup, M.D. Poulsen, C.Z. Bisgaard, S.S. Viftrup, H. Stapelfeldt, Alignment of symmetric top molecules by short laser pulses, Phys. Rev. A, 72, 043402, 2005.

Filter Design for Detectors and Sources

N S Swift, J F Clare, K M Nield, and D M J Cochrane

Measurement Standards Laboratory (MSL), Industrial Research Ltd, Lower Hutt, New Zealand
Corresponding e-mail address: n.swift@irl.cri.nz

Many photometric and radiometric applications require the use of detectors and sources which provide defined spectral response or irradiance distributions, within narrow tolerances. The Measurements Standards Laboratory (MSL) has established coloured-glass filter design and fabrication capabilities with which we can produce detectors and sources more tightly specified than those available commercially. In recent years, this has been used for the design and manufacture of filters for photopic and scotopic detectors and a CIE D65 light source.

INTRODUCTION

The design process optimises filter thicknesses based on their internal transmittance. Calculations are performed with an algorithm which accounts for reflection from each glass-glass and air-glass interface, with no consideration given to the effects of glues between filter layers [1].

Designs with narrow tolerances require precise fabrication. The thinnest filter we accomplished was 69 µm thick, achieved by bonding it to a thicker filter within the designed stack. Although within 1 µm of its design, thicknesses of this magnitude can only be controlled to around 5 µm, glass type and surface area influencing how well this can be achieved. Parallelism between the two faces is important to maintain filter transmittance uniformity. We are typically able to achieve 20 arc seconds for a 50 mm diameter filter. These values compare with typical commercial tolerances of ± 0.1 mm in thickness and 3 arc minutes in parallelism.

DETECTOR: SCOTOPIC FILTER DESIGN

The response of the human eye varies with luminance and can be considered to be adapted to one of three regions: photopic, scotopic and mesopic response. At high luminance levels the response is considered to be photopic, at low luminance levels it is scotopic. Under mesopic conditions, the response of the eye is somewhere between photopic and scotopic. Two methods have been pursued recently to measure mesopic response: a brightness matching approach and a visual task performance approach. The latter culminated in CIE Technical Report 191:2010 [2] and requires measurement of the scotopic to photopic ratio. Good quality photopic instruments are well established, however demand for quality scotopic instruments is relatively new.

In line with the value most manufacturers quoted, the spectral mismatch of each design was assessed by calculation of the f_1' value, as performed when assessing photopic filters. Aiming to create filters of similar quality to these, values less than 3% are considered high quality [3], with some commercially available photopic instruments reported to have values less than 2% [3].

All commercial products examined appear to comprise a filter and photodiode configuration. The best was the Gigahertz-Optik VL-3705, which had a stated f_1' value of less than 5% with no further spectral data provided. Based on reading points from charts in manufacturers' literature, the International Light SPM068 and the Solar Light SL3101-02 were calculated to be around 5.8% and 8.8% respectively.

In contrast, our design shown in Figure 1 has a designed f_1' value of 1.66%. It is based on a combination of a silicon photodiode with three Schott coloured glass filters. Based on previous experience in creating photopic filters, it is anticipated the completed filters will be within 0.2% of this designed value.

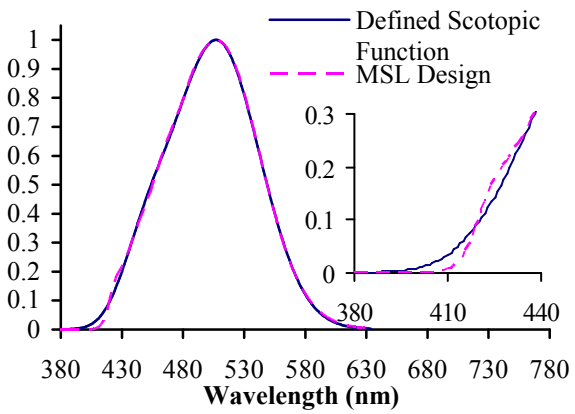

Figure 49. Comparison between the CIE defined scotopic response curve and the MSL designed scotopic

SOURCE: D65 FILTER DESIGN

The CIE D65 light source is defined to replicate daylight with a correlated colour temperature of 6500 K, its principal use being in colour measurement applications. A two-character rating is used to report the degree to which a source spectral distribution matches the D65 specification: the first character rates match within the visible range, and the second within the UV range of the spectrum, each rating being on a scale of A (excellent) to E (poor) [4]. Corrons [6] has created a D65 filter using a tungsten source with Schott filters and achieved a BB rating. Powell [7,8] designed a filter with a perfect AA rating using a multilayer interference filters but it is not clear if this was ever created and may suffer from temperature susceptibility. We require an implementation of this source with a BC rating or better to test the colour and luminance factor of high visibility fluorescent safety garments, as per the standard AS/NZS 1906.4:1997.

Filtered Tungsten lamps with a second UV source and fluorescent lamps are the most commonly used D65 sources today but can have their drawbacks [9]. The D65 source designed here is based on a filtered Xenon-arc source, Figure 2. The spectrum is matched in the visible and UV sections by a mosaic filter, consisting of a blue and a UV cut-off filter, in a manner similar to that employed by Corrons.

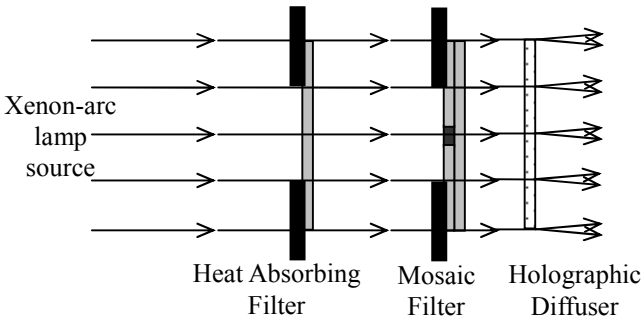

Figure 2. Configuration of MSL D65 filter.

In our design the mosaic components were placed in line with each other, rather than side by side, with the UV cut-off filter being in the form of a cross. This cross is designed to cover 36% of the total blue glass surface area when illuminated with a 35 mm beam. As the lamp ages and its spectral distribution changes, the diameter of the beam can be varied by means of the iris diameter to adjust the visible to UV filter ratio, thus maintaining the quality of the D65 source with age.

The spectral distribution of the final source in Figure 3 has a BA rating, meeting the spectral requirements for our intended use and is comparable in spectral quality with the best commercial sources as assessed to CIE 51.2. Using a 5 degree angle holographic diffuser, the source is designed to output light at less than 8 degrees divergence from normal and be spatially uniform with regards to intensity and spectral shape.

CONCLUSIONS

We have established a facility to meet the needs for high quality filter design and fabrication capabilities. The scotopic filter design is superior to commercial products reviewed before commencing work on the design. The D65 light source is spectrally comparable to the best in commercial products but has the advantages of improved uniformity and being adaptable to lamp ageing.

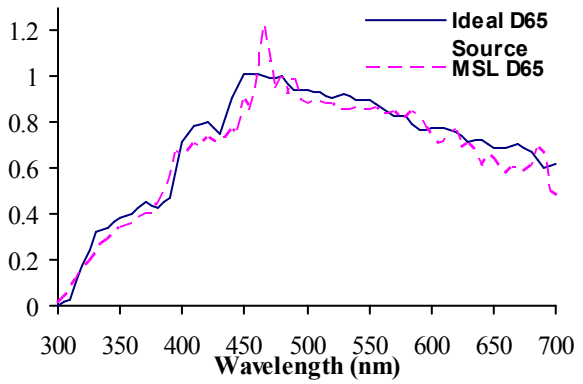

Figure 3. Comparison of the relative spectrum of the MSL-created D65 source with the defined CIE D65 source.

REFERENCES

1. J. F. Clare, Industrial Research Ltd Report 542, 1996.
2. CIE Technical Report: Recommended System for Mesopic Photometry Based on Visual Performance, CIE 191:2010.
3. C. DeCusatis, Handbook of Applied Photometry
4. CIE Technical Report: A Method for Assessing the Quality of Daylight Simulators for Colorimetry, CIE 51.2 - 1999.
5. Australian/New Zealand Standard: Retroreflective materials and devices for road traffic control purposes Part 4: High-Visibility materials for safety garments, AS/NZS 1906 4:1997.
6. A. Corrons, A. Pons, Applied Optics, **26**, 2867-2870, 1986.
7. I. Powell, Applied Optics, **35**, 6708-6713, 1996.
8. I. Powell, Applied Optics, **34**, 7986-7997, 1995.
9. CIE Technical Report: Practical Daylight Sources for Colorimetry, CIE 192:2010.

Research on Optical Return Loss Measurement Technologies

Zhixin Zhang, Jianwei Li, Nan Xu, Jian Li

National Institute of Metrology, Beijing, China

zhixinzhang@nim.ac.cn;lijw@nim.ac.cn;xunan@nim.ac.cn;jianl@nim.ac.cn;

This article promotes a new method to measure optical return losses using an optical circulator rather than a coupler. Comparing with the conventional coupler method, this solution can improve measurement precision significantly, and enable large-scale and continue measurements by adjusting the attenuator.

INTRODUCTION

In optical communication, optical transmission in devices is always accompanied by reflection. Optical return losses are optical powers lost in transmitters. Mainly caused by Fresnel reflection (produced by refractive index changes), Rayleigh backscattering (produced by impurity particles), direction and other factors, a return loss can be calculated as the difference between optical power of the incident ray and that of the reflected ray at an optical channel's input end. Disturbing optical communication or resulting in unstable source power, return losses harm reliability of optical communication networks. Comparing with the conventional coupler method, the circulator method, promoted in this article, can not only improve measurement precision, but also calibrate high-precise optical return loss meters.

MEASUREMENT SYSTEM

(1) Coupler Method for Optical Return Loss Measurement

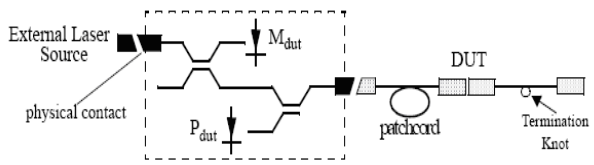

Figure 1. The principle of the coupler method

The principle of the coupler method is shown as figure1. An incident ray from the source comes into the 3dB coupler at the first input end, and goes out at the first output end, and then connects devices under test; and the ray reflected comes out of the coupler at the second input end, and then enters an optical d etector. Having measured out the photocurrent value by the optical detector, we can calculate out the optical return loss value. At present, most commercial optical-return-loss measuring instruments are abiding by this principle; in order to give correct readings, they must be calibrated before use by testing samples with known reflectance.

The major advantage of these instruments is low cost. Their disadvantages are：(a) the ray reflected disturbs the ray incident at input ends and results in unstable incident optical power；(b) optical signals reflected between 4 ends of the coupler always produce large noises; (c) optical signals always suffer high attenuation after crossing the 3dB coupler twice, so the measurement signals are weak, and the signal-to-noise ratio falls much.

The following diagram shows measurement results of optical return loss in a reflect mirror with tail fiber by the coupler method. Having measured 21 times, the standard deviation is 0.1dB.

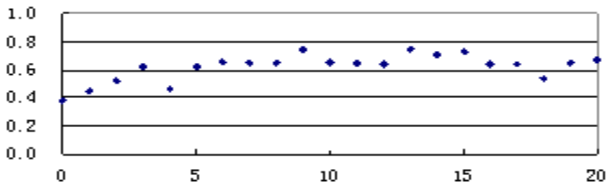

Figure 2. Results of Optical Return Loss Measured in Coupler Method

(2) Circulator Method for Optical Return Loss Measurement

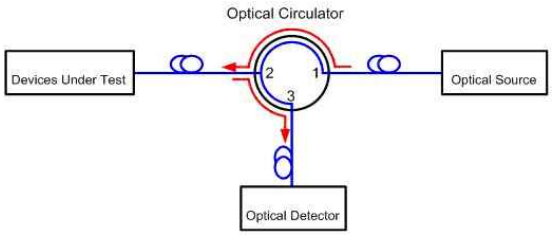

Figure 3. The circulator measurement method

The principle of the circulator measurement method is shown in Figure3. An incident ray enters the circulator at End 1, leaves at End 2, and connects devices under test; the ray reflected starts from End 2, leaves at End 3, and enters an optical detector finally. Having measured out the photocurrent value by the optical detector, we can calculate out the device's optical return loss value easily. An optical circulator features unidirectional transmission and low insertion

losses, signals can be transmitted from End 1 to 2 and from 2 to 3 only, reverse transmissions are forbidden. Having measured out the output optical power at End 2 and 3, and the insertion loss value from End 2 to 3, we can calculate out the sample's optical return loss precisely.

This method is superior in：(a) unidirectional laser transmission can eliminate interference phenomena, so can guarantee high stability; (b) low optical signal attenuation can guarantee strong signals, a high signal-to-noise ratio, and high measurement precision.

The following diagram shows optical return loss values of a reflect mirror with tail fiber measured by a circulator loss meter. After having measured 31 times, the standard deviation is 0.027dB, the precision has been improved greatly.

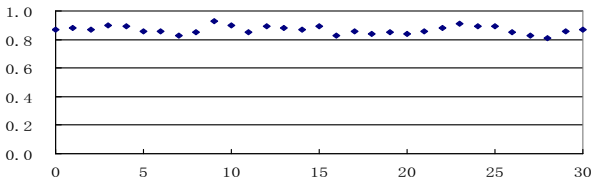

Figure 4. Optical return loss values of a reflect mirror with tail fiber measured by a circulator loss meter

(3) Circulator Method to Calibrate Optical Return Loss Meters

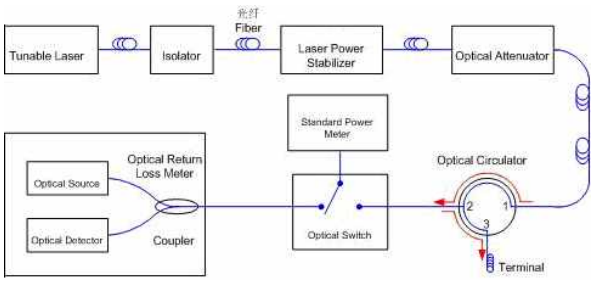

Figure5. The principle of the circulator calibration method

The principle of the circulator calibration method is shown in Figure5. Having measured the output power of an optical return loss meter with a standard power meter, if adjust the optical attenuator to unify the output power of the loss meter and the output power at End 2 of the circulator, and connect the loss meter to End 2, the optical power received by the loss meter, at this moment, will completely be the output power at End 2 of the circulator. If the power at End 2 equals the power received by the loss meter, the attenuator should read 0dB. Adjust the attenuator to unify the tow powers; values indicated on the attenuator will be the loss meter's actual readings. Thus, the loss meter can be calibrated by the standard power meter actually.

We have calibrated several imported optical return loss meters manufactured by various foreign companies; and each meter can be traced to a globally famous measurement standard laboratory. Small deviations of measurement results prove the accuracy of our calibration method from another point of view. The measurement results are as follows：

Table 1. Sample of RIFOCS's 585RL Mod Optical Return Loss Meter

Wave Length(nm)	Standard Value(dB)	Value Calibrated(dB)	Deviation(dB)
1310	5.5	5.6	0.1
1310	10.0	10.1	0.1
1310	20.0	20.1	0.1
1310	30.0	30.1	0.1
1310	40.0	40.1	0.1
1310	50.0	49.9	-0.1
1310	60.0	57.4	-2.6

Table 2. Sample of AI's AI9503A Mod Optical Return Loss Meter

Wave Length(nm)	Standard Value(dB)	Value Calibrated(dB)	Deviation(dB)
1300	5.000	4.91	-0.09
1300	10.000	9.90	-0.10
1300	30.000	29.93	-0.07
1300	50.000	49.89	-0.11
1300	60.000	59.94	-0.06
1550	10.17	10.16	-0.01

CONCLUSION

The conventional calibration method to test samples with known reflectance has the disadvantage of low precision which is caused by low accuracies of these samples' known reflectance and their susceptibility to application condition. The circulator calibration method can trace the loss meter to the standard power meter directly, so can prove the calibration precision greatly, and enable large-scale and continue measurements by adjusting the attenuator.

REFERENCES

1. Noutsios,P.C. Optical return loss measurements and simulation of an arbitrary array of concatenated reflective elements on field-installed optical links, 1697-1702,Journal of Lightwave Technology, 24(4),2006.

Characterization of Low Reflectance of NiP Ultra Black by FDTD Calculation

Kuniaki Amemiya[1], Daiji Fukuda[1], Takayuki Numata[1], Minoru Tanabe[1], and Yoshiro Ichino[1]

[1]*National Metrology Institute of Japan, Tsukuba, Japan*

Corresponding e-mail address: k.amemiya@aist.go.jp

NiP ultra black is used as an optical absorber of electrical substitution radiometers of NMIJ because of its excellent low reflectance for wide spectral range. However the origin of the low reflectance has not been clarified. Assuming a model of surface morphology of NiP ultra black, its spectral reflectance was calculated by finite-difference time domain (FDTD) method. It has been found that there exists a condition showing low reflectance of near and below 0.1 % for visible and near infrared region. Thickness and complex permittivity of absorption layer and aspect ratio of surface morphology are important parameters to determine the reflectance.

INTRODUCTION

NiP ultra black [1, 2] is used as an optical absorber having quite low reflectance of near and below 0.1 % for wide spectral range of visible and near infrared. It is used in electrical substitution radiometers of NMIJ such as laser calorimeters because it can be used as absorption plate, not optical trap cavity, and this leads to great advantage in high thermal equivalence of electrical substitution at room temperature, as well as low reflection loss.

Although NiP ultra black has such excellent properties, there are only some qualitative explanations about the low reflectance of NiP such that the oxidized nickel surface absorbs incident light and the surface random morphology assists as optical trap, and theoretically quantitative mechanism of the low reflectance has not been clarified in any reports.

In this paper, we report the results of theoretical calculation on the spectral reflectance of NiP ultra black by finite-difference time domain (FDTD) method assuming a model of its surface morphology.

FDTD CALCULATION

In this study, freely available FDTD calculation software package MEEP [3] was used. With MEEP, light wave propagation in dielectric materials can be calculated through *Scheme* script programming. In the script three-dimensional calculation field can be constructed by combining basic shaped volume

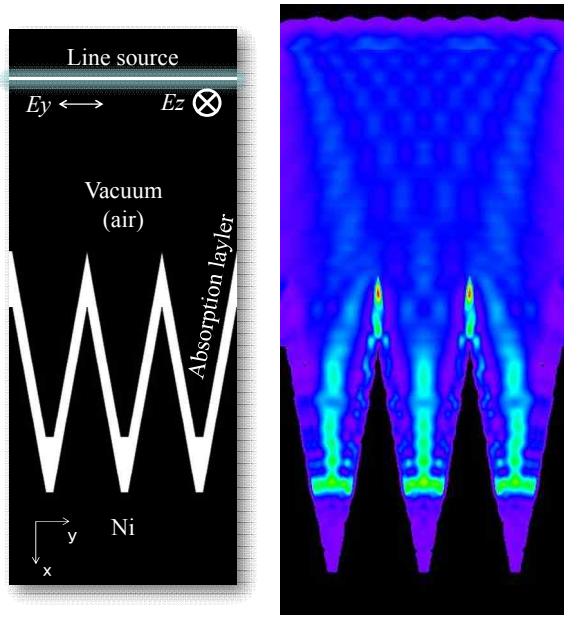

Figure 50. (Left) A model for FDTD calculation used in this study. (Right) An example of FDTD calculation result: electric field energy distribution.

elements (blocks, cylinders, cones and so on). We modelled surface morphology of NiP ultra black as shown in Fig. 1 (left). There are cone shaped pits on Ni metal substrate, and absorption layer of black nickel oxide on their surfaces: this model is based on a report by Brown et. al. [2].

Second, MEEP requires dielectric functions of corresponding target materials as parameters expressed in Lorentz model:

$$\varepsilon(\omega,\mathbf{x}) = (1 + i\sigma_D(\mathbf{x})/\omega)\times$$

$$[\varepsilon_\infty(\mathbf{x}) + \sum\nolimits_n \sigma_n(\mathbf{x})\omega_n^2/(\omega_n^2 - \omega^2 - i\omega\gamma_n)] \quad (1)$$

For Ni metal, the reported complex permittivity data [4] and Lorentz fitting parameters [5] were used. For black nickel oxide, the reported complex permittivity data [6] were used to derive Lorentz fitting parameters. Fig. 1 (Right) shows an example of FDTD calculation result, electric field energy distribution.

Calculations were performed in two-dimension (within x-y plane). Linear polarization of light source (line source) was assumed. Light wave of s-polarized (Ez) and p-polarized (Ey) to the cross section of absorber surface were investigated. Then spectral

reflectance was calculated for wavelength range from 400 nm to 1550 nm.

RESULTS

The calculated spectral reflectance is shown in Fig. 2. Thickness of absorption layer was about 600 nm, pit diameter and depth were 1 μm and 5 μm, respectively. For p-polarized light wave, the model showed quite low reflectance of near and below 0.1 % for wide spectral range from visible to near infrared. For s-polarized light, the model tends to have larger reflectance especially at near infrared region of over 1000 nm. Average of these two results may correspond to the reflectance for unpolarized light. Actual NiP ultra black shows quite low reflectance of about 0.1 % even at near infrared region, therefore the model used in this study was not so sufficient. Brown [2] reported that thickness of absorption layer is important for longer wavelength. Actually we also calculated for thinner absorption layer of about 300 nm and the spectral reflectance was larger especially at near infrared region. A little larger reflectance is also observed at shorter wavelength. This is probably because large imaginary part of permittivity at shorter wavelength causes large reflectance. It is reported [1, 2] that actual NiP ultra black products have as small reflectance at shorter wavelength (400 nm –) as at medium wavelength (600 nm – 1000 nm). In this simulation, assumption of smooth surface of absorption layer may affect the calculation results although actual surface morphology of NiP ultra black is more complicated. Aspect ratio of absorption pit in calculation model was also found to be important. This implies that the absorption pit should work as optical trap for quite low reflectance.

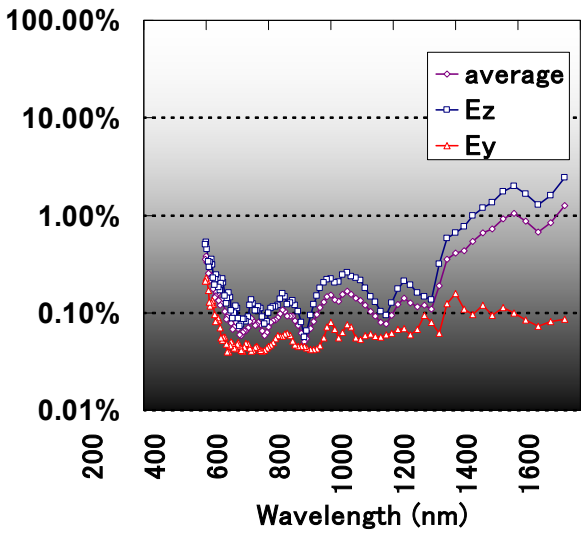

Figure 51. Calculated spectral reflectance of the NiP ultra black model.

CONCLUTION

We have demonstrated theoretical calculation on the spectral reflectance of NiP ultra black by FDTD method. It has been found that there exists a condition showing low reflectance of near and below 0.1 % for visible and near infrared region. To obtain quite low reflectance for wide spectral range, (1) thicker absorption layer enough to absorb most of incident light of longer wavelength, (2) not too large imaginary part of permittivity of absorption layer at shorter wavelength and (3) appropriate aspect ratio of absorption pit to work as optical trap are important. Actual NiP ultra black products probably satisfy these conditions. The simulation model used in this study was not so sufficient to explain the quite low reflectance especially at longer wavelength (1200 nm –). Further simulation with more practical model of surface morphology and its validation comparing with experimental data is future work, and it will be helpful to quantification and its uncertainty analysis of the reflectance of NiP ultra black.

REFERENCES

1. S. Kodama, M. Horiuchi, T. Kunii, K. Kuroda, Ultra-black nickel-phosphorus alloy optical absorber, IEEE IM, 39, 230-232, 1990.
2. R.J.C. Brown, P.J. Brewer, M.J.T. Milton, The physical and chemical properties of electroless nickel-phosphorus alloys and low reflectance nickel-phosphorus black surfaces, Journal of Material Chemistry, 12 2749-2754, 2002.
3. A.F. Oskooi, D. Roundy, M. Ibanescu, P. Bermel, J.D. Joannopoulos, S.G. Johnson, MEEP: A flexible free-software package for electromagnetic simulations by the FDTD method, Computer Physics Communications 181, 687–702, 2010.
4. Landolt-Börnstein, New Series III/15b, Metals: Electronic Transport Phenomena: Electrical Resistivity, Thermoelectrical Power and Optical Properties, 1985.
5. W.H.P. Pernice et al., An FDTD method for the simulation of dispersive metallic structures, Optical and Quantum Electronics 38, 843–856, 2006.
6. T.D. Kang, H.S. Lee, H. Lee, Optical properties of black NiO and CoO single crystals studied with spectroscopic ellipsometry, J. Korean Phys. Soc., 50, 632-637, 2007.

ARGon^3 – "3D Appearance Robot-based Gonioreflectometer" at PTB

Andreas Höpe, Tatsiana Atamas, Dirk Hünerhoff, Sven Teichert and Kai-Olaf Hauer

Physikalisch-Technische Bundesanstalt (PTB), Bundesallee 100, 38116 Braunschweig
Corresponding e-mail address: andreas.hoepe@ptb.de

At the Physikalisch-Technische Bundesanstalt (PTB) a new facility for measuring appearance-related quantities has been built-up. The acronym ARGon^3 stands for "3D Appearance Robot-based Gonioreflectometer". There are two main features within the new setup. A photometric luminance camera with a spatial resolution of 28 µm on the device under test, enables spatially high-resolved measurements of luminance and colour coordinates. A line-scan camera mounted to a spectrograph provides measurements of the radiance factor, respectively the BRDF, in full $V(\lambda)$-range with arbitrary angles of irradiation and detection relative to the surface normal, on a time scale of about 2 minutes.

INTRODUCTION

The visual appearance of commercial products is becoming more and more relevant to industry. There are increasing requirements from such different branches like for instance automotive, cosmetics and printing industry. Driving force behind this common ground are new goniochromatic materials which have a strong angular dependent reflection behaviour and hence show an colour impression that depends on the spatial arrangement of illumination and observation relative to the surface of the artefact.

Based on this conditions an increased demand on multi-geometry calibrations exceeding the conventional geometries of 45:0 and 0:45 recommended by CIE are noticed. In order to describe the colorimetric behaviour of effect pigmented surfaces, multitude reflection spectra for varying geometric configurations must be recorded. Typical calibration times for the spectral radiance factor in a certain geometry in $V(\lambda)$-range exceed several hours, with iteration measurements in order to have statistical significance, a whole day for data from one geometry must be estimated. With these constraints it is nearly impossible to adequately describe goniochromatic materials where dozens of geometric configurations must be mapped.

This was the reason for setting up a new facility at PTB especially for the measurement and calibration of appearance-related quantities. The main goals were to speed up measuring time and to improve spatial resolution on the device under test.

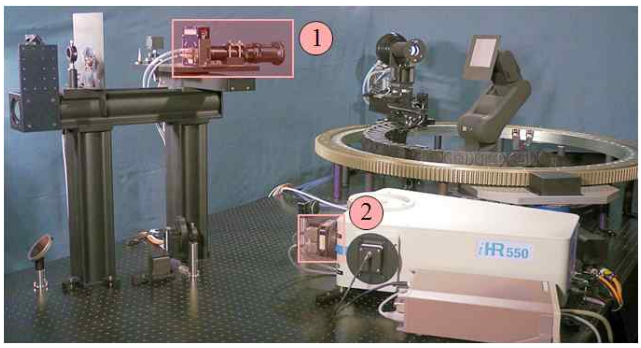

Figure 52. Photo showing the setup of the ARGon^3 facility. ① is a high-resolution video photometer system. ② is a line-scan camera module attached to an imaging spectrograph.

TECHNICAL DATA OF THE NEW FACILITY

The basic layout of the new facility is similar to the already existing and in several publications well described standard robot-based gonioreflectometer at PTB [1- 4]. It as well consists of a large rotation stage carrying the irradiating lamp, which is a small integrating sphere equipped with an internal 400 W quartz halogen lamp. In addition, a second lamp producing a D65-like illuminant is applied for measurements with the luminance camera system. In the centre of the rotation stage a five-axis industrial robot is located. This robot serves as a holder for the

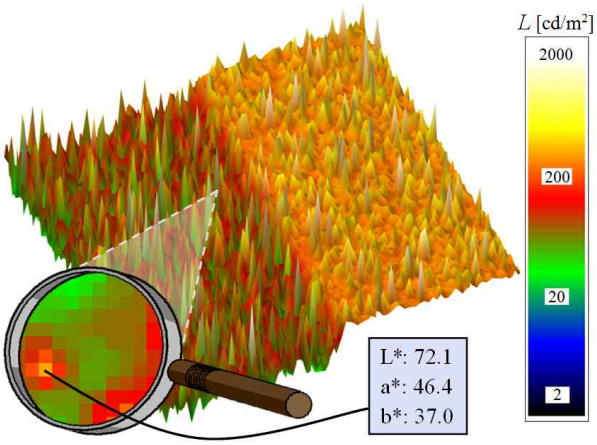

Figure 2. Spatially high resolved luminance distribution of an effect pigment (Xirona® Volcanic Sparks) applied on two different backgrounds (black/white).

sample under test (see Fig. 1). The combined adjustment of the rotation stage and the robot allows full angular control of the incident and reflected radiation within the full half space above the surface of the sample, accomplishing also measurement of "out-of-plane" reflection, where the direction vectors of irradiation and observation and also the vector of the sample normal are not lying in a common plane.

The main features of the new facility are two different camera systems as can be seen in Fig. 1. Device number ① is a video photometer system with an implemented CCD-sensor with 1364 x 1030 Pixels, having a field of view of 38 x 28 mm. It is capable to measure spatially resolved luminance distributions $L(x,y)$ with a resolution on the sample under test of approx. 28 µm. By means of the build-in filter wheel also tristimulus values can be determined. This enables the imaging measurement of chromaticity coordinates with the same spatial resolution, which can be given in user-defined colour spaces. Fig. 2 shows a high resolution luminance picture displayed in 3D-false colour presentation of an effect pigmented lacquering measured in 15:0 "in-plane" geometry. The pigment is applied on two different groundings (black and white) where the lower luminance values belong to the black background. The needle-like structure, which is called "sparkling", comes from semitransparent or transparent layers applied on metal oxide-coated aluminium or mica. If one zooms into the picture colour coordinates in L*a*b*-colour space can be determined with the spatial resolution of the imaging system of about 28 µm (see Fig. 2).

Device number ② is a 1036 Pixel, 16 Bit, line-scan camera module attached to the ½-meter imaging spectrograph in the detection path for measuring the spectral radiance factor. With a 150 g/mm grating the spectral coverage in the visible range is 290 nm in a single-shot. Fig. 3 shows a measurement of the spectral radiance factor composed of two parts. The centre wavelengths were adjusted to 500 nm and 700 nm (blue arrows in Fig. 3) giving the green and red colored curves which results together in full $V(\lambda)$-range resolution. The sample under test is a mica-based effect pigment (Iriodin® 7215 ultra red) printed on a black paper (Pop´Set 87). For the non-standard measurement geometry 65:-80 radiance factor values of up to a value of 9.77 were achieved, showing the strong non-lambertain reflection behavior of the interference effect pigment. From the displayed spectrum CIELab colour coordinates were calculated, giving L* = 228 ; a* = 10.8 ; b* = 24.2 for the 2° standard observer under illuminant D65. The time frame for acquiring this absolute measurement of the spectral radiance factor in full $V(\lambda)$-range was about 2 minutes. This is about a factor of 100 faster as with our standard gonioreflectometer when measuring with a monochromator and a single element detector at a wavelength spacing of the data points of 10 nm [5].

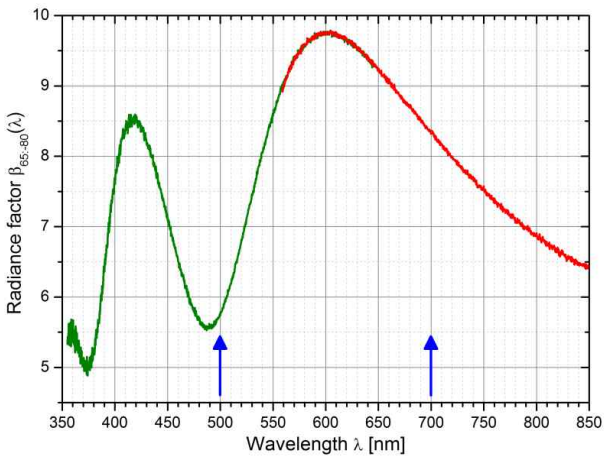

Figure 3. Spectral radiance factor of a printed effect pigment (Iriodin® 7215 ultra red printed on Pop´Set 87 black) measured in 65:-80 geometry.

ACKNOWLEDGMENTS

The authors thank B. Campe for construction and building several parts of the new facility.

Tatsiana Atamas appreciates the support of the Braunschweig International Graduate School of Metrology (IGSM).

REFERENCES

1. D. Hünerhoff, U. Grusemann, A. Höpe, New robot-based gonioreflectometer for measuring spectral diffuse reflection, Metrologia, 43, S11-S16, 2006.
2. S. Holopainen, F. Manoocheri, E. Ikonen, K.-O. Hauer, A. Höpe, Comparison measurements of 0:45 radiance factor and goniometrically determined diffuse reflectance, Applied Optics, 48, 2946-2956, 2009.
3. K.-O. Hauer, A. Höpe, High-Grade Uniform Light Source for Radiometric and Photometric Applications, MAPAN - Journal of the Metrology Society of India, 24, 175-182, 2009.
4. A. Höpe, K.-O. Hauer, Three-dimensional appearance characterisation of diffuse standard reflection materials, Metrologia, 47, 295-304, 2010.
5. A. Höpe, K.-O. Hauer, T. Atamas, K. Kehren, Appearance of printed interference effect ink in commercially used multi-geometry configurations, 2nd CIE Expert Symposium on Appearance - When

appearance meets lighting…, Ghent, Belgium, 08. - 10. September 2010.

Comparison of the bidirectional diffuse reflection scales of PTB and NRC in the $V(\lambda)$-range

Réjean Baribeau[1], William S. Neil[1], Kai-Olaf Hauer[2] and Andreas Höpe[2]

[1]*NRC Institute for National Measurement Standards, 1200 Montreal Road, Ottawa, Canada*
[2]*Physikalisch-Technische Bundesanstalt (PTB), Bundesallee 100, 38116 Braunschweig*
Corresponding e-mail address: rejean.baribeau@nrc-cnrc.gc.ca

The scales of goniometric determined spectral diffuse reflection, referred as radiance factor or bidirectional reflectance distribution function (BRDF), of the Physikalisch-Technische Bundesanstalt (PTB) and the National Research Council (NRC) has been compared in the $V(\lambda)$-range. The comparison includes measurements in five distinct geometries. These are the bidirectional geometries of 45:-30, 45:-20, 45:0, 45:30 and 45:65 as recommended in DIN 6175-2 and ASTM E2539-08. Both institutes operate similar layouts of robot-based gonioreflectometer facilities, but with different types of detection of the reflected radiation. Four different types of samples have been investigated: A matt white ceramic tile, a primed barium sulphate standard, an opal glass and a standard made of vapour-blasted aluminium.

INTRODUCTION

The scales of diffuse reflection in different geometrical configurations, like integrating sphere and goniometric setups, have manifold applications in various industrial areas. Due to extended customer requirements, there is currently an increased demand on goniometric measurements. Especially multi-geometry calibrations exceeding the conventional geometries of 45:0 and 0:45 recommended by CIE are of interest. This is given by the fact that so called goniocromatic materials and paints are entering more and more the product line-up of consumer goods.

International standardization has responded by the formulation of standards with an extended number of recommended goniometric reflection geometries. In DIN 6175-2 and ASTM E2539-08 [1, 2], a total number of five geometries is approved. All of them are so called "in-plane"-geometries, were the direction vectors of incidence, reflection and surface normal are all lying in one plane. They comprise an irradiation of the sample under 45°, followed by a detection at selected reflection angles of -30°, -20°, 0°, 30° and 65°, leading to the angular pairs of 45:-30, 45:-20, 45:0, 45:30 and 45:65 in CIE-notation (CIE: International Commission on Illumination).

INSTRUMENTATION AND LAYOUT OF THE FACILITES

PTB and NRC are both operating robot-based gonioreflectometer facilities which are able to perform measurements on the bidirectional diffuse reflection within the full half-space above the sample under test [3, 4]. In both setups a small 5-axis

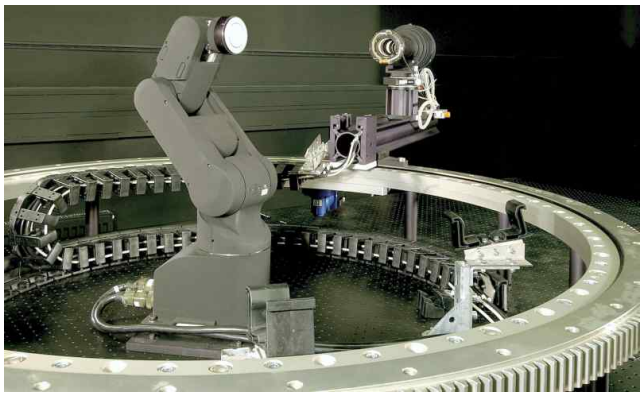

Figure 1. Photo showing part of the setup of the robot-based gonioreflectometer at PTB.

industrial robot (Mitsubishi Electric RV-2AJ) serves as the specimen holder (see Fig. 1 and 2). Also the lamp design for the irradiation of the sample is similar for both systems. PTB uses a mid-sized water cooled integrating sphere (inner diameter 150 mm)

Figure 2. Photo of the setup of the robot-based gonioreflectometer at NRC.

internally coated with barium sulphate and equipped with a 400 W quartz halogen lamp [5]. The extended uniform light source at NRC is realized by a 100 W lamp mounted inside of a 100 mm integrating sphere.

There are differences in the layout of the detection systems between the PTB and NRC setups. PTB uses a mirror-based imaging system to couple the reflected light into a triple grating monochromator. In order to span the wavelength range from 250 nm to 1700 nm it can be equipped with four different single element detectors. The detection system at NRC consists of a diode array imaging spectroradiometer that is capable to record a complete spectrum between 380 nm and 780 nm in a single measurement.

ARTIFACTS OF THE COMPARISON AND ACCOMPLISED MEASUREMENTS

For the comparison a set of 4 different types of reflection standards was selected in order to have a variety of materials and surface structures. The artefacts comprise two samples from each institute. They are measured first at the home-institute and then exchanged for the comparison. The investigated samples are: A matt white ceramic tile from CERAM, a barium sulphate based standard made of primed $BaSO_4$-powder manufactured at PTB, a SRM 2017 opal glass and a vapour-blasted aluminium standard prepared at NRC.

The standards were measured for their spectral radiance factor in the 5 previous mentioned geometries in $V(\lambda)$-range. Beside this, a reflection indicatrix for 45° incidence angle with angular resolved reflection every 2° in the range of $\alpha_r = \pm 85°$ relative to the sample normal was measured for wavelengths between 400 nm and 700 nm with a wavelength spacing of 50 nm (see Fig. 3).

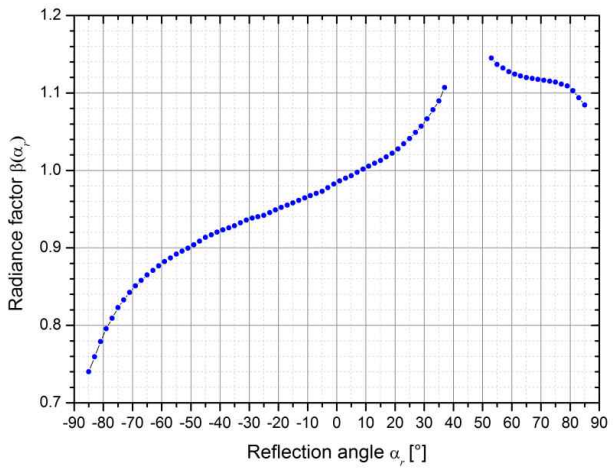

Figure 3. Angular resolved reflection indicatrix for a primed barium sulphate reflection standard at a wavelength of 550 nm measured at PTB.

At the conference we will present the full results of the comparison measurements, including uncertainty budgets and an analysis of the data.

REFERENCES

1. DIN 6175-2 Farbtoleranzen für Automobillackierungen - Teil 2: Effektlackierungen (Tolerances for automotive paints - Part 2: Goniochromatic paints), 2001-03, Beuth Verlag GmbH, 10772 Berlin.
2. ASTM E2539 - 08 Standard Practice for Multiangle Color Measurement of Interference Pigments, ASTM International, West Conshohocken, PA, 2008.
3. D. Hünerhoff, U. Grusemann, A. Höpe, New robot-based gonioreflectometer for measuring spectral diffuse reflection, Metrologia, 43, S11-S16, 2006.
4. R. Baribeau, W.S. Neil, E. Côté, Development of a robot-based gonioreflectometer for spectral BRDF measurement, Journal of Modern Optics, 56, 1497-1503, 2009.
5. K.-O. Hauer, A. Höpe, High-Grade Uniform Light Source for Radiometric and Photometric Applications, MAPAN - Journal of the Metrology Society of India, 24, 175-182, 2009.

The measurement of the Centre of Gravity of six absorption lines in an M-42 filter at cryogenic temperatures for the NIRSpec instrument.

C. J. Chunnilall[1], E. Theocharous[1], J. Ireland[1] and R. Cole[2]

[1]*National Physical Laboratory, Teddington, TW11 0LW, UK*
[2]*MSSL, UCL, Holmbury St. Mary, RH5 6NT, UK*
Corresponding e-mail address: christopher.chunnilall@npl.co.uk

An erbium-doped M-42 filter is to provide the wavelength calibration of the NIRSpec instrument to be flown in space as part of the James Webb Space Telescope (JWST). This paper describes the measurement of the Centre of Gravity (CoG) of six spectral absorption lines of such a filter in the 1.45 μm to 1.55 μm wavelength range with an uncertainty of less than 1 part in 100,000 of the centre wavelength. These measurements were carried out at five different cryogenic temperatures.

METHOD

An M-42[2] filter is being used for the wavelength calibration of the spectrometer to be flown in space as part of the NIRSpec instrument on the JWST. NPL was asked to measure the Centre of Gravity[3] (CoG) of six spectral absorption lines in the M-42 filter in the 1.45 μm to 1.55 μm wavelength range with an uncertainty of 1/100,000 of the centre wavelength at five different cryogenic temperatures in the 30 K to 50 K temperature range to identify any temperature dependency in the CoG of these lines.

Figure 1 shows the experimental set-up. The filter was illuminated using a tungsten strip lamp with a 2 mm wide filament. The lamp filament was imaged using a spherical mirror, M1, onto a small circular aperture so that the real image of the filament overfilled this aperture. Radiation passing through this aperture was steered using a plane mirror M2 and re-imaged using a gold-coated spherical mirror M3. Radiation was incident on the M-42 filter in an f/28 configuration. The two spherical mirrors were operated with the off-axis angles as small as possible in order to minimise aberrations.

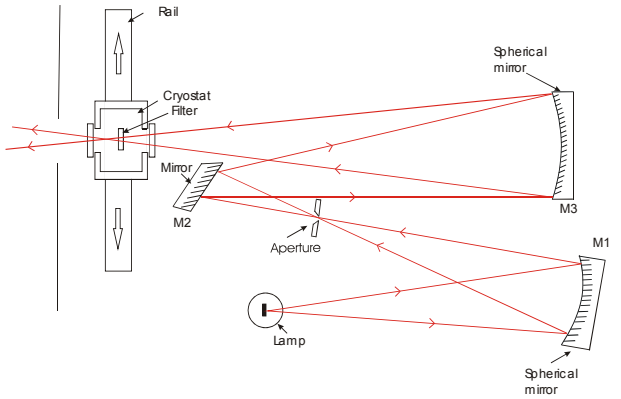

Figure 53: Layout for the measurement of the CoG of the absorption lines of the M-42 filter at different cryogenic temperatures.

A Bomem DA8.2 FT spectrometer was used to analyse spectrally the radiation transmitted by the M-42 filter, since the high wavelength accuracy and spectral resolution of an FT spectrometer was suited to this task. The spectrometer had an f/4 acceptance cone so all radiation passing through the filter was captured by the spectrometer. An instrumental line width of 0.5 cm^{-1} (0.11 nm – 0.12 nm) was used.

The M-42 filter was 18 mm in diameter and 0.38 mm thick. It was mounted on the cold finger of an Oxford Instruments mechanically cooled CCC1104 cryostat controlled by an ITC503 temperature controller. The cryostat was mounted immediately in front of the entrance aperture of the FT spectrometer on a linear translation stage which allowed the periodic insertion of the cryostat assembly into the optical beam and its subsequent removal from the beam. This allowed the measurement of the combined transmission of the filter plus cryostat windows.

Measurements were carried out at 30 K, 35 K, 40 K, 45 K and 50 K. At each change in temperature, the sample was allowed to stabilise overnight prior to taking measurements. The temperature of the cold finger of the cryostat was actively controlled. A second calibrated temperature sensor (LakeShore

[2] The "M-42" filter is a monocrystalline erbium-doped YAG $[(Y_{1.5}\ Er_{1.5})Al_2(AlO_4)_3]$, supplied by Nelson Gemmological Instruments, 1 Lyndhurst Road, London NW3 5PX, UK.

[3] Centre of Gravity (CoG) of a spectral line is defined as the intensity-weighted mean of the wavelength over the core of the line, i.e. over its full width at half maximum (FWHM).

Rh-Fe sensor Model No RF-100T-BC-4L) was used to read the temperature of the block on which the M-42 filter was mounted. The uncertainty with which this temperature was measured was ±0.025 K.

The wavelength axis of the spectrometer was calibrated using the tabulated atmospheric absorption lines of H_2O[4]. The uncertainty budget also took account of the other significant factors, viz. the angular illumination of the M-42 filter, the refractive index variation of air, filter temperature effects and stray light. The effects of atmospheric absorption, window transmittance, inter-reflections, polarisation, beam displacement due to introduction of the sample into the beam, and sample fluorescence were all found to be insignificant to the accuracy of the wavelength axis.

RESULTS

The M42 filter has numerous absorption lines in the 1.45 μm to 1.55 μm wavelength range. Six of these lines were selected for measurement of their CoG.

Figure 2 shows the transmission profiles of the M-42 filter in the 1.44 μm to 1.5 μm wavelength range, recorded at 30 K, 35 K, 40 K, 45 K and 50 K.

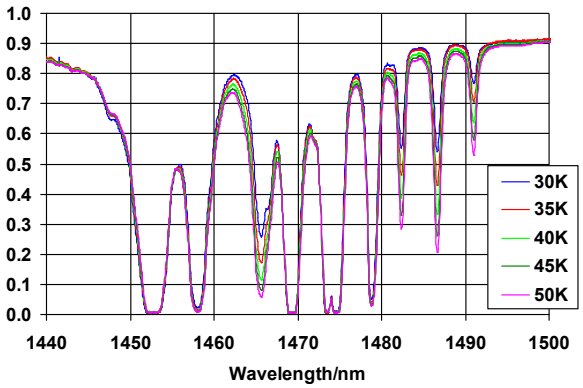

Figure 2: Transmission profiles of the M-42 filter in the 1.44 μm to 1.5 μm wavelength range at five different temperatures.

Figure 3 shows the transmission profile of the M-42 filter in the vicinity of the 1487 nm absorption line at five different temperatures. From this data, the values of the CoG of this line were calculated at these temperatures. The procedure used to calculate the CoG of these absorption lines is described elsewhere [1]. Figure 4 shows the plot of the CoG of the 1478.8 nm band measured at the five temperatures, along with the best straight line fit. From this plot, the temperature coefficient of the CoG of this line was calculated.

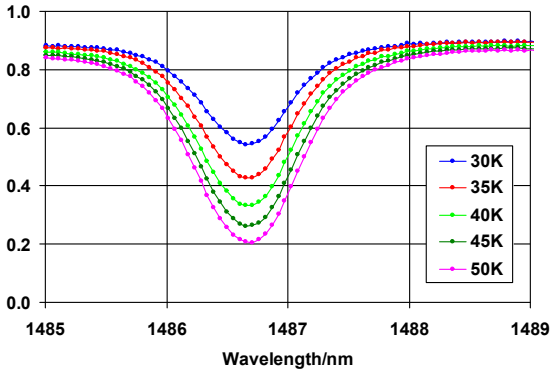

Figure 3: Transmission profile of the M-42 filter in the vicinity of the 1487 nm absorption line, recorded at five different cryogenic temperatures. For clarity, every fourth data point is shown.

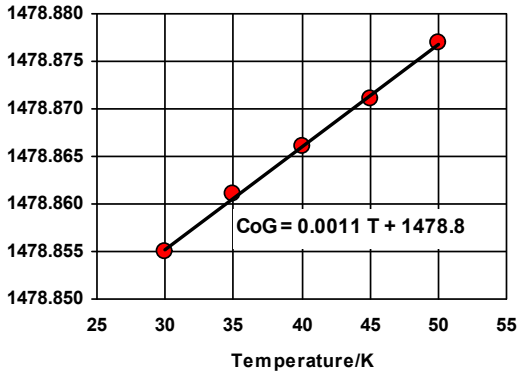

Figure 4: Plot of the measured CoG of the 1478.8 nm band versus filter temperature.

The Centre of Gravity of six spectral absorption bands in an erbium-doped M-42 filter was measured in the 1.45 μm to 1.55 μm wavelength range with an uncertainty of better than 1 part in 10^5 between 30 K and 50 K. The temperature dependence of five of the features was found to be less than 0.001 nm K^{-1}, the exception being the feature at 1478 nm. It was also observed that the intensity of some features increased with temperature, while that of others decreased. This can be explained in terms of the thermal population of the energy states involved in these transitions. The experimental process and its uncertainties, together with the observed temperature-dependant spectral behaviour of the filter will be discussed.

REFERENCES

1. D G Cameron, J K Kauppinen, D J Moffat and H H Mantsch, Precision in Condensed Phase Vibrational

[4] http://cfa-www.harvard.edu/HITRAN/

Spectroscopy, Applied Spectroscopy, 36, 245-250, 1982.

Spectral and geometrical comparison of the Bidirectional Reflectance Distribution Function (BRDF) of diffuse reflectance standards

Alejandro Ferrero, Ana M. Rabal, Joaquín Campos, Alicia Pons, M. Luisa Hernanz, Antonio Corróns

Instituto de Óptica, Consejo Superior de Investigaciones Científicas (CSIC), Madrid, Spain.
Corresponding e-mail address: alejandro.ferrero@csic.es

A spectral and geometrical comparison of the Bidirectional Reflectance Distribution Function of three common diffuse reflectance reference materials (Barium Sulphate, Spectralon and white Russian opal glass) is accomplished through this work. BRDF measurements were carried out using the new gonio-spectrophotometer developed at Instituto de Óptica in CSIC that allows for spectral, absolute and out-of-incidence-plane BRDF determination.

INTRODUCTION

Realization, maintenance and dissemination of the diffuse reflectance scale are important issues of Radiometry and Photometry. The transfer of this scale is done by the calibration of diffuse reflection standards in specific illumination-reflection directions. A spectral and geometrical comparison of the reflectance distribution of some of these standards is accomplished through this work.

The reflection of the incident optical radiation by a surface is characterized by its Bidirectional Reflectance Distribution Function (BRDF) that expresses the radiation reflected by the surface in every direction by irradiance unit in every illumination direction [1]. This function depends both on the illumination-reflection geometry as well as on the wavelength. The new gonio-spectrophotometer developed at Instituto de Óptica in CSIC allows spectral (380 nm -780 nm), absolute and out-of-incidence-plane BRDF measurements of samples to be made in a fast and automatic way [

2].

The diffuse reflection materials characterized in this work were:

(1) Polished white Russian opal glass, used by.NIST for its Multi-Angle White Reflectance Standards
(2) Spectralon: sintered polytetrafluoroethylene (PTFE).
(3) Pressed barium sulphate ($BaSO_4$) powder: prepared in our laboratory prior to the measurement.

RESULTS

BRDF measurements of Barium Sulphate, Spectralon and polished white russian opal glass at 500 nm on the incidence plane are shown in Fig. 1 (the half plane containing the incident direction corresponds to negative θ_i and the half plane containing the specular direction to negative θ_i). For the sake of the comparison, the ideal constant value $1/\pi$, i.e. the

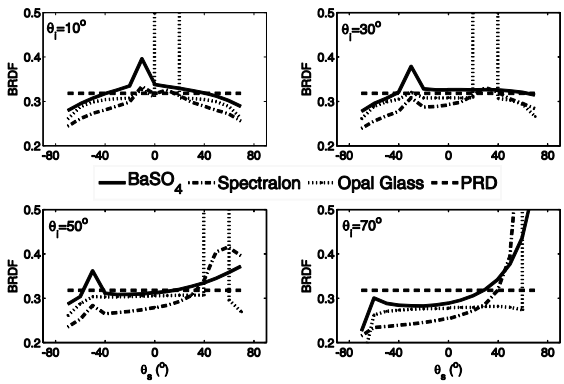

Figure 1. BRDF measurements of Barium Sulphate, Spectralon and polished white Russian opal glass at 500 nm, on the incidencet plane.

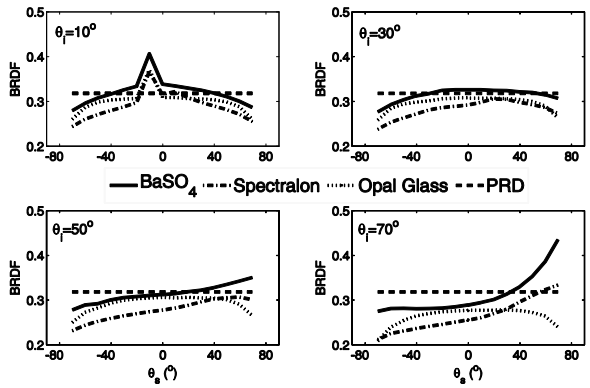

Figure 2. BRDF measurements of Barium Sulphate, Spectralon and polished white Russian opal glass at 500 nm, in the half planes 30º apart from the half planes containing incident direction and specular reflection.

BRDF for the Perfectly Reflecting Diffuser (PRD) is also plotted.

In a similar way, out-of-plane BRDF measurements are shown in Fig. 2. In this case, the half planes 30º apart from the half planes containing incident direction (negative θ_i) and specular reflection (positive θ_i) are represented.

Since the present spectral fingerprint correction of our non-scanning spectral system is not enough to distinguish the small spectral features of these materials, the comparison was made relative to the Barium Sulphate. An illumination/reflection configuration was chosen where Barium Sulphate's BRDF is almost $1/\pi$ (45:30, in the half plane containing the illumination direction) and a flat spectral BRDF was assumed. Under this assumption, dividing a sample's BRDF by Barium Sulphate's BRDF is exactly the radiance factor. The radiance factor of NIST standard was calculated way for the configuration 45:30 and is shown in Fig. 3. The NIST-certificated data for the NIST standard is also plotted (expanded uncertainty = 0.64%). The comparison proves that our system and procedures allow absolute BRDF measurements to be carried out.

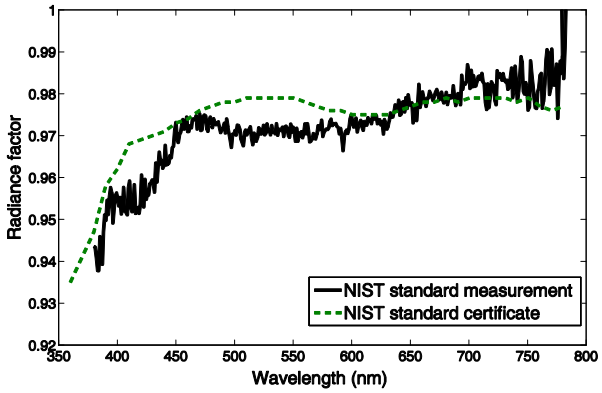

Figure 3. Measured spectral radiance factor of NIST standard (measured and NIST-certificated). Configuration 45:30, in the half plane containing the illumination direction.

DISCUSSION

According to Fig. 1 and Fig. 2, the BRDF measurements show that pressed Barium Sulphate has a higher BRDF than white Russian opal glass, but that this latter is more lambertian (flatter). These three materials have a higher BRDF at the retro-reflection direction, higher in Spectralon and Barium Sulphate than in opal glass. In addition, these two last materials have a higher BRDF in directions near the specular direction, the higher when the higher is the incidence angle. Spectralon has a poorer radiance factor than expected. This may be explained by degradation [
4].

CONCLUSIONS

The gonio-spectrophotometer developed at Insituto de Óptica in CSIC is able to perform diffuse object´s absolute spectral BRDF measurements with high accuracy and angular versatility (on incidence plane and out of incidence plane).

Geometrical comparison of the BRDF of pressed Barium Sulphate, Spectralon and white Russian opal glass are presented in this work. The results are consistent with the NIST standard certificate. In a future work, the dependence of the spectral distribution of the BRDF on the illumination/reflection configurations will be studied for these materials.

REFERENCES

1. F. E. Nicodemus, J. C. Richmond, J. J. Hsia, Geometrical considerations and nomenclature for reflectance, Natl. Bur. Stand. Monogr. 160, 1977.
2. A. M. Rabal, A. Ferrero, J. L. Fontecha, A. Pons, J. Campos, A. Corróns, A. M. Rubiño, Gonio-Spectrophotometer for Low-Uncertainty Measurements of Bidirectional Scattering Distribution Function (BSDF), CIE Tutorial and Expert Symposium on "Spectral and Imaging Methods for Photometry and Radiometry", 30- 31 August 2010, Bern, Switzerland.
3. A. Ferrero, J. Campos, A.M. Rabal, A. Pons, J. L. Fontecha, A. Corróns, Principal Components Analysis on the spectral Bidirectional Reflectance Distribution Function, CIE session 2011, 10-15 July 2011, Sun City, South Africa.
4. A. Höpe, K-O. Hauer, Three-dimensional appearance characterization of diffuse standard reflection materials, Metrologia, 47, 295-304, 2010.

Correction for the Thickness in Auxiliary Integrating Sphere Method for the Realization of Diffuse Reflectance

Guojin Feng [1], Yu Wang [1], Tingting Guo [2], Ping Li [1] and Chundi Zheng [1]

[1] *Spectrophotometry Laboratory, National Institute of Metrology, Beijing 100013, China,* [2] *Agricultural Department, China Agricultural University, Beijing, China*

Corresponding e-mail address: fengguojin@nim.ac.cn

To realize spectral diffuse reflectance scale in 0/d geometric condition at national institute of metrology in China (NIM), a facility based on auxiliary integrating sphere method has been built up and a correction method for the influence on the thickness of PTFE coating at the port of auxiliary integrating sphere is mainly discussed. From analysis in this paper, the error caused by thickness can makes the scale relatively 0.5% lower. The uncertainty of spectral diffuse reflectance in NIM is approximately 0.25 % (*k*=2) in 380nm to 800nm.

INTRODUCTION

Spectral diffuse reflectance is one of the key comparisons in CCPR listed in BIPM. This property of materials plays an important role in lighting engineering, textile and construction, the field of remote sensing and space technology. Currently, there are many kinds of methods [1-7] for the realization of spectral diffuse reflectance, including auxiliary integrating sphere method (or double-sphere method), Korte method, Sharp-Little method and so on. Auxiliary Integrating Sphere (AIS) method can be easily achieved in many instruments without too many changes, such as CARY 5E used in our laboratory for the simple principle and structure.

In the process of realizing diffuse reflectance by AIS method, there are many factors causing the deviation from the ideal result. For example: (1) the shape deviation of the inner wall of AIS to an ideal sphere one, see figure 1; (2) the reflectance uniformity of the inner surface of AIS; (3) the sphere-wall coating is never a perfect Lambertian diffuser; (4) the diameter deviation between exit port and entrance port; (5) the misalignment between exit port and entrance port; (6) the effect of light scattering and so on.

The main factors have been discussed in previous articles[1, 2, 8, 9]. This paper will focus on the neglected one, the thickness of PTFE coating at the port of AIS, discussing on the impact and the correction method.

THE THICKNESS INFLUENCE REFLECTANCE RESULTS ON THE AIS PORT

Generally, there are two kinds of materials used for the wall of integrating sphere, barium sulfate and PTFE. Now barium sulfate has been mostly replaced by PTFE, because of its relatively low reflectance in near infrared waveband. However, certain PTFE with a little translucent, to prevent integrating sphere shell material impact on the reflectance spectrum, requires a certain thickness. Then, a certain thickness at AIS port exists inevitably. Of course, this thickness also can be made into a blade-like shape, but it seems much more difficult to analyse the translucent influence.

The relationship between the thickness at the port and the total reflectance is more complicated, and it has been neglected before by cutting the port to a knife edge. We mainly analyze this problem following two respects : (1) Comparing to ideal integrating sphere, when there is a certain thickness at the port on the AIS, the solid angle of light, φ, reflected from AIS must be less than 2π to the probe sphere. See figure2. So, Qs will decrease. (2) The surface of port will reflect the light incident on itself. The reflected flux will increase the flux reflected from AIS relatively.

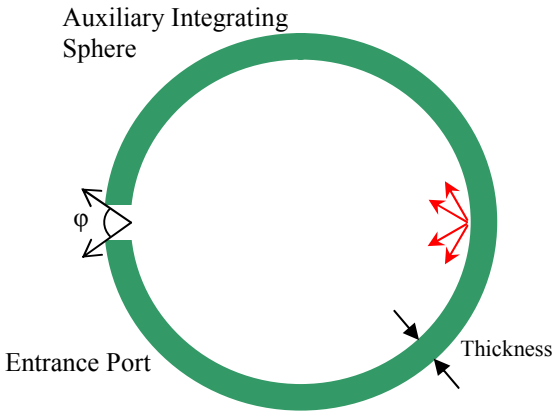

Figure 1. Real emission solid angle of AIS

CORRECTION FOR THE THICKNESS AT OPENING PORT

Due to space limitations, here only gives conclusions. Details are given later.

In ideal condition, from the secondary to the radiation flux reflected by AIS to the probe integrating sphere should be $\rho_S \Phi_0$, due to the thickness at the opening port, the actual optical radiation is η_D, so the formula can be replaced with the following statements

$$\rho = \frac{1}{1-f} - \frac{f}{1-f}\frac{Q_F}{Q_S'/\upsilon} \quad (where, \quad \upsilon = A + B\rho\frac{K_1 - B\rho_s K_3 K_1 \rho + A\rho_s K_3}{1-(K_2 + B\rho_s K_3)\rho}) \qquad (1)$$

Formula (1) is a transcendental equation, its analytical solution is difficult to work out, but it can be calculated with the help of computer programming.

RESULTS AND DISCUSSION

In realization, 20 flat samples with the same material, PTFE, and processing technique as the auxiliary integration sphere were made. The average measured value of 20 flat samples as a standard flat reflector measured value Q_F , whereas, the average value of 20 times readings with auxiliary integration sphere are used as a standard sphere reflector Q_S' , additionally, by formula (1, the theoretical reflectance can be calculated.

Again the various factors mentioned in revision to be amended, the absolute reflectance could be more accurate. Using this result and the relative measurement method, absolute reflectance of various other kinds of samples can be measured.

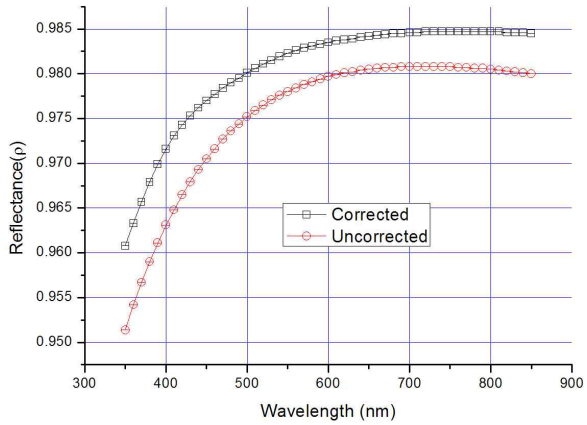

Figure 2. Comparison before and after correction

Figure 2 shows the comparison between corrected and uncorrected results. It is obviously that nearly 0.5% changing after correction.

Our AIS system and method presented in this paper is one that can be reasonably easily implemented on and adapted to most spectrophotometers in VIS-NIR regions. By comparing to the traditional double sphere method, the correction method is proved to be correct. In addition, the method can be readily implemented for use in monochromatic instrumentation with a reasonable cost. However, to get better performance and potentially higher-accuracy data, all factors that may influence the result should be carefully analyzed to ensure the accuracy.

ACKNOWLEDGMENTS

This work was supported by the Basic Science Research Foundation in NIM.

REFERENCES

[1] Goebel DG.Generalized Integrating-Sphere Theory: Applied Optics.Vol. 6 (1967):p.125-128.

[2] De Vries G, Beek JF, Lucassen GWandVan Gemert MJC.Effects of light losses in double integrating spheres on optical properties estimation: IEEE Journal on Selected Topics in Quantum Electronics.Vol. 5 (1999):p.944-947.

[3] Zerlaut GAandAnderson TE.Multiple-Integrating Sphere Spectrophotometer for Measuring Absolute Spectral Reflectance and Transmittance: APPLIED OPTICS.Vol. 20 (1981):p.3797-3804.

[4] Shitomi HandSaito I.A new absolute diffuse reflectance measurement in the near-IR region based on the modified double-sphere method: Metrologia.Vol. 46 (2009):p.S186-S190.

[5] Nevas S, Manoocheri FandIkonen E.Gonioreflectometer for measuring spectral diffuse reflectance: APPLIED OPTICS.Vol. 43 (2004):p.6391-6399.

[6] Lovell DJ.Theory and Applications of Integrating Sphere Technology: Laser Focus/Electro-Optics.Vol. 20 (1984):p.86-96.

[7] Chunnilall CJ, Deadman AJ, Crane LandUsadi E.NPL scales for radiance factor and total diffuse reflectance: Metrologia.Vol. 40 (2003):p.S192-S195.

[8] Clarke FJJandCompton JA.Correction Methods for Integrating-Sphere Measurement of Hemispherical Reflectance: Color Research and Application.Vol. 11 (1986):p.253-262.

[9] White HandTaylor J. The effect of instrument design on diffuse reflectance measurements. 9th Congress of the International Colour Association, June 24, 2001 - June 29, 2001. Rochester, NY, United states: SPIE; 2001. p. 761-764.

Gonio-spectrophotometer for Bidirectional Scattering Distribution Function (BSDF) Measurements in both hemispheres

A. M. Rabal[1], A. Ferrero[1], J. L. Fontecha[2], A. Pons[1], J. Campos[1], A. Corróns[1] and A. M. Rubiño[3]

[1]Instituto de Óptica, CSIC, Madrid, Spain, [2]Instituto de Física Aplicada, CSIC, Madrid, Spain, and [3]Dpto. de Óptica, Universidad de Granada, Granada, Spain

ana.rabal@csic.es

A gonio-spectrophotometer developed and built at the Institute of Optics of CSIC by the research group GiMRO is described. It was designed to allow absolute radiometrical measurements to be carried out within the hemispheres behind and in front of the sample, being the primary interest the measurement of the Bidirectional Scattering Distribution Function (BSDF) of materials. The instrument is fully automated and capable to perform actual retro-reflectance measurements.

INSTRUMENT DESCRIPTION

The gonio-spectrophotometer presented in this work, shown in Fig. 1,consists of [1] four subsystems:

(1) Illumination subsystem

Formed by a super-quiet Xenon High Intensity Discharge lamp and a Köhler optical system that produces a uniform spot of about 3 cm in diameter on the sample surface with a very small solid angle ($5x10^{-3}$ str.). Its periscope-shaped arrangement with a beamsplitter allows to measure the radiation scatterd by the sample in the incidence direction, which is the main difference with other present gonio-spectrophotometers [2-6]. A filter wheel is installed to attenuate the beam up to 100 times when required.

(2) Positioning subsystem

Based on an industrial robot arm of 6 joints that allows linear and rotation movements of the sample respect to a three orthogonal axes system. In opposition to other instruments, it is the sample that moves respect to the illuminating beam and not vice versa [3]. This allows more versatility for the illumination system regarding the type of source to be used.

(3) Detection subsystem

A spectroradiometer, coupled to a ring-shaped rail (1,03 m in diameter) moves around the centre of the sample. It can be full-automatically located at any point on the rail, allowing to change the illumination/observation angle. This degree of freedom cannot be changed by the robot-arm and is required to carry out a complete BSDF measurement. A transformation should be accomplished to obtain the spherical coordinates at sample reference surface from the robot arm rotations and the detector rotation [4, 6].

(4) Alignement subsystem

Two laser beams following directions along two different diameters of the ring define with negligible uncertainty the rotation centre of the spectroradiometer at their crossing point. This is the point where the centre of the sample should be located.

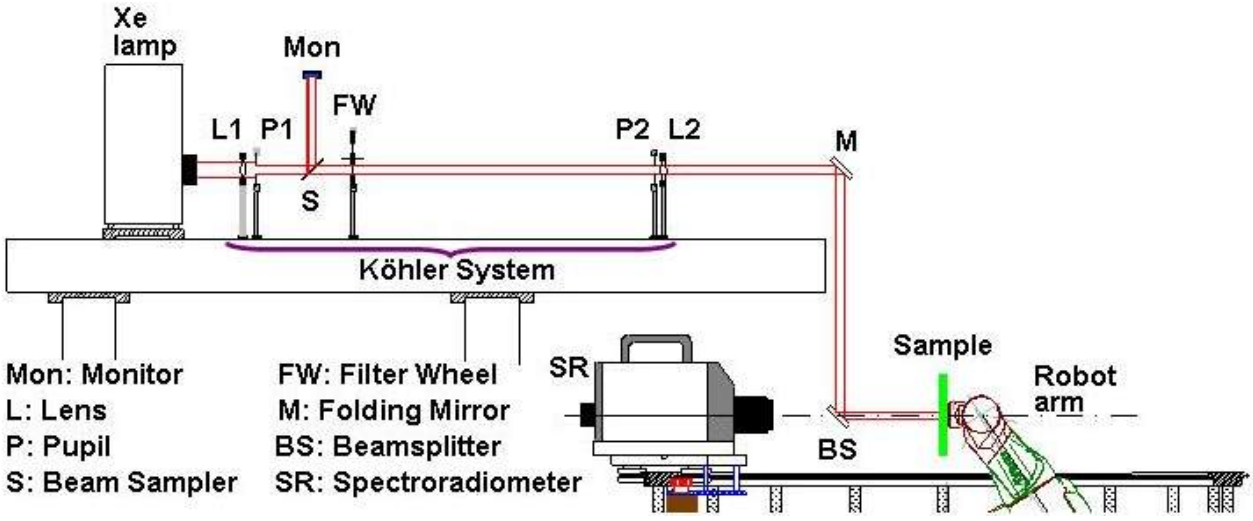

Figure 54. GEFE, instrument for radiometric measurements in both hemispheres.

METROLOGICAL FEATURES

The gonio-spectrophotometer carries out absolute measurements of the BSDF in all directions of incidence/viewing up to 75º with respect to the normal to the sample surface. It allows both reflectance and transmittance measurements to be carried out; it is able to perform actual retro-reflection measurements; it acquires simultaneously the visible spectrum and it is fully automated to do around 5 scanning positions per second.

GEFE has a partial occlusion angle of the radiation re-emitted by the sample in the region near the incidence direction, i.e. retro-reflection region, but has not got any blind spot as other gonio-spectrophotometers [2-6]. Fig. 2 top shows spectroradiometer's relative response at positions near the incidence direction, where 0º correspond to the position just behind the beamsplitter centre and 10º corresponds to a position outside the beamsplitter. We can see that 3,2º apart from incidence is the position where the spectroradiometer begins to get behind the beamsplitter's frame (opaque), and for angles greater than 7,5º apart, the spectroradiometer has left the critical region. Note that the relative response is higher than 20% in the region of greatest occlusion. Fig. 2 bottom shows the repeatability of the measurement. A slight noise increase behind the beamsplitter is seen, although it is always less than 1%.

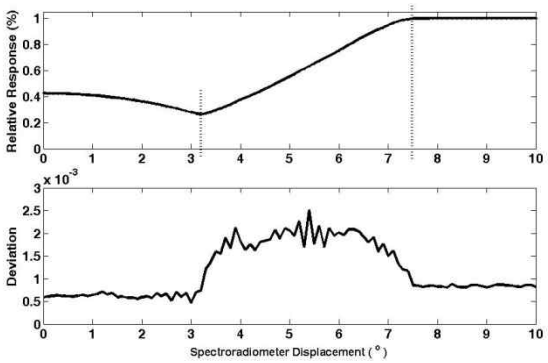

Figure 55. Variation of spectroradiometer relative response as a function of angular displacement respect to the incidence direction (top) and repeatability of the measurement in the region behind beamsplitter (down).

The light backscattered by the beamsplitter is due to the interreflections between its surfaces. This light is proportional to the power of the beam and has the same spectral distribution. It was found that the signal was $4 \cdot 10^{-5}$ times lower than the illuminaton signal. When the spectroradiometer is outside the region of the beamsplitter, there is another type of stray light due to the different elements and devices of the laboratory. This light has a different spectral distribution, and its value is between 10^{-7} and 10^{-8} times lower than the illumination signal.

CONCLUSIONS

A gonio-spectrophotometer developed in CSIC (GEFE) is presented. It allows absolute radiometric measurements (even at the direction of incidence) in both hemispheres to be done, being the primary interest the measurement of the Bidirectional Scattering Distribution Function (BSDF) of surfaces.

The main metrological features of this device are presented in this work. Null occlusion angle, god signal to noise ratio and low scattered radiation are among the primary characteristics of this device.

ACKNOWLEDDGEMENTS

The authors are grateful to "Plan Nacional de Física" for funding this work (FIS2007-66671-C02-01), to Dr. Armada form IAI (CSIC) for his advice on the mechanical design and placement subsystem, and to the JAE Program from CSIC for awarding us with a researcher in formation.

REFERENCES

1. A. M. Rabal, A. Ferrero, J. L. Fontecha, A. Pons, J. Campos, A. Coróns, Gonio-spectrophotometer for bidirectional scattering distribution function (BSDF) measurements, Opt. Pura y Apl., 44, 2011.
2. Fréderic B. Leloup, Stefan Forment, Philip Dutré, Michael R. Pointer, and Peter Hanselaer, Design of an instrument for measuring the spectral bidirectional scatter distribution function, Applied Optics, 40, 29, 2008.
3. D. Hünerhoff, U. Grusemann, and A. Höpe, New robot-based gonioreflectometer for measuring spectral diffuse reflection, Metrologia, 43, S11-S16, 2006.
4. G. Obein, R. Bousquet, and M. E. Nadal, New NIST reference goniospectrometer, Proc. SPIE, 5880, 241-250, 2005.
5. M. R. Pointer, N. J. Barnes, P. J. Clarke and M. J. Shaw, A new goniospectrophotometer for measuring gonio-apparent materials, Color Technol., 121, 96-103, 2005.
6. T. A. Germer and C. C. Asmail, Goniometric optical scatter instrument for out-of-plane ellipsometry measurements, Rev. Sci. Instrum., 70, 3688-3695, 1999.
7. F. E. Nicodemus, J.C. Richmond, and J. J. Hsia, Geometrical Considerations and Nomenclature for Reflectance, Natl. Bur Stand. Monogr., 160, 1977.

Towards novel AlN and GaN based single photon sources

A. M. Racu[1], S. Peters[1], W. Schmunk[1], H. Hofer[1], S. Kück [1], A. Behrends[2], A. Bakin[2], A. Waag [2], J. K. Mishra[3], U. Rossow, A. Hangleiter[3], K. Trunov[4], and A. Wieck[4]

[1]Physikalisch Technische Bundesanstalt, Braunschweig, Germany, [2] Institute of Semiconductor Technology, University of Technology Braunschweig,Germany, [3] Institute of Applied Physics, University of Technology Braunschweig, Germany, [4]Institute of Applied Physics, Ruhr University Bochum, Germany

Corresponding e-mail address: Stefan.Kueck@ptb.de

We present first results on optical characterization of impurity centers in a GaN and AlN matrix in order to obtain novel single photon sources. The samples under investigation are Zn-doped GaN and Cr implanted AlN. Spectroscopically we found typical emission lines of the corresponding impurities. Using confocal PL mapping we studied the formation of conglomerates of emitters and their characteristics depending on the doping parameters. Consequently, we discuss the potential of these systems for single photon emission.

INTRODUCTION

Single photon sources have gained increased interest due to their potential applications in different fields of science, technology and metrology. Highly efficient emitters working at room temperature are demanded for practical use in quantum cryptography, quantum computation [1], and fundamental physics [2]. Single photon generation has already been demonstrated in several systems such as N-V [3] and Si-V [4] defect centres in diamond or single quantum dots [5] in III-V heterostructures. Other materials, well known from the fields of lasers and LEDs, might be suitable candidates for novel single photon sources due to strong photoluminescence or electroluminescence signals. The challenge is to find the doping parameters for an appropriate density of quantum emitters in the semiconducting matrix in order to obtain single photon sources. Here, we present results from a confocal PL imaging study combined with micro-PL spectroscopy for energy levels related to GaN doped with Zn as well as AlN doped with Cr.

EXPERIMENTAL

A sketch of the experimental setup is presented in Figure 1. The exciting laser beam is focused on the sample using a microscope objective with 100X magnification and numerical aperture of 0.7. The laser wavelength is 532 nm for measurements of AlN:Cr and 375 nm for GaN:Zn (below band gap excitation in both cases). The PL emission from the sample travels back through the microscope objective and a dichroic beam splitter and is directed via a fiber optic splitter towards a single photon detector (SPAD) and a spectrometer. Different filters can be used to select the spectral range of interest. For PL scans a xyz-piezoelectric stage was used. The temperature of the sample can be changed from 4 K to 300 K using a He flow-cryostat.

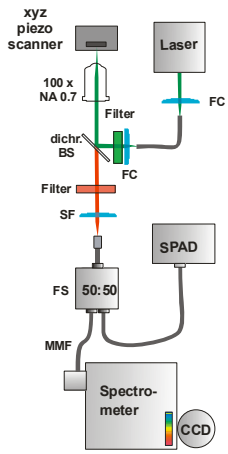

Figure 56. Experimental setup used for the optical characterisation of the samples.

Further, the same setup can be used to determine the single photon character of the emitted light. For this, the spectrometer will be replaced by a second SPAD in a Hanbury Brown Twiss [6] configuration.

RESULTS AND DISCUSSION

A promising material for single photon emission is Zn doped GaN. Moreover, it is also attractive for the realization of electrically driven single photon sources based on GaN LEDs. Zn is a well known deep level in GaN, which has formerly been used for the fabrication of blue LEDs. The PL spectra show a broad emission around 2.9 eV which decreases with decreasing Zn-flow [8]. The lifetime of this blue luminescence is 77 ns, which is sufficiently fast for single-photon emission.

Figure 2a presents a confocal PL image of a Zn:GaN sample. We observe a homogeneous background with small bright spots with dimensions of only several micrometers. The corresponding spectra are shown in Figure 2b. Here, we have used a filter with an edge around 450 nm in order to eliminate the strong contribution from the back reflected laser light.

In order to get single-photon emission a drastic reduction of the Zn-concentration is required. This can be realized by reducing both Zn-flow and the layer thickness of the Zn-doped region.

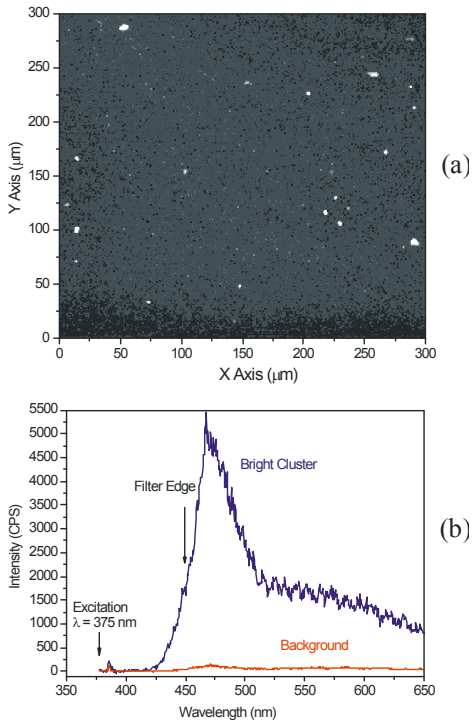

Figure 2. Confocal scan (a) and spectrometer data (b) for Zn doped GaN.

Figure 3a shows a confocal PL scan of a Cr implanted AlN layer on a sapphire substrate. Dark and bright regions represent low and high emission, respectively. A spectroscopic analysis of these regions reveals different types of spectra which are plotted in Figure 3b. The dark background shows two sharp peaks, identified as the R1 and R2 lines of the sapphire substrate, visible through the transparent AlN film. The spectra corresponding to the bright spots 1 and 2, marked by arrows in Figure 3a are tentatively assigned to the red to near infrared emission from Cr^{3+} in AlN [7], but it needs to be further confirmed. The spot dimensions are around 20 µm, not yet compatible with single photon emission, but the reduction of the Cr concentration may lead to the formation of smaller centres.

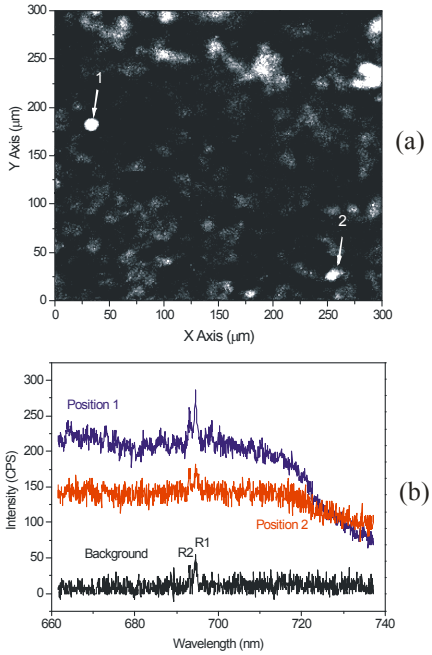

Figure 3. Confocal scan (a) and micro-PL measurements (b) for Cr implanted AlN. The broad emission is tentatively assigned to Cr^{3+} in AlN.

SUMMARY

In conclusion, we have characterized two potential candidates for semiconductor based single photon sources. We found clusters of emitters displayed as bright spots in the PL images. However, the concentration of dopants still has to be optimized for single photon emission. Experiments on samples with lower concentrations are in progress and the results of photon statistics will be shown at the conference.

We acknowledge financial support from the project BMBF 45004 EPHQUAM.

REFERENCES

1. Y. Yamamoto, C.Santori, G. Solomon, J. Vuckovic, D. Fattal, E. Waks, E. Diamanti, Progress in Informatics 1, 5-37, 2005.
2. C. Braig, P. Zarda, C. Kurtsiefer, H. Weinfurter, Appl. Phys. B 76, 113-116, 2003.
3. C. Kurtsiefer, S. Mayer, P. Zarda, H. Weinfurter, Phys. Rev. Lett. 85, 290, 2000.
4. C. Wang, C. Kurtsiefer, H. Weinfurter, B. Burchard, J. Phys. B: At. Mol. Opt. Phys. 39, 37-41, 2006.
5. D. Richter, R. Roßbach, W. Schulz, E. Koroknay, C. Kessler, M. Jetter, and P. Michler, Appl. Phys. Lett. 97, 063107, 2010.
6. R. Hanbury Brown and R. Q. Twiss, Nature London 178, 1447, 1956.
7. M. Maqbool, E. Wilson, J. Clark, I. Ahmad, A. Kayani, Applied Optics 49, 653, 2010.
8. A Behrends, M. Al-Suleiman, A. Bakin, A. Waag, S. Peters, A. M. Racu, W. Schmunk, H. Hofer, S. Kück, ICNS, 2011.

Theoretical Study of Integrating Sphere-based Absolute Photoluminescence Quantum Efficiency Measurement

Yoshiro Ichino[1]

[1]*National Metrology Institute of Japan (NMIJ), Tsukuba, Japan*
Corresponding e-mail address: y.ichino@aist.go.jp

Spectroradiometric instruments coupled with integrating spheres are widely used to measure absolute photoluminescence quantum efficiencies of phosphor materials for white LEDs. Basic sphere theory in conjunction with several assumptions for simplicity is employed to formulate internal photoluminescence quantum efficiency. When the difference between the diffuse reflectance on the surface of the phosphor at the excitation wavelength and that at the emission one is taken into account, a correction factor, which is required to obtain a theoretically exact quantum efficiency value from the experimentally determined apparent value, is calculated. This factor is found to be far from negligible in particular cases.

INTRODUCTION

Solid state lighting technology using white light-emitting diodes (LED) has attracted extensive attention worldwide. Improvement of photo-luminescence quantum efficiency (PQE) of phosphor materials, as well as of quantum efficiency of a LED chip and of light extraction efficiency from a LED package, plays a key role for improving total efficiency of the white LED. As the development of high-PQE phosphors becomes much competitive, more precise and reliable measurement method of PQE has been required. Practically, it had been sufficient for LED phosphor manufactures to obtain PQE only relatively against their local standard phosphor materials, brightest available in most cases. Such competitive R&D, however, has induced interlaboratory comparison of measurement results, and absolute measurement of PQE has been more crucial. Instruments employed for PQE measurement should be appropriately calibrated against reference standard light sources or detectors traceable to national standards. An integrating sphere with a sample holder together with an array spectroradiometer is usually used to measure absolute PQE value. In this study, internal PQE, defined as the ratio of photoluminescence photon numbers to excitation photon numbers absorbed by the sample, is theoretically derived as functions of various optical parameters only by employing the basic sphere theory.

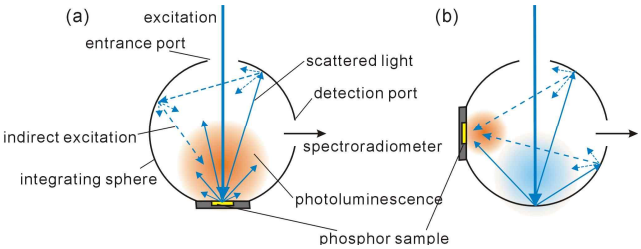

Figure 57. Integrating sphere-based PQE measurement setup: (a) sample excitation geometry, and (b) re-excitation correction geometry.

FORMULATION

Figure 1(a) illustrates a basic measurement geometry assumed in this study. A phosphor sample is attached onto the sphere and excited by monochromatic light. For simplicity, photoluminescence is assumed as monochromatic and separable completely from the excited light by a calibrated spectroradiometer which measures relative spectral irradiance at the detection port of the sphere. In addition, both scattering onto the sample and the photoluminescence are assumed as Lambertian, and the diffuse reflectance inside the sphere is wavelength-independent and thoroughly uniform. On this geometry, not only the photoluminescence caused by the direct excitation onto the sample but also that from the sample indirectly excited by diffused light inside the sphere is detected by the spectroradiometer. This extra indirect component results in overestimating PQE value and thus should be properly taken into account [1, 2]. A sophisticated experimental method to correct such overestimation was developed by de Mello et al. [3] and has been widely applied for transparent organic thin films. This method includes three experimental geometries: irradiating a sphere wall without a sample (geometry A), irradiating the wall with the sample attached at the center of the sphere (B) and directly irradiating the sample (C). The geometry shown in Fig. 1(a) corresponds to the modified de Mello's geometries A and B, where the white reflectance standard is replaced with the

phosphor sample for geometry A. In the same manner, geometry C is modified as the one shown in Fig. 1(b). The direct excitation geometry (Fig.1(a)) gives the internal PQE, η_{in} as follows:

$$\eta_{in} = \frac{E_{PF}}{\frac{E_W}{\rho_W} - E_{PS}} \cdot \frac{1}{1 + f_P(1-\alpha)\frac{\rho_s(1-f_O)}{1-\rho_s(1-f_O)}} \qquad (1)$$

where E_{PF} and E_{PS} are measured irradiance of photoluminescence and scattered light, respectively, with the phosphor sample attached, E_W is that of scattered light with the white standard attached whose diffuse reflectance is ρ_W, and ρ_s, α, f_P and f_O correspond to the diffuse reflectance of the sphere wall, absorptance of the phosphor and the fractions of the sample surface area and the total are of the opening ports to the total surface area of the internal sphere wall, respectively. This means the internal PQE is not determined only by the geometry shown in Fig. 1(a).

When the geometry depicted in Fig. 1(b) is employed together with that in Fig. 1(a), PQE is expressed as

$$\eta_{in} = \frac{E_{PF} - \rho_s(1-f_O)\cdot\frac{E_{PS}}{E_W}\cdot E_{IF}}{\frac{E_W}{\rho_s} - E_{PS}} \qquad (2),$$

where E_{IF} is the irradiance component of the photoluminescence for Fig. 1(b). Eq. (2) indicates that determination of PQE requires some optical parameters, which should be obtained by additional experiments.

CORRECTION FACTOR

The modified de Mello's method shown above does not consider the difference between the diffuse reflectance on the surface of the phosphor at the excitation wavelength, namely 1-α, and that at the emission one ρ_{PF}, which is far from actual properties of high-performance phosphors. When such difference is taken into account, internal PQE value cannot be expressed in an analytical form. Correction factors required to be applied to the "apparent" PQE value $\eta_{in}^{demello}$, experimentally obtained by means of modified de Mello's method, are calculated as a function of absorptance of the phosphor for several sets of optical parameters as shown in Fig. 2. This result clearly shows that the correction factor can be far from negligible in particular cases, dependent on parameters, absorptance and diffuse reflectance for the phosphor sample, as well as on diffuse reflectance of the sphere wall.

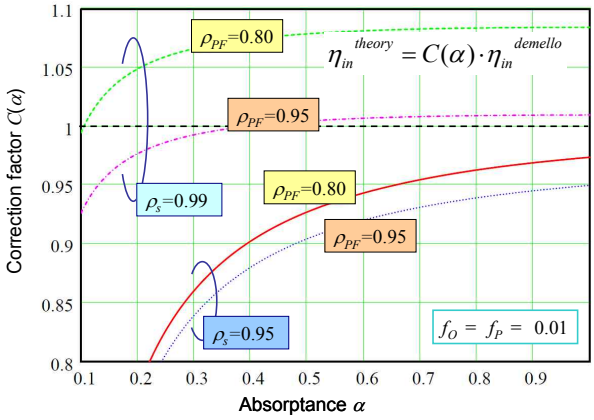

Figure 2. Correction factors to derive theoretically exact PQE from the experimentally obtained value.

Imperfectness of the integrating sphere, such as baffles and boundary between two hemispheres, may contribute to the correction factor, which requires another numerical calculation [4] or a ray-tracing simulation and is not taken into consideration in this study.

REFERENCES

1. K. Ohkubo and T. Shigeta, Absolute Fluorescent Quantum Efficiency of NBS Phosphor Standard Samples, J. Illum. Engng. Inst. Jpn., 83, 87-93, 1999.
2. J. Horigome, T. Wakui and T. Shirasaki, A Simple Correction Method for Determination of Absolute Fluorescence Quantum Yields of Solid Samples with a Conventional Fluorescence Spectrophotometer, BUNSEKI KAGAKU, 58, 553-559, 2009.
3. J.C. de Mello, H.F. Wittmann and R.H. Friend, An Improved Experimental Determination of External Photoluminescence Quantum Efficiency, Adv. Mater., 9, 230-232, 1997.
4. R. Westsphaling, P. Ullrich, J. Hoffmann, H. Kalt, C. Klingshirn, K. Ohkawa and D. Hommel, Measurements of the Absolute External Luminescence Quantum Efficiency in ZnSe/ZnMgSSe Multiple Quantum Wells as a Function of Temperature, J. Appl. Phys., 84, 6871-6876, 1998.

Fiber-Coupled Cryogenic Radiometer with Carbon Nanotube Absorber[5]

David Livigni, Nathan Tomlin, Christopher L. Cromer, John H. Lehman

National Institute of Standards and Technology, Laser Radiometry, Boulder, Colorado USA
Corresponding e-mail address:lehman@boulder.nist.gov

A cryogenic radiometer was constructed for direct-substitution optical fiber power measurements. The cavity is intended to operate at the 3 K temperature stage of a dilution refrigerator system along with other radiometric detectors operating at or below 3 K. The cavity features micromachined silicon spacers to thermally isolate the optical fiber as well as an absorber made from micromachined silicon on which vertically aligned carbon nanotubes were grown. Measurements of electrical substitution, optical absorption and temperature change indicate that the radiometer is capable of measuring 10 nW power levels with a responsivity of 160 nW/K.

INTRODUCTION

Measuring light directly from an optical fiber using a cryogenic radiometer is important for two reasons; for the calibration (absolute, traceability) of optical fiber power meters, and for comparison with emerging low-temperature superconducting detectors [1]. In the past, calibration of optical fiber power meters was accomplished with a two-step process consisting of: (1) a free-field based calibration of a transfer standard (photodiode trap detectors having high coupling efficiency), and (2) direct comparison of fiber-coupled meters (one transfer standard, one device under test). A cryogenic radiometer that is directly coupled to optical fiber presents an opportunity to eliminate some of the larger uncertainty contributions inherent to a radiometer having a window and a large-area cavity.

RADIOMETER DESCRIPTION

The radiometer was operated in a cryogen-free dilution refrigerator (DR) made by Oxford Instruments.[†] The first two cooling stages were cooled by a Cryomech pulse tube, with 1W of cooling power at 3K. The dilution unit consists of three colder stages - the still at 600-800 mK, coldplate ~100 mK, and the mixing chamber with a base temperature of ~12 mK. The mixing chamber has a cooling power of 225 μW at 100 mK. For the present evaluation, the coldest four stages were shorted together using copper wiring and braid, and only the pulse tube cooler operated while the dilution unit was off. All stages of the refrigerator were thus stabilized at 3.5K. The experiment was contained in a DR to demonstrate the compatibility with other DR-based optical-detector experiments in the range of 10 mK.

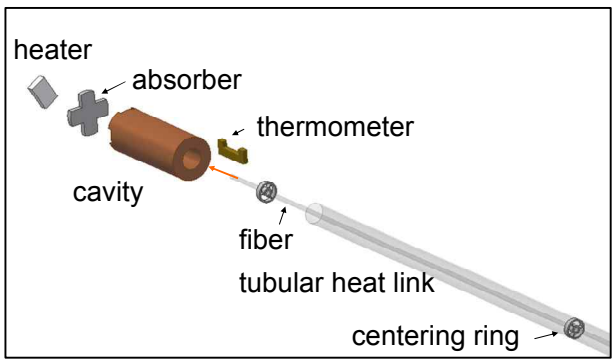

Figure 1. Exploded view of the radiometer cavity, optical fiber, heat link, thermometer and heater.

The fiber-coupled radiometer cavity, shown in Fig. 1, was assembled and installed into the DR. The present design is optimized for measuring a temperature change proportional to the optical power emitted from the fiber. The radiometer components are described by the following. A micromachined silicon chip the shape of a plus sign (absorber, Fig. 1) constitutes the closed end of a copper tube (cavity) painted with proprietary black paint (Aeroglaze Z302). Two concentric polyimide tubes link the optical fiber and the cavity; an outer tube mechanically supports and provides thermal isolation (tubular heat link, Fig. 1) of the cavity while the inner tube holds the optical fiber. Micromachined silicon

[5] Publication of NIST, an agency of the US government, not subject to copyright.

[†] Trade names are identified only for reference purposes and does not represent or imply an endorsement by NIST.

rings (centering ring, Fig. 1), each resembling a three-spoked wheel, mechanically center the tubes such that the optical fiber is suspended inside the cavity a distance of 7 mm from the absorber.

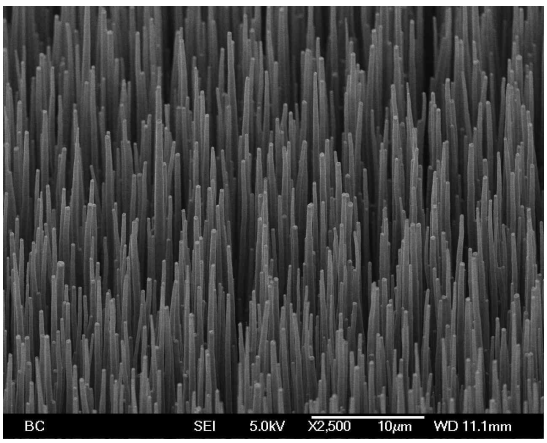

Figure 2. Vertically aligned carbon nanotubes grown on micromachined silicon.

In the past, we demonstrated that CNTs provide an excellent absorber for thermal detectors.[2] Today, such coatings on silicon are readily available commercially. The CNT coating was prepared commercially by Nanolab and the silicon absorber was populated with nanotubes approximately 40 um long, with a nanotube density of 10^9 tubes per cm^2. A scanning electron micrograph of the coating is shown in Fig. 2. For this work, the specular reflectance at 1574 nm (1 mW) is estimated to be 0.8 %. This was measured using a germanium photodiode with chopped input at 82 Hz at approximately 1 mW at near-normal incidence and at room temperature. This measurement does not provide an adequate evaluation for the purposes of estimating uncertainty. Additional characterization of this material is described elsewhere. [3]

RESULTS

The response of the fiber radiometer was determined optically and electrically (by heating). Optically, the radiometer was characterized by coupling light from a 1550 nm diode laser into an optical fiber (SMF28) and comparing the radiometer response by direct substitution with an optical fiber power meter outside the DR. Electrically, the radiometer was characterized by applying a known current to the heater (1012.6 Ω metal foil resistor). The cryogenic radiometer's open-loop response was measured at approximately 1 nW, 10 nW and 100 nW. The temperature response to 9.8 nW of optical and electrical power, shown in Fig. 3, is 61 mK, Therefore the sensitivity is 160 nW/K, with a 1/*e* rise time of 13 min. The 1 nW input is qualitatively similar to the 10 nW and 100 nW measurement results, with temperature fluctuation noise of less than 3 mK (peak to peak).

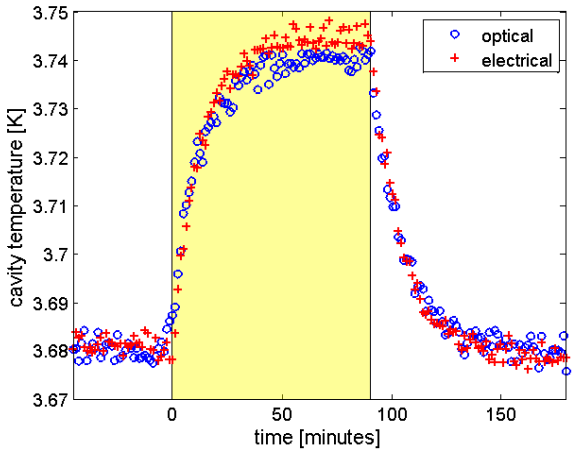

Figure 3. Cavity response with respect to time for optical and electrical heating at 9.8 nW. The shaded region indicates the duration of optical or electrical heating.

DISCUSSION AND CONCLUSION

We have demonstrated the first fiber-based cryogenic radiometer of its kind, and a novel application of vertically aligned CNTs. We incorporated micromachining of silicon to provide mechanical support and thermal isolation. By measuring the cavity temperature with respect to time for optical power emitted from an optical fiber, we have demonstrated 160 nW/K sensitivity and excellent thermal isolation. The cavity and heat link may be optimized for an absolute cryogenic radiometer by reducing the thermal time constant and adding temperature controls [4]. In addition, evaluation of the cavity's response at 100 mK in the DR will be undertaken. Complete uncertainty analysis is required, including low-temperature reflectance measurements and characterization of optical coupling losses into the DR.

REFERENCES

1. A.E. Lita, A.J. Miller, S.W. Nam, "Counting near-infrared single-photons with 95% efficiency," Optics Express, 16, 3032-3040, 2008
2. J. Lehman, A. Sanders, L. Hanssen, B. Wilthan, J. Zeng, C. Jensen, "Very Black Infrared Detector from Vertically Aligned Carbon Nanotubes and Electric-Field Poling of Lithium Tantalate" Nano Letters, 10, 3261–3266, 2010.
3. Chunnilall, et al., "Absolute IR reflectance of carbon nanotube mats and arrays," submitted Newrad 2011.
4. E. D. West and K. L. Churney, "Theory of Isoperibol Calorimetry for Laser Power and Energy Measurements," J. Appl. Phys. 41, 2705-2712, 1970.

Absolute High-Power Laser Measurements with a Flowing Water Power Meter*

Christopher L. Cromer, Xiaoyu Li, Marla Dowell, John H. Lehman

National Institute of Standards and Technology, Boulder, Colorado USA
Corresponding author: lehman@boulder.nist.gov

ABSTRACT

We describe a novel flowing water optical power meter (FWOPM) for high-power laser radiometry in the range of 50 W to 10 kW. The FWOPM has several design features: a rotating mirror oriented at 45° with respect to the incoming radiation, a conical light-trapping cavity coated with a multiwall carbon nanotube composite and a modular electrical heater for calibration. The design is modular to facilitate shipment to the laser facility and for scaling of measurements up to 100 kW. We have demonstrated 1 % relative uncertainty with laser power measurements near 5 kW at 1.06 µm and 10.6 µm wavelengths.

INTRODUCTION

Lasers designed to operate in the range of 10 kW/cm^2 are typically used in manufacturing for cutting or welding and for military applications. Therefore, designing an absolute laser power meter that is intended to efficiently absorb such high irradiance linearly and without damage is challenging. We have developed a flowing water optical power meter (FWOPM) that is capable of measuring 10 kW with very low uncertainty, minimal backscatter and absolute calibration traceable to electrical standards. The FWOPM consists of several modular subsystems: a receiver to absorb the incident laser power, a water system to supply cooling water to the receiver, and an electronic system for data acquisition and control. A separate high accuracy water heater provides calibration of the system traceable to electrical standards. In the 1970s, NIST scientists developed a 100 kW isoperibol calorimeter (referred to as the BB calorimeter)[1] based on the thermal capacitance of a large volume of water surrounding an optical cavity. This system is nearly forty years old, slow (a few measurements per day) and difficult to transport. Others have built volume-absorbing calorimeters that are based on the thermal capacitance and differential thermometry.[2] Other calorimeter systems exist that are not well documented in the literature, but are based on well-known thermodynamic principles.

DESCRIPTION

The concept of the FWOPM is based on the idea of heat balance calorimetry [3], which in this instance relies on measuring the temperature change of cooling water flowing in a closed system that surrounds an optical cavity. The equation for this system is:

$$P = (T_{out} - T_{in})\, \rho\, c_p ,$$

where ρ is the mass flow rate in (kg/s), c_p is the specific heat of water in (J/(kg K)), and T_{in} and T_{out} are the measured input and output water temperatures in (K).

Laser light entering the cavity is absorbed and converted to heat, which is transferred to the cooling water. Similarly, for calibration, the optical cavity is replaced with an electrical heater and water flows in a closed system that surrounds the heater. We used commercial encapsulated thermistors that can readily measure water temperature changes of a few mK with 10 mK uncertainty. The specific heat of water with respect to temperature is well known. The mass flow rate is directly measured with a Coriolis-type flow meter which measures mass flow with an accuracy of 0.1% over its range. The calibration of the thermistors and the flow meter are not required since we use an electrical heater to provide a whole system calibration, but the thermistors and flowmeter provide an independent check of the results. During operation, the dynamic range of the optical power measurements is improved by increasing the flow rate as the optical power increases. Dual voltmeters are used to measure the thermistor's resistance and to measure the voltage and current (with a shunt resistor) applied to the heater during calibration.

The optical cavity is shown in Fig. 1. The cavity is designed such that collimated light entering the cavity is incident on the rotating mirror at 45°. The 45° front cone and the 22.5° rear cone provide for

trapping of the laser beam inside the cavity. The input aperture is 50 mm. We measure the reflectance of the cavity at 1064 nm at 0.03%, and estimate the reflectance at 10.6µm to be less than 0.1 %.

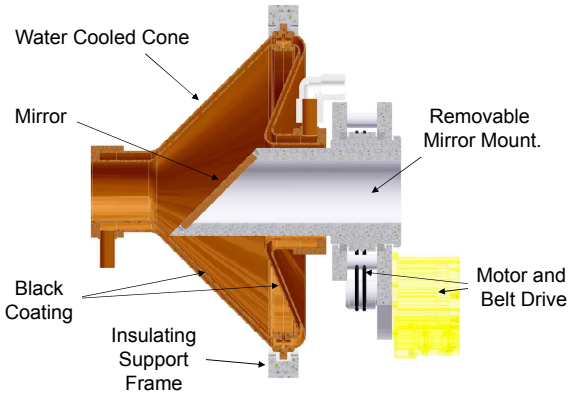

Figure 1. Cross section view of the FWOPM. The optical axis is horizontal with the laser entering the cavity from the left.

The inside of the cavity is coated with a black absorber consisting of a shell-core composite made from polymer derived silicon carbon nitride (the shell) and multiwall carbon nanotubes (the core). The details of this material are described elsewhere.[4] Briefly, the coating is optimized for high optical absorption efficiency (95 % at 1 µm) and high laser damage threshold of approximately 10 kW/cm^2.

The rotating mirror section is thermally insulated from the cavity to simplify the thermal characteristics of the system. Thus it is important that the mirror absorb as little of the incident laser beam as possible, so each laser wavelength requires a separate high reflectance mirror. Each mirror is elliptical in shape coincident with the circular section of the rotating mirror mount. Quartz (for 1.06 and 3 µm) and silicon carbide (for 10.6 µm) substrates are coated with a combination of metal and dielectric layers to achieve ultra-high reflectivity (>99.99 %).

The pump and flow meter are packaged in a shippable rack mount container. The shippable rack mount electronics package contains the voltmeters, shunt resistor, flow meter transceiver, variable speed pump motor driver, and 4 kW DC power supply. Communications between a laptop running a custom program is done with an Ethernet router connected to various serial and GPIB converters in the electronics package. The 4 kW DC power supply is used to check the system in the field and a separate 15 kW DC power supply is used to calibrate the system in the lab. The receiver head and heater are shipped in custom fit containers as well as a 100 gallon plastic water tank (which is shipped empty).

MEASUREMENT RESULTS

We have undertaken several comparisons of the FWOPM over a range of wavelengths and power levels referenced to the electrical calibration. The FWOPM was compared to an existing primary standard at NIST (K-series calorimeter) [5] and to the BB calorimeter at Wright Patterson Air Force Base.

Table 13. Summary of FWOPM comparisons to other standards.

Reference	Wavelength (µm)	Power (kW)	Result (offset)
K	1.064	0.5	0.9983
K	10.6	0.5	1.002
BB	1.064	4	1.009
BB	10.6	1 - 4	0.999
System	Electrical	.1 – 3.8	0.998

CONCLUSION

We have described a novel power meter for high-power laser radiometry. The FWOPM has several design features to manage laser irradiance up to the level of 10 kW/cm^2, including a rotating mirror to spread the incoming beam within a light trapping cavity and a custom MWCNT composite coating. A separate modular electrical heater is used to calibrate the system traceable to SI units. We have demonstrated 1 % relative uncertainty with laser power measurements near 10 kW at 1.06 µm and 10.6 µm wavelengths. Presently we are undertaking the construction of a 100 kW FWOPM with a 150 mm input aperture with the same design strategy, which will use the same system but with a larger pump (85 lpm) and flow meter.

REFERENCES

1. R. L. Smith, T. W. Russell, W. E. Case, A. L. Rasmussen, "A Calorimeter for High-Power CW Lasers," IEEE Trans, Instrum. Meas., vol. IM-21 (1972).
2. S.R. Gunn, "Volume-Absorbing Calorimeters for High-Power in Laser Pulses," Rev. Sci. Ins., 45, 936-943, 1974.
3. M.C.H. McKubre, F. Tanzella, "Mass Flow Calorimetry," Int'l Conf. on Condensed Matter Nuclear Science, ICCF-14, Washington, DC, 1-15, 2008.
4. J. H. Lehman, K. E. Hurst, G. Singh, E. Mansfield, J. D. Perkins, C. L. Cromer, "Core–shell composite of SiCN and multiwalled carbon nanotubes from toluene dispersion," J. Mater. Sci. 45, 4251–4254, 2010.
5. D. E. West and L. B. Schmidt, A System for Calibrating Laser Power Meter for the Range 5-1000 W, NBS Technical Note, 685, (1977).

Goniospectroradiometry of Modern Lamps

M. Lindemann, R. Maass, G. Sauter

Physikalisch-Technische Bundesanstalt, Braunschweig, Germany
Corresponding e-mail address: matthias.lindemann@ptb.de

A newly developed photometer head equipped with integrated input optics in combination with a robot goniophotometer system allows precise spectroradiometric measurements of modern lamps.

NEW PHOTOMETER HEADS

Goniophotometry has a long tradition at the Physikalisch-Technische Bundesanstalt (PTB). The first goniophotometer was installed in the fifties of the last century. As long ago as 1997 the former universal-mounted-goniophotometer was equipped with an additional array spectrometer to measure the relative power distribution of the lamp under test synchronized to the illuminance distribution. But the photometer and the input optic of the array spectrometer had different fields of view and slightly different positions on the goniophotometer system which complicated and restricted the final data analysis.

In 2006 the first robot goniophotometer was installed in the new photometric laboratory of PTB. This new goniophotometer system consists of three robots with 7 degrees of freedom for the positioning of the lamp and the detectors. Two robots are used for the measurements and the third serves as an active lamp-holder. Parallel to the development of the robots, special newly developed photometer heads were designed to measure photometric, colorimetric, radiometric and spectral data, synchronously. The new photometer heads (fig. 1) are optimized for high optical throughput and, therefore, the system is well prepared to measure modern light sources such as single high power LEDs, large LED-clusters, discharge lamps or, of course incandescent lamps, which will probably survive in their role as transfer standards for photometric and colorimetric quantities.

This paper provides information especially about the design of the new combined highly sensitive photometer heads allowing synchronized photometric and spectroradiometric measurements. The measurement results demonstrate the capabilities of this new facility related to conventional and modern sources.

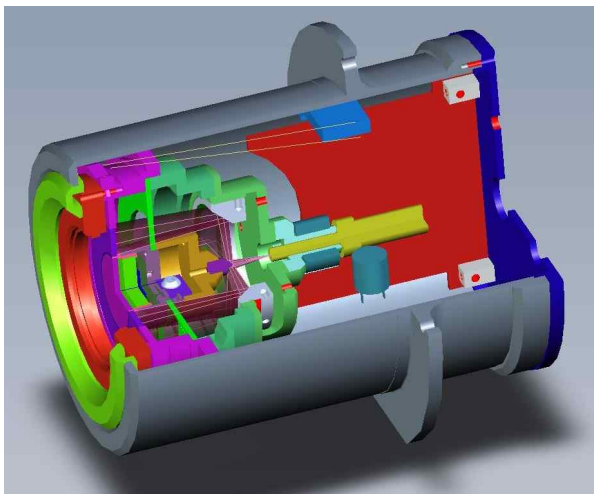

Fig. 1.: Photometer head with integrated input optics attachable via fibre to an array spectrometer

REFERENCES

1. G. Sauter, *Goniophotometry: new calibration method and instrument design*, Metrologia, 32 (1995/96), 685-688
2. M. Lindemann, *Photometrie-Seminar - Goniophotometrie, Ver. 1.2*, internal PTB publication, Physikalisch-Technische Bundesanstalt, May 2008

An absolute detector-based spectrally tunable radiometric source

Steven W. Brown[1], Zhigang Li[2], and Robert D. Saunders[3]

[1]*National Institute of Standards and Technology, Gaithersburg, MD USA,* [2]*Space Dynamics Laboratory, North Logan, UT USA,* [3]*DSK Science, Inc., Poolesville, MD USA*

Corresponding e-mail address: swbrown@nist.gov

In this talk, we describe an absolute, spectrally tunable, detector-based broad-band radiometric calibration source whose expanded (*k*=2) uncertainties in spectral radiance may approach those of reference detectors, on the order of 0.1 %. The conceptual framework of the source, characterization and radiance validation data, trending of the source radiance over time, and the combined standard uncertainty in the source spectral radiance will be presented.

INTRODUCTION

The radiance of narrow-band sources can be determined with expanded (*k*=2) uncertainties on the order of 0.1 % using transfer standard radiance meters traceable to a cryogenic radiometer while the current expanded uncertainty in the spectral radiance of broad-band lamp-illuminated sources is on the order of 0.4 %. On the other hand, broad-band sources are much simpler to operate and maintain than the suite of lasers on the NIST facility for Spectral Irradiance and Radiance responsivity using Uniform Sources (SIRCUS), for example. An ideal source configuration would be one that could be calibrated in narrow-band mode using detectors calibrated on SIRCUS, then operated in broad-band mode for Device Under Test (DUT) measurements.

The Absolute Detector-based spectrally tunable radiance Source (ADbS) makes use of both narrow-band and broad-band configurations, enabling it to be calibrated with uncertainties commensurate with narrow-band sources and operated with the ease of broad-band sources. In the ADbS concept, the spectral radiant flux (or radiance of an integrating sphere source (ISS)) is measured in quasi-monochromatic bands with calibrated radiance meters. The same source then generates broad-band flux DUT measurements. In this way, the uncertainties of detector-based calibrations are achieved while the benefits of a broad-band source calibration are maintained.

If the ADbS was based on a conventional monochromator, the corollary would be to measure the flux spectrally, with the exit slit narrowed, then opening the exit slit and collecting all the transmitted light to provide a broad-band source for calibration of the DUT.

SPECTRALLY TUNABLE SOURCES (STS)

STS's with user-definable output, often called Spectral Light Engines [1], have recently been developed and are available commercially over the spectral range from 380 nm to 1600 nm [1-3]. These sources use a multi-element programmable array of user-selectable reflectance or transmittance elements (e.g. Digital Micromirror Device (DMD) [1-3] or Liquid Crystal on Silicon (LCOS) arrays [4]) in a modified spectrograph configuration, see Fig. 1. In the first half of the Spectral Light Engine, the DMD is placed at the focal plane of a spectrograph. Dispersed incident radiation is imaged across the array of elements at the focal plane. By changing the reflectance (or transmittance) of an element, flux incident on that element can be re-imaged at the output of the device – or not – thereby controlling the radiant intensity from that element. Different columns of elements project different spectral components of the incident light. By adjusting the number of elements that are turned 'on' within the column of elements where the imaged is formed, the intensity of the flux at that particular wavelength can be varied. Controlling all elements at the focal plane, then, results in a user-definable output spectrum, limited to some degree by the spectral content of the input source and the spectral throughput of the spectrometer.

The STS can be operated in 'monochromator-mode' by turning on only one (or a few) columns at a time. Knowing the wavelength, the resultant output radiant flux can be measured absolutely with a calibrated photodiode. By measuring the output of the source across the array (turning elements in each column on) and co-adding the measured flux, it is possible in principle to place an absolute spectral radiant power scale on the integrated output of the source; that is, on a broad-band source. We thus have a tunable radiometric source whose absolute

calibration is traceable to detector standards that are in turn traceable to the SI.

A REALIZED PROTOTYPE ADBS

Figure 1 is a schematic diagram of the ADbS while Fig. 2 is a photograph of a realized prototype ADbS. The ADbS requires an STS, an integrating sphere, and one or more transfer radiometers. A OneLight Spectral Engine* with a spectral range from 430 nm to 630 nm is used as the STS. It is illuminated by an internal Xe arc lamp. The scale is realized using three silicon Gershun-tube radiometers calibrated for spectral radiance responsivity on the NIST SIRCUS facility over the spectral range from 380 nm to 950 nm. There is an internal monitor silicon detector and an internal monitor spectroradiometer mounted on the sphere wall. The monitor spectroradiometer is an Instrument Systems Vis-NIR CAS 140CT-153 compact spectrograph. It has a spectral resolution of 3 nm and a spectral range from 380 nm to 1040 nm. A second CAS instrument with a radiance scale tied to NIST's Facility for Automated Spectral Calibrations (FASCAL) facility periodically measures the spectral radiance of the source. It is used as the primary standard reference instrument to validate the concept.

Data sets consisting of radiance meter measurements, internal and external CAS measurements and monitor photodiode measurements have been acquired weekly for over 6 mos. Results showing the ability of the radiance meters to track changes in the source distribution will be presented along with an estimate of the uncertainty in the broad-band spectral radiance of the source.

CONCLUDING REMARKS

The ADbS is an absolutely calibrated, spectrally tunable detector-based source of spectral radiance. The source radiance is traceable to the International System of Units (SI) through detector standards based on cryogenic radiometry. A detector-based radiance scale is simple to maintain using multiple transfer standard radiometers while offering the possibility of reduced uncertainties in the spectral radiance of integrating sphere sources with broad spectral distributions over conventional source-based radiance scale derivations. In the ADbS approach, changes in the spectral distribution of the source(s) and changes in the throughput of the Integrating Sphere are automatically accounted for. Finally, because the source spectral distribution is user-definable, the ADbS offers unique possibilities as a performance validation artifact.

* Identification of commercial equipment does not imply recommendation or endorsement by the National Institute of Standards and Technology, nor does it imply that the equipment identified is necessarily the best available for the purpose

REFERENCES

1. N. MacKinnon, U. Stange, P. Lane, C. MacAulay and M. Quatrevalet, Spectrally programmable light engine for invitro on in vivo molecular imaging and spectroscopy, Appl. Opt. 44, 2033-2040 (2005); OneLight Corporation, Vancouver, BC, Canada..
2. Gooch and Housego OL 490 Agile Light Source, http://www.goochandhousego.com/products/systems/spectral-imaging-synthesis/ol-490-agile-light-source..
3. S. W. Brown, J. P. Rice, J. E. Neira, B. C. Johnson, Spectrally tunable sources for advanced radiometric applications, J. Res. Natl. Inst. Stand. Technol. 111, 401-410 (2006)..
4. Teresa Ewing, Boulder Nonlinear Systems, Lafayette, CO.

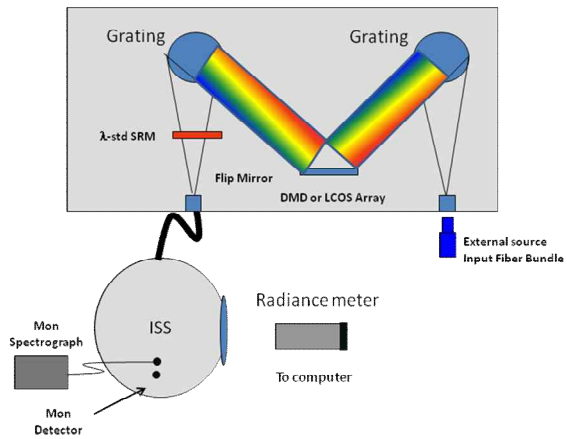

Figure 58. Schematic diagram of the ADbS.

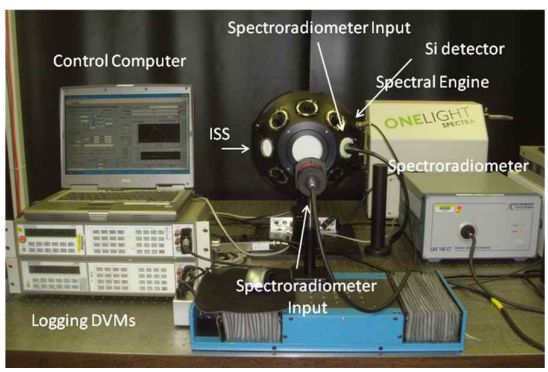

Figure 2. Photograph of the realized ADbS.

The evaluation of multi-walled carbon nanotube coatings using pyroelectric detectors

E. Theocharous[1] and J. Lehman[2]

[1]*National Physical Laboratory, Hampton Road, Teddington, TW11 0LW, UK*
[2]*National Institute of Standards and Technology, Boulder, Colorado 80305, USA*
Corresponding e-mail address: e.theo@npl.co.uk

The characterisation of pyroelectric detectors with and without black coatings can provide information on the physical properties of the coating. This was demonstrated by studying the radiometric properties of a pyroelectric detector based on a 60 μm thick $LiTaO_3$ crystal, with and without a sprayed Multi-Walled Carbon NanoTube (MWCNT) coating. Information gained included the spectral absorption characteristics of the coating, the spatial uniformity of its thickness, and its suitability as a black coating for that particular detector substrate. The spatial uniformity of response of the bare detector improved as the modulation frequency increased from 4 Hz to 70 Hz, whereas that of the coated detector deteriorated. The uncoated detector was found to have a "super-linear" response whereas the coated detector had a "sub-linear" response. The origin and implications of this behaviour are discussed.

INTRODUCTION

Black coatings are applied to thermal detectors to increase their absorptivity, at the cost of increasing their thermal mass [1]. Black coatings must also have high thermal conductance to ensure that a large fraction of the heat generated by the incident radiation passes to the transducer where it is converted into an electrical signal. As the thickness of a particular coating deposited on a pyroelectric crystal increases, the detector response will at first increase because of the higher absorbance, but beyond a certain thickness the responsivity will decrease as the thermal mass of the coating becomes dominant. The main requirements of black coatings for thermal detectors are fulfilled by carbon nanotube (CNT) coatings and pyroelectric detectors coated with these coatings have been studied [2]. A pyroelectric detector with a 3 mm diameter active area was assembled from a 60 μm thick $LiTaO_3$ crystal coated with a spayed MWCNT coating. The thickness of the pyroelectric crystal was sufficiently robust to allow the removal of the MWCNT coating and therefore the evaluation of the same detector could be repeated on the bare (uncoated) pyroelectric crystal.

A variety of MWCNT coatings are currently deposited on substrates as black coatings, but there is little information on the actual thickness of the coating, whether the thickness of the coating is optimum for the type of application used, or whether the thickness of the coating is spatially uniform. This work sought to evaluate the feasibility of characterising some of the physical properties of sprayed black coatings by applying them on a pyroelectric crystal and characterising the radiometric properties of the resultant pyroelectric detector, with and without the black coating.

We describe and discuss the evaluation of the spectral responsivity in the wavelength range from 0.9 μm to 24 μm, and the evaluation of the linearity of response which showed that whereas the uncoated detector was observed to have a "super-linear" response, the linearity of response characteristics of the coated detector was shown to be "sub-linear".

RESULTS AND DISCUSSION

The spatial uniformity of response of the coated and uncoated detector was measured on the NPL spatial uniformity of response facility [3], using a 0.16 mm diameter spot to scan the active area of the test detector. Figures 1, 2, 3, 4 and 5 show the normalised spatial uniformity of response of the pyroelectric detector, with the sprayed MWCNT coating and with the coating removed, measured at modulation frequencies of 4 Hz, 8 Hz, 16 Hz, 40 Hz and 70 Hz, respectively.

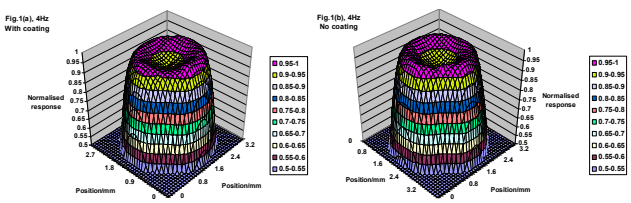

Figure 1: Spatial uniformity of response of the pyroelectric detector, with and without the MWCNT coating, at 4 Hz.

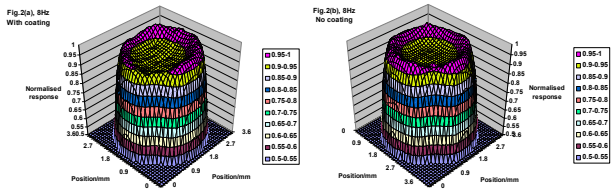

Figure 2: Spatial uniformity of response of the pyroelectric detector, with and without the MWCNT coating, at 8 Hz.

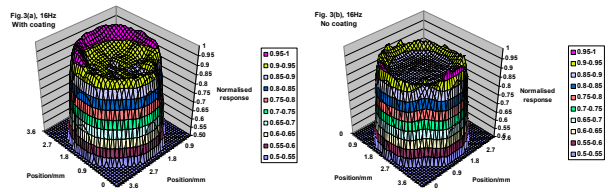

Figure 3: Spatial uniformity of response of the pyroelectric detector, with and without the MWCNT coating, at 16 Hz.

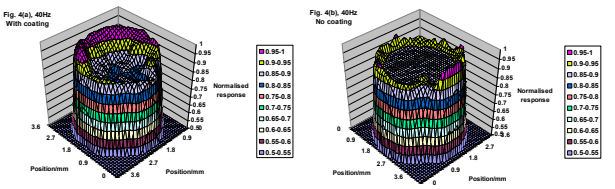

Figure 4: Spatial uniformity of response of the pyroelectric detector, with and without the MWCNT coating, at 40 Hz.

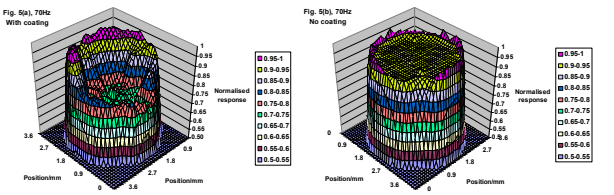

Figure 5: Spatial uniformity of response of the pyroelectric detector, with and without the MWCNT coating, at 70 Hz.

The spatial uniformity of response profiles of the detector at 4 Hz, with and without the MWCNT coating, are similar (Figure 1). However, as the modulation frequency was increased, the spatial uniformity exhibited by the uncoated detector improved, whereas the spatial uniformity exhibited by the coated detector deteriorated. At 70 Hz (Figure 5), the spatial uniformity of the uncoated pyroelectric detector was excellent (a 5% increase in the response around the perimeter of the active area is visible, with the variation over the central 90% of the active area of the detector limited to less than 2%). On the other hand, the spatial uniformity of the coated pyroelectric detector at 70 Hz is very poor, with variations of over 30% of the peak response evident. The spatial non-uniformities in the response of the coated detector can only be due to the MWCNT coating applied to the detector, and in particular spatial variations in the thickness of the coating. Confirmation of this is provided by the fact that at low modulation frequencies, the penetration depth is large so the variations in the coating thickness are less important. As the modulation frequency increased the penetration depth decreased and became comparable to the thickness of the MWCNT coating. The spatial inhomogeneities in the black coating resulted in the spatial non-uniformities of response observed at high frequencies. In the case of the bare detector, the pyroelectric crystal did not have any spatial inhomogeneities so the spatial uniformity remained good at all modulation frequencies [4].

A study of the linearity characteristics of the coated and uncoated detector showed that the uncoated detector had a "super-linear" response whereas the linearity of response of the coated detector was shown to be "sub-linear" [4].

REFERENCES

1. W. R. Blevin and J. Geist, "Influence of black coatings on pyroelectric detectors", Applied Optics, **13**, 1171-1178, 1974.
2. E. Theocharous, R. Deshpande, A.C. Dillon, and J. Lehman, "The evaluation of a pyroelectric detector with a carbon multi-walled nanotube black coating in the infrared" Applied Optics, **45**, 1093-1097, 2006.
3. E. Theocharous, F. J. J. Clarke, L. J. Rodgers and N. P. Fox, "Latest techniques at NPL for the characterisation of infrared detectors and materials", Proc. SPIE, **5209** "Materials for Infrared Detectors III", 228-239, 2003.
4. E. Theocharous and J. Lehman, "The evaluation of a pyroelectric detector with and without a sprayed multi-walled carbon nanotube coating", to be published.

Absolute linearity measurements on a PV HgCdTe detector in the infrared

E. Theocharous

National Physical Laboratory, Hampton Road, Teddington, TW11 0LW, UK

Corresponding e-mail address: e.theo@npl.co.uk

The linearity of response characteristics of a photovoltaic (PV) HgCdTe detector were investigated at a number of wavelengths in the infrared wavelength region using the NPL detector linearity of response characterisation facility. The deviation from linearity in the generated photocurrent was shown to be independent of wavelength, but very dependent on the area of the detector being illuminated. This behaviour is similar to that exhibited by photoconductive (PC) HgCdTe detectors, indicating that Auger recombination is the dominant source of the deviation from linearity observed in the PV HgCdTe detector.

INTRODUCTION

The characterization of the linearity response of photodetectors is one of the most important requirements for accurate radiometry and radiation thermometry**.** The linearity of response characteristics of PC HgCdTe detectors has been found to be poor and dependent on the photon irradiance rather than the total radiant power incident on the detectors [1]. Furthermore, in the case of PC HgCdTe detectors, the contribution due to the thermal background radiation was shown to strongly affect the linearity characteristics of these detectors [2]. Although the linearity characteristics of PV HgCdTe have been briefly mentioned [1], they have never been studied systematically. This is mainly because the active area of these detectors is typically limited to 1 mm in diameter or less, although PV HgCdTe detectors with 2 mm diameter active areas are now being fabricated. It is generally accepted that the linearity characteristics of PV HgCdTe detectors are superior to those of PC HgCdTe detectors, hence their widespread use in Fourier transform (FT) spectrometry. The purpose of this contribution is to report the results of an investigation carried out at NPL into the linearity of response characteristics of a 2 mm diameter PV HgCdTe detector.

APPARATUS AND METHOD

The NPL linearity of response measurement facility [3] was used to characterise the linearity of response of the test detector at four different wavelengths, 10.3 μm, 4.7 μm, 3.8 μm and 2.2 μm. A tungsten strip lamp with a sapphire window was used for wavelengths up to 5 μm while a Nernst source was used for longer wavelengths. Narrow band-pass filters were used to select quasi-monochromatic radiation.

The photocurrent generated by the test detector was amplified using a transimpedance amplifier and gains of 10^4 and 10^5 V A^{-1} were used during this evaluation. The amplified output was fed into a digital lock-in amplifier for rectification. The linearity of the transimpedance amplifier and lock-in amplifier was checked using standard techniques [4]. A 70 Hz modulation frequency was used for all measurements. The operation of the facility was fully automated.

The test detector had a 2 mm diameter active area and was mounted inside a side-looking liquid nitrogen-cooled cryogenic Dewar for operation at 77 K. The Dewar was fitted with a ZnSe window and a cold field-stop which restricted the detector field of view to approximately 60^o (full angle) to limit the noise contribution due to thermal background radiation.

RESULTS AND DISCUSSION

Figure 1 shows the plot of the linearity factor [1] of the PV HgCdTe detector, measured with the active area of the test detector overfilled, at three different wavelengths, 10.3 μm, 4.7 μm and 2.2 μm. Also shown in Figure 1 is the best straight line fit to the measurements acquired at 2.2 μm. All data were normalised for 10^5 V A^{-1} amplifier gain and 1 V lock-in amplifier sensitivity. The good overlap of the three plots corresponding to the three different wavelengths indicates that the wavelength of the incident radiation is not a factor when the linearity factor is plotted as a function of the lock-in amplifier

output. Since the generated photocurrent is directly proportional to the lock-in amplifier output, plots of the linearity factor as a function of generated photocurrent at different wavelengths also overlap. This behaviour is similar to that observed in PC HgCdTe detectors [1].

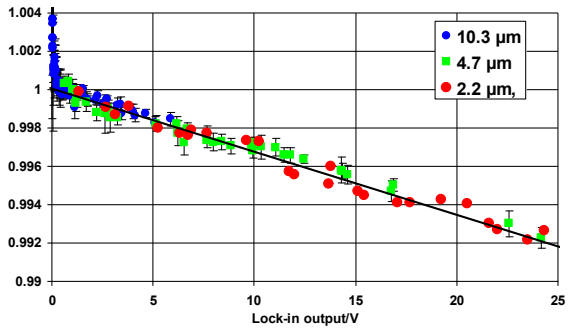

Figure 1: Linearity factor of the PV HgCdTe detector versus lock-in output, measured at 10.3 µm, 4.7 µm and 2.2 µm.

Figure 2 shows the data shown in Figure 1 plotted on a logarithmic abscissa. Also shown in Figure 2 is the best straight line fit to the measurements taken at 2.2 µm. Figure 2 shows that for small lock-in amplifier outputs (output less than 0.1 V) the test detector exhibits a super-linear response. The origin of this behaviour is unknown at present. This, in combination with the deviation from linearity observed for high lock-in amplifier outputs (output higher than about 10 V), shows that the dynamic range of the test detector is relatively low compared to photodetectors responding at shorter wavelengths, such as silicon detectors.

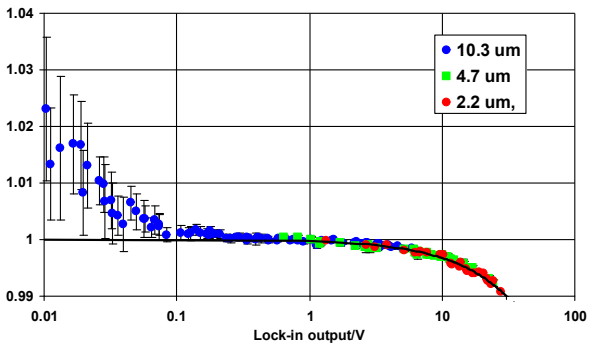

Figure 2: Linearity factor of the PV HgCdTe detector versus lock-in output plotted on a logarithmic abscissa, and measured at 10.3 µm, 4.7 µm and 2.2 µm.

In earlier studies [1], the low spectral radiance available from thermal sources around 10 µm prevented the full evaluation of the linearity of response characteristics of detectors at these long wavelengths. The realization that the linearity characteristics of the PV HgCdTe detector are independent of wavelength allowed the measurements to be repeated at shorter wavelengths where the spectral radiance available from thermal sources was much higher. The linearity factor of the PV HgCdTe detector was measured at 2.2 µm with different areas of the test detector being illuminated. Measurements of the linearity factor were made with 0.4 mm, 0.6 mm, and 1.0 mm diameter spots as well as with the active area of the test detector overfilled. The results, shown in Figure 3, indicate that the linearity factor is a strong function of the illuminated area. This behaviour is similar to that exhibited by PC HgCdTe detectors [1]. When the data shown in Figure 3 was re-plotted as a function of incident irradiance, the plots corresponding to the different illuminated areas exhibited a superior overlap, demonstrating the importance of the area being illuminated and confirming that Auger recombination is the dominant source of the observed deviation from linearity.

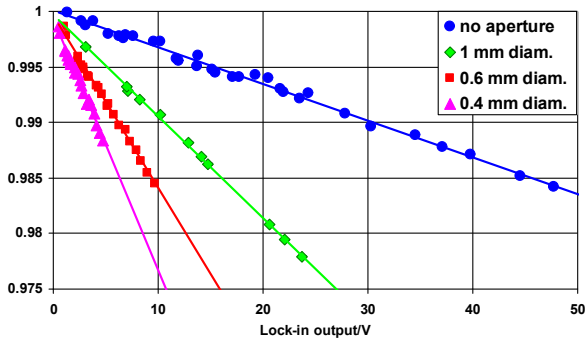

Figure 3: The linearity factor of the PV HgCdTe detector measured at 2.2 µm as a function of lock-in amplifier output. Measurements were made with 0.4 mm, 0.6 mm, 1.0 mm diameter spots as well as with the active area of the test detector overfilled.

REFERENCES

1. E. Theocharous, J. Ishii and N. P. Fox, Absolute linearity measurements on HgCdTe detectors in the infrared, Applied Optics, 43, 4182-4188, 2004.
2. E. Theocharous and O. J. Theocharous, Practical limit of the accuracy of radiometric measurements using HgCdTe detectors, Applied Optics, 45, 7753-7759, 2006.
3. E. Theocharous, F. J. J. Clarke, L. J. Rogers, N. P. Fox, Latest measurement techniques at NPL for the characterization of infrared detectors and materials, Proc. SPIE, 5209, 228-239, 2003.
4. E. Theocharous, Absolute linearity calibration of lock-in amplifiers, Applied Optics, 47, 1090-1096, 2008.

Nonlinearity measurement of filter radiometers using water-cooled LED radiation sources

W. Dong[1, 2], Z. Yuan [2], P. Bloembergen[2], X. Lu[2], Y. Duan[1]

[1] *Key Laboratory for Thermal Science and Power Engineering of MOE, Tsinghua University, Beijing, China*

[2] *National Institute of Metrology, Beijing, China*

correspondence e-mail address: dongw@nim.ac.cn

The nonlinearity of filter radiometers is critically involved and has to be corrected for when measuring radiometric thermodynamic temperatures; the uncertainty in the correction should be adequately specified. In this paper the nonlinearity has been measured by means of the superposition method, involving two water-cooled LEDs with high radiance output as radiation sources. A new method, the step-mode operation with fixed phase shift between the LEDS in question, is introduced. The junction temperature of the LEDs was controlled by a thermostatic bath. The system error caused by the differences in quasi-linear drift between the LEDs is corrected for by means of a model, described in the paper. The results of the nonlinearity and its associated uncertainty, as derived for the filter radiometer in study, are reported.

INTRODCUTION

The nonlinearity of filter radiometers inherent in the detector and associated electronics is one of the main components in the uncertainty budgets proper to the measuring of thermodynamic temperature. Flux doubling by the superposition method [1,2] is widely used to measure nonlinearity.

Using LEDs as radiation sources to measure the non-linearity of detectors or detector based instruments has been firstly reported by D.J Shin et.al[3], and subsequently further developed by us in [4].

EXPERIMENTAL

Two high-intensity LEDs with nominal 645 nm peak wavelength were utilized as radiation sources to substitute the conventional tungsten-strip lamps, and to measure the nonlinearity of the filter radiometer with nominal 633nm peak wavelength. Since the LEDs respond fastly to current supply transients, commonly within a few micro-seconds, the shutters applied in conventional NL measurement systems, in conjunction with tungsten -strip lamps, can be skipped, so as to avoid the system error caused by the changes in interreflections between the tungsten-strip and the shutter, especially at high radiance levels.

By properly switching the bias currents of the LEDs, irradiating the radiometer via a beam-splitter, flux addition can be attained.

Fig1 shows schematic diagram of the NL measurement system using water-cooled LEDs as radiation sources.

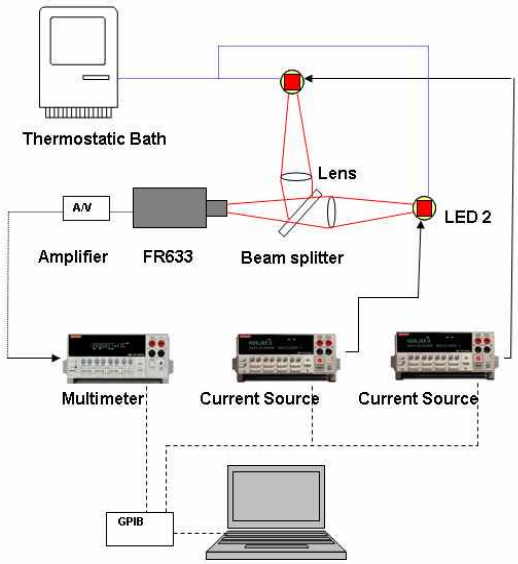

Fig1. A schematic diagram of the nonlinearity measurement system

In [4], we measured the spectral distribution of LEDs and characterized the radiation emitted by the LEDs. Also the measurement and the characterization of the drift in their radiant intensity, in dependence of the bias current, are described. Still the drift in spectral-radiance observed after switching on the LEDs has to be taken into account and corrected for, since this drift, interfering during the superposition procedure, could corrupt the sum rule for the fluxes involved, which is the crux of the superposition method. Therefore experimental research has been carried out in [5] to characterize the drift of LEDs operated in the

pulse mode with fixed phase shift. However, a shift in the LEDs' peak wavelength can be induced by the residual increase in temperature associated with the increase in dissipated power with increasing bias current[5]. In this paper we describe the effect of introducing a water bath to control the junction temperature of the LEDs.

The results obtained indicated that the drift could be roughly specified in terms of two characteristic time intervals: non-linear drift in the first tens of seconds followed by a quasi-linear drift in the subsequent time interval. The cross-over time from non-linear to quasi-linear drift could be ascertained by experiment.

Only the quasi-linear part of the drift was involved in the nonlinearity measurement model. This allowed us to correct system errors introduced by the differences of quasi-linear drift between the two LEDs. The system error δ_{NL} ,under LED1 lightening first condition, can be expressed as

$$\delta_{NL} = \frac{\int_0^{\infty} 2\Delta t(k_1 - k_2) R_{12}(\lambda) d\lambda}{\int_0^{\infty} \phi_1(\lambda) R_1(\lambda) d\lambda + \int_0^{\infty} \phi_2(\lambda) R_2(\lambda) d\lambda}$$

where k_1 , R_1 , ϕ_1 denote the linear drift coefficient ,spectral responsivity, and spectral radiance of LED1, respectively; Δt denotes the quasi-linear drift regime. If we assume that the differences of quasi-linear drift between the two LEDs remain constant while switching the LEDs, the system error can be eliminated.

RESULTS

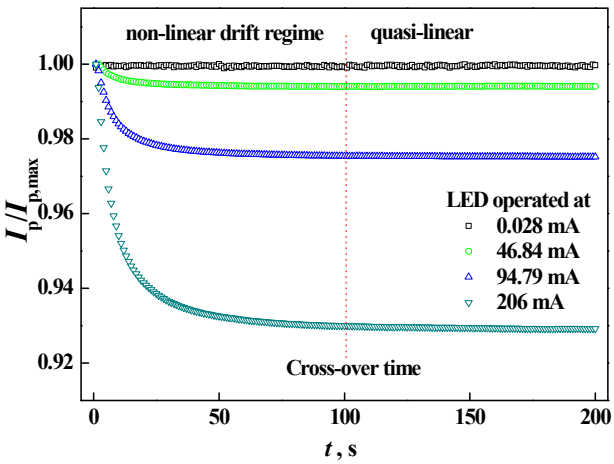

Fig2. The spectral radiation drift of the LED measured by the FR633

Fig2 shows the spectral radiation drift of a LED measured by the filter radiometer FR633, with the junction temperature of the LEDs being controlled at 20 °C i.e. at room temperature.

Fig 3 shows the integral nonlinearity of the FR633 and its associated uncertainties.

FIG3. The integral nonlinearity of the FR 633 and its associated uncertainty

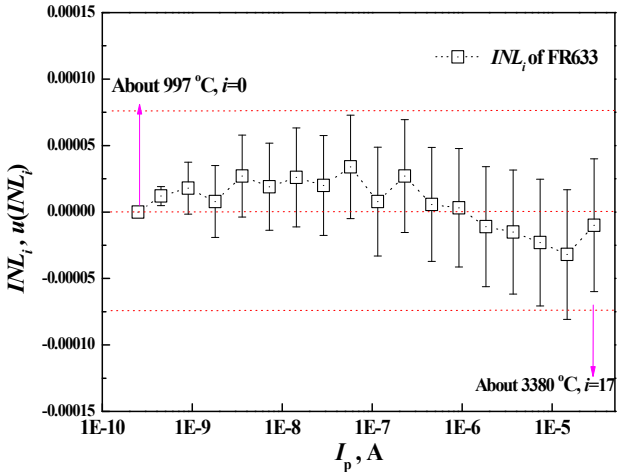

CONCLUSION

1) The nonlinearity of a filter radiometer FR 633 and its associated uncertainty were studied by a novel method employing water-cooled LEDs as radiation sources.

2) Controlling the LEDs junction temperature by water-cooling can restrain the drift and reduce the system error on the NL measurement.

3) The system error caused by the drift of the LEDs involved, is corrected for by means of a model, described in the paper.

4) The standard uncertainty of the integral nonlinearity, corresponding to (thermodynamic) temperature measurements (at NIM) from 997 to 3380 °C, was better than 5×10^{-5}.

REFERENCES

1. D. R. White, M. T. Clarkson, P. Saunders, et al, Metrologia, **45**, pp. 199-210(2008)
2. H. Jung, Metrologia,**15**, pp. 173-181(1979)
3. D. Shin, D. Lee, C. Park, et al, Metrologia,**42**, pp. 154(2005)
4. W. Dong, Z. Yuan, P. Bloembergen, et al, Submitted to Int. J. Thermophysics (2010)
5. P. Manninen, P. Orrevetelinen, Appl. Phys. Lett., **91**(18), pp. 181121-1 ~ 3(2007)

Calibration of a Photodiode Array Spectrometer against the Copper-Fixed Point

Saber S G R Salim[1,2,3], Nigel P. Fox[2], Kenneth T. V. Grattan[3], Tong Sun[3]

[1] *National Institute for Standards (NIS), Tersa Street, El-Haram, Giza, PO Box 136, Egypt*
[2] *The National Physical Laboratory (NPL), Hampton Road, Teddington, Middlesex, TW11 0LW, UK*
[3] *City University London, School of Engineering and Mathematical Sciences, Northampton Square, London, EC1V 0HB, UK*

A photodiode array-based spectrometer is a dispersive instrument with multiple-optical sensors that enables simultaneous acquisition of spectral power over a particular spectral range. Such instruments are, in general, characterized by their small size, low cost and lightweight nature. In addition, they have the key advantage of being able to capture a spectrally resolved signal over a wide spectral range in a very short time, compared to many mechanical scanning spectrometers. This has led to their widespread use in applications where signals are low, unstable, and/or short-lived.

Although diode array spectrometers are increasingly being used in many applications, they are considered, in many cases, instruments of low efficiency due to their poor stray light performance and large nonlinearity coefficient. There have been lately considerable efforts made to account for these two limitations, and, successfully, accurate corrections have been created to improve the quality of the signal level they deliver.

Usually array spectrometers are calibrated against working standard lamps from a National Metrology Institute or even against the manufacturer's working standards. This, in turn, in spite of the acknowledged effort carried out in improving their performance, makes the signal they deliver is usually associated with a large level of uncertainty compared to that delivered by single element photodiodes. As a result, this has limited their use in applications where high accuracy is required along with fast acquisition and wide spectral coverage – such as for in-the-field measurements.

This paper describes the calibration of a photodiode array spectrometer against the copper-fixed point. As a fixed-point blackbody source, it is characterized by excellent emissivity and high stability during the duration of its freezing plateau. The paper shows the system used in the calibration process, in addition to discussing the associated uncertainty factors and their evaluations, showing the value of such an approach for practical applications.

Uncertainty contribution images - A new method to evaluate the measurement uncertainty for ILMD and IRMD

Udo Krüger[1], Peter Blattner[2] and Franz Schmidt[1]

[1]TechnoTeam Bildverarbeitung GmbH, Ilmenau, Germany, [2]METAS Bern, Switzerland
Corresponding e-mail address: udo.krueger@technoteam.de

The evaluation of the measurement uncertainty for ILMD and IRMD [6] requires an extended approach due to the image information and the relation of different parts of the image to each other which has to be taken into account. With the introduction of uncertainty contribution images (UCI) the authors evaluated a first approach to describe the uncertainty contribution from the imaging measurement device for different sources of measurement uncertainty contributions.

The UCIs containing information which are separated in five different contributions differenced by the kind of spatial and temporal correlation and their dependence from the signal level and their spatial position.

Using some measurement examples for a luminance and temperature measurement the authors will explain their new approach.

INTRODUCTION

Imaging measurement devices are widely used for luminance, colour and temperature measurements. However the estimation of measurement uncertainties for the measurement results is not possible at the moment - only simple uncertainty models are available [1].

The correlations between single measurement values and correlations caused by the capturing and correction algorithms influencing the measurement uncertainty estimation. Therefore in a first attempt the uncertainty contributions from the measurement device are of interest. Here the manufacturer of the measurement device should collect data during the calibration and adjustment process of the system. With the help of this information a first estimation of the measurement uncertainty contribution from the measurement device is possible.

NOTATIONS

For image data it is necessary to consider the temporal and spatial context. For a single pixel (i,j), the measurement value can change over time (with and without correlations to other influences) and the value can depend on the values of the neighbouring pixel.

In particular it is necessary to calculate a co-variance matrix for the image information. This is in general not possible or very complicated due to the complex structure of the devices and the difficult interrelationship between the signals of different parts of the image. Therefore the following approach takes only uncorrelated or fully correlated processes and influences into account.

– Influences to the image signal effecting repeated measurements similarly are called temporal correlated effects.
– Influences to the image signal effecting the surrounding of a selected pixel are called spatial correlated effects.

OBJECTIVE OF THE WORK

The result of a measurement using an IxMD[7] is not only the luminance/colour or radiance image $\mathbf{L}(i,j)$ but also an associated uncertainty contribution image (UCI) $\mathbf{u}_{\mathrm{L}}(i,j)$. This image (or theses images) containing all contributions of the measurement system to the measurement value $\mathbf{L}(i,j)$, which can be calculated from the properties of the measurement system estimated during the calibration/adjustment and the working conditions (e.g. system temperature T, spectral radiation function $S(\lambda)$, …).

However UCIs don't contain all contributions to the measurement uncertainty. Contributions resulting from the properties of the measurement object and interactions between the measurement object and the measurement device are not included.

MODEL AND UNCERTAINTY CONTRIBUTIONS

Using a modified model equation from [1]

[6] ILMD … Image luminance measuring device, IRMD … Image radiance/temperature measuring device

[7] IxMD is used as a general term and means ILMD, IRMD or ICMD (Image colour measuring device).

$$\mathbf{L} = \frac{1}{A_{\mathrm{P}} \cdot \overline{\mathbf{PP}}_{\mathrm{L}}} \cdot k_{\mathrm{L}} \cdot \frac{f_{\mathrm{NL}}(\mathbf{S} - \overline{\mathbf{D}}) \cdot (\mathbf{S} - \overline{\mathbf{D}})}{k_{\mathrm{Sys}} \cdot t_{\mathrm{I}}} \qquad (1)$$

As a first attempt five different contributions to the measurement uncertainty can be indentified.

Table 14. Summary of selected uncertainty contributions

		temporal	
		correlated	Not correlated
Spatial	correlated	$u_{\mathrm{rel,c}}(L)$ $\mathbf{u}_{\mathrm{rel,c}}(\mathbf{L})$	$\mathbf{u}_{\mathrm{t}}(\mathbf{L})$
	Not correlated	$\mathbf{u}_{\mathrm{s}}(\mathbf{L})$	$\mathbf{u}_{\mathrm{st}}(\mathbf{L})$

- Uncertainties which are temporal and spatial correlated to all pixels and not spatial or signal depended, hence can be represented by a single scalar (relative uncertainty contribution: $u_{\mathrm{rel,c}}(L)$)
- Uncertainties which are temporal and spatial correlated for all pixels and spatial or signal depended. (relative UCI: $\mathbf{u}_{\mathrm{rel,c}}(\mathbf{L})$)
- Uncertainties which are not correlated for spatial averaging but for temporal averaging (absolute UCI: $\mathbf{u}_{\mathrm{s}}(\mathbf{L})$)
- Uncertainties which are not correlated for temporal averaging but correlated for spatial averaging (absolute UCI: $\mathbf{u}_{\mathrm{t}}(\mathbf{L})$)
- Uncertainties which are not correlated for spatial and temporal averaging. (absolute UCI: $\mathbf{u}_{\mathrm{st}}(\mathbf{L})$)

The index of the uncertainty contribution images describes the quantity for which the uncertainty contribution can be reduced by averaging.

Table 15. Examples for uncertainty contributions

		temporal	
		correlated	Not correlated
spatial	correlated	**B1** calibration Factor, k_{L} **B2** nonlinearity, $f_{\mathrm{NL}}()$	**B4** not known at the moment
	Not correlated	**B3** Dark signal non uniformity (DSNU, $\overline{\mathbf{D}}$)	**B5** Photon shot noise k_{Sys}

The measurement values $\mathbf{L}(i,j)$ and the associated uncertainty contributions ($u_{\mathrm{rel,c}}$, $\mathbf{u}_{\mathrm{rel,c}}(\mathbf{L})$, $\mathbf{u}_{\mathrm{s}}(\mathbf{L})$, $\mathbf{u}_{\mathrm{t}}(\mathbf{L})$ und $\mathbf{u}_{\mathrm{st}}(\mathbf{L})$) of a region (area of interest, AOI) with N_{s} pixel and the temporal averaging using N_{t} images can be expressed by the following equations :

$$^{s}\overline{L} = \frac{1}{N_{\mathrm{s}}} \sum_{i,j \in \mathbf{I}} \begin{cases} L(i,j) & (i,j) \in AOI \\ 0 & (i,j) \notin AOI \end{cases} \qquad (2)$$

$$u^2\left(^{s}\overline{L}\right) = \underbrace{\mathrm{u}^2_{\mathrm{rel,c}} \cdot {}^{s}\overline{L}^2}_{(B1)} + \underbrace{\left(^{s}\overline{\mathbf{u}_{\mathrm{rel}}(\mathbf{L}) \cdot \mathbf{L}}\right)^2}_{(B2)} + \underbrace{\underbrace{\left(\frac{^{s}\overline{\mathbf{u}_{\mathrm{s}}(\mathbf{L})}}{N_{\mathrm{s}}}\right)^2}_{(B3)} + \underbrace{\left(\frac{^{s}\overline{\mathbf{u}_{\mathrm{t}}(\mathbf{L})}}{N_{\mathrm{t}}}\right)^2}_{(B4)} + \underbrace{\left(\frac{^{s}\overline{\mathbf{u}_{\mathrm{st}}(\mathbf{L})}}{N_{\mathrm{s}} N_{\mathrm{t}}}\right)^2}_{(B5)}}_{(B3')} \qquad (3)$$

With:

$^{s}\overline{L}$ Spatial mean value (luminance, temperature, colour) in a region (measurement value)

N_{s} Number of pixels in the region

N_{t} Number of camera images used for the evaluation of the measurement value

In their full paper the authors will explain the concept in a more detailed manner. Furthermore some known and classified uncertainty contributions will be shown by means of examples. The authors will present selected effects for instance: the influence of the photon shot noise and the lens shading. For each contribution the calculation of the uncertainty

contribution image and the combination to the combined measurement uncertainty will be showed.

REFERENCES

1. Krüger, U. and Schmidt, F.: The impact of cooling on CCD-based camera systems in the field of image luminance measuring devices. NewRad2008 published in Metrologia 46 S252-S259, 2009.

A New Method for Measurement of Window Transmittance of Cryogenic Radiometer

Xuebo Huang and Gan Xu

National Metrology Centre, Agency for Science, Technology and Research, Singapore

Corresponding e-mail address: huang_xuebo@nmc.a-star.edu.sg

Abstract. This paper described a new method to measure the window transmittance accurately using a modified window chamber of cryogenic radiometer so as to improve calibration uncertainty of trap detector especially at UV and NIR wavelengths. The measurement uncertainty of transmittance of a synthetic fused silica window is better than 0.003%.

INTRODUCTION

The measurement of window transmittance is an important task in the calibration of trap detectors using cryogenic radiometer especially at UV and NIR wavelengths as it is a big challenge to adjust the incident laser beam on the window at Brewster angle by minimising the reflecting beam through human eyes.

DESIGN AND METHOD

The main body of cryogenic radiometer was modified as shown in figure 1. A measuring chamber was designed and assembled in between the window chamber and cryogenic cavity. The window chamber, measuring chamber and cryogenic cavity were mounted in a movable stage. A trap detector used to measure laser power was attached to a holder with fine adjustment mechanism along X, Y and Z axes.

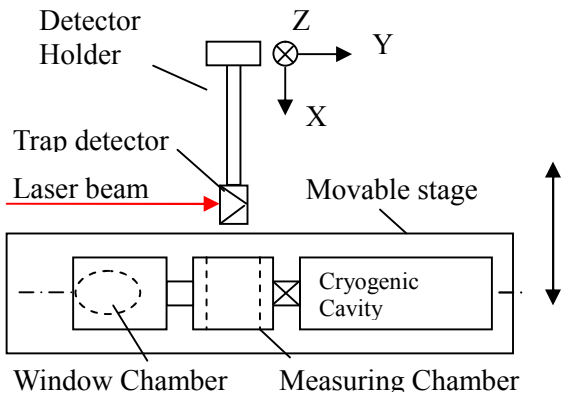

Figure 1. Top view of the setup to measure laser power directly

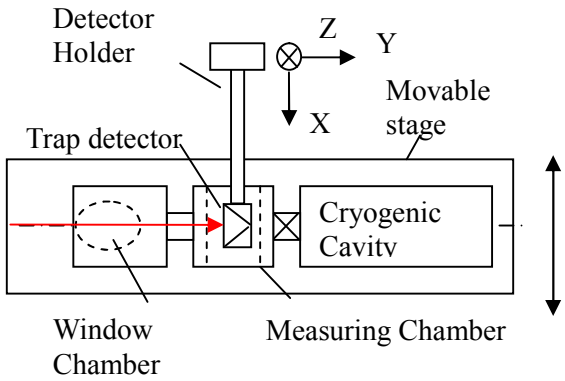

Figure 2. Top view of the setup to measure laser power inside measuring chamber

The laser power was directly measured by the trap detector as shown in Figure 1 and recorded as P_1. Then the trap detector was raised up to certain height (h) which was caused by laser beam displacement after passing through the window. The movable stage was moved forward until the laser beam passed through the window and reached to the trap detector again as shown in Figure 2. The laser power was measured again and recorded as P_2. The window transmittance at certain wavelength $T(\lambda)$ can then be calculated using equation (1):

$$T(\lambda) = \frac{2(P_2 - P_D)}{(P_{1B} - P_D) + (P_{1A} - P_D)} \qquad (1)$$

where P_{1B} and P_{1A} are direct power readings before and after the power measurement inside the measuring chamber. P_D is the dark power reading.

The laser beam displacement before and after passing through the window or the height (h) that trap detector should be raised is determined as shown in Figure 3.

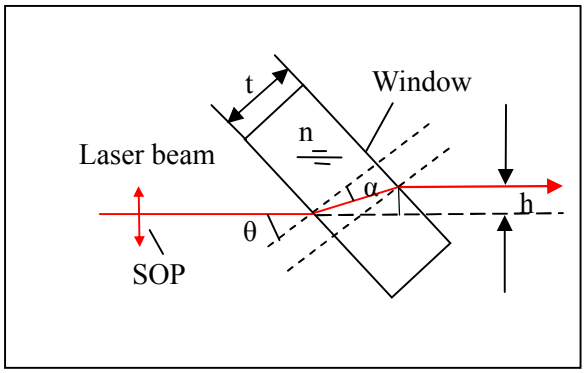

Figure 3. Diagram of laser beam displacement (h) before and after it passes through the window. (t: thickness of window; n: refractive index of window; θ: laser beam incident angle; **α**: laser beam refractive angle; SOP: state of polarisation of laser beam)

Under a visible laser (e.g. He-Ne laser at 632.8nm) with linear polarisation (its SOP as shown in Figure 3), the incident laser beam at Brewster angle (θ) can be easily determined by adjusting the angle of the window to minimise reflective beam by eyes. The Brewster angle of the window can be calculated in equation (2):

$$\tan(\theta) = n(632.8nm) \qquad (2)$$

where *n(632.8nm)* is the refractive index of the window material at wavelength of 632.8 nm.

Then displacement (h) can be calculated using equation (3) according to the geometrical optics shown in Figure 3.

$$h = t\sin(\theta - \alpha)/\cos(\alpha) \qquad (3)$$

where

$$\alpha = \sin^{-1}[\sin\theta / n(\lambda)] \qquad (4)$$

When the incident angle (θ) is fixed, the displacement of laser beam (h) can also be calculated at other wavelengths especially UV or NIR using equations (3) and (4). The example of calculation at 632.8 nm and 356.4 nm was shown in Table 1.

Table 16. Calculation of laser beam displacement before and after passing through the window

laser wavelength (λ)	632.8 nm	356.4 nm
Thickness of window (t)	10.047 mm	10.047 mm
Refractive index of window material, $n(\lambda)$ [1]	1.45702	1.47587
Incident angle (θ)	55.5369 degree	55.5369 degree
Refractive angle (α)	34.4631 degree	33.9623 degree
Laser beam displacement (h)	4.38 mm	4.45 mm

UNCERTAINTY EVALUATION

The main sources of measurement uncertainty were evaluated in Table 2.

Table 2. Uncertainty budget for transmittance measurement

Source of uncertainty	**Type**	**Value of Standard uncertainty (%)**
Repeatability of transmittance measurements	A	0.001
Spatial uniformity of trap detector (±0.05mm)	B	0.0017
Spatial uniformity of window glass (±0.05mm)	B	0.0004
Accuracy of refractive index of window glass(±3x 10e-5) [1]	B	0.0014
Thickness measurement of window glass (±0.002mm)	B	0.0014
Combined Uncertainty(k=1)		0.0028

CONCLUSION

The window transmittance of cryogenic radiometer was measured by using a new method through a modified window chamber. The main sources of uncertainty were investigated theoretically and experimentally. The measurement uncertainty of the window transmittance is 0.0028% (k=1).

REFERENCE

1. www.mellesgriot.com/products/optics/mp_3_2.htm

The concept of PTB's next generation solar cell and detector calibration facility

Stefan Winter, Dirk Friedrich, Thomas Fey

Physikalisch-Technische Bundesanstalt, Braunschweig, Germany
Corresponding e-mail address: Stefan.Winter@ptb.de

The Differential Spectral Responsivity (DSR) method has been successfully used at PTB for the primary calibration of solar cells since the 1980s [1]. But due to increasing requirements, there is presently a strong need for significant improvements. Thus, a new concept for the next generation of the solar cell and detector calibration facility has been developed: the LASER-DSR facility. It will decrease the relative uncertainty of I_{STC} of 156x156 mm² large reference solar cells from 1.6% to about 0.6%.

INTRODUCTION

Due to the high market volume of solar modules, an uncertainty of 1 % in efficiency measurement causes an uncertainty of many 100 millions of Euro per year in the product value. Hence PTB has repeatedly been approached with the request of a lower measurement uncertainty, even though PTB - as a qualified World Photovoltaic Scale (WPVS) laboratory - already belongs to the institutes serving the lowest uncertainty for the primary calibration of reference solar cells worldwide while being traceable to the SI.

In this contribution, we will present our concept for a new improved setup for the calibration of solar cells and detectors that meets the needs of industry for decreased uncertainty levels.

APPROACH

A completely new facility for the primary calibration of reference solar cells has been designed and is being built at PTB. The new facility is based on the successful Differential Spectral Responsivity (DSR) method that allows the determination of the absolute spectral responsivity and nonlinearity of the solar cell with the lowest uncertainties [2]. By using a tunable laser (see Fig. 1), the new setup avoids the main problem of the lamp-based system, the low optical power of the monochromatic beam.

RESULTS

During preliminary measurements by means of a tunable laser, a factor of 100(!) of higher irradiance in comparison with the lamp-based facility was reached. The high power allows the solving of the subsequent problems of low monochromatic power such as: a low signal-to-noise ratio for large solar cells at a high bias radiation level, the difficulty of achieving a good uniformity, the high bandwidth of the monochromatic beam, and the interpolation error when merging absolute and relative measurements. These improvements will lead to a reduction of the relative uncertainty of the short circuit current of large reference solar cells (156x156 mm²) from 1.6% to 0.6%, thus to the uncertainty that is reachable today only for 20x20 mm² reference solar cells. The reduction is reached mainly due to the improved uniformity of monochromatic radiation field and the better signal to noise ratio at high bias levels. The presentation will show the concept, the first measurements and the solution of new laser induced problems like interferences, outer-band peaks (see Fig. 2), and especially how the high peak power of fs pulses is smoothed to a constant cw signal.

CONCLUSION

Because a large number of calibration and testing labs worldwide are customers of PTB, a large part of the whole PV community will benefit from these improvements at the starting point of the PV calibration chain.

With the realization of this new concept, PTB will meet the needs of the PV industry, concerning a significant reduction of measurement uncertainties. The end of the complete validation and the start of the regular calibrations are expected for 2012.

REFERENCES

[1] J. Metzdorf: “Calibration of solar cells 1: The differential spectral responsivity method” Appl. Optics 26 (1987) 1701

[2] S. Winter, T. Wittchen, J. Metzdorf: Primary Reference Cell Calibration at the PTB Based on an Improved DSR Facility; in “Proc. 16th European Photovoltaic Solar Energy Conf.”, ed. by H. Scherr, B. Mc/Velis, E. Palz, H. A. Ossenbrink, E. Dunlop, P. Helm (Glasgow 2000) James & James (Science Publ., London), 4 p., ISBN 1 902916 19 0

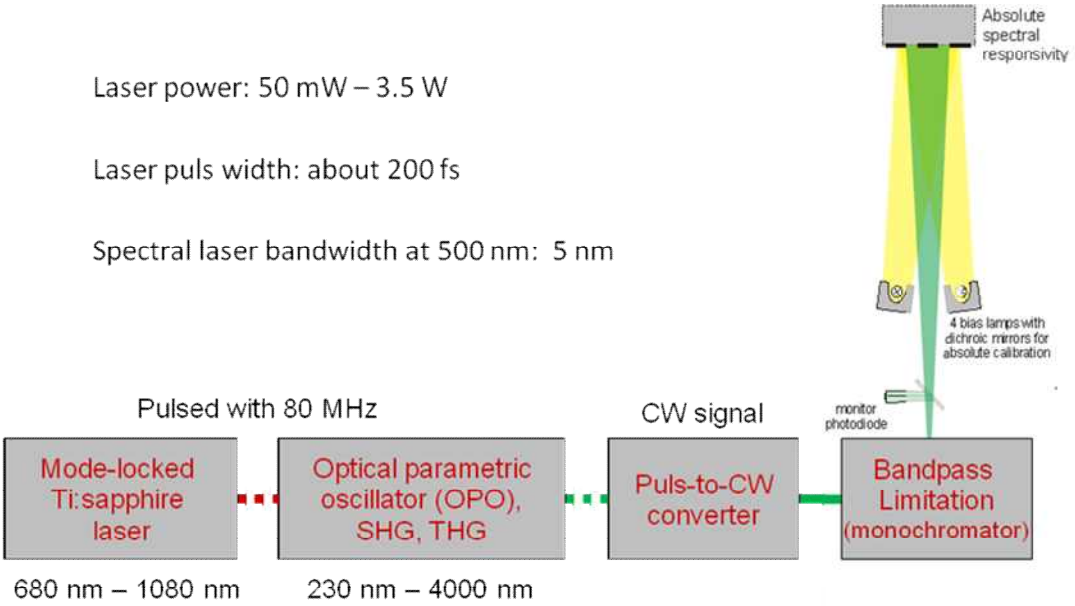

Fig. 1: Schematic diagram of the new Laser-DSR facility: The beam starts at a hands-free widely tunable mode-locked Ti:sapphire laser. Depending on the needed wavelength the beam passes through an optical parametric oscillator (OPO) and/or a second harmonic generator (SHG) or a third harmonic generator (THG). The pulsed signal is smoothed to a cw signal at a special pulsed-to-cw-converter developed at PTB. The bandpass is limited by a monochromator (see Fig. 2).

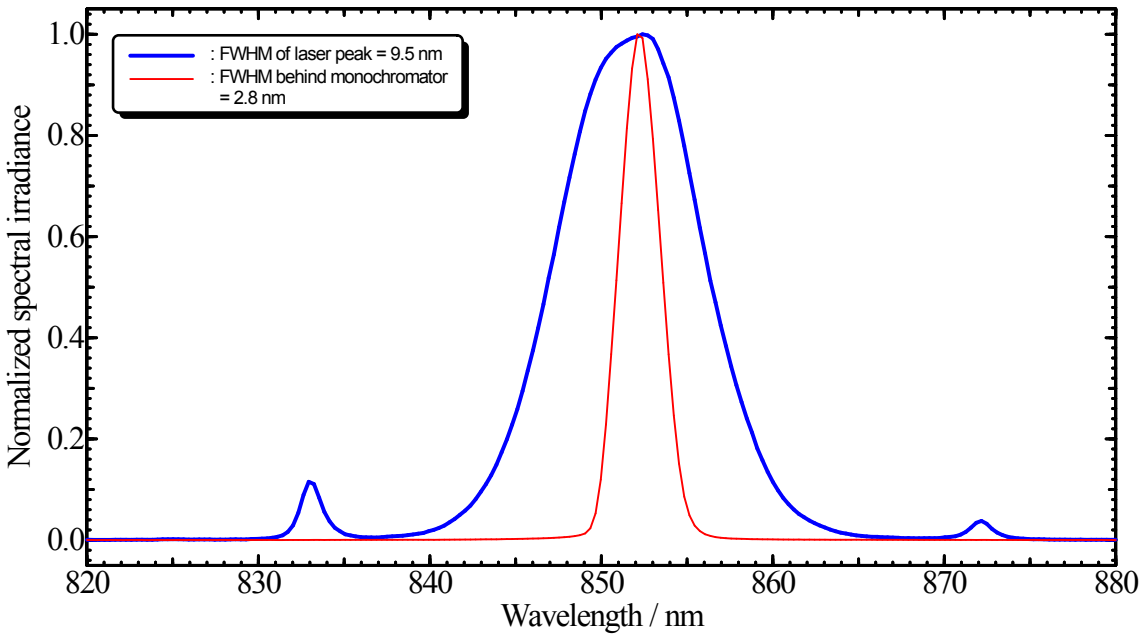

Fig. 2: Because the pulsed laser spectrum has
a) a too high bandwidth,
b) outer-band peaks (partly more than 10 % of the maximum signal) and
c) a small part of the SHG signal in the THG signal
a monochromator is applied to achieve a well-defined signal. Nevertheless, this signal is up to 100 times higher than the monochromatic signal of the old monochromator-based setup.

Design of an instrument for accurate measurements of pulsed optical power

Yabai He, Anura Gajaweera, and Peter Manson

National Measurement Institute, Sydney, NSW 2070, Australia
Corresponding e-mail address: yabai.he@nmi.gov.au

Accurate power measurements of pulsed optical radiation by photodiode-based detectors are more difficult than for continuous-wave (cw) radiation, as photodiode outputs vary in time and dynamic pulse response of detectors may lead to larger measurement uncertainties. Here, we describe the design of a new photodetector circuit board for improving measurement accuracy of pulsed optical power. The new detector is based on two matched photodiodes and a passive capacitor-integration technique, complemented by a feedback loop for maintaining a constant bias voltage across the photodiodes. The new device will be tested under a wide range of laser pulse conditions to demonstrate its performance.

INTRODUCTION

Semiconductor photodiodes are widely used to convert optical radiation of a certain wavelength range directly into an electric current. A measurement of this generated current, either directly or indirectly after some further processing by electronic circuits such as preamplifiers, enables a determination of the input optical power, provided the absolute spectral responsivity of the photodiode system is known. That calibration is generally performed by comparison with e.g., a reference cryogenic radiometer [1]. This measurement technique is quite straightforward for continuous-wave (cw) radiation. However, care should be taken when measuring the average power of pulsed laser radiation. This explains why commercial optical power meters available on the market are usually classified for either cw or pulsed radiation measurement, as the temporal profile of optical pulses can affect measurements.

At the National Measurement Institute (NMI) Australia, we have a need for an accurate optical power detector to cover a wide range of laser pulse conditions (e.g. repetition rate and temporal pulse profile). This has prompted us to develop a new circuit based on photodiode detectors. The new device should be capable of making accurate optical power measurements of both cw and pulsed laser radiation, with minimal dependence on the radiation pulse characteristics. This paper reports on this development and its performance.

INSTRUMENT DESIGN

We have designed the new instrument based on two photodiodes and a passive capacitor-integration technique, complemented by a feedback loop for maintaining a constant bias voltage across the photodiodes. A passive integrating capacitor is not subject to the critical time response issues associated with active components as in the case implemented with an operational amplifier coupled with a feedback capacitor. This makes the instrument applicable to a wide range of laser pulse conditions (repetition rate and pulse profile). Another factor that affects performance of a photodiode is its dark current which is not constant but depends on temperature. To reduce this impact we have implemented a dual matched photodiode configuration. Two biased photodiodes are connected in series; one photodiode charges the capacitor while a second photodiode discharges it. The current flowing through each of the photodiodes is monitored optionally by two sets of inline pick-up resistors and differential instrumental amplifiers. This balanced-photodiode configuration cancels the impact of dark currents of the photodiodes. One or two input optical beams are converted by the two photodiodes into electric currents which charge or discharge the passive capacitor. The resulting voltage across the capacitor is then monitored by a buffer amplifier with extremely high input impedance and very low input bias current. The capacitor is resettable via an analog switch controlled by an electronic TTL signal.

A feedback loop is included to adjust the voltage applied to the other electrode of each of the two photodiodes automatically, so that the bias voltage across each photodiode remains constant at pre-set values, while the capacitor voltage changes due to charge or discharge. This ensures that the operation condition of the photodiode stays unchanged. A schematic of the new photodetector circuit board is presented in Fig.1.

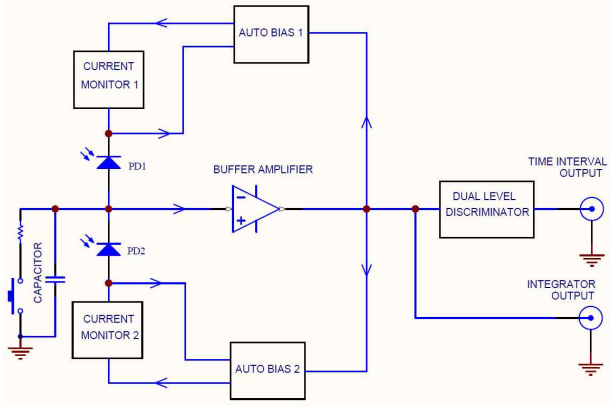

Figure 1. Schematic of the new photodetector circuit

This instrument has three operation modes:
(1) single beam input,
(2) dual beam input,
(3) low-pass resistor-converter.

(1) Single-beam mode

In the single-beam mode, only one photodiode is exposed to input optical radiation. The PD current charges the capacitor and the voltage across the capacitor is monitored by the buffer amplifier.

The buffered capacitor voltage increases monotonically as each laser pulse is received. This output voltage is compared precisely against two pre-set voltage levels. The time taken (or the number of pulses within this time interval) for the capacitor voltage to pass from one preset reference voltage level to a second level is inversely proportional to the average power of the laser pulses.

The total number of pulses integrated should ideally be larger than the inverse of the required relative uncertainty. However, the detector can make single pulse measurement as well, by recording the voltage value at the end of the pulse.

The conversion factor of this time measurement to the optical power can be calibrated against a cw reference beam.

(2) Dual-beam mode

In the dual-beam mode, each photodiode monitors a separate input beam. This enables direct comparison of the two optical beam powers without knowing the spectral responsivities of the two photodiodes. One configuration is for one detector to receive pulsed radiation to be measured, while the second photodiode receives a cw reference radiation of the same wavelength. One of the two photodiodes charges a capacitor, while the second one discharges the same capacitor. The power of the cw beam will be adjusted so that the capacitor voltage behaves the same way as when both beams are blocked. Then the cw beam power will be measured by an independent cw power measurement system (e.g. reference photodiode in combination with a picoammeter). A second similar measurement will be obtained after swapping the two photodiode channels or the two beams. By doing this, the final value of the pulsed beam power can be calculated as a geometric average of the two readings, and the spectral responsivity function of the two photodiode channels will become irrelevant.

(3) Low-pass resistor converter mode

A resistor will be connected to the capacitor in parallel to turn it into a current-to-voltage converter with the capacitor performing a passive low-pass filtering function. The current-to-voltage conversion occurs at the resistor to generate a voltage output. The high-input-impedance amplifier buffers the voltage across the resistor to an output port.

RESULTS AND DISCUSSION

We have constructed a photodetector based on the new design. Its functionality has been verified. Currently it is undergoing various tests under a wide range of laser pulse conditions, to verify its measurement accuracy and the influence of pulse shape. Detailed results will be reported at the conference.

As photodiodes are used to detect light, the new photodetector will be limited to receiving sub-mW low power radiation without saturation [2,3]. High power optical beam needs to be attenuated beforehand. We have therefore also developed a method to determine optical attenuation accurately so that the photodetector can be used over an extended optical power range.

REFERENCES

1. J.M. Houston, J.P. Rice, "NIST reference cryogenic radiometer designed for versatile performance" Metrologia 43, S31-S35 (2006).
2. R. Stuik, F. Bijkerk, "Linearity of P-N junction photodiodes under pulsed irradiation," Nuclear Instruments and Methods in Physics Research A 489, 370-378 (2002).
3. R.E. Vest, S.B. Hill, S. Grantham, "Saturation effects in solid-state photodiodes and impact on EUVL pulse energy measurements," Metrologia 43, S84-S88 (2006).

The Infrared Integrating Sphere (IRIS) Radiometer for Atmospheric Longwave radiation Measurements

Julian Gröbner[1]

[1]*Physikalisch-Meteorologisches Observatorium Davos, World Radiation Center*
Davos Dorf, Switzerland
Corresponding e-mail address:julian.groebner@pmodwrc.ch

The IRIS radiometer is a new transfer standard instrument for the measurement of atmospheric longwave irradiance. The requirement for irradiance measurements required the development of a novel integrating sphere concept with integrated shutters and a pyroelectric detector. The radiometer is traceable to SI via the calibration by a well characterised cavity. Simultaneous outdoor measurements with four independently calibrated IRIS radiometers gave consistent measurements to within ±1 Wm^{-2}.

INTRODUCTION

Downwelling atmospheric longwave radiation between 4 µm and 100 µm is a key component of the surface radiation budget. Measurements are usually performed with pyrgeometers, consisting of a blackened thermopile and a silicon dome to protect the instrument from the harsh environment. In the past, pyrgeometers were calibrated by radiation from blackbody cavities. However significant uncertainties due to the spectral transmission features of the dome in combination with the significant differences between the Planck radiation from the calibrating cavity and the atmospheric longwave radiation spectrum were observed [1]. Therefore, pyrgeometers are now calibrated in-situ, using longwave radiation measurements by transfer standard radiometers, which do not suffer from these limitations.

MEASUREMENT PRINCIPLE

The IRIS radiometer was conceived as transfer standard radiometer for atmospheric longwave irradiance. The schematic drawing is shown in Figure 1. IRIS consists of a 60 mm diameter gold plated integrating sphere with three apertures; the aperture facing upwards measures the irradiance from the upper hemisphere, while the aperture at the bottom receives radiation from a small reference blackbody cavity. An SPH-40 series windowless pyroelectric detector from Spectrum Detector Inc. is placed behind the third aperture, located 90° from the other two. The radiation entering the integrating sphere is switched with a nominal frequency of 27 Hz between the upper and lower aperture using two gold plated shutters mounted within the integrating sphere. Effectively, the measurement principle consists in measuring the incoming downwelling radiation relative to the radiation emitted by the reference cavity.

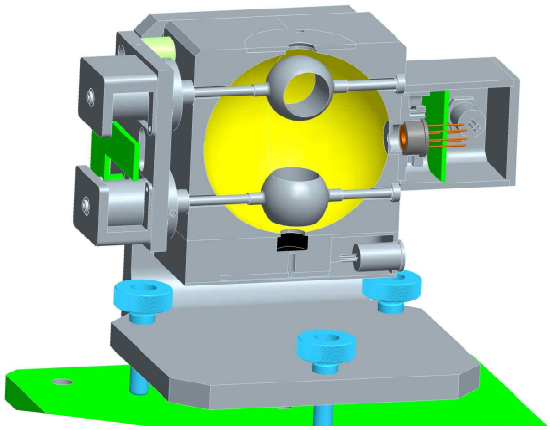

Figure 1 Schematic layout of the IRIS radiometer.

The Infrared Radiometry Section of the World Radiation Center at PMOD/WRC has constructed five prototype IRIS radiometers of which the last four have nominally identical specifications and will be discussed here. They are operated at ambient temperatures during night-time only since they are operated without any windows. At regular intervals, they are calibrated in the blackbody cavity BB2007 which was designed and built by PMOD/WRC [2].

IRIS#2 has been in operation since October 2009, while the remaining three were put in operation in March 2011. Figure 2 shows the calibration history of IRIS#2. As shown in the figure, the repeatability of the responsivity calibration of the radiometer is ±0.7% which corresponds to a stability of ±0.7 Wm^{-2} in atmospheric downwelling longwave radiation.

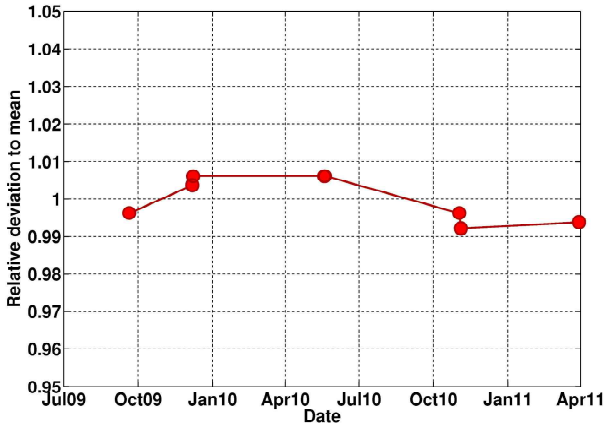

Figure 2 Relative variability of the Sensitivity of the IRIS#2 Radiometer obtained from calibrations using the BB2007 blackbody cavity.

UNCERTAINTIES

The uncertainty budget of the IRIS Radiometer is summarized in Table 1. The main uncertainty components are the responsivity based on the calibration with the blackbody cavity, ±0.6%, and the uncertainty of the temperature sensitivity of the pyroelectric detector of -0.08±0.025%K^{-1}. The latter is important since the calibration is performed in the laboratory at 20 °C, while the measurements are performed at ambient temperatures, between -20 °C and +20 °C. Thus, the overall uncertainty of atmospheric longwave radiation measurements with the IRIS Radiometer is ±1.2%, which corresponds to an uncertainty of ±1.2 Wm^{-2} for a net radiation flux of 100 Wm^{-2} representative for clear sky conditions.

Table 17. Expanded relative uncertainty components (k=2) for the IRIS radiometer.

Uncertainty component	u (95%)
Responsivity	0.6%
Reference surface	0.02 %
Temp. coefficient for 40 K range	1.0%
Total	1.2%

MEASUREMENTS

The four IRIS Radiometers were calibrated in turn in the blackbody cavity BB2007 and installed on the outdoor measurement platform for several clear sky nights. The measurements are shown in Figure 3 while the differences and standard deviations of the four IRIS radiometers during the measurement period are summarised in Table 2. Measurements are taken every 10 seconds and consist of 10 samples of which the average is displayed in the figure. As can be seen, the radiometers IRIS#2 IRIS#3 and IRIS#5 measure atmospheric longwave radiation with differences less than ±1 Wm^{-2} between each other, which is consistent with the estimated uncertainties. The larger scatter of

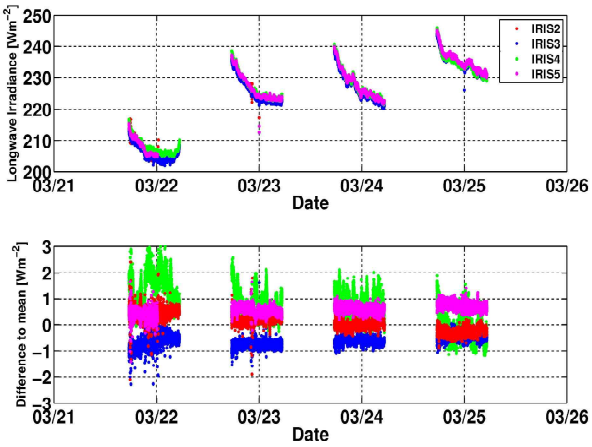

Figure 3 Atmospheric longwave irradiance measured with IRIS #2, #3, #4, #5 in Davos, March 21 to 25, 2011.

IRIS#4 on the other hand could be traced to a faulty detector which had to be replaced.

Table 2. Atmospheric longwave measurements by four IRIS Radiometers during four clear nights at Davos in March 2011.

	Difference to mean [Wm^{-2}]	Standard deviation [Wm^{-2}]
IRIS#2	0.10	0.31
IRIS#3	-0.63	0.19
IRIS#4	0.68	0.73
IRIS#5	0.59	0.19

CONCLUSION

A new transfer standard radiometer for atmospheric longwave irradiance measurements was designed and tested. The measurement uncertainty was estimated to ±1.2 Wm^{-2}, which is consistent with outdoor measurements between four prototypes which agreed within ±0.7 Wm^{-2} during four clear sky nights. The stability of one radiometer was tested over more than one year and showed a stability of better than ±0.7% over this time period.

REFERENCES

1. Gröbner, J, and A. Los, Laboratory Calibration of pyrgeometers with known spectral responsivities, Applied Optics, 46, 7419-7425, 2007.
2. J. Gröbner, Operation and Investigation of a tilted bottom cavity for pyrgeometer characterizations, Applied Optics, 47, 4441-4447, 2008.

Characterization of SiC photodiodes for high irradiance UV radiometers

Stefan Nowy[1], Bettina Barton[1], Sven Pape[1], Peter Sperfeld[1], Dirk Friedrich[1], Stefan Winter[1],

Gabriel Hopfenmüller[2], and Tilman Weiss[2]

[1] *Physikalisch-Technische Bundesanstalt, Braunschweig, Germany,*
[2] *sglux SolGel Technologies GmbH, Berlin, Germany*
Corresponding e-mail address: stefan.nowy@ptb.de

For monitoring high UV irradiance, silicon carbide (SiC) based photodiodes are used. In this paper, we describe the characterization of novel SiC UV photodiodes in terms of their spectral and integral responsivity. Special attention is paid to the aging behavior of the photodiodes due to high UV irradiance. Artificial aging of the samples is performed by illumination with a high power medium pressure mercury discharge lamp.

INTRODUCTION

The monitoring of UV irradiances is necessary in many industrial applications, e.g., in lacquer or glue hardening, UV curing, and the disinfection of water. Suitable photodiodes are based on silicon carbide (SiC), as their spectral responsivity peaks in the UV range. Additionally, SiC photodiodes offer a very good blindness in the visible and infrared spectral range, low dark current, high speed, and low noise.

Despite their usefulness, the sole manufacturer of SiC UV photodiodes, Cree, Inc., stopped production in 2007. Since 2009, the company sglux SolGel Technologies GmbH produces new SiC photodiodes which offer an improved visible blindness and similar properties as the Cree photodiodes.

In this paper, we will investigate new SiC photodiodes for their use in high irradiance UV radiometers.

PRELIMINARY STUDIES

Prior to the detailed investigation, several SiC photodiodes were exposed to extremely high UV irradiance levels for about 65 hours in order to observe the magnitude of the relative change in responsivity. The high irradiance levels were achieved by placing the photodiodes at a distance of 5 cm from the housing of a medium pressure mercury discharge lamp, having a nominal electrical power of 2 kW.

Two types of SiC photodiodes of different area (0.04 mm² and 1 mm²) were used. In general, both types of photodiodes showed similar behavior. For further studies, large area photodiodes were chosen.

INVESTIGATION OF THE AGING BEHAVIOR

A new setup was constructed for the artificial degradation of SiC photodiodes. As UV radiation source, the 2 kW medium pressure mercury discharge lamp was used.

During the UV irradiation, the photodiodes were mounted on a water-cooled heat sink to minimize degradation effects due to increased temperatures of photodiodes' housing. One of the UV photodiodes was used for online photocurrent measurements. All other photodiodes were short-circuited. An additional monitor photodiode and a novel UV sensor (sglux Digiprobe, also based on a SiC photodiode) were used to observe the UV lamp's stability. For comparison, some photodiodes were not exposed to UV light.

For a quick examination of the photodiode aging between degradation intervals, another setup using a low pressure mercury discharge lamp was built. This allows the measurement of the integral responsivity changes of the samples by using a reference photodiode.

The spectral responsivity of the photodiodes is obtained at the differential spectral responsivity (DSR) facility at the Physikalisch-Technische Bundesanstalt (PTB) [1]. Usually, this setup is used for solar cells and has been modified for the measurements in the UV range.

After measuring the initial spectral responsivity of new SiC photodiodes at the DSR facility, the measurement cycle was as follows: 1) artificial degradation, 2) measurement of the integral responsivity change, 3) optional: measurement of the

spectral responsivity, and 4) continuation of artificial degradation.

SUPPLEMENTARY MEASUREMENTS

We will show a detailed analysis of the aging behavior of SiC photodiodes exposed to high UV irradiance levels concerning the spectral responsivity and relative change in responsivity. Additionally, we are investigating the degradation behavior of filters for UV-C, which eventually are used in UV photodiodes. Filtered photodiodes will be investigated consecutively. Finally, to fully characterize the SiC photodiodes for their use in high irradiance UV radiometers, their linearity in irradiance levels as well as the homogeneity of different batches are being investigated.

ACKNOWLEDGEMENT

The authors wish to thank the "Zentrales Innovationsprogramm Mittelstand" (ZIM) for providing funding (Förderkennzeichen KF2303704RR9).

REFERENCES

1. Metzdorf, Winter, Wittchen, *"Radiometry in photovoltaics: calibration of reference solar cells and evaluation of reference values"*, Metrologia **37** (2000) 573.

Irradiance Responsivity Measurement of a 900 nm Filter Radiometer

X. Lu[1], Z. Yuan[1], J. Zhang[2]

[1] *National Institute of Metrology, Beijing, China,* [2]*North China Electric Power University, Beijing, China*
Corresponding e-mail address: luxf@nim.ac.cn

For the radiometric measurement of thermodynamic temperature, a 900 nm centre filter radiometer is studied based on the irradiance responsivity measurement facility. The filter radiometer is calibrated against the trap detector which is traced to the cryogenic radiometer. The irradiance responsivity of the filter radiometer has been obtained over a dynamic range of nearly six decades from 450 nm to 1200 nm. The wavelength accuracy, the polarization effect, and the out-of-band blocking region are also discussed. The uncertainty of the integrating irradiance responsivity is estimated to be less than 1×10^{-3} at the 1σ level.

INTRODUCTION

The irradiance responsivity of a filter radiometer is an essential parameter which needs to be measured accurately in the radiometric determination of the thermodynamic temperature. At the National Institute of Metrology of China (NIM), the spectral irradiance comparator was established and slightly improved [1] for the irradiance responsivity measurement of filter radiometers. The schematic diagram of the facility is shown in Figure 1. The filter radiometer is calibrated against the standard trap detector by the substitution method. And the absolute responsivity of the trap detector was measured on the cryogenic radiometer system at several tuneable laser lines between 800 nm and 1000 nm [2].

Figure 59. The spectral irradiance comparator facility

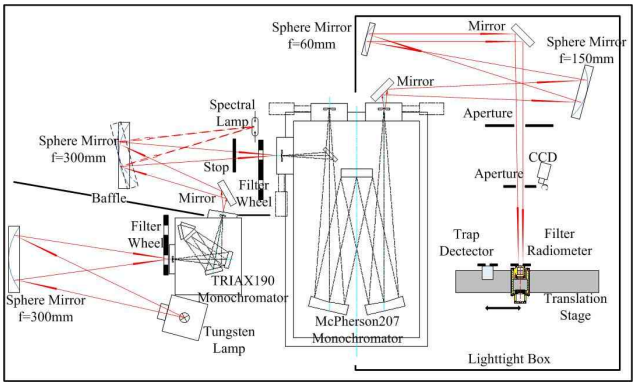

For the contrast of temperature measurement with the 633 nm filter radiometer, a 900 nm centre filter radiometer was built with a careful control of the temperature. The basic components of the filter radiometer are a precision aperture, an interference filter and a windowless silicon photodiode. The precision aperture is knife-edged and its nominal diameter is 5 mm. The interference filter is custom-made with a centre wavelength of 900 nm, a spectral bandwith of 40 nm and an out-of-band blocking of more than six orders of magnitude. A Hamamatsu silicon photodiode with active area of 10 mm × 10 mm is tilted by an angle of 5° to avoid inter-reflections between the surface of the photodiode and the interference filter.

From the measured photocurrents, the irradiance responsivity of the filter radiometer $R(\lambda)$ was calculated according to:

$$R(\lambda) = s_{\text{trap}}(\lambda) I_{\text{FR}}(\lambda) A_{\text{trap}} / I_{\text{trap}}(\lambda) \qquad (1)$$

where, A_{trap} denotes the accurate area of the aperture of the trap detector, $s_{\text{trap}}(\lambda)$ is the interpolated spectral responsivity of the trap detector [3].

EXPERIMENT RESULT

Before the calibration of the filter radiometer, the alignment of both detectors is done by using a laser beam, a CCD camera and a length gauge. The positions of both detectors in the direction of the optical axis are adjusted in such way that the apertures of both detectors are in the same plane, to ensure both detectors have the same irradiance.

To minimise the effect of room temperature drift, the wavelength of the monochromator is calibrated before and after each calibration of filter radiometer. The doubled 435.834 nm spectral line of the mercury lamp and the 914.867 nm of the neon lamp are used as they are near the centre wavelength of the filter radiometer. The result shows that the around 900 nm wavelength accuracy of the monochromator is better than 0.03 nm in the whole process.

The beam from the exit slit of the grating monochromators had a small degree of polarization

[4]. To overcome any possible remaining influence of polarization effects, the filter radiometers were measured by inserting the Glan-Thompson prism between the two apertures near the CCD camera. The difference was found within the repeatability of 3 $\times 10^{-4}$. So the polarization should have no great influence on the measured results.

The characteristic behaviour of the spectral responsivity of the filter radiometer is shown in Figure 2. For the determination of the thermodynamic temperature, the integrating signal of the irradiance responsivity is the mainly cared parameter [5]. So the irradiance responsivity is separated into two wavelength regions: the bandpass and the out-of-band blocking. The bandpass is arbitrary defined as the wavelength region in which the responsivity decreases about 4 orders of the magnitude with respect to the maximum. Due to the very strong blocking capability of the filter, the integrating signal contribution from the out-of-band is very small comparative to the one from the bandpass. Therefore the irradiance responsivity calibrations in the out-of-band wavelength region were performed only a few times.

Figure 2. Spectral irradiance responsivity of the 900 nm filter radiometer

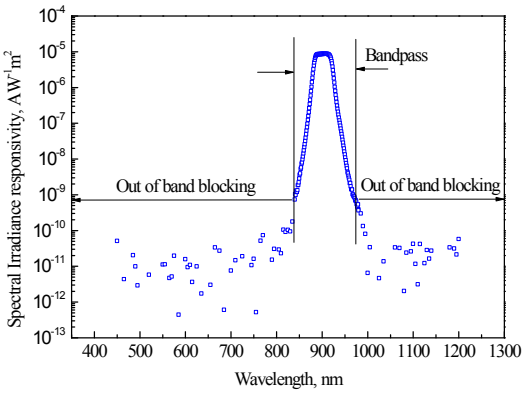

The uncertainty of integrating responsivity of the 900 nm filter radiometer is estimated in Table 1. They are analyzed from the contributions of the trap detector, the filter radiometer, light beam and the amplifier.

Table 18. Contributions to the relative uncertainty of the irradiance responsivity

Source of contribution	Detail	$\Delta s/s$
Trap	Responsivity at laser lines	2×10^{-4}
detector	Interpolation	3×10^{-4}
	Area of trap aperture	3×10^{-4}
	Nonlinearity	1×10^{-4}
Beam	Diffraction	0.5×10^{-4}
	Distance from exit slit	0.3×10^{-4}
	Polarization	1×10^{-4}
	Accuracy of wavelength	3×10^{-4}
	Stability of lamp	3×10^{-4}
	Bandwidth effect	0.5×10^{-4}
Filter radiometer	Out of band transmittance	1×10^{-4}
	Temperature coefficient	0.3×10^{-4}
	Repeatability	5×10^{-4}
Amplifier	Voltmeter	$0.\ 1\times10^{-4}$
	Gain of Amplifier	1×10^{-4}
	Standard uncertainty	9×10^{-4}

CONCLUSION

For the contrast of temperature measurement with the 633 nm filter radiometer, a 900 nm centre filter radiometer was built and calibrated on the spectral irradiance comparator at NIM. The irradiance responsivity of the filter radiometer has been obtained over a dynamic range of nearly six decades in the wavelength range from 450 nm to 1200 nm. The wavelength accuracy, polarization effect and the out-of-band region are discussed. The relative standard uncertainty of the integrating irradiance responsivity is estimated to be less than 1×10^{-3} at the 1σ level.

REFERENCES

1. X.Lu, Z.Yuan, X.Hao etc, Calibration of the irradiance responsivity of a filter radiometer for T measurement at NIM, *Int. J. Thermophysics*, 32, 278-284, 2011
2. L.Werner, J. Fischer, U. Johannsen and J. Hartmann, *Metrologia* 37, 279-284, 2000
3. D. R. Taubert, R. Friedrich, J. Hartmann and J. Hollandt, *Metrologia* 40, S35-S38, 2003
4. R. Friedrich, J. Fisher and M. Stock, *Metrologia* 32, 509-513, 1995
5. J. Hartmann, *Physics Reports* 469, 205-269, 2009

Stray Light Correction Algorithm for Multi-channel Spectrographs

S. W. Brown[1], Y. Zong[1], P.-S. Shaw[1], K. R. Lykke[1], B. C. Johnson[1], S. J. Flora[2], M. E. Feinholz[2], M. A. Yarbrough[2], D. K. Clark[3]

[1]National Institute of Standards and Technology, Gaithersburg, MD USA, [2]Moss Landing Marine Laboratories, Moss Landing, CA USA, [3]Marine Optical Consulting, Arnold, MD USA

Corresponding e-mail address: swbrown@nist.gov

We describe an algorithm, based on characterization measurements using a tunable laser system, to correct a multi-channel fiber-coupled spectrograph for stray or scattered light within the system and apply it to a multi-channel spectrograph system. This is the first scattered light correction of a multi-channel spectrograph.

INTRODUCTION

Multi-channel spectrometers such as multiple fiber input spectrographs allow the simultaneous acquisition of spectrally resolved data sets from spatially distinct targets. They are widely distributed throughout a number of industries with applications ranging from product quality assurance to high throughput medical diagnostics. As multi-channel non-imaging systems (and imaging systems) are increasingly used in quantitative metrological applications, the need for an understanding of the radiometric performance of the instrument increases.

Scattered light within an input channel (along the spectral or dispersion direction) as well as channel-to-channel cross-talk (spatial direction) arising from improperly imaged, or scattered, optical radiation within an instrument is difficult to properly characterize and is often a dominant measurement error. A 1-d (non-imaging, single input) Stray Light Correction (SLC) algorithm has been developed previously [1, 2] and the foundation has been laid for a 2-d SLC algorithm [3]. In this talk, a 2-d SLC algorithm is developed for a multiple input spectrograph. It is a special case of the SLC algorithm for hyperspectral imaging systems [3].

MULTI-CHANNEL SPECTROGRAPH

The multi-channel system is based on a Horiba Jobin Yvon CP140 f/2.0 spectrograph, uses a concave reflective grating as the dispersion element and has an Andor CCD detector at the focal plane. The CCD has 1024, 25 μm pixels in the dispersion direction and 256 pixels along the slit height (spatial direction). The system has four 1 mm core diameter input fibers; the fibers, aligned with the entrance slit, formed separate images or tracks on the CCD. Responses of all 4 input tracks to a broadband spectral source are shown in Fig 1. The image covers the spectral range from 326 nm to 965 nm. The CCD counts are integrated over the slit direction for each track, resulting in spectra for each fiber input; the dark rectangular boxes define each track.

The non-zero signal between tracks is an indication of cross-track coupling. Fig. 2 shows the system response from all 4 tracks with a single track

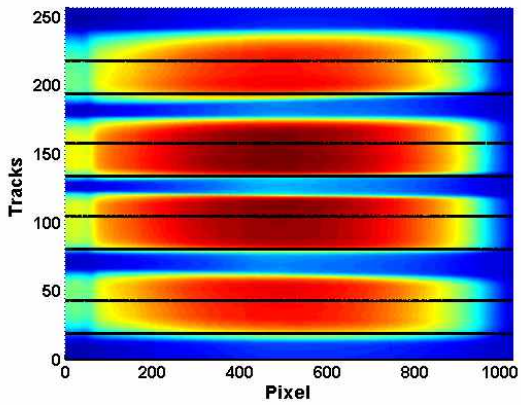

Fig. 1. Multi-track image from the CP140 system. Tracks are images of 1000 μm fibers separated by approximately 500 μm The solid black lines in the figure illustrate the fractions of the images averaged to create track spectra.

(Track 2) illuminated. In Fig. 3, the signal from Tracks 1, 3, and 4 are shown ratioed to the signal from Track 2. The cross-track coupling is on the order of 1 % for all tracks in the center of the image, increasing dramatically when the signal from the illuminated track decreases significantly, e.g. for pixels 0 to 100 and 700 to 1024. The magnitude of the cross-track coupling would increase if the full width of each track image was used.

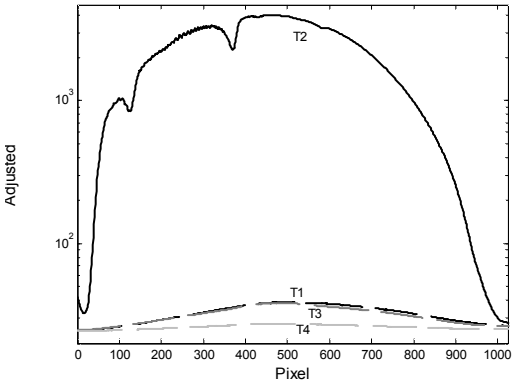

Fig. 2. Signal from CP140 system with a single track, Track 2, illuminated.

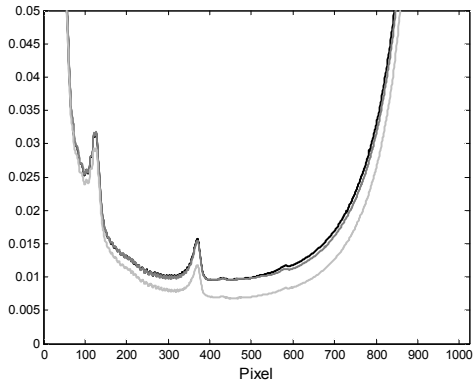

Fig. 3. Ratio of Tracks 1, 3, and 4 to illuminated Track 2.

STRAY LIGHT CORRECTION ALGORITHM

To correct the instrument for stray light, it is necessary to know the relative stray light response of element (*i, j)* for every excitation wavelength (*i, k*$_\lambda$), where *i* corresponds to the Track (*i*=1 to 4), *j* to the along track CCD element (*j*=1 to 1024) and *k* corresponds to the peak in-band element for wavelength λ (*k*=1 to 1024). For the 1-d SLC algorithm, this is known as the Stray light Distribution Function (SDF) matrix. For the 2-d SLC algorithm, there are separate 2-d scattered light matrices for along-track and cross-track coupling. For Track 1, there would be one matrix describing scattered light within the track, and 3 matrices describing the stray light from Tracks 2, 3, and 4 scattering into Track 1. Each matrix has 1024x1024 elements. The SDF matrix elements for each track consist of 4 2-d scattering matrices. Fig. 4 shows the 2-d scattered light matrix for Track 3 with light incident on Track 4. In contrast to the along-track matrices, the cross-track matrix elements around the diagonal of the array are not set to 0 [1-3].

In the 1-d algorithm, the scattered light signal is represented by the column vector Y_{meas},

$$\boldsymbol{Y}_{meas}=\mathbf{D}\cdot\boldsymbol{Y}_{\mathrm{IB}}, \qquad (1)$$

where $\boldsymbol{Y}_{meas}$ is the 1024x1 stray light signal, **D** is the 1024x1024 stray light distribution matrix and $\boldsymbol{Y}_{IB}$ is the 1024x1 in-band signal from each detector element. For the 2-d stray light correction algorithm, the 4 channels are merged into a 4096x1 array; $\boldsymbol{Y}_{IB}$ and $\boldsymbol{Y}_{meas}$ both have dimensionality of 4096x1 while the SDF matrix is a 4096x4096 matrix.

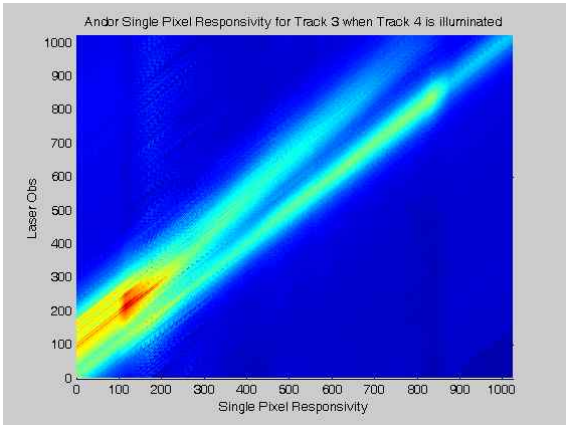

Fig. 4. 2-d scattered light matrix for Track 3 when Track 4 is illuminated.

CONCLUDING REMARKS

In this talk, we describe the development of the stray light correction matrix from the SDF matrix, apply the correction to the 4-channel spectrograph system and present data showing the efficacy of the technique. This is the first application of the 2-d SLC algorithm to a multi-channel system. In its fullest application, the algorithm is a point-spread correction algorithm for imaging systems.

REFERENCES

1. Zong, Y., Brown, S. W., Johnson, B. C., Lykke, K. R., Ohno, Y., Simple spectral stray light correction method for array spectrometers, Appl. Opt. 45, 1111-1119 (2006).
2. Feinholz et al., Stray light correction of the Marine Optical System, J. Atmos. Oceanic Technol. 26, 57-73 (2009).
3. Zong, Y., Brown, S. W., Meister, G., Barnes, R. A., Lykke, K. R., Characterization and correction of stray light in optical instruments, Proc. SPIE 6744, 67441L (2007).

Predictable Quantum Efficient Detector II: Characterization Results

I. Müller[1], G. Brida[5], J. Gran[3], S.S. Hoem[3], E. Ikonen[2], T. Kübarsepp[4], U. Linke[1], F. Manoocheri[2], M. Sildoja[2], M. Smîd[6], L. Socaciu-Siebert[1] and L. Werner[1]

[1]Physikalisch-Technische Bundesanstalt (PTB), Berlin, Germany, [2]Aalto University and Centre for Metrology and Accreditation, Espoo, Finland, [3] Justervesenet, Kjeller, Norway, [4]AS METROSERT, Tartu, Estonia, [5] Istituto Nazionale di Ricerca Metrologica, Torino, Italy, [6] Ceský metrologický institut, Prague, Czech Republic

Ingmar.Mueller@ptb.de

The Predictable Quantum Efficient Detector (PQED) is intended to improve optical power measurements in the wavelength range from 450 nm to 900 nm. Characterization results for two produced batches of photodiodes that will be used in the PQED are presented. These results will be used to develop a model to predict the response of the PQED to optical radiation.*

INTRODUCTION

One of the major objectives of the project "Candela: Towards quantum based photon standards" of the European Metrology Research Programme [1], is the development and validation of a Predictable Quantum Efficient Detector (PQED) that is intended to have an internal quantum deficiency (IQD) at the 1 ppm level [2]. To achieve this level of IQD, photodiodes with a p-n-junction induced by surface charges in the passivation silicon oxide layer [3] are used. Because of very low doping concentrations at the 10^{12} cm^{-3} level, the main recombination channel for light generated electron-hole-pairs, the recombination at impurities, is highly suppressed. This is a significant advantage in terms of modelling aspects since the IQD and therefore the uncertainties of a possible model of the IQD can be very small. The characterization results presented here in combination with calculations presented in a complementing paper [4] might eventually lead into a new model of photodiode response with a very low uncertainty [5].

The PQED consists of two photodiodes in a reflection trap design allowing for seven internal, specular reflections and thus high external quantum efficiency [6].

MEASUREMENTS

At the PTB, photodiodes from two batches produced within the project have been characterized. The uniformity and linearity of the spectral responsivity of the photodiodes as well as the dependence of these quantities on bias voltage and temperature has been investigated at a wavelength of 760 nm. A power-stabilized distributed feedback diode laser system has been used as radiation source.

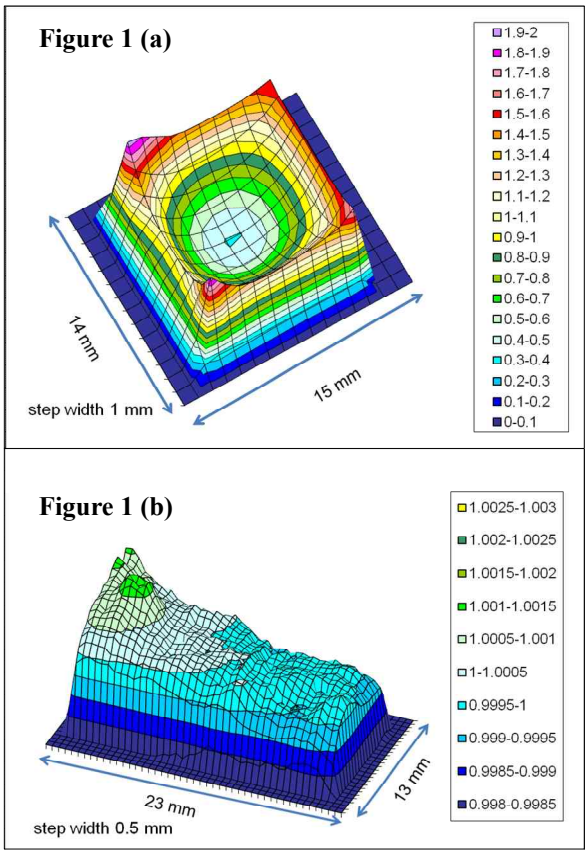

Figure 60 Relative uniformity of (a) 100 nm oxide layer photodiode of the first batch and (b) 210 oxide layer photodiode of the second batch at 760 nm and room temperature. Note that the scales of (a) and (b) differ by a factor of 400.

The option to operate the photodiodes at low temperatures down to 80 K and the demands on diode cleanliness to avoid scattering losses require the use of cryostats as housing. A fixed Brewster window was used to minimize the influence of the mandatory window, especially on the uniformity measurements. In the first batch of photodiodes, two different thicknesses of the passivation layer were chosen. According to optimum reflectivity behavior of the

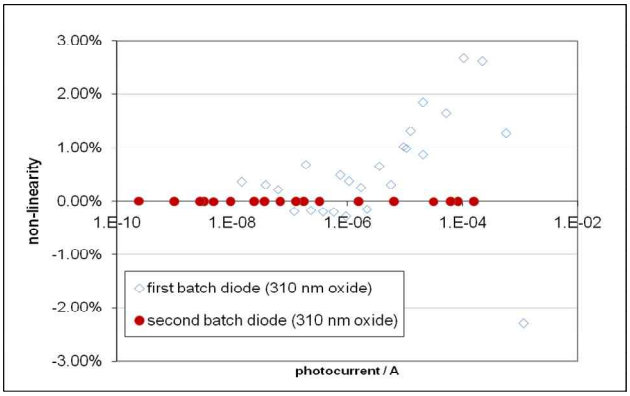

Figure 2 Comparison of the linearity of two photodiodes from the first and second batch at a wavelength of 760 nm.

PQED calculated in [6] and the requirements for the formation of a p-n-junction given in [3], two types of photodiodes with 100 nm and 310 nm passivation layer were produced.

The uniformity measurements and calculations [5] showed that there was no sufficient formation of the p-n-junction in the photodiodes with the oxide thickness of 100 nm (see Fig. 1a), in contrast to the other type of photodiodes of the first batch. It is assumed that the expected surface charge density could not be induced in the first production process. An improved production process was chosen for the second batch to overcome this problem. The photodiodes of the second batch have sufficient density of induced charges and very good uniformity. The standard deviation of the uniformity in the central part (18x8 mm^2) of the most homogenous photodiode was (0.042 ± 0.0043) % (see Fig. 1b). The improved production process also had an effect on the linearity of the diodes (see Fig. 2). While the first batch of photodiodes showed a supralinearity up to 3 % at room temperature with a bias voltage of 5 V, there was no significant supralinearity within the standard uncertainty (0.0025 %) in the linearity measurements of the second batch of photodiodes under these conditions. This is of special importance as supralinearity is usually connected to recombination losses in the bulk which decrease with increasing optical power [7]. Thus, a considerable supralinearity would indicate an IQD of similar magnitude at power levels below the range of power where the supralinearity occurs.

In addition, the external quantum efficiency of a PQED built from the first batch photodiodes has been measured against reference trap detectors at a wavelength of 760 nm and at a temperature of 78 K with a reverse bias voltage of 5 V. An external quantum efficiency of 99.4 % with a standard uncertainty of 0.094 % was determined. The total uncertainty of the quantum efficiency is dominated by the contribution associated with the non-uniformity of the PQED test version of 0.09 %, possibly caused by displacement of one of the photodiodes. The deviation of the external quantum efficiency from unity might be caused by recombination losses which are also responsible for the supralinearity. These effects are less important at shorter wavelengths and might explain that an external quantum efficiency of 100 % is achieved at 488 nm [4]. However, this still has to be investigated.

The promising results of the second batch of photodiodes in terms of spectral uniformity and linearity indicate the possibility of PQED operation at the 1 ppm IQD level. There is ongoing work to determine the external quantum efficiency of a PQED against PTB and CMI laser-based cryogenic radiometers.

CONCLUSION

Two batches of induced junction photodiodes were characterized. The characterization results of the first batch were used to improve the understanding of induced junction photodiodes and to improve the production process for the second batch of photodiodes. The second batch characterization results show that PQED operation at the 1 ppm IQD level might be achievable. Finally the PQED will be characterized and its external quantum efficiency will be determined against a cryogenic radiometer.

*The research leading to these results has received funding from the European Community's Seventh Framework Programme, ERA-NET Plus, under Grant Agreement No. 217257.

REFERENCES

1. www.quantumcandela.org
2. J. Geist et al, “Prospects for improving the accuracy of silicon photodiode self-calibration with custom cryogenic photodiodes”, Metrologia, 40, 132-135, 2003.
3. T. E. Hansen, “Silicon UV-Photodiodes Using Natural Inversion Layers” Phys. Scripta 18, 471-475, 1978.
4. M. Sildoja et al., Predictable Quantum Efficient Detector I: Photodiodes and Design, these proceedings.
5. J. Gran et al., these proceedings.
6. M Sildoja et al, “Reflectance Calculations for Two-Photodiode Predictable Quantum Efficient Detector”, Metrologia, 46, 151–154, 2009.
7. K. D. Stock, “Si-photodiode spectral nonlinearity in the infrared”, Applied Optics, Vol. 25, No. 6, 830-832, 1986.

Standard resistor based calibration of new reference photocurrent-meters and DC low-current sources with 0.006 % (k=2) uncertainty

G. P. Eppeldauer, D. G. Jarrett, T. C. Larason, and H.W. Yoon

National Institute of Standards and Technology
Gaithersburg, Maryland, USA
Corresponding e-mail address: george.eppeldauer@nist.gov

Low-current calibration service is not available from most NMIs even if the lowest possible current measurement uncertainty is needed in optical radiometery, especially in radiation thermometry. In order to solve this problem at NIST, reference current-to-voltage converters were designed and constructed. A new calibration procedure was developed for the reference converters. The converter design and calibration issues and the uncertainties are discussed here. The new converters were compared to a previous generation converter and also to a commercial current source. Now, DC current measurements between 10 pA and 10 μA can be performed with uncertainties lower than 0.006 % (k=2) upto a signal-gain of 10^{10} V/A. The uncertainty of the calibration was improved by one order of magnitude for a high-performance commercial current-source at currents lower than 100 nA. Based on the described procedure, low DC-current routine calibrations are suggested to NMIs. A calibrated travelling current-source can be used for gain calibrations of test current-to-voltage converters.

INTRODUCTION

In order to transfer the radiant-power responsivity from a primary-standard cryogenic-radiometer to a transfer standard radiometer, a photocurrent measurement uncertainty of less than 0.01 % (k=2) is needed. This is a demanding requirement especially in radiation thermometry where the responsivity scale must be converted from radiant-power to irradiance and radiance measurement modes and frequently low signal levels are to be measured. A photocurrent-to-voltage converter calibration method was published [1] where the expanded uncertainty was 0.046 % (k=2) at 10 pA. Using high quality silicon or InGaAs photodiodes [2], relative signal measurements could be performed down to about 10 pA photocurrent with less than 0.01 % (k=2) uncertainty [2, 3]. Accordingly, the absolute current-to-voltage (I-V) conversion must have similarly low uncertainty.

The reference I-V converters have calibration traceability to NIST electrical standards.

DESIGN OF NIST REFERENCE I-V CONVERTER

The feedback resistors of the I-V converters were selected for temperature and voltage dependence, drift and settling time. The 1 GΩ and 10 GΩ resistors were heat treated. The resistors were "in-situ" calibrated against NIST high-resistance standards using substitution in a guarded dual-source bridge. This resistance calibration includes (in addition to the feedback resistor) the printed circuit board (PCB), the gain-switch of the converter, and the packaging in the calibration. Contamination-free high-resistance materials and components were selected and the PCB traces were well-separated and cleaned to minimize leakage currents. During calibration, the operational amplifier of the converter is isolated using jumpers that are removed. The converter is permanently mounted in a shielded enclosure with suitable terminations. The calibration happened in an air bath of regulated temperature and humidity. The obtained resistance is defined as a standard resistor that produces the current conversion.

COMPARISIONS

The figure shows the comparison results of current calibrations performed with the commercial (Keithley 6430) and the new reference I-V converter. While the uncertainty of the tested high-quality commercial current-source was 0.05 % at nA levels, the uncertainty of the current as measured by the NIST reference I-V converter was 0.006 % (k=2) at 1 nA.

While the highest gain of the first generation reference I-V converter was 10^8 V/A, that of the new generation converter was 10^{10} V/A. The current measurement uncertainty at the highest gain of the

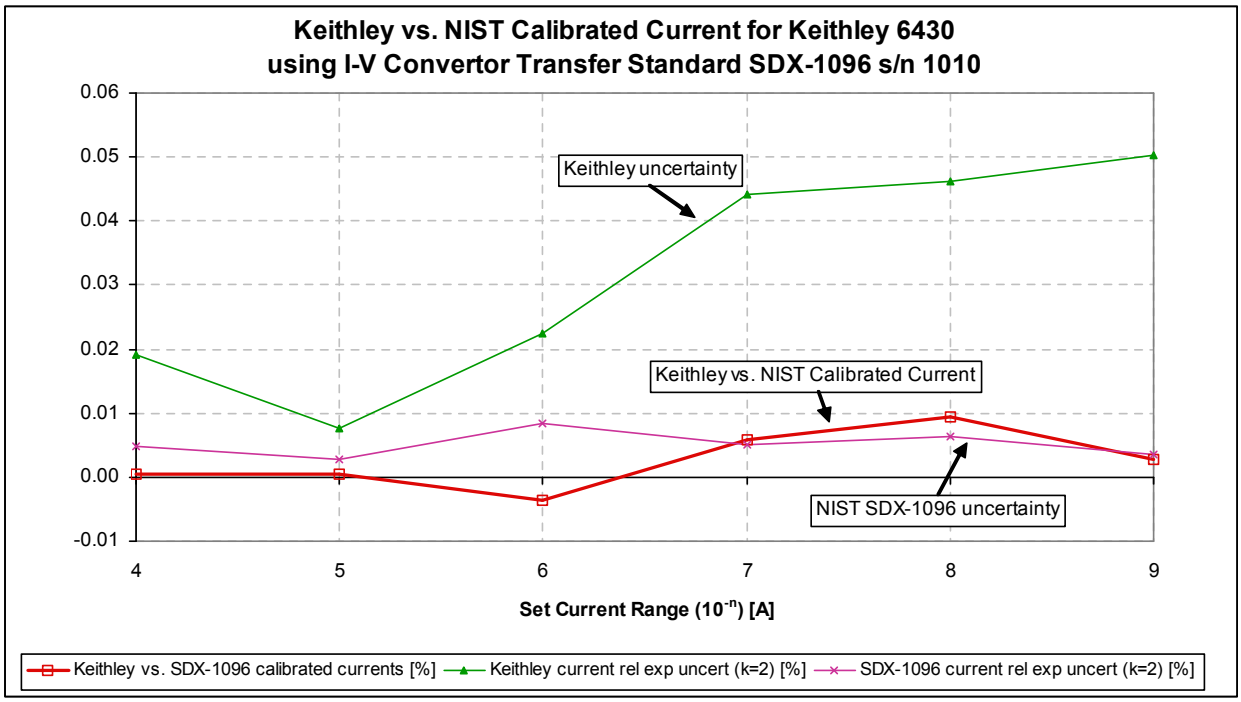

Figure 1. Calibration of a high-quality current source with the NIST reference I-V converter (SDX-1096).

first-generation converter was 0.012 % (k=2) [4] and 0.006 % of the new converter at its highest gain.

The neighbouring resistance and output-voltage ratios were compared and agreed within 0.010 %.

The calibration uncertainty of the two highest feedback resistors (1 GΩ and 10 GΩ) were 0.0018 % and 0.005 % (k=2).

UNCERTAINTY BUDGET

The expanded total uncertainty of DC current measurement with the second-generation I-V converter is 0.0064 % (k=2) at the 10^{10} V/A gain. The expanded total uncertainty is 0.004 (k=2) at the 10^{9} V/A gain, and 0.0022 (k=2) at the 10^{8} V/A gain.

The uncertainty was 0.012 % (k=2) at the 10^{8} V/A gain with the first-generation I-V reference converter.

The uncertainty of the commercial current source was 0.103 % (k=2) at 50 pA.

The uncertainty of the signal-gain of a test I-V converter at 10^{10} V/A gain using the commercial current-source with a 10^{13} Ω output resistance was 0.0082 % (k=2).

The validation of the new low-DC-current scale is to be made.

DISCLAIMER

Certain commercial equipment, instruments, or materials are identified in this paper to foster understanding. Such identification does not imply recommendation or endorsement by the NIST, nor does imply that the equipment are necessarily the best available for the purpose.

REFERENCES

1. P. Sipila et al, NEWRAD Proc. p. 223, 2005.
2. G. P. Eppeldauer, NIST Technical Note # 1438, 2001.
3. H.W. Yoon et al, Metrologia, **40**, S154, 2003.
4. G. P. Eppeldauer, MAPAN – Journal of Metrology Society of India, **24**, No. 3, p. 193, 2009.

Extension of the NIST spectral power-responsivity calibration service to 2500 nm

G. P. Eppeldauer, H. W. Yoon, J. Zeng, T. C. Larason, J. M. Houston, and V. Khromchenko

National Institute of Standards and Technology,
Gaithersburg, Maryland,
Corresponding e-mail address: george.eppeldauer@nist.gov

NIST is extending the detector spectral power-responsivity calibration-service to 2500 nm based on extended-InGaAs (EIGA) transfer- and working-standard radiometers and low-NEP pyroelectric transfer-standards. The extended scale is traceable to the electrical-substitution cryogenic radiometer through the transfer-standard EIGA radiometers. In order to perform low responsivity-uncertainty, the EIGA radiometers have been characterized for spatial-response, temperature-dependent spectral-responsivity, linearity, noise, drift, and stability. They can measure both radiant-power and irradiance in either AC or DC measurement modes. The EIGA working standards hold the extended scale and are used as reference detectors for the Spectral Comparator Facility (SCF) where the calibration service is being extended from the present 1800 nm limit. The EIGA radiometers are operated in DC measurement mode at the SCF. An improved uncertainty budget is discussed for test-detector calibrations within the 1650 nm to 2500 nm range.

INTRODUCTION

At several national measurement institutes (including NIST) the spectral irradiance and spectral radiance calibrations have already been extended to 2500 nm. In addition to these source-based calibrations the spectral power-responsivity calibration service at NIST also needs extension to 2500 nm. Extension of the detector-based calibrations is needed not only for the solar-photovoltaic industry (since most of the solar radiation is in the short-wave infrared range) but also for many military applications where measurements are to be made within the 2000 nm to 2500 nm atmospheric window. This is the first spectral-responsivity calibration service for the SW-IR range.

At present, NIST offers spectral responsivity calibration service only to 1800 nm. The uncertainty of the present scale will be improved at wavelengths longer than 1650 nm based on this work.

EIGA RADIOMETER STANDARDS

Both transfer and working standard EIGA radiometers were developed to realize an improved responsivity scale for the long wavelength end of the near-infrared range and to extend the low-uncertainty scale to 2500 nm. An integrating sphere was attached to the detector input of the transfer standards to achieve spatially uniform input for radiant power measurements and to convert the spectral power responsivity to irradiance responsivity using an aperture of known area at the entrance-port of the sphere. The working standards were built using 5 mm diameter EIGA detectors. All detectors were cooled with a 4-stage thermoelectric cooler to about -70 ^{o}C +/- 0.05 ^{o}C. The dissipated heat was removed with either side fan or circulated water from a radiator.

CHARACTERISTICS OF RADIOMETERS

Both the electronic and radiometric characteristics of the new generation EIGA radiometers have been tested to minimize measurement uncertainty for both radiant-power and irradiance responsivities in both AC and DC measurement modes.

The temperature dependent responsivity of the EIGA detectors was measured to determine the temperature stability needed for the detector at the cold operating temperature. Figure 1 shows the measured and then calculated temperature coefficients of responsivity versus wavelength. The results show that the temperature instability cannot be larger than 0.05 ^{o}C if a responsivity change of less than 0.5 % is needed at 2500 nm.

The spatial non-uniformity of responsivity was also measured at several wavelengths. As shown in

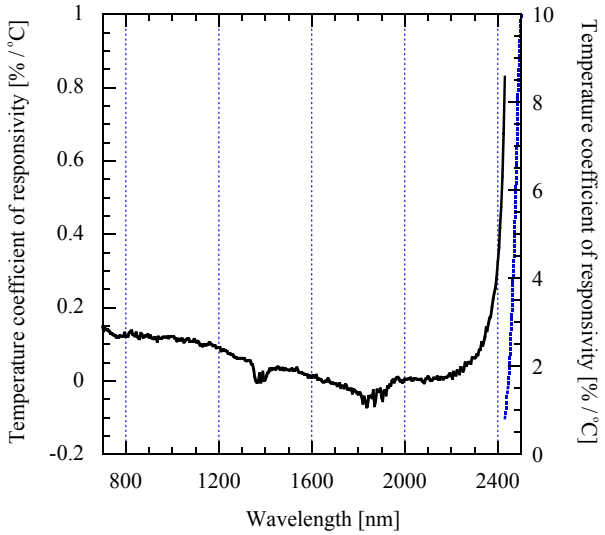

Fig. 1. Temperature coefficient of responsivity versus wavelength of a 5 mm diameter EIGA detector.

Fig. 2, the spatial non-uniformity of responsivity was 0.5 % (max-to-min) at 2100 nm. The non-uniformity

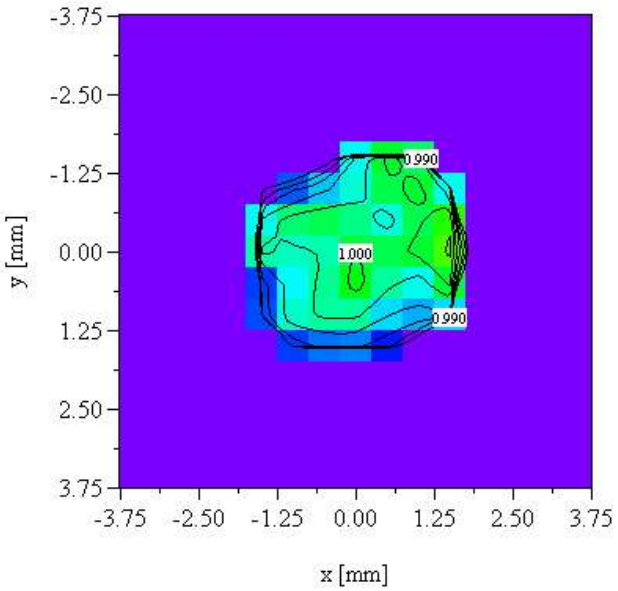

Fig. 2. The responsivity uniformity of a 5 mm EIGA detector at 2100 nm is illustrated with 0.2 % contours.

was similar between 1300 nm and 2300 nm. However, it increased to a max-to-min of 1.5 % at 2400 nm and 25 % at 2500 nm. The max-to-min non-uniformity was 2.5 % at 900 nm. The spot size used was 1.1 mm diameter and the step increments were 0.5 mm.

The linearity of EIGA detectors was tested on the Beam Conjoiner [1]. The signal-to-flux ratio in one run is shown at different AC signal levels on Fig. 3.

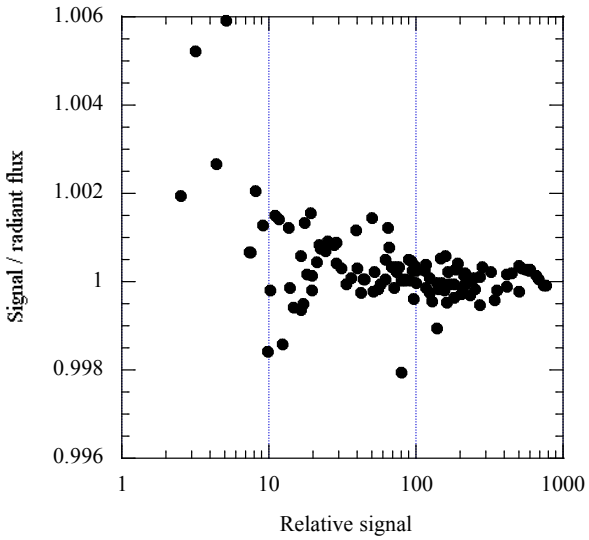

Fig. 3. One run of a linearity test of an EIGA detector.

CALIBRATIONS

The new responsivity scale is based on the SIRCUS [2] measured power-responsivity points, the SCF [3] spectral power responsivity scale to 1600 nm, and the low-NEP pyroelectric transfer standard radiometer [4] (as measured on the IR-SCF). The spectral power responsivity of the sphere-input EIGA transfer standard is shown in Fig. 4. The uncertainty of the wavelength dependent scale is less than 1 % (k=2).

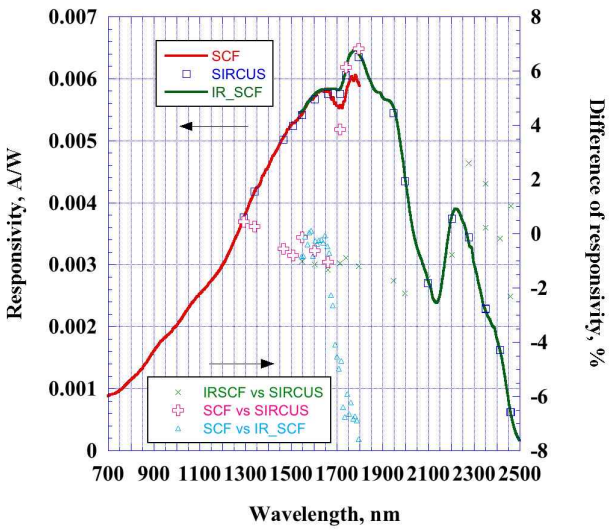

Fig. 4. The spectral power responsivity of a sphere-input EIGA transfer-standard radiometer determined from three scales.

REFERENCES

1. H.W. Yoon et al, Metrologia, **40**, S154, 2003.
2. S.W. Brown et al, Appl. Opt., **45**, # 32, p. 8218, 2006.
3. T.C. Larason et al, NIST SP 250-41, 2008.
4. G. P. Eppeldauer et al, Metrologia **46,** S155, 2009.

Development of new-generation transfer-standard pyroelectric radiometers for monochromator use

G. P. Eppeldauer, Jinan Zeng, and L. M. Hanssen

National Institute of Standards and Technology
Gaithersburg, Maryland, USA
Corresponding e-mail address: george.eppeldauer@nist.gov

Transfer standard pyroelectric radiometers with NEPs close to 1 nW/Hz$^{1/2}$ have been developed for monochromator-use to extend the NIST spectral power responsivity scale for routine calibrations to 25 μm. The main steps to obtain low NEP, without using liquid-nitrogen cooled quantum detectors, are described. Since the low-NEP single-element pyroelectric hybrid detectors have structured spectral responsivities, dome-input radiometers with low-NEP have been developed. The new devices are described and compared for spectral responsivity and NEP. The infrared spectral responsivity scale uncertainty has been decreased to less than 1 % (*k*=2).

INTRODUCTION

There are no room-temperature detectors available with low enough noise-equivalent-power (NEP) to measure less than 1 μW radiant-power levels of monochromators in the infrared range. Radiometers with NEP of about 1 nW/Hz$^{1/2}$ are needed for the spectral responsivity scale extension (without any wavelength gaps) to 25 μm. Pyroelectric trap detectors (both wedge and dome versions) developed earlier [1] have high NEPs (larger than 40 nW/Hz$^{1/2}$) and cannot be used at monochromator outputs. They need laser sources. Tuned-laser calibrations are slow and expensive. The earlier developed cryogenic bolometers are not user friendly.

RADIOMETER DESIGN

Pyroelectric detectors with large and spatially uniform area are selected. Low-reflectance (<6 %) organic-black coatings were used for frequency compensation. As a result of the frequency compensation, feedback resistors of 10 GΩ could be used for photocurrent conversion and spectrally constant responsivity can be achieved to about 100 Hz (3 dB) roll-off frequency. In order to eliminate structures in the spectral responsivity function (caused by the black coating), a reflecting dome-input is attached to the detector.

The construction of the dome-input pyroelectric radiometer is shown in Fig. 1.

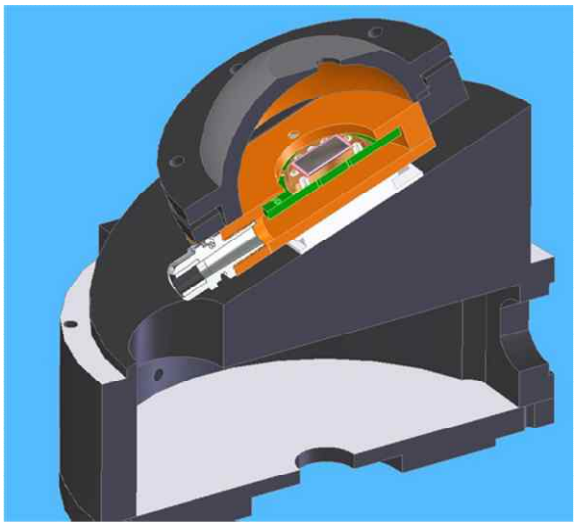

Figure 1. Front-design of the dome-pyroelectric radiometer.

The detector is tilted and temperature controlled with a thermoelectric cooler. There is a 4 mm diameter opening at the dome-entrance. The radiometer can accept f/4 incident beam to match the input geometry to the monochromator. Because of the multiple input reflections, most of the incident radiation is absorbed by the detector-coating. The high absorption makes it possible to smooth out the structures from the spectral responsivity.

The NEP was decreased by increasing the responsivity. Table 1 shows how the responsivity increased with decreasing thickness on single element $LiTaO_3$ detectors. The responsivity of the 25 μm detector increased by a factor of seven compared to the traditionally used 100 μm thick detector. The shown V/W responsivities include the increased value (by a decade) of the feedback resistor. As a result of the responsivity increase, the NEP was improved to about 1 nW/Hz^{½}. The stray capacitance parallel to the feedback resistor was decreased with the compact hybrid detector arrangement [2] to 0.1 pF resulting in

spectrally flat responsivity to the shown 3 dB roll-off frequencies. In the hybrid arrangement the crystal and the current-to-voltage converter were located in the same (transistor) metal can. In the dome-arrangement, the metal can was not used and the stray capacitance was 0.2 pF. The area of the detectors (crystals) was minimized for a given design to minimize noise boosting (amplification for the input noise). The NEP was further decreased by decreasing the electrical bandwidth of the applied lock-in amplifiers.

Table 1. Responsivity increase with decreasing crystal-thickness of single-element $LiTaO_3$ detectors.

Detector#	Coating	Size mm dia.	Thickness (μm)	3 dB rolloff (Hz)	Responsivity (V/W)
2	OB	5	100	100	5059 (785 nm)
3	OB	5	50	109	16985 (1.32 μm)
5	OB	3	50	60	16352 (1.32 μm)
6	OB	3	25	128	35879 (1.32 μm)

RADIOMETER TESTS

The reflectance of the single-element pyroelectric detector [3] and the signal ratio of the dome-detector to the single-element detector is shown versus wavelength in Fig. 2. The two curve shapes are in good agreement. The structures in the spectral reflectance curve can be seen well.

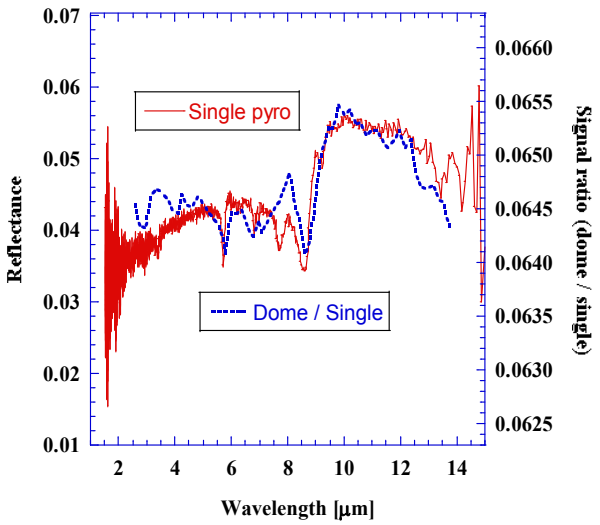

Figure 2. Reflectance of single-detector and signal ratio of dome-detector to single-detector.

The low-NEP domed radiometer was calibrated against the old domed radiometer and also against the single-element radiometer. Figure 3 shows the comparison of the spectral responsivities.

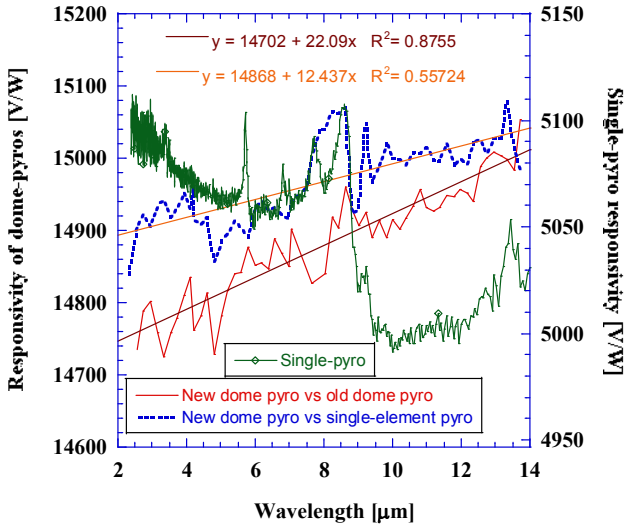

Figure 3. Comparison of spectral responsivities of pyroelectric radiometer standards.

The structure in the responsivity of the single-element detector cannot be seen in the responsivity curves of the domed radiometers. The difference between the responsivity from the two calibrations is about 0.5 %. The larger difference at the short wavelength-end is caused by the difference in the input geometries between the domed and single-element radiometer inputs at calibrations.

REFERENCES

1. G. P. Eppeldauer, J. Zeng, and L. M. Hanssen, Development and calibration of pyroelectric radiometer standards at NIST, SPIE Proc. Vol. 6201, p. 620119-1 to 620119-12, 2006.

2. G. P. Eppeldauer, J. Zeng, and H. W. Yoon, Low NEP pyroelectric radiometer standards, SPIE Proc., Vol. 6940, p. 694036-1 to 694036-9, 2008.

3. G. P. Eppeldauer, J. Zeng, H. W. Yoon, B. Wiltham, T. C. Larason, and L. M. Hanssen, Extension of the NIST spectral responsivity scale to the infrared using improved-NEP pyroelectric detectors, Metrologia, Vol. 46, p. S155-S159, 2009.

Temporal instability of photodiodes in the UV

Lutz Werner, Peter Meindl

Physikalisch-Technische Bundesanstalt (PTB), Braunschweig and Berlin, Germany
Corresponding e-mail address: lutz.werner@ptb.de

The temporal stability of the spectral responsivity of different types of UV photodiodes has been investigated at PTB within the last five years. Significant instabilities have been found depending on the type of the detector and on the wavelength. These changes in responsivity can be linearly fitted at each desired wavelength. Since the temporal drift prevalently exceed the uncertainty of the spectral responsivity calibration, these linear fits can be used to correct the spectral responsivity and therefore to decrease the uncertainty of the dissemination of the spectral responsivity.

INTRODUCTION

Photodiodes are the detectors of choice for radiometric purposes in the visible (vis) and near infrared (NIR) spectral region. However, some of the convenient properties of photodiodes as e.g. stability and uniformity diminish in the ultraviolet spectral range (UV). This can be caused by the higher photon energy and the fact that the absorption of incident photons takes place in the very vicinity of the photodiode surface. The semiconductor crystal is of poorer quality near the surface compared to the bulk crystal because the surface per se is a defect of the crystal structure. Furthermore, the crystal can be influenced and even changed near its surface by the environmental conditions. This is in particular of importance when windowless photodiodes are used as it is usually the case in precision radiometry.

The stability of the spectral responsivity is of special relevance because it decides about the reliability of the spectral responsivity value obtained in a calibration after the detector has been used several times or has been stored over a certain period of time. It has been reported by several authors [1-4] that the spectral responsivity of Si photodiodes changes when these diodes are exposed to UV radiation. This change usually occurs not only at the wavelength of exposure but also at other wavelengths in the UV and even in the vis and NIR and in positive as well as in negative sense [4]. Since this effect mainly depends on the exposure it can be kept small by keeping the level of irradiance as well as the duration of exposure as small as possible. However, there is in addition a responsivity change that is proportional to time even when the photodiode is not irradiated at all. This temporal drift of the spectral responsivity is the subject of this paper.

MEASUREMENTS AND RESULTS

The spectral responsivity scale of the PTB in the UV at wavelengths above 200 nm is realized by a cryogenic-radiometer-based facility utilizing the monochromatized radiation of an argon arc plasma [5]. Several types of detectors as e.g. three-element reflection trap detectors based on Si photodiodes of type Hamamtsu S1337 (T-S13), Hamamtsu S5227 (T-S52) and Schottky-type PtSi-nSi photodiodes of type SUV 100 (T-SUV) as well as single-element SUV 100 photodiodes (SUV) have been calibrated at this facility in the UV about once a year over a period

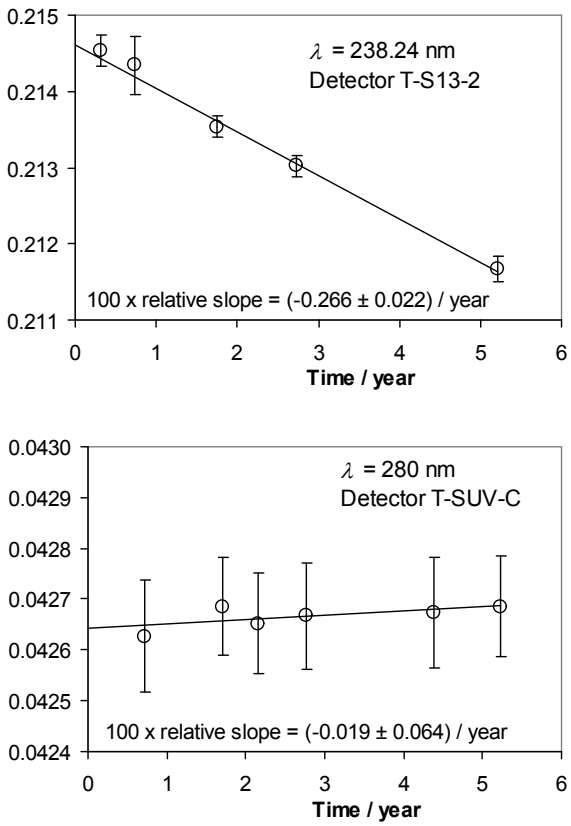

Figure 61. Temporal drift of the spectral responsivity of two detectors at two calibration wavelengths over a period of five years. The data are fitted by assuming a linear temporal dependence.

of more than five years. The temporal drift of the responsivity values at each calibration wavelength has been fitted using a linear model by assuming a linear temporal dependence. The examples in fig. 1 show that the responsivity change can be well described within this linear model. Up to five responsivity values obtained over a period of about five years have been fitted. The linear drift model has been applied to 9 detectors of the four types mentioned above and at 50 to 60 calibration wavelengths for each detector. Furthermore, the statistical consistency of each data set within the linear drift model has been checked by the chi-square test.

The relative annual drift of the spectral responsivity in the past including its standard uncertainty has been gathered from the linear fits and is displayed for five different detectors in fig. 2. The responsivity drift per year ranges from +0.1% to -0.1% for T-SUV and SUV detectors and from -0.1% to -0.3% for Si photodiode based trap detectors (T-S13 and T-S52). Detector SUV-8 shows an unusual large drift and has therefore been suspended for the dissemination of the spectral responsivity at PTB.

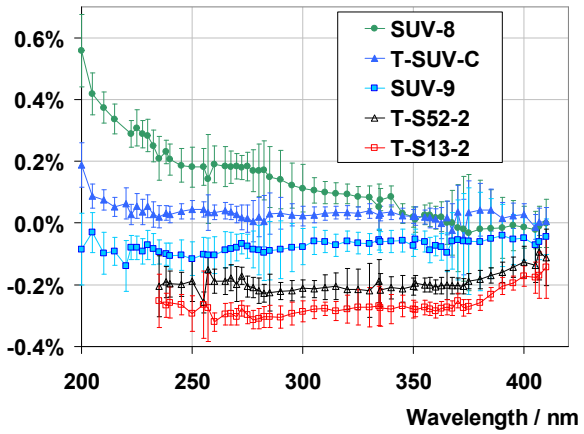

Figure 2. Relative annual drift of different types of photodiodes in the UV. The error bars indicate the standard uncertainty of the relative annual drift.

The standard calibration uncertainty of the spectral responsivity of the detectors used for the dissemination of the spectral responsivity is in general about 0.1% at wavelengths above 240 nm and increases down to 200 nm to about 0.2% [5]. Thus the change in responsivity due to the temporal drift one year after a calibration can be comparable or even considerably larger than the calibration uncertainty originally achieved. As a consequence, the responsivity calibration has to be repeated after rather short time intervals or the responsivity has to be corrected for the temporal drift. The latter option should be preferred having in mind the rather large effort for calibrations in the UV at 50 to 60 different wavelengths. Since the temporal drift depends on the wavelength, this correction has to be performed at each desired wavelength.

SUMMARY

The temporal drift of the spectral responsivity of different types of UV photodiodes has been investigated at PTB. The drift depends on the type of the detector and is dependent on the wavelength. As a good approximation the drift can be linearly fitted. This has to be done at each desired wavelength and enables to correct for temporal changes. A significant improvement of the uncertainty of the dissemination of the spectral responsivity can be achieved in this way when temporal changes exceed the uncertainty of the calibration of the detectors.

REFERENCES

1. Fu Lei, J. Fischer, Characterization of Photodiodes in the UV and Visible Spectral Region Based on Cryogenic Radiometry, Metrologia, 30, 297-303, 1993
2. R. Goebel, R. Köhler, R. Pello, Some effects of low-power ultraviolet radiation on silicon photodiodes, Metrologia, 32, 515-518, 1995/1996
3. N.M. Durant, N.P. Fox, Evaluation of solid-state detectors for ultraviolet radiometric applications, Metrologia, 32, 505-508, 1995/1996
4. L. Werner, Ultraviolet stability of silicon photodiodes, Metrologia, 35, 407-411, 1998
5. P. Meindl, A.E. Klinkmüller, L. Werner, U. Johannsen, K. Grützmacher, New UV spectral responsivity scale of the PTB based on a cryogenic radiometer and an argon plasma arc radiation source, Metrologia, 43, S72-S77, 2006

Spectral properties of semiconductor photodiodes/solar cells

Terubumi Saito[1]

[1]*Tohoku Institute of Technology, Sendai, Japan, 982-8577*
Corresponding e-mail address: terubumi.saito@hotmail.co.jp

The efficiency of photodiodes and solar cells should be as high as possible for better signal –to-noise ratio and better energy conversion, respectively. Theoretical and experimental evaluations of the two major losses of optical losses (reflectance, dead layer absorption and substrate partial absorption) and carrier recombination loss have been conducted as a function of wavelength and of some other parameters like angle of incidence for reflectance. The results show that both losses steeply change in the UV range. For reflectance, the change is brought by the change in both optical indexes of the surface layer and of the substrate. For surface recombination, the change is only brought by the change in absorption coefficient of the substrate. In conclusion, it is essential to characterize any property not only for the above two factors but also other properties like uniformity, linearity, etc. at each wavelength in interest since it depends on the wavelength.

INTRODUCTION

Geist et al. [1] proved in their work on self-calibration that the spectral internal quantum efficiency is very close to unity in the wavelength range approximately from 400 nm to 800 nm and major deficiencies are reflectance loss, surface recombination and incomplete absorption in the substrate. The second and the last losses can be called optical losses. For the optical losses, it should be noted that most photodiodes can be optically modelled by a simple layered structure consisting of a sensing semiconductor substrate covered by a thin surface layer [2-4]. For instance, a p-n junction silicon photodiode consists of a silicon dioxide film on silicon substrate and a GaAsP Schottky photodiode consists of a gold film on GaAsP substrate. Even with a single layer, optical properties of the whole system can be very different from those for a substrate without surface layer due to the interference effect and absorption by the surface layer.

Probability of surface recombination is typically dominant and becomes high when absorption in the substrate becomes strong, that is, in the UV and VUV regions. On the other hand, probability of rear recombination which is responsible for incomplete absorption in the substrate is typically high in the infrared region where photon absorption is weak.

In this paper, spectral properties mainly of optical losses and carrier recombination are discussed and theoretical and experimental results are presented.

OPTICAL LOSSES

The optical losses are classified into the loss of photons due to reflection from the surface, due to absorption in a dead layer in front of the sensitive region, and due to transmission through the sensitive region. The last case only occurs when the photon absorption coefficient is small and therefore it is negligible in the UV or VUV region because of the strong absorption. Among the optical losses, the reflection loss can be determined also by a simple reflectance measurement. However, the absorption loss cannot be determined by experiment. If the optical constants of the composing materials and the geometry are known, the optical losses can be evaluated by calculation based on the optical model.

Consider that a photodiode is placed in vacuum ($\tilde{n}_0 = 1$) and is composed of a slab of semiconductor ($\tilde{n}_2 = n_2 - ik_2$, where n_2 is a real part and k_2 is an imaginary part of the optical constant) whose thickness is large compared to the absorption length of photons considered, and a film ($\tilde{n}_1 = n_1 - ik_1$) with thickness, d, on the slab. When the angle of incidence on the photodiode is ϕ_0, transmittance, T, reflectance, R, and absorptance, A, of the film are given theoretically.

An example of the calculation results for normal transmittance, T, absorptance, A, and reflectance, R, of a Si photodiode which has a 30 nm-thick SiO_2 on Si, is shown in Fig. 1. The detector is almost insensitive in the range from 60 nm to 120 nm due to the absorption by the SiO_2 layer. The major loss mechanism of photons is absorption below about l20 nm, and reflection above 120 nm. In the longer wavelength region, a change in thickness of the SiO_2 layer greatly alters the shape of the transmittance and reflectance curves due to the interference effect.

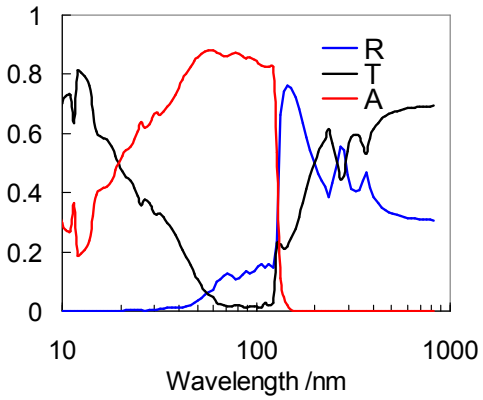

Figure 62. Calculated spectra of transmittance (*T*), reflectance (*R*) and absorptance (*A*) for 30 nm-thick SiO_2 film on Si.

CARRIER RECOMBINATION LOSS

Hovel reported on carrier transport model in solar cells as a function of absorption coefficient of the incident radiation [5]. Carrier collection efficiency for photodiodes is given as a function of wavelength via absorption coefficients based on his model. Suppose that an n-on-p photodiode is irradiated by monochromatic radiation of wavelength λ. Carrier collection efficiency, $C(\lambda)$, which is defined by collected number of carriers divided by number of photo-generated carriers, is given by

$$C(\lambda) = C_p(\lambda) + C_{dr}(\lambda) + C_n(\lambda) \quad (1)$$

where $C_p(\lambda)$, $C_{dr}(\lambda)$, and $C_n(\lambda)$ are carrier collection efficiencies contributed from the front region before the depletion region by hole current, from the depletion region, and from the rear region after the depletion region by electron current, respectively. Each contribution is given by analytical solution to the carrier transport equations. Calculation results for a p-on-n silicon photodiode are shown in Fig. 2.

As explained before, spectral dependence is brought only by the change in absorption coefficient of the semiconductor as a function of wavelength. Corresponding to the strong absorption about from 60 nm to 400 nm, collection efficiency is steeply dropped. It is known that decrease in collection efficiency becomes nearly saturated after reaching a certain level of absorption. It is clear that contribution from the front region is dominant in most of the spectral range, especially in the region mentioned above. For such a situation, one of the most important parameter to govern the efficiency is the surface recombination velocity. As Fig. 2 shows, contrary to the large difference in efficiency the UV, change in the surface recombination velocity affects little the efficiency in the visible.

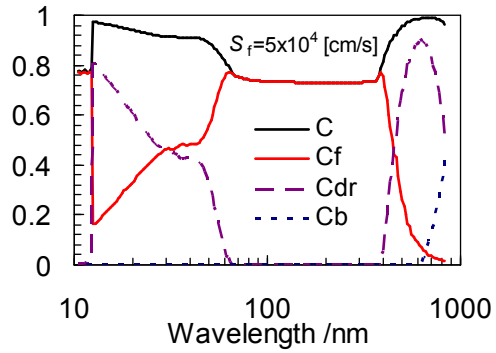

Figure 2. Calculated carrier collection efficiency spectra for a silicon photodiode. (a): Total (*C*) a nd each contribution from the front region (C_f), deletion region (C_{dr}), back region (C_b).

CONCLUSION

The loss mechanisms in efficiency of semiconductor photodiodes and solar cells can be classified mainly as optical loss and carrier recombination loss. The validity of the optical model was verified by comparison with the experiments. The experimental and theoretical results show that angular/polarization dependence does not change much as a function of wavelength in the visible but steeply changes in the UV due to the change in optical indices of the composing materials. The proportion of surface recombination loss shows a steep increase near the ultraviolet region and becomes constant with respect to the wavelength.

REFERENCES

1. J. Geist, E. F. Zalewsky, A. R. Schaerer, Appl. Phys. Lett. 35, 1979.
2. T. Saito, K. Katori, and H. Onuki, Physica Scripta 41, 783-787, 1990.
3. T. Saito, M. Yuri, and H. Onuki, Metrologia 32, 485-489, 1996.
4. T. Saito, H. Shitomi, and I. Saito, CIE Tutorial and Expert Symposium, Bern, CIE, 2010.
5. H. J. Hovel, Solar Cells in Semiconductors and Semimetals vol. 11 edited by A. C. Willardson, Academic, New York, 24-, 1975.

New Method for Spectral Irradiance and Radiance Responsivity Calibration using Pulsed Tuneable Lasers from 210 nm to 2500 nm

Yuqin Zong, Steven Brown, George Eppeldauer, Keith Lykke, and Yoshi Ohno

National Institute of Standards and Technology, Gaithersburg, Maryland, USA
Corresponding e-mail address: yuqin.zong@nist.gov

Continuous wave (CW) tuneable lasers are expensive and hard to operate. To address this issue, we developed a new, electric charge measurement-based method for spectral irradiance and radiance responsivity calibration by using affordable and automated pulsed lasers. A current integrator is used for both standard detector and test detector to measure the total charge of a pulse train. The estimated expanded uncertainty of this method is below 0.1 % (*with a coverage factor k=2*) for spectral irradiance and radiance responsivity calibrations.

1. INTRODUCTION

Continuous wave (CW) tuneable lasers have been used for spectral irradiance and radiance responsivity calibrations for over 10 years [1]. The CW laser-based calibration facility is capable of achieving the lowest uncertainty for spectral irradiance and radiance responsivity calibrations. However, CW tuneable lasers are expensive and difficult to operate and maintain. Furthermore, CW tuneable lasers typically have extremely narrow bandwidths; interference fringes from optical elements of detectors (e.g. windows) and instruments (e.g. filters) can result in large calibration errors if not properly mapped out.

The newly developed 1000 Hz repetitive rate optical parametric oscillator (OPO) tuneable lasers are affordable and easy to operate compared to CW tuneable lasers. However, the pulse duration of this type of OPO tuneable lasers is only a few nanoseconds and thus its duty cycle is extremely small. The small duty cycle causes problems in a conventional measurement system consisting of a detector, a transimpedance amplifier, and a digital multimeter. To avoid saturation at the peak laser power, the averaged signal from the detector must be low, and the gain of the transimpedance amplifier and the range of the digital multimeter must be set to be several orders of magnitude higher than that for the corresponding DC signal which results in a large measurement uncertainty. Furthermore, a significant error may be introduced when a multimeter is used to measure the extremely spiky signals from the kHz laser system in DC mode.

In this paper we describe an electric charge measurement-based method that can be used for measurement of pulsed lasers. By using this new measurement technique a fully automated system is being developed at NIST for calibration of spectral irradiance and radiance responsivity from 210 nm to 2500 nm.

2. THE ELECTRIC CHARGE MEASUREMENT BASED METHOD

Instead of directly measuring the averaged DC photocurrent of a detector (unit: ampere), the new method measures a detector's response for total electric charge (unit: coulomb) of its photocurrent pulse train by using a current integrator. The diagram of the measurement circuit is shown in **Figure 1**.

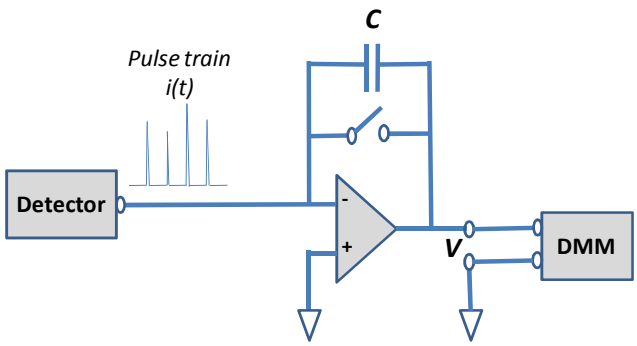

Figure 1. Schematic of a current integrator.

The capacitor's total charge, Q, over a known period of integration time, T, is

$$Q = \int_0^T i(t)dt = C \times V \,. \quad (1)$$

For the spectral irradiance and radiance calibration, the spectral responsivity of the test detector, R_{test}, can be obtained by

$$R_{\text{test}} = R_{\text{standard}} \times Q_{\text{test}} / Q_{\text{standard}} \,, \quad (2)$$

$$\text{or} \quad R_{\text{test}} = R_{\text{standard}} \times V_{\text{test}} / V_{\text{standard}} \,, \quad (3)$$

assuming that the same integrator and the same integration time, T, is used. Note that the integration time error does not contribute to the calibration uncertainty as long as the integrator catches the same pulse train of a pulse laser.

3. THE OPO TUNEABLE LASER SYSTEM

An 1000 Hz OPO tuneable laser based system is being developed at NIST to perform fully automated spectral irradiance and radiance responsivity calibration from 210 nm to 2500 nm. The schematic is shown in **Figure 2**.

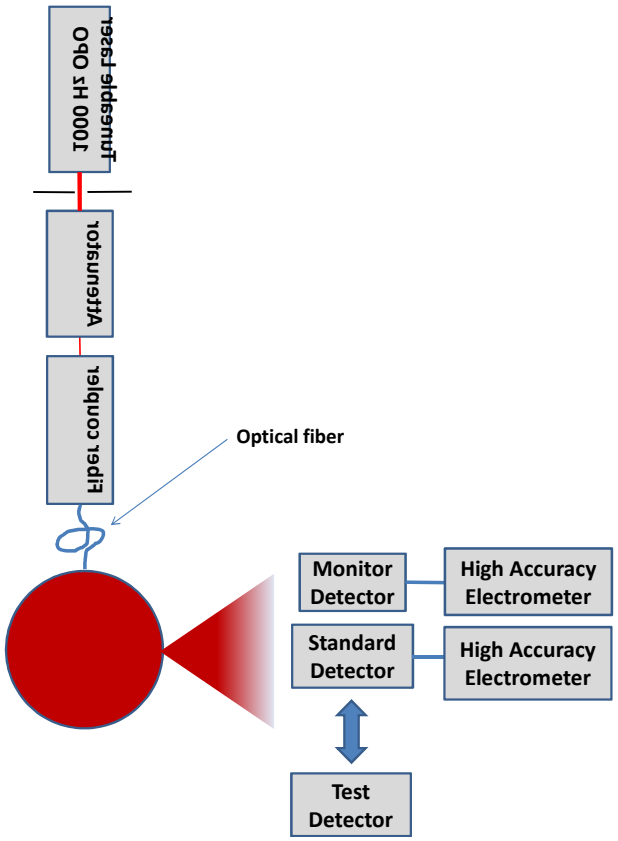

Figure 2. Schematic diagram of the kHz laser-based calibration system.

Flux from the OPO laser is coupled into an integrating sphere through an optical fiber to form a uniform irradiance or radiance source. A monitor detector is placed on the edge of the laser beam to monitor the change of the laser. Two high accuracy electrometers are used to measure total charge, Q, from the two detectors. The laser shutter and the two electrometers are synchronized to control the integration time. For a spectral irradiance or radiance calibration, first the standard detector and the monitor detector are used to measure the laser beam for $Q_{\text{standard, opo}}$ and $Q_{\text{monitor, standard}}$, and then the standard detector is replaced by the test detector and the laser beam is measured again using the test detector and the monitor detector with the same integration time for $Q_{\text{test, opo}}$ and $Q_{\text{monitor, test}}$. The spectral resonsivity of the test detector can be calculated by using **Equation 2**, where $Q_{\text{standard}} = Q_{\text{standard, opo}} / Q_{\text{monitor, standard}}$ and $Q_{\text{test}} = Q_{\text{test, opo}} / Q_{\text{monitor, test}}$ to correct for changes in the laser output during the calibration. Note the systematic errors of the electrometers are cancelled because both the test detector and the standard detector use the same electrometer, and the same monitor and its electrometer are used for both measurements. Furthermore, the integration time error does not contribute to the calibration uncertainty because both the standard detector (or the test detector) and the monitor detector measure the same number of laser pulses.

The pulse width of the OPO tuneable laser is approximately 5 ns. Due to multiple reflections inside the integrating sphere, the pulse width of the radiant flux out of the sphere can be more than 10 times longer. For the case where the integrating time is 1000 ms, the peak photocurrent of the detector is limited to be 0.1 mA (well below the saturation level), the time-averaged detector current is 5 nA which can be measured by the high accuracy electrometers with a small uncertainty.

4. SUMMARY

A new, electric charge measurement-based method for spectral irradiance and radiance responsivity calibrations is described. This method is immune to the systematic errors from the current integrator and integration timer which are dominant uncertainty for a charge based measurement system, and thus small calibration uncertainties can be achieved. Based on the new technique, a fully automated calibration system using a 1000 Hz OPO tuneable laser with a continuous tuneable range from 210 nm to 2500 nm is being developed. The estimated relative expanded uncertainty for spectral irradiance and radiance responsivity calibration is expected to be below 0.1 % (with a coverage factor k=2). This system can be used to calibrate detectors for spectral irradiance and radiance responsivities. It can also be used to perform detector-based calibrations for spectroradiometers and imaging instruments over a wide spectral region, from 210 nm to 2500 nm. We are exploring the use of this technique with cryogenic radiometers for the calibration of trap detectors.

REFERENCES

1. S. W. Brown, *et al*, NIST facility for spectral irradiance and radiance responsivity calibrations with uniform sources, Metrologia, 37, 579–582, 2000.

Fully Lithographic Fiber-coupled Cryogenic Radiometer for Picowatt Powers*

Nathan Tomlin, John Lehman, Sae Woo Nam

National Institute of Standards and Technology, Boulder, Colorado USA
Corresponding e-mail address: ntomlin@boulder.nist.gov

A new type of absolute cryogenic radiometer has been fabricated at the microscale level for direct substitution optical fiber power measurements. It consists of three parts: an absorber, electrical heater, and thermometer all on a single micro-machined membrane. The device has been shown to be sensitive to power levels down to 1 pW.

INTRODUCTION

Current state-of-the-art absolute cryogenic radiometers (ACRs) at NIST and other national metrology institutes (NMIs) can measure optical power levels down to 1 μW with low uncertainties. However, there are many emerging industries that utilize detectors and sources operating at much lower power levels, for which NIST and other NMIs are currently unable to provide optical power traceability. Conventional radiometers consist of macroscopic components that are painstakingly assembled by hand. It is extremely challenging for a conventional ACR to provide metrology at lower power levels due to surrounding blackbody radiation and thermal gradients in the macroscopic components.

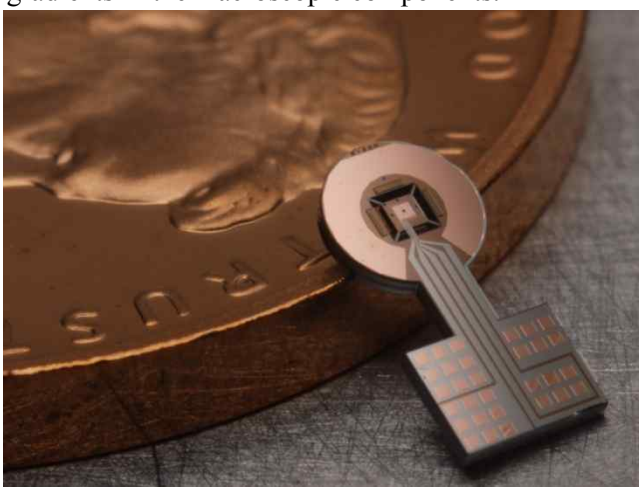

Figure 1. Microscale radiometer chip next to a penny for scale.

Instead of continuing to push conventional radiometers to smaller sizes, we have instead taken a completely different approach and designed a radiometer fabricated completely at the microscale level. The microscale radiometer is designed to measure power levels down to 1 pW, many orders of magnitude lower power than current ACRs.

The lithographic fabrication makes the microscale radiometer quite versatile. Hundreds of identical devices can be fabricated on a single wafer, which is desirable for inter-comparisons and dissemination to other NMIs. Alternatively, multiple variations in the design of the absorber, thermometer, and membrane can be produced on the same wafer.

RADIOMETER DESCRIPTION

All components of the radiometer are fabricated lithographically on a double-side polished silicon wafer. The weak thermal link is provided by a micro-machined silicon-nitride membrane. The thermometer, heater, and absorber are all on the membrane, with thin-film superconducting wiring providing electrical connections (Fig. 1 & 2). A portion of the bulk silicon is left hanging on the underside of the membrane to ensure that all parts of the radiometer are thermalized to the same temperature.

Figure 2. Membrane containing the thermometer, absorbers, and heater.

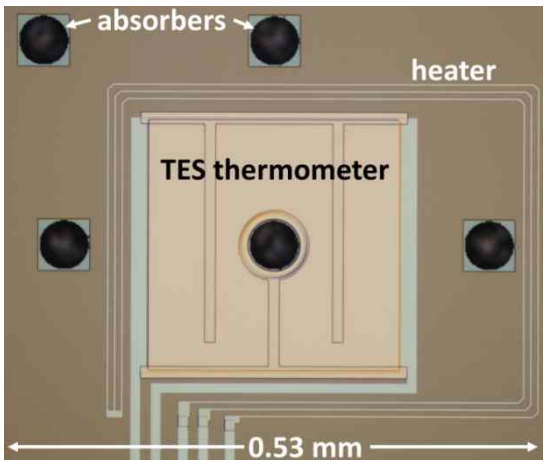

The thermometer is a thin-film superconducting Transition-Edge Sensor (TES), which can be stably biased in the superconducting transition using negative electro-thermal feedback and read out using superconducting quantum interference devices (SQUIDs) [1]. The steep change in resistance with respect to temperature at the superconducting critical temperature (T_c) makes the TES an extremely sensitive thermometer. The TES is made from a bilayer of Molybdenum and Copper. The thicknesses

of the metals can be adjusted to engineer the bilayer T_c, which for the current devices is 150 mK.

The electrical heater is a thin-film PdAu trace surrounding the TES and having a resistance of 10 kΩ. The resistor is used to heat the membrane for the electrical substitution measurement.

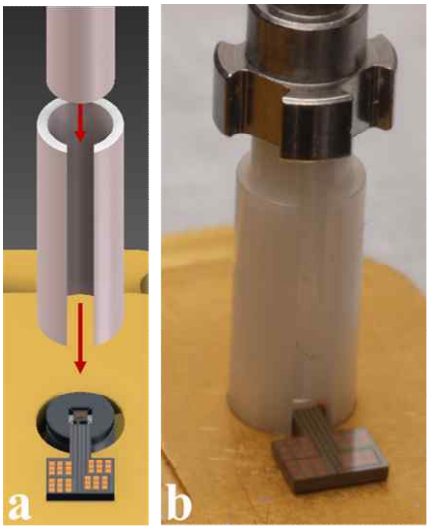

Figure 3. (a) Assembly drawing showing alignment of the fiber core to the center of the radiometer. (b) Picture showing aligned radiometer.

The absorber consists of silicon roughened to increase light absorption (black silicon) [2]. In the center of the TES, we etch a 50 μm diameter circle with a random lithographic pattern into the silicon using a Bosch process plasma etch. Incident radiation is coupled to the absorber through a standard 9 μm core, single-mode telecommunication fiber. The distance between the fiber and radiometer is set by 10 μm thick SU-8 epoxy posts surrounding the device. The device chip is etched in the shape of a circle in order to fit inside of a fiber ferrule, which aligns the optical fiber tip to the center of the absorber to within a few micrometers (Fig. 3) [3]. Additional absorbers are etched at varying distances from the center of the radiometer in order to check that all the components on the membrane are properly thermalized.

The complete membrane radiometer package is operated at a temperature of less than 100 mK using a cryogen-free dilution refrigerator with a base temperature of ~12 mK.

RESULTS

The response of the microscale radiometer was determined electrically by applying a known current to the heater. Fig. 3 & 4 show the TES response to electrical input powers from 1-200 pW. The measured responsivity of the device is 450 pW/K.

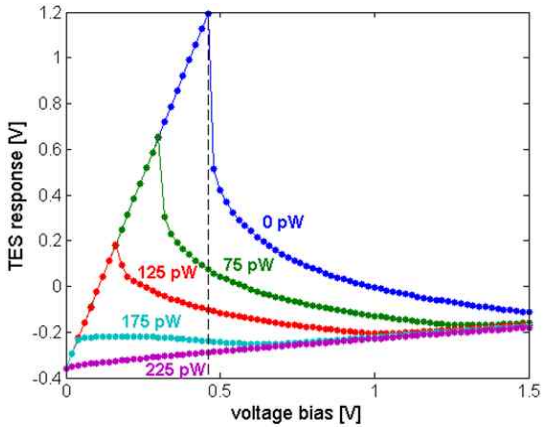

Figure 4. TES response vs. bias at different electrical heater powers.

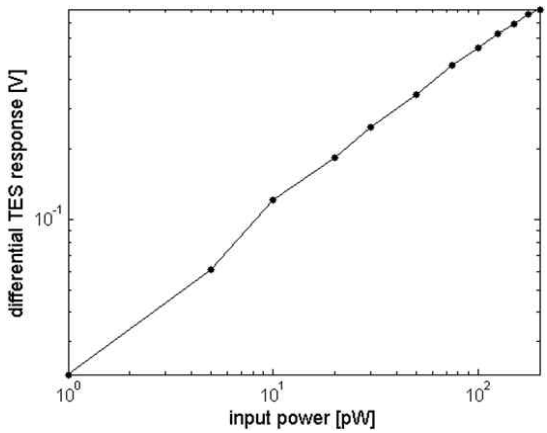

Figure 5. TES differential response vs. electrical heater power obtained at the bias point shown by the dashed line in Fig. 4.

DISCUSSION AND CONCLUSION

The microscale radiometer is a new tool which enables the use of conventional radiometric techniques at the very lowest power levels. We have shown sensitivity to electrical powers down to 1 pW.

REFERENCES

1. K.D. Irwin, An application of electrothermal feedback for high-resolution cryogenic particle-detection, Applied Physics Letters, 66, 1998, 1995.
2. K. Jung, W. Song, H.W. Lim, C.S. Lee, Parameter study for silicon grass formation in Bosch process, Journal of Vacuum Science & Technology B, 28, 143-148, 2010.
3. A. Miller, A. Lita, B. Calkins, S. Nam, Compact cryogenic self-aligning fiber-to-detector coupling with losses below one percent, Optics Express, accepted for publication, 2011.

Luminous Efficacy Measurement Setup for Solid State Lamps

Tuomas Poikonen[1], Tomi Pulli[1], Anna Vaskuri[1], Tuomo Hyvönen[1], Petri Kärhä[1,2], and Erkki Ikonen[1,2]

[1]*Aalto University School of Electrical Engineering, Espoo, Finland*

[2]*Centre for Metrology and Accreditation, Espoo, Finland*

Corresponding e-mail address: tuomas.poikonen@aalto.fi

We present a setup for luminous efficacy measurements of E27-base solid state lamps (SSL). The setup is based on a 1.65-m integrating sphere, originally designed for luminous flux measurements of incandescent lamps. The sphere setup was slightly modified, and a regulated AC power supply and an electrical power meter were added for measuring the power consumption of the lamps. Test measurements were conducted for a group of 15 SSLs. The measured luminous efficacies varied between 25 and 64 lm/W. The waveform measurements of the luminous flux and the AC-current showed large differences in the quality of the switching power supplies used in the lamps. The measurement uncertainty for the luminous efficacy of an SSL is 1.5 – 3.0 % (k = 2).

INTRODUCTION

Luminous efficacy, defined as the luminous flux produced by a lamp divided by its active electrical power, is an essential quantity in determining the energy consumption of light sources. Luminous flux measurement setups have been typically characterized for DC-operated incandescent light sources [1,2]. Luminous efficacy measurements of solid-state lamps (SSL) require special care due to their optical and electrical properties that differ from incandescent lamps. SSLs have built-in switching power supplies, which draw short pulses of current at each power line cycle [3]. This results in current waveforms that contain harmonic distortion at high frequencies. Depending on the current driver topology used in the lamp, the luminous flux may have pulsed shape also.

In this paper, we present our luminous efficacy measurement setup and the results of the test measurements for a group of 15 different types of 230 V SSLs with an E27-base.

MEASUREMENT SETUP

The luminous efficacy measurement setup is presented in Figure 1. It is based on a 1.65-m integrating sphere, originally designed for luminous flux measurements of incandescent lamps [2]. The lamp holder of the sphere and its electrical wiring were renewed for 230 V AC-voltage. The sphere has three ports: a detector port, a reference flux port, and an auxiliary port.

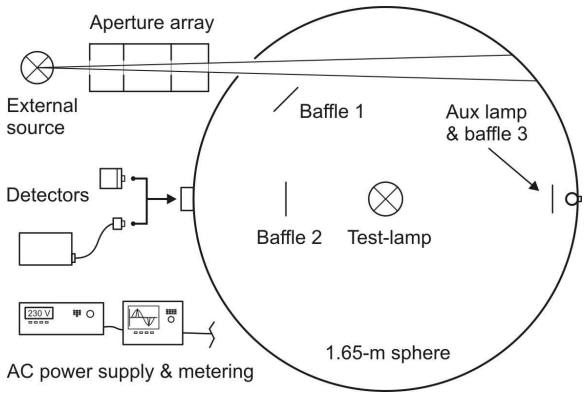

Figure 1. The luminous efficacy measurement setup.

The luminous flux responsivity of the system is calibrated by introducing a known external flux to the sphere through an opening, and by measuring the photocurrent of the sphere photometer, mounted in the detector port [1,2]. In order to minimize the burn times of the external standard source, the responsivity is measured only once with an empty lamp holder [4].

The spectral throughput of the sphere has been measured using a spectroradiometer and a diffuser head in the detector port. An incandescent luminous flux standard lamp was used as the light source, mounted in the lamp holder of the sphere. The relative spectral responsivity of the photometer head has been calibrated using our reference spectrometer facility. A motorized scanner is used for mapping the internal reflectance profile of the sphere.

A programmable AC power source is used for regulating the operating voltage for the SSL-lamp. A digital power meter is used for monitoring various parameters of the AC-line, such as voltage, current, power factor and total harmonic distortion (THD). The standard uncertainty of electrical power obtainable in typical SSL measurements is 0.5 %.

The luminous flux signal is measured with the photometer head and a current-to-voltage converter with adjustable bandwidth. The spectra of the lamps are measured with a spectroradiometer, and a self-absorption measurement is carried out using a halogen lamp in the auxiliary port. The self-absorption caused by the SSL can be measured either with the photometer or the spectroradiometer. For

spatial nonuniformity correction, the angular intensity distribution of the SSL is measured using a rotary stage and a photometer. The measurement uncertainty of a luminous efficacy measurement is between 1.5 % and 3.0 % ($k = 2$), depending on the properties of the SSL-lamp.

TEST MEASUREMENTS

In order to test the setup, and to get information about the variety of SSLs available in the market, luminous efficacies of 15 E27-base SSLs were measured after a 100-h burn-in period. The lamps were driven by a regulated 230 V power supply at a line frequency of 50 Hz. Due to the long stabilization times, the lamps were turned on for at least 1 hour before measuring the final values. The study revealed large variations in the luminous efficacy values and other parameters between different lamps, suggesting that the internal structures of the lamps may differ drastically from each other. The measured luminous efficacy values for the group of lamps were between 25 and 64 lm/W. The THD of the current waveforms were in the range of 30 – 260 %. The power factors ($\cos\varphi$) were between 0.35 and 0.95.

The luminous flux measurements were made with and without low-pass filtering to study possible flickering of the light output. In addition, the measurement gives information of how the built-in switching power supply drives the LEDs. The measured luminous flux values showed maximum deviations of 0.06 % – 105 % from the mean value of the flux. This indicates that some lamp use AC-LEDs or very simple rectifier circuits, whereas the others use more advanced switching stages and filtering to achieve a stable output [3,5]. For this group of lamps, the test measurements did not show correlations between the measured luminous efficacy, THD or power factor values.

The electric current and luminous flux waveforms of one of the studied SSL-lamps are presented as a function of phase in Figure 2. The regulated 230 V voltage is shown for illustrative purpose. Most of the studied lamps draw a similar sharp current pulse around the phase angles of 90° and 270° of the power line cycle. For this lamp, the THD of the current was 90 %, and the maximum deviation of the luminous flux from the mean value was 2.6 %.

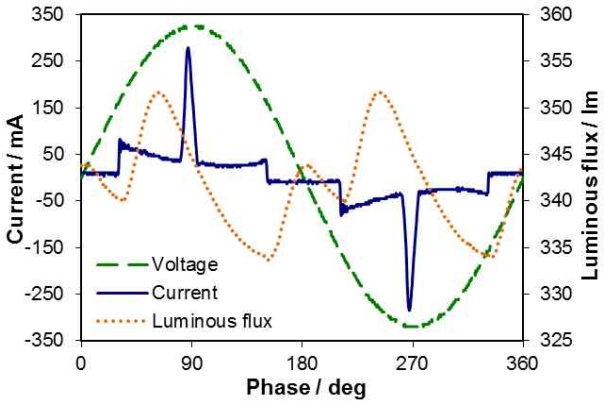

Figure 2. Measured waveforms of the AC-current and the luminous flux signal of one of the studied lamps.

CONCLUSIONS

We have developed a setup for luminous efficacy measurements of E27-base SSLs. Our existing 1.65-m integrating sphere was utilized for the setup with slight modifications. A programmable AC power source and a digital power meter were added to the setup to allow stable operation and characterization of the electrical power of the lamps. Test measurements were conducted for 15 SSLs after an ageing period of 100 h. The results showed significant variations in the measured luminous efficacies between different lamp types, as well as in the shape of the luminous flux and the electrical power consumption. Most of the measured lamps had pulsed light output. In addition, it was found out that SSLs produce large amounts of THD to the electrical network.

REFERENCES

1. Y. Ohno, Detector-based luminous-flux calibration using the absolute integrating-sphere method, Metrologia, 35, 473-478, 1998.
2. J. Hovila, P. Toivanen, and E. Ikonen, Realization of the unit of luminous flux at the HUT using the absolute integrating-sphere method, Metrologia, 41, 407-413, 2004.
3. H. van der Broeck, G. Sauerländer, M. Wendt, Power driver topologies and control schemes for LEDs, Proc. IEEE Applied Power Electronics Conf., 1319-1325, 2007.
4. T. Poikonen, P. Manninen, P. Kärhä, and E. Ikonen, Multifunctional integrating sphere setup for luminous flux measurements of light emitting diodes, Rev. Sci. Instrum., 81, 023102, 2010.
5. H.M. Jung, J.H. Kim, B.K. Lee, and D.W. Yoo, A New PWM dimmer using two active switches for AC LED lamp, Proc. IEEE Power Electronics Conf., 1547–1551, 2010.

Predictable Quantum Efficient Detector I: Photodiodes and Design

Meelis Sildoja[1], Farshid Manoocheri[1], Mikko Merimaa[1], Erkki Ikonen[1], Ingmar Müller[2], Lutz Werner[2], Jarle Gran[3], Toomas Kübarsepp[4], Marek Smîd[5] and Maria Luisa Rastello[6]

[1]Aalto University and Centre for Metrology and Accreditation, Espoo, Finland, [2]Physikalisch-Technische Bundesanstalt (PTB), Berlin, Germany, [3]Justervesenet, Kjeller, Norway, [4]AS METROSERT, Tartu, Estonia, [5]Český metrologický institut, Brno, Czech Republic, [6]Istituto Nazionale di Ricerca Metrologica, Torino, Italy

Corresponding e-mail address: meelis.sildoja@aalto.fi

We present the design and construction of a Predictable Quantum Efficient Detector (PQED), suggested to be capable of measuring optical power with an uncertainty of 1 ppm. The detector is based on custom-made inversion layer photodiodes operated at low temperatures using a reverse bias mode. Encouraging quantum efficiency results are obtained from three-dimensional modelling of a cylindrically symmetric photodiode. A constructed test PQED was compared with a silicon trap detector at the temperatures of 77 K, 173 K and 300 K with varied reverse biases from 0 V to 8 V. Our preliminary results show that the quantum efficiency at 488 nm is 1 within the measurement uncertainty of 500 ppm.*

INTRODUCTION

Geist *et al*. [1] have proposed a set of methods to reduce the internal quantum deficiency of inversion layer silicon photodiodes [2,3] to the 1 ppm level. Zalewski and Duda [4] developed already in 1983 close to 100 % external quantum efficiency (EQE) detector based on similar inversion layer type photodiodes. They showed that 0.999 ± 0.002 quantum efficiency is achievable.

The novelty of the present work consists of putting the ideas of [1] into an experimental test with a practical realization of the PQED to reduce the internal quantum deficiency by several orders of magnitude as compared with [4]. This involves manufacturing custom photodiodes with very low doping to reduce recombination losses in bulk silicon, improved modeling of the photodiode performance, designing the detector structure to reduce the specular reflectance [5], maintaining the cleanliness of the diodes' front surface and lowering the operating temperature to reduce the dark signal with reverse bias.

DESIGN OF THE PHOTODIODES AND PQED

The processing of photodiodes was subcontracted to the Technical Research Center of Finland (VTT) after public calls for tenders. VTT carried out two processing rounds to optimize the properties of the photodiodes for PQED. Figure 1 shows the cross section of the manufactured photodiodes. The impurity density of the p-type substrate is $2 \cdot 10^{12}$ cm^{-3} (6.6 kΩ cm resistivity). The active area of the photodiodes is either 11 x 11 mm^2 or 11 x 22 mm^2 and the thickness of the oxide layer is between 100 and 300 nm for different diodes. Detailed test results on single-photodiode performance are reported in the related papers [6] and [7].

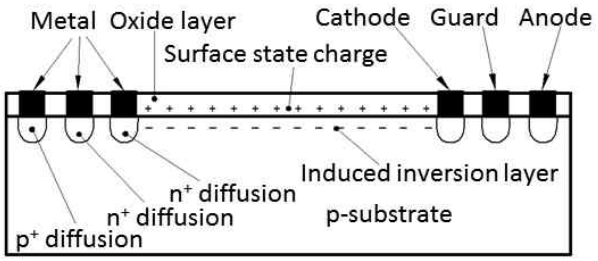

Figure 1. Cross section of the induced layer photodiode.

The PQED consists of two photodiodes aligned in such a way that 7 specular reflections take place before light leaves the detector [5]. The remaining reflectance of 60 ppm offers some visibility of the back-reflected beam for alignment purposes. For operation between 77 K and 300 K, the two-photodiode trap detector was mounted into liquid nitrogen cryostat equipped with a Brewster window.

MODELLING OF OPERATION

The expected quantum deficiency was calculated using Synopsis TCAD software for a cylindrically symmetric photodiode of 1 mm^2 active area. Figure 2

shows the results for temperatures between 100 K and 300 K at varying reverse bias voltage. The irradiance of 272 μW/cm^2 and wavelength of 730.5 nm (the same value as in [1]) were used in modeling. In Figure 2 it is seen that the internal quantum deficiency below 1 ppm is predicted below 250 K. The results of this three-dimensional calculation are in approximate agreement with those obtained using one-dimensional PC1D software [8].

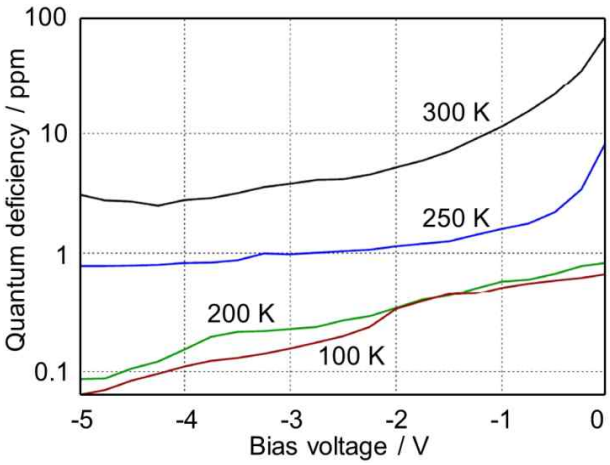

Figure 2. Synopsis TCAD simulation of the quantum deficiency for a 1 mm^2 inversion layer photodiode as a function of bias voltage at temperatures between 100 K and 300 K. The charge carrier lifetime is 2 ms, surface recombination velocity 100 cm/s and impurity density $4 \cdot 10^{12}$ cm^{-3}. The absorption coefficient value at 300 K is used for all temperatures.

PRELIMINARY TEST RESULTS

We have conducted preliminary test measurements of the PQEDs constructed using photodiodes from both processing rounds. As the radiation source a stabilized Ar+ laser with the beam diameter of ~2.5 mm ($1/e^2$) at the wavelength of 488 nm was used. The external quantum efficiency of PQED was measured against a calibrated trap detector. Results in Figure 3 for the first processing round photodiodes with the oxide thickness of 310 nm indicate that the target value of 1 is achieved within 500 ppm measurement uncertainty (k=1) with sufficient reverse bias voltage.

Similar results at 488 nm were obtained also for the second round photodiodes. The 500 ppm uncertainty in these measurements is mainly due to window transmittance, in addition to the trap detector calibration and instability of the laser power.

CONCLUSIONS

We have demonstrated that low-doped inversion layer silicon photodiodes, when arranged into trap configuration, can have external quantum efficiency values close to 1. Preliminary measurement results indicate that values above 0.999 are achievable up to room temperature when the reverse bias voltage is higher than 3 V. Ongoing comparisons of the PQEDs and cryogenic radiometers will allow more stringent tests of the achieved external quantum efficiency.

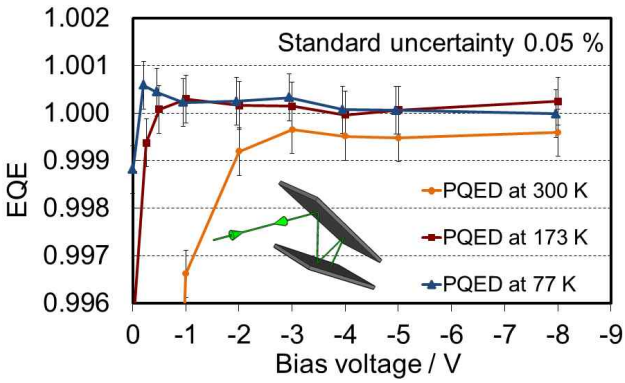

Figure 3. Measured external quantum efficiency (EQE) of PQED at the laser power of 285μW at 488 nm. The inset shows arrangement of the photodiodes.

*The research leading to these results has received funding from the European Community's Seventh Framework Programme, ERA-NET Plus, under Grant Agreement No. 217257.

REFERENCES

1. J. Geist, G. Brida and M. L. Rastello, Prospects for improving the accuracy of silicon photodiode self-calibration with custom cryogenic photodiodes, Metrologia, 40, 132-135, 2003.
2. T. E. Hansen, Silicon UV-Photodiodes using natural inversion layers, Phys. Scripta 18, 471-475, 1978.
3. J. Geist, E. Liang and A. R. Schaefer, Complete collection of minority carriers from the inversion layer in induced junction diodes, J. Appl. Phys. 52, 4879-4881, 1981
4. E. F. Zalewski and C. R. Duda, Silicon photodiode device with 100% external quantum efficiency, Applied Optics, 22, 2867-2873, 1983.
5. M. Sildoja, F. Manoocheri and E. Ikonen, Reflectance calculations for a predictable quantum efficient detector, Metrologia, 46, S151-S154, 2009.
6. I. Mueller et al, PQED II, these proceedings.
7. S. Hoem et al, Physics of self-induced photodiodes, these proceedings
8. J. Gran et al, Simulations of PQED with PC1D, these proceedings.

Temperature coefficients of multi-element trap detectors

F. Shindo[1], K.M. Nield[1], N. Swift[1], A. Koo[1]

[1]*Measurement Standards Laboratory of New Zealand, Industrial Research Ltd.*
Corresponding e-mail address: k.nield@irl.cri.nz

Measurements were made of the temperature coefficients of 5-, 3- and single element configured Hamamatsu S1337 silicon photodiode detectors. Comparisons of these data were made with previously published data for similar detector configurations.

INTRODUCTION

Until recently detector responsivity measurements of MSL's reference detectors have not been corrected for temperature variations during scale realization or upon transfer of the MSL scale. This was due to the good temperature stability in our laboratory space (± 0.5 °C) and the known low temperature sensitivities in the visible wavelengths and up to 900 nm [1, 2]. However, following our participation in CCPR-K2c, improvements in our UV detector responsivity scale, the extension of this scale beyond 900 nm, and the fact that the MSL reference scale is held on 5-element silicon trap detectors [3] (for which there is no specific data), it became more important to evaluate our reference detectors for their temperature coefficients.

MEASUREMENTS

The measurements were carried out on the MSL Detector Responsivity System (DRS). This consists of a McPherson 2035 double monochromator in additive dispersion mode with f/4.8. In addition, a beam splitter in the system allows monitoring of the light source so that source temporal drift may be corrected for. A combination of deuterium and tungsten sources was used to cover the wavelength range from 240 nm to 1000 nm in 10 nm intervals.

The temperatures of the detectors under test (DUT) (Hamamatsu S1337 photodiodes configured respectively as: one single photodiode, one 3-element trap and one 5-element trap) were controlled using the MSL constructed heat-pipes [4]. In this way all the DUTs were stable to better than 0.01 °C during the measurements. A second 5-element trap served as reference and was operated at the normal MSL laboratory temperature of 20 °C.

RESULTS

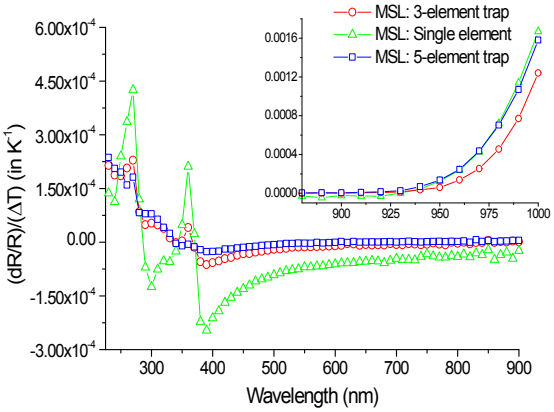

Figure 1. Temperature coefficients measured for three MSL detectors based on S1337 photodiodes configured in single element, 3-element and 5-element trap geometry.

Measurements were performed over a range of temperatures from 21 °C to 35 °C with a relative standard deviation in the mean of the temperature coefficients better than a few parts in 10^5. These temperature coefficients are shown in figure 1.

The temperature coefficients of the 5-element trap in the UV and visible regions were lower in magnitude than those of either the 3-element or single photodiodes, which correlates with the wavelength dependency of the front surface reflectance loss of these variously configured detectors [5]. In addition, the temperature coefficients for the latter two types of detectors compare well with previously published temperature coefficients for both single S1337 photodiodes and photodiodes housed in three-element geometries from 240 nm to 1000 nm [1, 6], see figure 2.

However, at longer wavelengths, where front surface reflectance loss is less significant, the 5-element trap measured for this work exhibited higher temperature coefficients than those of the 3-element trap studied. As these two detectors were fabricated at different times from different batches of photodiodes, it is likely that the difference in temperature coefficients may be due to other properties of the individual diodes used in these trap

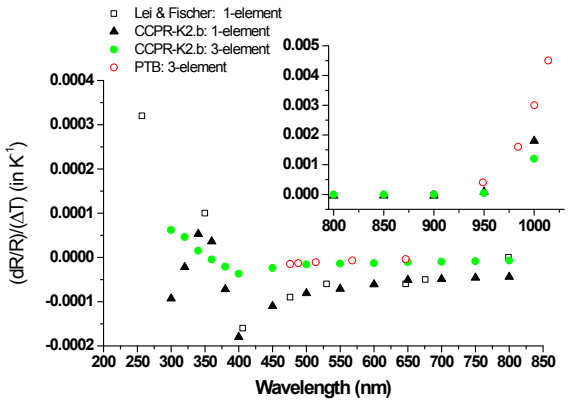

Figure 2. Temperature coefficients for single diode and three-element traps collected from Lei and Fischer [1], CCPR-K2.b [6] and PTB [7, 8].

detectors, and not simply the front surface reflectance loss. Indeed, a model for the temperature sensitivity of silicon photodiodes, proposed by Hartmann *et al*. [8], shows that the diode thickness and back reflectance of a silicon photodiode strongly influence the temperature coefficients at these wavelengths. This is in keeping with the model for

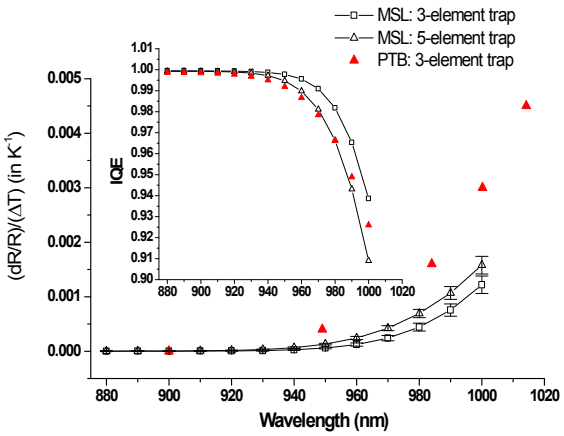

Figure 3. Temperature coefficients of MSL 3- and 5-element traps against a PTB 3-element trap [7, 8] beyond 875 nm. IQEs of the three detectors are indicated in upper left graph over the same wavelength range.

internal quantum efficiency (IQE) of silicon photodiodes as stated by Gentile *et al*. [9] and extended by Werner *et al*. [7].

Using the model for IQE we have calculated the IQEs for the PTB detector from the parameters given by Hartmann *et al*., and compared these with the IQEs for the MSL trap detectors. As can be seen in figure 3, the IQE curves of the MSL 5-element trap and the PTB 3-element trap detectors exhibit a steeper decrease starting at shorter wavelength than the IQE curve determined for the MSL 3-element trap. This correlates with the wavelength at which the temperature coefficients increase for these two detectors.

CONCLUSIONS

The temperature coefficients of MSL's reference silicon detectors have been evaluated from 240 nm to 1000 nm. This initial study confirms that a 5-element trap has lower temperature coefficient from UV to visible due to lower reflectance losses. However, to maintain this advantage beyond 900 nm, individual diodes should be tested and selected for their temperature coefficients.

Further work will be conducted to validate the model of Hartmann *et al*. for MSL detectors, and to determine if temperature coefficient data may be used to support the extrapolation of modelling of the IQEs of silicon photodiodes at wavelengths beyond 900 nm at laboratories where absolute responsivities are not easily determined.

REFERENCES

1. F. Lei and J. Fischer, "Characterization of Photodiodes in the UV and Visible Spectral Region Based on Cryogenic Radiometry", Metrologia, 30, 297-303, 1993.
2. T. C. Larason *et al*., " Spectrometric Detectors Measurements", NIST Special Publication 250-41, 1998.
3. A. Bittar *et al*., "New Five-Element Reflection Traps As Transfer Detectors for Monochromator, Laser and Filter Radiometry", Newrad, 1999, Madrid, Spain.
4. R. Mason *et al*., "Heat-Pipe Temperature Stabilisation System for Detectors and other Calibration Artefacts", submitted to Newrad 2011.
5. A Bittar, "Extension of a Silicon-based Detector Spectral Responsivity Scale in to the ultraviolet", Metrologia, 32, 497-500, 1996.
6. R. Goebel and M. Stock, "Report on the Key Comparison CCPR-K2.b of Spectral Responsivity Measurements in the Wavelength Range 300 nm to 1000 nm", BIPM Report, 2004.
7. L. Werner *et al*., "Accurate determination of the spectral responsivity of silicon trap detectors between 238 nm and 1015 nm using a laser-based cryogenic radiometer", Metrologia, 37, 279-284, 2000.
8. Hartmann *et al*, "Analytical Model for the Temperature Dependence of the Spectral Responsivity of Silicon", J. Opt. Soc. Am. B, 18, 942-947, 2001.
9. T. R. Gentile *et al*., "Realization of a scale of absolute spectral response using the National Institute of Standards and Technology high-accuracy cryogenic radiometer", Applied Optics, 35, No. 22, 4392-4403, 1996.

Impulse Spread Functions of Array Spectrometers Obtained by Deconvolutions of Measured Spectra of Calibration Lamps

Shau-Wei Hsu, Chin-Chai Hsiao, Kuei-Neng Wu and Yen-Liang Chen

Center for Measurement Standards, Industrial Technology Research Institute, Hsinchu, Taiwan
Corresponding e-mail address: SWHsu@itri.org.tw

A linear regularized deconvolution process has been developed to find the impulse spread functions (ISF) of array spectrometers by using line-spectral light sources. Experimental results show that the solutions of ISF are free of fluctuation if the spectral outputs are wavelet-denoised first. The wavelength dependent ISF of a spectrometer, and its application to the deconvolution of original outputs were also demonstrated.

1. INTRODUCTION

The array spectrometers are frequently used for radiometric and colorimetric measurements of LEDs, general lightings, displays, traffic signals, etc [1-3]. Because of entrance slit width, detector width, diffraction phenomena, aberrations, stray light, quality of components and alignment, the array spectrometers would have broaden and distorted spectral outputs compared with the input spectra. There are many methods to correct the measured outputs by using the impulse spread functions [2-6], which are the spread shapes of impulse inputs. However, because the impulse spread function is wavelength dependent, it is usually found out them by expensive wide-band tuneable lasers.

In this paper, we present another method for obtaining wavelength-dependent impulse spread function. It is done by deconvolutions of spectral output of common Ne, Ar, and Hg calibration lamps. The experimental data for this method are same as wavelength calibration of array spectrometer.

2. THEORY AND EXPERIMENTS

Figure 1 demonstrates a line-spectral input **x,** the impulse spread function $\mathbf{h_c}$ of a spectrometer, and the spectral output **y**, which can be expressed as following

$$y(i) = \sum_{k=1}^{K} x(i-k)h_c(k), \quad i = c - I \sim c + I \qquad (1)$$

where *y(i)* is the *i*-th output, *x(i-k)* is the *(i-k)*-th input, $h_c(k)$ is the impulse function around *c*-th channel. For the line-spectral source, **x** can be expressed as a collection many impulses. $h_c(k)$ can be solved with the equation

$$\mathbf{h_c} = (\mathbf{H}^T\mathbf{H} + \alpha\mathbf{Q}^T\mathbf{Q})^{-1}\mathbf{H}^T\mathbf{y} \qquad (2)$$

where the matrix **H** is constructed by *x(i-k)* and with dimensions of *(2I+1)*×*K*, *Q* is a linear regularization matrix, α is a small positive number [6].

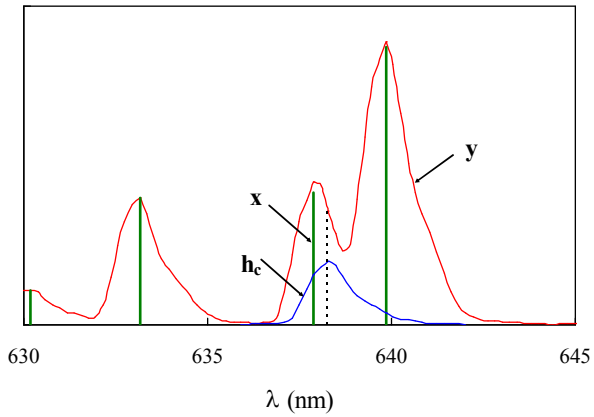

Figure 1. Demonstration of line-spectral input **x,** impulse spread function $\mathbf{h_c}$ of a spectrometer, and spectral output **y**.

Two commercial array spectrometers denoted as **A** and **B** were selected to find their ISF. Three commercial Ne, Hg, and Ar calibration lamps were used as the line-spectral sources. The lights form the lamps were homogenized by an integrated sphere, and then guided with a fiber into the spectrometers.

The impulse heights of the input **x** were estimated from the output **y** with Gaussian broaden assumption. To reduce the fluctuation from deconvolutions, the measured spectral outputs were firstly processed with wavelet denoised. A Matlab program was written for the calculations in this work.

3. RESULTS AND DISCUSSIONS

Figure 2 shows the obtained ISF of spectrometer **A** around λ = 667 nm with Ne lamp. The ISF in this work was normalized to have unit integral. It is observed that in a range of parameters *K* and *I*, the ISF is slightly invariant. The nearly smooth ISF is reached by wavelet denoise on the spectral output **y** to prevent fluctuation caused from deconvolution calculations.

The wavelength dependent ISF of spectrometer **A** is shown Fig. 3. As wavelength increased, the full width at half maximum of the ISF is increased, and the shape of ISF is less symmetric. The shape of ISF is not triangular for all wavelengths, and then the bandpass correction methods with the triangular assumption may not be used for the spectrometer **A**.

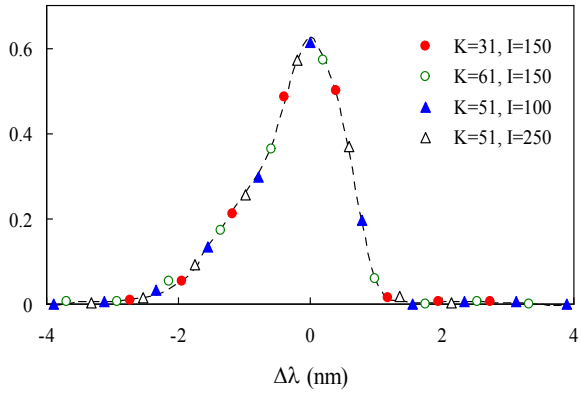

Figure 2. Impulse spread function around λ = 667 nm of spectrometer **A**. Dashed line is a guide to eyes.

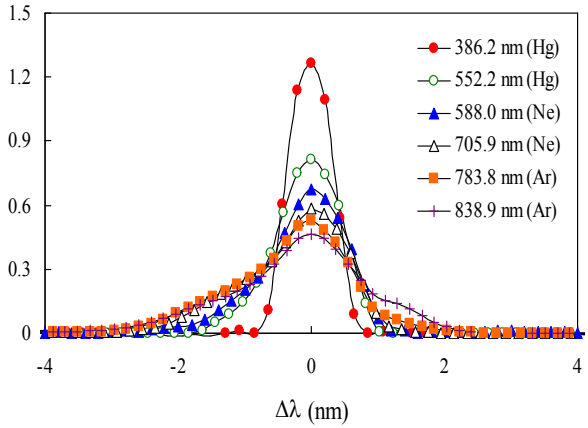

Figure 3. ISF of spectrometer **A** around various wavelengths.

A result of application of ISF around λ = 625 nm to the deconvolution of spectral outputs of Ne-lamp by spectrometer **A** is shown in Fig. 4. The iterative positive deconvolution algorithm was used in the calculation [6]. It can be observed that the ideal line-spectral of Ne-lamp was recovered for wavelength lower than 650 nm and higher than 600 nm. As the wavelength far from that of ISF (e.g., 650 nm in this case), the line shape will not be recovered.

Compared with spectrometer **A**, as shown in Fig. 5, the ISF of another spectrometer **B** is broader and more symmetric around 650 nm. This difference is retained for all common wavelengths of these two spectrometers, and may be caused from systematic variations such as entrance slit width or detector width.

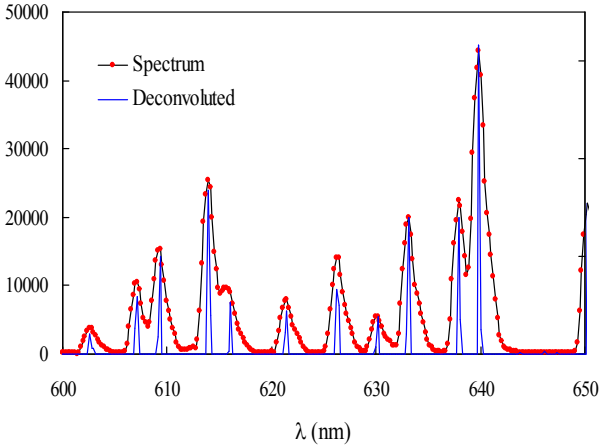

Figure 4. Use of the obtained ISF to deconvolute the measured spectrum of the Ne-lamp with spectrometer **A**.

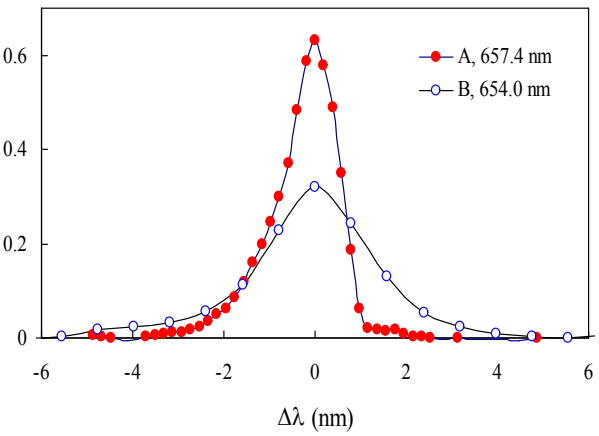

Figure 5. Comparison of ISF between spectrometers **A** and **B** around wavelength about 650 nm.

REFERENCES

1. Y. Ohno, Ch. 5: Spectral color measurement in *Colorimetry: understanding the CIE system*, 101-134, 1997.
2. L. P. Boivin, Study of bandwidth effects in monochromator-based spectral responsivity measurements, *Appl. Optics*, 41, 1929-1935, 2002.
3. Y. Zong, S. W. Brown, B. C. Johnson, K. R. Lykke and Y. Ohno, Simple spectral stray light correction method for array spectroradiometers, *Appl. Optics*, 45, 1111-1119, 2006.
4. J. L. Gardner, Bandwidth correction for LED chromaticity, *Color Res. Appl.*, 31, 374-380, 2006.
5. P. B. Crilly, A quantitative evaluation of various iterative deconvolution algorithms, *IEEE Trans. Instrum. Meas.*, 40, 558-562, 1991.
6. M. Morhaˇc and V. Matoušek, "Complete positive deconvolution of spectrometric data", Digital Signal Processing, 19, 372–392, 2009.

Beam properties of trap detectors

Toomas Kübarsepp[1], Malcolm White[2], Priit Jaanson[3]

[1]*Metrosert AS/TUT, Tallinn, Estonia,* [2]*National Physical Laboratory,Teddington, UK,*
[3] *AALTO University, Espoo, Finland*
Corresponding e-mail address: tkubarsepp@metrosert.ee

We have studied the first ten photodiode transmission trap detector at the laser wavelength 647.1 nm. The beam of 1/e^2-diameter 1.9 mm and overall diameter about 3 mm, was directed into the device in both *s*- and *p*-polarisation states. The output beam was measured using a scanning technique. A change in diameter less than 0.1 mm was observed. The output beam maintained a Gaussian distribution profile of the optical intensity along the propagation direction.

BEAM PROPERTIES

In high accuracy optical measurements, it is desirable to understand possible distortions of a travelling light beam undergoing multiple reflections.

A laser beam can be described in terms of a Gaussian distribution of the optical radiant power intensity along the direction of propagation

$$I = I_0 \exp\left(\frac{-2r^2}{w^2}\right) \qquad (1)$$

where I_0 is the maximum intensity, r the beam radius and w the beam waist radius.

Our intention was to study multiple reflection effects on the Gaussian shaped laser beam in the ten-element transmission trap detector reported in [1].

MEASUREMENTS

We used a Coherent type I302 Krypton ion laser, emitting at 647.1 nm, as the source. This beam was stabilised and then measured with a CCD camera. The beam radius was w = 0.95mm ± 0.05 mm which gave as an estimation for the laser beam 1/e^2 diameter d_i = 1.9 mm. The overall input beam diameter was measured to be 2.5 mm.

A PerkinElmer Optoelectronics model MP962 channel photomultiplier, fitted with a 0.2 mm diameter aperture, was used to measure the profile of the output beam. The aperture limited the maximum count rate of the multiplier to 850,000 counts per second, corresponding to 0,85 pW of optical power.

The CPM was mounted on a pair of automated linear translation stages, enabling the device to be moved in the *x* and y directions. An area 4 mm x 4 mm was scanned behind the detector to study the optical intensity profile of the exiting beam for both, *s*- and p-polarised incoming beam.

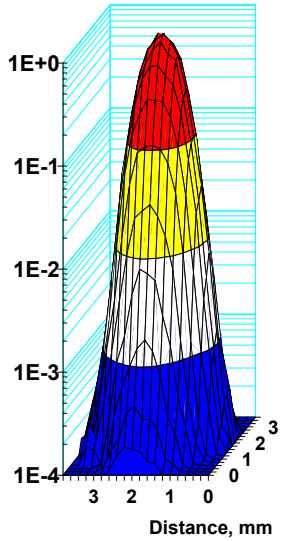

Fig.1 The measured profile of the beam at the output of ten-element transmission trap detector for *p*-polarised input beam. The *p*-polarised light at the wavelength of 647.1 nm is attenuated approximately 10^6 times due to ten reflections in the trap detector before exiting.

The analysis of the measurement results revealed that the profile of the beam was not distorted after ten reflections in the transmission trap detector under study and preserved a Gaussian distribution profile (Fig 1).

This study was part of a larger EURAMET joint research project which received funding from the European Community's Seventh Framework Program, ERA-NET Plus, under Grant Agreement No. 217257.

REFERENCES

1. T. Kübarsepp, M. White, "Ten-element photo-detector for optical power and attenuation measurements," Appl. Opt. 49, 3774-3779 (2010).

The use of the Allan deviation for noise and drift measurements in radiometry applications

Andrew Levick[1], Marin Dury[1], Jane Ireland[1], Emma Woolliams[1] and Nigel Fox[1]
[1]National Physical Laboratory, Teddington, United Kingdom
Corresponding e-mail address: Andrew.Levick@npl.co.uk

We have used the Allan deviation method to measure the noise and drift in the power of a supercontinuum laser with and without power-stabilisation feedback control. The Allan deviation method clearly shows that the feedback control removes drift. The random uncertainty in the mean stabilized laser power, determined using the Allan deviation method, is <0.01 % for averaging times longer than 100 s.

INTRODUCTION

All measurement systems have a resolution limited by random fluctuations (noise) or by variations in parameters with time (drift). Noise and drift can take a variety of forms having different measurement times or frequency dependencies. Gaussian or 'white noise', flicker or '1/*f*' noise, and random walk drift are examples commonly met in electronic measurement devices. The noise in a signal is usually quantified by computing the standard deviation; however this is a single value, and gives no information about the type and timescales of the noise and/or drift. The mean and standard deviation are only meaningful quantities when white noise dominates. When there is significant drift, the mean and standard deviation are not relevant quantities and averaging does not reduce the random uncertainty.

ALLAN DEVIATION METHOD

The Allan deviation method [1] allows different noise and drift types to be readily identified at various timescales. Consider a signal, $y(t)$, measured many times uniformly spaced by an interval Δt. The Allan variance is the variance of the differences between successive averages of $y(t)$:

$$\sigma_y^2(\tau) = \frac{1}{2N}\sum_{k=1}^{N-1}\left(\overline{y_{k+1}} - \overline{y_k}\right)^2$$

where

$\overline{y_k} = \frac{1}{\tau}\sum_{t=t_k}^{t=t_k+\tau} y(t)\Delta t$ and $\overline{y_k}$ is the average of a series of measurements $y(t)$ over time τ, and is computed for: $1\Delta t$,$2\Delta t$, $4\Delta t$, $8\Delta t$….

The plot of $\log(\sigma_y(\tau))$ versus $\log(\tau)$ is the **Allan deviation plot**, and the slopes in the plot are interpreted as follows:

Noise or drift model	Slope
Linear drift	1
Random walk	0.5
Flicker or drift	0
Gaussian or white noise	-0.5

SUPERCONTINUUM LASER STABILISATION

As an example application of the Allan deviation, we describe the power-stabilisation feedback control of a supercontinuum laser. The noise and drift associated with the laser power were calculated with the Allan deviation method.

Supercontinuum lasers, which emit over a broad wavelength range (e.g. 400 nm – 2200 nm), are being investigated as potential sources for metrology [2]. They could replace lamps and blackbodies, being more robust and portable, and having a low optical invariance (entendue). However, commercial products have comparatively poor power stability.

Figure 1 is a schematic diagram of the apparatus. The supercontinuum laser (Fianium FemtoPower SC450) is coupled into an integrating sphere (50 mm diameter) on to which are attached two stable filter radiometers (wavelength 800 nm, bandwidth 20 nm). Using two radiometers allows a distinction to be made between different sources of drift (i.e. drift associated with the laser and drift associated with the radiometers). Standard high accuracy interference-filter based filter radiometers were used. These were actively temperature stabilised.

The laser consists of three main sub-systems: a passively mode-locked low power fibre laser at 1064 nm, a high power cladding-pumped fibre amplifier and a high nonlinearity supercontinuum generator. The latter generates supercontinuum radiation in the range 450 nm – 2200 nm. The laser generates up to 4 W of power over this wavelength range.

For power-stabilisation feedback control, the laser was actively power-stabilised using a feedback

control from one of the filter radiometers (FR1) to the pumped fibre amplifier within the laser. The other filter radiometer (FR2) was used as an independent monitor. The signals from the two filter radiometers were continuously monitored and then analysed using the Allan deviation method.

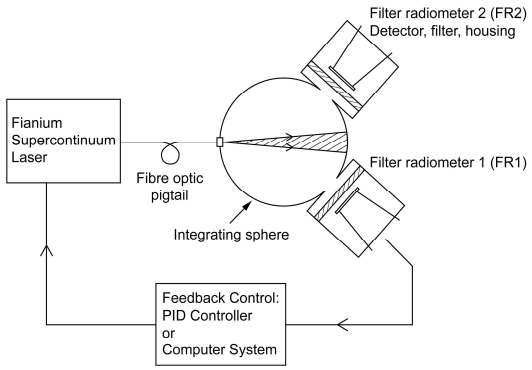

Figure 1. Schematic diagram of the experiment

RESULTS

Figure 2 shows the filter radiometer signals **with** the stabilisation feedback control applied. Neither the feedback radiometer signal, nor the independent monitor radiometer signal shows drift, demonstrating the absolute stability of the stabilisation. The signals have noise with standard deviation of 0.1 %.

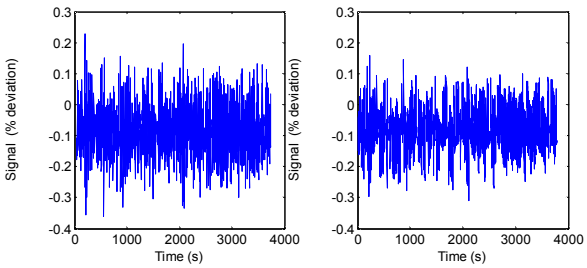

Figure 2. Signal (% deviation) versus time for filter radiometers (FR1 left graph, FR2 right graph) **with** stabilisation.

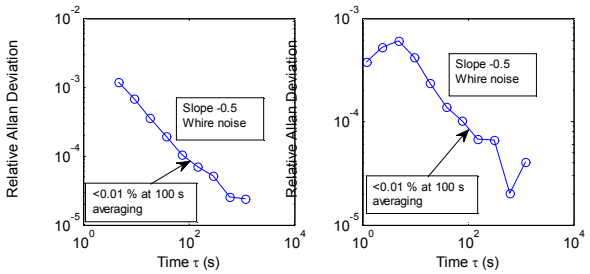

Figure 3. Relative Allan deviation plots for signals in figure 2.

Figure 3 shows the relative Allan deviation plots for the signals in figure 2. Both plots have gradients approaching -0.5, indicating that white noise is dominant and drift is negligible. This means that averaging is appropriate and figure 3 shows that the random uncertainty in the mean signal value is <0.01 % for averaging times longer than 100 s.

In contrast, figure 4 shows the filter radiometer signals **without** the stabilisation feedback control applied. Both signals show drift, which is correlated and thus associated with the laser. This drift is 0.9 % over time period of 5000 s in this case, and can be much larger especially when the laser is stabilising after start up. Figure 5 shows the Allan deviation plots for the signals in figure 4. Both plots have gradients >0, indicating drift and/or random walk. It would not be appropriate to average these signals.

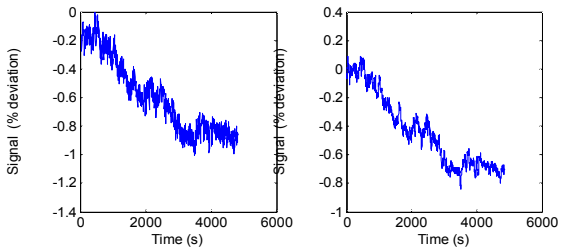

Figure 4. Signal (% deviation) versus time for filter radiometers (FR1 left graph, FR2 right graph) **without** stabilisation.

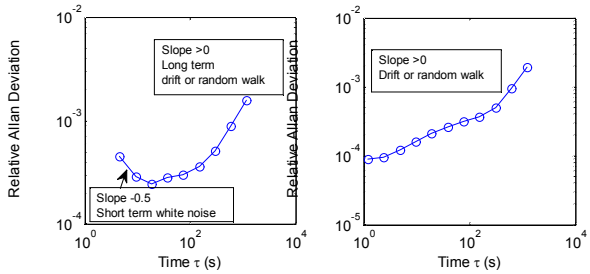

Figure 5. Relative Allan deviation plots for signals in figure 4.

CONCLUSION

We have used the Allan deviation method to measure the noise and drift in a supercontinuum laser with and without power-stabilisation feedback control. The Allan deviation plots indicate that the stabilisation clearly removes the drift. The Allan deviation gives more information than the standard deviation value alone.

REFERENCES

1. D. W. Allan, Statistics of atomic frequency standards, Proc IEEE, 51, 221-30, 1966.
2. J. T. Woodward, A. W. Smith, C. A. Jenkins, C. Lin, S.W. Brown and K. R. Lykke, Supercontinuum sources for metrology, Metrologia, 46, S277-S282, 2009.

The Agreement Results of Optical Fiber Power Meter Traceable to Absolute Radiometer and Cryogenic Radiometer

Jianwei Li, Zhixin Zhang, Jian Li, Nan Xu, Liang Lv

National Institute of Metrology, Beijing, China

lijw@nim.ac.cn； zhixinzhang@nim.ac.cn; jianl@nim.ac.cn; xunan@nim.ac.cn; lvliang@nim.ac.cn

We describe the agreement results of optical fiber power meter traceable to Cryogenic Radiometer and Absolute Radiometer of NIM. We trace optical fiber power measurements at nominal wavelengths of 1310nm and 1550nm. Measurement results are shown that the relative deviation is less than 0.3%. Two methods of traceability have good agreement.

INTRODUCTION

The optical fiber power is traced to absolute radiometer, but NIM has established the cryogenic radiometer with more accuracy. In order to ensure the agreement of the results, the two tracing methods are applied.

MEASUREMENT SYSTEM

1. Traceability of Optical Fiber Power to the Absolute Radiometer

For absolute radiometers have high requirements on environmental stability, so we shall adopt a spectrum measuring system which has an optical fiber power monitor (module of optic attenuator) function to compare **optical fiber power values and absolute radiometer readings. And then, values from the optical fiber power monitoring module will be transferred to a reference optical fiber power meter. The following figure shows the principle:**

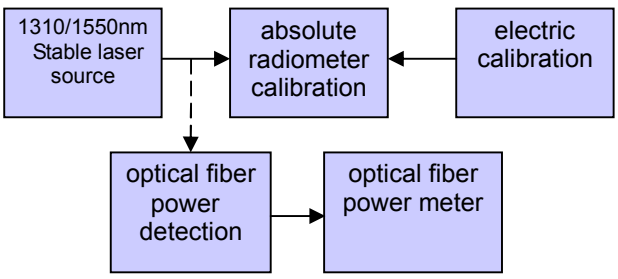

Figure 1. Absolute radiometer calibrate reference optical fiber power meter schematic

When using the absolute radiometer calibrate optical fiber power meter, the light source in the testing process requires good wavelength stability and power stability, the stable laser source is used in the experiment module for the optical output F-P type semiconductor lasers which central wavelengths are 1310nm and 1550nm, the wavelength is measured using a calibrated spectrum analyzer, the power stability for high-precision reference power meter detector test results are 0.037% and 0.017%.

The experiment using two different models of reference devices (absolute radiometer) to calibrate three reference optical fiber power meters, each calibration process are used on-site electronic calibration methods, and then getting the optic power meter correction factors, the 1310nm and 1550nm wavelength optical fiber power meter wavelength correction factors are shown in Table 1.

Table 1. 1310nm wavelength optical fiber power meter correction factors.

1310nm	
reference power meter correction factors	1.0065
	1.0097
	1.0077
	1.0079
average	1.0080
relative standard deviation of average	0.07%

Table 2. 1550nm wavelength optical fiber power meter correction factors.

1550nm	
reference power meter correction factor	0.9774
	0.9793
	0.9771
	0.9761
average	0.9775
relative standard deviation of average	0.13%

2. Traceability of Optical Fiber Power to the Cryogenic Radiometer

We will calibrate a trap detector using a high-stable light source which will radiate to the cryogenic radiometer, and then transfer responsivity values at 1310nm and 1550nm

wavelength points to a reference optical fiber power meter through a pyroelectric detector which has a flat spectral response. See the following figure for the principle:

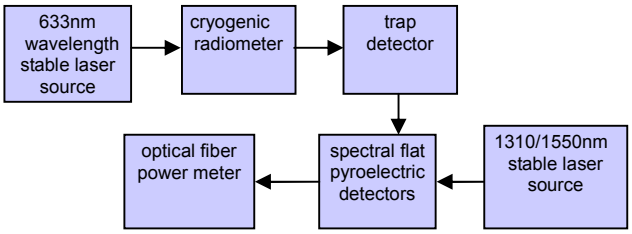

Figure 2. Cryogenic radiometer calibrate reference optical fiber power meter schematic.

The 1310nm wavelength calibration test results of optical fiber power meter are as follows:

Table 3. 1310nm wavelength optical fiber power meter calibration results.

1310nm pyroelectric detector/1310nm optical fiber power meter (RS5900 / 81618A)	
average	0.9983
relative standard deviation	0.04%
correction factor of the trap detector to the reference power meter	1.0074

The 1550nm wavelength calibration test results of optical fiber power meter are as follows:

Table 4. 1550nm wavelength optical fiber power meter calibration results.

1550nm pyroelectric detector / 1550nm optical fiber power meter (RS5900 / 81618A)	
average	0.9705
relative standard deviation	0.02%
correction factor of the trap detector to the reference power meter	0.9792

Since the pyroelectric power meter in the 633nm-1550nm spectral response is not completely flat. Therefore, according to its spectral reflectance get the amendment value as 1.001. Reference power meter final correction factors are shown in Table 5.

Table 5. Final correction factors of reference power meter.

Wavelength (nm)	cryogenic radiometer / reference power meter
1310	1.0084
1550	0.9802

RESULTS

As shown in the following table, we will get two different correction factors (A and B) for the reference optic power meter using above the two evaluation methods.

Table 6. Correction factors A and B.

	A	B	B/A
wavelength (nm)	cryogenic radiometer	absolute radiometer	/
1310	1.0084	1.0080	0.9996
1550	0.9802	0.9775	0.9972

For the relative deviation of result A and B is less than 0.3%. Therefore, the two methods of traceability have good agreement.

REFERENCES

1. F.Manoochehri, P.Karha, Characterisation of optical detactors using high-accuracy instruments, 327-337, Analytica Chimica Acta 380, 1999.
2. Stefania Castelletto, Luminous and photo standards by trap detactors, IEEE.TIM, 900-906, 1998.
3. Thomas C. Larason, Responsivity calibration methods for 365-nm irradiance meters, IEEE.TIM, 474-477, 2001.

Detector-based radiometry in the VUV spectral range

Alexander Gottwald, Udo Kroth, Hendrik Kaser, Gerhard Ulm

Physikalisch-Technische Bundesanstalt (PTB), Berlin, Germany
Corresponding e-mail address: alexander.gottwald@ptb.de

Monochromatized synchrotron radiation provides access to the vacuum-ultraviolet (VUV) spectral range (i.e, wavelenghts below 200 nm), which can not be completely covered with conventional laboratory radiation sources. With the 630 MeV electron storage ring Metrology Light Source (MLS), PTB owns a dedicated source for the UV, VUV and EUV spectral ranges. Already since 2008, a UV and VUV beamline for detector calibration is in operation. In 2011, a new undulator beamlime will become operational, providing UV and VUV radiation with higher radiant power. At both beamlines, a cryogenic electrical substitution radiometer is used as primary detector standard. The modular cavity absorber of the radiometer will be modified to match the different spectral and power conditions. For radiometric validation, detector and source-based comparisons were conducted.

INTRODUCTION

The absolute calibration of photodetectors regarding their spectral responsivity by using monochromatized synchrotron radiation (SR) and an electrical substitution radiometer as primary detector standard has been established by PTB since the early 1990s [1,2]. Currently, PTB operates two different radiometers for the dedicated use with SR. These instruments have a modified design compared to conventional radiometers for use with, e.g., laser radiation. While one of the radiometers was optimized for the (soft-)X-ray spectral range, the other instrument is particularly designed for the VUV spectral range, and operated at PTB's MLS storage ring [3]. Besides an existing beamline at a bending magnet of the MLS [4], currently an additional beamline at the undulator is in the final set-up phase. It will provide a larger spectral range down to the extreme ultraviolet (EUV) at radiant powers more than two orders of magnitude higher. To cover the enhanced dynamic range, the thermal coupling parameters of one cavity module can be changed for optimizing the performance.

MLS BEAMLINES FOR VUV DETECTOR-BASED RADIOMETRY

At the MLS, two beamlines will be available for detector calibration in the (extended) VUV spectral range: The normal-incidence monochromator beamline is located at one of the bending magnets. It covers the spectral range from 40 nm to 400 nm, and is in operation since 2008 (Fig. 1, [4]). The monochromator is a 1 m, 15° McPherson type monochromator with three different spherical gratings in a turret mount. The three gratings differ in line density and coating, and must be chosen with respect to the desired wavelength interval. Besides the gratings, different combinations of pre-mirrors, refocusing optics, bulk- and rare gas- filters can be chosen in order to suppress higher order contributions from the grating and to optimize the spectral purity of the monochromatized beam over the whole wavelength range covered.

In 2011, a second beamline will become available, which covers at least the same wavelength range, however, with quite different characteristics. The MLS storage ring offers one long straight section

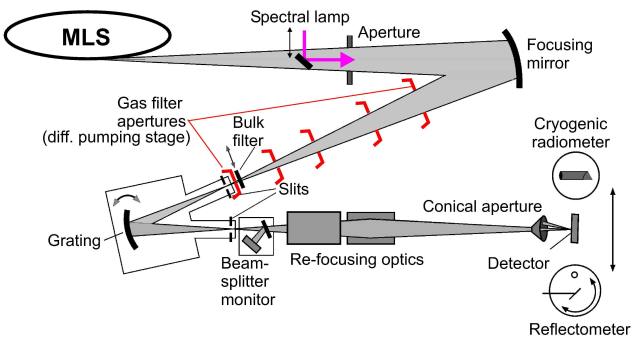

Figure 63. Schematic view of the normal-incidence monochromator beamline at the MLS.

in which the U180 undulator [5] is placed. The undulator is a periodic magnetic structure (21 periods, 180 mm period length). The spectrum of the undulator is dominated by harmonics with high intensities but limited spectral width. By changing the magnetic field parameter (i.e., the current of the electromagnets) the wavelength of emission can be

tuned over a wide range. For the use of the radiation between 4 nm (EUV) to 400 nm (UV), a dedicated beamline currently is under construction. It combines a grazing-incidence plane grating monochromator operating in collimated beam with an integrated normal-incidence configuration for the long-wavelength range.

THE SYRES II RADIOMETER

At its laboratory at the MLS, PTB operates the cryogenic electrical substitution radiometer SYRES II (Synchrotron Radiation Electrical Substitution radiometer) as the primary detector standard. This radiometer is particularly designed for the requirements in UV and VUV radiometry. The cavity absorber is made of thin (100 µm) electroformed copper with a 1 µm gold overcoat, so that the total mass and therefore the heat capacity is kept small, in particular at temperatures where the electrical connectors is in a superconducting state. The thermal connection to the heat sink (which is kept at liquid Helium temperature) is made by a thin wire with low heat resistance to obtain the desired values for sensitivity and time constant. In the standard configuration, the sensitivity is set to a value of about 100 mK/µW. This limits the maximum absorbed radiant power to about 40 µW. For higher powers, the temperature will become too high for superconducting conditions. By adjusting the length of the wire, the heat link can be modified, thus in particular the sensitivity can be adapted to the expected radiant powers of a few 100 µW at the undulator beamline.

VALIDATION OF THE SPECTRAL RESPONSIVITY SCALE

By use of monochromatized SR and the cryogenic radiometer as primary detector standard, a scale of spectral responsivity of semiconductor photodiodes is maintained and disseminated by PTB for wavelengths below 400 nm down to 0.02 nm. For the spectral range from 135 nm to 250 nm, a bilateral detector comparison was conducted between PTB and NIST [6]. Although these measurements still had been performed at the BESSY II facility, internal measurements validated the measurement capabilities at the MLS facility (Fig. 2). Nevertheless, the detector-based comparisons revealed that one critical issue is the detector stability in the VUV spectral range. The development of suitable new detector types is one of the current demands [7].

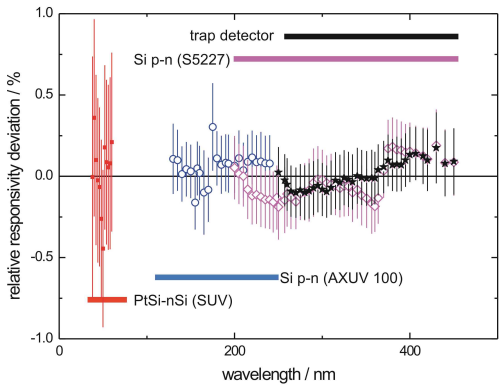

Figure 2. Relative deviation between calibrations at MLS and BESSY II with standard uncertainties.

A second approach for validation is the comparison of the cryogenic radiometer as primary detector standard to the MLS storage ring as primary source standard of calculable radiation [8]. Here, the non-dispersed total radiant power as measured by the radiometer is compared to the storage ring emission as calculated by the Schwinger equation. By this, the equivalence of both radiometric approaches (detector- and source-based radiometry) was shown to a level of uncertainty of currently about 1 %.

REFERENCES

1. H. Rabus et al., Synchrotron-Radiation Operated Cryogenic Electrical-Substitution Radiometer as High-Accuracy Primary Detector Standard in the Ultraviolet, Vacuum Ultraviolet and Soft X-ray Spectral Ranges Appl. Opt., 36, 5421-5440, 1997.
2. A. Gottwald et al., The PTB High-Accuracy Spectral Responsivity Scale in the VUV and X-Ray Range Metrologia, 43, S125-S129, 2006.
3. R. Klein et al., The Metrology Light Source operated as a primary source standard, Metrologia, 46, S266-S271 2009.
4. A. Gottwald et al., Ultraviolet and vacuum-ultraviolet detector-based radiometry at the Metrology Light Source, Meas. Sci. Technol,. 21, 125101, 2010
5. R. Klein et al., The PTB electromagnetic undulator for BESSY II, J. Synchrotron Rad 5, 451-452, 1998.
6. A. Gottwald et al., Bilateral NIST-PTB Comparison of Spectral Responsivity in the VUV, Metrologia, 48, Tech. Suppl. 02001, 2011
7. L. Shi et al., Optical performance of B-layer ultra-shallow-junction silicon photodiodes in the VUV spectral range, Procedia Engineering, 5, 633-636, 2010
8. R. Klein et al., Radiometric comparison of the primary source standard MLS to a primary detector standard, Metrologia, *submitted*

Characterization of the Surface Reflectance and Quantum Losses of Germanium Photodiodes for Determination of Optical Responsivity

Özcan Bazkır, A. Kamuran Türkoğlu
TUBITAK-UME
Optics Laboratory, Gebze/KOCAELİ
Phone: +90 262 679 50 00
Fax: +90 262 679 50 01
ozcan.bazkir@ume.tubitak.gov.tr
kamuran.turkoglu@ume.tubitak.gov.tr

Abstract

Responsivity of a photodiode is simply its current/voltage response to the incident optical power. Optical reflection losses, carrier recombinations, defects, passivating layer thickness, doping level, polarization dependency, etc. can be considered as the important parameters that affect the responsivity. Accurate determination of responsivity mainly depends on the measurement of optical power and current/voltage response of detection element. Since single photodiodes possess high reflectance losses, polarization dependency and also low stability, multiple trap configurations are preferred as the reference standard for the responsivity measurements.

In this work, we present our characterization and measurement results of germanium photodiode based trap detectors to use as reference standard. This optical detection element was constituted by geometrically oriented 3 windowless Ge photodiodes in reflective configuration. Large area (10 mm x 10 mm) photodiodes were employed in order to obtain larger field of view, linearity and responsivity. The number of photodiodes and their replacement configurations were aligned to reduce reflectance losses and polarization dependency.

After enabling the polarization independence and low reflectivity in the detection element, characterization of the front surface reflectance and determination of internal quantum losses were carried out. Front surface reflectance of Ge photodiodes was calculated using Fresnell's reflection, transmission equations and their optical constants (n,k). The calculated reflectance data were fitted to the measured data by adjusting the thickness of SixNy anti reflecting coating parameter. The internal quantum losses of photodiodes due to recombination of carriers were calculated from drift and diffusion current of carriers in the p-n photodiode. Here Ge photodiode having a very thin p layer ($p<<n$) was studied by considering negligible amount of recombination's in the p and depletion regions. The results indicate that high reflectance values of Ge photodiodes can be reduced bellow 1,0 % using the combinations of photodiodes in the trap configuration, which improve both responsivity and stability and therefore preferred to be used as reference standard for the determination of optical responsivity of detectors within its spectral range.

Key Words: Germanium Photodiode, Reflectance, Responsivity

Correction algorithm for interference affected measurement data

Michaela Schuster, Saulius Nevas, Armin Sperling

Physikalisch-Technische-Bundesanstalt, Braunschweig, Germany
Corresponding e-mail address: michaela.schuster@ptb.de

A method based on discrete Fourier transform (DFT) and digital filtering techniques is presented to correct tuneable laser-based measurement data for interference effects numerically. The method relies on well established digital signal processing algorithms rather than a physical modelling of the interference effects. An example of the algorithms applied to correct interference-affected measurement data of a radiance meter at the TULIP setup of PTB is provided. Finally, the uncertainty contribution arising from the digital filtering is discussed.

INTERFERENCE PROBLEM

Calibration and characterisation results of photometric and radiometric detectors using cw-lasers, for example at the TULIP setup [1] at PTB, are often affected by interference. This is due to multiple reflections of the narrow-band coherent radiation within the optical components of the optical radiation detectors. The interference effects are typically observed if no diffusing element is used as the foremost optical component of the detector. As a result, the constructive and destructive interfering parts of the radiation field superimpose as spectral oscillations (interference fringes) on the responsivity function of the detectors. Different techniques are known to reduce the unwanted interference fringes or to deal with them when measured: (i) The use of a diffusing element at the entrance window of the detector [2] or of wedged filters or filters with antireflection coating [3] will remove or reduce the interference effects. However, such extensions in detector design are often undesired or simply not feasible. (ii) Depending on the experimental data, a cancellation of the interference structure can be accomplished by either an average over every single period or a moving average with an appropriately selected averaging period along the measured signal [3,4]. This procedure may be sufficient for some applications. However, it is not a simple task to evaluate the detailed uncertainty contribution caused by such a method because these fringes are not simple sine-waves with fixed periods.

CORRECTION ALGORITHM

The idea behind the suggested correction algorithm is shown in the block diagram of Fig. 1. It is based on digital filtering approach, which is known from digital signal processing [5].

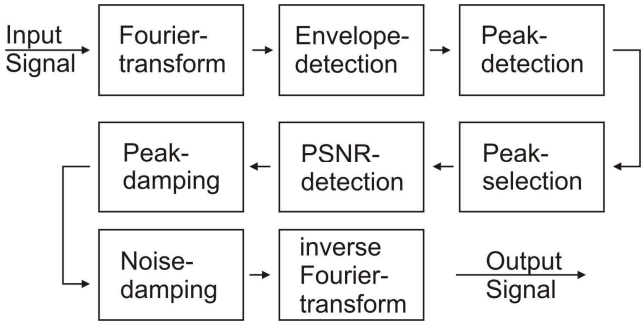

Figure 64. Block diagram of the digital filtering algorithm for correcting interference effects in laser-based measurement data.

To get information about the frequency components of the determined spectral responsivity function, the discrete responsivity values have to be transformed into the spatial frequency domain using a DFT. The transformation shows a main peak at around 0 cycles/nm containing information about the filter function of the detector and additional higher frequency components caused by the interference effects. Applying an envelope detection gives information about the peak values of the signal components and their position in the spatial frequency domain as well as their bandwidths. For the selected values of the interference peaks, the peak-signal-to-noise ratio (PSNR) is calculated. Out of this information a digital IIR (infinite impulse response) filter can be calculated which can be used to selectively damp the frequency components caused by the interference oscillation. The filtering can be either done by a multiplication in the spatial frequency domain or by a convolution in the wavelength domain. A low-pass filter can be additionally applied to reduce the remaining noise level. After the calculation in the frequency domain an inverse Fourier transform has to be applied to get the filtered output signal in the wavelength domain.

APPLICATION EXAMPLE

The radiance responsivity of a pyrometer of type LP3 was measured with a wavelength step of 0.01 nm in the wavelength range between 620 nm and 680 nm. The measured radiance responsivity with the interference oscillations and the associated measurement uncertainty are plotted in Fig. 2. Fig. 3 (blue curve) shows the measured signal transformed into the spatial frequency domain.

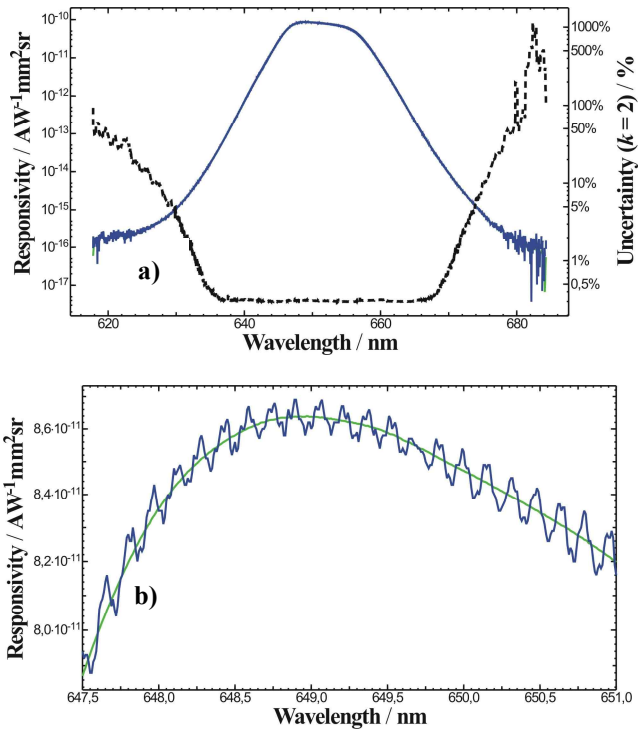

Figure 2. a) Measured spectral radiance responsivity of the pyrometer LP3 (blue curve, left axis), the data filtered by applying the digital filtering algorithm (green curve, left axis), and the associated measurement uncertainty (dashed black curve, right axis). b) Close up on the measurement data within the spectral range between 647.5 nm and 651 nm.

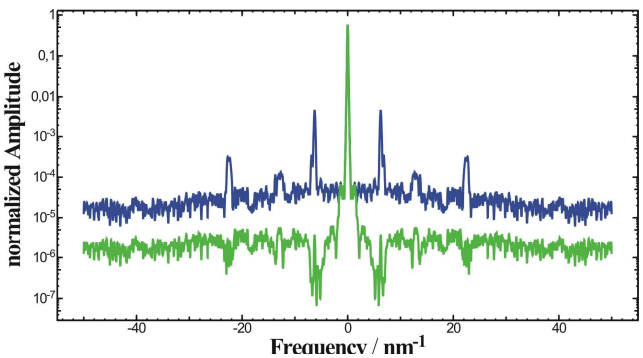

Figure 3. Spectrum of the measured radiance responsivity of the pyrometer before (blue curve) and after (green curve) applying the digital filtering algorithm for the interference correction.

Beside the peak at around 0 cycles/nm, two other peaks at around 6 cycles/nm and 22 cycles/nm are detected. The unwanted frequencies caused by the interference oscillations are damped with two band stop filters. Furthermore, a low pass filter is applied to damp the noise components. The resulting output data in the spatial frequency domain as well as the output data in the wavelength domain are shown as green curves in fig. 3 and fig. 2, respectively.

UNCERTAINTY CONTRIBUTION

The effectiveness of the digital filtering algorithm and the propagation of uncertainty of input quantities through this algorithm have been tested using simulations. For this purpose laser-based measurements of a photodiode with a protective window were simulated.. The filtered data were compared with the interference effects–free measurement data of the photodiode carried out at a monochromator-based setup. It was found that the deviation between the filtered signal and the measured data was about 0.05 %. This is in good agreement with the uncertainties associated with measurements using the TULIP setup.

ACKNOWLEDGEMENT

We thank our colleagues Klaus Anhalt and Thada Keawprasert from working group “7.31 High Temperature Scale” of the Berlin Institute of PTB for supporting the measurements of the radiance meter.

REFERENCES

1. A. Sperling, O. Larionov, U. Grusemann, and S. Winter, Stray-light correction of array spectroradiometers using tunable pulsed and cw lasers, Proc. of NEWRAD: 9th International Conference on New Developments and Applications in Optical Radiometry, 2005.
2. L.P.Boivin, Diffusers in silicon-photodiode radiometers, Appl. Opt. **21**, 918-923, 1982.
3. N. Noorma, P. Toivanen, F. Manoocheri, and E. Ikonen, Characterization of filter radiometers with a wavelength-tunable laser source, Metrologia **40**, S220-S223, 2003.
4. V. Ahtee, S. W. Brown, T. C. Larason, K. R. Lykke, E. Ikonen, and M. Noorma. Comparison of absolute spectral irradiance responsivity measurement techniques using wavelength-tunable lasers, Appl. Opt. **46**, 4228-4236, 2007.
5. A. Quinquis, Digital signal processing using MATLAB, ISTE, London, 2008.

Long-Term Stability of Gold Black Bolometers

Errol Atkinson and Ian C.M. Littler

National Measurement Institute, Sydney, Australia
Corresponding e-mail address: Errol.Atkinson@measurement.gov.au

Gold black bolometers are used at NMIA as standards of relative spectral responsivity. The possible drift in the spectral responsivity of reference bolometers arising from extended usage requires a means of checking their spectral stability. We describe a comparison between the responsivity of solid state photodetectors obtained using cryogenic radiometry and the responsivity obtained using bolometers. The results of the comparison show evidence that the reference bolometers have maintained their original calibration within the uncertainties of the measurements, even after extended use.

INTRODUCTION

Bolometers have been used as standards of relative spectral responsivity at NMIA since 1964 [1]. The current series of bolometer standards were first calibrated in 1996. The calibration of each bolometer involved spectrophotometric characterisation of the spectral transmittance and reflectance losses of the bolometer sensitive element and transmittance of the bolometer window. Since then each bolometer has accumulated between 300 and 510 hours of use. A photograph of one of the current series of bolometers is shown in Figure 1.

The issue of stability of the bolometers has been raised with the major concern being the possibility that use of the bolometers at raised temperature produces gradual physical changes in the structure of the gold-black absorption layer of the bolometer sensitive elements and consequential drift in spectral characteristics.

The active elements of the bolometers are extremely fragile when exposed so removing the elements from their housings for direct spectrophotometric measurement presents an undesirable risk.

Instead, a check was performed by measuring the relative spectral responsivity of a windowless silicon photodiode and a windowless InGaAs photodiode utilising the bolometer references and comparing these results with responsivity values obtained directly from the NMIA cryogenic radiometer over a wide wavelength range.

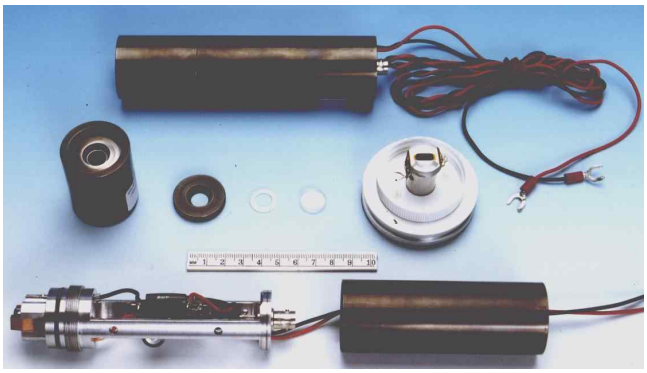

Figure 1. A reference bolometer and its components

METHODOLOGY

Four reference bolometers were compared with a Hamamatsu S1337-1010 silicon photodiode and a Hamamatsu G8370-10 InGaAs photodiode in the NMIA double monochromator incoherent spectral responsivity measurement system using radiant flux of approximately 10 μW.

For each of the photodetectors, approximately thirty spectral responsivity transfers were performed against each bolometer allowing the noise associated with a single transfer to be greatly reduced by averaging. The responsivity values obtained were based on the average of the response from all four bolometers and provided data over the wavelength range between 250 nm and 1700 nm at 5 nm intervals.

The silicon and InGaAs photodiodes were compared with the NMIA cryogenic radiometer at ten laser wavelengths between 476 nm and 1308 nm at radiant flux levels of approximately 200 μW.

RESULTS

Linear interpolation between the values obtained for the relative response of each of the photodetectors based on bolometer measurements was used to calculate values of relative response at each of the laser wavelengths used with the cryogenic radiometer. These values were then compared with the absolute response values obtained. The ratios of relative response values are presented in Table 1 and Table 2 and plotted in Figure 2.

Table 19. Ratio of silicon photodetector absolute responsivity values to relative responsivity values at selected laser wavelengths, normalised to the mean value of the ratio.

Wavelength (nm)	Responsivity Ratio	Uncertainty (±) (k=2)
476.49	0.9997	0.0013
487.99	1.0001	0.0020
496.51	0.9992	0.0016
514.53	0.9985	0.0013
632.82	1.0006	0.0014
656.19	1.0005	0.0015
807.65	1.0003	0.0025
912.45	1.0005	0.0014
975.42	0.9993	0.0017

Table 2. Ratio of InGaAs photodetector absolute responsivity values to relative responsivity values at selected laser wavelengths, normalised to the mean value of the ratio.

Wavelength (nm)	Responsivity Ratio	Uncertainty (±) (k=2)
912.45	1.0011	0.0013
975.42	0.9992	0.0015
1307.83	0.9997	0.0011

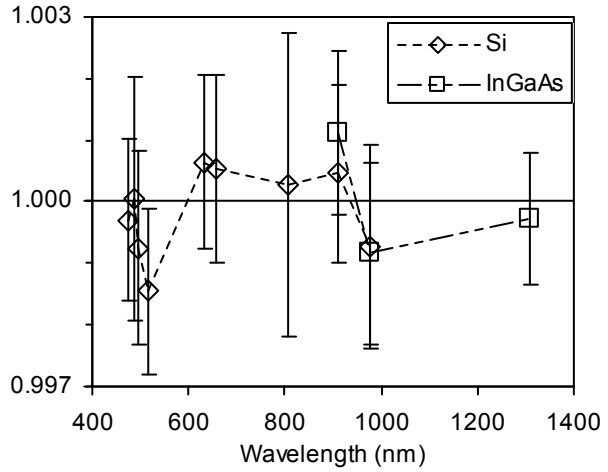

Figure 2. Variation of the relative spectral responsivity of the NMIA gold-black bolometer references with associated uncertainties. Dashed lines are provided as a guide to the eye.

CONCLUSION

The responsivities measured with the bolometers and those measured with the cryogenic radiometer show excellent agreement between the methods for both photodetectors. Based on these measurements the NMIA reference bolometers have maintained their spectrophotometric calibration within the claimed uncertainties for the wavelength range tested even after extended use over a period of fifteen years.

REFERENCES

1. W.R. Blevin and W.J. Brown, Large-area bolometers of evaporated gold, Journal of Scientific Instruments, 42, 19-23, 1965.

Characterization of Nonlinearity of a Thermal Detector by Attenuation Method for High Laser Power Calibration

Takayuki Numata, Minoru Tanabe, Kuniaki Amemiya, Daiji Fukuda, and Yoshiro Ichino

National Metrology Institute of Japan (NMIJ)
National Institute of Advanced Industrial Science and Technology, Tsukuba, Japan
Corresponding e-mail address: t.numata@aist.go.jp

Range of calibration service of laser power at NMIJ has been extended to 100 W at wavelengths of 1.1 μm and 10.6 μm. A water-cooled thermal detector has been newly employed as a reference standard detector for the high power-level calibration. The nonlinear behaviour of the detector depending on irradiation power was characterized by attenuation method using an optical chopper. Calibration uncertainty of user's detector is estimated approximately 1.9 % (*k*=2).

INTRODUCTION

We have developed laser power standard calorimeters which allow precise evaluation of absolute laser power[1][2]. Each of the calorimeters measures laser power by means of temperature-controlled electrical substitution method, where temperature of optical absorber is kept at a room temperature using thermo-electric coolers and an electric heater. This method is effective to reduce uncertainty factors originated from thermal issue in measurement. However, the maximum measurable range of laser power is limited to around 10 watts due to performance of the electric elements. Therefore, introduction of a reference standard detector to extend range of laser power measurement is required. In this presentation, we report on investigation of nonlinear behaviour of a water-cooled thermal detector which we employ as the reference standard (RS) detector for laser power calibration service up to 100 W at wavelengths of 1.1 μm and 10.6 μm.

PRINCIPLE

Since responsivity of thermal detectors shows non-linear behaviour according to irradiated laser power, characterization of the nonlinearity becomes essential for high laser power measurement. Thus, absolute laser power measured using the RS detector is formulated taking the nonlinearity into account as following equation,

$$P = \frac{V_{rs}}{R_{rso} \cdot C(V_{rs})} \tag{1}$$

where, P is the absolute laser power, R_{rso} is the responsivity of the RS at a basis power level (1 W) measured by primary standard calorimeter, V_{rs} is the output voltage, and $C(V_{rs})$ is the relative nonlinearity of the RS against the basis power level as a function of its output voltage.

Nonlinearity of the detector at a discrete power level is evaluated by comparing an optical attenuation applied to incident laser power with corresponding detector's output voltage, that is,

$$C(V_{rsi}) = \frac{\alpha}{A_i} = \frac{\alpha}{\left(\frac{V_{rsi-1}}{V_{rsi}}\right)} \tag{2}$$

where, α is attenuation factor, V_{rsi-1} and V_{rsi} represent output voltages for with and without attenuation, respectively. Then, the relative nonlinearity accumulated from the basis to n-th power level is derived by multiplication of the discrete nonlinearity as follows.

$$C(V_{rsn}) = \prod_{i=1}^{n} C(V_{rsi}) = \frac{\alpha}{(A_1)} \cdot \frac{\alpha}{(A_2)} \cdot \cdots \cdot \frac{\alpha}{(A_n)} = \frac{\alpha^n}{\prod_{i=1}^{n} A_i} \tag{3}$$

The nonlinearity of the RS was investigated throughout the objective power range changing incident laser power step by step. Then, a nonlinear character function, $C(V_{rs})$, is derived from the discrete experimental data set by means of least square sense fitting. This operation enables interpolation of nonlinearity character of the RS as a function of its output voltage, and thus, allows calibration service of laser power meters at arbitrary power.

EXPERIMENT

In this study, an optical chopper was employed for a laser power attenuator because of its wavelength independent attenuation factor and durability for high power laser irradiation. The chopper disc was cut out of a 5052 aluminium alloy plate by wire discharge machining and the surface was polished to give high reflectivity for infrared lasers. Two 90 degrees sectoral openings on periphery of the disc produce

transparent beam with rectangular on/off modulation with frequency twice of axis rotation. Attenuation factor of the optical chopper attenuator was measured at sub-watt level by another high-sensitive thermal detector, whose linear response was verified prior to the measurement of attenuation factor. Irradiation power for measurement was adjusted appropriately considering S/N and linearity of the detector, and thermally ineffective to chopper disc material. Then, we defined the attenuation factor as,

$$\alpha = \alpha_o \cdot \upsilon = \frac{V_l \cdot \upsilon}{V_h \cdot NL} \quad (4)$$

where, α_o is attenuation factor at measurement power level derived from of V_l , V_h, and NL, designating output voltages of the detector for with and without attenuator, and nonlinearity correction factor of the detector, respectively. Also, we have introduced correction factor for irradiation power dependence ν, which is examined by means of pump-probe method using two beams, i.e. one is high power-density beam for heating the chopper disc and the other is precisely power-stabilized small intensity beam for probing subtle change of the attenuation factor in dimension at the heating spot. These two beams were superposed and irradiated at a same spot on the rotating chopper disc. Since the probe beam showed no noticeable change for heating laser irradiation, the power dependence factor was evaluated to be small enough and negligible in this measurement. Attenuation factor α was measured to be 0.5000±0.0002 for 1.1 μm and 0.4997±0.0005 for 10.6 μm.

Linearity of the RS was investigated at power range between 1 W and 128 W. Measurement setup is depicted in Fig. 1. Size of measurement beams was adjusted to be 5 mm in diameter and the flow rate of cooling water for the RS was 2 L/min at a temperature of 22 °C.

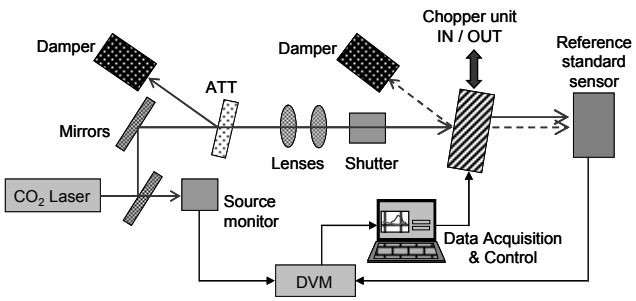

Figure 1 Schematic diagram of linearity investigation setup at 10.6 μm.

RESULTS

As shown in Fig.2, the RS exhibited a positive nonlinearity, i.e. responsivity of the RS gradually increases according to incident laser power. It reaches 2 % for incident power over 100 W. In addition, the nonlinear behaviour showed different for laser wavelength. Possible reasons of them are temperature-dependent character of thermopile and wavelength-dependence of optical absorber. The $C(V_{rs})$ is calculated from these experimental data considering uncertainty of each point and the relative nonlinearity to be unity at the basis level.

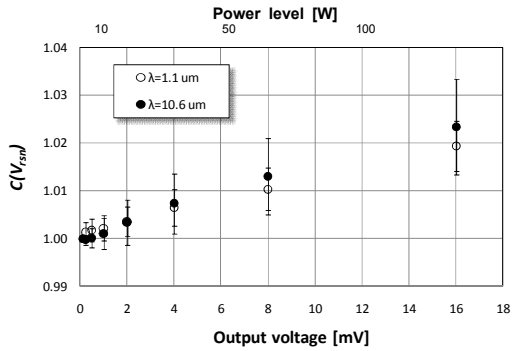

Figure 2 Nonlinearity characters of the RS.

SUMMARY

Attenuation method using an optical chopper was applied to linearity investigation of a water-cooled thermal detector, which we employed as the reference standard detector to extend power range of calibration service. The nonlinearity was characterized as a function of detector's output voltage and used to compensate itself. Based on this investigation, we have established laser power standard up to 100 W at wavelengths of 1.1 μm and 10.6 μm and opened calibration service for domestic users. Calibration uncertainty of user's detector is estimated approximately 1.9 % (k=2).

REFERENCES

1. T. Inoue, I. Yokoshima, and A. Hiraide, "Highly Sensitive Calorimeter for Microwatt-Level Laser Power Measurements", IEEE Trans. Instrum. Meas., 36, 623-626 (1987).
2. M. Endo, and T. Inoue, "A Double Calorimeter for 10-W Level Laser Power Measurements", IEEE Trans. Instrum. Meas., 688-691(2005).

Quantum efficiency characterization of silicon trap detectors

LIN Yandong, LÜ Liang
National Institute of Metrology(NIM), Beijing, China

linyd@nim.ac.cn

Abstract. To achieve spectral responsivity with high accuracy, silicon trap detectors are measured using a cryogenic radiometer at ten laser wavelengths. The uncertainty of the effective heating power measured by the cryogenic radiometer is experimentally determined by virtual optical heating method in a direct and accurate way. The spectral internal quantum efficiency is fitted with T. Gentile's model using the measured external quantum efficiency results at the laser wavelengths. The maximum deviation between the modeled and measured results is 1.5×10^{-4} from 488nm to 900nm.

INTRODUCTION

Photodetectors play an important role in photometry and radiometry. To achieve photodetector spectral responsivity with high accuracy, one way is to model the quantum efficiency from the discrete quantum efficiency measurement results obtained using a cryogenic radiometer at laser wavelengths and the detector surface reflectance. [1,2] This paper presents (1) the responsivity measurement results of silicon trap detectors at laser wavelengths from 476.5nm to 950nm and (2) the spectral quantum efficiency results fitted using the model introduced by T. Gentile[2].

RESPONSIVITY MEASUREMENT

The experiment setup for responsivity calibration of a photo detector based on cryogenic radiometer is illustrated in Figure 1. It is situated in an air conditioned clean room with ambient temperature at 23±0.5˚C. An oxford cryogenic radiometer (Radiox) is used as the primary standard. Three laser sources are implemented for the experiment: a He-Ne laser, an Ar/Kr mixed gas ion laser, and a Ti:Sapphire tunable laser. A laser power controller stabilizes the laser power to 3×10^{-5} for the gas lasers. A spatial filter is used to collimate the beam and minimize the scattered light. A prism beam splitter is used to distribute the laser power to the feedback detector and the monitor detector, respectively. The cryogenic radiometer and the trap detectors are mounted on an automated translation stage with high-precision positioning capability.

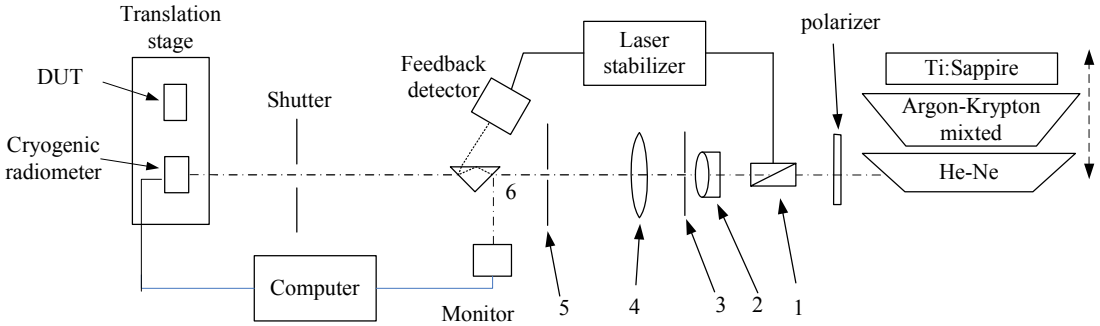

Figure 1. Schematic illustration of the responsivity calibration facility:
1- polarizer, 2- micro-objective lens, 3- pin hole, 4- collimation lens, 5- aperture.

The cryogenic radiometer is operated in the static mode and the optical heating power is a linear interpolation of the electrical power versus the temperature. To evaluate the uncertainty of the effective heating power measured by the cryogenic radiometer, a precisely measured dosage of electrical heating power is applied to the cavity by the electrical heater. Thus, the heating power measured by the cryogenic radiometer can be directly calibrated with the electrical power derived from the voltage across the heater and the current through it. Accuracy of the effective heating power measured by the cryogenic radiometer can be evaluated and the systematic bias can be determined by this method. The uncertainty of the effective heating power measurement of the cryogenic radiometer is within 3×10^{-5}.

The scattered light is characterized using a photodiode with a <6 mm size central hole. The

photodiode is placed at the same distance from the beam splitter as the cavity of the cryogenic radiometer. The scattered light power is measured while changing the diameter of the aperture in front of the detector. Typically, the effect from the scattered light is less than 0.003%.

Three methods have been applied to check the transmittance measurement of the Brewster window of the cryogenic radiometer. (1)The window is detached and mounted separately. (2) The window is attached to the cryogenic radiometer during the experiment. The trap detector for the transmittance measurement is placed at the cavity distance and at the position of the opening of a vacuum chamber between the window and the vacuum valve in the former case. The transmittance results of the 3 methods agreed within 2×10^{-5}. The transmittance is usually between 0.9997 and 0.9998 during the trap detector calibration.

The spatial non-uniformity of the responsivity of the cryogenic radiometer is characterized by horizontally scanning the cryogenic radiometer across the stabilized beam at 0.2mm interval in ±1.8mm range with the same detector calibrated at each position. The uniformity is within 4×10^{-5} in the measurement range. Taking the repeatability of cryogenic radiometer measurement and precision of reposition into account, the effect of spatial non-uniformity of the cryogenic radiometer is estimated to be 2×10^{-5}.

The responsivity of the trap detectors are measured at 10 laser wavelengths from 476.5nm to 950nm. The result is shown in Figure 2.

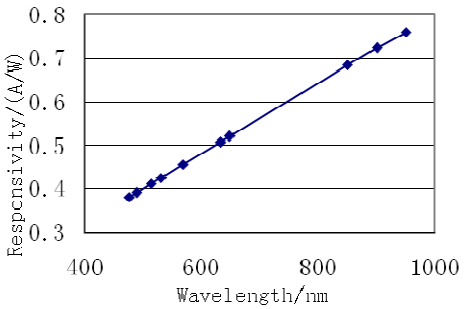

Figure 2. Responsivity measurement result (dots) and the linear fitting (line).

QUANTUM EFFICIENCY MODELLING

The dominant difference between the external quantum and the internal quantum efficiency is the surface reflectance. Reflectance at 488nm, 514nm, and 633nm are measured at an incident angle of less than 3 degree from normal incidence. The thickness of the thin silicon dioxide layer is calculated and spectral reflectance is modeled.

The internal quantum efficiency at each laser wavelength is derived from the external quantum efficiency measured by the cryogenic radiometer and the surface reflectance of the trap detector. The internal quantum efficiency model proposed by T. Gentile is applied to evaluate the internal quantum efficiency results. The fitting result in the wavelength range between 488nm and 900nm is illustrated in Figure 3. The maximum deviation of the model from the measurement result is 1.4×10^{-4}. However, the model significantly deviates from the measurement results at 476.5nm and 950nm. Measurements at more laser lines are needed to improve the accuracy.

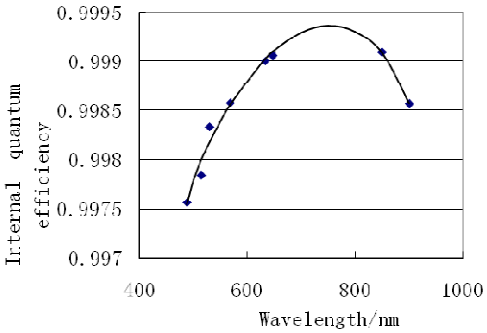

Figure 3. The internal quantum efficiency measurement (dots) and fitting (line) results.

SUMMARY

The spectral responsivity of trap detectors are calibrated using cryogenic radiometer. The uncertainty of the effective heating power measured by the cryogenic radiometer was experimentally determined using direct and accurate virtual optical heating method. The spectral quantum efficiency modeling result is derived and presented. The maximum deviation between the modeled and experimental results is 1.5×10^{-4} in the wavelength range between 488nm and 900nm.

REFERENCES

1. Gentile T. R., Houston J. M., Cromer C. L., Realization of a scale of absolute spectral response using the National Institute of Standards and Technology high-accuracy cryogenic radiometer, Applied Optics, 35, 4392-4403, 1996
2. L. Werner, J. Fischer, U. Johannsen et al, Accurate determination of the spectral responsivity of silicon trap detectors between 238 nm and 1015 nm using a laser-based cryogenic radiometer, Metrologia, 37, 279-284, 2000

Tristimulus head for measuring the long-term stability of the chromaticity of high-power LEDs

M. López, M. Lindemann, D. Linder, S. Winter and A. Sperling

Physikalisch-Technische Bundesanstalt, Braunschweig, Germany
Corresponding e-mail address: marco.lopez@ptb.de

A tristimulus head composed of four sensor heads to determine the long-term stability of the chromaticity of high-power LEDs is presented. The sensor heads are equipped with different filters which fit the colour-matching functions $\bar{x}(\lambda)$, $\bar{y}(\lambda)$ and $\bar{z}(\lambda)$. The stability of the tristimulus head observed over an operation time of 10 000 h is ≤ 0.3 % .

INTRODUCTION

High-power LEDs are today used in many lighting applications, e.g. automotive, building and road lighting, because of their high luminous flux, high efficiency, long lifetime, space savings, etc. It has been shown that the light emission of the LEDs depends not only on the temperature and forward electrical current but also on the packaging [1]. Because of the wide variety of different types and packaging of high-power LEDs commercially available, complex measurement systems are often required to evaluate their radiation emission accurately. Furthermore, high-power LED transfer standards are often requested by LED manufacturers and users to achieve traceable photometric and colorimetric measurements. Here, the long-term stability of their photometric and colorimetric quantities, e.g. the luminous intensity and the chromaticity, is required to reach reproducible reference values.

For that purpose, a high quality tristimulus head that achieves a high responsivity and a high long-term stability was developed by an industrial partner. This tristimulus head forms part of the LED-aging set-up developed in 2009 at PTB to investigate the long-term behaviour of the photometric and colorimetric quantities of several types of high-power LEDs [2]. In this paper we present the construction of the tristimulus head and the calibration results. Furthermore, as an example, the measurements of the chromaticity of a set of high-power LEDs carried out over 10 000 h is also shown.

TRISTIMULUS HEAD

The tristimulus head is built of four sensor heads like the one shown in Figure 1. The spectral responsivity of the sensor heads is corrected by glass filters to the CIE colour-matching functions $\bar{x}(\lambda)$, $\bar{y}(\lambda)$ and $\bar{z}(\lambda)$. In order to obtain a better signal ratio, $\bar{x}(\lambda)$ is achieved by means of two sensor heads, each one optimized for $\bar{x}_{\text{short}}(\lambda)$ and $\bar{x}_{\text{long}}(\lambda)$, respectively. The sensitive surfaces of the sensor heads are limited by precision apertures with an 8 mm diameter. In order to avoid any responsivity variation of the head due to changes of the environmental temperature, the photodiode and the filter are thermoelectrically stabilized, e.g. at 35 °C, by means of an aluminium thermal block placed just behind the photodiode. The temperature control is carried out by means of two heating transistors and a temperature sensor.

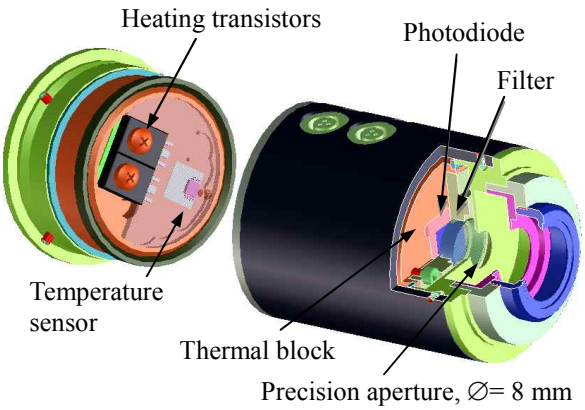

Figure 1. Right: Single sensor head of the tristimulus head. Left: Rear view of the thermal block.

The luminous responsivity s_v of the sensor heads was determined by calibrating the heads against an incandescent lamp at the CIE illuminant A (2856 K). For light sources with a spectral distribution different to the illuminant A, a spectral correction factor is required to correct the spectral mismatch of the sensor heads with respect to the CIE colour-matching functions. The spectral responsivity of the heads is shown in Figure 2. For incandescent lamps, a simple illuminance match index m can be found to account for the spectral deviation due to filament

temperatures different from 2856 K and other material characteristics. In this case the correction factor is finally given by the determined temperature ratios with the index m as an exponent. The values for s_v and the match index m obtained from the calibration of the heads are listed in Table 1. For non-Planckian sources a colour mismatch factor F_{cc}, taking into account the spectral mismatch of the spectral distributions of the source and the detectors with respect to illuminant A and $V(\lambda)$, respectively and expressed by the well-known fourfold integral equation [4], has to be determined. As an example, in Table 2 the mismatch correction factors calculated for three different coloured LEDs are shown. As expected, the mismatch correction factors for the channels depend strongly on the distribution of the LED spectrum and the spectral mismatch of the sensor head involved in the measurement.

Table 20. Luminous responsivity s_v and match index m of the head sensors for the CIE illuminant A. The index m is zero for a perfect spectral match of the head.

Channel	$s_v \times 10^{-9}$ A/lm	m
X_{short}	6.43812	0.1026
X_{long}	1.93734	0.0302
Y	3.87840	0.0145
Z	1.64483	0.1348

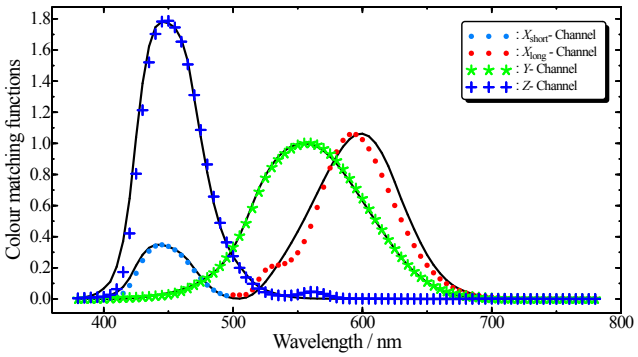

Figure 2. Relative spectral responsivity functions of the four used channels. Solid line: 2-deg Colour matching functions $\bar{x}(\lambda)$, $\bar{y}(\lambda)$ and $\bar{z}(\lambda)$ (CIE, 1931) [3].

Table 2. Mismatch correction factors F_{cc_i} of the sensor heads for three different spectrums generated with three colour LEDs.

	F_{cc_i}		
Channel	Blue	White	Red
X_{short}	0.97765	0.96919	1.00797
X_{long}	0.75415	0.99782	1.11366
Y	1.06650	1.00136	0.99493
Z	0.99485	0.98996	0.38406

LONG-TERM CHROMATICITY OF HIGH-POWER LEDs

As an example, in Figure 3 the chromaticity coordinates x and y of three different high-power cool-white LEDs measured by the different detector channels over 10 000 hours of operating time are shown. It has to be noted that for most of the LEDs investigated, after a certain stabilization phase, the variation of the chromaticity coordinates x and y with $\Delta x = 0.003$ and $\Delta y = 0.004$ is almost negligible. In general, the drift of the chromaticity coordinates of the LEDs appears to be in the range of $\leq 9 \cdot 10^{-7}$ / h.

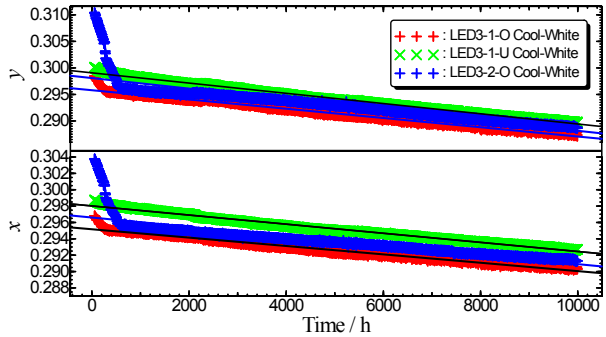

Figure 3. Chromaticity coordinates x and y of three different white high-power LEDs measured up to 10 000 h. Solid lines represent a linear fit.

The stability of the detector heads was checked periodically by means of calibrated incandescent lamps and high-power LEDs operated only once a day for a short period of time. The change in the responsivity of the heads appears to be lower than 0.3% over 10 000 h.

REFERENCES

1. Hsu, Y.C, et. al., Failure Mechanisms Associated with Lens Shape of High-Power LED Modules in Aging Test, Laser and Electro-Optics Society (LEOS) The 20th Annual Meeting, Lake Buena Vista, Florida, 2007.
2. M. López, M. Lindemann, N. Betzhold, M. Dämmig, A. Sperling: "Aging of photometric and colorimetric quantities of high-power light emitting diodes", Light and Lighting Conference with special emphasis on LEDs and solid state lighting, Budapest, May 2009.
3. Colorimetry, 3rd Edition, CIE 15:2004.
4. Georg Sauter, Tutorial: Determination of Measurement Uncertainties in Photometry; Annex A, CIE-M3, in Proceedings of the 2nd CIE Expert Symposium on Measurement Uncertainty. CIE x029:2006, page 51.

Laser Radiometry for High Power Lasers in the 1-µm Spectral Range

Friedhelm Brandt, Holger Lecher, Stefan Kück

Physikalisch-Technische Bundesanstalt (PTB), Bundesallee 100, 38116 Braunschweig, Germany
Corresponding e-mail address: stefan.kueck@ptb.de

High power lasers in the kW-power range are nowadays widely used in industrial applications like cutting, welding, melting and hardening. In this presentation we report on the measurements of laser diode power of fibre coupled diode laser radiation at 1065 nm in the multi-kW power range. The calibration setup, the standard detector, the uncertainty budget and first results will be presented and discussed. By using transfer detectors with spectral independent responsivity, traceability also for laser power measurements for other industry-relevant lasers in the 1-µm spectral range (Nd:YAG, Yb:YAG, Yb-fibre) is established.

INTRODUCTION

Lasers in the 1-µm spectral range with output powers in the kW-power range, e.g. Nd:YAG lasers, Yb:YAG lasers, Yb-fibre lasers and recently also diode lasers are nowadays widely and still increasingly used for industrial applications such as cutting, welding, melting and hardening, especially in machine building, automotive and related branches. Hence, caused by quality control and quality management purposes, there is an increasing interest and requirement from the industry, from operators as well as from detector manufacturers to establish a measurement and calibration service for laser power meters for purposes of production control, standardization and safety regulations during investigation, testing and production. Currently, such a calibration service is being established at the Physikalisch-Technische Bundesanstalt (PTB), the German national metrology institute. In this presentation, the setup used for the experiments and calibrations will be described in detail.

CALIBRATION CHAIN AND SETUP

The traceability chain for measurements in the 1-µm spectral range in the kW-power range is shown in Figure 1. As starting device, the cryogenic radiometer is listed, which operates at 633 nm (HeNe laser) at power levels around 1 mW. The scale of laser power is then transferred via a Silicon-based trap detector, the LM7 thermal cone detector and the HLR301 flat-absorber thermal detector, which is the standard detector for 1-µm laser radiation up to 120 W. It is cooled with water of 20 °C with a flow rate of approx. 3 l/min.

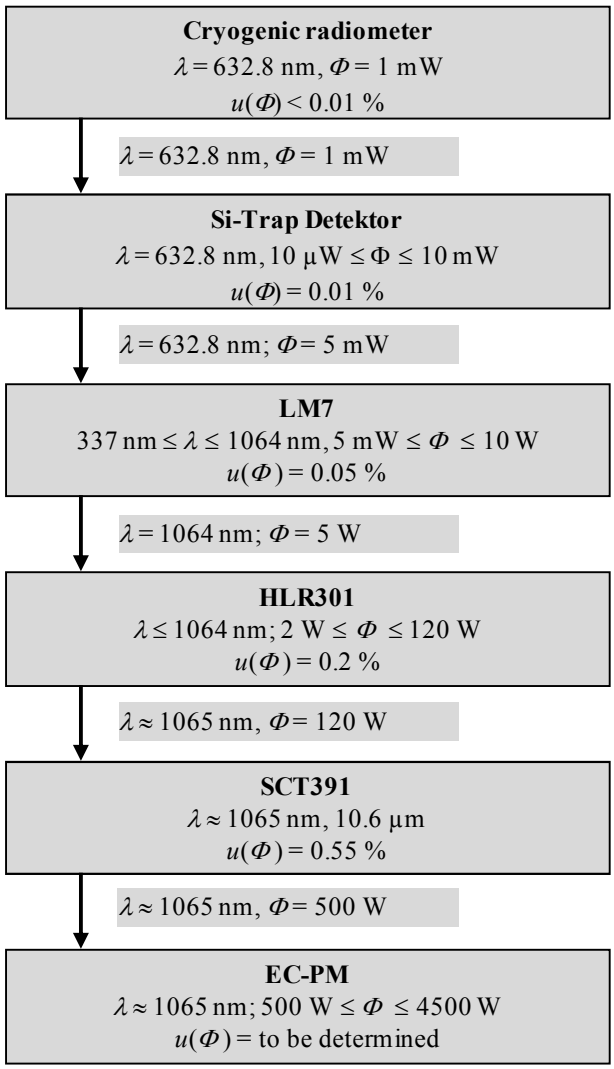

Figure 1. Calibration chain for laser radiometry.

The expansion in terms of power is performed via electrical nonlinearity measurements: the absorber of the detector is heated by electrical power via heating elements. The detector responsivity as a function of the applied electrical power is measured, from which the corresponding nonlinearity coefficient is determined. Thus for the HLR301 detector:

$$s_N = s_0(\lambda) \cdot (1 + \beta_\Phi \cdot V_N) \qquad (1)$$

with $s_0(\lambda)$: responsivity of HLR301 at $V_0 = 0$ mV, V_N: signal (thermoelectric voltage) of HLR301 (corrected for offset voltage, when detector is not illuminated), β_Φ: power coefficient.

In a further step, the scale of the laser power is transferred from the HLR301 to the SCT391 standard detector [1] by calibration at a wavelength of 1064 nm and a power level of approx. 120 W. The SCT391 consists of a cylindrical absorber tube, in which the incoming power is almost completely absorbed. The cooling water flows through a metal cooling coil, which is attached outside the absorber tube. The temperature difference ΔT of the cooling water at the exit and at the entrance of the coil is measured with a resistance thermometer (Pt100). Furthermore, an electrical heating coil is attached to the absorber tube in order to determine the electrical responsivity s_0 and nonlinearity coefficient β_S (for powers between 100 W and 1000 W) of the SCT391. It should be noted that the temperature increase is also dependent on the flow rate V_s of the cooling water, thus this flow needs to be measured and corrected to a reference flow rate V_{s0} of 1.5 l/min. Thus, the total responsivity s with respect to radiation is:

$$s = s_0 f_k \left(1 + \beta_s \cdot \Delta T\right)\left(V_{s0} / V_s\right), \qquad (2)$$

where f_K is a wavelength dependent correction factor determined from the calibration with the HLR301, that takes into account the absorbance of the absorber tube.

As standard for the measurements of laser power > 1000 W for wavelengths around 1 µm a commercial power meter is used, i.e. the EC-PM (Electronic Calibrated Power Monitor, PRIMES). As shown in Figure 1, this power meter is directly calibrated by the SCT391 in the power range between 500 W and 1000 W. The operation principle of this device is as follows: the incoming laser radiation is focused with a concentrating reflector through a small pinhole into a cavity absorber, where it is almost completely absorbed. Also here, the absorber is water cooled and the temperature rise ΔT and the absolute water mass flow V_m is measured. The displayed laser power value Φ is then calculated by:

$$\Phi = V_m c_m \Delta T\,, \qquad (3)$$

where c_m is the specific heat capacity of water. From this displayed value and the laser power determined by the SCT391, the correction factor for the EC-PM is calculated. Additionally, the EC-PM is calibrated electrically in the power range between 300 W and 4500 W, thus the nonlinearity coefficient can be determined and finally also responsivity up to 4500 W. First measurements revealed a negligible power coefficient.

The optical setup for the calibration of laser power meters in the > 1-kW-range in the wavelength region around 1 µm is setup as follows, see also Figure 2. The laser radiation of the diode laser operating at approx. 1065 nm is coupled into a fiber with a core diameter of 1000 µm, which transmits the radiation to a collimating optics. This optics contains a protective glass at its exit and a beam splitter in order to reflect a small part of the laser radiation to a monitor detector, which monitors the power stability of the laser radiation. After the collimation optics, the beam has a diameter of approx. 22 mm and is transmitted through an aperture of also approx. 22 mm. This aperture is finally imaged with a lens of approx. 500 mm focal length to the detector plane, where the standard detector (SCT391 or EC-PM) and the device under test (EC-PM or customer transfer detector) are alternately moved into the beam for its calibration.

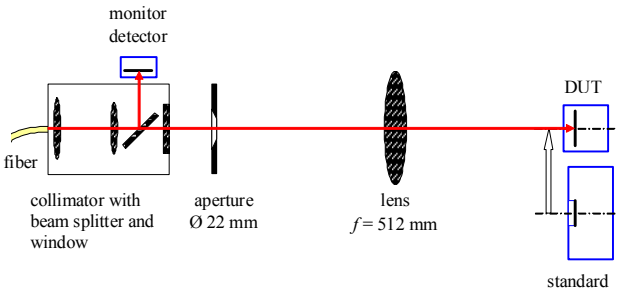

Figure 2. Scheme of the optical setup for the calibration of laser power meters in the > 1-kW-range ($\lambda \sim 1$ µm).

SUMMARY

We will present the new setup for the calibration of high power laser radiation in the 1-µm spectral range for laser power in the kW-range. The calibration chain and the measurement uncertainties at the different stages within the calibration chain will be discussed in detail. The standard detectors will be characterized, included nonlinearity measurements.

REFERENCES

1. F. Brandt, K. Möstl, Kalibrierung von Leistungsmeßgeräten für Hochleistungslaser, in Laser in Forschung und Technik, edited by W. Waidelich, 730-733, Springer-Verlag, Berlin, 1996.

Analysis and study of optolectronics characteristics of InP photodetectors.

Ana Luz Muñoz Zurita, Joaquin Campos Acosta,

J. Didier Marin Cardenas, Juan I. Larruquert.

[1]**Facultad de Ingeniería Mecánica y Eléctrica, U .Torreón**
Universidad Autónoma de Coahuila (México)
[2]**Instituto de Física Aplicada IFA-CSIC (España).**

The InP-photodiodes from different manufacturers have got rather low noise level, good response uniformity over the sensitive surface and a wide dynamic range. As in any photodiode, the spectral short-circuit responsivity is determined by the wavelength and the photodiode's reflectance and internal quantum efficiency. Then if these quantities were known, the photodiode's responsivity would be known without being compared to another standard radiometer; i. e. the photodiode would be an absolute radiometer for optical radiation measurements. This idea was firstly developed for silicon photodiodes in the eighties, once the technology was able to produce low defects photodiodes. Following this reference, the reflectance could be approached from a superimposed thin layers model. By knowing the thicknesses of the layers and the optical constants of the materials, it is possible to determine the device reflectance. However, this information is not completely available for InP photodiodes: the actual thickness of the layers is not known and optical constants of materials are only approximately known for bulk. Nevertheless it's possible to measure reflectance at some wavelengths and to fit the thicknesses of a layer model that would reproduce those experimental values. Therefore the attainable scope at present is just to obtain a model to be able to calculate spectral responsivity values at any wavelength. To get this, a model has been developed to calculate reflectance values from experimental ones at some wavelengths and another model has been developed to interpolate spectral internal quantum efficiency values from some values got from reflectance and responsivity measurements at some wavelengths. Both models will be presented in this communication.

FBG stabilised diode lasers for near infra-red cryogenic radiometry

Ian C.M. Littler
National Measurement Institute, Sydney, Australia

Corresponding e-mail address: ian.littler@measurement.gov.au

Cryogenic radiometers are used as primary standards for calibration of photo-electric detectors. The calibration process requires power-stable, spectrally pure, spatially confined radiation at a number of wavelengths across the detector range in order to provide absolute anchors for the wavelength responsivity. We show that inexpensive FBG stabilised diode lasers, available from 650 nm to 1000 nm, are suitable sources.

INTRODUCTION

Photo-detectors are calibrated by comparison of their responsivity to that of a liquid Helium (LHe) cooled electrical-substitution Radiometer. The accuracy of this measurement is typically a few parts in 10^4, which places high stability requirements on the power of the source during the responsivity transfer. In addition, since the photo-diode response is wavelength dependent, the source should be spectrally pure. The source also needs to be collimated and confined such that the light can reach inside the LHe shielding and so that the amount of light falling on the photo-diode is the same as absorbed by the radiometer.

Traditionally, ion lasers have provided a number of fixed wavelength lines throughout the visible region on which the detectors have been calibrated. Noise-eaters reduce the power fluctuations from a few percent to parts in 10^5. Other approaches use optical parametric oscillators and tuneable Ti:Saph lasers to generate a narrow band coherent source through the visible and near infra-red [1].

Since the powers required for a calibration are generally small (few 100 μW), diode lasers are an attractive alternative, providing an inexpensive and reliable way of generating a range of fixed wavelength points. Simple Fabry-Perot (FP) type lasers have unpredictable spectra which would have to be measured precisely for each calibration. On the other hand, DFB type diode lasers provide spectrally pure, monochromatic radiation with acceptable intrinsic power stability. Unfortunately, they are only available cheaply (~$300) in the telecommunications bands. Custom DFB diode lasers at other wavelengths cost around $10,000 per device which can be prohibitive in volume.

Fiber Bragg grating (FBG) wavelength stabilised diode lasers promise to have similar properties to the DFB lasers and with a price-tag ($1000) closer to a simple FP type laser. In this paper it is shown that their intrinsic performance is not as good as first thought but they can be used successfully for calibration purposes with a little intervention.

METHODOLOGY

FBG wavelength stabilised lasers are extended cavity FP lasers where a fiber coupled Bragg grating forms a wavelength selective end mirror to the laser device. This forces oscillation in a narrow range and provides side-lobe suppression but leads to peculiar behaviour.

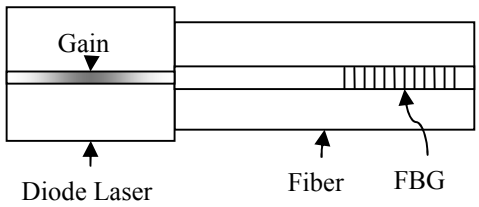

Figure 65. Schematic of an FBG stabilised diode laser

RESULTS

Key parameters important for laboratory use were measured as follows.

Tuning Characteristics

Figs 2 and 3 show the tuning characteristics of the laser. In Fig. 1, as expected the power increases with current. However, at ~75 mA there is a kink in the slope which coincides with a mode-hop, seen as a jump in wavelength. From the figure, the current tuning coefficient is ~1.6 pm. mA^{-1}.

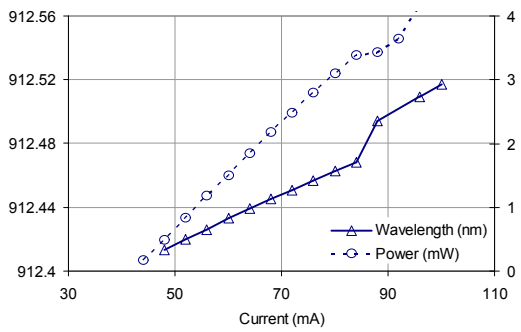

Figure 2. Current tuning and output power

As the temperature is tuned the laser also tunes, but exhibits a wavelength flip-flopping mode-hopping behaviour. The tuning rate is ~20 pm.K^{-1} between mode hops and ~10 pm.K^{-1} overall. Note that the power reaches a maximum between mode-hops where the wavelength dependent loss curve is lowest. At the mode-hop position, the laser exhibits multi-longitudinal mode operation.

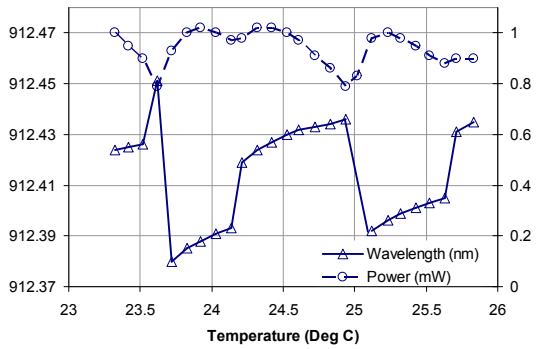

Figure 3. Temperature tuning and output power

For practical operation, the current is first set for the desired output power and then the temperature adjusted to a stable region by maximising the power.

Laser Spectrum

The laser spectrum is shown in Fig. 4, with the spectrum of a DFB laser for comparison. From the figure, the side-lobe suppression of the FBG stabilised laser is 30 dB. The DFB laser is much better with suppression of 50 dB. However, the side-lobe suppression is sufficient for cryo-radiometry.

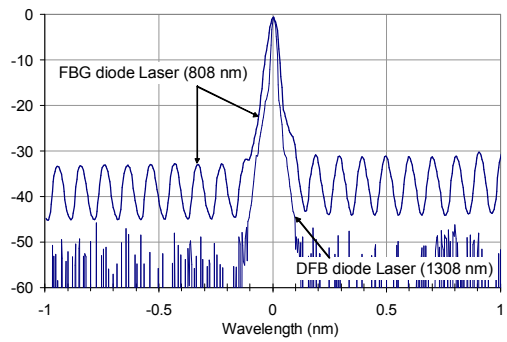

Figure 4. FBG laser vs DFB laser spectrum

Polarisation Instability

An unexpected feature of the FBG stabilised laser is significant wobble in the output polarisation. To examine the temporal behaviour, the orthogonal linear polarisation components were independently recorded over time. The result is shown in Fig. 5. This polarisation wobble creates significant power instability when the beam interacts with polarisation components.

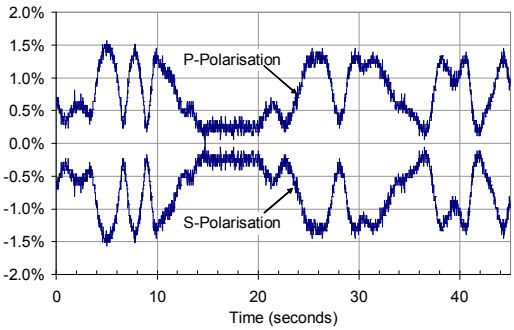

Figure 5. Polarisation wobble with time

By tuning the temperature of the laser, the polarisation was found to cover twelve oscillations per 100 mK. Thus, temperature stability of much better than 10 mK would be required for stable operation of the laser. The polarisation effect is most likely tied to birefringence in the fiber and/or FBG.

Power Stability: Effect of Noise-eater

In Fig. 6, the free running laser is seen to fluctuate in power by ±0.5% due to the polarisation instability. However, with the use of a polarisation rotating noise-eater (Brockton LPC), which can be used with many such lasers, the drift is 0.02% over 15 minutes and much better over a single radiometer measurement which takes around 2 to 4 minutes.

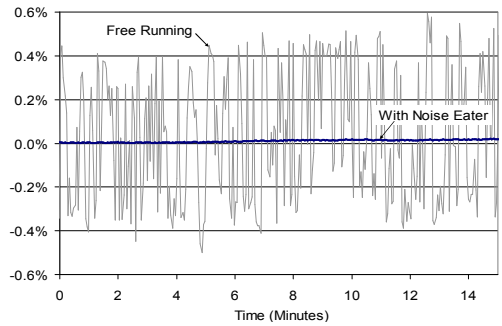

Figure 6. Output power fluctuations: noise-eater effect

CONCLUSION

FBG stabilised diode lasers display unfavourable polarisation instability which feeds into significant power fluctuations. However, coupled with a noise-eater, the characteristics are suitable for high accuracy cryogenic radiometry.

REFERENCES

1.T.R. Gentile, J.M. Houston and C.L. Cromer, Realization of a scale of absolute spectral response using the National Institute of Standards and Technology high-accuracy cryogenic radiometer, Appl. Opt. 35, 4392-4403, 1996.

Study of the spectral responsivity of a silicon photodiode.

Ana Luz Muñoz Zurita[1], Joaquin Campos Acosta[2],

Noel I. Toto Arellano[3], Alicia Pons Aglio[2].

[1]Facultad de Ingeniería Mecánica y Eléctrica, U .Torreón
Universidad Autónoma de Coahuila (México)
[2]Instituto de Física Aplicada IFA-CSIC (España)
[3]Centro de Investigaciones Opticas CIO (Mexico)

Silicon photodiodes are more sensitive and quicker than thermal detectors. For these reasons silicon photodiodes are used to maintain scales of spectral responsivity in the spectral range (300 nm – 1000 nm) in many international Laboratories. The spectral responsivity of a photodiode depends on the reflectance and the internal quantum efficiency, so a good approach to determine responsivity is to know both reflectance and internal quantum efficiency. Because of that, in this work we present a study about the reflectance of silicon photodiodes, with two goals: To study the variability of reflectance among photodiodes from a single batch, and to study the reflectance ageing of some silicon photodiodes used as standards during six years. In some radiometric applications, the reflectance of individual photodiodes plays an important role because they have to match to a pair or minimized or maximized, as it is the case for silicon trap radiometers. The ageing of silicon photodiodes has been studied for several authors and all them looked at the stability of the internal quantum efficiency rather than to the reflectance.

To approach the first objective, we restricted the study to a single manufacturer, because the reflectance is linked to the structure and thickness of the passivation layer. We chose photodiodes from Hamamatsu, because they are the most stable and used in many National Laboratories. Furthermore we have used photodiodes from just one batch to avoid as much as possible changes in the oxide thickness which in turn produces different reflectance values.

To achieve the second goal, the ageing of photodiodes, we have measured the reflectance of three silicon photodiodes, from the same manufacturer, that are used to maintain the scale of spectral responsivity of Institute for Applied Physics (CSIC).

The results obtained show that we have an outstanding change between the reflectance of the photodiodes of the same batch, which indicates that it is necessary to measure the reflectance of every individual photodiode if accurate reflectance knowledge is needed.

Validation of two absolute integrating sphere methods for luminous flux scale by comparison with the gonio-photometer method in KRISS

Yong-Wan Kim[1,2], Seongchong Park[1], Seung-Nam Park[1], Dong-Hoon Lee[1], and Min Yong Jeon[2]

[1]*Division of Physical Metrology, Korea Research Institute of Standards and Science (KRISS), Daejeon, Rep. Korea*
[2]*Department of Physics, Chungnam National University, Daejeon, Rep. Korea*
Corresponding e-mail address: dh.lee@kriss.re.kr

We report the experimental validation of two absolute integrating sphere (IS) methods realized in KRISS for luminous flux measurement: one method at a large IS photometer with a diameter of 2 m for conventional lamps, the other at a smaller IS photometer with a diameter of 30 cm for LEDs. The results of the absolute integrating sphere methods are compared with those of the gonio-photometer method via two groups of tungsten lamps. As all three methods are traceable to the same detector-based scale of KRISS, any disagreement in this comparison indicates a systematic error. Agreement within the claimed uncertainties is verified, and the origins of the differences are discussed.

LUMINOUS FLUX SCALE OF KRISS

The luminous flux scale of KRISS is realized based on three different methods. The first "classical" one is the gonio-photometer method, which measures the angular distribution of luminous intensity by spatially scanning a calibrated illuminance meter over the 4π-solid angle at a constant distance. This is currently declared as the primary method for the KRISS luminous flux scale [1]. In practice, the gonio-photometer calibrates only the transfer standard lamps of 100 W tungsten type, and the test lamps are calibrated in an IS photometer with a diameter of 2 m by direct substitution with a standard lamp.

The other two methods are the absolute IS method in which the flux responsivity of an IS photometer is absolutely calibrated in the unit of reading/lm based on the external reference flux [2-4]. The main challenge of the absolute IS method is the accurate measurement of spatial response distribution function (SRDF) of the IS photometer to correct the spatial mismatch between the external reference flux and the internal flux of the test lamp.

We realized the two absolute IS methods with the same traceability as the gonio-photometer method by using photometric detectors calibrated against the spectral responsivity scale of KRISS. Therefore, we could validate the accuracy of the absolute IS method by comparing the result with that of the gonio-photometer method.

ABSOLUTE INTEGRATING SPHERE METHODS

The first absolute IS method is realized at a large IS photometer with a diameter of 2 m. Figure 1 schematically shows the experimental setup of the large absolute IS method.

A 1000 W FEL-type tungsten lamp provides the reference flux into the IS through a precision aperture.

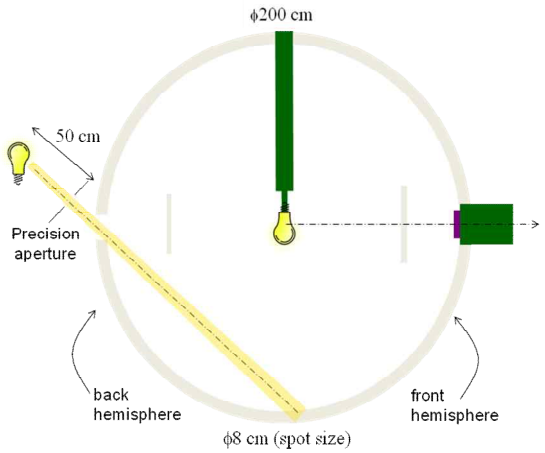

Figure 66. Schematic setup of the absolute IS method with a large IS photometer and an overfilled measurement of the reference flux.

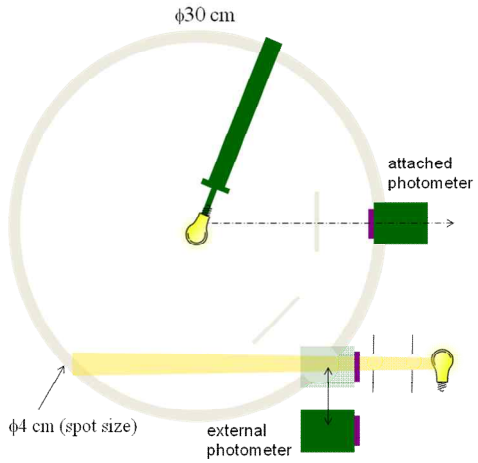

Figure 67. Schematic setup of the absolute IS method with a small IS photometer and an underfilled measurement of the reference flux.

The reference flux is determined by multiplying the illuminance at the aperture position with the area of the aperture. The illuminance is measured either by using a calibrated illuminance meter in an overfilled condition or from the calibrated spectral irradiance data of the FEL lamp. The results of both the detector-based and source-based measurements showed an agreement within 0.2 %. In the validation experiment, however, we use the result based on the illuminance meter to keep the traceability as same as that of the gonio-photometer method.

Figure 2 shows the experimental setup of the other absolute IS method at a small IS photometer with a diameter of 30 cm. This method is applied to the small-sized sources such as LED lamps [4]. The difference to Fig. 1 is that a collimated beam from a tungsten lamp is used as the external reference flux, which is measured by a photometer in an underfilled condition based on its calibrated spectral responsivity.

The SRDF of each IS photometer is measured by using an angular scanning collimated lamp mounted at the position of the test lamp.

COMPARISON OF THE METHODS

Each of the absolute IS method is compared to the gonio-photometer method by using two groups of test lamp. The first group, two 100 W tungsten lamps with a nominal value of 1100 lm, is measured by the gonio-photometer and by the large absolute IS setup of Fig. 1. The measurement uncertainty is evaluated to be 1.2 % and 2.4 % for each method, respectively ($k = 2$).

The second group, two 2 W tungsten halogen lamps with a nominal value of 40 lm, is measured by the relative method in the 2-m IS photometer against the 100 W lamp from the gonio-photometer and by the small absolute IS setup of Fig. 2. Note that the 2 W lamps could not be measured directly by the gonio-photometer due to its small flux level. The measurement uncertainty is evaluated to be 1.8 % and 2.4 %, respectively ($k = 2$). The uncertainty of the gonio-photometer method is increased due to the additional step of the relative measurement in the IS photometer.

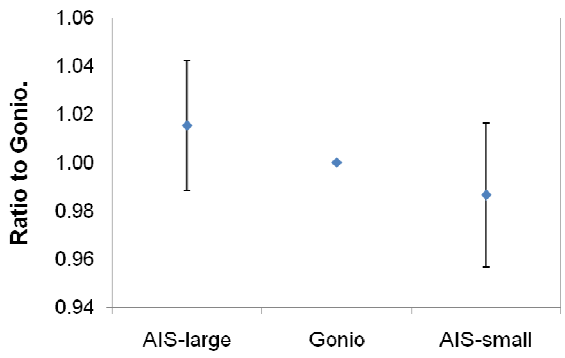

Figure 68. Result of comparison as the ratio of the two absolute IS methods with respect to the gonio-photometer method. The error bars indicate the uncertainty values of the ratios ($k = 2$) which contain also the uncertainty of the gonio-photometer method.

Figure 3 shows the result of the comparison as the ratio of luminous flux values measured by each absolute IS method with respect to the gonio-photometer method. The large IS method measures 1.5 % higher than the gonio-photometer method, while the small IS method 1.3 % lower than the gonio-photometer method. These differences are smaller than the uncertainty of the ratios indicated by the error bars in Fig. 3.

DISCUSSION

Three methods for the luminous flux realization are compared by using two groups of tungsten lamps. By taking the gonio-photometer method as the primary standard, the two absolute IS methods showed a disagreement of up to 1.5 %, which is smaller than the measurement uncertainty of 2.4 % for the absolute IS methods. However, as all three methods are traceable to the same detector-based scale of KRISS, any disagreement in this comparison can indicate a systematic error of each implementation.

The dominant uncertainty components of the absolute IS methods are the spatial mismatch correction (0.7 % ~ 0.9 %), near field absorption (0.5 %) and the photometer responsivity (0.5 %). The spatial mismatch correction is currently limited by the accuracy of the SRDF measurement of each IS, which can be improved either by increasing the resolution or by increasing the spot size of the reference flux beam.

REFERENCES

1. Final report of APMP.PR-K4, to be published in KCDB (draft B in review).
2. Y. Ohno, Detector-based luminous-flux calibration using the absolute integrating-sphere method, Metrologia, 35, 473–478, 1998.
3. J. Hovila, P. Toivanen, and E. Ikonen, Realization of the unit of luminous flux at the HUT using the absolute integrating sphere method, Metrologia, 41, 407–413 2004.
4. S. Park, D.-H. Lee, Y.-W. Kim, and S.-N. Park, Absolute integrating sphere method for total luminous flux of LEDs, in Proceedings of the 10th NEWRAD, 215-216, KRISS, 2008.

Physics of self-induced photodiodes

Stian Samset Hoem[1], Jarle Gran[1], Meelis Sildoja[2], Farshid Manoocheri[2], Erkki Ikonen[2] and Ingmar Müller[3]
[1]*Justervesenet, Kjeller, Norway,* [2]*Aalto University and Centre for Metrology and Accreditation, Espoo, Finland,*
[3]*Physikalisch-Technische Bundesanstalt (PTB), Berlin, Germany*
Corresponding e-mail address: ssh@justervesenet.no

Presented here is a simple one-dimensional model for describing the behaviour of self-induced photodiodes, used as detectors in the PQED (Predictable Quantum Efficient Detector). Calculations based on this model are compared with results of PC1D simulation software, and used to explain actual measured data on the photodiodes' behaviour.*

INTRODUCTION

The self-induced photodiode consists of a p-type substrate of low impurity concentration, and a grown oxide layer with fixed positive charges, Q_{ss}. These surface charges are located within d=20 nm of the interface [1], and will induce negative depletion charge Q_B and inversion layer Q_n in the silicon, thus creating a structure similar to an n-p-junction. Since the surface charge region d and the oxide thickness x_0 are both finite, a mirror charge Q_G is also induced on the outside of the oxide [2], see Figure 1.

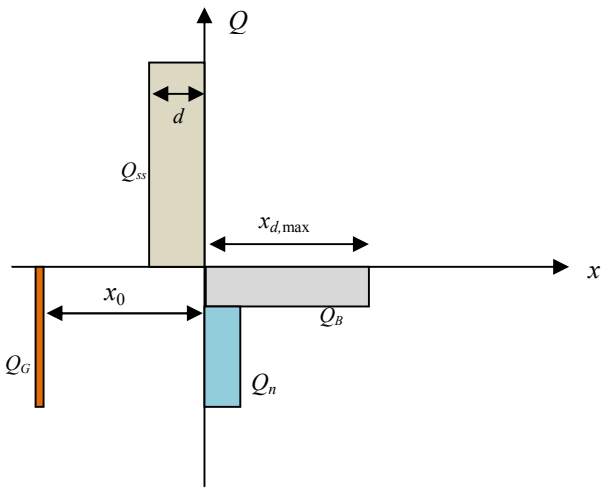

Figure 1. An illustration of the charge distribution in an induced junction photodiode. The y-axis marks the interface between the oxide and the semiconductor.

The induced inversion layer Q_n, described by Hansen with the following equation in [2], must be negative to allow the device to operate as a diode:

$$Q_n = -Q_{SS}\left(1-\frac{d}{2x_0}\right)-Q_B\left(1+\frac{\varepsilon_{ox}x_{d,\max}}{2\varepsilon_S x_0}\right). \quad (1)$$

Here $x_{d,\max}$ is the width of the depletion layer, which for a given bias voltage has a finite maximum extension. Parameters ε_{ox} and ε_S are the permittivity for the oxide and the silicon, respectively.

MODELLING THE SELF-INDUCED DIODE

Equation (1) tells us that thinner oxides will lower the electron concentration in the inversion layer, and that this concentration is also strongly dependent on the surface charge Q_{ss}. By using this model with semiconductor theory one can numerically calculate the electrostatic potential and electric field across the diode. Figure 2 shows a plot of the electric field calculated by this model, and also the field given by PC1D simulation software [3], with the same physical parameters. The qualitative agreement between the two simulations indicates that PC1D can be used to easily extract numerical values for further calculations [4].

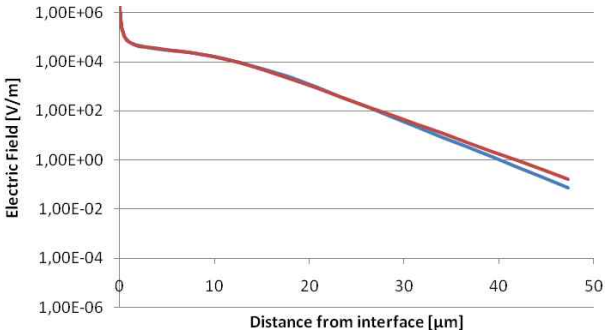

Figure 2. The electric field in silicon, plotted logarithmically as a function of distance from the interface. The plotted values come from PC1D calculations (blue line) and numerical calculations based on Hansen's model (red). Differences between the curves can only be seen deep in the bulk. This plot is for V_{bias}=0 V, bulk doping density N_A=2·10^{12} cm^{-3} and temperature T=300 K.

COMPARISON WITH MEASUREMENTS

In the first PQED production batch [5], the photodiodes were grown with two different oxide layers: one 'thin' layer (100 nm oxide) and one 'thick' (310 nm oxide). The responsivity of these test detectors was measured by uniformity scans with

monochromatic light at λ=760 nm, spot diameter ≈0.5 mm and step size 1 mm [6], see Figure 3. The results indicate a much lower response for the 'thin' diode, less than half of the 'thick' diodes response at 300 K. This large difference in responsivity can be explained by the one-dimensional model of Figure 1. A thinner oxide will give less induced inversion charge, and by that give less charge separation force in the p-n-junction and a lower responsivity.

According to the model, lower temperatures will reduce the diode properties of the device. Figure 4 shows a plot of Q_n as a function of Q_{ss} for different oxide thicknesses at 78 K. To have a working diode according to Equation (1), Q_n must be negative. The manufacturer specifies that the test diodes have oxide surface charges between $2{\cdot}10^{11}$ - $4{\cdot}10^{11}$ e/cm^2. For this interval Figure 4 indicates weak and strong diode structures for the 100 and 310 nm oxides, respectively. When measuring the 'thin' diode in Figure 3a at 78 K, it appeared to be fully switched off in the central area, which can be interpreted as the loss of the diode structure according to Figure 4.

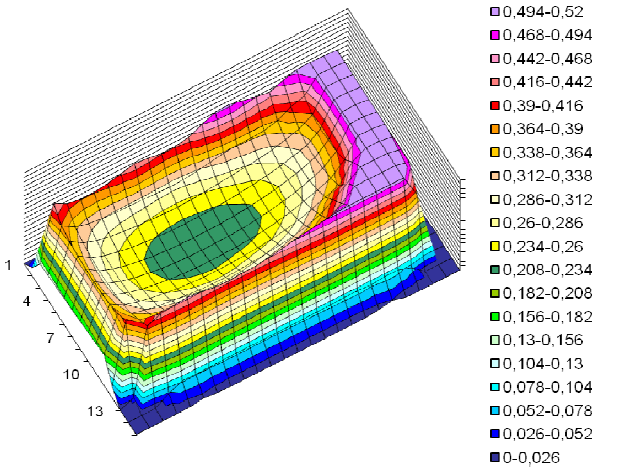

a) 'Thin' diode, response measured at 300 K with V_{bias} = 0 V

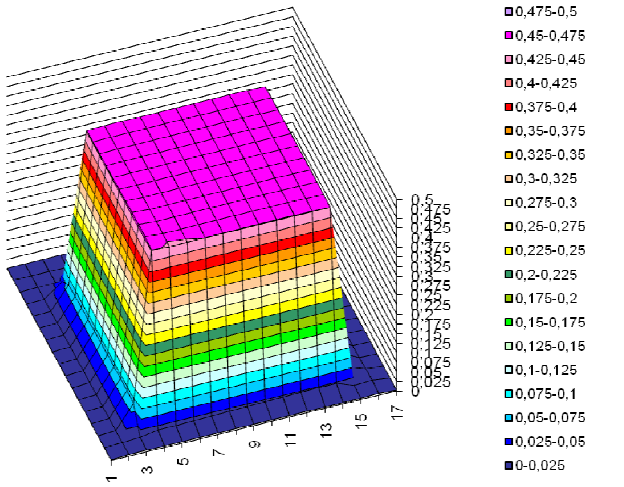

b) 'Thick' diode, response measured at 78 K with V_{bias} = 0 V

Figure 3. Response uniformity results from measurements on test diodes.

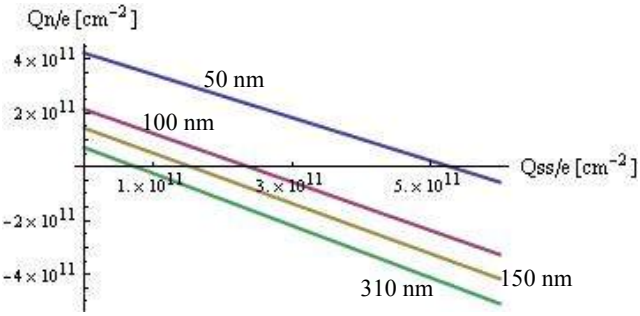

Figure 4. Induced charge as a function of surface charge for different oxide thicknesses. Applied voltage V_{bias} = 0 V, doping density N_A=2·10^{12} cm^{-3} and temperature T=78 K.

SUMMARY

A one-dimensional model of the self-induced diode gives a good understanding of the basic physical principles that lie behind the design and operation of the photodiodes used in the PQED. This relatively simple model has been compared with actual measured data and can give a qualitative explanation of the photodiodes' behaviour with different oxide thicknesses, surface charges, temperatures and bias voltages. Calculated values are in good agreement with values from the more comprehensive PC1D software, and this program should be able to give sufficiently accurate values for calculations on self-induced photodiodes.

*The research leading to these results has received funding from the European Community's Seventh Framework Programme, ERA-NET Plus, under Grant Agreement No. 217257.

REFERENCES

1. B.E. Deal et al, Characteristics of the Surface-State Charge of Thermally Oxidized Silicon", J. Electrochem. Soc., Vol. 114, 266, 1967.
2. T.E. Hansen, Silicon UV-Photodiodes Using Natural Inversion Layers, Physica Scripta, Vol. 18, 471–475, 1978.
3. PC1D Version 5: 32-bit Solar Cell Modelling on Personal Computers, 26th IEEE Photovoltaic Specialists Conference, Anaheim, Sep-Oct 1997, pp.207- 210.
4. J. Gran et al, Simulations of Predictable Quantum Efficient Detectors with PC1D, these proceedings
5. M. Sildoja et al, PQED I, these proceedings
6. I. Müller et al, PQED II, these proceedings

Measurement of Thermodynamic Temperature of High-Temperature Blackbody

B.B. Khlevnoy, V.R. Gavrilov, M.L. Samoylov, D.A. Otryaskin
All-Russian Research Institute for Optical and Physical Measurements (VNIIOFI), Moscow, Russia

Corresponding e-mail address: khlevnoy-m4r@vniiofi.ru

We describe a radiometric method for a high temperature black body temperature measurement through the use of a filter radiometer calibrated in terms of spectral irradiance responsivity against a trap detector, which directly linked to a cryogenic radiometer. The accuracy of the temperature measurement is estimated by the Monte Carlo method.

INTORODUCTION

VNIIOFI's spectral radiance, spectral irradiance and spectral radiant intensity primary measurement standard is based on a high temperature black body (HTTB) [1] as a primary standard source whose spectral radiance can be determined by the Planck law:

$$L_{BB}(\lambda,T)=\frac{\varepsilon_{eff}\cdot c_1}{\pi\cdot\lambda^5\cdot n^2}\cdot\left[\exp\left(\frac{c_2}{\lambda\cdot T\cdot n}\right)-1\right]^{-1} \quad (1)$$

Here λ is the wavelength in vacuum, T is the thermodynamic temperature of the HTTP, ε_{eff} is the effective emissivity of the HTTB, n is the air refractive index, c_1=3.74177·10^{-16} W·m^2, c_2=1.4388·10^{-2} K·m.

Here we describe a radiometric method for the HTTB temperature measurement through the use of a filter radiometer (FR) calibrated in terms of spectral irradiance responsivity against a trap detector (TD), which directly linked to a cryogenic radiometer. Moreover, we evaluate the accuracy of the temperature measurement using the Monte Carlo method.

MEASURING PRINCIPLE

The FR is a silicon photodiode of S1227 type with a broadband glass filter and a 5 mm aperture. The range Λ of spectral responsivity is about from 400 nm to 600 nm with a maximum at 510 nm. The temperature of the filter radiometer is stabilized be means of a liquid thermostat during the HTTB radiation measuring. If the FR is installed against the HTTB with aperture of diameter D at a distance l, the FR signal i_{FR} may be calculated by the formula:

$$i_{FR}=\frac{D^2}{l^2}\cdot\int_{\Lambda}L_{BB}(\lambda,T)\cdot S_{FR}(\lambda)\cdot d\lambda \quad (2)$$

Here $S_{FR}(\lambda)$ is the FR irradiance spectral responsivity, which typically represents the curve shown in Figure 1.

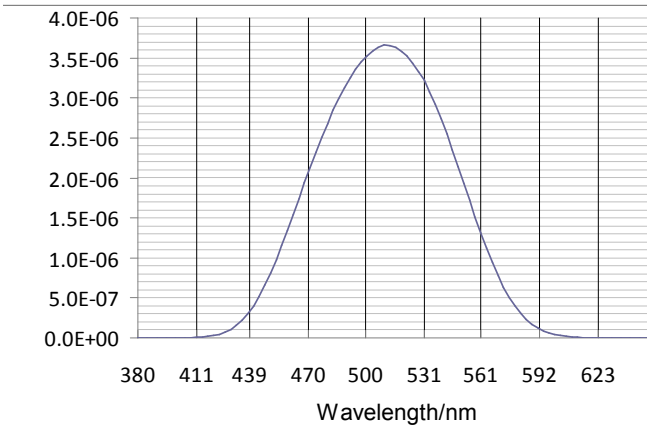

Figure 21. FR's irradiance spectral responsivity.

The FR is calibrated in terms of irradiance spectral responsivity against the TD, which is directly linked to a cryogenic radiometer and consists of 3 silicon photodiode of S1337 type. The FR-TD comparison facility is based on a precise 1 m double diffraction monochromator with the scattered light level of order 10^{-14}.

EVALUATION OF TEMPERATURE UNCERTAINTY

The temperature T we need to find is a result of numerical solving the equation (1) containing the following input quantities: the measured values i_{FR}, D, l, ε_{eff} and the function $S_{FR}(\lambda)$, specified by measured values at a set of points of the spectral interval Λ. Note that the usual procedure of uncertainty estimation described in [2] implies a given explicit functional relationship between an output quantity and input quantities, so it is not applicable here. In our case we apply the Monte Carlo (MC) method [3] to evaluate the temperature uncertainty. An implementation of the MC method implies a random draw for each input quantity and the subsequent numerical calculation of the temperature T by the equation 1. This uses the measured values for the

input quantities and their uncertainties. Many MC trials are performed, i.e. the process is repeated many times N, to obtain values $T_1,\ldots,T_N$. After that the values $T_1,\ldots,T_N$ are used to obtain the estimate of the temperature T, the combined standard uncertainty $u_c(T)$ and the expanded uncertainty $U(T)$.

Finally, we present the uncertainty budget of the temperature measurement in Table 1.

Table 22. Uncertainty budget of the thermodynamic temperature measurement.

Input quantity	Type of uncertainty	Component, K
i_{FR} – FR' signal	A и B	0.25
ε_{eff} – effective emissivity of HTTB	B	0.05
D – diameter of HTTB aperture	B	0.03
l – distance between FR and HTTB apertures	B	0.02
$S_{FR}(\lambda)$ – FR's irradiance spectral responcivity	B	0.5
Standard uncertainty (k=1) $u_c(T)$		0.56

REFERENCES

1. Sapritsky V.I., Khlevnoy B.B., Khromchenko V.B., Lisiansky B.E., Mekhontsev S.N., Melenevsky U.A., Morozova S.P., Prokhorov A.V., Samoilov M.L., Shapoval V.I., Sudarev K.A., Zelener M.F. Precision blackbody sources for radiometric standards // Applied Optics. 1997. V. 36. № 19. P. 1-6.
2. BIPM, IEC, IFCC, ISO, IUPAC, IUPAP and OIML 1995 Guide to the Expression of Uncertainty in Measurement (Geneva, Switzerland: International Organisation for Standardisation) ISBN 92-67-10188-9.
3. BIPM, IEC, IFCC, ILAC, ISO, IUPAC, IUPAP, OIML. Evaluation of measurement data Supplement 1 to the "Guide to the expression of uncertainty in measurement" Propagation of distributions using a Monte Carlo method. JCGM 101:2008.1.

Simulations of Predictable Quantum Efficient Detector with PC1D

Jarle Gran[1], Toomas Kübarsepp[2], Meelis Sildoja[3], Farshid Manoocheri[3], Erkki Ikonen[3], Ingmar Müller[4]

[1]*Justervesenet (JV), Kjeller, Norway,* [2]*Metrosert,* [3]*Aalto University,* [4]*Physikalisch-Technische Bundesanstalt, Berlin*

Corresponding e-mail address: jag@justervesenet.no

The spectral responsivity of Predictable Quantum Efficient Detector (PQED) is calculated based on the responsivity of an ideal quantum detector and taking into account reflection losses from the surface of the photodiode and internal charge carrier losses inside the diode. The internal quantum deficiency (IQD) is obtained from simulations with PC1D using the material data of the produced PQED photodiodes. The simulations suggest that less than 1 ppm uncertainty is achievable with PQED photodiodes mounted in a trap configuration consistent with [1].*

INTRODUCTION

The spectral responsivity of a quantum detector is given by

$$R(\lambda) = \frac{e \cdot \lambda}{h \cdot c}\left(1-\rho(\lambda)\right)\left(1-\delta(\lambda)\right)\left(1+g(\lambda)\right) \quad (1)$$

The factor $e\lambda/hc$ is the responsivity of an ideal quantum detector expressed by fundamental constants and the vacuum wavelength λ of the applied radiation. Parameters $\rho(\lambda)$ and $\delta(\lambda)$ describe the spectrally dependent reflection and IQD, respectively, whereas $g(\lambda)$ is the quantum gain.

The PQED is a quantum detector and consists of two induced-junction silicon photodiodes with custom-made design parameters. The diodes in the PQED are aligned so that 7 reflections take place before the non-absorbed fraction of light leaves the detector.

From (1) we see that by reducing both internal and external losses/gains and predicting their magnitude we express the responsivity in terms of fundamental constants and predictable quantities and hence have a primary standard. Analysis on the achievable uncertainty in each of the factors in (1) will be treated in the following.

UNCERTAINTY OF IDEAL RESPONSIVITY

The dominating uncertainty in $e\lambda/hc$ is the knowledge of the vacuum wavelength λ. For an applied radiation of 760 nm a 0.3 pm uncertainty in the wavelength would give a 0.4 ppm relative uncertainty in the responsivity. As the speed of light is defined exact, the ratio of e/hc is known from CODATA with the relative uncertainty of 0.022 ppm.

REFLECTANCE

Experimental results show that the diffuse reflectance of the PQED photodiodes is less than 1 ppm [2]. Different strategies can be applied to achieve the 1 ppm uncertainty of the specular reflectance. One could reduce the reflectance loss to an insignificant level or have a moderate number of reflections and measure the residual reflectance at one wavelength.

Analysis of a 7 reflection trap detector is made in [3]. The total reflectance of a 7 reflection trap would be a few tens of ppm which means that the reflectance has to be known with a few percent uncertainty to achieve 1 ppm uncertainty in the responsivity.

INTERNAL QUANTUM DEFICIENCY

The estimate of the internal quantum deficiency is produced using PC1D v.5, which is the same method as used in [1]. Simulation of an induced diode's IQD at different temperatures vs. reverse bias is shown in Fig. 1. The irradiance was 272 μW/cm^2, with a wavelength of 730.5 nm, filling the entire active area of the detector. A surface charge density of $5 \cdot 10^{11}$ e/cm^2 and bulk lifetime of 2 ms, with a surface recombination velocity of 100 cm/s were applied as input parameters. These parameters were the same as those given in the simulations performed in [4].

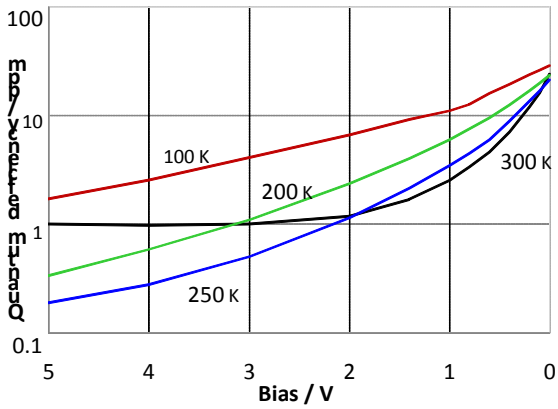

Figure 1. PC1D simulations of PQED quantum deficiency at 730.5 nm vs. applied bias voltage at different temperatures, Na=3.3·10^{12} cm^{-3}.

The PC1D simulations at 5 V reverse bias at 300 and 250 K agree reasonably well with the simulations made in [4] with more complex software. The discrepancies at lower temperatures are related to the temperature dependent absorption coefficient at 730 nm in PC1D and the depletion width of the diode.

In the following, the material parameters for the PQED photodiodes are used in the PC1D simulations (Figs. 2 and 3). Trapped front surface charge density is $6.2 \cdot 10^{11}$ e/cm^2 on a 525 µm thick wafer with doping concentration of $2 \cdot 10^{12}$ cm^{-3}. The bulk lifetime was given to be 1.5 ms and the measured effective lifetime was found to be approximately 500 µs. The measured effective lifetime is a combination of bulk lifetime and surface recombination velocity and gives a front surface recombination velocity of 35 cm/s for the PQED diodes. Oxide thicknesses are 221.9 and 302.8 nm. The optical power was set to 10 µW on an active area of 10 mm^2. The wavelength is 760 nm and reverse bias 5 V.

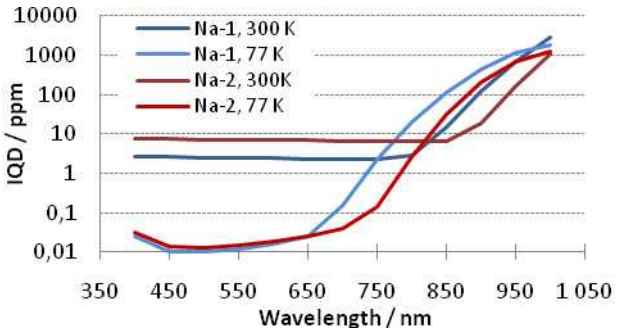

Figure 2. PC1D simulations of PQED's IQD plotted with wavelength at different temperatures with two different doping levels Na-1 = $2 \cdot 10^{12}$ cm^{-3} and Na-2 = $0.7 \cdot 10^{12}$ cm^{-3}.

From PC1D simulations we expect to have less than 10 ppm IQD even at room temperature. Reducing the temperature from 300 to 77 K, we expect a reduction in the IQD by two orders of magnitude over the spectral range from 400 to 650 nm.

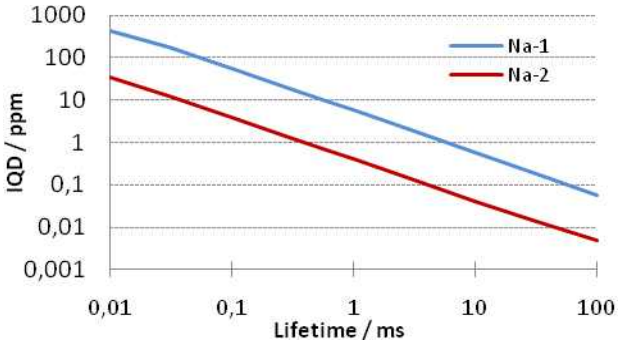

Figure 3. PC1D simulations of PQED's IQD vs. electron hole lifetime at 760 nm and 77 K with two different doping concentrations Na-1 = $2 \cdot 10^{12}$ cm^{-3} and Na-2 = $0.7 \cdot 10^{12}$ cm^{-3}.

The IQD of the PQED photodiodes at 77 K is sensitive to the bulk lifetime of electron hole pairs and the substrate doping concentration in the spectral range from 700 to 800 nm as shown in Fig. 3.

QUANTUM GAIN

There is a strong electric field at the oxide-silicon interface of induced diodes [5]. This field can potentially cause impact ionization producing secondary carriers which contribute to the total photocurrent registered. By knowing impact ionization rate α as a function of electric field in the device, the relative increase in photocurrent can be estimated [6]. By using the device parameters of the present study, the estimated relative contribution to the photocurrent is rather weak reaching the level of about 0.01 ppm at temperatures below 100 K.

SUMMARY

Predicting the responsivity of a PQED is performed starting with an ideal photodiode and taking into account corrections due to reflections, internal losses and gains. For the ideal photodiode the vacuum wavelength must be measured with sub picometer accuracy to achieve ppm level relative uncertainty in the responsivity. The reflectance of a 7 reflection trap detector must be known with a few percents accuracy to achieve 1 ppm uncertainty in the responsivity. The IQD is evaluated with PC1D using the actual material parameters for the PQED. Over a broad spectral range from 400 to 700 nm less than 0.3 ppm IQD is predicted by PC1D at 77 K. Even at room temperature values less than 10 ppm seem achievable over the same spectral range. The quantum gain is at the 0.01 ppm level and therefore insignificant.

*The research leading to these results has received funding from the European Community's Seventh Framework Programme, ERA-NET Plus, under Grant Agreement No. 217257.

REFERENCES

1. J. Geist et.al.:Prospects for improving the accuracy silicon photodiode self-calibration with custom cryogenic photodiodes, Metrologia, 40, S132-135, 2003.
2. E. Ikonen et. al.:, Photon-to-Electron Converter with 1 ppm Quantum Deficiency, Proceedings of the Northern Optics 2009 Conference (Vilnius 2009) p. 114.
3. M. Sildoja et. al.: Reflectance calculations for a predictable quantum efficient detector, Metrologia, 46, S151-S154, 2009.

4. M. Sildoja et. al.: Predictable Quantum Efficient Detector I: Photodiodes and Design, these proceedings.
5. S. Hoem et. al.: Physics of self-induced photodiodes, these proceedings
6. S. M. Sze, Kwok K. NG, Physics of semiconductor devices, 3rd Ed. John Wiley & Sons, NY, 2007.

Current Capabilities at the Metrology Light Source

Alexander Gottwald, Roman Klein, Ralph Müller, Mathias Richter, Frank Scholze, Reiner Thornagel, and Gerhard Ulm

Physikalisch-Technische Bundesanstalt (PTB), Berlin, Germany
Corresponding e-mail address: alexander.gottwald@ptb.de

The Physikalisch-Technische Bundesanstalt (PTB) has set up in close cooperation with the Helmholtz-Zentrum Berlin (HZB) the 630 MeV electron storage ring Metrology Light Source (MLS). This electron storage ring is in regular user operation since April 2008 and is dedicated to synchrotron-radiation-based metrology and technological developments in the far-IR/THz, IR, UV, VUV and EUV spectral range. In 2011, the first phase of instrumentation set-up will be finished, thus providing access to a large range of measurement capabilities.

INTRODUCTION

PTB has been employing synchrotron radiation from electron storage rings for metrological purposes for more than 25 years [1]. At present, - mainly for metrology in the X-ray range - PTB is operating nine experimental stations in its laboratory at the electron storage ring BESSY II. These potentials are complemented by the MLS and its instrumentation, which are optimized to cover the spectral range from the far-IR to the EUV [1, 2].

A substantial feature of synchrotron radiation is that its spectral properties can be calculated from classical electrodynamic relations. Therefore, electron storage rings with calculable bending magnet radiation according to the Schwinger theory are used as primary source standards for radiometry at several national metrology institutes, thus, considerably expanding the spectral region as compared to that covered by blackbody radiators. The major applications of the calculable radiation are the calibration of radiation sources - many of them for astrophysical purposes -, energy-dispersive detectors or wavelength dispersive spectrometers.

Another main focus of PTB is on the calibration of non energy-dispersive detectors, e.g. semiconductor photodiodes [3]. This is based on the comparison to primary detector standards, i.e. cryogenic radiometers. Here it is very important that the monochromatized synchrotron radiation has a high spectral purity, i.e. a low portion of higher order radiation or stray light. These requirements are also mandatory for reflectometry, a further major activity of PTB. All these activities are being pursued at dedicated beamlines at the MLS.

Besides basic radiometric methods, in particular in the (far-)IR spectral range, the synchrotron radiation is used for spectrometric and spectro-microscopic applications, taking advantage of the unique combination of radiant power and source size.

STATUS OF THE RING FACILITY

The MLS is designed for metrology and technological applications mainly in the spectral range from the far IR to the VUV. The electron beam is directly injected into the storage ring from a 105 MeV microtron. The electron beam can then be ramped in the storage ring to any desired electron energy value up to 630 MeV, giving a high flexibility in adjusting the synchrotron radiation spectrum. This is especially important for the suppression of higher diffraction orders or stray light or for the mitigation of the radiation load on optics and the possible degradation related with it.

Furthermore, the electron beam current can be adjusted within a range of more than 11 decades, i.e. from one stored electron, which is equivalent to a current of 1 pA, up to the design value of 200 mA. By this, the radiant intensity of the synchrotron

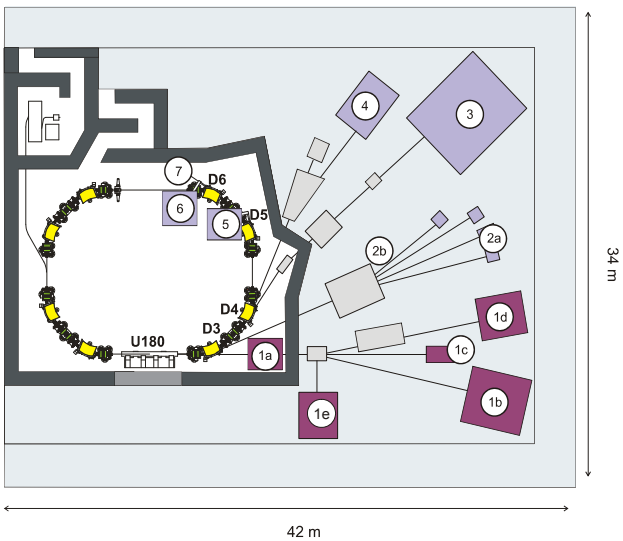

Figure 69. MLS beamlines and experimental stations.

radiation can be adjusted accordingly without changing the shape of the spectrum. These possible variations in the spectral shape and intensity of the synchrotron radiation spectrum enable PTB to tailor a source for the various applications. Moreover, in a special operation mode, the so-called low-α mode, short electron bunches can be set in order to create the so-called coherent synchrotron radiation in the FIR/THz spectral range [4].

STATUS OF THE BEAMLINES AND INSTRUMENTATION

In 2011, the first set-up period for the instrumentation in the experimental hall will be finalized (Fig. 1). Twelve experimental stations at seven beamline ports will become operational, covering the spectral region from the FIR/THz up to the EUV, thus, expanding the measurement capabilities on the low-energy side considerably as compared to the instrumentation at the PTB laboratory at BESSY II. The beamlines with related typical application examples and the present status of the beamline operation are listed in Table 1.

Table 23. Beamlines and its applications at the MLS.

No.	Application and wavelength range
1a	IR undulator radiation 0.6 μm to 70 μm, IR bending magnet edge radiation; Compton-backscattering
1b	deflected undulator radiation
1c	direct undulator radiation; Compton-backscattering
1d	UV/VUV plane-grating monochromator for undulator radiation 4 nm to 400 nm
1e	IR undulator radiation 0.6 μm to 20 μm
2a	direct bending magnet radiation
2b	UV/VUV monochromator 7 nm to 400 nm, source calibration
3	EUV plane-grating monochromator 5 nm to 50 nm
4	UV/VUV NIM monochromator 40 nm to 400 nm, detector calibration/reflectometry
5	THz beamline 100 μm to 7 mm
6	IR beamline 0.6 μm to 7 mm
7	diagnostics front-end

The use of the MLS as a primary source standard is essential for PTB. Therefore, PTB is operating equipment for the accurate measurement of all parameters needed for the calculation of the emitted spectral photon flux or spectral radiant power. This exceeds by far the equipment normally present at other electron storage rings. E.g., at station #7 a highly sensitive system for the optical imaging of the electron beam, even with one stored electron, is in operation [5]. The undispersed, calculable radiation from a bending magnet can be used either at a white light beamline (station #2a), e.g. for the calibration of energy-dispersive detectors or wavelength-dispersive or selective spectrometers or, at station #2b, for the calibration of radiation sources, which is planned to be put into operation in 2011.

For calibrations of detectors and reflectometry in the UV and VUV spectral range, a normal incidence monochromator beamline (#4) was successfully put into operation already in 2008 [6]. A dedicated beamline for the EUV spectral range (#5), will be put into operation in 2011. The undulator with a 180 mm period length is already in operation and produces radiation from the IR (70 μm at 105 MeV electron energy) up to the EUV. The related monochromator beamline (#1d) will be also operational in 2011, and provide highly intensive radiation in the wavelength ranges from UV to EUV. Provision is taken to utilize non-dispersed undulator radiation at stations #1b (VUV) and #1e (IR), e.g. for high flux experiments. Located at the roof of the storage ring bunker are two other operational beamlines for the use of IR (#6) and THz radiation (#5) bending magnet radiation. These are equipped with a rapid scan Fourier transform spectrometer and an IR microscope for life and materials science investigations.

REFERENCES

1. B. Beckhoff et al., A quarter-century of metrology using synchrotron radiation by PTB in Berlin, Phys. Status Solidi B. 246, 1415–1434, 2009.
2. R. Klein et al., The Metrology Light Source operated as a primary source standard, Metrologia, 46, S 266-S271 2009.
3. A. Gottwald et al., The PTB High-Accuracy Spectral Responsivity Scale in the VUV and X-Ray Range, Metrologia, 43, S125-S129, 2006.
4. J. Feikes et al., Metrology Light Source: The first electron storage ring optimized for generating coherent THz radiation, Phys. Rev. ST Accel. Beams, 14, 030705, 2011.
5. C. Koschitzki et al., Highly sensitive beam size monitor for pA currents at the MLS electron storage ring, Proc. of IPAC'10, 894, 2010.
6. A. Gottwald et al., Ultraviolet and vacuum-ultraviolet detector-based radiometry at the Metrology Light Source, Meas. Sci. Technol., 21, 125101, 2010.

Lens transmission measurement for Absolute Radiation Thermometer

Hao Xiaopeng, Yuan Zundong, Lu Xiaofeng, and Dong Wei

Division of Thermometry and Materials Evaluation, National Institute of Metrology, Beijing, China
Corresponding e-mail address:haoxp@nim.ac.cn

The lens transmission for the absolute radiation thermometer is measured by a hybrid method. The results of lens transmission are 99.002% and 86.792% for filter radiometers with centre wavelengths 633-nm and 900-nm, respectively. These results, after correcting for diffraction factors and the size-of-source effect, can be used for the radiometric measurement of the thermodynamic temperature. The standard uncertainty of our measurement system has been evaluated. It is 6.5E-4 for both diameters 25 mm and 40mm at 633 nm, and 6.6E-4 and 6.9E-4 for diameters 25 mm and 40 mm, respectively at 900 nm.

INTRODUCTION

A lens is a very important optical device. The transmission of a lens, just as its focal length, its focus curvature and radius, its materials etc., is a very important parameter. There are several methods to measure this parameter [1-3]. But lens transmission measurement results are influenced by several factors, such as the incidence angle, source stability, diffraction effect, size-of-source effect (SSE) and so on.

At the National Institute of Metrology of China (NIM), the absolute radiation thermometer (ART) is a simple device consisting of a linear arrangement of a 50-mm diameter doublet lens coated with MgF_2, a 25-mm diameter diamond-turned aperture directly behind the lens, and a filter radiometer (as described in [4]) at a distance of 1450 mm from the lens. A thermodynamic temperature measurement by the ART requires the determination of several parameters, such as lens transmission, aperture area, emissivity of the cavity, responsivity of the filter radiometer, gain of the amplifier etc. In this paper we introduce the method for measuring the transmission of the lens and evaluate its uncertainty.

RESULTS AND UNCERTAINTY

In our measurement of the lens transmission of the ART we used the hybrid method shown in figure 1. The source is an integrating sphere with uniformity of 5E-4 over an area of 48 mm × 48 mm. In the radiance mode (figure 1a), a 10-mm diameter aperture is placed in the object plane of the ART to obtain the signal V_{rad}. In the irradiance mode, the lens and the 10-mm diameter aperture are removed from the ART and from its object plane, respectively, to obtain the signal V_{irrad}. The lens transmission τ_{opt} is then calculated according to equation 1:

$$\tau_{opt} = \frac{V_{rad}/SSE}{V_{irrad}/F_{diff}} \quad (1)$$

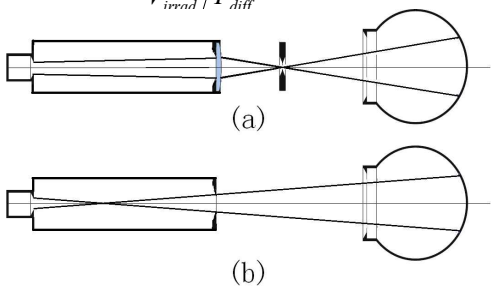

Figure 70. Sketch of our hybrid lens transmission measurement method, a) radiance signal with lens, V_{rad} b) irradiance signal without lens, V_{irrad}

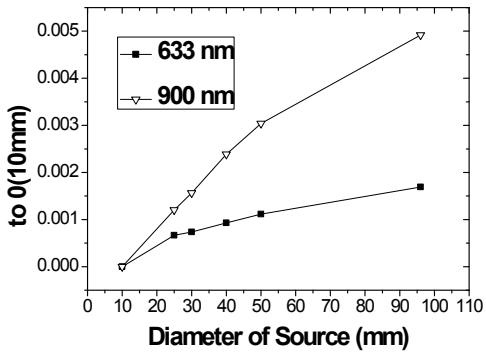

Figure 2. SSEs for 633-nm and 900-nm centre wavelength temperature measurements.

The SSE of the ART needs to be measured so that V_{rad} can be corrected. If the source diameter changes from 10 mm to 96 mm, the SSEs are 0.169% and 0.492% for the filter radiometers with 633-nm and 900-nm centre wavelengths, respectively (cf. figure 2).

The diffraction factor for correcting V_{irrad} is calculated following Edward's model [5, 6]. The radius of the source (r_s), the radii of the lens (r_a) and of the detector (r_d), the distance between source and

lens (d_s), and the distance between lens and detector (d_d) are given for the ART. The r_s, r_a and r_d are 48 mm, 12.5 mm, and 2.5 mm, respectively. The resulting diffraction factors are listed in table 1.

Table 24. Diffraction factors for different measurement parameters.

Wavelength (nm)	d_s (mm)	d_d (mm)	Factor
633	1600	1200	0.99945
900	1600	1200	0.99921
633	1000	1425	0.99987
900	1000	1425	0.99981

The lens transmission, measured 7 times per day during 4 days, is 99.002% for the 633-nm centre wavelength filter radiometer; the standard deviations (SD) are below 7.1E-05 for one day. For the 900-nm centre wavelength filter radiometer the result is 86.792%, with an SD below 2.9E-5.

Table 2. The lens transmissions τ for the 633-nm and 900-nm centre wavelength filter radiometers.

Wavelength (nm)	Data	τ_{opt} d = 25mm	τ_{opt} d = 40mm
633	2010/12/1	99.068%	99.097%
	2010/12/2	99.042%	99.071%
	2010/12/3	99.055%	99.084%
	2010/12/9	99.041%	99.070%
900	2010/12/3	86.877%	86.979%
	2010/12/9	86.888%	86.990%

The ART was used to measure high temperature points. Because the aperture diameter is different for the measurements at the fixed points of silver and the metal carbon eutectics, the SSE must be corrected. The lens transmissions, corrected for SSEs and diffraction factors, are listed in table 2. Given the source sizes of 40-mm diameter for the silver fixed point, and 25-mm for metal carbon eutectic point, τ_{opt} needs to be corrected by SSEs from 10 mm to 25 mm and 40 mm.

The uncertainties, which include the effects of repeatability, uniformity of source, diffraction correction and SSE correction are shown in table 3. The SD, 6.5E-4, of results taken over the duration of one month characterizes the repeatability. The combined uncertainty is then 6.5E-4 for the 633-nm centre filter radiometer and source diameters 25 mm and 40 mm, 6.6E-4 for the 900-nm centre filter radiometer and source diameter 25 mm, and 6.9E-4 for the 900-nm centre filter radiometer and a source diameter of 40 mm.

Table 3. Uncertainties of the lens transmissions. (D and d are given in millimetres.)

Source of Uncertainty	λ = 633 nm		λ = 900 nm	
	D=25	d=40	d=25	d=40
Repeatability	6.5E-4	6.5E-4	6.5E-4	6.5E-4
Uniformity of source	5.0E-6	5.0E-6	5.0E-6	5.0E-6
Diffraction	1.3E-5	1.3E-5	1.9E-5	1.9E-5
SSE	6.4E-5	9.3E-5	1.2E-4	2.4E-4
Combined	6.5E-4	6.5E-4	6.6E-4	6.9E-4

CONCLUSION

We have measured the lens transmission of the ART that is used for the radiometric measurement of the thermodynamic temperature by a hybrid method. The lens transmission is 99.002% and 86.792% for the 633-nm and 900-nm centre wavelengths of our filter radiometers, respectively. These results, corrected for diffraction factors and size-of-source effect are used in thermodynamic temperature measurements at NIM. The uncertainties are 6.5E-4 at 633-nm with aperture diameters 25 mm and 40 mm, and 6.6E-4 and 6.9E-4 at 900 nm for aperture diameters of 25 mm and 40 mm, respectively.

REFERENCES

1. E.R. Woolliams, D.F. Pollard, N.J. Harrison, E. Theocharous, N.P. Fox, New facility for the high-accuracy measurement of lens transmission, Metrologia, 37, 603-605, 2000.

2. Liu Fei, Novel method for measuring the spectral transimission of a photographic lens, Optical Engineering, 47, 113602, 2008.

3. R. Winkler, E. R. Woolliams, W. S. Hartree, S.G. R. Salim, N.P. Fox, J.R. Mountford, M. White, S. R. Montgomery, Calibration of an absolute radiation thermometer for accurate determination of fixed-point temperatures, Int. J. Thermophys, 28, 2087-2097, 2007.

4. X.Lu, Z.Yuan, X. Hao, Y.Lin, J.Yang, Calibration o f the irradiance responsivity of a filter radiometer for T measurement at NIM, Int. J. Thermophys. 32, 278-2 84, 2011.

5. P. Edwards, M. McCall, E. Usadi, Use of the single wavelength approximation in radiometric diffraction loss calculations, Proceeding of SPIE, 5189, 36-44, 2003.

6. P. Edwards, M.McCall, Appl. Opt. 42, 5024-5032, 2003.

LED near-field goniophotometer at PTB

M. López[1*], K. Bredemeier[2], N. Rohrbeck[3], C. Véron[3], F. Schmidt[2] and A. Sperling[1]

[1]*Physikalisch-Technische Bundesanstalt, Germany,* [2]*TechnoTeam Bildverarbeitung GmbH, Germany*
[3] *ZETT OPTICS GmbH, Germany*
[*]*Corresponding e-mail address: marco.lopez@ptb.de*

Today, near-field goniophotometers are commonly used to measure the luminance distribution of solid state light sources, e.g. LEDs. These measurements are employed for generating ray data ("ray files") used for the design of modern luminaries. At present, there is still a lack of traceability for such measurements. In order to meet this demand, PTB has recently installed a near-field goniophotometer. As a first "validation" of the near-field goniophotometer, the luminous intensity distribution of an LED was determined from near-field measurements and compared to one carried out separately in far-field with a photometer. This comparison is presented in this paper.

INTRODUCTION

The first near-field goniophotometers were developed in the 1990s to determine the luminous intensity distribution and the total luminous flux of a light source from luminance distribution measurements [1, 2]. By using a CCD-based imaging photometer as a detector on a goniophotometer, such a near-field goniophotometer is able to determine the starting point and the direction of the rays from the emitted radiation of the light source (near-field model). These measurements are today used for generating ray data ("ray files"), which are commonly employed for optical simulation tools (ASAP, Zemax, etc.) for the design of modern luminaries, e.g. headlamps which use LEDs as light sources [3, 4].

Until now, manufacturers of near-field goniophotometers and users of the ray data have not been able to achieve confident photometrical values due to a lack of traceability of such measurements. In order to meet this need, at PTB a near-field goniophotometer has recently been installed. It will be used to evaluate novel light sources like LEDs or OLEDs for their suitability as transfer standards. The near-field goniophotometer is still under characterization. However, the first near-field measurements carried out with this goniophotometer were compared to the ones carried out in far-field conditions. The results of this comparison are presented in this paper.

MEASUREMENT PRINCIPLE OF A NEAR-FIELD GONIOPHOTOMETER

A near-field goniophotometer uses a special camera (luminance measuring camera) which captures the luminance distribution $L(x_S, y_S, z_S, \vartheta_E, \varphi_E)$ [8] of a light source for all directions in which the light is emitted. The measurements are carried out by moving the measuring camera with the mechanical system of a goniophotometer on an imaginary spherical surface around the light source (see Figure 1). Each pixel (i, j) in the luminance image defines a solid angle element $d\Omega_{Pixel}(i, j)$, and an area element $dA(\vartheta, \varphi)$ which defines a luminous flux portion $d\Phi(i, j)$. These luminous flux portions can be regarded as ray data. Knowing the camera position $\{\vartheta_k, \varphi_k\}$, the image coordinates $\{x', y'\}$ in the CCD matrix can be determined too. With this information, the image data can be converted into rays with respect to the goniophotometer coordinate system (device coordinates). Furthermore, the luminous intensity distribution $I(\vartheta, \varphi)$ and the total luminous flux Φ_v of the light source can also be determined from the ray data [5].

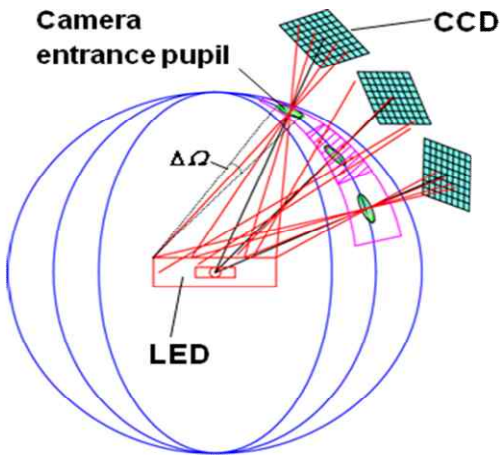

Figure 1. Principle of a near-field goniophotometer.

[8] $L(x_S, y_S, z_S, \vartheta_E, \varphi_E) = \frac{d\Phi}{dA(x_S, y_S, z_S) \cdot \cos\vartheta_E \cdot d\Omega(\vartheta_E, \varphi_E)}$

NEAR-FIELD GONIOPHOTOMETER AT PTB

PTB developed a special LED goniophotometer setup to be able to measure all kinds of LEDs under far-field conditions as well as under all the different conditions given in CIE 127:2007. Recently, this facility was expanded to carry out near-field goniophotometric measurements by adding a luminance measuring camera (see Figure 2). Unlike typical near-field goniophotometers, in this setup the luminance camera is maintained at a fixed position while the source (LED) is moved over the angles $\{\vartheta, \varphi\}$ during the measurement. The luminance camera is equipped with several objectives which allow the capturing of measurement objects (e.g. organic LEDs) with a diameter of up to 100 mm. Spectrally resolved near-field measurements can also be carried out by adding a bandpass filter to the luminance camera. The ray data is determined by using the algorithm described in [5]. However, it is planned to implement new algorithm modules to evaluate the ray data and to support the versatility of this facility. By substituting the camera with a spectroradiometer, with its fibre input mounted on the rotary stage (see Figure 2) adjacent to the photometer, the light source can also be characterized spectrally in the far field.

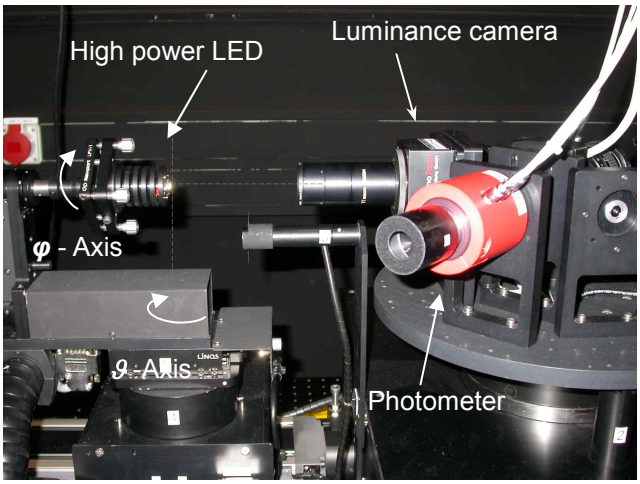

Figure 2. Far- and near-field goniophotometer at PTB.

COMPARISON OF NEAR-FIELD AGAINST FAR-FIELD GONIOPHOTOMETRICAL MEASUREMENTS

Figure 3 shows a comparison of the luminous intensity distribution of a high-power LED determined from measurements carried out in the near and far field. In the near field, a set of 1 million rays was used to calculate the luminous intensity distribution. In order to reduce the noise generated when the accumulation of the ray is carried out near to the pole, i.e. for small area elements, a resolution of the areas of 3° was used for this comparison. The far-field measurement was carried out with a photometer with a limited aperture of 10.5 mm diameter. The LED (nearly Lambertian) was placed 600 mm away from the photometer for far field measurements.

As can be observed in Figure 3, the average difference between both measurements is ≤ 4%. LEDs with non-lambertian luminous intensity distribution will be measured in order to obtain more information about the measurement errors caused, e.g. by a misalignment of the light source, axis, etc. The complete study will be presented at the conference.

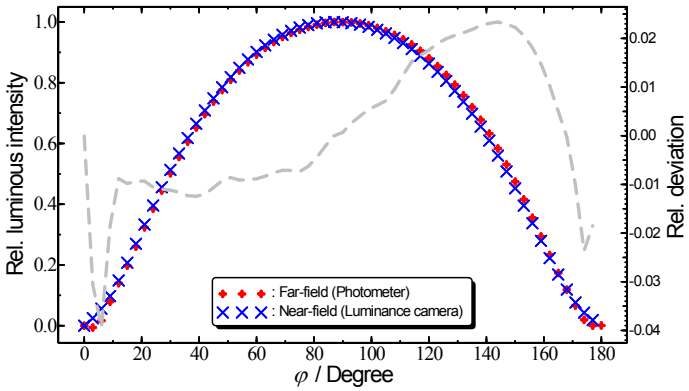

Figure 3. Comparison of the luminous intensity distribution of a high-power LED obtained from far- and near-field goniophotometrical measurements over the polar angle ϑ = 0-180°.

REFERENCES

1. "Near-field photometric method and apparatus", Ian E. Ashdown, U.S. Patent Number: 5,253,0036, 1993.
2. Manfred Riemann, Franz Schmidt, Ralf Poschmann, "Zur Bestimmung der Lichtstärkeverteilung von Leuchten innerhalb der fotometrischen Grenzentfernung mittels eines bildauflösenden Goniometers", LICHT 7-8 S.592-597 (1993).
3. Bredemeier Knut, Jordanow Wladimir and Franz Schmidt, "Messung der Ausstrahlcharakteristik (Strahlendaten) von LED" LICHT 2008, Ilmenau 10-13.Sept. 2008, Tagungsband, pp. 130-137.
4. Ian Ashdown and Marc Salsbury, "A Near-field Goniophotometer for LED Measurements", SPIE-OSA, Vol. 6342, 2006, pp. 634215 – 6363226.
5. "Imaging-photometer-based near-field goniophotometer", CIE Draft No.1, TC 2-62, 2010.

Equivalence of published GLS solutions to comparison analysis

Annette Koo and John F. Clare

Measurement Standards Laboratory, Lower Hutt, New Zealand
Corresponding e-mail address: a.koo@irl.cri.nz

Several implementations of the Generalised Least Squares (GLS) approach to the analysis of the data from inter-laboratory comparisons have been reported. A proof of their equivalence and the implications for CCPR comparisons are discussed.

INTRODUCTION

MSL was recently granted the task of piloting the next CCPR-K6 regular spectral transmittance comparison. In preparation for the work, and as part of putting together the technical protocol for the comparison, an investigation of published approaches to analysis of the results was carried out.

While the CCPR guidelines [1] include a worked example of the 'step-by-step' approach to analysis, a nod is also made to the generalised least squares (GLS) approach which has been used once [2] for a CCPR comparison, and is in regular use for mass comparisons. Despite its growing usage, the GLS approach has aroused concern owing to its perceived lack of transparency.

At first glance, the GLS approach promised to be more auditable, statistically defensible and simpler to implement, especially in the face of complex protocols or correlations between measurements. However a closer look at the literature showed that three distinct treatments of data had been carried out in each of the three publications containing a guide to the application of GLS to comparison data [2, 3, 4]. Notwithstanding the apparent advantages of GLS considerable disagreement persists over its implementation.

Ambiguity in the treatment of data has reduced confidence in the GLS approach and made it difficult to persuade the community of its efficacy for comparison analysis. However, on analysing some sample data sets using each of these implementations, we found that both the numerical results for artefact values and participant bias and the estimates of their uncertainty were identical. This equivalence held for a wide range of data sets, leading to the hypothesis that the three implementations were equivalent. Further work led to a general proof of that equivalence [5].

RESULTS

Every measurement made during a comparison between L participants may be modelled with the measurement equation

$$y_{\lambda jr} = \theta_j + \Delta_\lambda + e_{\lambda jr} \qquad (1)$$

where $y_{\lambda jr}$ is a single measurement result of participant λ for artefact j and round (or repeat) r, θ_j is the 'true value' of artefact j, Δ_λ is the bias of participant λ, and $e_{\lambda jr}$ is the error associated with the measurement which may include the intrinsic variability of the artefact itself for that particular measurement (e.g. drift, contamination or random fluctuations). A constraint in the form of a definition of the Key Comparison Reference Value (KCRV) is required for a unique solution and is chosen to be

$$\sum w_\lambda \Delta_\lambda = 0 \text{ where } \sum w_\lambda = 1 \qquad (2)$$

as per the CCPR guidelines [1] where the w_λ are the weights assigned to each participant.

Equation (1) can be expressed in a matrix form,

$$\mathbf{y} = X\boldsymbol{\beta} + \mathbf{e}, \qquad (3)$$

where $\mathbf{y}$ is the column vector of all measurement results $y_{\lambda jr}$, X is the design matrix with each row representing a single measurement, $\boldsymbol{\beta}$ is a column vector of the unknown θ_j and Δ_λ, and $\mathbf{e}$ is a column vector containing the errors $e_{\lambda jr}$ associated with each result. The GLS solution

$$\hat{\boldsymbol{\beta}} = (X'V^{-1}X)^{-1}X'V^{-1}\mathbf{y} = Z\mathbf{y} \qquad (4)$$

will be the best linear unbiased estimate of the unknowns where V is the covariance matrix associated with the errors. It is constructed from the information given by participants regarding the components of uncertainty in their results. The covariance matrix associated with the estimate is given by

$$\mathrm{cov}(\hat{\boldsymbol{\beta}}) = ZVZ' \qquad (5)$$

The difference between the published treatments of comparison data lies in the construction of V.

Sutton [3] includes all components of error, taking into account any components of error correlated between measurements of a particular participant, as well as between the measurements of more than one participant.

Woolliams *et al*. [2] on the other hand consider the errors correlated between all measurements of any participant to be systematic and therefore modelled by the bias, Δ_λ, in equation (1) so the errors, $e_{\lambda jr}$, and consequently V in equation (4), include only the 'random' components of error reported by the participants. When it comes to calculating the covariance matrix associated with the estimate however, the full covariance matrix is used in equation (5).

White [4] also considers the errors correlated between all measurements of a participant to be accounted for by Δ_λ so uses the same reduced covariance matrix as Woolliams in calculating the estimates (4), and also uses the reduced covariance matrix in equation (5), adding an extra term to the final calculated uncertainty of the participant biases to account for the systematic components of error.

By requiring that the comparison be internally linked, i.e., any two artefacts $\mathcal{A}_1$ and $\mathcal{A}_2$ are linked through a sequence of participants who measured $(\mathcal{A}_1,\mathcal{A}_3),(\mathcal{A}_3,\mathcal{A}_4),\ \ldots\ ,\ (\mathcal{A}_{n-1},\mathcal{A}_n),$ $(\mathcal{A}_n,\mathcal{A}_2)$ respectively, we have been able to show that the estimator $Z\mathbf{y}$ in equation (4) is the same whether the full or reduced covariance matrix is used. Further, the difference between the covariance matrix associated with the estimate calculated using the full measurement covariance matrix and that using the reduced covariance matrix was shown to be equal to the additional term used by White to account for the systematic errors. These two results show the equivalence of the three distinct approaches of Sutton, Woolliams *et al*. and White.

DISCUSSION AND CONCLUSION

The results that we have demonstrated constitute a considerable advance in the understanding of metrological comparisons and provide a definitive answer for the values of participant biases. However, in the authors' minds, a question remains as to whether the common result of the approaches discussed provides the most appropriate or useful estimate of uncertainty in participant biases. The inclusion of the effects of the bias in two terms of the model, namely the unknown bias term and the error term, appears to be 'double counting'. Accounting for this by including the correlated errors at later points in the calculation is not convincingly justified either. Appropriate treatment of these correlated errors is an issue not only in the use of GLS, but also when using the 'step-by-step' approach.

The somewhat controversial view that, owing to the 'trade' purposes of a comparison, inter-laboratory correlations should not be considered in the analysis of the results has avoided the complexity of taking these correlations into account using the step-by-step method. Using GLS makes accounting for these correlations straightforward, and this report shows that the estimated values of the biases are not affected.

To date, CCPR comparisons have mostly followed a 'star' format in which participants are linked only through the pilot laboratory. A format incorporating several 'sub-pilots' and measurements of artefacts by several participants would reduce vulnerability to pilot laboratory problems and be more statistically robust. That the analysis of such comparisons by the traditional 'step-by-step' approach is more difficult and less auditable does not now matter as the GLS approach is available.

The metrological community can now adopt GLS for comparison analysis without ambiguity with respect to the three published methods. The issue of how these methods take account of correlated errors in the GLS approach to determining degrees of equivalence is resolved: these components have no influence on the values of the unknowns, and their contribution to the final uncertainties is the same for all three. Potentially then, an agreed-upon algorithm could be constructed and software made available for the analysis of measurement comparison data by the whole community.

REFERENCES

1. CCPR-KCWG *Guidelines for CCPR Comparison Report Preparation,* available at www.bipm.org/utils/common/pdf/Guidelines_for_CCPR_KC_Reports.pdf, 2009
2. E.R. Woolliams *et al*., Metrologia, **43**, S98-S104, 2006; E.R. Woolliams *et al*., CCPR K1.a Final Report, available at http://kcdb.bipm.org/appendixB/appbresults/ccpr-k1.a/ccpr-k1.a_final_report.pdf, 2006.
3. C.M. Sutton, *Metrologia*, **41**, 272–277, 2004
4. D.R. White, *Metrologia*, **41**, 122–131, 2004
5. A. Koo and J.F. Clare, IRL Report # 2471, 2011

Absolute Calibration of a Linear Pyrometer (LP3) Traceable to a Cryogenic Radiometer

A.D.W. Todd and D.J. Woods

Institute for National Measurement Standards, National Research Council of Canada,

Ottawa, Ontario Canada

Corresponding e-mail address: andrew.todd@nrc-cnrc.gc.ca

With the goal of measuring the absolute melting temperatures of the high temperature eutectic fixed points Co-C, Pt-C and Re-C, a linear pyrometer (LP3) has been calibrated using a filter radiometer (FR1) near the transition temperatures of the fixed points. FR1 is absolutely calibrated with traceability to the National Research Council Canada's cryogenic radiometer. A high temperture blackbody (HTBB) was used to tranfser the FR's calibration to the LP3.

INTRODUCTION

Working Group 5 (WG5) of the Consultative Committee for Thermometry (CCT) is working toward the measurement of the absolute melting temperatures of the high temperature fixed points of Co-C, Pt-C and Re-C for inclusion in the *Mise en pratique* for the definition of the kelvin.

The approaches used by researchers around the world vary, but all rely on a calibration chain that is traceable to an electrical substitution cryogenic radiometer. At the National Research Council Canada, the initial approach adopted sees the NRC LP3 calibrated against a HTBB for which the radiance temperature has been determined by a FR that has had its spectral responsivity measured via a transfer detector calibrated against the cryogenic radiometer. This approach is similar to that reported by Anhalt *et al*. [1].

Here, the transfer calibration of the LP3 against the FR and the uncertainties associated with this calibration will be discussed. This calibration scheme was used in order to measure the transitions temperature of the fixed points and not to absolutely calibrate the pyrometer at other temperatures.

PROCEDURES AND RESULTS

Figure 1 shows a block diagram of the procedure used to absolutely calibrate the LP3 at the temperatures of interest. Details of the calibration of the Si transfer detector against the cryogenic radiometer can be found in Ref. 2. The filter radiometer used in this work has a coloured glass filters with a peak wavelength of nominally 650 nm (FR1). Details of the filter radiometer can be found in Ref. 3.

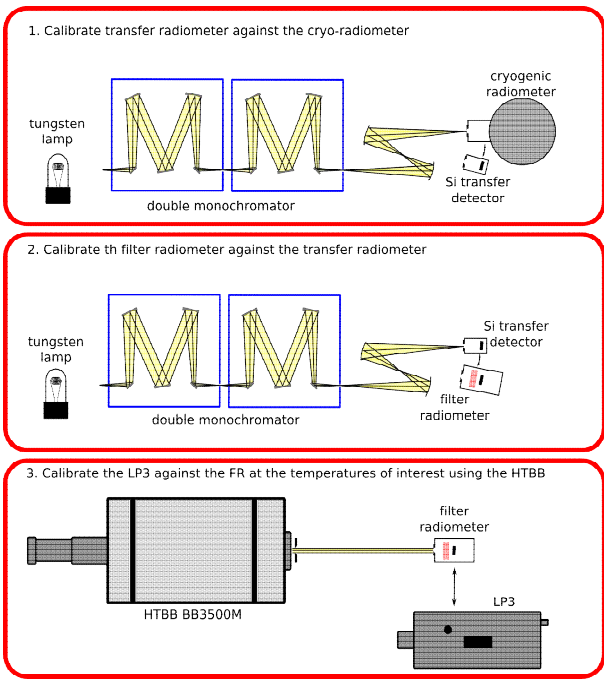

Figure 1: Schematic of the approach to calibrate the LP3 at approximately 1358 K, 1597 K, 2011 K, and 2747 K.

A precision aperture (8.560 mm in dia. with an uncertainty of 0.0005 mm (k = 1)) housed in a water cooled copper housing was installed in front of the opening and behind the feedback control sensor of the HTBB. A gauge bar of length 913.063 mm was used to align the HTBB aperture to the aperture integrated into FR1 and to set the distance between the two apertures. A temperature controlled circulator filled with distilled water was set to 19.5 ºC and connected to the HTBB feedback control sensor and the HTBB aperture housing. The temperature of the FR was maintained at 30.0 °C using the integrated thermo-electric coolers.

The HTBB (BB3500M, see Ref. 4) was brought close to the desired operating temperature by slowly ramping up the HTBB current to a value that was previously determined to be near the required

temperature. When the temperature (as measured by the LP3) began to stabilize near the desired temperature the feedback stabilization mode was enabled.

The LP3 was focused at the centre of the HTBB aperture a distance of 70 cm from the LP3's front lens. Once it was determined that the HTBB was stable a measurement with the LP3 was made for approximately five minutes followed immediately by a five minute measurement using the FR. A measurement of the FR dark current was made while the LP3 measurement was taking place and before the FR was moved in front of the HTBB.

Figure 2 shows the deviation of the temperature measured by the LP3 from that determined by FR1 near the temperatures of interest. Table 1 shows the uncertainty budget for the transfer of the calibration of the FR to the LP3.

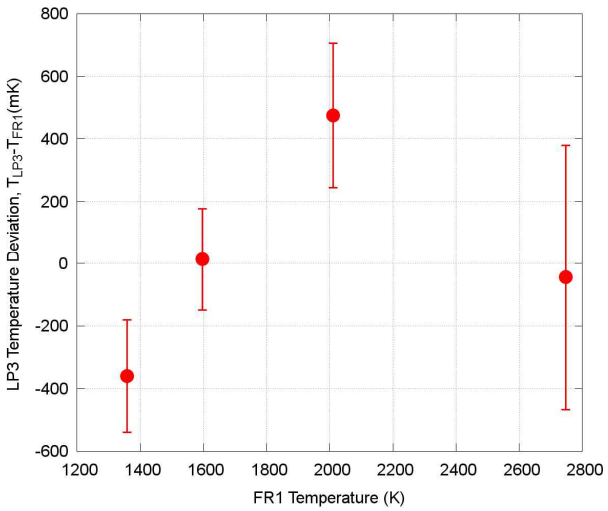

Figure 2: The deviation of the temperature measured by the LP3 near the melting points of Cu, Co-C, Pt-C and Re-C from the absolute temperature measured by FR1

CONCLUSIONS

The NRC's LP3 has been absolutely calibrated near the melting temperatures of Cu, Co-C, Pt-C and Re-C in order to measure the melting temperatures of these fixed points. Corrections to the LP3 temperature and an uncertainty in the correction are given in Table 2.

Table 25: Correction and uncertainty in the correction for the LP3 at the tempertures of interest.

FR1 Temperature (K)	Correction T_{LP3}-T_{FR1} (mK)	Uncertainty (k = 1) (mK)
1358.264	-360	184
1597.118	13	171
2010.633	475	237
2747.157	-44	428

REFERENCES

1. K. Anhalt, J. Hartmann, D. Lowe, G. Machin, M. Sadli and Y. Yamada, Thermodynamic temperature determinations of Co-C, Pd-C, Pt-C and Ru-C eutectic fixed-point cells, Metrologia, 43, S78-S83, 2006.
2. L.P. Boivin and K. Gibb, Monochromator-based cryogenic radiometry at the NRC, Metrologia, 32, 565-570, 1995/96.
3. L.P. Boivin, C. Bamber, A.A. Gaertner, R.K. Gerson, D.J. Woods and E.R. Woolliams, Wideband filter radiometers for blackbody temperature measurements, J. Modern Optics, 57:17, 1648-1660, 2010.
4. S.A. Ogarev, B.B. Khlevnoy, M.L. Samoylov, V.I. Shapoval, V.I. Sapritsky and M.K. Sakharov, New high-temperature pyrolytic graphite blackbody sources for precision measurements in radiation thermometry, in Proceedings of the 9th Symposium on Temperature and Thermal Measurements in Industry and Science Dubrovnik-Cavtat, Croatia, June 22-25, 2004.

Table 26: Uncertainties for the absolute calibration of the LP3.

Source	FR Response (%)	u in T at T = 1357 K (mK)	u in T at T = 1597 K (mK)	u in T at T = 2011 K (mK)	u in T at T = 2747 K (mK)
FR Calibration		80	103	160	293
HTBB Emissivity	0.05	47	64	100	183
HTBB Stability		54	33	6	42
Refractive Index		20	20	20	20
FR Optical Alignment	0.06	56	77	120	220
Noise in FR Signal		94	43	31	46
Noise LP3 Signal		86	48	31	61
HTBB Aperture Area	0.02	19	26	40	73
Radiance Non-uniformity		50	50	50	50
Total		**184**	**171**	**237**	**428**

International Comparisons of Optical Fiber Power Measurements*

I. Vayshenker, D. J. Livigni, X. Li, and J. H. Lehman

National Institute of Standards and Technology, Boulder, USA

e-mail address: igor@boulder.nist.gov

We discuss the results of optical fiber power meter (OFPM) measurements at 1310 nm and 1550 nm made by NIST and seven national measurement institutes (NMIs). We also describe transfer standards and the associated uncertainties. The comparisons show a reasonably good agreement between the participating laboratories, with relative differences that are within the standard (*k*=1) combined uncertainties.

INTRODUCTION

In our previous work we have reported international comparisons of optical fiber power with several NMIs [1-7] at 1310 nm and 1550 nm. In this paper we present new measurement results from National Institute of Metrology (NIM-China) and summarize previous fiber-based power measurements.

For OFPM calibrations, the NIST primary standard is the cryogenic radiometer [8], which has an expanded measurement uncertainty of absolute optical power of 2 parts in 10^4. NIST reference standards are calibrated against the primary standard by the use of collimated (free field) beams, but are typically used with divergent beams characteristic of laser light exiting an optical fiber.

TRANSFER STANDARDS

We used two germanium (Ge) trap-based detectors [1-6] and one commercial optical power meter [7] in the comparisons. The transfer standards may be broadly described as "trap detectors" [9]. In the present case, our trap detectors, known as the "4×trap", are two Ge photodiodes and a spherical mirror. It has been shown in [10] that such a configuration provides a uniform response over a wide field of view and therefore requires no correction for beam geometry. This design increases the coupling efficiency for larger values of numerical apertures [11].

The transfer standards were calibrated at the participating laboratories against their reference standards at approximately 100 µW, or -10 dBm. We employed a direct-substitution method for the measurements. NIST's measurement system is described in detail in [12].

RESULTS

We present the results of the responsivity comparisons and their associated standard combined uncertainties (as error bars, *k*=1) in Fig. 1. The standard uncertainties for the optical power measurements were evaluated in accordance with the International Organization for Standardization Guide to the Expression of Uncertainty in Measurement [13]. Fig. 1 shows the relative difference (expressed in percent compared to the measurement of the National Institute of Standards and Technology (NIST-USA)) at two laser wavelengths of 1310 nm and 1550 nm among seven NMIs: (1) National Physical Laboratory (NPL-UK), (2) All-Russian Research Institute for Optophysical Measurements (VNIIOFI-Russia), (3) Physikalisch-Technische Bundesanstalt (PTB-Germany), (4) National Metrology Institute of Japan/National Institute of Advanced Industrial Science and Technology (NMIJ/AIST-Japan), (5) Federal Office of Metrology (METAS-Switzerland), (6) Centro Nacional de Metrología (CENAM-Mexico), and (7) National Institute of Metrology (NIM-China). The comparisons show a reasonably good agreement between the participating laboratories, with relative differences that are within the standard (*k*=1) combined uncertainties.

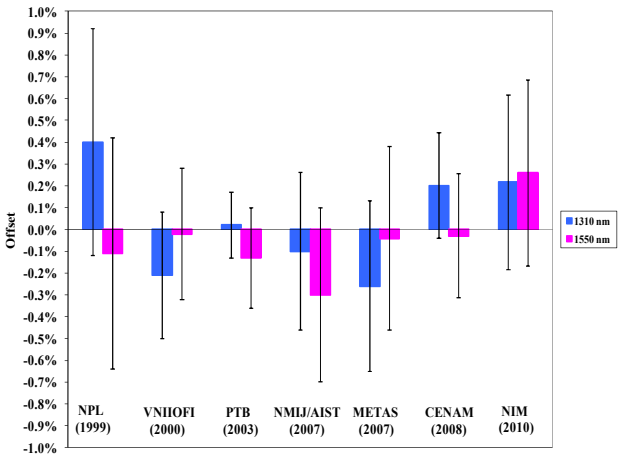

Figure 71. International comparison results (1999-2010; *k*=1). NIST results are represented by a horizontal line with an offset of 0%.

ACKNOWLEDGEMENTS

We thank NPL, VNIIOFI, PTB, METAS, NMIJ/AIST, CENAM, and NIM for providing the comparison data and uncertainty analysis.

*Partial contribution of the National Institute of Standards and Technology; not subject to copyright.

REFERENCES

1. S. V. Tikhomirov, A. I. Glazov, M. L. Kozatchenko, V. E. Kravtsov, A. B. Svetlichny, I. Vayshenker, T. R. Scott, and D. L. Franzen, "Comparison of reference standards for measurements of optical-fibre power," Metrologia, 37, 347-348, 2000.
2. I. Vayshenker, H. Haars, X. Li, J. H. Lehman and D. J. Livigni "Comparison of optical-power meters between NIST and PTB," Metrologia, 37, pp. 349-350, 2000.
3. I. Vayshenker, H. Haars, X. Li, J. H. Lehman, and D. J. Livigni, "Optical fiber-power meter comparison between NIST and PTB," Journal of Research of the NIST, 108, 391-394, 2003.
4. I. Vayshenker, J. H. Lehman, D. J. Livigni, X. Li, K. Amemiya, D. Fukuda, S. Mukai, S. Kimura, M. Endo, J. Morel, and A. Gambon, "Trilateral optical power meter comparison between NIST, NMIJ/AIST, and METAS," Appl. Opt. 46, 5, 643-647, 2007.
5. I. Vayshenker, D. J. Livigni, J. A. Hadler, and J. H. Lehman, "NIST optical fiber power measurements: intramural and international comparisons," Digest, Optical Fibre Measurement Conference, 97-100, October, 2007.
6. I. Vayshenker, J. C. Bermudez, J. C. Molina, Z. E. Ruiz, D. J. Livigni, X. Li, and J. H. Lehman, "Bilateral Optical Power Meter Comparison between NIST and CENAM," Journal of Research of the NIST, 113, 4, 1-4, July-August, 2008.
7. I. Vayshenker, J. Li, L. M. Xiong, Z. X. Zhang, D. J. Livigni, X. Li, and J. H. Lehman, "Optical fiber power meter comparison between NIST and NIM," Journal of Research of the NIST, 115, 6, 1-4, November-December, 2010.
8. D. J. Livigni, "High accuracy laser power and energy meter calibration service," NIST Special Publication 250-62, 2003.
9. N. P. Fox, "Trap detectors and their properties," Metrologia 28, 197-202, 1991.
10. J. H. Lehman and X. Li, "A transfer standard for optical fiber power metrology," Eng. and Lab. Notes in Opt. & Phot. News, Vol. 10, No. 5, May 1999, archived in Appl. Opt. Vol. 38, No. 34, pp. 7164-7166, 1999.
11. J. H. Lehman and C. L. Cromer, "Optical trap detector for calibration of optical fiber powermeters: coupling efficiency," Appl. Opt, 31, 6531-6536, 2002.
12. I. Vayshenker, X. Li, D. J. Livigni, T. R. Scott, C. L. Cromer, "Optical fiber power meter calibrations at NIST," NIST Special Publication 250-54, 2000.
13. "ISO, Guide to the Expression of Uncertainty in Measurement," International Organization for Standardization, Geneva, Switzerland, 1993

A long-period undulator at the Metrology Light Source as an IR radiation source

R. Klein, A. Gottwald, A. Hoehl, R. Müller, M. Ries and G. Ulm

Physikalisch-Technische Bundesanstalt (PTB), Berlin, Germany
Corresponding e-mail address: roman.klein@ptb.de

At the electron storage ring Metrology Light Source (MLS) the Physikalisch-Technische Bundesanstalt operates a long-period undulator with a period length of 180 mm. In combination with the rather low electron energy of the MLS, this gives the unique possibility of generating undulator radiation in the IR spectral region, with a potential extension of the spectral range into the FIR. The status and perspectives are reported.

INTRODUCTION

For more than a quarter of a century the Physikalisch-Technische Bundesanstalt (PTB) has been performing synchrotron radiation-based radiometry and metrology [1], using various electron storage rings. Since the start of operation of its own electron storage ring, the Metrology Light Source (MLS) [2], PTB has at hand an ideal source which can be flexibly operated, e.g. at any electron beam energy between 105 MeV and 630 MeV or at any electron beam current from 1 pA (single electron) up to 200 mA. Installed at the MLS is an undulator with a period length of 180 mm (U180) [3], which, in combination with the tuneable electron energy, can span a wide wavelength range, reaching from the VUV as far as into the FIR spectral region. In this paper the properties of the undulator radiation in the MIR and FIR spectral range are described, with the intention of a possible radiometric use in the wavelength range above 10 µm, which is only sparely covered by laser lines.

THE UNDULATOR U180

The U180 is an electro-magnetic undulator and its main parameters are summarized in Table 1. The U180 radiation can be exploited at several beamlines [4, 5], so, e.g., direct U180 radiation or radiation deflected by a plane mirror can be used. The wavelength of the nth undulator harmonics is given by

$$\lambda_n = \frac{\lambda_{undulator}}{2n\gamma^2}\left(1+\frac{K^2}{2}+(\gamma\Theta)^2\right)$$

with $\lambda_{undulator}$ being the undulator period length, K the undulator parameter and $\gamma = W / m_e c^2$, with W being the electron energy and $m_e c^2$ the electron rest mass; Θ is the observation angle with respect to the forward direction ($\Theta = 0$). The wavelengths of the harmonics are therefore tuneable by variation of K or W, a larger K or a lower W shifts the harmonics to longer wavelengths. The undulator radiation spectral intensity can be calculated numerically. The radiation is emitted into a narrow cone in the vertical and horizontal direction, the characteristics of which rapidly changes with wavelength. For higher K, many harmonics are present, so that for specific applications some kind of wavelength selection might be necessary by filters or by a dispersive element.

Table 1. Main undulator parameters.

Parameter	value
Period length / m	0.18
Number of full periods	21
Max. K-parameter	8.3
Max. current	150 A
Max. magnetic induction	0.495 T
Wavelength of 1st harmonics	
K = 0.1, W = 630 MeV	60 nm
K = 8.0, W = 630 MeV	2.0 µm
K = 8.0, W = 105 MeV	70.2 µm

CURRENT STATUS

Figure 1 shows the absolute measurement of the direct, undeflected U180 radiation by means of a well-characterized filter radiometer (FR) at 1.595 µm centre wavelength [6]. The 1st undulator harmonics

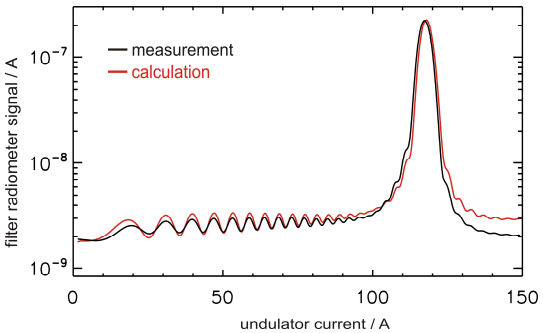

Figure 1. U180 radiation measured with a calibrated filter radiometer compared to the corresponding calculation.

was spectrally tuned by variation of K (by means of varying the undulator current) through the band pass of the FR and the measured FR signal was compared to that calculated from the undulator, storage ring and geometry parameters. A good absolute agreement was found, which confirms that the U180 performance can be properly modelled. Figure 2 shows the U180 spectrum measured with a FTIR at the U180-IR beamline [5]. This beamline is currently terminated by a ZnSe-window which only transmits wavelengths shorter than about 20 μm. Therefore, the undulator and storage ring parameters were chosen in such a way, that the 1st undulator harmonics wavelength is just transmitted. The first and higher harmonics can clearly be identified as expected.

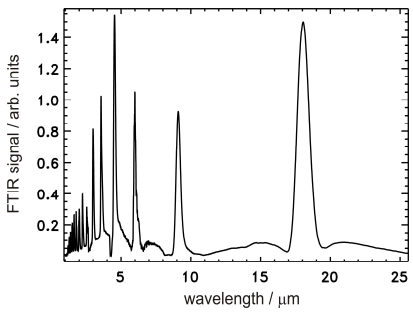

Figure 2. Undulator spectrum measured with a FTIR at 200 MeV electron energy and $K = 7.6$.

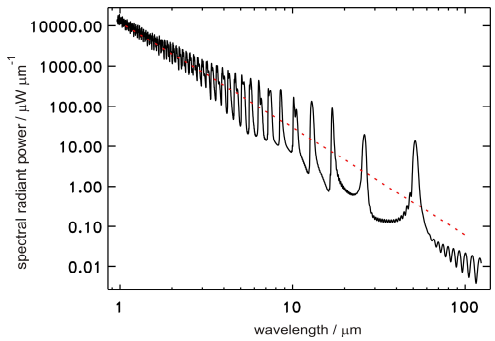

Figure 3. Calculated undulator spectrum at 125 MeV electron beam energy for $K = 8$. The dashed red line shows the spectral radiant power calculated for the same geometry for the U180 considered as a series of bending magnets.

FUTURE OPTIONS

Up to now, the MLS has been optimized for undulator operation at electron energies above 200 MeV. Since the undulator operation in the storage ring is more demanding for lower electron energies, a first step will be the optimization of the storage ring performance at a lower electron energy of, e.g., 125 MeV. Then, the 1st harmonics for $K = 8$ is at $\lambda_1 = 54$ μm. Figure 3 shows the spectrum calculated for these parameters and - as for all following figures - an electron beam current of 100 mA. The angular acceptance (h: ±5 mrad, v: ±3.33 mrad) was chosen to accommodate almost the entire radiation cone. Since the angular spread is rather large, provision must be taken to reduce diffraction during application. Figure 4 shows, e.g., the radiant intensity at 54 μm. The wavelength of the 1st harmonics can be further shifted to a longer wavelength by a reduction of the electron beam energy. Ultimately at 105 MeV, the 1st harmonics is at 70 μm, even longer wavelengths are possible by a slight off-axis observation. Figure 5 shows the calculated available radiant power in the 1st harmonics for the U180 operated at $K = 8$, the wavelength is varied by tuning the electron energy from 630 MeV to 105 MeV.

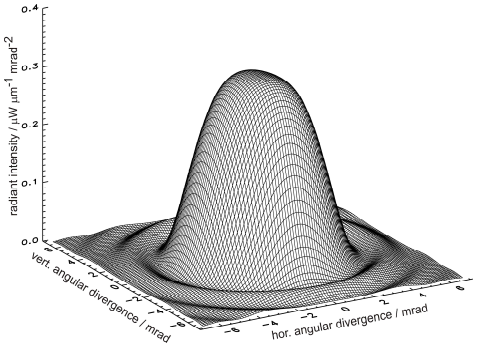

Figure 4. Calculated radiant intensity at 54 μm wavelength (λ_1) for the spectrum as shown in Fig. 3.

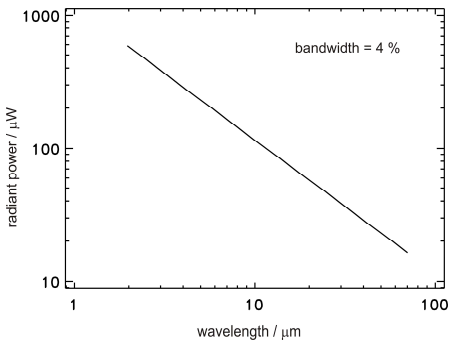

Figure 5. Calculated radiant power in the 1st harmonics as a function of its wavelength for angular acceptance of the entire radiation cone. The bandwidth $\Delta\lambda/\lambda = 4$ % roughly relates to the spectral width of the 1st harmonics.

REFERENCES

1. B. Beckhoff et al., Phys. Status Solidi B 246, 1415, 2009.
2. R. Klein et al., Phys. Rev. ST – Accel. Beams 11, 110701, 2008.
3. R. Klein et al., J. Synchrotron Rad 5, 451, 1998.
4. R. Klein et al., Metrologia 46, S266, 2009.
5. R. Müller et al., AIP Conf. Proc. 1214, 32, 2010.
6. M. Ries, Diploma thesis, Humboldt University, Berlin, Germany, 2010.

Heat-Pipe Temperature Stabilisation System for Detectors and other Calibration Artefacts

R Mason, K M Nield, F Shindo, D R White

Measurment Standards Laboratory of New Zealand, Industrial Research Ltd, Lower Hutt, New Zealand
Corresponding e-mail address: k.nield@irl.cri.nz

A temperature stabilisation system, based on a pair of heat-pipes and a commercially available thermoelectric control system, has been developed for the temperature control of photodetectors. Initial measurements with the system show that stability better than 10 mK can be achieved over at least a 12 hour period. The largest temperature differences observed between diodes in a five-element silicon trap detector were no greater than 25 mK

INTRODUCTION

Historically, at MSL we have chosen not to temperature control the silicon detectors used for the establishment of our radiometric scales, other than in photometers. This has been possible because the temperature sensitivity of the response of silicon detectors over the visible wavelengths is small [1], and in the ultraviolet region the impact of temperature variations on the accuracy of the MSL scale has been modest compared with other errors in the measurement process. However more recently, due to to improvements in the realization of our detector responsivity scale and a need to extend this scale beyond 900 nm, we have initiated a study into the temperature sensitivity of response of our various multi-element configured silicon photodiode detectors from 240 nm to 1000 nm [2]

This note describes the temperature stabilisation system developed to provide a known and uniform temperature in the area occupied by all the detectors housed in either single- 3- or 5-element silicon trap detector systems [3, 4].

HEAT-PIPE SYSTEM

A heat-pipe is a heat transfer system that exploits the latent heat associated with evaporation and condensation to efficiently transfer heat between locations. The effective thermal conductivity of heatpipes exceeds that of copper by many orders of magnitude [5]. Two heatpipes are used for the application described here (see Figure 1). The first heatpipe is the enclosure for the detector housing and gives a much greater temperature uniformity than possible with a water jacket. Initially, we fabricated a brass heat-pipe filled with acetone as the working fluid, which can be efficiently used from -50 °C to 145 °C [6, 7]. Subsequently, we used pre-fabricated heat-pipe sheets [8] (also using acetone as the working fluid) that can be formed to fit the the detector housing (as shown in Figure 1).

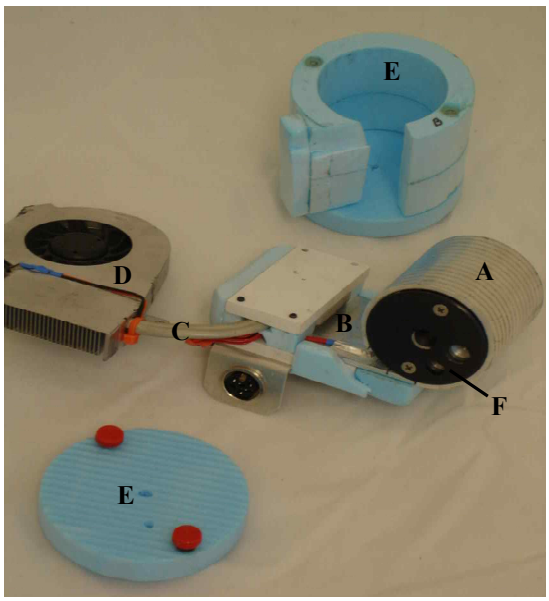

Figure 72. Heat-pipe system using (A) pre-fabricated heat pipe-sheet shaped to fit the detector housing, (B) Peltier element, (C) secondary heat-pipe, (D) fan, (E) thermal insulation. A 5-element trap detector (F) is shown inserted into the primary heat-pipe.

The heating and cooling for the system is provided by a Peltier device mounted on the base of the heat-pipe. One of the advantages of Peltier devices is that they provide both heating and cooling and can therefore work near ambient temperatures. An Electron Dynamics Peltier driver and temperature controller (model TCM-5) [9] was used to drive the system. A 100 ohm platinum resistance temperature sensor (PRT), affixed to the heat-pipe, was used to monitor the temperature for the controller.

A second heat-pipe assembly is used to sink heat to and from the rear side of the Peltier device, ensuring that there is a low-thermal-impedance heat sink for the Peltier device and that performance of

the Pelteir device is not compromised by thermal feedback. The second heatpipe and heat sink assembly is cooled by a fan.

MEASUREMENT RESULTS

During the assessment of the temperature sensitivity of response of a variety of detectors the heat-pipe assemblies were operated in excess of 12 hours at time. Over such time periods, while temperature variations in laboratory were of the order of ± 600 mK peak to peak, the temperature of the detectors remained within 10 mK of their set-point (as shown on Figure 2). Averaged results suggested that the control system reduced the influence of

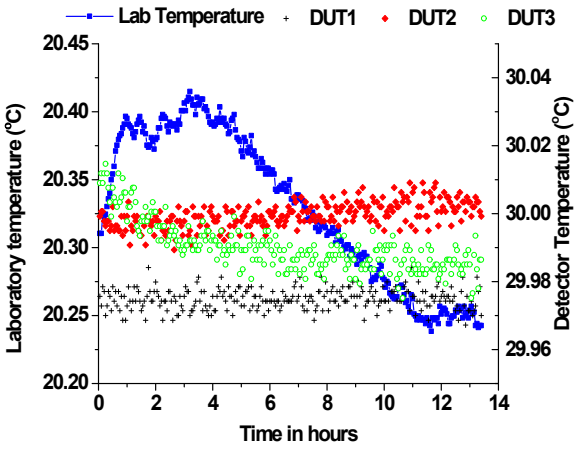

Figure 2. Laboratory temperature stability compared to temperature stability of the heat-pipe housed detectors.

variations in the ambient temperature by a factor of about 100.

The temperature uniformity of the heat-pipes was checked within the frame of a 5-element trap detector using two independent methods. The temperature uniformity was assessed by measuring the temperature of two photodiodes housed in the trap frame with spatial position assumed to span the largest expected temperature distribution. In the first measurement, the temperature of each diode was monitored with the same calibrated PRT with the heat-pipe running at constant temperature. A difference of 60 mK was observed between the two diodes. In the second method, each photodiode was connected to one of the legs of a thin (0.25 mm diameter) differential Type-T thermocouple. For a Type-T thermocouple, the Seebeck coefficient is approximately 40 μV/K. The voltage arising from the temperature gradient was recorded with a nanovolt DVM: all connections between the thermocouple and the DVM were made in copper with the joins insulated with bubble wrap to reduce thermal EMFs. A zero offset of 0.5 μV in the measurement system was determined by immersing the thermocouple legs in an ice point. For all operating temperatures in the range 20 °C to 35 °C the temperature gradient observed in the various detectors and heat-pipes assemblies was less than the resolution of the measurements, approximately 25 mK (1 μV).

CONCLUSIONS

A novel system for the temperature stabilisation of photodetectors has been designed utilising a combination of heat-pipes and thermoelectric heating/cooling. The prototypes applied to a five-element trap detector have demonstrated 24-hour temperature stabilities within 10 mK and temperature uniformities of better than 25 mK.

Other applications proposed for this system have been: the stabilisation of photometers, where uniformity of temperature u from aperture entrance, to filter and detector could be useful; and the stabilisation of capacitors for MSL's Electrical Standards group.

Currently the system is being used in the Quantum Candela Project, T1 J2.3 of the iMERA Plus Programme [10], to improve the detectivity of standard transfer detectors in the calibration of photon counting systems at low level fluxes (in the order of 500 kc/sec).

REFERENCES

1. F Lei and J Fischer, "Characterization of Photodiodes in the UV and Visible Spectral Region Based on Cryogenic Radiometry", Metrologia, 30, 297-303, 1993.
2. F Shindo et al., "Temperature Coefficients of Multi-Element Trap Detectors", submitted to Newrad 2011.
3. N Fox, "Trap Detectors and their Properties", Metrologia, 28, 197-202, 1991.
4. A Bittar et al., "Five-Element Reflection Trap Detectors as Transfer Standards for Monochromator, Laser, and Filter Radiometry", Newrad 1999, Madrid, Spain.
5. C A Busse et al., "The Gas-Controlled Heat Pipe : A Temperature-Pressure Transducer", in Temperature Measurement 1975, edited by B F Billing and T J Quinn, 428-438, Institute of Physics, London, 1975.
6. P D Dunn and D A Reay, "Heat Pipes", 4th edition, Pergamon Press, 1996.
7. A Faghiri, "Heat Pipe Science and Technology", Taylor & Francis, Bristol, 1995.
8. http://www.amecthermasol.co.uk/
9. http://www.electrondynamics.co.uk/e/
10. http://www.quantumcandela.org/project.html

Realization of candela using trap photometer at two wavelengths

Liu Hui, Lin Yandong, Yu Jing, lv liang, Ma Yu, Liu Zilong, Jiang Xiaomei, Ma Yan, Zhao Weiqiang,

Liu Jian

National Institute of Merology, Bei Jing, China
Corresponding e-mail address:liuhui@nim.ac.cn

A kind of photometric trap-detector was developed, and used to realize the luminous intensity unit candela in two wavelengths 514.54nm, 632.82nm at NIM. The candela newly realized essentially agrees with our current maintained unit which is based on room-temperature radiometer and maintained by a group of incandescent lamps. The deviation of the realization value at two wavelengths is 0.14%, and to the current unit is 0.18%.

INTRODUCTION

Candela is one of the seven base units of SI unit system, which is adopted by CGPM in 1954 and formed base for all photometric quantities[1]. In 1979, CGPM redefined candela by relating it to the radiometric unit (watt). With the new definition, candela has been realized using detector-based standards instead of source based standard [2].

At NIM, luminous intensity unit of candela was realized using a group of room-temperature electrically calibrated radiometers and maintained by BDQ8 and BDQ7 gas-filled tungsten filament lamps since 1983[3]. Cryogenic radiometers which could provide much lower measurement uncertainty than room-temperature radiometer, and improvements in spectral-responsivity have also occurred with the introduction of trap detectors[4], many national laboratories now trace luminous intensity quantities to this device. The measurement uncertainty of spectral responsivity of trap detector using cryogenic radiometer arrive 0.03%(k=2) at NIM, opportunity was taken to re-determine candela before the new international luminous intensity comparison.

DESCRIPTION OF TRAP PHOTOMETRIC - DETECTOR

In order to realize luminous intensity unit of candela and establish detector-based photometric measurement system, a kind of photometric trap detector was designed, characterized and used. The structure of the detector is shown in Fig. 1.

The basic components of this detector is an aperture, a V(λ) filter and a photodiode based trap detector, special designed mechanic ring make the trap detector easy to be re-assembled with the V(λ) filter and the aperture. Absolute responsivity of the trap detector was measured by cryogenic radiometer using two laser sources, Ar-Kr (514.54nm) and He-Ne (632.82nm) respective. The absolute spectral transmittance of the V(λ) filter traced to the NIM spectral transmittance standard. Aperture area was measured by the length division of NIM.

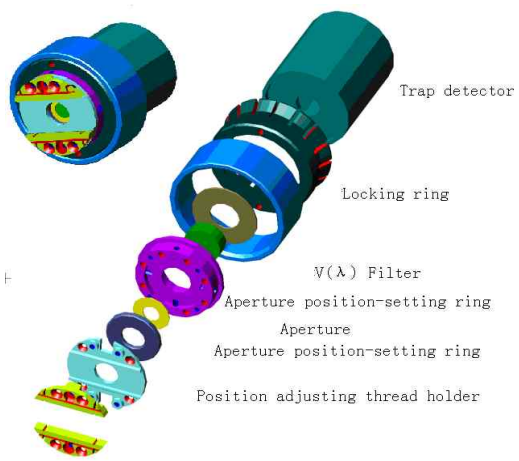

Figure 73. Structure of the photometric trap detector.

REALIZATION THE LUMINOUS INTENSITY UNIT CANDELA

The realization experiment carried out on 7-meter long photometer bench. The luminous intensity lamp and detector were mounted on stages having five degrees of freedom that allows accurate positioning the lamp filament and the aperture of the detector perpendicular to the optical axis of the photometer bench, using an optical image system. The BDQ7-82-563 luminous intensity is placed at a distance l(m) from the detector, which has a limiting aperture area of A(m^2) then the luminous intensity of source I(cd) can be calculated from the measured

photocurrent I(A) of the detector according to the equation 1.

$$I_V = E_V \cdot l^2 = \frac{K_{(\lambda)} F I l^2}{s(\lambda) A} \quad (1)$$

Where K(λ) is the spectral luminous efficiency of photopic vision at the wavelength λ, s(λ) is the transmittance of V(λ) filter at wavelength. λ.

$$F = \frac{\int_{380}^{780} P(\lambda) V(\lambda) d\lambda}{\int_{380}^{780} P(\lambda) R_{rel}(\lambda) d\lambda} \quad (1).$$

F is color correction factor, the effect of difference between the V(λ) curve and the relative spectral responsivity of the trap photometric detector. P(λ) spectral power distribution of the BDQ7-82-563, R_{rel}(λ) relative spectral distribution of the photometric detector. The character of the photometric detector and calculate luminous intensity show in table 1.

Table 27. Character of the photometric detector and derived luminous intensity

Parameter	Wavelength: 632.82nm	Wavelength: 514.54nm
K(λ)	160.7338659	400.8984738
F	1.03553	1.03553
I(A)	2.3542E-07	2.3542E-07
l (m)	4.193023	4.193023
s (λ)	0.50844	0.40688
Diameter of the aperture (m)	0.00599841	0.00599841
Spectral transmittance of the V (λ) filter	0.1030737	0.321659
Luminous intensity (cd)	465.18	464.59
Deviation from the current value	0.18%	0.04%

CONCLUSION

A kind of trap photometric detector was developed , the basic components of it is an aperture, a V(λ) filter and a photodiode based trap detector, special designed mechanic ring make the trap detector easy to be re-assembled with the V(λ) filter and the aperture. BDQ7 incandescent lamp was used to conduct the realization experiment. The responsivity of the trap detector and the transmittance of the V(λ) filter measured at the wavelength 514.54nm and 632.82nm. The candela was realized at these two wavelengths, deviation of them is not significantly different from the current room-temperature radiometer and well within the uncertainty of components. Various sources of uncertainties and their contributions to the luminous intensity unit of candela are listed as an uncertainty budget in Table 2. The basis realization of candela at NIM will transferred to power measurement with a cryogenic radiometer at the imminent international comparison.

Table 2. Standard uncertainty components for the realization of luminous intensity unit of candela

Parameter	Standard uncertainty
Relative spectral responsivity of photometric trap detector	0.1
Spectral power distribution of lamp	0.1
Absolute responsivity of trap detector	0.015
Spatial non-uniformity of trap detector	0.005
Transmittance of V(λ) filter	0.075
Aperture area	0.01
Distance measurement	0.022
Lamp Current	0.09
Alignment repeatability of the detector	0.01
Stray light	0.01
Photocurrent measurement	0.025
Combined standard uncertainty	**0.20**

REFERENCES

1.Ohno Y. Improvement photometric standards and calibration procedures at NIST. J Res Natl Inst Stand Technol 1997;102:323-31

2. Farhad Samedov, Filter-radiometer-based realization of candela and establishment of photometric scale at UME, Optical and lasers in Engineering 43(2005) 1252-1266

3. Gao Zhizhong, Realization of the Candela by Electrically Calibrated Radiometers,Metrologia, 1983, 19.

4. J.L.Gardner, New Realization of the candela, Metrologia, 1998,35,235-239.

Measurement of Angular Nonuniformity of an Integration Sphere under 2π Illumination Geometry

Kenji Godo[1], Kazuki Niwa[1], Tatsuya Zama[1], Yuqin Zong[2], and Yoshi Ohno[2]

[1] *National Metrology Institute of Japan, National Institute of Advanced Industrial and Technology, 1-1-1 Umezono, Tsukuba, Ibaraki, JAPAN*

[2] *National Institute of Standards and Technology, 100 Bureau Drive, Gaithersburg, MD, USA*

Corresponding e-mail address: kenji-goudo@aist.go.jp

We measured angular nonuniformity of a 2.5 m integrating sphere under 2π illumination geometry for measurement of lighting emitting diodes (LED) and solid-state lighting (SSL) products. An LED-based compact beam scanner was developed and used for this measurement. The beam scanner was temperature-controlled and was stable within 0.1 % over 8 h measurement time. The correction factors for angular nonuniformity associated with various LED beam profiles were analyzed. The difference between the correction factor for a 30 degree narrow beam LED and that for a 150 degree wide beam angle LED is less than 0.35 % for the 2.5 m integrating sphere.

INTRODUCTION

Many SSL sources have large heat sinks and have only forward light. Therefore, integrating spheres are increasingly used to measure such light sources for total flux (angular-integrated) under 2π illumination geometry where a light source is mounted on a sphere port. Similar to the conventional 4π geometry method by which the light source is mounted at the center [1][2], the sphere needs to be characterized for angular nonuniformity under 2π illumination geometry in order to correct the error arising from the difference of the beam profiles of a standard source and a test source. However, such characterization has never been performed, resulting in an unknown uncertainty component, which may be significant.

In this work, we describe a compact beam scanner which can be used to measure the angular nonuniformity of an integrating sphere under the 2π geometry. The angular nonuniformity of the NIST 2.5 m integrating sphere under 2π illumination geometry is presented

DEVELOPMENT OF THE BEAM SCANNER

Figure 1 shows the beam scanner for measurement of angular nonuniformity of an integrating sphere under 2π illumination geometry. The scanning beam is a collimated white high-power LED source. The beam scanner rotates with inclination angle from 0 deg to 90 deg and azimuth angle from 0 deg to 360 deg. The beam scanner is mounted on a tripod and is positioned onto a port of the integrating sphere.

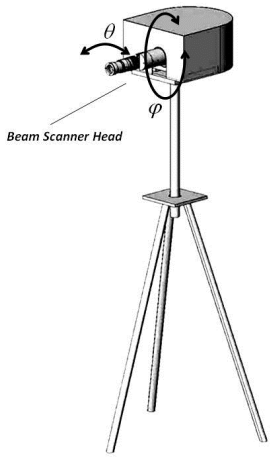

Figure 1. Beam scanner for measurement of angular uniformity of a sphere under 2π illumination geometry

The LED source is temperature-controlled by a thermal-electrical cooler is and its stability is less than 0.1 % over the 8 h measurement time. The angular nonuniformity is measured with a scanning step size of $\Delta\theta$ = 5 deg and $\Delta\phi$ =5 deg.

ANGULAR NONUNIFORMITYOF THE NIST 2.5 M INTEGRATING SPHERE

The angular nonuniformity of the NIST 2.5 m integrating sphere was measured under 2π illumination geometry. Figure 2 shows the arrangement of the NIST 2.5 m integrating sphere. Baffle 3 and Baffle 4 were required and added for the 2π illumination geometry. The port near the Baffle 4 was used for mounting light sources and the beam scanner.

The angular nonuniformity of the 2.5 m integrating sphere is plotted in Figure 3. The locations of Baffle 3, Baffle 4, the auxiliary lamp, and the lamp post can be easily identified.

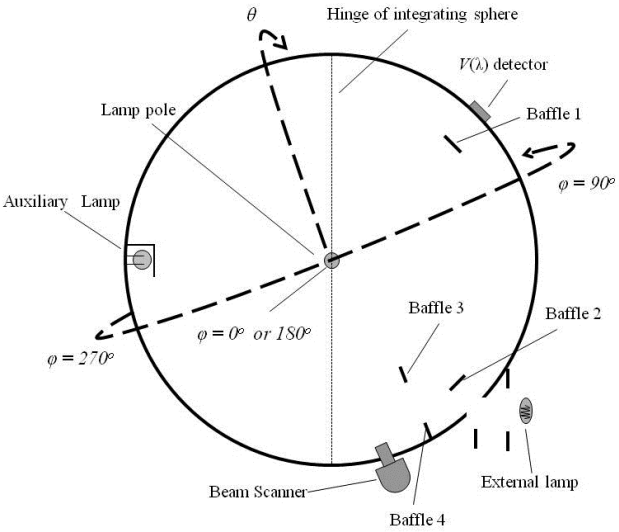

Figure 2. NIST 2.5m integrating sphere system arranged.

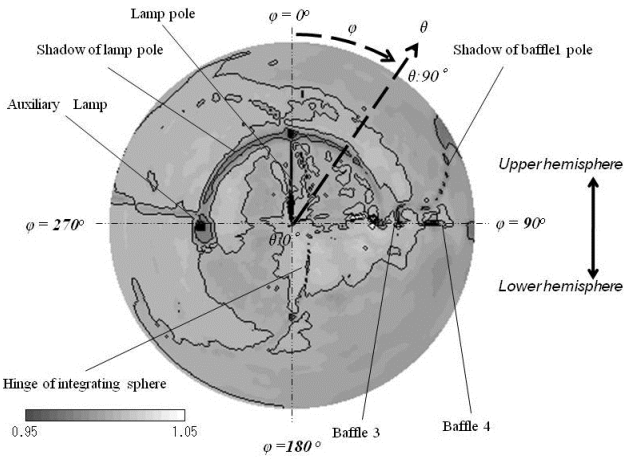

Figure 3. SRDF of NIST 2.5 m integrating sphere with the beam-scanner for the 2π-geometry. The radius of circle mapping is vertical angle (θ) of beam-scammer, the central angle of circle mapping indicate horizontal angle (ϕ) of it.

The correction factors for angular nonuniformity of the NIST 2.5 m integrating sphere. is plotted in Figure 4. The beam angle of the standard source is 120°. Figure 4 shows that the error due to the angular nonuniformity of the sphere is less than 0.35 % when the beam angle of a test source changes from 30° to 150°.

CONCLUTION

Integrating spheres are increasingly used under 2π illumination geometry for measurement of SSL sources. We developed a compact beam scanner for measurement of angular nonuniformity of an integrating sphere under 2π illumination geometry. By knowing the angular nonuniformity of an integrating sphere, the measurement error arising from the angular nonuniformity can be analyzed and corrected.

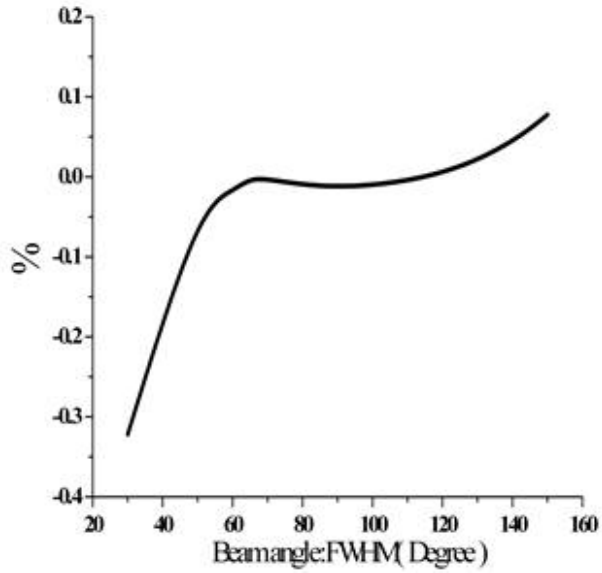

Figure 4. The calculation results of a spatial correction factor for models of varied beam angle.

REFERENCES

1. IES LM-79-08, Approved Method: Electrical and Photometric Measurements of Solid-State Lighting Products, IESNA, 2008.

2. Y. Ohno, R.O. Daubach, Integrating Sphere Simulation on Spatial Nonuniformity Errors in Luminous Flux Measurement, Journal of the Illuminating Engineering Society, 30-1, 105-115, 2001.

The evaluation of two InGaAsP/InP Geiger-mode avalanche photodiodes at NPL

E. Theocharous[1], M. A. Itzler[2], C. J. Chunnilall[1], J. Cheung[1] and J. Mountford[1]

[1]*National Physical Laboratory, Teddington, UK*
[2]*Princeton Lightwave Inc., Cranbury, USA*
Corresponding e-mail address: e.theo@npl.co.uk

There is a wide and growing demand for photon-counting detectors, driven by the need to measure low radiant powers. The NPL uniformity of response and linearity of response facilities have recently been upgraded to accommodate photon counting detectors. Two nominally identical Single Photon Avalanche Photodiode photon counting systems based on InGaAsP/InP single-photon avalanche photodiodes have been evaluated. It was found that they exhibited a spatially non-uniform response which was dependent on the applied bias voltage, as well as nonlinearity which was due to pulse collisions.

INTRODUCTION

The performance of two nominally identical Single Photon Avalanche Photodiode (SPAD) Model id400 photon counting systems based on InGaAsP/InP single-photon avalanche photodiodes was evaluated. Each id400 detection system is based on the PGA285 avalanche photodiode fabricated by Princeton Lightwave. The two systems were designated as id400-A and id400-B detection systems. Each InGaAsP/InP Avalanche PhotoDiode (APD) had a circular active area of 80 µm diameter and was sensitive to radiation in the 900 nm to 1150 nm range. The SPADs were cooled to –40 °C using 3-stage thermoelectric coolers. They were operated under three different single photon detection probability values (7.5 %, 15 % and 30 %), which correspond to three different bias voltages. The systems were investigated for 1 µs and 10 µs dead-time settings. Both id400 detection systems were operated in the "free-running" Geiger mode.

SPATIAL UNIFORMITY OF RESPONSE

The spatial uniformity of response was measured on the NPL spatial uniformity of response characterisation facility [1]. An 8 µm diameter spot was used to illuminate the active area of the test detector. The F/number of the incident beam was limited to F/30. A bandpass filter whose transmission peaked at 1064 nm (Full Width Half Maximum of 15 nm) was used to spectrally filter the output of the tungsten filament source.

Figures 1 and 2 show the spatial uniformity of response for the id400-A SPAD for single photon detection probability values of 7.5 % and 30 % respectively (all plots correspond to measurements using a 10 µs dead-time). Figures 1 and 2 confirm the significant influence of the single photon detection probability value on the spatial uniformity of response of this detector.

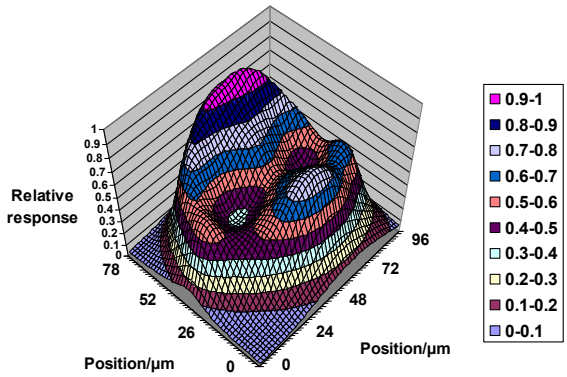

Figure 1: The spatial uniformity of response of the id400-A detector measured at 1064 nm, with 10 µs dead-time and a 7.5 % single photon detection probability value.

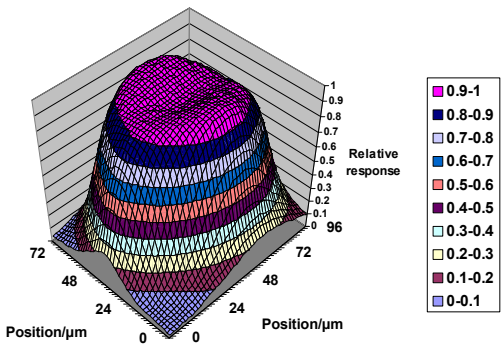

Figure 2: As in Figure 1 but with a 30% single photon detection probability value.

When the spatial uniformity of response of the id400-A detector was measured at 1064 nm, with 1 µs and 10 µs dead-times (a 7.5 % single photon detection probability value was used for both occasions), the response exhibited near identical profiles confirming that the dead-time setting had no significant effect on the spatial uniformity of this detector. Similar behaviour was observed for id400-

B SPAD. Repeating the measurements using a 900 nm band-pass filter showed that the spatial uniformity of response of both detectors did not to vary significantly with wavelength. The spatial uniformity of the id400-A detector was measured (using a 10 μs dead-time and a 7.5 % single photon detection probability) for three different output count rates (33,000, 13,000 and 4,800 counts per second). The responses had similar profiles, hence the spatial uniformity of response of this detector was not significantly dependent on the output count rates in the 4,800 to 33,000 counts per second range. The spatial uniformity of response characteristics of id400-B (which was fabricated on the same wafer as id400-A) were also evaluated and found to be quantitatively similar to those of id400-A.

The strong dependence of the spatial uniformity of response of detectors id400A and id400 B on the single photon detection probability value has been linked to the non-uniformity in the breakdown voltage V_b across the active area of the SPAD [2]. The planar diode structure is fabricated using a dopant diffusion technique, and a quasi-cylindrical junction profile that forms at the perimeter of a planar diffusion tends to enhance the local electrical field amplitude. Due to the very sensitive dependence of avalanche gain on electric field, this local field enhancement in the device periphery leads to higher avalanche gain at the device edge and to the so-called "edge breakdown" effects. A full discussion on the origins of these effects can be found elsewhere [2].

LINEARITY OF RESPONSE

The linearity of response characteristics of the id400 systems were evaluated on the NPL detector linearity of response characterisation facility [1] which measures the linearity factor of photodetection systems using the "flux-superposition" method. Figure 3 shows the plot of the linearity factor of id400-A as a function of the output count rate with the single photon detection probability value set at 7.5 % and dead-time settings of 1 μs and 10 μs (note logarithmic abscissa). The 1 μs dead-time data follow a logarithmic fit. The two sets of data agree for count rates below about 4,000 counts per second but diverge for higher count rates, with the data acquired with a 10 μs dead-time exhibiting a much higher non-linearity (the value of the linearity factor moves away from unity).

Figure 3 indicates that there are two mechanisms responsible for the non-linear behaviour of the id400-A detection system. The first is logarithmic and occurs for all output count rates evaluated, when the dead time was 1 μs. The same mechanism was also observed for output count rates below 4000 counts per second when the dead time was 10 μs. However, for output count rates higher than 4000 counts per second (and 10 μs dead time) a second, stronger non-linear mechanism becomes apparent. A clue to the origin of the larger non-linearity is provided by treating the linearity factor for a 1 μs dead-time as a background, i.e. it is subtracted from the non-linearity measured for a 10 μs dead-time. The difference was shown to arise due to pulse collisions [2,3] for the 10 μs dead time, assuming Poisson statistics for the photon arrival times. This second mechanism is as yet not understood.

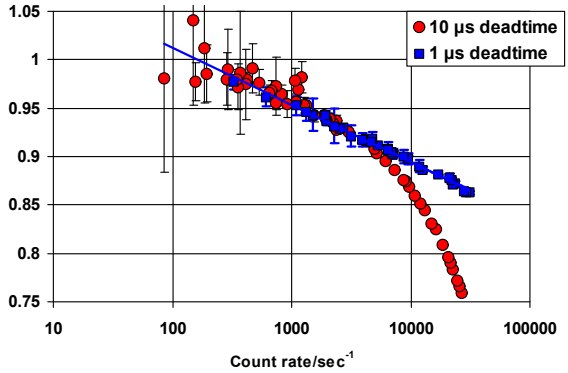

Figure 3: The linearity factor of the id400-A detector measured at 1064 nm, 1 μs and 10 μs dead-time (single photon detection probability set to 7.5 % for both plots).

REFERENCES

1. E. Theocharous, J. Cheung, C. Chunnilall, "Characterisation of photon counting systems at NPL", Photon Counting Techniques IV, SPIE 7681, 768105 [1-12], 2010.
2. E. Theocharous, M. A. Itzler, J. Cheung and C. J Chunnilall, "The characterisation of the linearity of response and spatial uniformity of response of two InGaAsP/InP Geiger-mode avalanche photodiodes" IEEE Journal of Quantum Electronics, 46,(11), 1561-1567, 2010.
3. D. P. Donovan, J. A. Whiteway and A. I. Carswell, "Correction for nonlinear photon-counting effects in lidar systems", Applied Optics, 32, 6742-6753, 1993.

Traceable calibration of Si-avalanche photodiodes using synchrotron radiation

I. Müller, R. Klein, J. Hollandt, G. Ulm and L. Werner

Physikalisch-Technische Bundesanstalt (PTB), Berlin, Germany
Ingmar.Mueller@ptb.de

Calibration of single photon detectors traceable to primary standards, i.e. cryogenic radiometers, is difficult due to the very different optical power levels of power measuring classical radiation detectors and single photon detection systems. In this paper we present a new substitution method based on the unique properties of synchrotron radiation and the Metrology Light Source (MLS) of the PTB. The MLS is used as a light source with a dynamic range of 11 orders of magnitude to bridge the gap in optical power measurement between a cryogenic radiometer and a single photon detector.

INTRODUCTION

There is a growing demand for traceable calibration of single photon detectors (SPDs). The emerging field of quantum cryptography and quantum communication with its high security concerns depends on certified/calibrated systems. For instance, the SARG04-protocol [1], applied in commercial quantum key distribution (QKD) systems, requires detectors with known quantum efficiency (QE) to establish secure communication [2]. Therefore traceable calibration of SPDs is a key component for secure communication of the users of QKD systems. The QE of detectors used in a commercial QKD system directly influences performance and operation distance of such a system and is a figure of merit to compare systems.

To perform traceable calibrations of SPDs one can choose between traceability to a primary standard or to a primary method. For an SPD calibrated against a primary standard, relative standard uncertainties of 0.17 % (k=1) [3] have been reported. With a primary method as the "spontaneous parametric down conversion (SPDC)" relative standard uncertainties of 0.18 % [3] have been achieved. Both methods have some difficulties. For the substitution method, i.e. the measurement of the same optical power with a calibrated reference detector and a counting detector as the device under test (DUT), the DUT needs to be well characterized in terms of dead time. In addition, the linear response of the reference detector needs to be known down to a very low optical power level where precise measurements, especially linearity investigations of classical detectors, are hardly possible. In case the SPDC is used for this, the losses in the optical path and the uniformity of the applied crystal etc. need to be measured with high accuracy and limit the achievable uncertainty.

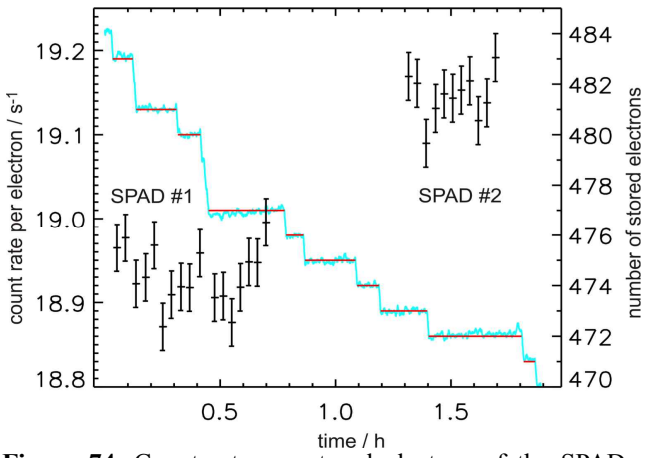

Figure 74. Count rate per stored electron of the SPADs (scattered points) and the number of stored electrons (line).

In this paper the unique properties of the synchrotron radiation from the electron storage ring MLS are used [4, 5] to perform the calibration of two single photon avalanche photodiodes (SPAD) traceable to a cryogenic radiometer.

MEASUREMENTS AND RESULTS

According to the Schwinger equation [6] the photon flux emitted by a storage ring is directly proportional to the number of stored electrons while the emitted spectrum is independent of the ring current [4, 5]. To perform the calibration of a free space SPD the synchrotron radiation has been monochromatized by a filter with a central wavelength of 650 nm, spatially limited by an aperture with a free diameter of 50 mm and focussed on the reference detector (trap detector) and the DUT. The beam focus had a FWHM of 40 µm. The number of photons per time and per stored electron in the focus is determined using a trap detector calibrated to a cryogenic radiometer at a ring current I_{high} of about 140 mA. At this level the ring current can be measured with a relative standard uncertainty of $5 \cdot 10^{-4}$ by parametric current transformers. The ring current is then reduced (I_{low}) to several hundred pA, i.e. several hundred stored electrons. The ring current I_{low} is the product of the revolution frequency and the

number of stored electrons determined via counting with cooled monitor diodes [5]. The count rate of the DUT (see Fig.1) per stored electron is measured for different electron numbers. Thus, the wide dynamic range of the MLS is used to bridge the gap between the optical power level used in classical radiometry to the few photons/s level. Using this calibration method no attenuators (that have to be characterized) are needed and the linearity of the transfer detection system (trap detector and amperemeter) has to be known only in the µW power regime.

The calibration of the SPAD is then performed by calculating the following relation:

$$QE^*_{APD} = \frac{count\ rate_{APD} / number\ of\ stored\ electrons\ (I_{low})}{photon\ rate_{Trap} / number\ of\ stored\ electrons\ (I_{high})} \qquad (1)$$

From the known spectral responsivity of the trap detector and the measured ring current I_{high} the photon rate per stored ring electron can be calculated. QE^*_{APD} is a first approximation of the quantum efficiency. Several corrections are needed to get the true QE of the SPAD and its uncertainty. First the photon statistic must be taken into account. This must be done for the reference detector and the SPAD that is unable to resolve the number of photons per pulse. Additionally the influence of the different sizes of active areas of

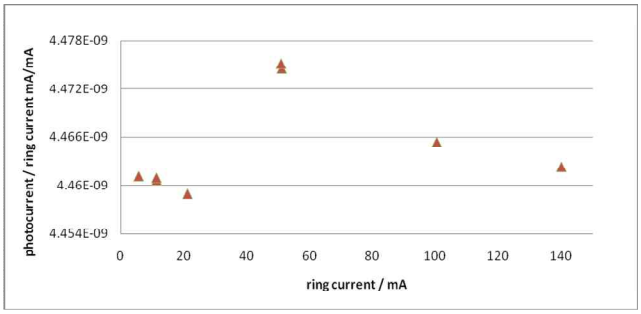

Figure 75. Stability of transmission of synchrotron radiation through a 200 µm pinhole. The spike at 50 mA ring current arises from a short instability of the cooling system of the MLS and is neglected.

the reference detector and the SPAD is estimated. Therefore two measurements were performed. First: The stability of the transmission of the synchrotron radiation through a pinhole of 200 µm diameter (about the active diameter of the SPAD) when normalized to the ring current was measured (see Fig. 2). With the results of these measurements the influence of the possibly different electron beam size at different electron beam currents can be estimated and thus, the necessary correction for the different detectors sizes of the trap and the DUT. The relative standard deviation of the measured photocurrents was below $5 \cdot 10^{-4}$, i.e. limited by the uncertainty of the ring current monitors. Second: The signal of a photodiode irradiated by the monochromatized synchrotron radiation passing through pinholes of 150 µm and 200 µm in diameter was measured together with the signal without pinhole to correct for the different detector sizes. Finally, the value for QE^*_{APD} still contains "false" counts due to after-pulsing. The uncertainty arising from this fraction of false counts contributes at this time with u=0.3 % (k=1) to the uncertainty budget. This uncertainty will be further reduced by additional measurements and corrections for after-pulsing.

Two SPADs have been calibrated at a wavelength of 650 nm. The preliminary achieved relative standard uncertainty of the corrected quantum efficiency QE is 0.37 % (k=1).

CONCLUSION

With the unique properties of synchrotron radiation and the broad dynamic range of 11 orders magnitude of the MLS two SPADs were calibrated at a wavelength of 650 nm traceable to a cryogenic radiometer. This is an independent method to calibrate single photon detectors that can be used in the VIS and NIR. Thus it allows for the validation of the results given by the SPDC method and the substitution method as given, e.g. in [3]. The achievable uncertainties of this method are only limited by the uncertainties of the measurement of the ring current and of the calibration of the reference detector. This method will further be used to perform calibrations of fibre coupled single photon detectors at 1.55 µm.

REFERENCES

1. V. Scarani, "Quantum Cryptography Protocols Robust against Photon Number Splitting Attacks for Weak Laser Pulse Implementations", Phys. Rev. Lett., 92, 057901, 2004.
2. C. Branciard, "Security of two quantum cryptography protocols using the same four qubit states" Phys. Rev. A, 72, 032301, 2005.
3. S. Polyakov and A. Migdall, "High accuracy verification of a correlated photon based method for determining photon counting detection efficiency", Optics Express, 15, 1390-1407, 2007.
4. R. Klein et al., "Operation of the Metrology Light Source as a primary radiation source standard", Phys. Rev. ST Accel. Beams, 11, 110701, 2008.
5. R. Klein et al., "From single photons to milliwatt radiant power – electron storage rings as radiation sources with a high dynamic range", ***Metrologia,*** 47**,** R33-R40, 2010.
6. J. Schwinger, "On the Classical Radiation of Accelerated Electrons", Phys. Rev., 75, 1912–1925, 1949.

Extending Single-Photon Optimized Superconducting Transition Edge Sensors Beyond the Single-Photon Counting Regime

T. Gerrits[1], B. Calkins[1], N. Tomlin[1], A.E. Lita[1], A. Migdall[2], S.W. Nam[1], R.P. Mirin[1]

1. National Institute of Standards and Technology, Boulder, CO, 80305, USA
2. National Institute of Standards and Technology, Gaithersburg, MD, 20899, USA and Joint Quantum Institute, Univ. of Maryland, College Park, MD 20742, USA

Photon number resolving transition-edge sensors (TES) are the cutting-edge enabling technology for high quantum efficiency photon number counting. The TES developed at NIST reliably show system detection efficiencies of more than 95%, and even approach 99% for individual detectors [1]. Recently, efforts to directly tying existing optical power measurements to measurements at the single-photon level are being considered by some metrology institutions around the world with the goal of better uncertainties. An initial step in this direction would be to explore how far existing detectors can be extended beyond their usual operating regimes. One promising candidate under consideration for connecting these two regions is the TES, as it functions as a microcalorimeter and is therefore able, in principle, to measure optical powers from the single-photon-regime to picowatt levels.

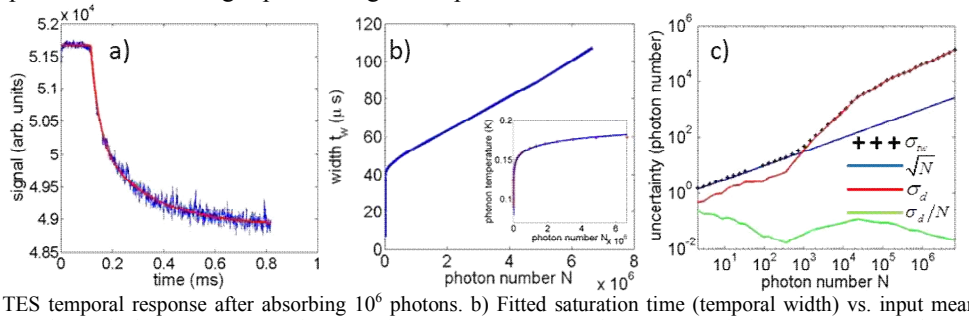

Fig. 1. a) TES temporal response after absorbing 10^6 photons. b) Fitted saturation time (temporal width) vs. input mean photon number; inset: phonon bath temperature as a function of input mean photon number. c) Uncertainties vs. input mean photon number; black crosses: total measured uncertainty; blue solid line: input state uncertainty; red solid line: inferred readout and detector uncertainty; green solid line: relative readout and detector uncertainty (σ_d/N)

We have tested a TES designed for single-photon counting in the regime far beyond the single-photon saturation point of the detector, *e.g.* > $7 \cdot 10^6$ photons or 0.9 pJ in a single pulse of coherent laser light. The laser pulse repetition rate is 1 kHz. The detection efficiency of this detector is 94 %, optimized for a wavelength of 1550 nm. After ~10 photons, the TES passes from the superconducting-normal transition region where single-photons are resolved to the normal resistance regime. At this point, all the current is diverted through the shunt resistor in our SQUID readout electronics and a constant voltage output is observed for a time t_w until the TES re-enters the transition region due thermal coupling of the electron system to the phonon system. t_w strongly depends on the amount of deposited energy, *i.e.* number of photons absorbed by the device. A typical TES trace after absorbing ~$5 \cdot 10^6$ photons is shown in fig. 1a. We fit the temporal response to a double-exponential whose decay is delayed by t_w (red solid line) [2]. When fitting all traces as function of input mean photon number (N), we find that t_w linearly depends on N, as can be seen in fig. 1b. We calculate that the electron system is heated to about 30 K after absorbing $7 \cdot 10^6$ photons. Due to the hot electron system and the long thermal decay of the phonon system, the phonon system experiences a cumulative increase in temperature. This is equivalent to raising the thermal bath temperature for the electron system. The phonon temperature rises steadily as a function of N until it reaches the electron superconducting transition temperature of ~180 mK at ~$7 \cdot 10^6$ photons. The inset in fig. 1b shows the inferred phonon temperature as a function of N. The dependence of the phonon temperature with respect to the laser pulse energy is: $T_{ph} = 0.009 \cdot \ln[2E/\gamma V] + 0.12$, where E is the energy absorbed by the TES, γ is the electron specific heat capacity and V is the TES volume. Figure 1c shows the uncertainty of t_w as a function of N. The uncertainty is given in units of photon number. The black crosses correspond to the standard deviation of t_w (σ_{tw}) obtained when fitting 20,000 individual traces to our model. Since, we use a coherent state input, the input state shot noise scales as $\sqrt{N}$ (solid blue line). After quadrature subtracting the input state shot noise from σ_{tw}, we obtain the readout plus detector uncertainty σ_d (solid red line). σ_d is below the input state shot noise up to $N \sim 1000$. Throughout the entire input state range, the relative uncertainty (σ_d/N) is below 10 % for the single-shot measurements (solid green curve).

We conclude that this technique can be very powerful when optical powers from the single-photon regime to the picowatt regime are used. The measured width depends linearly on N and the relative single-shot uncertainty remains below 10 % and can certainly be reduced by averaging traces.

References

1. Lita, A.E., A.J. Miller, and S.W. Nam, Opt. Express, 2008. **16**(5): p. 3032-3040.
2. Bennett, D.A., et al., Applied Physics Letters, 2010. **97**(10): p. 102504-3.

STUDYING PHOTON NUMBER DISTRIBUTION OF NV-CENTRE EMISSION IN NANO-DIAMONDS

W. Schmunk[1], M. Gramegna[3], G. Brida[3], I. P. Degiovanni[3], M. Genovese[3], H. Hofer[1], S. Kück[1], L. Lolli[3], M. G. A. Paris[4], S. Peters[1], M. Rajteri [3], A.M. Racu[1], A. Ruschhaupt[2], E. Taralli [3], P. Traina[3]

[1]*Physikalisch-Technische Bundesanstalt, Braunschweig, Germany*
[2]*Leibniz Universität Hannover, Hannover, Germany*
[3]*Istituto Nazionale di Ricerca Metrologica INRIM, Torino, Italy*
[4]*Università degli Studi di Milano, Milano, Italy*

Corresponding e-mail address: silke.peters@ptb.de

In the context of quantum communication security it is necessary to verify that a non-classical light source is a true single photon source. For that purpose several methods have been developed to analyse unknown quantum states, which in practise is still difficult. In the following contribution the photon number distribution of light emitted by NV-centres in diamond is studied by a detector based on a transition edge sensor (TES) and so-called 'on/off-measurements' in comparison to the $g^{(2)}(0)$-values obtained by Hanbury-Brown-Twiss (HBT)-measurements.

INTRODUCTION

One key element in further development of quantum information processing systems is the ability to prepare single photon states yielding high photon rates without diminishing communication security by multi-photon events, which an eavesdropper could exploit. In practise the use of attenuated laser light is a compromise between security and photon rate, due to its inherent photon statistics leading to an increasing probability of more than one photon being present. Also current single photon sources are imperfect, because of their non-vanishing autocorrelation $g^{(2)}(0)$-value at time-delay zero, implying residual multi-photon emission [1]. Thus, it would be desirable to verify that a given non-classical light source is a true single photon source (SPS).

In the present work we analyze the photon-number distribution of nitrogen vacancies (NV-centres) in nano-diamonds by a TES detector and the so-called 'on/off measurement'-technique. The investigated NV-centres provide photon rates up to 10^6 counts per second (cps) together with an excellent photo-stability at room temperature, what makes them useful for metrological characterisation of single photon detectors at appropriate spectral range [5].

EXPERIMENT

The emitted fluorescence of the investigated NV-centres was generated by pulsed or continuous wave laser excitation at a wavelength of 532 nm and observed by a confocal setup and spectral filtering at (697±37) nm. The second order correlation function was measured by a HBT interferometer consisting of two fibre coupled single photon avalanche photo-diodes (SPAD) and a fibre splitter.

To obtain the photon number distribution of NV-centres with different $g^{(2)}(0)$-values the diagonal elements of the optical density matrix were determined using a TES detector. This superconducting device produces an output signal proportional to the number of photons absorbed at a given wavelength and is described in detail in [2]. The detector was triggered by a signal of the pulsed laser at a frequency of 740 kHz in order to assure temporally well-defined photons striking the detector surface (TES energy resolution 0.41 eV @ 690 nm) .

Alternatively we performed 'on/off measurements' in order to obtain the photon statistics of a given signal using conventional non-photon-number-resolving SPADs. Their binary output is either 'on' or 'off' and a detector 'click' indicates the arrival of one or more photons. Information on the photon number distribution is gained from the ratio of 'no-click' events

$$p_0(\eta_\upsilon) = \sum_n (1-\eta_\upsilon)^n \rho_n \qquad (1)$$

to the total number of runs for different detection efficiencies η_υ, $\upsilon = 1,...,N$, where ρ_n is the probability of finding n photons. We consider the above expression as a statistical model for the parameters ρ_n

to be solved by Maximum-Likelihood estimations [3]. Experimentally the single photon source was operated in the pulsed excitation regime. Various detection efficiencies were modelled by inserting different calibrated neutral density filters on the optical path in front of the entrance of the SPAD.

RESULTS AND DISCUSSION

Figure 1 shows the photon number distribution of a given single NV-centre measured by the TES detector as well as using 'on/off'-statistics. The corresponding *g(2)*-function is depicted in the upper graph. By fitting the HBT-data according to [5] a $g^{(2)}(0)=0.06\pm0.03$ was determined. Thus, due to absent multi-photon components (see Figure 1(b)) it is comparable with a $g^{(2)}(0)$-value of approximately zero calculated from TES data by

$$g^{(2)}(0) = \sum_n (n^2 P_n - nP_n)/(\sum_n nP_n)^2. \quad (2)$$

Studying an additional centre, presumable consisting of two nitrogen vacancies, a non-zero two photon component resulting in a $g^{(2)}$-value of 0.5±0.1 was found in agreement to $g^{(2)}= 0.53\pm0.02$ measured by the HBT interferometer. The measurement uncertainties of the two methods are caused by the fitting process and a high fraction of trigger events, where no photon was detected. This results from the comparable low detection efficiency of the TES detector as well as an overall efficiency of the SPS setup in the range of 2% to 6%.

The photon number distributions measured by 'on/off–measurements' also exhibit a similar high zero-photon component, see Figure 1(c). From the experimental data obtained by the Maximum-Likelihood method single-photon component was estimated, determining the amount of the $g^{(2)}$-values (see Equation 2), while the multi-photon processes contribute in the range of 10^{-8}. This implies $g^{(2)}$-values close to zero for the two investigated centres, which agrees only partially with the previous results. Therefore, further measurements will be done investigating NV-centres providing brighter emission and higher multi-photon components in order to discuss in detail the applicability of the TES and 'on/off'- methods for the investigation of the photon statistics of single photon sources.

Acknowledgement to the ERA-NET Plus program (No. 217257), and the German Federal Ministry of Education and Research (No. 01BL0900).

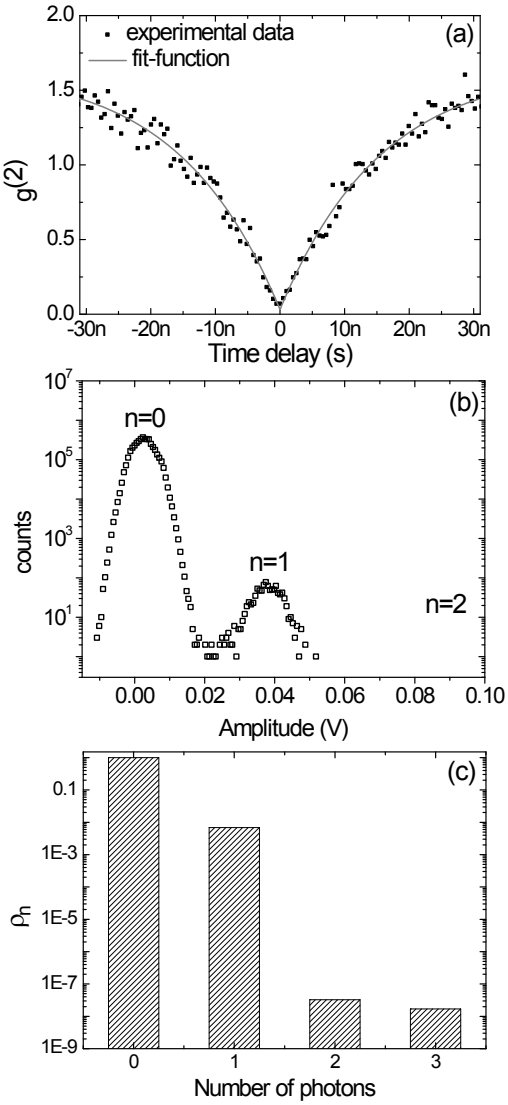

Figure 1. Photon statistic analysis of a single NV-centre: (a) *g(2)*-function, under continuous wave laser excitation an averaged photon rate of 250 kcps was achieved. The experimental data are fitted according to [5]. Photon number distribution, which was measured (b) by the TES detector and (c) obtained by 'on/off'-measurements.

REFERENCES

1. R. H. Hadfield, Single-photon detectors for optical quantum information applications, Nature Photonics 3, 696-705, 2009.
2. L. Lolli et al., Ti/Au Transition-Edge Sensors Coupled to Single Mode Optical Fibers Aligned by Si V-Groove, Applied Superconductivity, IEEE Transaction on 99, 1, 2011.
3. G. Zambra et al., Experimental reconstruction of photon statistics without photon counting, PRL 95, 06302-1, 2005.
4. C. Wang et al., Single photon emission from SiV centres in diamond produced by ion implantation, J. Phys. B: At. Mol. Opt. Phys. 39, 37–41, 2006.
5. W. Schmunk et al., Radiometric calibration of single photon counting detectors, Single Photon Workshop 2009, Boulder, USA, 2009.

Toward Traceable Few Photon Radiometry

G. Brida[1], J. Cheung[2], I. Degiovanni[1], M. Gramegna[1], T. Kübarsepp[3], M. G. Mingolla[1], I. Mueller[4], G. Porrovecchio[5], M. L. Rastello[1], M. Smid[5] and L. Werner[4]

[1]INRiM, Torino, Italy, [2]NPL, Teddington, United Kingdom, [4]AS Metrosert, Tartu, Estonia, [5]PTB, Berlin, Germany, [5]CMI, Prague, Czech Republic

Corresponding e-mail address:g.brida@inrim.it

We report on the calibration of a Single Photon Avalanche Detector (SPAD) with conventional calibration technique, directly against a Trap Transfer Detector (TTD), and by means of the correlated photon technique. We describe the measurement set-ups and experimental results.

INTRODUCTION

Classical low-light level applications (lidar, bioluminescence, for example) and emerging quantum information technologies demand for more accurate calibrations of photodetectors operating in photon counting regime. From the metrological point of view a successful linkage of the photon counting techniques to the conventional classical radiometry will be a significant step in demonstrating the viability of reformulating the candela in terms of a countable number of photons.

This work describes the measurements of the photon-counting detection efficiency of a SPAD, a Silicon photodiode operated in Geiger mode, performed with two different methods: (i) a conventional substitution calibration against a TTD directly tied to an absolute standard, a cryogenic electrical substitution radiometer; (ii) by means of a correlated photon pairs produced by Parametric Down-Conversion (PDC), an intrinsically absolute technique.

CALIBRATION AGAINST TTD

The procedure adopted was a direct comparison of the two detectors response using the same laser beam alternatively on TTD and SPAD. To operate SPAD within his maximum safe count rate (10^7 counts/s) it is necessary to perform the comparison at very low-power, few picowatt. For the TTD the measurement at such low power level, at an uncertainty comparable with the state of the art [1], is an high demanding task, requiring trap detectors with low dark-current, very sensitive current measurement electronics and finally a stabilized and strongly attenuated laser source that preserves beam shape and long-term stability.

The source was a DFB laser diode operating at the wavelength of 761 nm and power stabilized with a feedback system. A spatial filter reshape the beam profile to the desired diameter [2]. The relative standard deviation of the optical power of this source is below 5 ppm. The high power delivered from the source system is attenuated by means of a ten element trap detector retaining the quality of the incoming beam [3]. The Trap transfer standard and the SPAD are mounted on a linear translation stage and moved alternatively into the output beam of the attenuator. To reduce background light within the field of view of the detectors they are mounted inside a light tight enclosure. The laser beam travels through a small aperture inside the enclosure; an interferential filter centered at 761 nm was placed in front of the aperture to strongly reduce unwanted background light contributions incoming from the external environment. Trap transfer detector was temperature cooled down to 14 °C to reduce dark-current noise. The faint photocurrent output from the Trap transfer standard is converted into a voltage by means of a low-noise Switching Integrating Amplifier (SIA) [4]. A remote controlled shutter was placed on input side of the optical attenuator in order to measure alternatively background light and laser beam flux. To couple the laser beam, few millimeters of width, to the small sensitive area of the SPAD, 180 μm of diameter, a focusing lens was mounted in front of the detector. This coupling lens becomes hence an integrating part of the photon counting detector.

The readout of the two detectors, placed alternatively into the same laser beam power flux Φ allows the estimation of the SPAD quantum efficiency η_{SPAD}:

$$\eta_{SPAD} = \eta_{TTD} \cdot e \cdot R \cdot C / V \qquad (1)$$

where η_{TTD} is the quantum efficiency of the trap transfer detector, e is the electron charge, R is the transresistance gain of the SIA and finally C is the mean count rate of the SPAD, V is the output voltage from the SIA, both corrected for the background readouts. Measurements were performed at relatively large count rate for SPAD, at about 4 million counts/s and 1 million counts/s and the estimated SPAD quantum efficiency are 55,6 % and 64 %, respectively, with a good repeatability and an uncertainty below 0,2%. The uncertainty budget with this conventional measurement technique is dominated by the standard deviation of the trap photocurrent.

CALIBRATION WITH CORRELATED PHOTON PAIRS

The same SPAD was calibrated using correlated photon pairs produced by PDC, an inherently absolute measurement technique. The observation of one photon from a pair in a certain direction (signal) implies the presence of the other paired photon in the conjugated direction (idler). The non-detection of this idler photon is due to the non-ideal quantum efficiency of the idler detector, which can be measured in this way [1,5-6]. The absolute detection efficiency of the SPAD, η_{SPAD} is

$$\eta_{SPAD} = N_{coincidendence} / N_{trigger} \quad (2)$$

where $N_{coincidence}$ and $N_{trigger}$ are the total number of counts accumulated over the measurement time interval on coincidence and trigger detectors, respectively. The efficiency estimated in this way is the efficiency of the entire detection channel and includes losses from the interferential filters and losses in the non-linear crystal. To compare the calibration with PDC to the conventional substitution calibration these losses have been accurately measured and accounted for in the uncertainty budget.

Photon pairs were generated pumping a BBO non-linear crystal, 10 mm of thickness, by means of an Argon ion laser operating at 351 nm. Interferential filters are placed in front of the detectors: a filter centered at 761 nm, 20 nm FWHM of bandwidth in front of the SPAD under calibration, a filter centered at 652 nm (the conjugated wavelength), 5 nm FWHM, on the trigger detector. Measurements of the quantum efficiency have been performed at few different counting rates of the SPAD under calibration. The results, after proper correction for the losses in the inferential filter and inside the non-linear crystal, are summarized in Figure 1. The main contribution on the uncertainty budget for the calibration of the SPAD photon-counting detection efficiency with PDC comes from the measurement, at 761 nm, of the non-linear crystal losses. The preliminary evaluation of the uncertainty budget gives a final uncertainty of about 0.3%, for the PDC method. The estimated values of photon-counting efficiencies with PDC are compatibles with the ones obtained with conventional substitution method.

CONCLUSIONS

In this work we have reported the calibration of a SPAD photon-counting efficiency with classical substitution method and with correlated photon pairs technique. The comparison between the results of the two methods shows agreement within the measurement uncertainties in spite of the difficulty of measuring losses in the non-linear crystal.

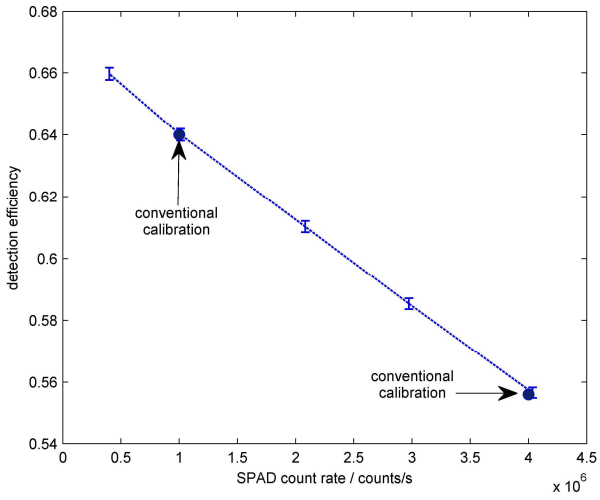

Figure 76. Detection efficiency of the SPAD vs count

ACKNOWLEDGMENTS

This work was supported by European Community's Seventh Framework Program, ERA-NET Plus, under Grant Agreement No. 217257.

REFERENCES

1. S. V. Polyakov, A. L. Migdall, High accuracy verification of a correlated-photon- based method for determining photoncounting detection efficiency, Optics Express, Vol. 15 Issue 4, pp.1390-1407 (2007).
2. D.J. Butler, R. Kohler and G.W. Forbes, Diffraction effects in the radiometry of coherent beams, Applied Optics, Vol. 35, n. 13 (1996).
3. T. Kübarsepp and M. White, Ten-element photodetector for optical power and attenuation measurements, Applied Optics, Vol. 49, Issue 19, pp. 3774-3779 (2010).
4. J. Mountford, G. Porrovecchio, M. Smid, and R. Smid, Development of a switched integrator amplifier for high-accuracy optical measurements, Applied Optics, Vol. 47, Issue 31, pp. 5821-5828 (2008).
5. G. Brida, S. Castelletto, I. P. Degiovanni, C. Novero, and M. L. Rastello, Quantum Efficiency and Dead Time of Single-Photon Counting Photodiodes: a Comparison Between Two Measurement Techniques, Metrologia 37, 625–628 (2000)
6. G. Brida, S. Castelletto, I. P. Degiovanni, M. Genovese, C. Novero, and M. L. Rastello, Towards an Uncertainty Budget in Quantum-Efficiency Measurements with Parametric Fluorescence, Metrologia 37, 629–632 (2000)

A transfer standard for the low power / few photon regime – the trap detector plus switched integrator amplifier

G. Porrovecchio[1], J. Y. Cheung[2], C. J. Chunnilall[2], J. R. Mountford[2], M. Smid[1], M. G. White[2]

[1]*Czech Metrology Institute, Praha 5, Czech Republic*
[2]*National Physical Laboratory, Teddington, TW11 0LW, UK*
Corresponding e-mail address: gporrovecchio@cmi.cz

The use of photon counting technology is accelerating rapidly. There are currently no reliable transfer standards for calibrating detectors at the few photon level. We describe a transfer standard for measuring detection efficiency that is traceable to a primary radiometric standard, the cryogenic radiometer, through a reference silicon photodiode trap detector. The trap detector, when used in conjunction with a switched integrator amplifier, can detect signals down to 0.1 pW, or 3 x 10^5 photons per second. This provides a convenient route for providing calibrations at these levels across the visible optical spectrum (UV – near IR).

INTRODUCTION

Trap detectors consisting of three silicon photodiodes are optical detectors with the following useful properties: spectral coverage from 300 nm to 1100 nm, spatial uniformity better than 10 ppm, responsivity value measureable with an uncertainty of 0.02%, reflectance as low as 0.4%, and linearity better than 100 ppm from 100 µW down to a few tenths of a pW [1]. These features have led to them becoming the transfer standard of choice for optical power measurements, and they can be directly calibrated against a cryogenic radiometer primary standard. The trap configuration has been extended to comprise greater numbers of photodiodes, as well as the so-called transmission configuration, which has no specular back-reflection, and which can also be used as a calibrated attenuator [2]. The low, or negligible, reflectance of both trap configurations make them especially useful as measuring devices for an optical system, since they minimize the introduction of perturbations via back-action, i.e. inter-reflections, into the system.

THE SWITCHED INTEGRATOR AMPLIFIER

A trap detector is normally used with a transimpedance amplifier (TIA) in the mW to µW power regime. Operation is possible at lower power levels, however this is limited by the noise floor of the trap detector and TIA. The TIA does not perform optimally when coupled with a low shunt resistor detector at high V/I gain due to its noise gain, which is proportional to the ratio between its large value feedback resistor and the detector's shunt resistor. A switched integrator amplifier (SIA) has been shown [3] to have a lower noise equivalent power (NEP) compared to a TIA when used with a three element silicon photodiode trap detector in dark conditions. The SIA converts the photo-induced current i_L in the trap detector into a voltage, V_{out}, as shown in figure 1.

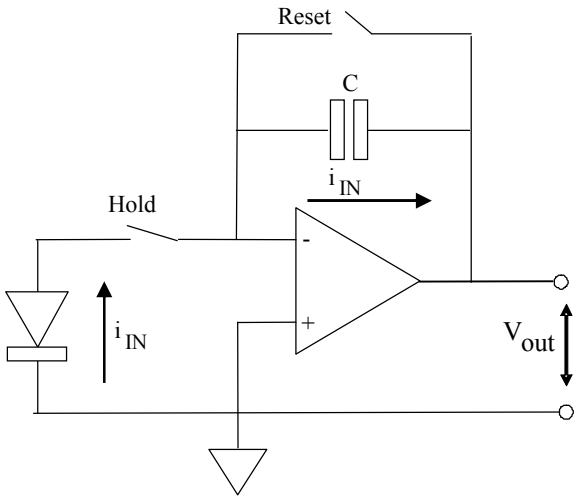

Figure 1. SIA + trap circuit diagram.

At time $t = 0$, the reset switch is opened, and the hold switch is closed, so that the current I_{IN} will charge the capacitor, of capacitance C, that has been kept discharged by the reset switch, i.e.

$$V_{out}(t=0)=0 \qquad (1)$$

A charge proportional to the current and time accumulates in the integration capacitor. The role of the amplifier is to hold one plate of the integration capacitor to the reference potential so the second plate will have a potential

$$V_{out}(t)=-\frac{t_{INT}}{C}I_{IN} \qquad (2)$$

where V_{out} is the SIA output voltage and t_{INT} is the integration period. The output voltage signal is proportional to the input current, and the V/I gain is:

$$G_{V/I} = -\frac{t_{INT}}{C} \quad (3)$$

The overall capacitance of a trap is the sum of the individual photodiode element junction capacitances. This high capacitance brings two benefits when the 'hold' switch is open. Firstly, for a given photocurrent, the diode output voltage is low, which reduces the leakage through the shunt resistance. Secondly, the low voltage reduces the risk of damaging the 'hold' switch, which must not be exposed to more than 700 mV.

Using equation (3) the SIA V/I gain calibration can be performed with low uncertainty at high gains. The SIA is calibrated at a low gain using a relatively high known input current where the signal to noise ratio is favourable, and at the same time the integration time t_{INT} is measured. From equation (3) the integration capacitance C is calculated, which characterizes completely the SIA current-voltage conversion behaviour. For higher gains one just measures t_{INT} and uses the calculated value of C to calculate the gain using (3). If a subfemto-amp source is used to provide the known input current [3], the fractional noise for a relatively high current of 100 nA and above is a factor of three less than for a 1 nA current. This therefore provides a potential factor of three increase in calibration accuracy for an SIA compared to a TIA.

The SIA is based on the Burr Brown ACF2101 chip that, with its internal 100 pF capacitor, can reach a V/I gain of 10^{11} with an integration period of 10 s [3]. Extension of the gain range can be obtained with the use of an external capacitor to reduce the integration capacitance: 10 pF extends the gain one order of magnitude, and 1 pF two orders of magnitude. The higher gain can however produce a correspondingly higher output offset voltage due to the charge injected by the reset and hold analogue switches, since the ACF2101 chip is optimized to minimize switch charge injection for its internal capacitor.

Other advantages of the trap + SIA combination include a shorter settling time at high gain settings and the use of an ultra stable clock to make the uncertainty in t_{INT} insignificant.

In Table 1 we report the results of the noise measurements at gain $\geq 10^9$ carried out with a three element silicon photodiode trap detector connected to SIAs with 100 pF and 1 pF external integration capacitors, and two different transimpedance amplifiers named TIA 1 and TIA 2 which are among the best commercially available. The trap detector has a measured shunt resistance of 160 MΩ at 23 ºC, which corresponds to an NEP value of about 10 fW/Hz^{½}. N_{PLC} is the number of power line cycles over which the digital multimeter integrates the SIA output, and NB is the noise bandwidth.

Amplifier	Gain [V/A]	t_{INT} [s]	DMM N_{PLC}	Noise [fA]	NB [Hz]	NEP [fW/Hz^{½}]
SIA 100pF	10^9	0.1	10	25	2.0	**35**
	10^{10}	1	10	20	0.5	**57**
	10^{11}	10	10	5	0.05	**45**
SIA 1pF	10^9	0.001	10	75	2.5	**95**
	10^{10}	0.01	0.5	70	50	**24**
	10^{11}	0.1	2	9	12.5	**28**
TIA 1	10^9		10	35	0.4	**45**
TIA 2	10^{10}		10	13	0.4	**60**
	10^{11}		10	130	0.4	**60**

Table 1. Comparison of NEP for trap detector with different amplifiers.

Discussion of these results will cover the derivation of the expression for NB, and the method for estimating the optimum integration time. Results of investigations into low temperature operation of the SIA will also be presented.

DETECTOR CALIBRATION

The trap + SIA combination was the basis of one of the techniques used in a cross-validation of two independent techniques for measuring the detection efficiency of photon counting detectors, the second being based on correlated photons. Agreement between the two techniques was found to be within 0.2%. The comparison, and the implementation of the two techniques, will also be discussed.

REFERENCES

1. N. P. Fox, Trap detectors and their properties, Metrologia, 28, 197-202, 1991
2. T. Kübarsepp and M. White, Ten-element photodetector for optical power and attenuation measurements, Appl. Opt., 49, 3774-3779, 2010
3. J. Mountford, G. Porrovechio, M. Smid, R. Smid, Development of a switched integrator amplifier for high-accuracy optical measurements, Appl. Opt., 47, 5821-5828, 2008.

Calibration of photomultiplier tubes for few photon applications using synchrotron radiation

Uwe Arp[1], Ping-Shine Shaw[1], Rob Vest[1], Lindsay Hum[2], and Michael L. Bishop[2]

[1]*National Institute of Standards and Technology NIST, Gaithersburg, MD, U.S.A.,* [2]*Naval Surface Warfare Center, Corona, CA, U.S.A*

Corresponding e-mail address: uwe.arp@nist.gov

Synchrotron radiation is routinely used to calibrate both detectors and sources in the ultraviolet spectral region. Here we report on studies of photomultiplier tubes for few photon applications in current and counting mode. To perform these comparisons, the storage ring had to be operated at low currents to allow counting.

INTRODUCTION

The Synchrotron Ultraviolet Radiation Facility SURF III [1] has been used to calibrate photodetectors since the 1960s. Currently, most of the detector calibrations are focused on solid-state photodiodes, which are calibrated using an electrical substitution absolute cryogenic radiometer [2]. More recently, we started calibrating photomultiplier tubes (PMTs) using the same beamline [3]. Since photomultiplier tubes saturate at much smaller signals than photodiodes, the storage ring had to be operated at a lower electron beam current than usual. These special accommodations of user's needs are the strength of synchrotron radiation sources dedicated to radiometric research, where the radiation output spectrum and intensity can be custom-tailored. At SURF we routinely change the energy of the stored electrons to shift the short wavelengths cut-off of the synchrotron radiation spectrum or reduce the stored electron beam current from its normal value of a few 100 mA to a few µA or even nA (1 stored electron is equivalent to 10 pA electron beam current). During standard operation on beamline 4 [4,5], the incoming radiation is monitored using a calcium-fluoride beamsplitter and a photodiode, which is place between the monochromator exit slit and the detector under study. At very low electron beam currents, this beam monitor signal is too small and the electron beam current is used to scale the signal.

In first experiments in 2008, tests of spatial uniformity and linearity were performed [3] on used and pristine PMTs. It was found that at high radiant exposure, the PMT response was not linear. Spatial uniformity maps of PMTs after significant exposure times showed significant loss of reponsivity in the exposed region.

In a new set of experiments we demonstrated the equivalence of the performance of PMTs operated in current mode, *i.e.* the generated photocurrent is measured, to counting mode, *i.e.* the photocurrent is converted into a count rate by use of a preamplifier, discriminator, and pulse shaper. Figure 1 shows the equivalence of the two measurements.

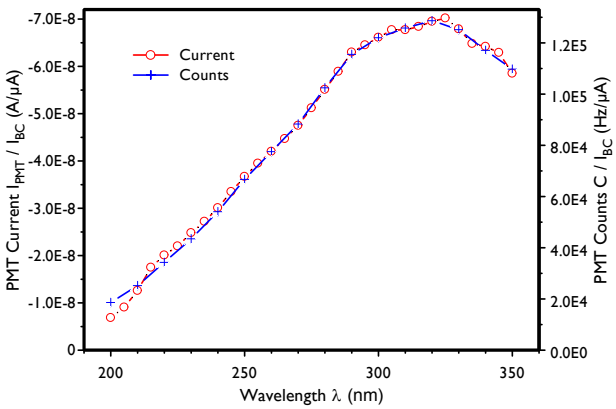

Figure 77. Comparison of the response of a photomuliplier in current (○) and counting (+) mode.

REFERENCES

1. U. Arp, C. Clark, L. Deng, N. Faradzhev, A. Farrell, M. Furst, S. Grantham, E. Hagley, S. Hill, T. Lucatorto, P. Shaw, C. Tarrio, and R. Vest, *Nuclear Inst. and Methods In Physics Research*, A 1-3 (2010).
2. P.-S. Shaw, K. R. Lykke, R. Gupta, T. R. O'Brian, U. Arp, H. H. White, T. B. Lucatorto, J. L. Dehmer, and A. C. Parr, *Metrologia* **35**, 301-306 (1998).
3. Lindsay Hum, Ping-Shine Shaw, Zhigang Li, Keith R. Lykke, and Michael L. Bishop, *Proceedings Of SPIE* **7304**, 730410-730410-8 (2009).
4. L Hughey, *Nuclear Instruments and Methods In Physics Research Section A: Accelerators, Spectrometers, Detectors and Associated Equipment* **347**, 294-298 (1994).
5. D. L. Ederer, B. E. Cole, and J. B. West, *Nuclear Instruments and Methods* **172**, 185-190 (1980).

Relative detection efficiency calibration of single photon avalanche photo detectors using non-classical light from nitrogen-vacancy defect centres in nano diamonds

Waldemar Schmunk, Mark Rodenberger, Silke Peters, Helmuth Hofer, Ana Maria Racu and Stefan Kück

Physikalisch-Technische Bundesanstalt (PTB), Bundesallee 100, 38116 Braunschweig, Germany
Corresponding e-mail address: stefan.kueck@ptb.de

We report on two different techniques for detection efficiency calibration of single photon avalanche photo diodes (SPAD). Both methods use a non-classical light source based on single nitrogen-vacancy (N-V) defect centres in nano-diamonds and utilise a fibre-coupled Hanbury Brown-Twiss (HBT) interferometer setup. The first calibration technique is based upon the fibre-coupled method adopted from optical telecommunication. The second one uses the coincidence counting method, measured on a single N-V defect centre by HBT in a pulsed excitation regime. We compare these two different techniques in order to determine the relative detection efficiency of a fibre-coupled SPAD.

INTRODUCTION

There is a rapid technological advance in recent years in the fields of single photon sources and detectors. The single photon technology has a wide field of application. From metrological point of view a variety of new questions and challenges are arising, dealing especially with the definition and the realisation of standards for sources and detectors on the single and few photon level.

The SPAD detection efficiency (DE) is one important parameter for the characterisation of the systems based on single and few photon sources. Most of the actually established methods for characterisation of the absolute DE are based upon the two-photon correlation technique generated by a parametrical down conversion (PDC) [1]. With these methods no calibrated standard detector is needed and thus no traceability to an absolute standard detector is necessary.

Relative calibration setups are widely used in order to realize reproducible and reliable DE calibration at low uncertainty level. In this work we report on two DE calibration methods for SPADs operated in the Geiger mode. The experimental setup for excitation and detection of single N-V centres [2] with a low value of second order correlation function at zero time delay is shown in Figure 1a. A band pass filter at (700 ± 10) nm spectrally confined the broad photoluminescence emission from the N-V single defect centre.

FIBRE EXCHANGE CALIBRATION METHOD

This fibre exchange method is commonly used for the fibre-coupled DE calibration in the optical telecommunication field for analogue detectors, described in detail in [3]. The experimental setup is shown in Figure 1b. The incoming optical flux Φ is split with a 50:50-fibre-optical coupler. The output arms A and B of the coupler are connected to the detector under test (DUT) and to the standard detector, respectively. The measured count rates $N_{S,A}$ of the standard and $N_{D,B}$ of the DUT detectors are proportional to the flux Φ as well as to the detection efficiencies η_S and η_D of the detectors and given by

$$\begin{aligned} N_{S,A}(\lambda) &= \Phi_A \eta_S(\lambda) = \Phi \beta_A \eta_S(\lambda) \\ N_{D,B}(\lambda) &= \Phi_B \eta_D(\lambda) = \Phi \beta_B \eta_D(\lambda) \end{aligned} \quad (1)$$

with the total transmittances β_A and β_B at the fibre end A and B, respectively. In the second run the fibre ends are interchanged and the count rates $N_{S,B}$ and $N_{D,A}$ are measured:

$$\begin{aligned} N_{S,B}(\lambda) &= \Phi_B \eta_S(\lambda) = \Phi \beta_B \eta_S(\lambda), \\ N_{D,A}(\lambda) &= \Phi_A \eta_D(\lambda) = \Phi \beta_A \eta_D(\lambda). \end{aligned} \quad (2)$$

For the known DE of the standard detector the relative DE of the DUT can be determined from the experimental data as follows

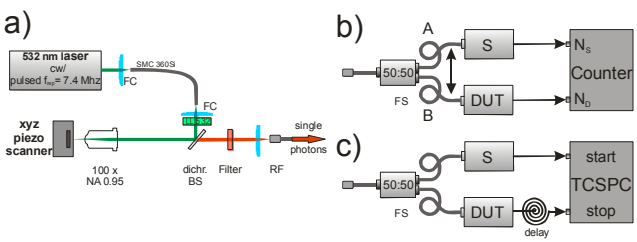

Figure 78. Experimental setups: a) single photon generation, b) setup for fibre exchange method and c) setup for coincidence count calibration method.

$$Q(\lambda)=\frac{\eta_D(\lambda)}{\eta_S(\lambda)}=\sqrt{\frac{N_{D,A}(\lambda)N_{D,B}(\lambda)}{N_{S,A}(\lambda)N_{S,B}(\lambda)}} \qquad (3)$$

COINCIDENCE COUNT TECHNIQUE

With the same fibre-based HBT setup and time correlated single photon counting (TCSPC) analysis (shown in Figure 1c) instead of simple photon counting one can measure the coincidence events $c_n(t)$. The distribution of the correlation function contains information about the overall detection efficiency η of the whole detection path. In pulsed excitation regime, the probability p_n to detect a photon in the n-th pulse is given by [4]

$$p_n = \eta \cdot (1-\eta)^{n-1}. \qquad (4)$$

The coincidence counts $c_n(t)$ are proportional to the probabilities p_n. However, in the experiment, $c_n(t)$ is not a δ-peak, but broadened due to the emitting centre lifetime. Thus, the area A_n of the n-th pulse are calculated as follows:

$$A_n = \int_{\text{n-th pulse}} c(t)dt = Kp_n, \qquad (5)$$

with K as an overall constant. Thus, the following equation for A_n holds:

$$\ln(A_n) = \ln(\tfrac{K\cdot\eta}{1-\eta}) + n\ln(1-\eta). \qquad (6)$$

From a linear regression on this equation, we obtain the slope $\kappa = \ln(1-\eta)$, from which the overall detection efficiency η is calculated:

$$\eta = 1 - e^{\kappa}. \qquad (7)$$

Here κ is the slope of the regression fit. Performing two separate coincidence measurements with different detectors at the stop channel of TCSPC module and a common reference detector at the start channel allow the determination of the ratio of the overall efficiencies, η_D/η_S, that is equal to the relative DE of the DUT.

RESULTS

We performed the above described two calibration techniques for a SPAD detector id100-50 module (idQuantique) as DUT and a SPCM-AQRH-13-FC module (PerkinElmer) as reference detector.

We found consistent results for both experimental calibration methods. With the fibre exchange calibration method we obtained a relative detection efficiency $\eta_D/\eta_S = 0.12 \pm 0.01$, see Figure 2.

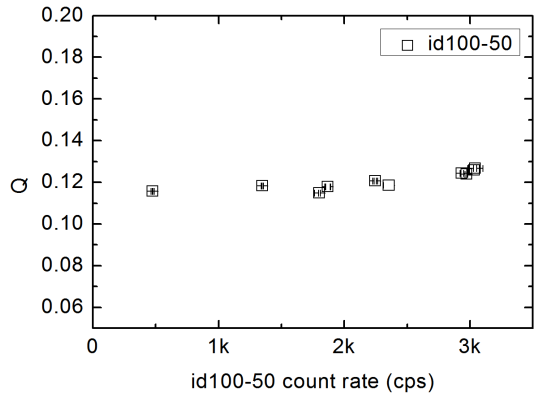

Figure 2. Experimental results for the id100-50 module with fibre exchange calibration method.

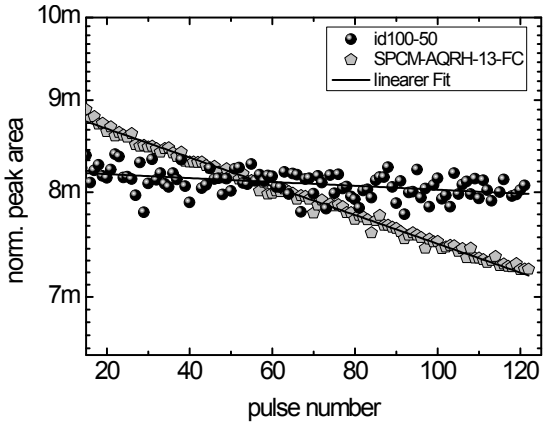

Figure 3. For coincidence count method the overall efficiencies for the id100-50 and SPCM-AQRH-13-FC modules were determined from linear fit of the coincidence peak areas resulting from the pulsed excitation.

The coincidence count method yielded a ratio of $\eta_D/\eta_S = 0.135 \pm 0.036$, see Figure 3.

In the presentation we report also the possible influence of the photon-counting distribution on the experimental results at higher mean photon numbers.

We acknowledge the ERA-NET Plus program under Grand Agreement No. 217257, the Braunschweig International Graduate School of Metrology, the Joint Optical Metrology Centre, and the German Federal Ministry of Education and Research under Grant No. 01BL0900.

REFERENCES

1. A. Migdall, "Correlated-Photon Metrology Without Absolute Standards" in Physics Today, 41 - 46 (1999)
2. www.qcvictoria.com
3. H. Hofer, M. Lopez, S. Kück, "Fiber-based power measurement for the optical telecommunication in a wide spectral range" in Proceedings of NEWRAD, 2008, 105-106
4. A. Beveratos, PhD thesis, University of Paris, (2002)